

Journal of Energy

ISSN 1849-0751 (On-line)
ISSN 0013-7448 (Print)
UDK 621.31

VOLUME 63 Number 1–4 | 2014 Special Issue

- 03** H. Passath, G. Leber, P. Hamberger, F. Bachinger
Direct current compensation – field experience under service conditions
- 13** P. Gabrić, A. Mikulecky, D. Ilić, V. Podobnik
Influencing factors in insulation model testing
- 22** Z. Godec, V. Kuprešanić
Temperature rise of power transformers: Comments and proposals to IEC 60076-2:2011
- 35** R. Sitar, Ž. Janić
Application of the temperature-time method for measurement of local power losses in transformer steel parts
- 43** A. Gamil, F. Schatzl
New method to optimize no-load noise of power transformers based on core design & transformer operating conditions
- 52** B. Bošnjak, M. Stuhne
Analysis and experimental verification of static tilting behavior of CTC in transformer windings
- 63** I. Žiger, D. Krajtner, Z. Ubrenkić
Pushing the boundaries of inductive voltage transformer design
- 74** B. Čučić, N. Meško, M. Mikulić, D. Trstoglavac
Design improvements in modern distribution transformers
- 82** E. Almeida, P. Pedro, P. Martins, C. Silva
Evaluation of different types of steel under high loading rates for short circuit applications
- 95** L. Štrac, F. Kelemen
Magnetizing current of a large power transformer and its harmonic spectrum in normal and GIC conditions
- 104** Z. Andjelic, R. Girgis, A. Fazlagić, A. Regalino, C. J. Lambert, A. Seidel, M. Ries
Structural-mechanics analysis of the 10g transformer impact
- 114** D. Brezak, D. Filipović-Grčić
Ultrasonic method for testing of power transformers
- 124** B. Németh, G. Csépes, I. Kispál, Z. Laczkó
Checking of the condition of transformers and the efficiency of oil regeneration with RVM (return voltage measurement)
- 135** V. Haramija, Dijana Vrsaljko, V. Đurina, Domagoj Vrsaljko
Thermal stability change of synthetic ester-based transformer oil
- 141** D. Bidwell, D. Skelly
New tools for enhanced diagnostics of DGA data
- 150** I. Šulc, R. Sitar, A. Mikulecky
An aspect of transformer inrush current
- 156** L. A. Darian, V. P. Polistchook, A. V. Shurupov
Testing of models of explosion protection system for high-voltage oil-filled electrical equipment
- 166** D. Šegović, F. Kelemen
Estimation of zero sequence impedance in power transformers using 2D and 3D FEM
- 172** S. Selvaraj, R. Mertens, G. Caluwaerts, M. B. Varrier, R. Mathersa
Investigation of impact of magnetic shunt parameters on temperature distribution in transformer tanks
- 179** R. Wittmaack
CFD simulation of pressure loss in HVDC transformer winding
- 189** B. Bošnjak, A. Hauck, H. Landes
Coupled magneto-mechanical finite element analysis of a power transformer in short circuit conditions
- 199** K. Capuder, G. Plišić, Ž. Štih
Generic approach to calculation of short circuit currents in power transformers
- 209** R. Plátek, G. Juszkwicz
Seismic analyses for power transformers
- 217** M. Marković, I. Radić, V. Matun
Statistical and numerical analysis of transformer oil ac breakdown
- 227** M. Marković
Insulation optimization of power transformer leads
- 235** J. Smajic, R. Obrist, M. Rüegg, B. Cranganu-Cretu, C. Roy, B. Weber, E. Rahimpour
Lightning impulse modeling and simulation of dry-type and oil-immersed power- and distribution transformers
- 244** G. Plišić, K. Capuder
Influence of winding capacitances to ground modelling on the calculation of transferred voltages in power transformer
- 252** V. Larin, D. Matveev, A. Volkov
Study of transient interaction in a system with transformer supplied from network through a cable: assessment of interaction frequencies and resonance evolution
- 262** B. Jurišić, I. Uglešić, A. Xemard, F. Paladian, Ph. Guuinic
Case study on transformer models for calculation of high frequency transmitted overvoltages

Journal of Energy

Scientific Professional Journal Of Energy, Electricity, Power Systems

Online ISSN 1849-0751, Print ISSN 0013-7448, VOL 63

Published by

HEP d.d., Ulica grada Vukovara 37, HR-10000 Zagreb

HRO CIGRÉ, Berislavićeva 6, HR-10000 Zagreb

Publishing Board

Robert Krklec, (president) HEP, Croatia,

Božidar Filipović-Grčić, (vicepresident), HRO CIGRÉ, Croatia

Editor-in-Chief

Goran Slipac, HEP, Croatia

Associate Editors

Helena Božić HEP, Croatia

Stjepan Car Končar-Electrical Engineering Institute, Croatia

Tomislav Gelo University of Zagreb, Croatia

Davor Grgić University of Zagreb, Croatia

Mičo Klepo Croatian Energy Regulatory Agency, Croatia

Stevo Kolundžić Croatia

Vitomir Komen HEP, Croatia

Marija Šiško Kuliš HEP, Croatia

Dražen Lončar University of Zagreb, Croatia

Goran Majstrovic Energy Institute Hrvoje Požar, Croatia

Tomislav Plavšić Croatian Transmission system Operator, Croatia

Dubravko Sabolić Croatian Transmission system Operator, Croatia

Mladen Zeljko Energy Institute Hrvoje Požar, Croatia

International Editorial Council

Franco Barbir University of Split, Croatia

Tomislav Barić J.J. Strossmayer University of Osijek, Croatia

Anastasios Bakirtzis University of Thessaloniki, Greece

Frank Bezzina University of Malta

Tomislav Capuder University of Zagreb, Croatia

Ante Elez Končar-Generators and Motors, Croatia

Dubravko Franković University of Rijeka, Croatia

Hrvoje Glavaš J.J. Strossmayer University of Osijek, Croatia

Mevludin Glavić University of Liege, Belgium

Božidar Filipović Grčić University of Zagreb, Croatia

Dalibor Filipović Grčić Končar-Electrical Engineering Institute, Croatia

Josep M. Guerrero Aalborg Universitet, Aalborg East, Denmark

Dirk Van Hertem KU Leuven, Faculty of Engineering, Belgium

Žarko Janić Siemens-Končar-Power Transformers, Croatia

Igor Kuzle University of Zagreb, Croatia

Niko Malbaša Ekoneg, Croatia

Matislav Majstrovic University of Split, Croatia

Zlatko Maljković University of Zagreb, Croatia

Predrag Marić J.J. Strossmayer University of Osijek, Croatia

Viktor Milardić University of Zagreb, Croatia

Srete Nikolovski J.J. Strossmayer University of Osijek, Croatia

Damir Novosel Quanta Technology, Raleigh, USA

Hrvoje Pandžić University of Zagreb, Croatia

Robert Sitar Končar-Electrical Engineering Institute, Croatia

Damir Sumina University of Zagreb, Croatia

Elis Sutlović University of Split, Croatia

Damir Šljivac J.J. Strossmayer University of Osijek Croatia

Darko Tipurić University of Zagreb, Croatia

Bojan Trkulja University of Zagreb, Croatia

Nela Vlahinić Lenz University of Split, Croatia

Mario Vražić University of Zagreb, Croatia

INTRODUCTION

Journal of Energy special issue: Papers from 3rd International Colloquium "Transformer Research and Asset Management"

Welcome to this special issue, which is based on selected papers presented at the 3rd International Colloquium "Transformer Research and Asset Management", held in Split, Croatia, on October 15th -17th, 2014.

The International Colloquium was organized by the Croatian CIGRÉ National Committee in cooperation with the Faculty of Electrical Engineering and Computing in Zagreb and the Centre of Excellence for Transformers in Zagreb with support from CIGRÉ A2 Study committee (Transformers). The goal of the Colloquium was to share latest research in the in the areas of distribution, power and instrument transformers.

The Colloquium extended over three days. Two CIGRÉ tutorials were offered to all participants. In total there were 160 participants from 22 countries. All of the 50 accepted papers were presented in oral sessions, out of that there were three invited lectures. Participants from manufacturers, utilities and universities took part in discussions.

All the papers were divided into three sessions

Numerical Modeling

- Electromagnetic field
- Coupled fields
- Transients
- Numerical modeling in design, etc.

Materials, Components and New Technologies

- Insulating material
- Magnetic material
- Transformer components
- Transformer new technologies, etc.

Transformer Life Management

- Monitoring
- Diagnostics
- Failures
- Asset management, etc.

From the 50 papers presented at the Colloquium, 29 papers were accepted for publication in Journal of Energy after having undergone the peer-review process. We would like to thank the authors for their contributions and the reviewers who dedicated their valuable time in selecting and reviewing these papers. We hope this special issue will provide you a valuable source of newest achievements in transformer technology.

Guest Editor

ass. prof. dr. sc. Bojan Trkulja

University of Zagreb, Croatia

Faculty of Electrical Engineering and Computing

asst. prof. dr. sc. Žarko Janić

Končar Power Transformers

A joint Venture of Siemens AG and Končar d.d.

Helfried Passath
Siemens AG Österreich
Transformers Weiz
helfried.passath@siemens.com

Gerald Leber
Siemens AG Österreich
Transformers Weiz
gerald.leber@siemens.com

Peter Hamberger
Siemens AG Österreich
Transformers Linz
peter.hamberger@siemens.com

Florian Bachinger
Siemens AG Österreich
Transformers Linz
florian.bachinger@siemens.com

DIRECT CURRENT COMPENSATION – FIELD EXPERIENCE UNDER SERVICE CONDITIONS

SUMMARY

Modern grain oriented core steel used in power transformers has a very high magnetic conductivity. This advanced material makes the transformer susceptible even for small direct current (DC) in the power grid. Already minor DC increases the no-load noise and no-load losses of the transformer considerably. This effect is known as half-cycle saturation. In order to overcome these parasitic DC an active compensation method called “DC compensation” (DCC) was recently developed by Siemens [1].

The question about the origin of the DC is not fully answered yet. However the following sources have been already identified: power electronics, renewable power generation (wind, solar), HVDC transmission lines and DC operated railroad or subway systems. The parasitic direct currents can flow over the power lines to ground or asymmetrically in the power line phases only.

In this paper field data, a four-month DC load profile, of single-phase core type transformers, equipped with active DC compensation, are shown. The discussed unit, a bank of three single-phase autotransformers, is in service mainly exposed to DC flowing from the overhead lines through the windings to the common neutral. DC magnitude varies from 0.05 A to about 0.2 A DC per phase throughout the day. From factory tests we know that only 0.2 A DC causes a noise increase of 5.6 dB(A) compared to the noise level without any DC compensation. This might cause troubles at the substation when noise has to be below a guaranteed level.

Data analysis of the field data shows that the DC throughout the day follows a clear profile with its highest level during midnight and lunch time. This might indicate a correlation to the load and / or switching operations in the grid to adjust to the actual needed load.

However, the DC compensation equipment fully eliminates the direct flux in the core and thus the DC caused increase in noise.

Key words: Transformer – Direct current – DC bias – Saturation – Noise – No-load loss – Renewable power generation

1. INTRODUCTION

Modern power transformers use highly efficient grain oriented electrical core steel. The cores are manufactured by using most advanced core stacking techniques. These transformers are usually operated at low core flux densities and low excitation currents in order to achieve low no-load noise and no-load losses.

By using these optimization strategies excitation currents are small and therefore even small direct currents are influencing these transformers in a negative way [2]. Half cycle saturation may occur already when DC in the range of a few hundred milli-amps (mA) to a few amps (A) is applied. This results in a considerable increase of the no-load noise level and no-load losses. Reactive power consumption is increased as well. So far the origins of these small DC have not been completely investigated. However the following sources have been already identified: power electronics, renewable power generation (wind, solar), HVDC transmission lines [4] and DC operated railroad or subway systems. The direct currents may also be geo-magnetically induced (GICs). The case of GIC has been analyzed e.g. in [6], [7], [8] and [9]. The parasitic direct currents can flow between the power lines and ground or asymmetrically in the power line phases only. Three-phase three limb cores are relatively insensitive to symmetric direct currents but react strongly to DC asymmetries between the phases. This is the case for example for static VAr compensation (SVC). Transformers with high magnetic conductivity paths for zero sequence flux, like single phase and three phase five limb core transformers are most sensitive to the DC magnetization in any case.

An active compensation method was developed to overcome the problems with parasitic DC [1]. This paper shows four month of DC load field data of a bank of three single-phase autotransformers equipped with DC compensation (DCC) and gives another possible explanation of the cause of the DC.

2. INVESTIGATED TRANSFORMERS

A bank of three single phase autotransformer intertie transformers and one spare with a guaranteed noise level of 69 dB(A) with a specified DC level of 2 A per phase (table I) was delivered to a substation in the USA. All transformers have been equipped with DC compensation.

Table I – Transformer ratings

	unit	Transformer (single phase)
Rated power	MVA	134.4 / 134.4 / 44.8
Rated voltage	kV	230/ $\sqrt{3}$ / 120/ $\sqrt{3}$ / 13.2
Frequency	Hz	60
Core type (limbs- return limbs)		1-2

Since the transformers are single phase units, they are very sensitive to DC. Factory acceptance tests with DC in the range from 0 to 3.6 A DC have been carried out. The test setup was a back to back test configuration according figure 1. The transformers have been excited through the tertiary windings at the maximum tap position at both transformers. This setup allows injecting DC into the HV winding with an off the shelf DC source. DC was measured by current probes and shunts. The Resistor R_v is for grounding the second transformer in case of malfunctioning of the current source.

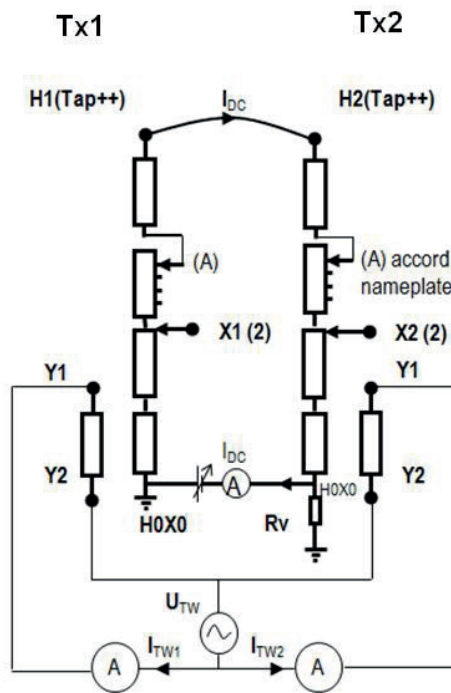


Figure 1- Back to back test setup

2.1. Effects of DC on the unit

The effects of DC on transformers are well known [2], [3] and [5]. In this paper we will focus only on the noise rise and the no-load losses rise since problems with eddy currents and therefore overheating in metallic parts nearby the core occur only at much higher DC levels like GIC.

2.1.1. No-load losses

An unwanted effect of DC is the increase of the no-load losses. For these transformers the increase was almost 30% at 2 A (DC compensation switched off) which is quite significant. The loss increase at higher DC levels flattens since the core is driven into the non-linear range of the B-H curve (figure 2).

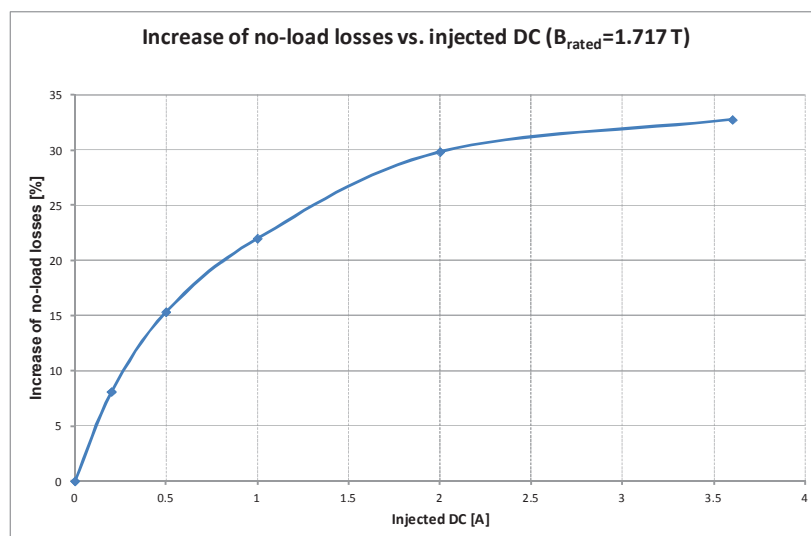


Figure 2 - Increase of no-load losses without DC compensation

2.1.2. Noise rise

In figure 3 the noise rise of the DC magnetized transformers is shown. At the specified DC level of 2 A the noise rise is more than 10 dB(A). Since the rated AC flux density of the unit is 1.717 T, the increase is lower than at transformers operated at lower AC flux density levels where the increase can be even above 20 dB(A) [3]. In figure 4 the transformer noise with DC load with and without DC compensation is shown. Without any compensation measures, the noise would be above the guaranteed level at approximately 100 mA DC. With active DC compensation the noise level is well below the guaranteed level in the entire specified DC range.

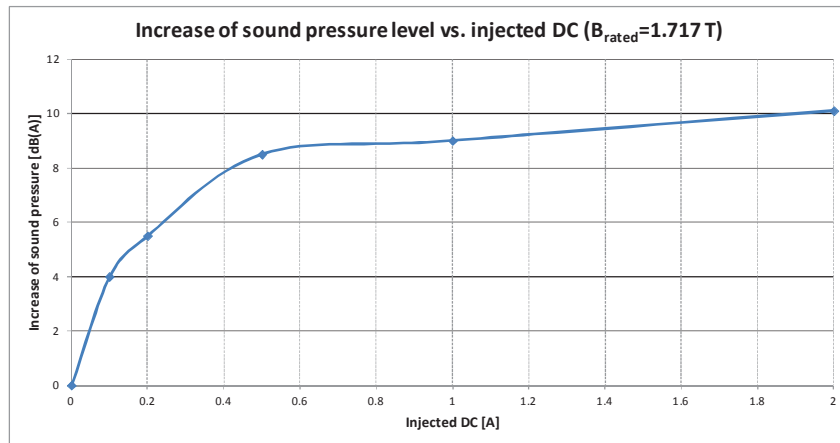


Figure 3 - Measured noise rise in relation to the injected DC

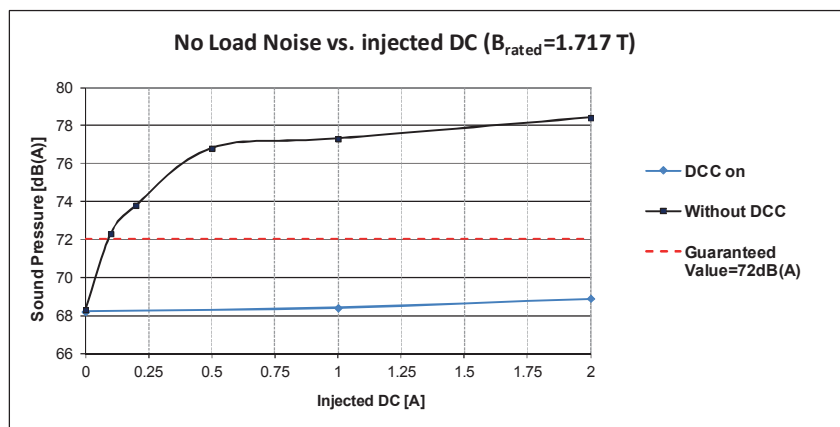


Figure 4 - Measured noise with DC and DC compensation

3. FIELD EXPERIENCE

As stated above the effects of DC on transformers are well known. So far the origin of the DC in the power grid is not fully investigated at the moment. Different sources have been identified but it is very difficult to identify the corresponding source of the DC for the considered transformers. The aim of this paper is to raise awareness of this problem at the manufacturers, customers and operators of transformers.

In this section a four month profile of the DC load of the 3 transformers equipped with DC compensation (table I) is presented. Data is available from 1st of September 2013 to the end of December 2013. In order to attenuate short spikes coming from switching operations in the grid, a moving average filter was applied to the raw data.

3.1. Analysis of field data

Figure 5 shows the (filtered) DC load from 3rd of September to the 6th of September. The shape of the profile is found in the entire four month data. The DC load is highest at around noon and higher than average in the night. In table II the average DC load in time and phases is shown. As from this table and figure 5 can be seen the DC in the transformer flows between the windings and the neutral and splits up almost symmetrically between the windings and therefore we concentrate in the following analysis on one phase (Phase A) only.

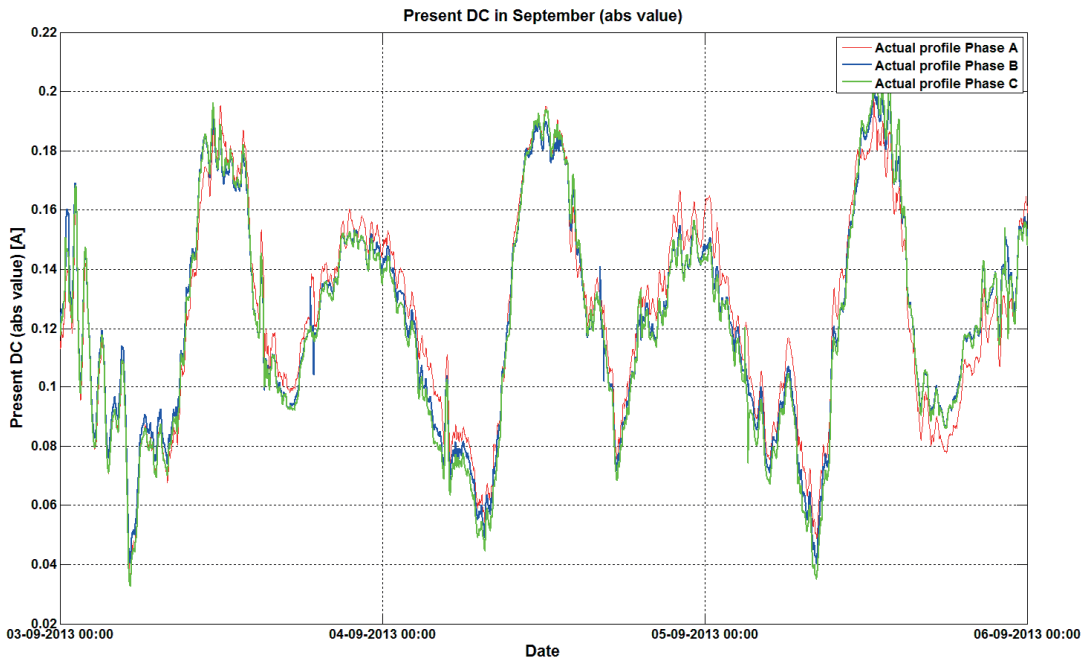


Figure 5 - Representative DC profile of September 2013

Table II – Average DC load

	unit	Phase A	Phase B	Phase C
September	A	0.123	0.12	0.119
October	A	0.118	0.118	0.118
November	A	0.113	0.112	0.115
December	A	0.095	0.103	0.105

Out of the obtained data, for each investigated month an average day profile has been calculated and correlated to the actual day profile. With this method it shall be proven that the DC in parts of the US grid and probably in the entire grid of the USA follows a clear profile which doesn't change significantly over time. The correlation was obtained by using the corrcoef function of Matlab[®] (MathWorks[®]). In order to get the quality of the correlation the coefficient of determination was calculated. This coefficient can be easily determined by the square of the correlation coefficient (R) and is called R² and is in the range between 0 and 1. Although different limits for this value are given in the literature, a value above 0.4 or better 0.5 should be taken into account. When the value of R² is 1, the data (in this case the average DC profile) fits perfectly with the actual DC profile. As a second test the hypothesis of no correlation was checked and was in all cases well below the 0.05 significance level.

Figures 6-11 show the coefficient of determination as described above. Unfortunately some days are missing due to problems with the remote data transmission system. For several periods this coefficient is above 0.4 which states that the actual daily profile doesn't change a lot in comparison to the average profile. In periods with low correlation it might be interesting to check the GIC activity and or load

conditions since these artifacts have a duration of several minutes up to a couple of hours. The periods of poor correlation also indicate the difficulty in determining all the sources of the parasitic DC.

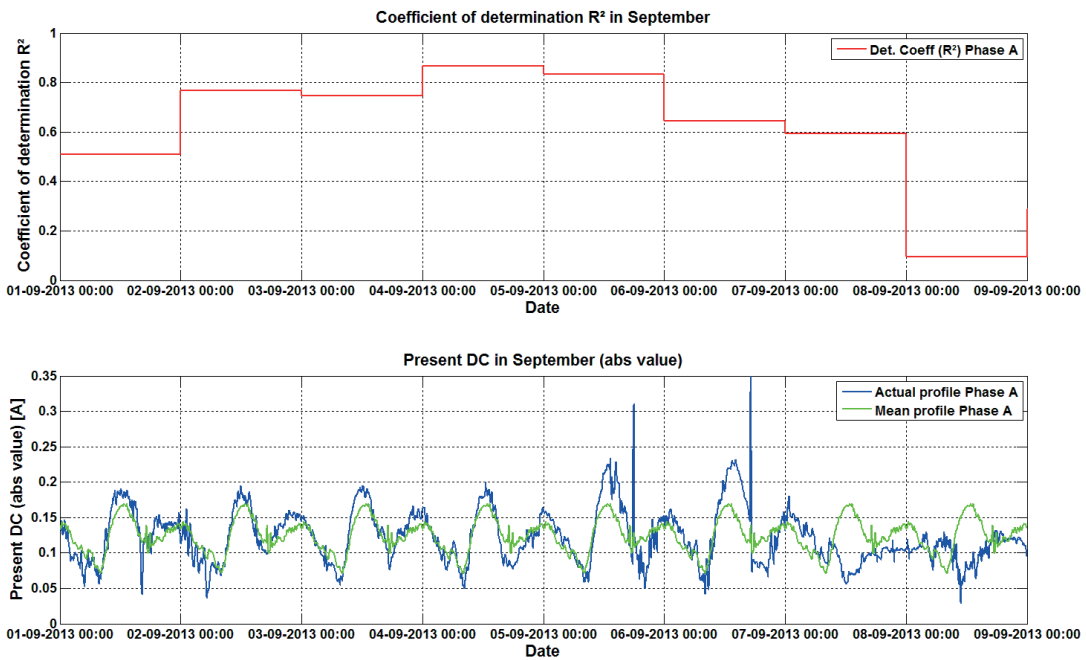


Figure 6 - Coefficient of determination and DC Profiles for September (Part 1)

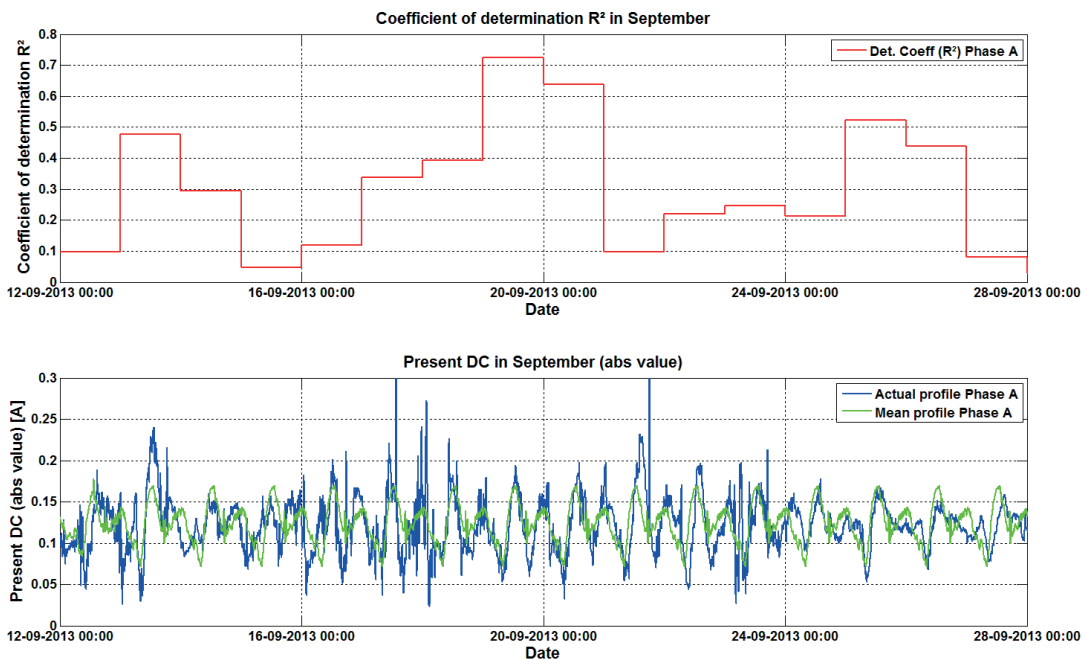


Figure 7 - Coefficient of determination and DC Profiles for September (Part 2)

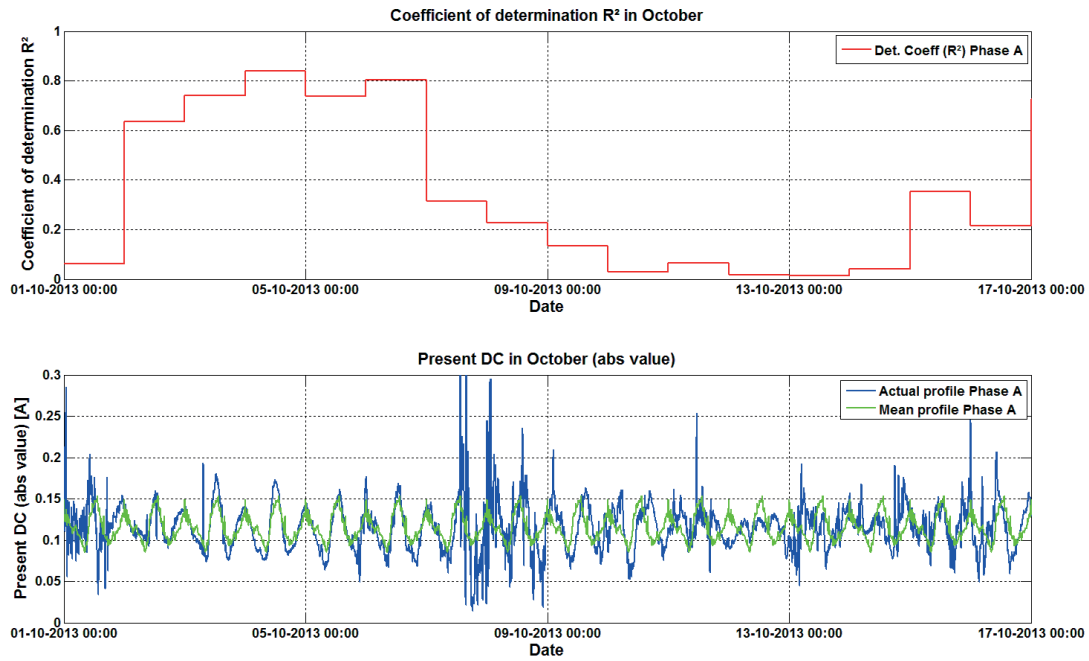


Figure 8 - Coefficient of determination and DC Profiles for October (Part 1)

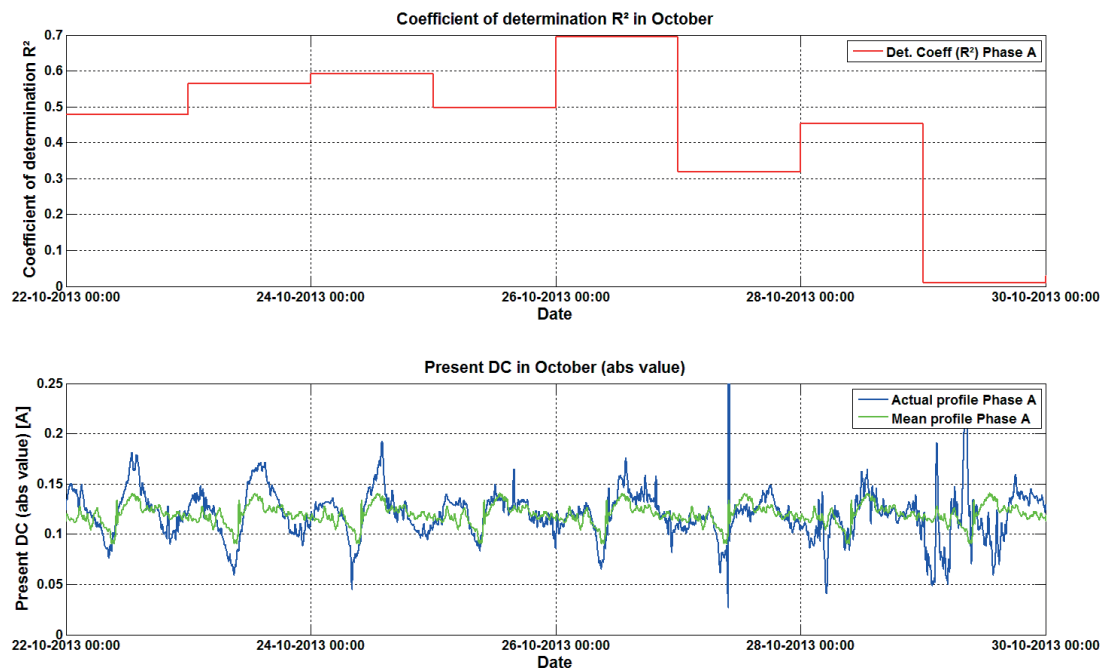


Figure 9 - Coefficient of determination and DC Profiles for October (Part 2)

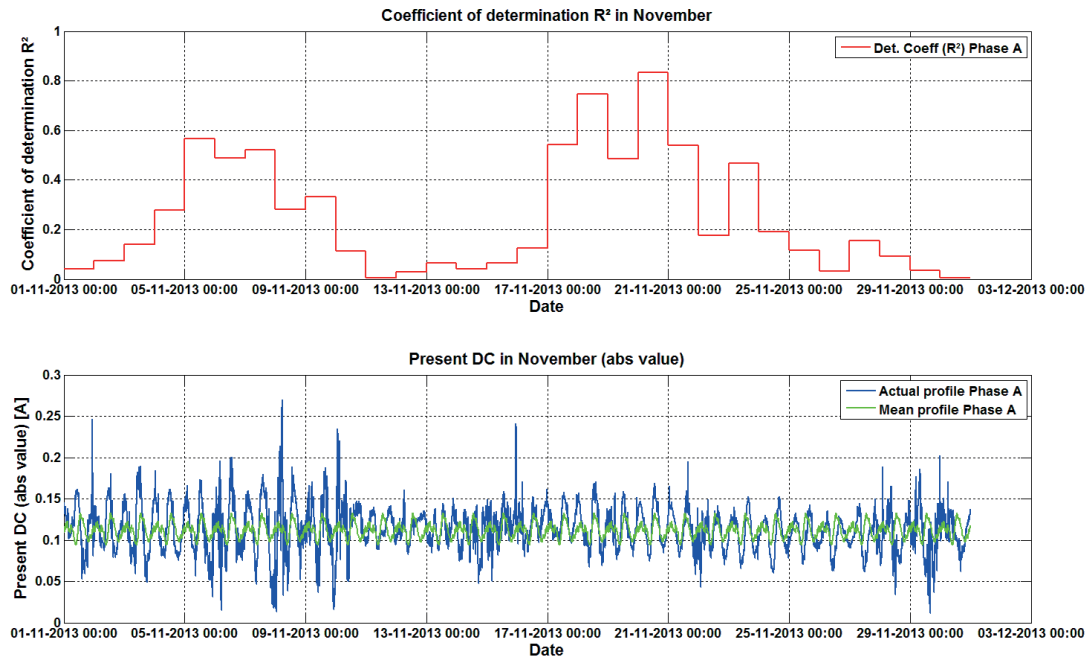


Figure 10 - Coefficient of determination and DC Profiles for November

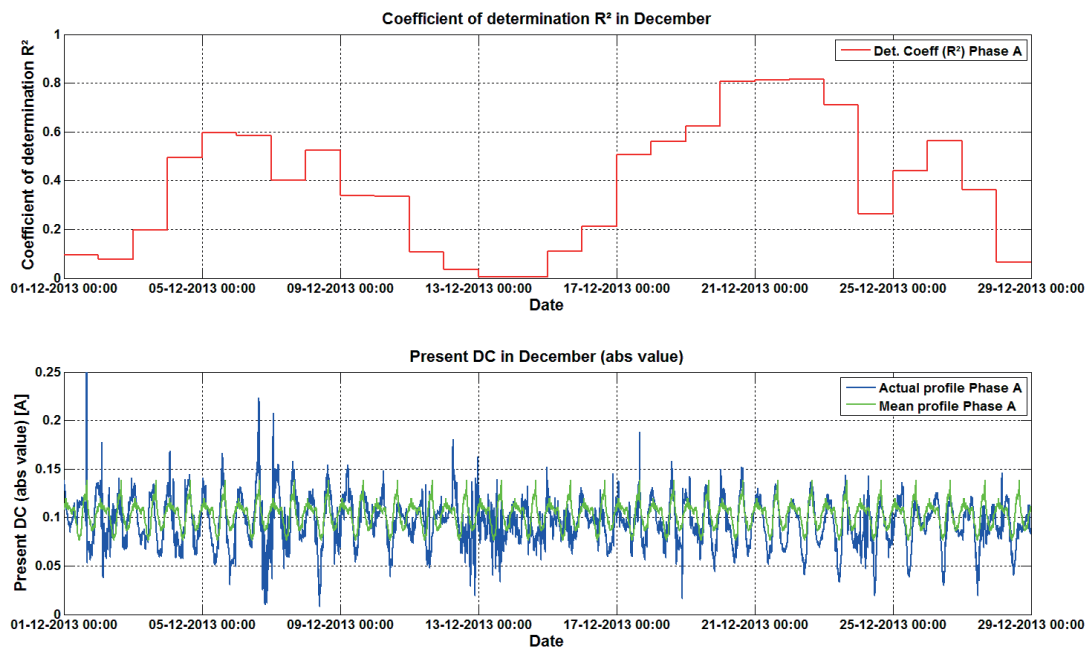


Figure 11- Coefficient of determination and DC Profiles for December

In figures 12 and 13 we compare DC profiles for July 2012 and September 2013. It can be seen that the DC load profile is quite the same although a year is between them and the shown profile of 2013 is an average one. The correlation shows a R^2 of 0.63 which is quite good.

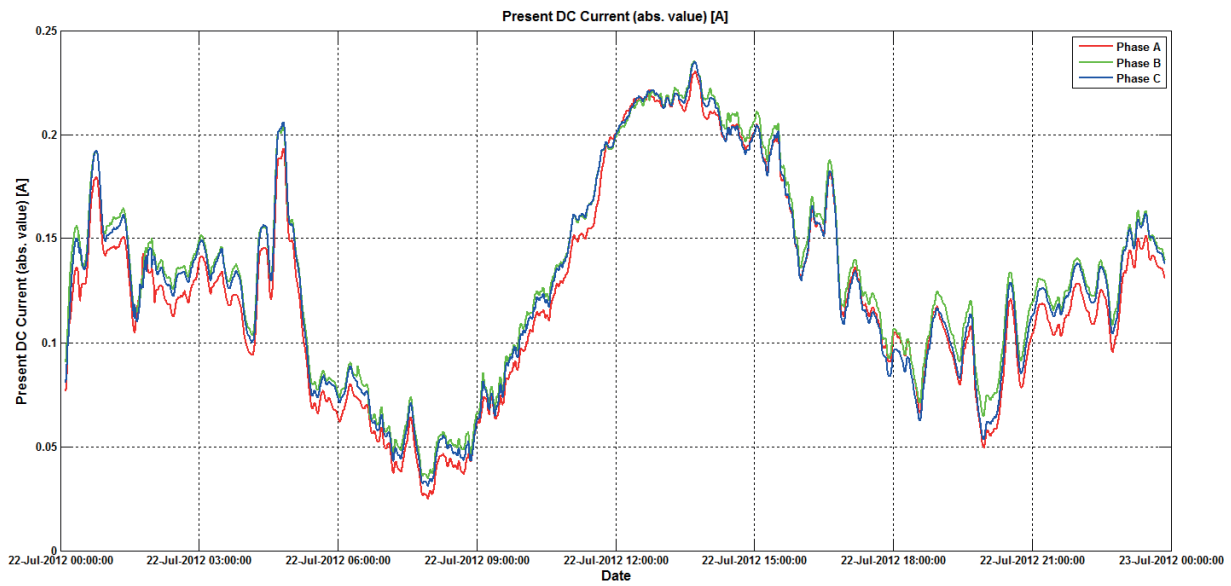


Figure 12 - DC profile of the 22nd July 2012

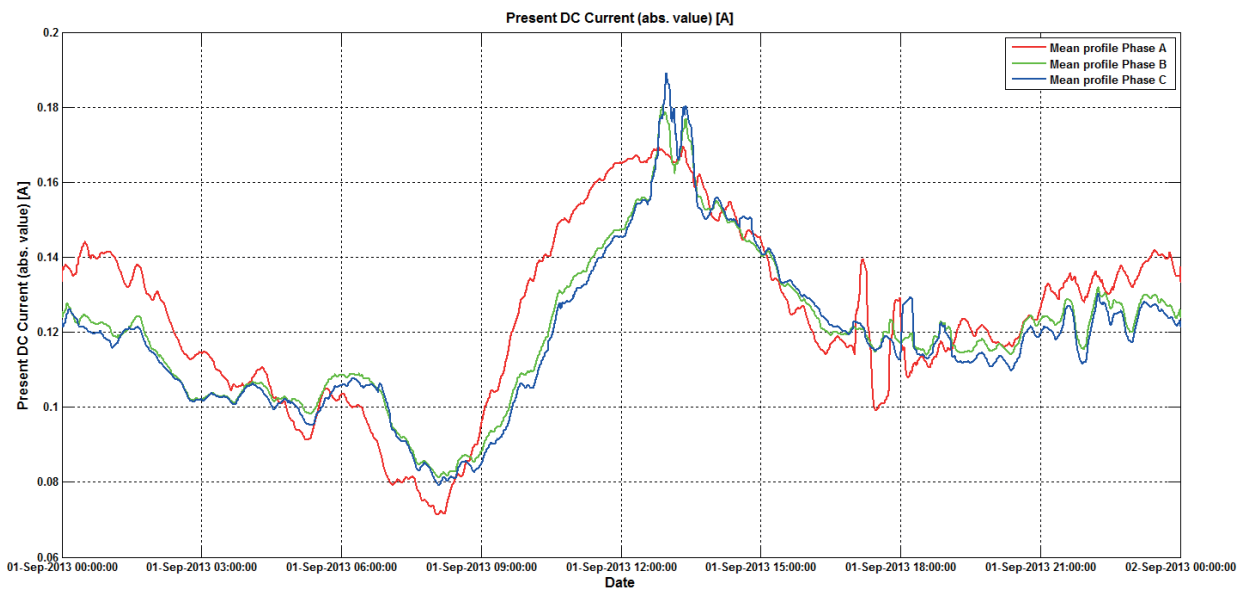


Figure 13 - Average DC profile of the first part of September 2013 data

4. CONCLUSION

Direct current was measured in an US power grid. The DC followed a clear profile as shown in figure 6-11. Due to this profile it might have a correlation to the load and or adjustments to the load (switching operations in the grid). The DC was in average smaller in December than in September which might be as well an indication that the load has an influence on the DC since there might be for example less air-conditioning in use in the winter season.

The DC was mainly in the range from 0.05 to 0.2 A per phase which is the same range measured a year before. The shape of the profile didn't change as well (figure 12 and 13). According figure 4, without DC compensation the transformers noise would have been almost the entire four month period above the guaranteed noise level.

The coefficient of determination shows clearly that the followed profile doesn't change its shape significantly over time. Some poor correlation was found when artifacts are in the actual profile. Better correlation might have been achieved by a segmentation of the data for calculation of the average profile. However, beside the correlation, it can be seen that there is a good relationship between the average and actual day profile. It must be pointed out that these artifacts are probably caused by other unidentified DC sources that do not behave in a periodic way.

Customer should take the DC phenomenon in AC grids into account. No-load noise and no-load losses are increased. With the DC compensation equipment, the noise can be kept at the original level without DC and the increase of the no-load losses is not significant.

As a next step measurements in the European grid will be performed. If the profile in Europe follows more or less the same profile it would be another indication that the DC is correlated to the load. The renewable power generation shall also be considered when analyzing the DC since there are some indications that at some locations the wind power generation is responsible as well for the DC. So far as the DC cannot be turned off, countermeasures have to be considered when operating parasitic DC affected transformers.

5. REFERENCES

- [1] F. Bachinger, A. Hackl, P. Hamberger, A. Leikermoser, G. Leber, H. Passath, M. Stoessl, "Direct current - effects and compensation", Proceedings of the CIGRE Session 2012 (Paris), no. A2-301(2012).
- [2] H. Inoue, S. Okabe, "Magnetic properties of grain oriented electrical steel in model transformer", Journal of Applied Physics 115, 17A332 (2014); doi: 10.1063/1.4866846
- [3] F. Bachinger, P. Hamberger, A. Leikermoser, G. Leber, H. Passath, "Direct current in transformers - experience, compensation", Paper PS1-34, CIGRE SC A2 & C4 JOINT COLLOQUIUM 2013 Zurich, Switzerland
- [4] G. Mei, Y. Sun, Y. Liu. "Simulation on DC current distribution in AC power grid under HVDC ground-return-mode" (Journal of Electromagnetics Analysis and Applications, vol. 2, no. 7, 2010, p. 418 – 423).
- [5] H. Pfützner, G. Shilyashki, F. Hofbauer, D. Sabic, E. Mulasalihovic, V. Galabov. "Effects of DC-bias on the loss distribution of a model transformer core" (Journal of Electrical Engineering, vol. 61, no. 7/s, 2010, p. 126 – 129).
- [6] M.A.S. Masoum, P.S. Moses. "Influence of geomagnetically induced currents on three-phase power transformers" (Proceedings of the Australasian Universities Power Engineering Conference AUPEC 2008).
- [7] P.R. Price. "Geomagnetically induced current effects on transformers" (IEEE Transactions on Power Delivery, vol. 17, 2002, p. 1002 – 1008).
- [8] X. Dong, Y. Liu, J.G. Kappenman. "Comparative analysis of exciting current harmonics and reactive power consumption from GIC saturated transformers" (Proceedings of the IEEE Power Engineering Society Winter Conference 2011, p. 318 – 322).
- [9] J. Kappenman. "Geomagnetic storms and their impacts on the U.S. power grid" (Meta-R-319, Metatech Corporation January 2010).

Petar Gabrić
Končar - Electrical Engineering Institute Inc.
pgabric@koncar-institut.hr

Damir Ilić
Faculty of Electrical Engineering
and Computing (FER), Zagreb
damir.ilic@fer.hr

Antun Mikulecky
Končar - Electrical Engineering Institute Inc.
amikul@koncar-institut.hr

Vladimir Podobnik
Končar Power Transformers Ltd.,
A joint venture of Siemens and Končar
vladimir.podobnik@siemens.com

INFLUENCING FACTORS IN INSULATION MODEL TESTING

SUMMARY

The aim of this paper is to examine different factors that influence the quality of insulation models high voltage testing results. These factors are related to model geometry and model testing procedures. Model geometry is visually checked, several influencing factors are detected and their influence on el. field calculation results is evaluated using finite element method (FEM) and cumulative method for oil-barrier insulation design. The procedure for model geometry uncertainty estimation is performed using first-order Taylor series approximation. Also, the influence of previous voltage exposure history of a specimen, so-called “memo effect”, is estimated with a cumulative exposure method.

Key words: oil-barrier insulation, cumulative method, influencing factor, model uncertainty, sensitivity coefficient, step-by-step method

1. INTRODUCTION

Power transformer insulation system is made of two basic materials - paper and mineral oil. These materials can be used in transformer in various forms such as impregnated paper between electrodes (usually between winding turns), oil impregnated paper in combination with oil gap (usually used for leads and many other application) and oil barrier insulation (used for insulation between windings and between windings and earthed parts in all oil immersed HV power transformers).

Transformer insulation design is based on insulation design curves which have been developed as a result of high voltage experiments on insulation models. Experimental curves are used because a well-proven and a widely accepted oil breakdown theory has not yet been found and published. Different types of physical insulation models are reported in literature. In majority of published papers authors use bare electrodes because these electrodes are cheaper and easier to produce. In this work insulation models with paper covered electrodes will be analyzed because of their importance in design curves development – majority of the high voltage insulation systems consist of paper covered electrodes due to better voltage properties. The basic difference between bare and paper covered electrodes, regarding experimental research, is the fact that series of breakdowns can be made between bare electrodes while only one breakdown can be made between paper covered electrodes. Another important difference between these two types of electrodes is related to model geometry – it is more difficult to obtain uniform model parameters in models with paper covered electrodes due to tolerances in manufacturing process. Non-uniformity of model parameters causes discrepancy in comparison to nominal model parameters as well as uncertainty in electric field analysis.

The aim of this paper is to present a model geometry analysis procedure to improve the quality of test results by estimating oil gaps width and paper insulation thickness as precise as possible. This is achieved by calculating mean values of model parameters and their uncertainty. Mean values of actual model parameters are used as input values in minimum safety factor calculation. Measuring uncertainties of these parameters are used to find standard measuring uncertainty of model's minimum safety factor.

Furthermore, the influence of multiple test voltage levels coexistence on insulation system is analyzed as another important factor that influences quality of test results. Insulation models are often tested up to breakdown by using step-by-step method (i.e. ramp in steps) in which voltage is raised every 60 seconds in 3-5% steps of reference voltage level. On the other hand, insulation design curves are usually defined for one-minute constant AC stress. Therefore, it would be useful to analyze the so-called "memo effect" in the insulation system.

2. MODEL GEOMETRY ANALYSIS

2.1. Cumulative method insulation design basics

In this paper safety factors in oil gaps are calculated with cumulative method. El. field values are obtained with FEM. According to cumulative method, oil gaps in transformer main insulation system are designed in a way that the average el. stress along each el. field line is lower than the permissible el. stress which is defined with insulation design curves [1]. Ratio of permissible and average el. stress across a field line is called the safety factor ($\sigma(x)$) or margine. Minimum safety factor (σ_{min}) is defined as:

$$\sigma_{min} = \min\{\sigma(x)\} = \min\left\{\frac{E_{perm}(x)}{\bar{E}(x)}\right\} \quad (1)$$

where $E_{perm}(x)$ is the permissible el. field and $\bar{E}(x)$ is the average el. field. Average el. field is a function of the el. field along an el. field line (which should be previously transferred to descending function if necessary) and x is the position on the el. field line ($x=0$ represents the starting point of the field line). $\bar{E}(x)$ is calculated as:

$$\bar{E}(x) = \frac{1}{x} \int_{x=0}^x E_{desc}(x) dx \quad (2)$$

where $E_{desc}(x)$ is descending el. field.

Cumulative insulation design method is explained in more detail in [2].

2.2. Model parameters influencing factors

As previously mentioned, actual parameters in the insulation models with paper covered electrodes are not uniform due to manufacturing tolerances which leads to discrepancies in comparison to models with nominal parameters. Visual inspection is performed on different types of models and factors that influence the model's minimum safety factor uncertainty (model uncertainty) are determined. For each model parameter the average value and standard measuring uncertainty is found. Also, the comparison of actual and nominal model parameters is made to demonstrate the influence of manufacturing tolerances. Model geometry analysis is performed on models that are used for oil-barrier insulation experiments reported in [3]. Figure 1 shows the cross section of the model and electrodes (oil gap is marked as d_{oil} and paper covering thickness as d_{paper}). In models with barrier, one 2 mm thick barrier is placed horizontally in the middle of the oil gap. In the following, several influencing factors are analyzed and it is shown that average values of all model parameters should be determined as precise as possible due to significant influence on test results.

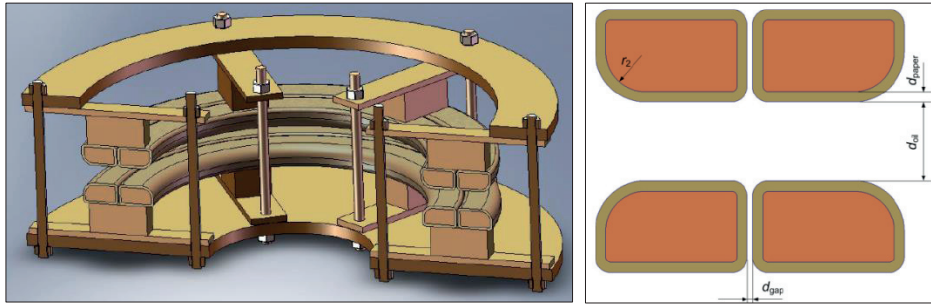


Figure 1 – Model cross section (left); electrodes cross section (right)

2.2.1. Spacer thickness

During the model drying process spacer thickness reduces which leads to reduction in related oil gap width. In order to obtain spacer thickness measures as precise as possible, measurements should be performed immediately after model drying in models with bulk oil gap (models without spacers - in this type of models spacers are used for oil gap width adjustment during the drying process and they are removed before impregnation with oil). In models with spacers in oil gap (for creepage testing) measurement should be performed immediately after the end of HV testing. Table I shows a few examples of nominal and measured values. Measurements are made on 12 samples for each group.

Table I – Spacer thickness measures

Nominal spacer thickness / mm	Average spacer thickness before drying / mm	Average spacer thickness after drying / mm	Relative measurement uncertainty of spacer thickness after drying / %
6	6,1	5,8	1,7
10	10,1	9,4	1,1
22	22,1	20,7	0,5
30	29,8	27,8	0,3

Table II shows σ_{min} values calculated with the cumulative method in the case when spacer thickness differs from nominal. In models with nominal parameters σ_{min} is equal to 1 for reference voltage (which is obtained with cumulative method and insulation design curve reported in [1]).

Table II - σ_{min} values for different spacer thicknesses

Nominal oil gap / mm	σ_{min}		
	Spacer thickness 5% lower than nominal	Spacer thickness equal to nominal	Spacer thickness 5% higher than nominal
3	1,00	1,00	1,00
6	0,99	1,00	1,01
10	0,99	1,00	1,01
18	0,98	1,00	1,02
22	0,98	1,00	1,02
30	0,98	1,00	1,02

From Table I and Table II it can be seen that discrepancies in actual and nominal spacer thickness result in different σ_{min} which means that test results should be recalculated to actual model geometry (average values of model parameters). For example, calculation with nominal parameters in the case of 30 mm oil gap compared to the calculation with measured spacer thickness (Table I) would lead to nearly 3% higher σ_{min} . For 3 mm oil gap spacer thickness change, in the observed range, practically does not affect σ_{min} .

2.2.2. Paper thickness

Electrodes paper covering thickness reduces during the drying process. In majority of cases it is not possible to directly measure paper thickness due to electrode design. Paper thickness is calculated as a difference between paper covered and bare electrode thickness and then an additional factor is applied which simulates the effect of paper drying. This factor depends on paper type and technology. In our experiment it was taken as 0,95 (paper thickness reduces by 5%). Another important fact is that paper thickness is not uniform across the electrode circumference because of manufacturing tolerances and it is advisable to measure these values on several places on each electrode. Table III shows σ_{\min} for different nominal oil gaps and depending on paper thickness (σ_{\min} is equal to 1 in the case of nominal paper thickness for each nominal oil gap).

Table III - σ_{\min} for different paper thicknesses

Nominal oil gap / mm	σ_{\min}		
	Paper thick. 5% lower than nominal	Paper thick. equal to nominal	Paper thick. 5% higher than nominal
3 mm	0,97	1,00	1,03
6 mm	0,98	1,00	1,02
10 mm	0,98	1,00	1,02
30 mm	0,99	1,00	1,01

Average values of paper thickness on electrodes reported in [3] are in the range of $\pm 5\%$ of the nominal value (which is 4 mm) and measurement uncertainty is in the range of 2,5-10%. From Table III it can be seen that the influence of these discrepancies is the highest in models with 3 mm oil gaps – errors up to 3% are possible and should be corrected by application of actual instead of nominal values. This component influences the model uncertainty significantly due to high relative measurement uncertainty. Its influence can be reduced only by reducing manufacturing tolerances.

2.2.3. Squeezing of paper insulation on electrodes

Figure 2 shows squeezing of paper insulation under the spacer (spacer is translated from its original position to show the effect of squeezing). The depth of squeezing in models is estimated to be up to 0,5 mm. Estimation is made by comparison with the thickness of an appropriate strip used as a caliber.

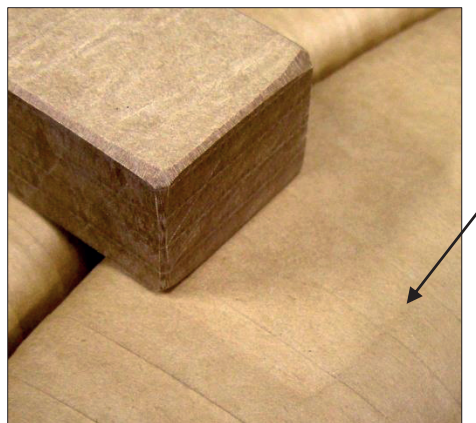


Figure 2 – Paper squeezing under the spacer

EI. field calculation (using FEM) is made to analyze the influence of paper squeezing on the experimental results. 10 mm oil gap with squeezing of 0,5 mm on each side of oil gap is modeled in Infolytica ElecNet, as shown in Figure 3.

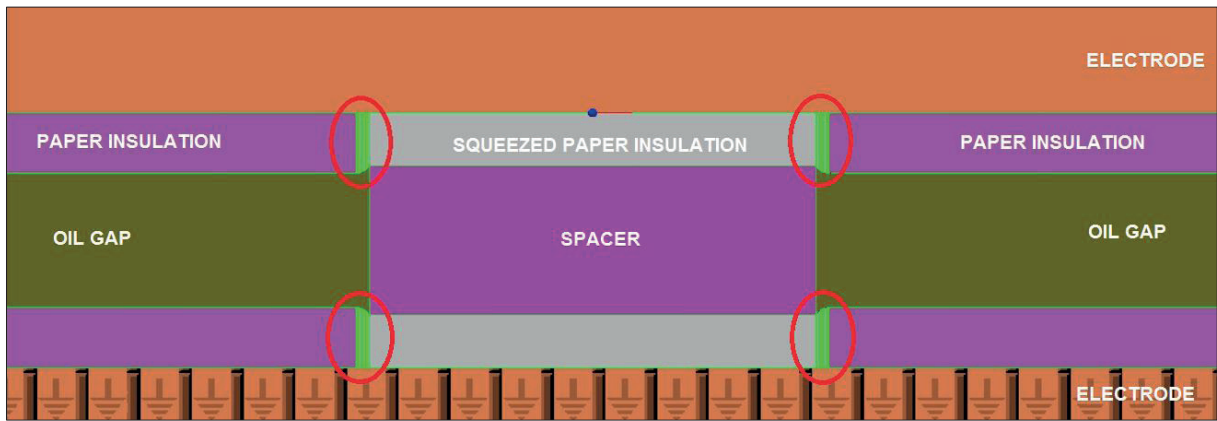


Figure 3 – Paper squeezing model made in Infolytica ElecNet

Paper squeezing has two major effects on model geometry parameters - oil gap width far from the spacer is reduced and paper permittivity is increased in the squeezed region due to paper density increase. Paper permittivity change is modeled in 10 steps (marked with red markers in Figure 3). The influence of paper squeezing is analyzed with cumulative method applied on simulation results, see Figure 4. σ_{\min} value in model with nominal parameters is equal to 1.

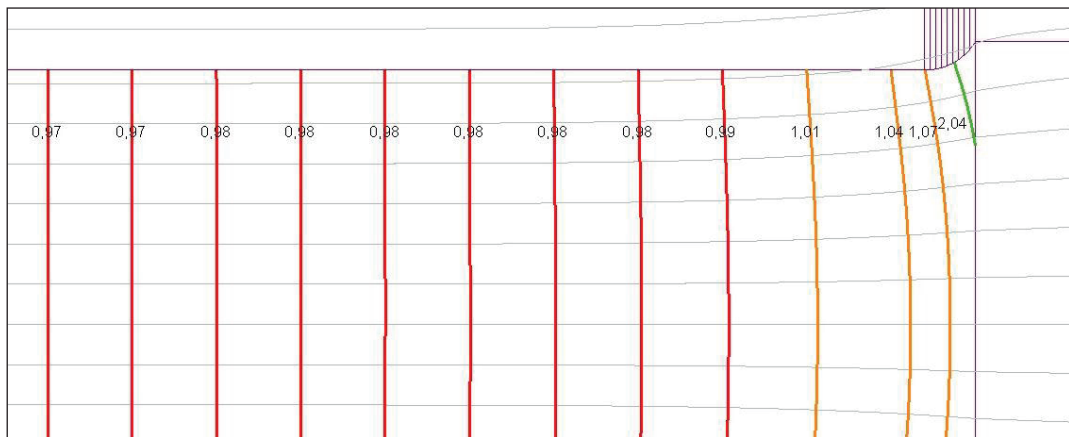


Figure 4 – Safety factors in 10 mm oil gap with 0,5 mm paper squeezing on each side

Figure 4 shows that safety factors in the vicinity of spacer are higher than in the model with nominal parameters which means that paper permittivity change effect can be neglected. On the other hand, oil gap width reduction effect should not be neglected because safety factors far from the spacer are lower than 1. Table IV shows σ_{\min} values for different values of paper squeezing.

Table IV - σ_{\min} for different values of paper squeezing

Nominal oil gap width / mm	σ_{\min}	
	No squeezing	0,5 mm squeezing on each side of oil gap
3	1,00	1,02
10	1,00	0,97
18	1,00	0,98
30	1,00	0,98

Table IV shows that paper squeezing results in lower σ_{\min} for models with larger oil gaps and in higher σ_{\min} for models with narrow oil gaps. This can be explained by the fact that the slope of the permissible el. field function is higher in the range of narrow oil gaps (permissible el. field in (1) increases in higher amount than the change of the average el. field caused by oil gap width reduction).

2.2.4. Barrier distortion

Figure 5 shows a photo of barrier distortion which was taken during the model disassembling. Barrier distortions are estimated to be between 0 and 1 mm by visual inspection of all models and by using an appropriate spacer as a caliber. Barrier distortion results in different oil gap widths which leads to lower minimum safety factors in actual oil gaps than in nominal models (nominal model consists of two oil gaps of equal width). Barrier distortion of 1 mm changes oil gaps in model from 4+4 mm nominal width to 3+5 mm (as in Figure 5) and lowers minimum safety factor by 8%. Table V shows minimum safety factors for barrier distortions of 0,5 mm and 1 mm in the cases of 4+4 mm, 8+8 mm and 10+10 mm oil gaps (2 mm thick barrier is placed between electrodes nominally in the middle of the oil gap).



Figure 5 - Barrier distortion (the most prominent photo)

Table V - σ_{\min} for different values of barrier distortion

Nominal oil gap / mm	σ_{\min}		
	0 mm distortion	0,5 mm distortion	1 mm distortion
4+4	1	0,96	0,92
8+8	1	0,97	0,95
10+10	1	0,98	0,96

According to Table V, models with narrower oil gaps are significantly influenced with barrier distortion. Hence, it is necessary to achieve a barrier distortion as small as possible during the model assembling and preparation phase.

2.2.5. Spacer shifting (in models with barrier only)

Oil gaps in model with barrier are formed with spacers placed between each insulated electrode and barrier. In ideal situation spacers are placed at the same positions in both oil gaps (complete overlap is achieved). However, it is not simple to put the spacers exactly on the same position without gluing and they are often displaced from "ideal position" by a few millimeters. Figure 6 shows safety factors in oil gaps for the cases when one spacer is kept in the fixed position and the other is shifted for 0, 2, 4 and 6 mm.

From Figure 6 it can be seen that greater spacer displacement reduces safety factors in oil gaps. In case of 2 mm shifting σ_{\min} is still higher than 1, but for 4 and 6 mm shifting σ_{\min} reduces to 0,97 and 0,93. According to this, during model assembling spacer displacement should be rigorously controlled and kept below 2 mm if possible. In case this is not possible, the influence of spacer shifting on el. field geometry should be taken into account and additional correction factors should be applied on test results.

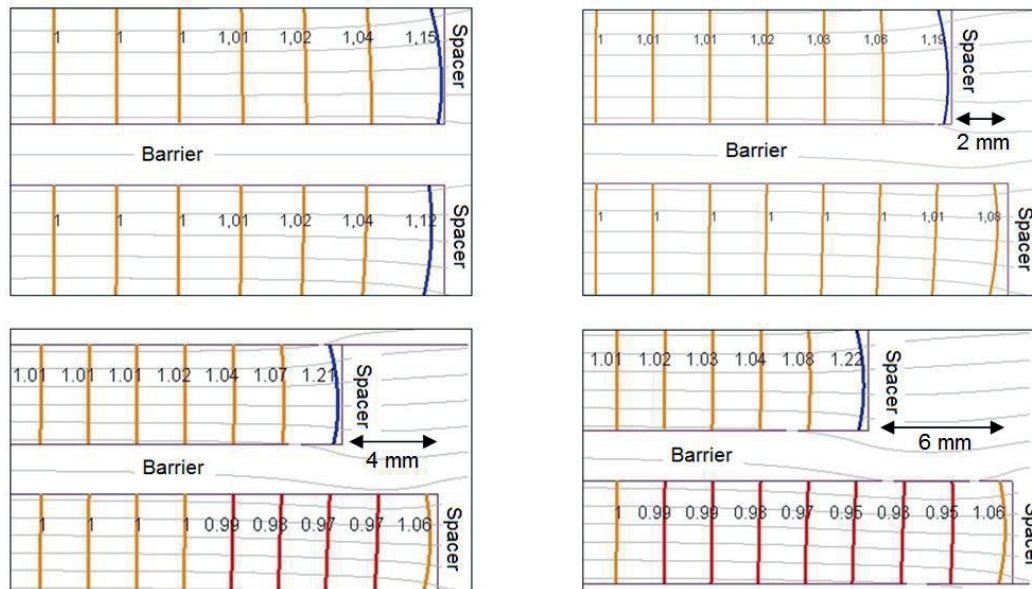


Figure 6 - Safety factors in oil gaps; upper spacer is shifted for 0, 2, 4 and 6 mm to the left side

2.3. Model uncertainty estimation

Relation between model parameters and model minimum safety factor can be expressed as $\sigma_{min} = f(x_1, x_2, \dots, x_i, \dots, x_n)$ where x_i is model parameter (influencing factor) defined with average value and measuring uncertainty. Function f is determined with cumulative method and FEM calculations made on model geometry. σ_{min} value should be calculated by using actual (average) values of model parameters as previously demonstrated. Model uncertainty (σ_{min} uncertainty) is estimated with Taylor series approximation because input parameters are independent variables. Input and output variables are considered to be linearly dependent and the first-order Taylor series approximation is used, [4]:

$$u(\sigma_{min}) = \sqrt{\sum_i \left(\frac{\partial f}{\partial x_i}\right)^2 \cdot u^2(x_i)} \quad (3)$$

where $u(\sigma_{min})$ is standard deviation of model minimum safety factor (model uncertainty), $\partial f / \partial x_i$ is sensitivity coefficient of i -th model parameter and $u(x_i)$ is measurement uncertainty of i -th model parameter.

Sensitivity coefficients in (3) are calculated from Tables II-V as:

$$\frac{\partial f}{\partial x_i} = \frac{\sigma_{min(1)} - \sigma_{min(2)}}{x_{i(1)} - x_{i(2)}} \quad (4)$$

where $x_{i(2)}$ is 5% higher value than nominal x_i and $x_{i(1)}$ is 5% lower value than nominal x_i . $\sigma_{min(1)}$ and $\sigma_{min(2)}$ are minimum safety factors in case when model parameter x_i is equal to $x_{i(1)}$ and $x_{i(2)}$ while other model parameters are equal to nominal values. For example, sensitivity factor for paper thickness is calculated from Table III and in the case of 6 mm oil gap we have:

$$\frac{\partial f}{\partial d_p} = \frac{0,98 - 1,02}{0,95 \cdot 4 - 1,05 \cdot 4} = 0,1 \text{ mm}^{-1} \quad (5)$$

Measuring uncertainty of spacer thickness and paper thickness is equal to standard measuring uncertainty based on 12 measurements. Paper squeezing and barrier distortion are modeled using uniform distribution between 0 and maximum estimated value. Average parameter values in these two cases are equal to max estimated value divided by 2, whereas measuring uncertainty is equal to max estimated value divided by $\sqrt{3}$.

For example, Figure 7 shows safety factors for model geometry with spacer thickness of $7,70 \pm 0,05$ mm, paper thickness of $3,84 \pm 0,41$ mm, paper squeezing of $0,25 \pm 0,14$ mm on each side of oil gap and with barrier distortion of $0,5 \pm 0,29$ mm. Voltage between electrodes is set to reference value which gives minimum safety factor equal to 1 for nominal model parameters. For actual model parameters minimum safety factor is equal to $0,95 \pm 0,026$ which means that el. field obtained with actual parameters are 5% higher than in model with nominal parameters and model geometry uncertainty is 2,6%. This result confirms necessity to perform geometry analysis in model with paper covered electrodes.

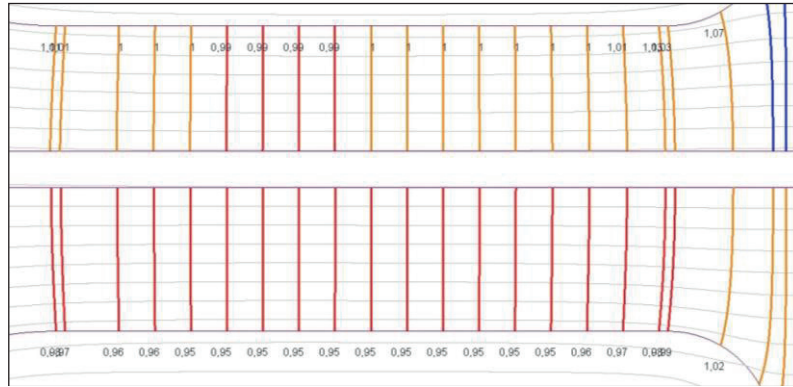


Figure 7 – Safety factors in oil gaps for model parameters as stated in the text

3. INFLUENCE OF THE MULTIPLE TEST VOLTAGE LEVEL

AC design curves for oil-barrier insulation system define permissible el. field strength for different oil gap lengths. Usually these curves are expressed for 1 min AC constant voltage stress (correction factors should be applied for different duration of voltage application). Testing with 1 minute AC constant stress is rarely performed in case of insulation model testing. Step-by-step (ramp in steps) test method is more effective because breakdown or PD inception is reached in a shorter period of time. In this method voltage is raised every 60 seconds in 3-5% steps of reference voltage level. The first voltage level is usually 60-70% of the reference voltage. Figure 8 shows a test voltage shape in step-by-step testing. Different authors reported that permissible el. fields could be underestimated without taking into account the previous exposure history of a specimen, a so-called “memo effect” [5,6].

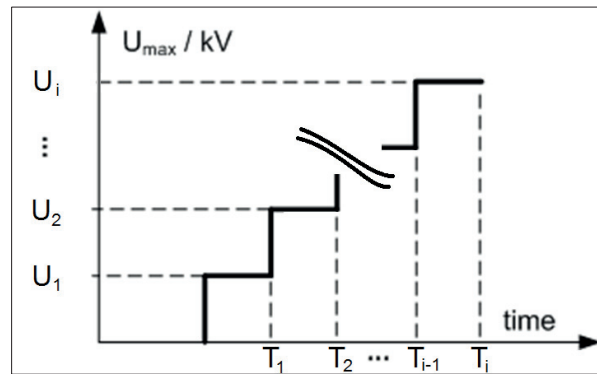


Figure 8 – Step-by-step (ramp in steps) test method

The influence of “memo effect“ is analyzed for the V-t characteristics of the oil-filled transformers. V-t characteristics can be approximated by $V^t t = K$, where K is a constant. It is assumed that cumulative fault probability in oil-barrier insulation conforms to the Weibull distribution. Inclination n of the V-t characteristics can be expressed as $n = m/a$, where m is a Weibull distribution voltage shape parameter and a is a Weibull distribution time shape parameter. The Weibull distribution for specimens at constant stress is:

$$P = 1 - \exp(-AV^m t^a) \quad (6)$$

where A is a constant. According to [5,6], cumulative fault probability should be retained when voltage changes. This is done by shifting to V-t characteristics with equal $V^n t$. In other words, in step-by-step method step 2 has an equivalent start time s_1 which would produce the same breakdown probability as step 1 within T_1 . The equivalent time s_1 at voltage V_2 is calculated from $V_2^n \cdot s_1 = V_1^n \cdot T_1$ and it is equal to

$$s_1 = \left(\frac{V_1}{V_2}\right)^n \cdot T_1 = \left(\frac{V_1}{V_2}\right)^{\frac{m}{a}} \cdot T_1 \quad (7)$$

Cumulative fault probability P in the second step (time region $T_1 \leq t \leq T_2$) is expressed with

$$P = 1 - \exp(-AV_2^m (t - T_1 + s_1)^a) \quad (8)$$

where s_1 is defined in (7).

In the step i ($T_{i-1} < t < T_i$), equivalent time s_{i-1} and cumulative fault probability are:

$$s_{i-1} = \left(\frac{V_{i-1}}{V_i}\right)^{\frac{m}{a}} \cdot (T_{i-1} - T_{i-2} + s_{i-2}) \quad (9)$$

$$P = 1 - \exp(-AV_i^m(t - T_{i-1} + s_{i-1})^a) \quad (10)$$

The influence of the “memo effect” can be estimated with analysis of the case when the one-minute fault probability is equal to cumulative fault probability in the step i . For 60 seconds voltage step intervals we can write:

$$-AV_i^m(60 + s_{i-1})^a = -AV^m60^a \quad (11)$$

$$V = V_i \cdot \left(\frac{60+s_{i-1}}{60}\right)^{\frac{a}{m}} = V_i \cdot \left(\frac{60+s_{i-1}}{60}\right)^{\frac{1}{n}} \quad (12)$$

where V is corrected voltage value and V_i is measured voltage value.

The “memo effect” influence is analyzed for the case where $n = 33,3$, $m = 10$ and $a = 0,3$ which are typical values for oil-filled transformer reported in literature [5]. Using (9) and (12) it is estimated that for the common test parameters (the first voltage level 60% of reference voltage, voltage step 3% of reference voltage) “memo effect” influence is 1-2% depending on the number of voltage steps before PD inception or breakdown. In case when voltage step is 5% this influence is 0,5-1% (which means that corrected voltage value V is up to 1% greater than measured PD inception or BD voltage V_i).

It is important to state that cumulative exposure model presented in this section has not been adequately verified by experimental research up to now and conclusions are made from theoretical considerations. According to previous, it should be stated that a bit lower permissible values are obtained by using step-by-step test method than in 1 min AC stress testing which means that step-by-step method results are on the safe side.

4. CONCLUSION

In this paper a model geometry analysis procedure is performed to improve the quality of test results by estimating oil gaps width and paper insulation thickness as precise as possible. This is achieved by estimating mean value and measuring uncertainty of model parameters. Sensitivity coefficients of influencing factors are calculated using FEM and cumulative method. It is shown that the difference between results obtained with nominal and actual model parameters can be significant. It is advised to make calculations with actual model parameters in models with paper covered electrodes. Furthermore, the influence of “memo effect” on insulation system is analyzed as another important factor that influences quality of test results. A permissible el. field values obtained with step-by-step test method are a bit lower than in 1 min AC stress testing which means that results are on the safe side.

REFERENCES

- [1] W. Dahinden, K Shultz, A. K uchler, “Function of Solid Insulation in Transformers”, Transform 98, 20.-21. April 1998, Forum der Technik, M unchen
- [2] F. Derler, HJ. Kirch, Ch. Krause, and E. Schneider, "Development of a design method for insulating structures exposed to electric stress in long oil gaps and along oil/Transformerboard interfaces", 7th Int'l. Sympos. High Voltage Eng. (ISH), Dresden, 1991.
- [3] P.Gabri c, M.Glavini c, A.Mikulecky, V.Podobnik, “Research of Transformer Main Insulation Design Rules”, International Colloquium Transformer Research and Asset Management, Dubrovnik, 2012.
- [4] Z.Godec, "Iskazivanje mjernog rezultata", Zagreb, Graphis, 1995.
- [5] T.Tsuboi, J.Takami, S.Okabe, "Influence of Voltage Application History on Insulation Test with One-Minute Step-up Method", IEEE Transactions on Dielectrics and Electrical Insulation Vol. 15, No. 5; October 2008
- [6] W.Nelson, "Accelerated Testing - Statistical Models, Test Plans and Data Analysis", John Wiley & Sons, 2004

Zdenko Godec
Končar - Electrical Engineering Institute Inc.
zgodec@koncar-institut.hr

Vjenceslav Kuprešanin
Končar - Electrical Engineering Institute Inc.
vkupresa@koncar-institut.hr

TEMPERATURE RISE OF POWER TRANSFORMERS: COMMENTS AND PROPOSALS TO IEC 60076-2:2011

SUMMARY

Two years ago, a new, third edition of IEC 60076-2 standard was published [1]. Over a period of two years, we have had the opportunity to evaluate this new standard in practice. In the paper, it is shown that the criterion for stagnation $1K/h + 3h$ is not entirely satisfying. Better criterion is $1K/3h$, or extrapolation to stagnation - as given in second edition of the standard. A formula for hot-spot determination is not complete and it is suggested how to improve it. In the new standard, three formulas for winding average temperature determination are given. Based on experiments, we conclude that the best formula is the simplest one, and two additional formulas are without any benefit. According to [1], paragraph 7.11, measurement uncertainty estimates of results should be given in test reports - but only as information. No procedure for measurement uncertainty estimation is given, and measurement uncertainty is not used in decision-making. Therefore, the third edition of the standard is uncompleted and not motivating in terms of efforts to increase the quality of the measurement results. In the paper, the procedure for measurement uncertainty estimation is proposed and suggestion is given for appropriate decision making.

Key words: Power transformers, temperature rise test, measurement uncertainty, decision-making

1. INTRODUCTION

A brief overview and comments on major changes in [1] is given in [2]. This paper emphasizes procedure for estimation of measurement uncertainties of characteristic temperature rises of transformer parts, and proposes some improvements in the standard [1].

2. THE PROCEDURE FOR ESTIMATING MEASUREMENT UNCERTAINTY OF TEMPERATURE RISES

2.1. Temperature rise test in short

The purpose of the transformer temperature rise test is to establish steady-state temperature rises of transformer characteristic parts. It is performed by the short-circuit method and consists, in principle, of two steps. In the first step, transformer is heated with total losses and steady-state oil temperature rise over the external cooling medium is determined. In the second step, transformer is heated with rated current to establish average winding to oil temperature gradient. Finally, the average

temperature rises of windings and windings hot spots over external medium are calculated, based on the simplified thermal model of transformer [1].

To evaluate the uncertainty of oil and windings temperature rises, it is necessary to pre-estimate the uncertainty of measurement of losses, alternating current, temperature and winding resistances.

2.2. Measurement uncertainty of losses

In the first part of the temperature rise test transformer is short-circuited and heated with total losses. Losses are measured using instrument transformers and power analyzer (PA). Standard uncertainties of measured total losses (sum of load losses and no-load losses) are estimated as:

$$u(P_{\text{tot}}) = \sqrt{[u(P_{\text{LL}})]^2 + [u(P_{\text{NLL}})]^2} \quad \text{and} \quad u(P_{\text{tot}})\% = \frac{\sqrt{[P_{\text{LL}} \cdot u(P_{\text{LL}})\%]^2 + [P_{\text{NLL}} \cdot u(P_{\text{NLL}})\%]^2}}{P_{\text{LL}} + P_{\text{NLL}}} \quad (1)$$

PLL are previously measured load losses at rated current and reference temperature \square_{ref} , and PNLL are previously measured no-load losses (corrected to a sine waveform voltage). The standard uncertainties $u(\text{PLL})\%$ and $u(\text{PNLL})\%$ are input parameters, which should be given in load loss and no-load loss test reports. Total losses should be maintained constant during the first part of the test (i.e. measured and controlled) to the moment when the rate of the change of top-oil temperature rise has fallen below 1 K/h and has remained there for a period of 3 h [1]. Due to the instability of the electrical source, losses vary and arithmetic mean value of the measured losses in the last hour of the first part of the test is declared relevant. Generally, measured and regulated heating losses PHL are:

$$P_{\text{HL}} = h \cdot P_{\text{tot}} \quad (2)$$

where the parameter h is not constant with no uncertainty, but varies depending on the measurement uncertainty of losses and uncertainty of the arithmetic mean of losses in the last hour of the first part of

the test:
$$u(h)\% = \sqrt{[u(P_{\text{HLm}})\%]^2 + [u(\bar{P}_{\text{HL}})\%]^2} \quad (3)$$

Thus, the total (standard) uncertainty of losses $u(P_{\text{HL}})$ consists of three components:

$$u(P_{\text{HL}})\% = \sqrt{[u(P_{\text{tot}})\%]^2 + [u(P_{\text{HLm}})\%]^2 + [u(\bar{P}_{\text{HL}})\%]^2} \quad (4)$$

- $u(P_{\text{tot}})\%$ uncertainty of the input data on the total losses which should heat transformer, according to equation (1)
- $u(P_{\text{HLm}})\%$ uncertainty of loss measurement estimated according to [3]
- $u(\bar{P}_{\text{HL}})\%$ uncertainty of arithmetic mean of measured losses in the last hour of the first part

of the test:
$$u(\bar{P}_{\text{HL}})\% = \frac{\sqrt{\frac{1}{n \cdot (n-1)} \sum_{i=1}^n (P_{\text{HL},i} - \bar{P}_{\text{HL}})^2}}{\bar{P}_{\text{HL}}} \cdot 100\% \quad (5)$$

n is the number of losses measurements in the last hour of the first part of the heating.

Losses P_{HL} are generally equal to the sum of PLL and PNLL, i.e. nominally is $h = 1$. Because of limited power of the power source, P_{HL} is sometimes less than required, which is taken into account by correction of steady-state oil temperature rise (19).

2.3. Measurement uncertainty of alternating current

In the second part of the temperature rise test transformer is heated with rated AC current for one hour with the purpose to determine winding to oil temperature rise.

Current is measured using current transformers and PA. Standard uncertainty of current $u(I)\%$ is estimated according to [3]. Rated current has no measurement uncertainty. Due to the instability of the power source the component of uncertainty caused by variation of the current through the last hour of heating should be added:

$$u(\bar{I})\% = \frac{\sqrt{\frac{1}{m \cdot (m-1)} \sum_{i=1}^m (I_i - \bar{I})^2}}{\bar{I}} \cdot 100 \% \quad (6)$$

m is the number of current measurements in the last hour.

Total (standard) measurement uncertainty of the current in the last hour is equal to:

$$u(I_{HC})\% = \sqrt{[u(I)\%]^2 + [u(\bar{I})\%]^2} \quad (7)$$

2.4. Uncertainty of temperature measurement

Temperatures of the transformer parts are usually measured in three ways:

- with thermocouples (or thermo resistances) and digital thermometers,
- with fibre optic thermometer, and
- indirectly, by calculating the average winding temperature based on the change of winding resistance

2.4.1. Uncertainty of temperature measurements with thermocouples

The most practical temperature measurement of coolant (oil, water and air) is with thermocouples and digital thermometer (DTM).

Copper-constantan thermocouples (type T) for measuring the temperature in the range from -40 °C to +350 °C are classified into two classes of accuracy (G_{TC}) [4]:

$$1) \pm 0.5 \text{ } ^\circ\text{C}, \text{ or } 0.004 \pm |\theta|.$$

(relevant is the higher value; for temperature range from -40 °C to +100 °C, $G_{TC} = \pm 0.5 \text{ } ^\circ\text{C}$),

$$2) \pm 1.0 \text{ } ^\circ\text{C}, \text{ or } \pm 0.0075 |\theta|.$$

For a relatively accurate DTM, accuracy (maximum permissible error) G_{DTM} is usually $\pm 1.0 \text{ } ^\circ\text{C}$ (for a period of one year and an ambient temperature in the range from 18 °C to 28°C).

Total (standard) uncertainty of temperature measurements by thermocouples and DTM is:

$$u(\theta) = \frac{1}{\sqrt{3}} \sqrt{G_{TP}^2 + G_{DTM}^2} = \frac{1}{\sqrt{3}} \sqrt{0,5^2 + 1^2} = 0,64 \text{ } ^\circ\text{C} \quad (8)$$

2.4.2. Uncertainty of measurement of temperature with fibre optic thermometer

Temperature of hot spots on transformer windings are directly measured with fibre optic thermometers. Since the fibre optics are made from electrical insulating material, measurement system is insensitive to the effects of electric and magnetic fields and the temperature measurements are possible even in the presence of high AC voltage. Usually the accuracy of fibre optic thermometers is $\pm 2 \text{ } ^\circ\text{C}$ in the temperature range from -30 °C to +230 °C. It is a direct measurement, and the (standard) measurement uncertainty according to [5] is estimated as:

$$u(\theta_h) = \frac{2}{\sqrt{3}} = 1,2 \text{ } ^\circ\text{C} \quad (9)$$

In addition, for measurement of winding hot-spot temperature, an indirect method is also used [1]. Procedure for estimation of temperature (or temperature rise) combined uncertainty is described in Chapter 2.8.1.

2.4.3. Measurement uncertainty of average winding temperature determined by measurement of winding resistance

It is an indirect method for measuring average winding temperature based on the measurements of winding resistance by V-C method of "cold" winding (to which reference temperature is associated) and hot winding resistance at the instant of shut down [1]. The average temperature of hot winding is determined using the change of resistance (see Chapters 2.6 and 2.7.).

2.5. Measurement uncertainty of oil temperature rise

Temperature rise of oil is not measured directly, but is calculated as a temperature difference:

$$\Delta\theta_{oil} = \theta_{oil} - \theta_a \quad (10)$$

θ_{oil} is measured oil temperature, and θ_a is measured external cooling medium temperature.

Estimation of uncertainty of determining the instantaneous temperature rise is based on the assumption that the measurements of oil temperature and external cooling medium temperature are mutually independent:

$$u(\Delta\theta_{oil}) = \sqrt{2} \cdot u(\theta) \quad (11)$$

According to [1] steady-state oil temperature rise $\overline{\Delta\theta_{oil}}$ is defined as the average temperature rise in the last hour. So the uncertainty of steady-state average oil temperature rise is equal to:

$$u(\overline{\Delta\theta_{oil}}) = \sqrt{[u(\Delta\theta_{oil})]^2 + \left[\frac{u_A(\Delta\theta_{oil})}{\sqrt{L}}\right]^2} \quad (12)$$

$u_A(\Delta\theta_{oil})$ is the component of the uncertainty of the individual measurements of temperature rise in the last hour of the first part of heating, and L is the number of readings in the last hour. When estimating the uncertainty of steady-state temperature rise, uncertainty of type B is dominant, while the second member in (12) can be neglected. Thus, the uncertainty of steady-state oil temperature rise will be equal to a measurement uncertainty of the single temperature rise measurement (11), because L values are correlated (as they are measured with the same sensor and the same channel of DTM) and the uncertainty caused by random influences $u_A(\theta)$ can be neglected:

$$u(\overline{\Delta\theta_{oil}}) = u(\Delta\theta_{oil}) = \sqrt{2} \cdot u(\theta) \quad (13)$$

Note. The new standard [1] does not provide extrapolation for determination of accurate steady-state oil temperature rise, as the old one does. The systematic error caused by criterion $1 \text{ K} / \text{h} + 3 \text{ h}$ depends on the thermal time constants of oil and is about -1.0 K for the thermal time constant of transformer oil not greater than three hours [6, 7]. If the heat run test is carried out successively for the transformer with two modes of cooling (e.g. ONAN/ONAF), and the steady-state temperature rise is greater for the first mode of cooling, the error is positive about $+1.0 \text{ K}$. The better criterion, with smaller systematic errors, will be $1 \text{ K} / 3\text{h}$ [6]. This systematic error will not be taken into account in here suggested procedure, because the standardized method [1] defines the steady-state oil temperature rise as average value in the last hour of heating.

The uncertainty of the instantaneous value of the top-oil temperature rise is:

$$u(\Delta\theta_o) = u(\theta) \sqrt{\frac{1}{m} + \frac{1}{n}} \quad (14)$$

because top-oil temperature rise is calculated as:

$$\Delta\theta_o = \frac{1}{m} \sum_{j=1}^m \theta_{tj} - \bar{\theta}_a = \frac{1}{m} \sum_{j=1}^m \theta_{tj} - \frac{1}{n} \sum_{i=1}^n \theta_{ai} \quad (15)$$

m is the number of thermometers on top of transformer tank and cooler inlets, and n is the number of thermometers to measure external cooling medium temperature.

Similarly, the uncertainty of instantaneous value of the bottom-oil temperature rise is:

$$u(\Delta\theta_b) = u(\theta) \sqrt{\frac{1}{p} + \frac{1}{n}} \quad (16)$$

p is the number of thermometers on cooler outlets.

And the uncertainty of instantaneous value of the average oil temperature rise is:

$$u(\Delta\theta_{om}) = \frac{\sqrt{[u(\Delta\theta_o)]^2 + [u(\Delta\theta_b)]^2}}{2} \quad (17)$$

Steady-state oil temperature rise according to [1] is calculated as the arithmetic mean of L measurements in the last hour of the first part of heating with

$$P_{HL}: \quad \bar{\Delta\theta}_{oil} = \frac{1}{L} \sum_{l=1}^L \Delta\theta_{oil,l} \quad (18)$$

This applies to all steady-state oil temperature rises, so index "oil" can be: "o" for top-oil temperature rise, "b" for bottom-oil temperature rise, and "om" for average oil temperature rise.

Temperature rise is then converted to the steady-state oil temperature rise at nominal total losses P_{TOT} :

$$\bar{\Delta\theta}_{oil,r} = \bar{\Delta\theta}_{oil} \left(\frac{P_{TOT}}{P_{HL}} \right)^x \quad (19)$$

The exponent x depends on the type of cooling (Table 3 in [1]), and $P_{TOT} = P_{tot}$ but now as a reference value ($u(P_{TOT})_{\%} = 0,0 \%$).

The total measurement uncertainty of oil temperature rises at a nominal total losses P_{TOT} ($\bar{\Delta\theta}_{o,r}$, $\bar{\Delta\theta}_{om,r}$, or $\bar{\Delta\theta}_{b,r}$) may be estimated with general expression:

$$u_T(\bar{\Delta\theta}_{oil,r})_{\%} = \sqrt{\left[\frac{u(\bar{\Delta\theta}_{oil})}{\bar{\Delta\theta}_{oil}} 100\% \right]^2 + [x \cdot u(P_{HL})_{\%}]^2} \quad \text{and} \quad u_T(\bar{\Delta\theta}_{oil,r}) = \frac{u_T(\bar{\Delta\theta}_{oil,r})_{\%}}{100\%} \cdot \bar{\Delta\theta}_{oil,r} \quad (20)$$

The uncertainties of steady-state oil temperature rises $u(\bar{\Delta\theta}_{oil})$ are calculated with (13).

2.6. Measurement uncertainty of winding resistance

The winding resistance is measured by DC V-C method, i.e. using two digital voltmeters (DMMs):

$$R = \frac{V}{I} = \frac{VR_S}{V_S} \quad (21)$$

V is the voltage across the winding, R_S is the resistance of the shunt, and V_S is the voltage on the shunt.

Measurement uncertainty (type B, according to [5]) of winding resistance R is estimated as:

$$u_B(R)\% = \frac{1}{\sqrt{3}} \sqrt{[G(V)\%]^2 + [G(V_S)\%]^2 + [G(R_S)\%]^2} \quad \text{and} \quad u_B(R) = \frac{u_B(R)\%}{100\%} \cdot R \quad (22)$$

where $G(V)\%$ and $G(V_S)\%$ are accuracies of DMM and $G(R_S)\%$ of shunt.

Repeating the measurement of winding resistance and calculating the average of n repeated measurements can reduce the random component of uncertainty and enable detection of substantial errors and transient induced voltages - which can disturb the measurement [8].

Total measurement uncertainty of cold (reference) winding resistance is determined as:

$$u(\bar{R})\% = \sqrt{[u_B(R)\%]^2 + [u_A(\bar{R})\%]^2} = \sqrt{[u_B(R)\%]^2 + \left[\frac{u_A(R)\%}{\sqrt{n}} \right]^2} \quad (23)$$

Winding resistance depends on temperature. Therefore the resistance of the winding should be associated with appropriate temperature. It is assumed that the average temperature of the windings is equal to the average temperature of the oil in the transformer in cold steady-state condition [9]. The uncertainty of determination of the resistance temperature consists of the uncertainty of determining the average oil temperature (25) and the uncertainty of association (u_Δ is estimated to be about 0,50 °C). The average temperature of the transformer oil is equal to:

$$\theta_{om} = \frac{\theta_o + \theta_b}{2} \quad (24)$$

and, consequently, uncertainty of average oil temperature is:

$$u(\theta_{om}) = \sqrt{\left[\frac{u(\theta_o)}{2} \right]^2 + \left[\frac{u(\theta_b)}{2} \right]^2} = \frac{1}{\sqrt{2}} u(\theta) \quad (25)$$

Then, total uncertainty of temperature associated to winding resistance is:

$$u(\theta_R) = \sqrt{[u(\theta_{om})]^2 + [u_\Delta]^2} \quad (26)$$

This temperature uncertainty should be transformed to the uncertainty of winding resistance:

$$u(R_{\theta R}) = \frac{R_\infty}{T + \theta_o} \cdot u(\theta_R) = \frac{R_{\theta R}}{T + \theta_R} \cdot u(\theta_R) \quad \text{and} \quad u(R_{\theta R})\% = \frac{u(\theta_R)}{T + \theta_R} \cdot 100\% \quad (27)$$

because

$$R_{\theta R} = \frac{R_\infty}{T + \theta_o} (T + \theta_R). \quad (28)$$

where R_{θ_R} is resistance at temperature θ_R , R_{θ_0} and θ_0 are reference resistance and temperature, and T is constant, for copper 235 K and for aluminium 225 K [1].

Finally, total uncertainty of winding resistance with associated temperature is:

$$u_T(R)_{\%} = \sqrt{[u(\bar{R})_{\%}]^2 + [u(R_{\theta_R})_{\%}]^2} \quad (29)$$

2.7. Measurement uncertainty of average winding temperature rise

Average temperature rise of winding over environment $\Delta\theta_W$, which manufacturer guarantees and which should be less than the agreed or standardized limit value, is obtained by adding the steady-state average oil temperature rise at nominal total losses $\overline{\Delta\theta_{om,r}}$ and winding to oil temperature rise at rated current g_r . So, measurement uncertainty of average winding temperature rise is:

$$u(\Delta\theta_W) = \sqrt{[u_T(\overline{\Delta\theta_{om,r}})]^2 + [u_T(g_r)]^2} \quad (30)$$

where $u_T(\overline{\Delta\theta_{om,r}})$ is total measurement uncertainty of steady-state average oil temperature rise at nominal total losses (20) and $u_T(g_r)$ is total measurement uncertainty of winding to oil temperature rise at rated current I_r which is calculated on the basis of

$$g_r = g \left(\frac{I_r}{I_{HC}} \right)^y, \quad (31)$$

as:

$$u_T(g_r)_{\%} = \sqrt{\left[\frac{u(g)}{g} 100\% \right]^2 + [y \cdot u(I_{HC})_{\%}]^2} \quad (32)$$

$u(g)$ is measurement uncertainty of average winding to oil temperature rise:

$$u(g) = \sqrt{[u(\theta_2^*)]^2 + [u(\theta_{om}^*)]^2} \quad (33)$$

Asterisk indicates temperatures at the instant of shutdown.

Instantaneous average winding temperature θ_2 is determined by measurement of winding resistance R_R at the reference temperature θ_R and winding resistance at the instant of shutdown R_2 :

$$\theta_2 = \frac{R_2}{R_R} (T + \theta_R) - T \quad (34)$$

To make estimation of measurement uncertainty easier, expression (34) can be rewritten as:

$$T_2 = \frac{R_2}{R_R} T_R \quad (35)$$

where $T_2 = T + \theta_2$, and $T_R = T + \theta_R$.

Resistances are measured by V-C method:

$$T_2 = \frac{V_2}{I_2} \frac{I_R}{V_R} T_R = \frac{V_2}{V_R} \frac{V_{Rs}}{R_s} \frac{R_s}{V_{2s}} T_R = \frac{V_2}{V_R} \frac{V_{Rs}}{V_{2s}} T_R \quad (36)$$

and

$$u(T_2)\% = \sqrt{\frac{1}{3} \left\{ [G(V_R)\%]^2 + [G(V_2)\%]^2 + [G(V_{Rs})\%]^2 + [G(V_{2s})\%]^2 \right\} + [u(T_R)\%]^2} \quad (37)$$

where G are limits of error (accuracies) of DMM, and

$$u(T_R)\% = \frac{u(T_R)}{T + \theta_R} 100\% = \frac{u(\theta_R)}{T + \theta_R} 100\% \quad (38)$$

Absolute measurement uncertainty of average winding temperature is then equal to

$$u(\theta_2) = u(T_2) = \frac{u(T_2)\%}{100\%} (T + \theta_2) \quad (39)$$

As the winding resistance (average temperature) cannot be measured at the instant of shutdown, it is measured several times during the cooling to permit extrapolation back to the instant of shutdown. Therefore, the uncertainty of average winding temperature at the instant of shutdown is greater:

$$u(\theta_2^*) = \sqrt{[u(\theta_2)]^2 + [u_{\text{ex}}(\theta_2^*)]^2} \quad (40)$$

$u_{\text{ex}}(\theta_2^*)$, uncertainty of extrapolation can be determined using the output values (mean square error and covariance matrix) of Levenberg-Marquardt algorithm for the best approximation of the measurement points on selected non-linear function using the least squares fit [10].

Winding temperature cooling curve is approximated as:

$$\theta_2(t) = \theta_{\text{om}}(t) + B \cdot e^{-\frac{t}{T_w}} \quad (41)$$

where the average temperature of the winding $\theta_2(t)$ depends on the time t , which is counted from the moment of shutdown. $\theta_{\text{om}}(t)$ is the average oil temperature during cooling, B is an estimate of temperature rise of windings over oil at the moment of shutdown, and T_w is the thermal time constant of winding to oil temperature rise.

The new standard [1] allows the selection of the average oil temperature cooling curves:

$$1. \text{ constant} \quad \theta_{\text{om}}(t) = A \quad (42a)$$

$$2. \text{ straight line} \quad \theta_{\text{om}}(t) = A - k \cdot t \quad (42b)$$

$$3. \text{ exponential curve} \quad \theta_{\text{om}}(t) = A \cdot e^{-\frac{t}{T_o}} \quad (42c)$$

where A is a constant, k is the difference between the average oil temperature at the beginning and at the end of the winding resistance measurement divided by the duration of the measurement of winding resistance during cooling ($[k] = \text{K} / \text{min}$), and T_o is the temperature time constant of oil.

Table I. – Results of winding cooling curves extrapolation

Type of cooling	Winding	Average oil temperature cooling curve	$\theta_2^*/I^\circ\text{C}$	$u_{\text{ex}}(\theta_2^*)/I^\circ\text{C}$	T_W/min	$u(T_W)/\text{min}$
ONAN	HV	constant	83.99	0.10	7.40	0.23
		straight line	84.09	0.10	6.24	0.19
		exponential	84.30	0.19	4.58	0.87
	LV	constant	74.59	0.21	5.08	0.26
		straight line	74.80	0.24	4.10	0.21
		exponential	74.86	0.38	3.90	1.0
ONAF	HV	constant	87.58	0.13	9.30	0.16
		straight line	87.89	0.13	7.77	0.13
		exponential	88.06	0.20	7.07	0.56
	LV	constant	82.75	0.14	7.92	0.16
		straight line	83.24	0.14	6.22	0.11
		exponential	83.68	0.22	5.19	0.33
OFAF	HV	constant	81.41	0.055	7.58	0.084
		straight line	81.54	0.060	6.60	0.077
		exponential	81.41	0.11	7.60	0.89
	LV	constant	67.59	0.45	4.51	0.30
		straight line	67.88	0.50	3.78	0.26
		exponential	67.50	0.71	4.80	1.85
ODAF	HV	constant	83.41	0.087	14.09	0.56
		straight line	83.46	0.090	11.51	0.45
		exponential	83.46	0.17	11.43	6.60
	LV	constant	74.19	0.18	6.92	0.35
		straight line	74.38	0.20	5.42	0.27
		exponential	74.68	0.36	3.95	1.0

Because in the new standard [1] no recommendation is given when to apply a particular method of extrapolation, we have investigated the properties of three methods. Table 1 shows the results of approximations using a nonlinear least-squares method of Levenberg-Marquardt (LabVIEW VI: "Nonlinear Curve Fit" or "Constrained Nonlinear Fit"). We have concluded that the first choice is a simple extrapolation of the exponential curve (42a). The other two methods are redundant, without any benefit.

2.8. Measurement uncertainty of winding hot-spot temperature rise

2.8.1. Indirect hot-spot winding temperature measurement

Winding hot spot temperature rise is calculated as [1]:

$$\Delta\theta_h = \overline{\Delta\theta_{o,r}} + H \cdot g_r \quad (43)$$

$\overline{\Delta\theta_{o,r}}$ is steady-state temperature rise of top-oil in the last hour of heating with total rated losses, H is hot-spot factor and g_r is average winding to oil temperature rise at rated current.

Measurement uncertainty is then:

$$u(\Delta\theta_h) = \sqrt{[u_T(\overline{\Delta\theta_{o,r}})]^2 + [H \cdot u_T(g_r)]^2 + [g_r \cdot u(H)]^2} \quad (44)$$

$u_T(\overline{\Delta\theta_{o,r}})$ is calculated using equation (20), $u_T(g_r)$ is calculated using equation (32), and $u(H)$ is assumed to be 10%. Uncertainty due to different oil temperature gradients in windings u_g (relative to the measured temperature gradient in the coolers) should be added to the expression (44). Consequently the total uncertainty of winding hot spot temperature rise is:

$$u_T(\Delta\theta_h) = \sqrt{[u(\Delta\theta_h)]^2 + u_g^2} \quad (45)$$

For ON.. and OD.. cooled transformers it is estimated that the uncertainty due to different temperature gradients of oil in the individual windings is approximately 2 K. For OF.. cooled transformers oil temperature gradient in windings is greater than the gradient of oil temperature in coolers, and systematic error is estimated to be approximately 10 K with an uncertainty of about 2 K.

2.8.2. Direct hot-spot winding temperature measurement

If the temperature of the hot-spot is measured directly with fibre optic thermometer, the hot-spot temperature rise is calculated as:

$$\Delta\theta_h = \overline{\Delta\theta_{o,r}} + \Delta\theta_{ho,r} \quad (46)$$

$\overline{\Delta\theta_{o,r}}$ is steady-state top-oil temperature rise in the last hour of heating with total losses and $\Delta\theta_{ho,r}$ is hot-spot winding temperature rise over top-oil recalculated to the rated current:

$$\Delta\theta_{ho,r} = \Delta\theta_{ho} \left(\frac{I_r}{I_{HC}} \right)^z \quad (47)$$

where the exponent z depends on the type of cooling (Table 3 in [1]), and $\Delta\theta_{ho}$ is winding hot-spot temperature rise over top-oil measured at current I_{HC} :

$$\Delta\theta_{ho} = \theta_h^* - \theta_o^* \quad (48)$$

Measurement uncertainty is then:

$$u(\Delta\theta_h) = \sqrt{[u_T(\overline{\Delta\theta_{o,r}})]^2 + [u_T(\Delta\theta_{ho,r})]^2} \quad (49)$$

$u_T(\overline{\Delta\theta_{o,r}})$ is calculated using equation (20), and $u_T(\Delta\theta_{ho,r})$ is on the basis of (47):

$$u_T(\Delta\theta_{ho,r}) = \frac{\Delta\theta_{ho,r}}{100\%} \cdot u_T(\Delta\theta_{ho,r})_{\%} = \frac{\Delta\theta_{ho,r}}{100\%} \cdot \sqrt{\left[\frac{u(\Delta\theta_{ho})}{\Delta\theta_{ho}} 100\% \right]^2 + [z \cdot u(I_{HC})_{\%}]^2} \quad (50)$$

Measurement uncertainty of winding hot-spot temperature rise over oil is calculated on the basis of (48):

$$u(\Delta\theta_{ho}) = \sqrt{[u(\theta_h)]^2 + \left[\frac{u(\theta)}{\sqrt{m}} \right]^2} \quad (51)$$

3. MEASUREMENT UNCERTAINTY AND DECISION MAKING

Measurement is a process which product is complete measurement result [5]. It consists of measured value $\{M\}$, standard measurement uncertainty $\{u\}$, coverage factor k and measurement unit $[M]$:

$$M = \{M \pm k \cdot u\} [M]. \quad (52)$$

Figure 1 shows the complete measurement result. The curve above is probability density function called Normal or Gaussian distribution. The area that encloses the curve above and the complete measurement result is equal to the probability that the true value of the measured quantity is within the complete measurement result (which is for $k = 2$ approximately 95%).

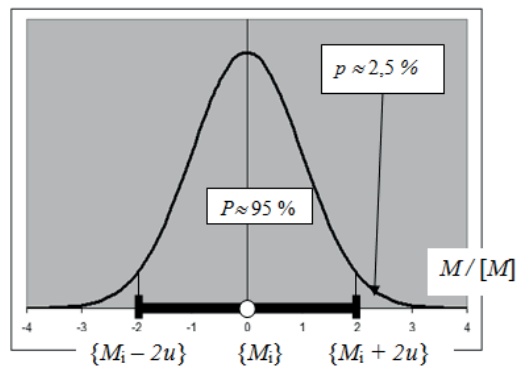


Figure 1. Complete measurement result and Gaussian probability density function

Measurement uncertainty is: (1) Universal and generally accepted numeric statement about the quality of the measurement results, (2) Condition for acceptance of the measurement results, (3) Main link in the chain of traceability, and (4) Basic parameter for making correct and reliable scientific and business decisions.

Due to measurement uncertainty, decision making on compliance of the measurement result with the specifications (limits) cannot be without risk of wrong decision. Therefore decision making is based on statistical tests. Statistical tests are procedures based on mathematical statistics that enable reasonable, objective and measurable decisions in cases of indeterminacy.

Figure 2 shows possible locations of complete measurement result in regard to a specified upper limit $\{UL\}$. For example $\{UL\}$ denotes guaranteed load losses, or guaranteed limit of top-oil or winding temperature rise. Between non-compliance and compliance zone is an area, width $4u$, called guard band (grey zone). For the measurement result in this indeterminate zone neither non-compliance nor compliance was demonstrated. Preferred formulations of assessment for cases shown in Figure 2 are:

a) **Compatible.** Measurement result marked with the letter A is compliant with the specification. It is likely that the measured property is below the upper specification limit value with probability greater than 95% (more specifically, 97.5%).

b) **Non-compatible.** Measurement result marked with the letter G is not compliant with the specification. It is likely that the measured property is above the specified limit with probability greater than 95% (more precisely, 97.5%).

c) **Indeterminate.** For the measurement results marked with B, C, D, E and F on the probability level of 95% is not possible to claim that the product meets or does not meet the specification.

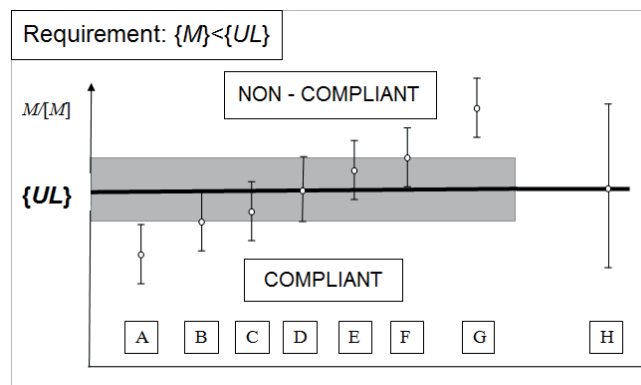


Figure 2. Assessment of compliance with an upper limit

Measurement result in grey zone can cause confusion, misunderstandings, disputes and costs. Practice needs simple solutions. A binary decision rule of conformity or non-conformity for all possible measurement outcomes is an answer. At this time widely accepted binary rule does not exist. Traditional decision rules, as well as decision rules that take into account measurement uncertainty in various ways [12] are used.

According to traditional decision rule, if the measured numerical value is less than the upper limit value, the measured result is compliant, and if not it is non-compliant (no matter how accurate measurement result is). In traditional decision rule measurement uncertainty is not taken into account. The consequence is that traditional decision rule does not guarantee acceptance of only those products that comply with the specification, or the rejection of only those products that do not comply with the specification. For example, if the measured value is equal to the limit value, there is a 50% probability that the product meets and the same probability that does not meet specified requirement. In addition, using traditional decision rule there is possibility of unacceptably large exceeding of the limit value (letter H in Figure 2). This decision-making rule is called shared-risk (in [12] is used the term "simple acceptance method", and in [13] "accuracy method").

The decision rules that take into account the measurement uncertainty use the so-called guard bands in various ways [12]. These rules are motivating to reduce measurement uncertainty and increase the quality of the measurement results. Reduction of uncertainty of measurement results reduces the grey zone, and are consistent with two of the eight major principles of quality management standard [11], that the organization must constantly improve processes (in this case measurement) and that the decision-making should use factual approach.

The new standard [1] for the first time requires that the test reports contain expanded uncertainty ($k = 2$) of characteristic temperature rises (steady-state temperature rise of top-oil, average winding temperature rise and hot-spot winding temperature rise), but the procedure for estimation of measurement uncertainty in the standard is not given. In addition, the standard notes that the uncertainty is listed as information only and is not used in decision-making. This means that, based on [13] traditional decision-making rule is used with all its shortcomings.

4. CONCLUSION

The paper points out an important fact that the new standard requires measurement uncertainty estimation for guaranteed values of temperature rise, but gives no estimation procedure. In the paper the procedure for measurement uncertainty estimation is proposed and suggestion is given for appropriate decision making. Also the criterion for stagnation $1K/h + 3h$ is criticized and it is experimentally showed that two formulas for winding average temperature determination are redundant. The new standard is incomplete and sketchy. It is not motivating in the sense of reduction of measurement uncertainty and increase of measurement results quality. In the next version we expect the procedure for estimating measurement uncertainties and if the traditional method of decision-making will be retained, at least the information of maximum permissible uncertainty of temperature-rise measurements.

REFERENCES

- [1] IEC 60076-2, Power transformers – Part 2: Temperature-rise for liquid-immersed transformers, February 2011
- [2] V. Kuprešanin, Z. Godec, I. Roketinec, „Temperature rise tests of oil-immersed power transformers according to new IEC and analysis of changes, A2-05, 11. HRO CIGRE, Cavtat, 2013. (in Croatian)
- [3] IEC/TS 60076-19, Power transformers – Part 19: Rules for the determination of uncertainties in the measurement of the losses on power transformers and reactors, March 2013
- [4] IEC 60584-2, Thermocouples – Part 2: Tolerances, January 1982
- [5] ISO/IEC Guide 98-3:2008, Uncertainty of measurement -- Part 3: Guide to the expression of uncertainty in measurement (GUM:1995)
- [6] Z. Godec, "Determination of steady-state temperature rises of power transformers", IEE Proceedings, Vol. 124, Pt. A, No. 10, December 1987
- [7] Z. Godec, „Steady-state temperature rise determination“, *Automatika* 33(1992)3-6, 129-134
- [8] Z. Godec, „Measurement of large power transformer winding temperature by inductive voltage correction method, *ETZ Archive*, 11(1989)2, 63-70
- [9] IEC 60076-1 Power transformers, Part 1: General, April 2011
- [10] C. M. Shakarji, „Least-Squares Fitting Algorithms of the NIST Algorithm Testing System“, National Institute, 1998

- [11] ISO 9001: 2008, Quality management system - Requirements
- [12] JCGM 106: 2012, Evaluation of measurement data – The role of measurement uncertainty in conformity assessment
- [13] IEC Guide 115: 2007, Application of uncertainty of measurement to conformity assessment activities in the electrotechnical sector

Robert Sitar
Končar – Electrical Engineering Institute Inc.
rsitar@koncar-institut.hr

Žarko Janić
Siemens E T TR LPT GTC RES
Končar - Power Transformers Ltd.
zarko.janic@siemens.com

APPLICATION OF THE TEMPERATURE-TIME METHOD FOR MEASUREMENT OF LOCAL POWER LOSSES IN TRANSFORMER STEEL PARTS

SUMMARY

Paper presents an application of temperature-time method for measurement of local losses in magnetic steel. Developed measurement system is described with focus on design of sensors and choice of instruments. Chosen equipment is tested on a DC circuit designed for measurement of losses in aluminum and copper conductors. Same measurement system is used for local loss measurement on magnetic steel rings. Measurement errors due to non-uniform loss distribution inside magnetic steel and heat dissipation to surrounding medium are analyzed and estimated.

Key words: local power loss, temperature-time method, magnetic steel, thermocouple, coupled calculation

1. INTRODUCTION

Stray losses in constructional steel parts are an important topic in transformer design process. High values of local loss densities in constructional elements can lead to temperature rises that can endanger transformer operation and lead to its failure. In order to determine local loss values, system with sensors for local measurement has to be used. One of appropriate methods for such measurements is the temperature-time method. The method relies on the fact that after a body has settled at a steady state temperature and internal heat source is suddenly removed or applied, initial rate of temperature change at any point is proportional to heat input (loss density) at that point. Correct application of this method thus allows both losses and their spatial distribution to be determined. So far method has found its application in measurement of losses in silicon-steel strips usually used for transformer cores [1] – [3]. Similar system has been used for measurement of stray losses in transformer tanks [4] and iron losses in induction motors [5].

2. TEMPERATURE-TIME METHOD

A possibility for determining local loss in constructional steel parts is to measure transient temperature-time curve and determine its initial slope. Example of determining the initial slope of a heated body is shown in Figure 1.

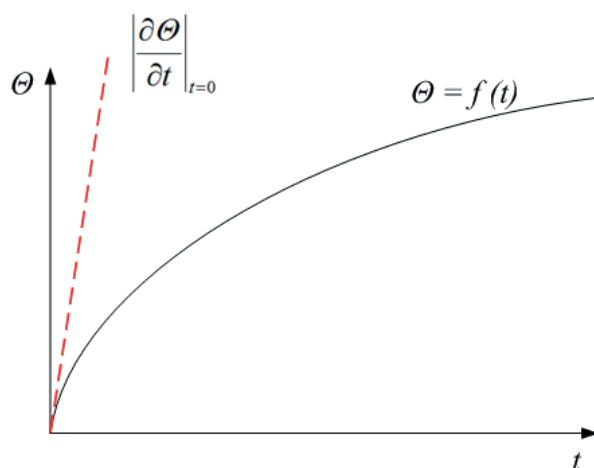


Figure 1 – Principle of determining initial slope of a heating curve

The curve shown in Figure 1 can be mathematically expressed by the heat diffusion equation in a simplified form

$$p = c\rho \frac{\partial\Theta}{\partial t} + q \quad (1)$$

where p is generated heat (power loss), Θ body temperature, c thermal capacitance, ρ mass density and q heat dissipated to surrounding regions. Surrounding regions to which heat dissipates are cold metal bodies (where generated heat is much lower than at the measurement point) and surrounding fluids (which cool the heated body by convection or radiation). Dissipated heat highly depends on temperature differences between the measurement point and surrounding regions. As temperatures of heated bodies grow dissipated heat from measurement points become higher and cause the initial straight line to turn into an exponential curve. So, if initial conditions consider all metal parts and the surrounding fluid at equal temperatures, for $t = 0$ it can be stated $q = 0$, and expression (1) can be written as

$$p = c\rho \left. \frac{\partial\Theta}{\partial t} \right|_{t=0} \quad (2)$$

Therefore, heat loss at any point can be obtained by multiplying the initial temperature gradient, mass density and thermal capacitance of the material under test. However, it is important to determine initial section where temperature-time curve can be considered as a straight line because of negligible heat dissipation. This will highly depend on type of convection cooling the heated parts are exposed to and how non-uniform power losses are in the body observed. The easiest solution would be to thermally isolate the observed body and to use the method only in cases of uniform heat sources inside the body. However, this is not easy to achieve in practice, such as in cases of power transformer.

3. DETAILS AND VERIFICATION OF THE MEASUREMENT SYSTEM

The first step when making a measurement system for the temperature-time method for loss measurement is to choose sensors for temperature measurements. The probes should be robust and have good thermal connection with the measurement point. Another important requirement is to be able to measure temperature instantly. Thus, sensors should have negligible heat capacity as recommended in [1] and [2]. To meet all of these requirements thermocouples were made from 0,08 mm thick constantan and copper wires. When working with AC power sources it is obligatory to twist the two wires together, so that AC pick-up in inductive loops of sensor leads is minimized. The measurement junction was placed and fixed on a point where losses are to be measured, while the reference junction was inserted in a water bath at a stable and known temperature. The main disadvantage of thermocouples is that they have relatively weak signal. For example, copper-constantan (T-type) thermocouples have sensitivity of about 43 $\mu\text{V}/^\circ\text{C}$. In order to detect temperature changes of 0,001 $^\circ\text{C}$, a so-called

nanovoltmeter with resolution of 1 nV was used. Thermocouple voltage was recorded every 0,2 s and processed by a LABVIEW [6] application on a computer. Full developed measurement system is shown in Figure 2.

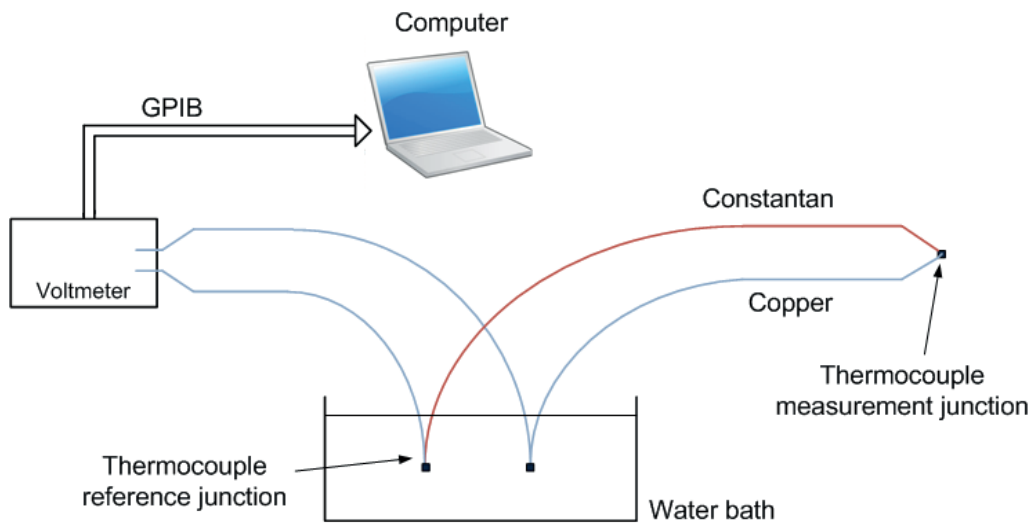


Figure 2 – Measurement system

In order to test applicability of chosen sensors and instrument for the loss measurement method, measurement system was first tested on aluminium and copper strips. Thermocouple measurement junction was fixed in the middle of 1000 mm long copper and aluminium strips, as shown in Figure 3. Circuit breaker was used to apply a DC voltage source suddenly to the strips, while resistors were used to change current in the circuit.

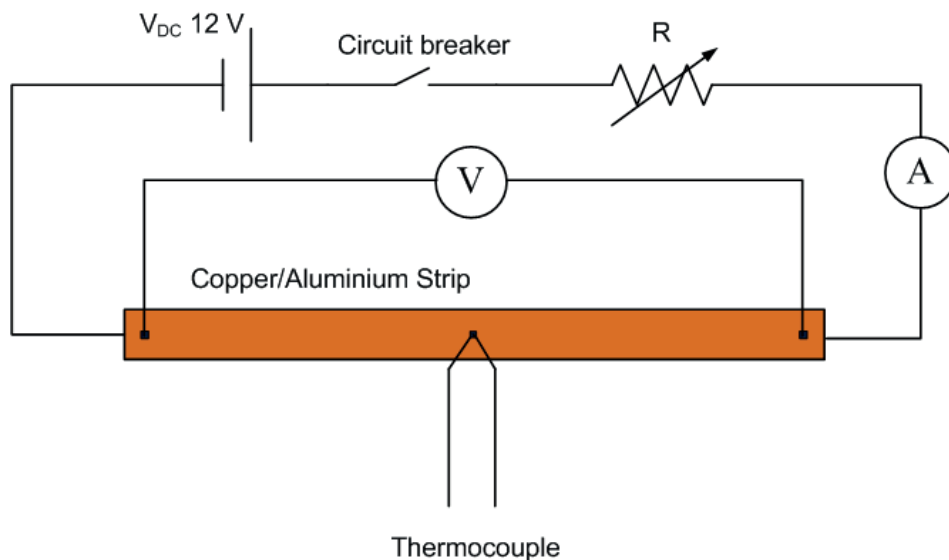


Figure 3 – Measurement of losses on copper and aluminium strips

An example of a recorder temperature-time curve is shown in Figure 4. Initial gradient for the curves was calculated from the temperature change in $\Delta t = 1 s$ after the voltage source was applied. From the measured temperature gradient and expression (2) value of local losses in W/m^3 were evaluated. Specific heat capacity of copper was $385 J/kgK$ and of aluminium $890 J/kgK$. Mass density of copper was $8940 kg/m^3$ and of aluminium $2700 kg/m^3$. At the same time current and voltage of tested conductors were measured. Total losses of conductors were evaluated by wattmeter and compared with results from the temperature – time method in Table I.

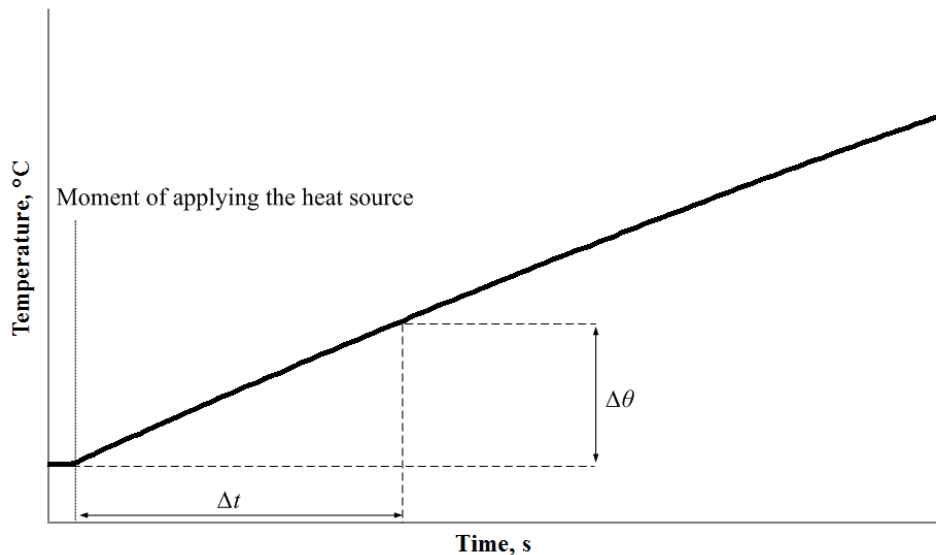


Figure 4 – Principle of determining temperature-time gradient

Table I – Measured losses in aluminium and copper conductors

Conductor	Current, A	Measured gradient, °C/s	Total losses, W		Ratio (1)/(2)
			Temperature-time method (1)	Wattmeter (2)	
Copper 1,0 x 15 mm ²	81,5	0,143	6,64	6,83	0,97
Copper 5,6 x 4,0 mm ²	98,3	0,098	6,80	6,80	1,00
Aluminium 2,0 x 15 mm ²	80,8	0,088	5,71	5,51	1,04
Aluminium 9,0 x 2,5 mm ²	95,0	0,230	12,43	11,30	1,10

Results from both measurement methods showed good agreement. Experiment has confirmed the suitability of thermocouples as sensors and nanovoltmeter as an instrument for local power loss measurement by the temperature-time method.

Here it should be emphasized that losses that were measured were distributed uniformly inside the heated object (copper/aluminium conductors). This is not the case when losses are caused by eddy currents in thick magnetic materials. Due to small skin depth (from 1 to 3 mm) of magnetic steel parts, losses are localized in a thin layer at surface of a magnetic part. Cold metal interior cools the surface layer, making value of the dissipated heat from equation (1) substantial.

Experiments with conductors were done in air. In case of transformers, metal parts are in most cases in contact with oil. Convection cooling by oil is much more efficient than convection by air. This can have additional influence on measurement results of the temperature-time method.

4. MEASUREMENT AND CALCULATION OF LOSSES IN MAGNETIC STEEL

When heat sources are non-uniform, errors in measured losses will occur if the temperature rise being measured is not completed before appreciable heat diffuses to or from other parts of different temperatures. The errors in these cases can be estimated by analysis of heat transfer on a simple geometry.

An experimental ring made of magnetic steel wound throughout its circumference with a copper conductor was considered as a model for evaluating possible measurement errors. Configuration is shown in Figure 4. Inner ring diameter D_i was 325 mm, outer diameter D_o 385 mm. By changing the thickness of the ring b , it was possible to better understand the influence of dissipation of heat to cold metal interior on the error of measurement. Coil wound around the ring was excited by a sinusoidal current source of frequency 50 Hz. Magnetic permeability of magnetic steel was modeled as a single-valued B-H curve, while electrical conductivity was 6,56 MS/m.

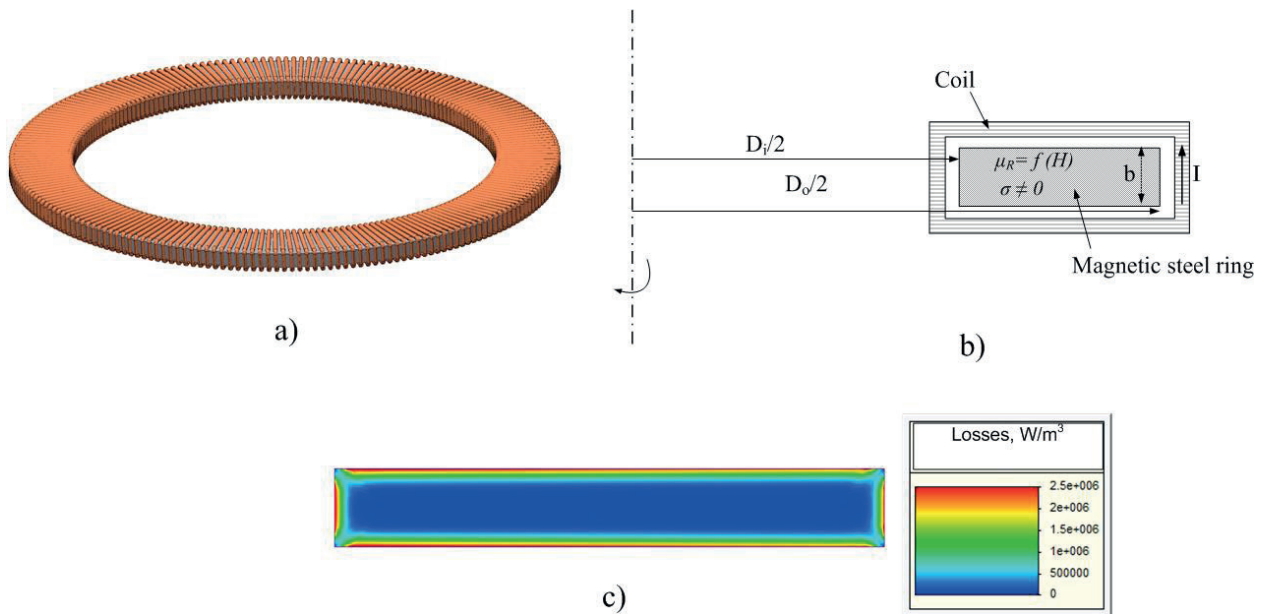


Figure 4 – a) Experimental magnetic steel ring, b) 2D model in MagNet, c) Loss distribution inside the ring (MagNet)

The model from figure 4 b) was also analyzed in thermal finite element method (FEM) software ThermNet [7]. Losses calculated in MagNet represented heat sources in ThermNet. Using a time “step-by step” (Transient) calculation in ThermNet it was possible to calculate temperature-time curves for different losses induced inside the ring. Heat dissipation to ambient was neglected in order to solely observe influence of non-uniform distribution of losses inside steel to the measured gradient. Since the losses were distributed non-uniformly it was necessary to analyze temperature-time curves on various positions inside the ring. The most interesting temperature-time curves were on the surfaces of the ring (where measurements with thermocouples can be made). Figure 5 a) shows the position where temperature-time curves were analyzed. In Figure 5 b)-c) calculation results are shown for 4, 8 and 12 mm thickness of steel ring. Curves show ratio of total ring losses determined from the initial slope of temperature-time curve after time Δt to total losses calculated by MagNet. Losses from temperature-time curves were evaluated by using expression (2) and considering temperature gradient as uniform inside the ring volume. Density of steel was 7850 kg/m^3 and specific heat capacity 460 J/kgK . Curves are shown for various total losses inside the ring. Losses in the ring were regulated by changing the current through the coil wound around the ring.

For three different thicknesses of the ring it is quite clear that after 5 to 10 seconds total losses determined from temperature gradient of the ring will not differ more than 10 % from calculated losses by MagNet. This is an interesting result from the practical point of view. Measurements can be made after couple of seconds when temperature rise becomes significant (from 0,1 to 1,0 °C) and enables a more accurate estimation of the initial temperature gradient.

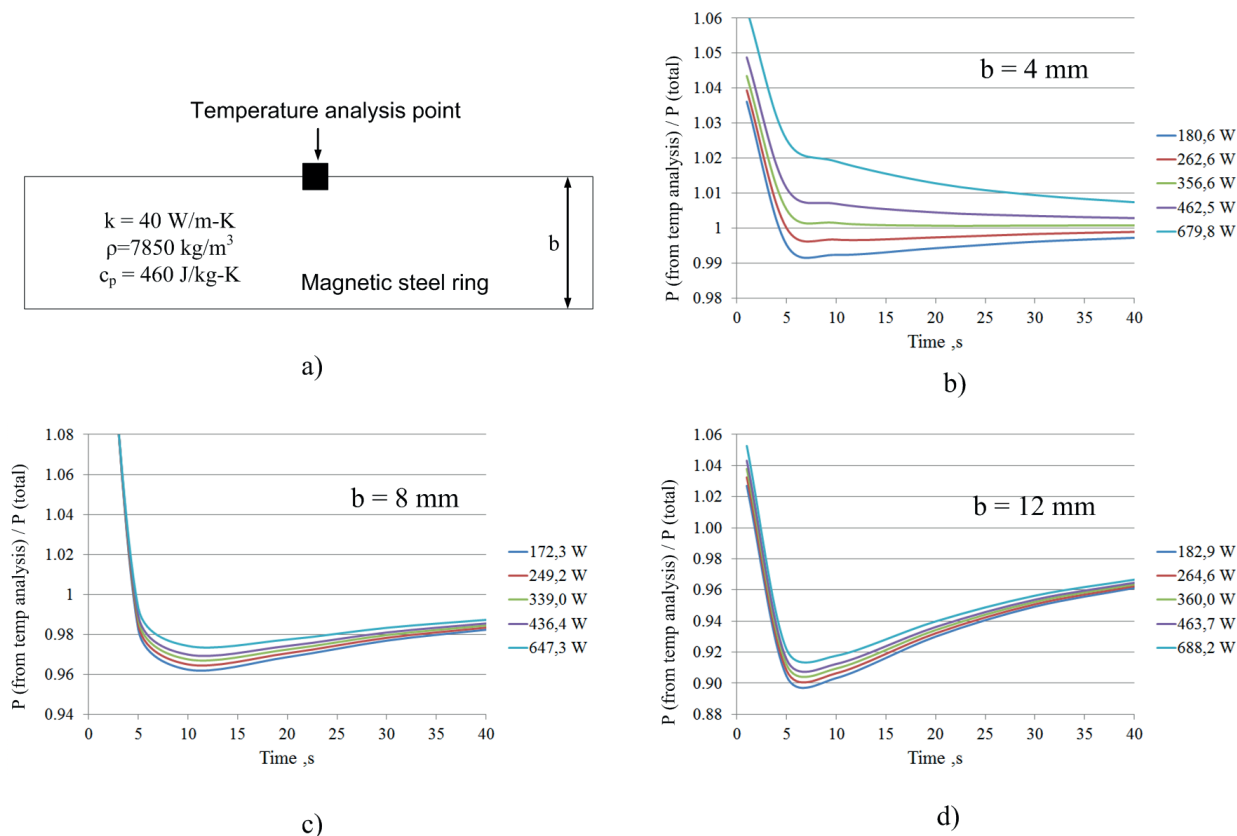


Figure 5 – Ratio of losses determined from temperature-time curves at different time instants to total losses

Model used for numerical calculation has been built and tested in laboratory. Basic idea was to measure total losses inside the ring (similarly as shown for copper and aluminium conductors) and compare with measurement from the temperature-time method. Experimental setup is shown in Figure 6.

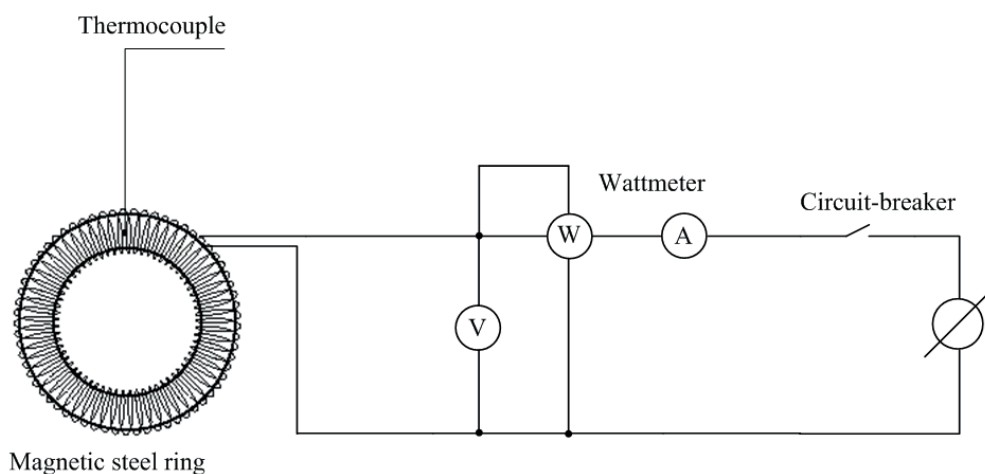


Figure 6 – Experimental setup for application of temperature-time method on magnetic steel ring

Total losses in the model were measured by a wattmeter and compared to measured losses by the temperature-time method. Measurements were made with steel ring in air and immersed in transformer oil. Usually transformer steel parts are in contact with oil, so influence of cooling conditions that are usually present in practice were observed. Steel ring in laboratory with thermocouples fixed on its surface is shown in Figure 7. The ring had the same inner and outer diameter as the numerical model, while the thickness was 8 mm. Coil wound on the steel ring had 100 turns. Clearances between adjacent turns of the coil were made in order to enable easier fixing of thermocouples on steel surface.



Figure 7 – Magnetic steel ring used for experiment

Results of temperature rise measurements in air and oil are shown in Table II. Results are presented for different values of magnetic field in the middle of the ring. Initial gradient of temperature-time curves was calculated from the temperature change $\Delta t = 10$ s after the voltage source was applied

Table II – Measurement results on magnetic steel

Magnetic field, A/m	Wattmeter losses (1), W	Air		Oil	
		Temperature-time method (2), W	Ratio (2)/(1)	Temperature-time method (2), W	Ratio (2)/(1)
2764	191,0	181,7	0,951	167,5	0,877
3430	272,6	261,6	0,960	244,9	0,898
4121	365,5	351,8	0,963	326,0	0,892
4825	465,4	452,3	0,972	425,3	0,914
6150	673,1	671,4	0,997	625,0	0,929

Results of the temperature-time method in air agree within 5% of measured wattmeter losses. Experiment has shown that when magnetic steel is immersed in oil, due to heat dissipation from magnetic steel to oil, measured temperature gradient decreases up to 8%. From practical point of view, this is an important result, since it is hard to evaluate heat transfer coefficients at positions where thermocouples are to be placed, especially in cases of small temperature differences between heated object and surrounding fluid.

5. CONCLUSION

Temperature-time method has found its application in various materials that are used in electrical machine and transformers. The paper has shown the potential of its application for determining local losses in magnetic steel usually used for constructional metal parts of transformers. Although losses in steel are mostly non-uniform and hard to measure locally, a simplification of the measurement method was proposed which solves this practical constraint. From results of electromagnetic and thermal FEM calculations it was possible to determine appropriate time instant at which temperature gradient can be calculated. From measured temperature gradient it was possible to determine total losses in the geometry and compare with wattmeter measurement. Difference between two measurement methods was not higher than 5 %.

Additionally, difference between measurement in air and oil was pointed out. Convection cooling by oil had additional influence on measured temperature when sensors were fixed on steel surfaces. Differences between measured temperature gradient in air and oil were not higher than 8 %.

Future research will be focused on application of the temperature-time method on transformer steel parts exposed to air and oil cooling (e.g. tanks) and comparison with FEM magnetic and thermal calculation.

REFERENCES

- [1] A. J. Gilbert, *A Method of Measuring Loss Distribution in Electrical Machines*, Proc. IEE - Part A: Power Engineering, vol.108, no.39, pp.239-244, June 1961
- [2] D. A. Ball, H. O. Lorch, *An Improved Method of Measuring Local Power Dissipation*, J. Sci. Instrum., vol. 42, pp. 90-93, 1965
- [3] H. Hamzehbahmani, A. J. Moses, F. J. Anayi, *Opportunities and Precautions in Measurement of Power Loss in Electrical Steel Laminations Using the Initial Rate of Rise of Temperature Method*, IEEE Transactions on Magnetics, Vol. 49, No. 3, pp.1264-1273, March 2013
- [4] N. Niewierowicz, J. Turowski, *New Thermometric Method of Measuring Power losses in Solid Metal Parts*, Proc. IEE, Vol 119, No. 5, pp. 629-635, May 1972
- [5] A. Bousbaine, *A Thermometric Approach to the Determination of Iron Losses in Single Phase Induction Motors*, IEEE Transactions on Energy Conversion, Vol. 14, No. 3, pp 277-283, September 1999
- [6] National Instruments LabVIEW, <http://www.ni.com/labview/>
- [7] Infolytica Corporation (2014), ThermNet & MagNet 7.4.1., <http://www.infolytica.com/>

Ahmed Gamil
SGB Regensburg, Germany
R&D Head Assistance
ahmed.gamil@sgb-trafo.de

Franz Schatzl
SGB Regensburg, Germany
Head of Technical Dept.
franz.schatzl@sgb-trafo.de

NEW METHOD TO OPTIMIZE NO-LOAD NOISE OF POWER TRANSFORMERS BASED ON CORE DESIGN & TRANSFORMER OPERATING CONDITIONS

SUMMARY

This paper introduces a new algorithm to calculate and optimize no-load noise (sound pressure) of power transformers, and to identify iron sheet parameters. The calculation consists of two steps: the **1st step** consists in calculating an initial sound pressure level (A-Evaluation) which has approx. 70 % accuracy within a tolerance interval of ± 2 dB (A). The **2nd step** consists in estimating the expected deviation from the initial calculation to reach 90 % accuracy in the final results. This deviation could be due to material handling, quality tolerance, core manufacturing, etc.

The optimization process consists of two parts: the **1st part** takes place before choosing a certain iron sheet for calculation to identify the sheet parameters required for computational accuracy ("Sheet Optimization"). The **2nd part** consists in considering a core design with an undesirable sound pressure level in order to reduce it to an acceptable limit. This part takes into account the other limitations such as no-load losses and transformer dimensions ("Design Optimization").

For new iron sheets in the market, there is no measurement history to rely on. However, the algorithm is also capable of identifying the sheet parameters for calculation based on the available algorithm data base and the magnetostriction measurements of the iron sheet manufacturer.

Key words: Sheet parameters, Limitation Factor, Magnetostriction, Noise Factors, 3D Parameter Model.

1. INTRODUCTION

1.1. Past & Present State

The problem of no-load noise of power transformers is discussed only in a very small number of items of transformer literature. In these cases, the problem handling process was focused in most cases on the accuracy of measurements. The estimation of the measured sound level of the core was introduced in analogy to the magnetostriction behavior of the material using empirical parameters.

Using the simulation tools which some software programming companies offer helps to a certain extent. There is no definition of the probability of deviation and the effective parameters inside these tools influence the variation of the sound pressure level to a certain extent. There is no guarantee for the final result. Moreover, in view of the time needed for one simulation case, these tools are not suitable for daily use in transformer manufacturing.

1.2. Need for a new technology

The acceleration in market and ecological requirements regarding noise restrictions and noise limitation obliges every transformer manufacturer to produce low-noise transformers.

In this paper, a new method is introduced to estimate no-load noise of power transformers (sound pressure) via direct calculation according to the iron sheet type, the core design, and the transformer operating condition. This new technology is capable of providing a 90 % precise result in practically no time and could be used in a simple calculator if the required information is available.

2. THE NEW METHOD

2.1. Calculation

2.1.1. Design influencing factors & iron sheet parameters

For a long period of time, the main determining factors for the sound level in cores has been the flux density and the limb length in analogy to the length variation detected by magnetostriction measurements. Later on, in terms of improvement of the calculation, the core weight was included for practical reasons.

Based on the transformer design, the new algorithm has constructed the whole design factors, which will influence the sound pressure level by 0.3m besides taking into account the flux density, namely:

- Core Volume Factor (V_f)
- Core Weight Factor (G_f)
- Tank Factor (K_f)

The initial value of the sound pressure level (SPL_{ini}) at a distance of 0.3 m is calculated by a function of these factors and the flux density.

$$SPL_{ini}(0.3m) = f(B, V_f, G_f, K_f, P_{1...N}) \quad \text{dB (A)} \quad (1)$$

Where

- B: Flux Density [T]
P_{1...N}: Iron Sheet Parameters

Through the optimization process explained in section 2.2, iron sheet parameters are detected as unique for each iron sheet type. Table I shows an example for different sheet types from different manufacturers.

Table I – Iron Sheet Parameters

Sheet Type	Thickness	P1	P2	P3
Type 1	0.23 mm	28,756	17,734	-3,906
Type 2	0.23 mm	31,189	19,819	-48,789
Type 3	0.23 mm	42.114	21.022	-3.317

It is evident that each iron sheet type has its own sheet parameters, which will be used according to the choice of sheet to determine the final value of the no-load noise of the transformer. However, equation (1) results in a so-called “Initial Value (dB_{ini})” which has a probability of approx. 70 % within a tolerance interval of $\pm 2dB$.

To reach a higher accuracy, the calculation should provide a final value which covers the reasons for the deviations (e.g. different sheet coil qualities, core production tolerances, measurement deviations, etc.). By relating these reasons for deviation to the core design and the operating condition, the deviation for each transformer design can be identified precisely.

2.1.2. Limitation factor of deviation

A certain “Deviation OffSet” (DOS) is detected as a function of the operation flux density [T] and a design limitation factor [m] based on core dimensions. This detection is taking place over the 3D surface illustrated in figure 1.

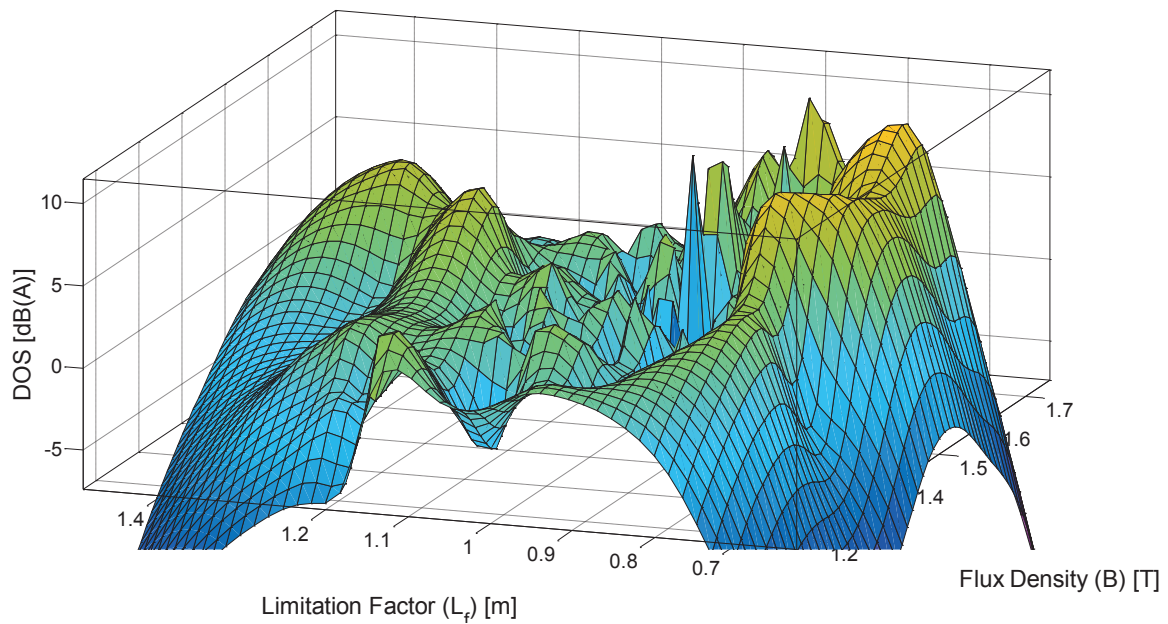


Figure 1 – Deviation surface for a sheet thickness of 0.23 mm

Depending on the value of DOS, a final sound pressure level is recognized as explained in equation (2):

$$SPL_{fin}(0.3m) = SPL_{ini}(0.3m) + DOS \quad \text{dB (A)} \quad (2)$$

$$DOS = f_{surf}(B, L_f) \quad (3)$$

The density and probability functions show the increase in computational accuracy by using the deviation surface. Without including DOS, the probability of deviation within a tolerance of $\pm 2\text{dB}$ amounts to 73.6 % whereby this probability is increased to 91.5 % as shown in figure 2(a, b) if DOS is included.

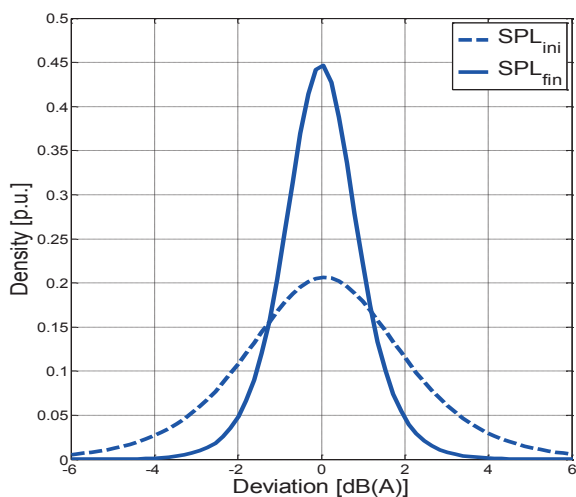


Figure 2a

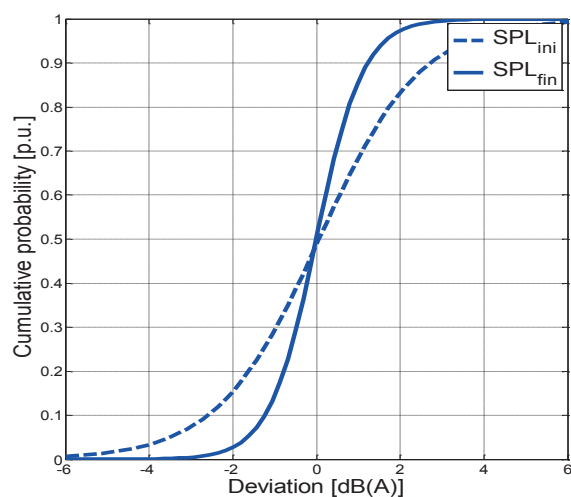


Figure 2b

Figure 2 – Density (2a) and probability (2b) functions of sheet thickness 0.23 mm

2.2. Optimization

2.2.1. Identification of known iron sheet

Depending on the measurement history of the no-load noise of power transformers, the parameters of the iron sheet used in the past for building the cores (“Known Iron Sheet”) can be identified. The algorithm uses the available information (measured sound pressure, design factors) to determine the iron sheet parameters, which together with the design factors result in the highest probability of a deviation of $\pm 2\text{dB}$ between the measured and the calculated sound pressure level. The flow chart of figure 3 shows the process of detection of each iron sheet type.

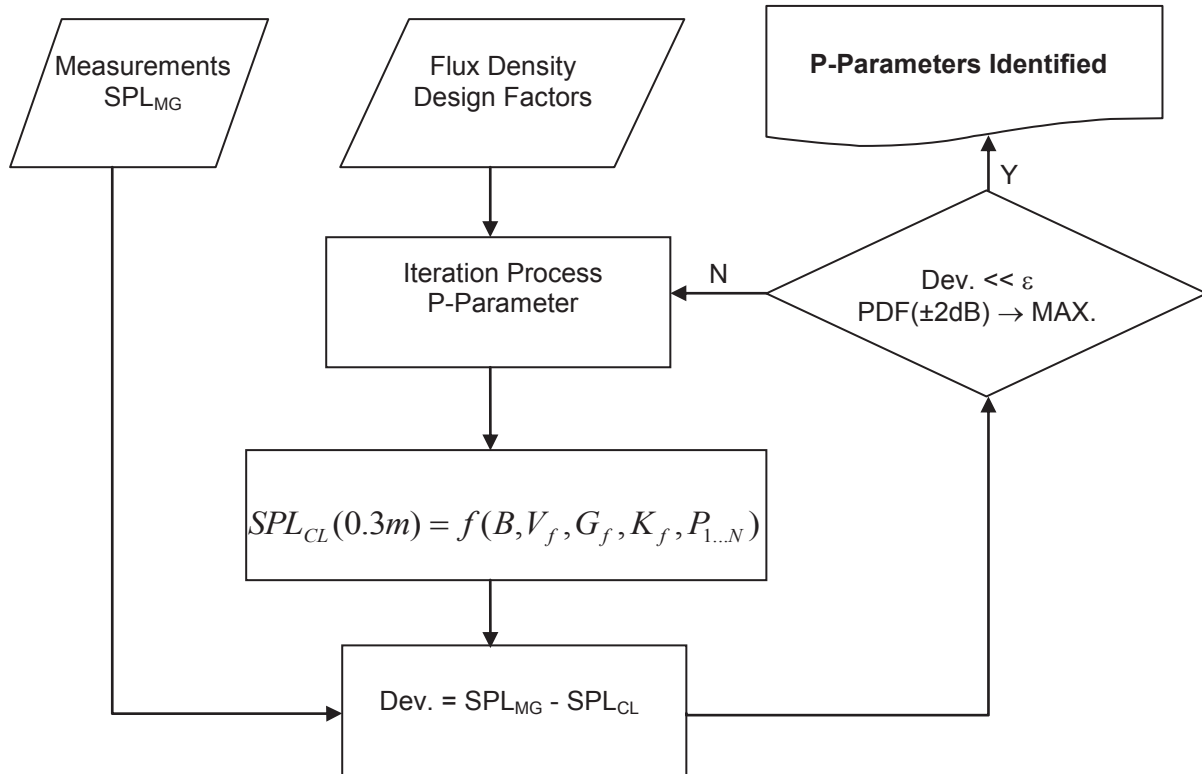


Figure 3 – Flow chart explaining the identification of iron sheet parameters

Where,

SPL_{MG} : Measured sound pressure level of different designs at a distance of 0.3 m.

SPL_{CL} : Calculated sound pressure level based on equation (1) during the iteration process.

PDF : Probability Distribution Function for adjusting the computational accuracy.

Although this process requires a certain extent of measurement history, this history could start from 3 different transformer designs with sound pressure measurements between 1.1 and 1.7T as a starting point for identifying the sheet parameters. However, the implementation of DOS requires at least 50 measurements.

In case of introducing iron sheet types without measurements history (“Unknown Iron Sheet”), i.e. if there is no transformer in which this material is used as a reference, another method is required to identify the sheet parameters, as will be explained in subsection 2.2.3.

2.2.2. Design optimization

According to sound level regulations, which have been subject to rapid changes recently, and because of the introduction of new manufacturers of iron sheet types, there is often a request for a previously manufactured transformer, however with enhanced noise restriction. For example, some customer had ordered a transformer two years ago with a guaranteed sound pressure value of 48 dB (A).

The calculation had provided a value of 46.9 dB(A) with a safety margin of 90 % (10 % risk of violation of that limit). The sound pressure measurement resulted in 46.3 dB(A).

The same customer asked again for the same transformer, however, with a new guaranteed SPL value of 46 dB(A). The target now consists in determining the design factors which result in an SPL reduction to 45 dB(A) with the same safety margin of 90 %. It should be kept in mind that the other limitations (e.g. no-load losses) should not be affected.

The algorithm fixes the value of K_f and tries to optimize the other design factors with the flux density to reach the desired $SPL_{fin} = 45$ dB(A). **That means reducing the sound level by 2 dB(A)**. The core of that transformer was modified successfully so that SPL reached the required value. The SPL measured at a distance of 0.3 m was 45.6 dB(A). Table II shows the design factors before and after optimization.

Table II – Design Factor Optimization

Design factors	Before optimization	After optimization	Change in %
B	1.573	1.512	-3.88
V_f	-0.0319	-0.0481	-3.66
G_f	-0.5858	-0.5877	-0.44
K_f	-0.415	-0.415	0.00

Even if this process takes no time to obtain these results also graphically as shown in figure 4, this optimization process is performed in critical situations where the use of a specified iron sheet is mandatory (normally origin-dependent). In most cases, another iron sheet from our data base is chosen instead, which is known as a lower noise sheet. However, for cost-saving reasons, it is frequent practice, due to sudden price increases, to change the iron sheet type used previously and to replace it by a cheaper one to keep the transformer price in an acceptable range.

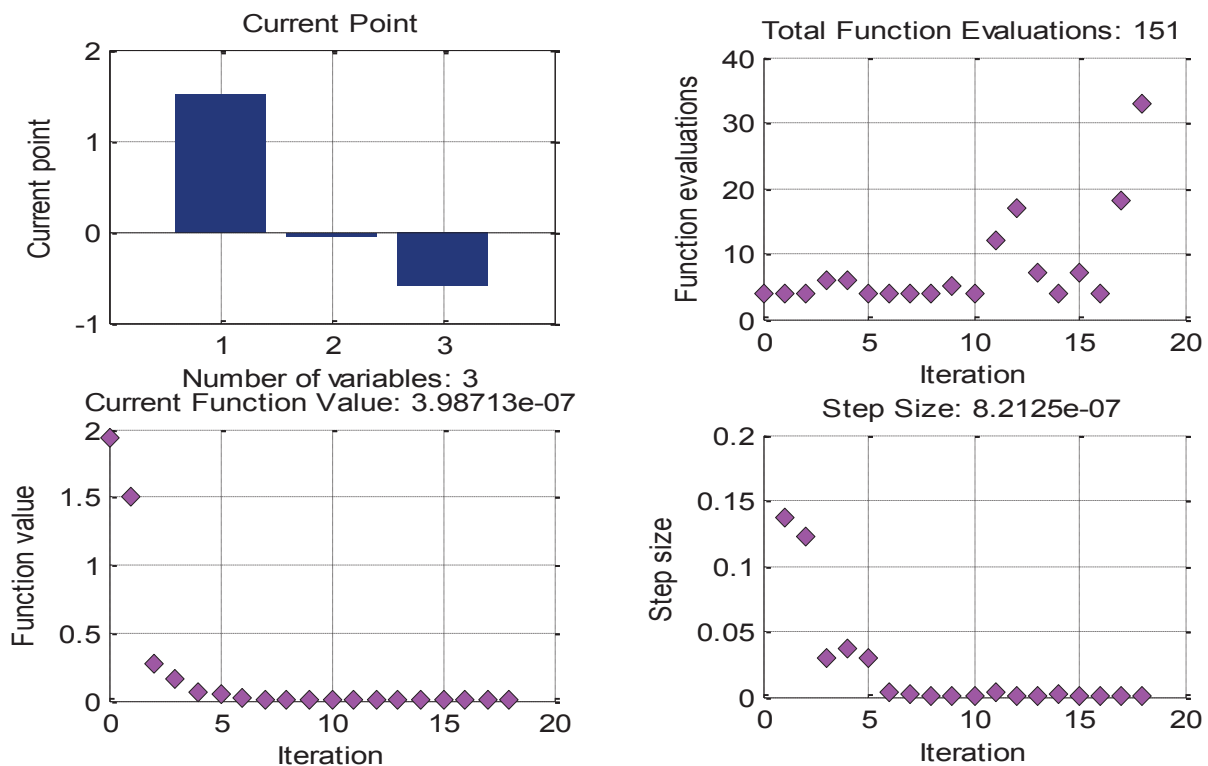


Figure 4 – Graphical illustration of the iteration process during design optimization

2.2.3. Identification of unknown iron sheet using the magnetostriction factor

Iron sheet manufacturers work continuously on improving the quality of their materials regarding both no-load losses and no-load noise. Therefore, almost every year, new iron sheet types are introduced into the transformer market at more attractive prices. Besides, iron sheet manufacturers use to confirm that the new sheet type in question is a low-noise type, based on their magnetostriction measurements.

On the part of transformer manufacturers, it is necessary to identify the sheet parameters in order to realize at least the initial SPL of the entire manufactured core using this new type. This is not possible because there is no measurement history of that new sheet. The information available is:

- Measurement history of Known Iron Sheets,
- Magnetostriction Measurements of Known Iron Sheets and
- Magnetostriction Measurement of Unknown Iron Sheet (new type).

Based on this information, the new algorithm is capable of detecting the iron sheet parameters for the new sheet type. By using the magnetostriction measurements, the algorithm calculates a so-called Magnetostriction Factor (M_f) which is recognized as characteristic value of the sheet. The available history of no-load noise measurements makes it possible to illustrate the 3D-Parameter Surface shown in figure 5 depending on sheet thicknesses and magnetostriction factors.

In case of new sheet types, the magnetostriction factor is determined from the magnetostriction measurements which are made available by the iron sheet manufacturer. Together with the known sheet thickness, the iron sheet parameter is recognized on the 3D-Parameter Surface. Figure 5 shows an example of detecting the volume factor parameter.

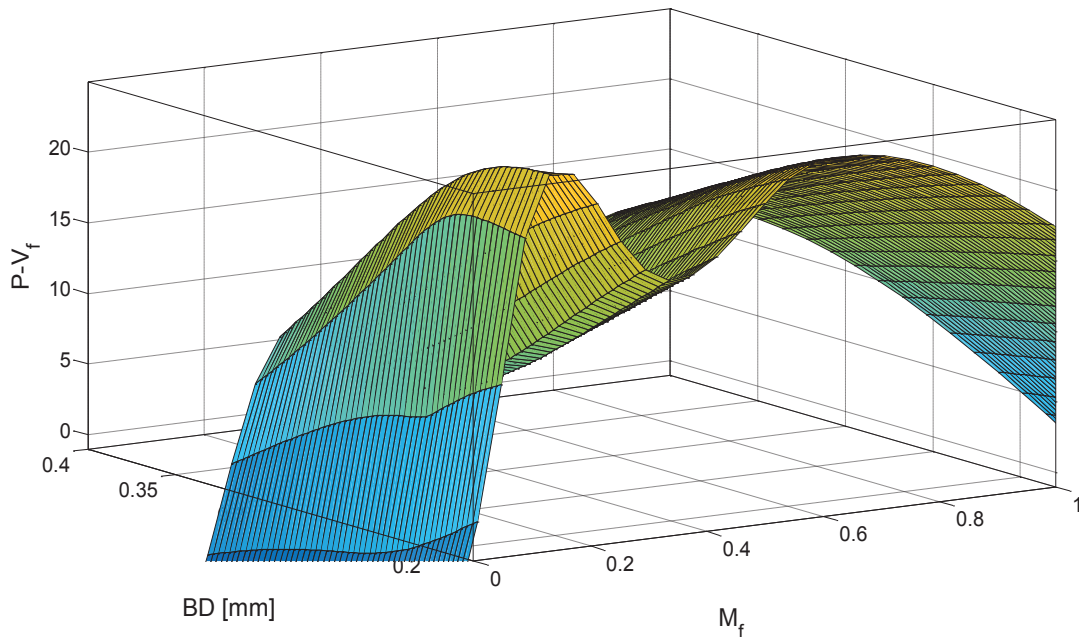


Figure 5 – 3D-Parameter Surface to detect sheet parameter for new types

One should keep in mind that the resulting parameter will construct equation (1), i.e. there is no way to detect DOS unless measurement data is available. Nevertheless, this is a good starting point to have an indication about the core noise performance of a new iron sheet type without having any past history of measurements. Table II shows the results of using two new iron sheets compared to the measurements and guaranteed values.

Table III – Adjusting Sheet Parameters

New Iron Sheet Types	Calculation (SPL_{ini})	Measurement (SPL_{MG})	Deviation
Type 1	53.2 dB(A)	51.9 dB(A)	-1.3 dB
Type 2	46.6 dB(A)	49.2 dB(A)	2.6 dB

3. RESULTS

3.1. Optimization Results

The results of the entire optimization process are clearly shown in figure 6 as an example of quality control based on the probability distribution of the measured deviation. If a higher degree of accuracy is required to avoid exceeding guaranteed values involving penalties, quality B will be preferred to quality A.

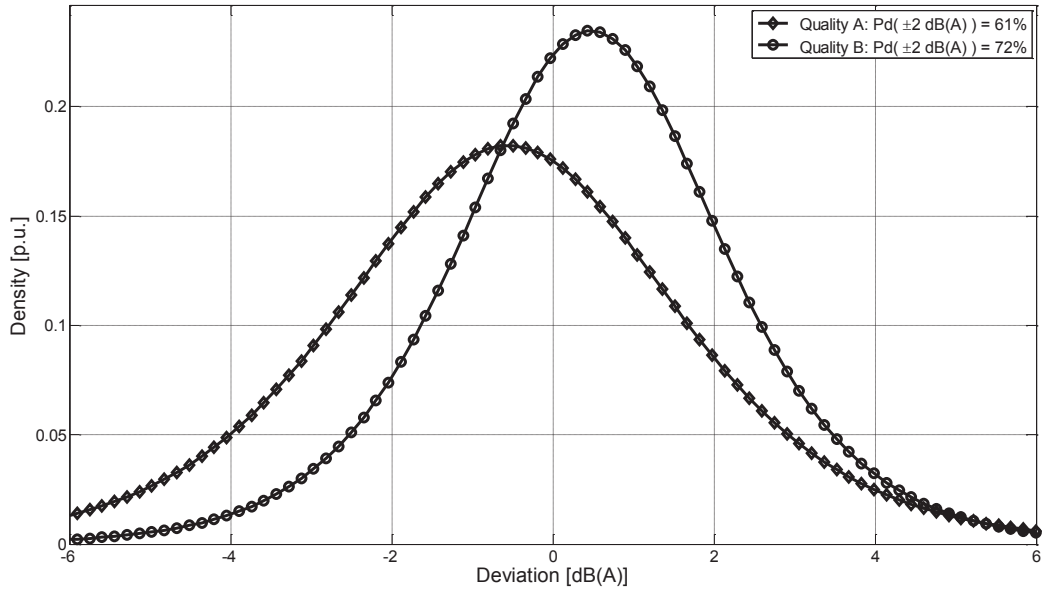


Figure 6 – Using the deviation probability as a measure of material quality

3.2. Practical results

The histogram shown in Figure 7 is the result of using the new algorithm over 2 years. The probability distribution is observed in range ± 3 dB(A), because the histogram contains all iron sheet types available at SGB for building the core. It provides a general view about the total scattering between measured and calculated SPL. The mean value (0.06 dB(A)) and the standard deviation (2.07 dB(A)) give a good indication of accuracy and the small range of scatter. The extreme deviating values are a result of new material used or sudden changes of the source quality.

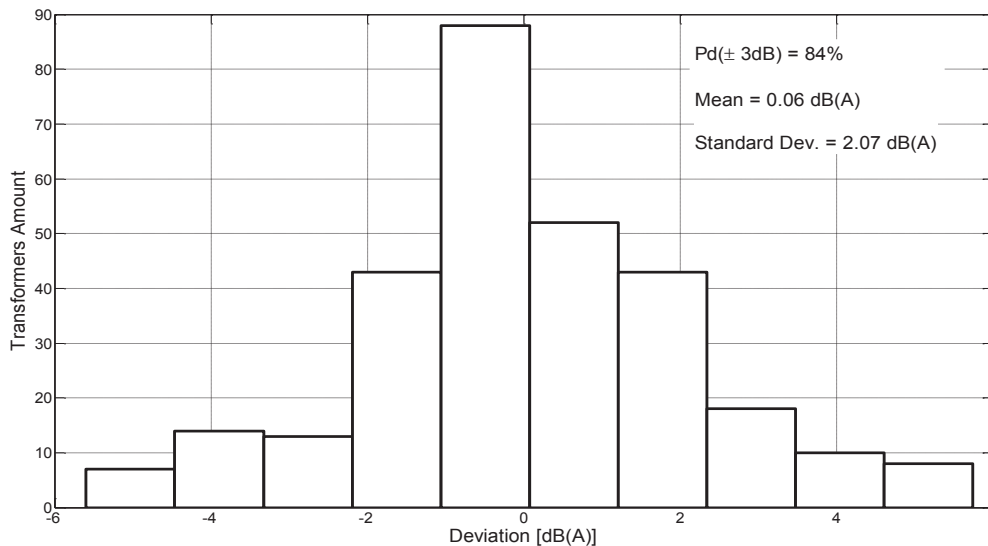


Figure 7 – Histogram of the deviation resulting of using all iron sheet types available

By taking a look on the direct influences of the new method on some of the transformers which were built in the past and have been redesigned over the past 2 years to decrease the deviation between the measured and calculated SPL, one can recognize the savings in material and cost resulting from this progress, due to the high accuracy of the new method as shown in Table IV.

Table IV – Effect of new method on core material savings

Transformer data	Built in	Rebuilt in	Iron savings [kg]
40MVA 115/10.5 kV ONAN/ONAF Guaranteed = 71 dB(A)	2007 Sound Power = 70.9 dB(A)	2011 Sound Power = 68.7 dB(A) Optimized to Sound Power = 70.2 dB(A)	797
25MVA 115/6.3 kV ONAN/ONAF Guaranteed = 66 dB(A)	2007 Sound Power = 65.6 dB(A)	2011 Sound Power = 64.0 dB(A) Optimized to Sound Power = 65.5 dB(A)	299

4. CONCLUSION

The method introduced in this paper permits to optimize the transformer core design under different operating conditions, and market and environmental requirements. Thanks to the high accuracy of the system and the elimination of almost any risk, it is now possible:

- to choose the right quality for each design.
- to have a starting point for new sheets.
- to optimize an existing design for any change in requirements.
- to identify the iron sheets with their magnetostriction characteristic values.
- to avoid in advance any critical deviation offset (DOS).

The good co-operation between SGB and its iron sheet manufacturers has played an important part in reaching that stage of developing a completely self-constructed algorithm which is able to cover all the previous aspects. The available data were separately analyzed based on the operational frequency (50, 60 and 16,667 Hz). However a simple offset might be sufficient to change over between 50 and 60 Hz.

REFERENCES

- [1] R. Küchler: "Die Transformatoren, Grundlagen für ihre Berechnung und Konstruktion", (1965)
- [2] S.V. Kulkarni: "Transformer Engineering, Practice and Design", (2004)
- [3] C.G. Kim: "Harmonics Analysis of Magnetostriction in 3% SiFe", Journal of Magnetism 3(4), 120-122(1998)
- [4] F. Bohn: "Magnetostriction in non-oriented magnetic steels", Physica B384, 294-296(2006)
- [5] F. Hofbauer: "Magnetostriction Distribution in a Model Transformer Core", Journal of ELECTRICAL ENGINEERING, VOL 61. NO 7/s, 130-132(2010).
- [6] D. Allan: "Electric Power Transformer Engineering", (2004)

Bruno Bošnjak
Siemens AG Power Transformers Nürnberg
bruno.bosnjak@siemens.com

Mario Stuhne
Končar - Power Transformers Ltd.
mario.stuhne@siemens.com

ANALYSIS AND EXPERIMENTAL VERIFICATION OF STATIC TILTING BEHAVIOUR OF CTC IN TRANSFORMER WINDINGS

SUMMARY

This paper presents a numerical model and experimental verification of the critical tilting force calculation for transformer winding conductors under static axial pressure. For the purposes of this investigation a structural finite element method model of a non-epoxy bonded continuously transposed conductor used for the construction of transformer windings was developed. The mechanical behaviour of two different transformer winding conductors under static axial pressure was simulated. The radial position of CTCs was varied according to manufacturer tolerances in order to closer correspond to the actual physical models. The displacements, stresses and strains obtained from the simulation are presented and analysed. This calculation is compared to existing analytical and empirical calculations in the IEC 60076-5:2006 and available literature. The results of these calculations were experimentally checked by pressing three physical winding models in a hydraulic press with the force corresponding to calculated critical tilting force and above. The resulting deformations of the winding conductors were photographed and compared to the results of the simulations.

Key words: Transformer, Windings, Short Circuit, Tilting, FEM, Structural Simulation

1. INTRODUCTION

Transformer windings consisting of current-carrying conductors are situated in the stray magnetic flux in the transformer window. Due to the interaction of the time-varying magnetic field and current flowing through the winding conductors, Lorentz forces are generated that act on the winding conductors. During a short circuit, if the axial compression exceeds a certain limit, a failure mode called tilting may occur which tilts the conductors of disk windings in a specific zig-zag pattern. This type of failure can damage the winding insulation, induce even higher forces due to conductor displacement and cause inter-turn short-circuits [1]. Currently, the calculation of the critical axial force under which tilting occurs is limited to analytical [2][3][4] and semi-empirical approaches [5]. This paper introduces a 2D finite element method calculation of stresses and corresponding displacements that occur during the pressing of two continuously transposed conductors (CTCs). The results of this calculation are compared to existing analytical calculations as well as to the experimental results. Primary object of this investigation was the characterisation of the mechanical behaviour of strandwise tilting [4].

2. EXISTING CALCULATIONS OF CRITICAL TILTING FORCE

2.1. Theoretical calculation approach

Current analytical calculations are primarily concerned with the calculation of the critical axial force under which tilting occurs. From [3], the following equation is available for the calculation of the critical axial force under which tilting occurs:

$$F_{tilt} = \frac{4}{3} E_0 \left[\frac{a_n \cdot \pi \cdot h_1^2}{D_{mean}} \left[1 + \frac{b_1^2}{h_1^2} \right] \cdot D_{mean}^2 - \frac{l_c}{L} + \frac{1}{4} \right] \cdot 10^{-3} [\text{kN}] \quad (1)$$

where

- E_0 - Young's modulus of elasticity for copper 113000 [N/mm²]
- a_n - width of the winding [mm]
- h_1 - height of the CTC strand [mm]
- b_1 - width of the CTC strand [mm]
- D_{mean} - mean winding diameter [mm]
- L - transposition distance in which one full transposition of all strands is completed [mm]
- l_c - distance over which one strand is transposed from one position to another [mm]
- μ - Poisson's ratio for copper

This analysis considers a winding made up of CTCs under the influence of an axial force from a theoretical standpoint, but does not take into account the additional complexities of the transformer winding geometry such as axial spacers, interaction between discs and material properties of paper and pressboard.

2.2. Semi-empirical calculation approach

IEC standard 60076-5 [5] prescribes the following equation for the calculation of the critical axial force under which tilting occurs:

$$F_{tilt2} = \left[\frac{E_0 \cdot n_r \cdot b_1 \cdot h_1^2}{2 \cdot D_{mean}} + K_2 \frac{n_r \cdot X \cdot \pi \cdot b_1^3 \cdot D_{mean} \cdot \gamma}{h_1} \right] \cdot K_3 \cdot K_4 \cdot 10^{-3} [\text{kN}] \quad (2)$$

where

- n_r - number of strands or twin conductors in the winding radial width
- K_2 - coefficient for the bedding term, 22 for non-bonded CTC [N/mm³]
- X - spacer coverage factor for disc- and helical-type windings $X = \frac{c \cdot z}{\pi \cdot D_{mean}}$
- c - radial spacer width [mm]
- z - number of radial spacers around the circumference
- γ - conductor shape constant; 1,0 for standard corner radius, 0,85 for fully rounded strands
- K_3 - factor accounting for the copper work hardening degree (see Table I)
- K_4 - factor accounting for dynamic tilting

Table I – Values for factor K_3

$R_{p0.2}$ MPa	K_3
Annealed	1.0
150	1.1
180	1.2
230	1.3
>230	1.4

Table II – Values for factor K_4

Conductor type	Winding type	
	Disc - helical	Layer
Strand or twin	1.2	1.1
Non-bonded CTC	1.7	1.3

For the purposes of this paper, the critical tilting forces were calculated with the dynamic tilting factor set at 1.0. This equation is based on a semi-empirical approach, stemming from theoretical considerations and statistical data.

2.3. Winding conductor data

Both analytical and numerical calculations were performed on the two types of continuously transposed conductor available. Experimental verification was performed on three winding models:

- Model 1 Winding
- Model 2 Winding
- Model 3 Winding – modified Model 2 winding with one less conductor in the radial direction in the top most disc

The basic data of each winding model is presented in the following table.

Table III – Winding and conductor model data

Model	Winding type	Spacers	n_{rad}	n_{CTC}	h_1	b_1	δ_{laq}	n_{paper}
Model 1	Disc winding	No	8	15	4,85	1,4	0,1	12
Model 2	Disc winding	Yes	3	47	9,05	1,42	0,1	6
Model 3	Disc winding	Yes	2	47	9,05	1,42	0,1	6

where

- n_{rad} - number of CTCs in the winding radially
 n_{CTC} - number of CTC strands
 δ_{laq} - thickness of the varnish layer
 n_{paper} - number of paper layers on the conductor

2.4. Analytical calculation results

Using equations (1) and (2), the following values of critical tilting force were calculated:

Table IV – Calculated critical tilting forces

Model	F_{tilt1} [kN] Theoretical	F_{tilt2} [kN] Semiempiric
Model 1	2435	3880
Model 2	3218	1242
Model 3	2124	822

3. NUMERICAL MODEL OF THE CONDUCTORS

The two conductor models, corresponding to the two types of conductor used in the calculations and the experimental verifications were modelled and solved using ANSYS R15.0 Workbench environment. Models are shown in Figure 1 and Figure 2.

Models developed were axially symmetric, with a force applied to structure at the top of the model which was modelled as a transformerboard object. Applied force had the amplitude of 2542 kN, which is the maximal pressing force applied in the consequent experiment.

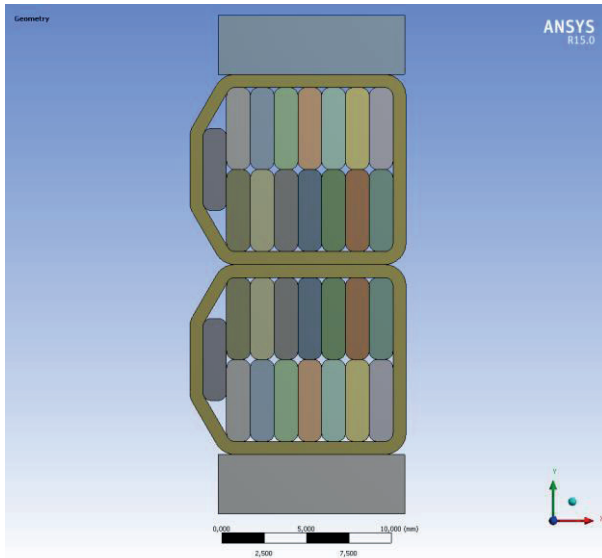


Figure 1 – Model 1 conductor geometry

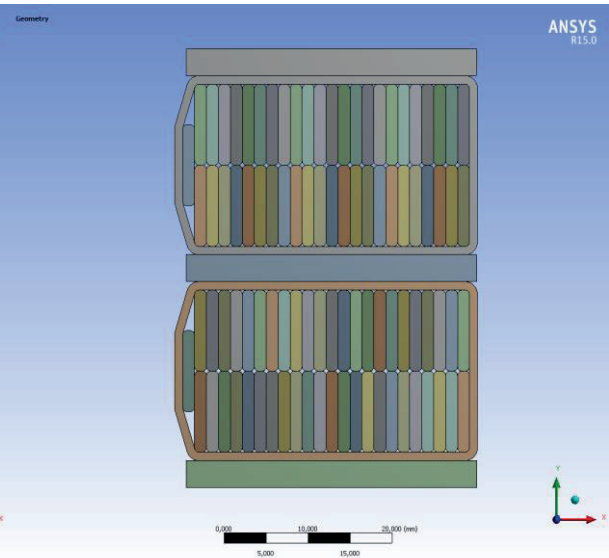


Figure 2 – Model 2 and 3 conductor geometry

Two additional conductor models were developed with a built-in horizontal offset of the CTC strands by 0.2mm according to the tolerances of conductor manufacturer. These models are shown in Figure 3 and Figure 4.

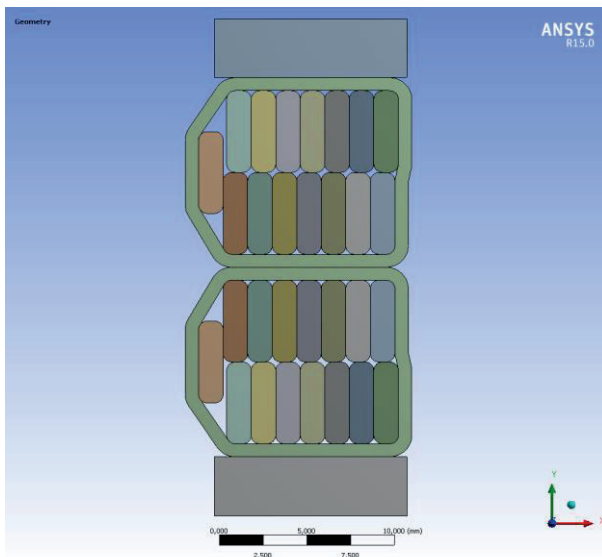


Figure 3 – Model 1 conductor geometry with a 0.2 mm horizontal offset

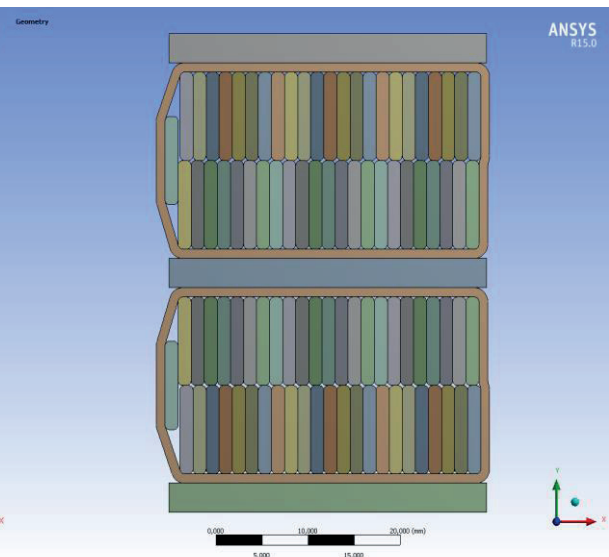


Figure 4 - Model 2 and 3 conductor geometry with a 0.2mm horizontal offset

4. SIMULATION RESULTS

The results of the static structural simulation are presented in the following figures. Displacement and stress are plotted for the both the case with perfect alignment and 0.2mm horizontal offset.

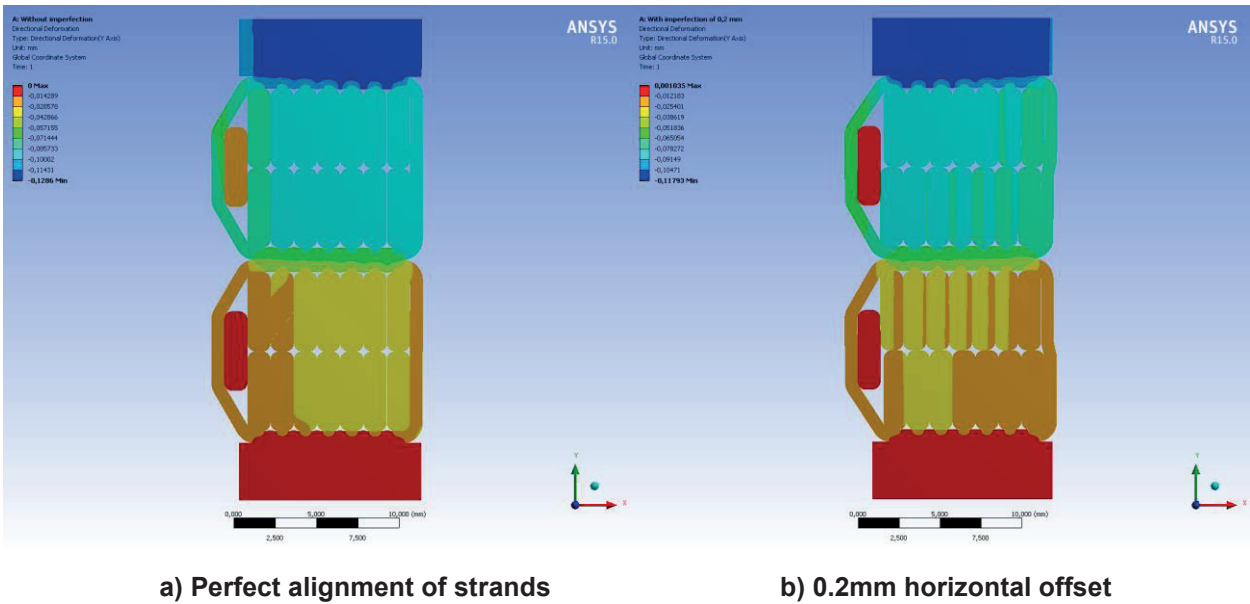


Figure 5 – Vertical displacement (y-axis) plots Model 1

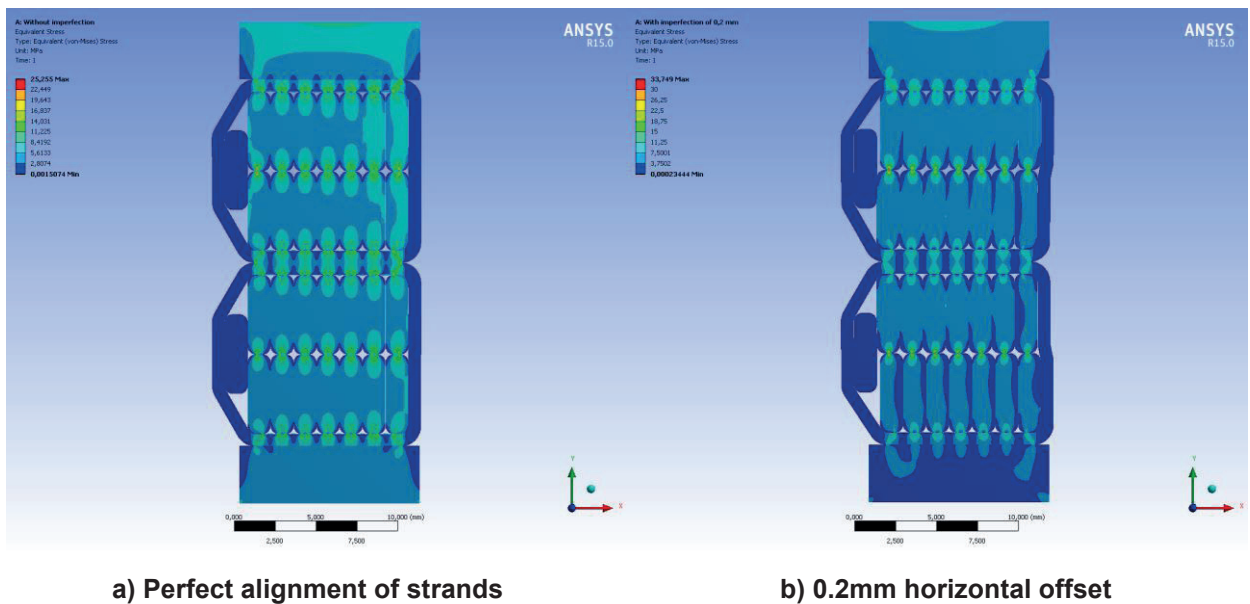
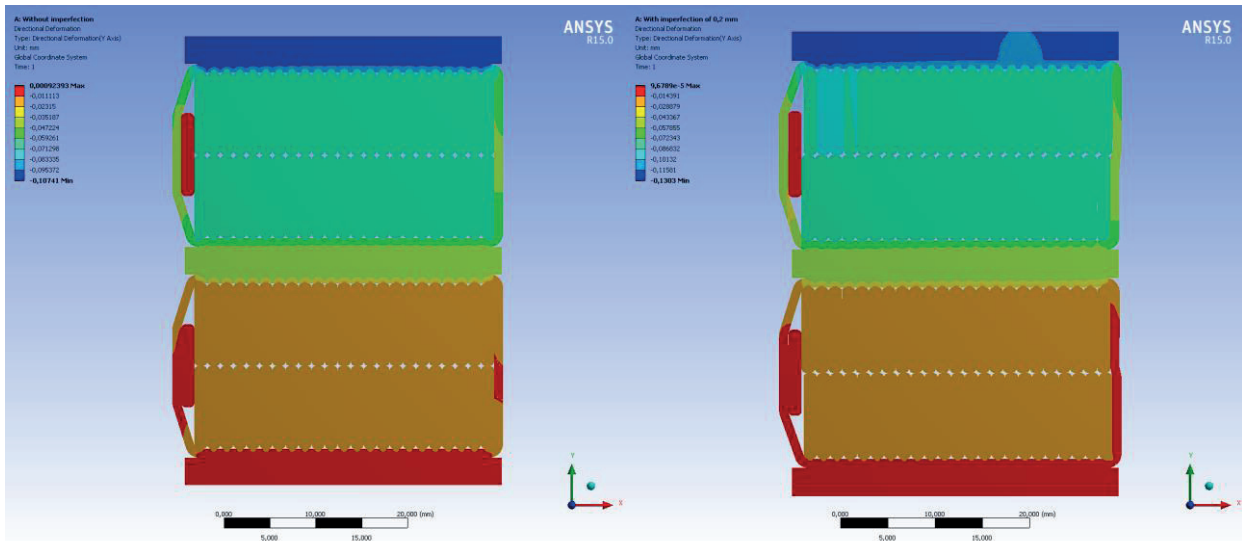


Figure 6 – Stress plots Model 1

The vertical displacement plot of Model 1 in Figure 5 shows the tendency of the top-most conductor to have the higher vertical displacements, i.e. the top most conductor experience the highest compression. Introduction of a 0.2 mm horizontal offset to the two conductor strand rows in Model 1 increases the maximum stress experienced by the conductor strands from 25,2 MPa to 33,7 MPa and changes the distribution of stress within the strands into a pattern more similar to the expected tilting stress patterns (Figure 6). Although the stress within the conductor is higher, the vertical displacement of the conductors is lower for the case with 0.2 mm offset. The 0.2 mm offset effectively causes the

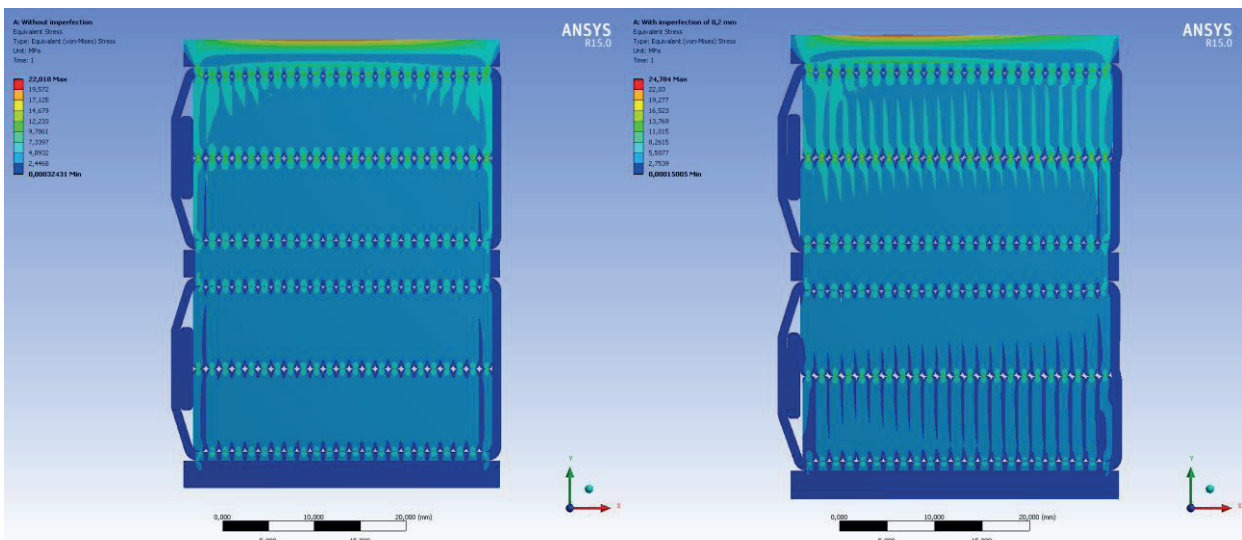
“wedging” of the conductor strands into one another to a certain degree, locking them into place. Therefore, in spite of higher maximum stress experienced in the contact points between the conductors, the average stress in each conductor strand is in fact lower when a 0.2 mm offset is present than when the conductor strands are perfectly aligned.



a) Perfect alignment of strands

b) 0,2mm horizontal offset

Figure 7 – Vertical displacement (y-axis) plots Model 2 and 3



a) Perfect alignment of strands

b) 0,2mm horizontal offset

Figure 8 – Stress plots Model 2 and 3

The simulation on conductor of Model 2 and 3 shows a similar general pattern of behaviour to the Model 1 regarding stress and displacement. The differences stem from the slenderer conductor strands and the higher number of strands overall. The higher number of strands means the maximum stress is lower and the overall distribution of stress and displacement is more even than for the Model 1. Also, no “wedging” effect is present and the vertical displacements are higher for the model with 0.2mm displacement which was the expected results. The equations (1) and (2), according to Table IV, give

contradictory results in regards to the tilting withstand capacity of this conductor. The numerical calculation yields results that are more line with the theoretical calculation from [2], i.e. equation (1).

These results indicate that the applied force of 2542 kN will not cause any observable tilting of either conductor used in the experiment, since the maximum displacement is in the 0.1 mm range.

Calculation of the critical tilting force for both winding models was performed for the models with the 0.2 mm horizontal offset of the CTC strands. For Model 1 conductor, critical tilting force was calculated to be at 4016 kN, or 103% of the calculated critical tilting force according to IEC (Table IV).

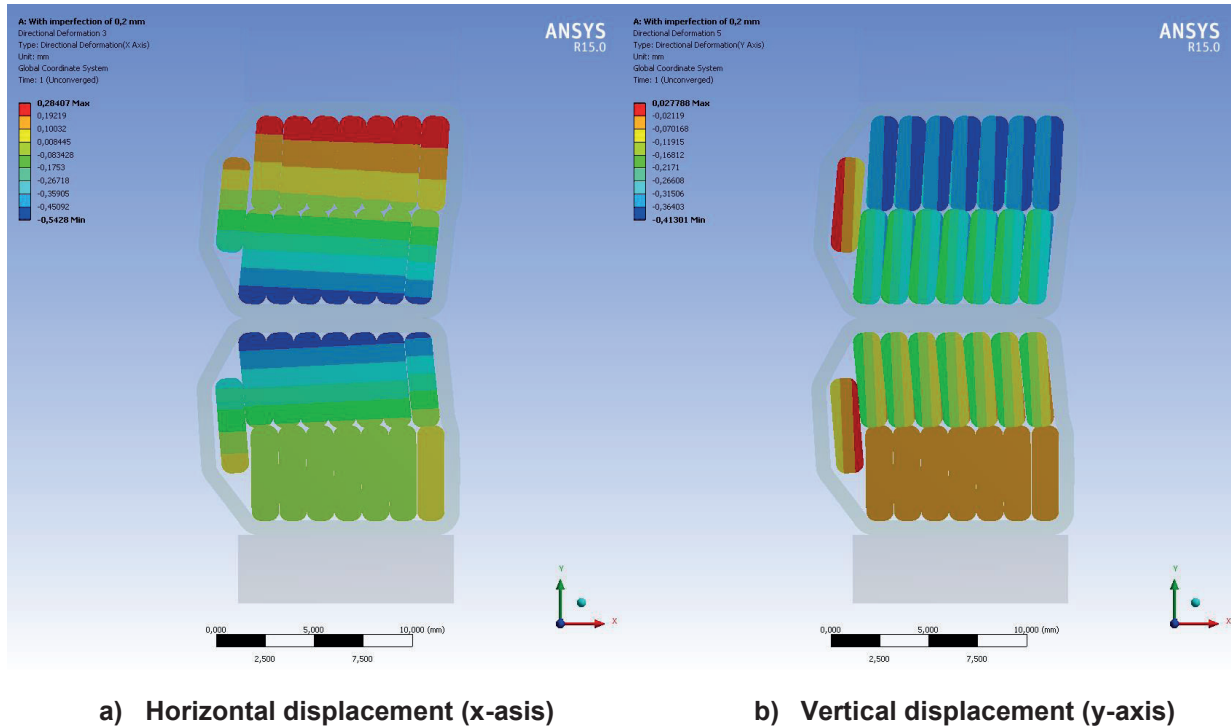
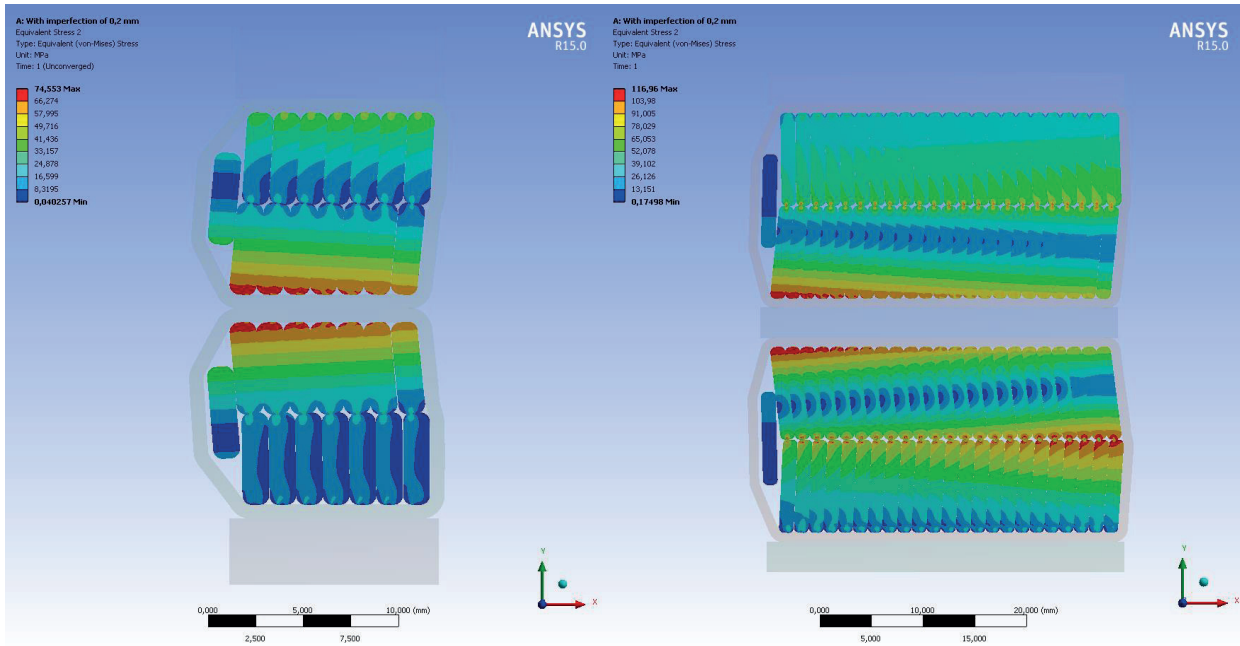


Figure 9 – Displacement plots for Model 1 winding conductor under 103% of the critical tilting pressing force according to IEC



Model 1 under 103% critical tilting force

Model 2 under 614% critical tilting force

Figure 10 – Stress plots for Models 1 and 2

Model 2 proved to be theoretically very resistant to tilting, as a complete tilt of the conductor was not achieved even at the force of 7626 kN which amounts 614% to of the critical tilting force according to IEC for Model 2 and 927% of the critical tilting force according to IEC for Model 3.

5. EXPERIMENTAL VERIFICATION

All three winding models were pressed using a hydraulic press with forces amounting to 50% and 100% critical tilting force according to IEC Standard 60076-5[5], calculated using the equation (2). For Model 1, since the 100% tilting force was at calculated at 3880 kN, the maximum allowed pressing forces were applied, amounting to 65% of the critical tilting force. The calculation results are presented in Table IV. All three winding models also were pressed using the maximum pressing force allowed on the hydraulic press due to safety regulation in the amount of 2542 kN. When subjected to 50% and 100% of the critical tilting force according to IEC Standard 60076-5, Model 2 and 3 exhibited no visible deformations of the copper conductors, even after a prolonged pressing time of 1 hour. The only visible deformation was the impressing of insulation paper into the radial spacers on Model 3 shown in Figure 11.



Figure 11 –Model 3 under the influence of the 100% of the critical tilting pressing force according to IEC

Under the influence of the maximum pressing force allowed on the hydraulic press (2542 kN, 309% of the IEC critical tilting force), visual deformations appeared on the winding conductors. The observed deformations were of within the elastic area of deformations, i.e. after the experiment, when the winding model was released from the press, they retained their previous state of mechanical stability. The winding conductors deformed in the shape precluding tilting, with the top conductor obviously under higher strain than the conductors below it (Figure 12).



Figure 12 – Model 3 under the influence of the 309% of the critical tilting pressing force according to IEC

The winding conductors exhibited an elastic deformation where the conductor strands were rotated around the axial axis of the winding in manner similar to tilting (Figure 13). Therefore, it is safe to assume that under the influence of higher force the winding model would plastically deform in the shape of tilting. The displacements observed were in the 1-4 mm range in the radial direction, which is an order of magnitude greater than the displacements predicted by the numerical simulation. The simulation correctly predicted the shape of the deformation. It is important to note the winding deformed in full-tilt mode [6].



Figure 13 – Model 3 under the influence of the 309% of the critical tilting pressing force according to IEC

Table V – Experiment with 50% of the critical tilting force applied

Model	F_{tilt2} [kN] Calculation according to [5]	F_{tilt1} [kN] Calculation according to [3]	F_{tilt13} [kN] Numerical calculation	F_{app} [kN] Applied Force	$\frac{F_{app}}{F_{tilt2}} \cdot 100$ [%]	Observed deformations of the copper conductors
Model 1	3880	2435	4016	1940	50%	No visible deformations
Model 2	1242	3218	>7626	621	50%	No visible deformations
Model 3	822	2124	>7626	411	50%	No visible deformations

Table VI – Experiment with 100% of the critical tilting force applied

Model	F_{tilt2} [kN] Calculation according to [5]	F_{tilt1} [kN] Calculation according to [3]	F_{tilt1} [kN] Numerical calculation	F_{tilt3} [kN] Numerical calculation	F_{app} [kN] Applied Force	$\frac{F_{app}}{F_{tilt2}} \cdot 100$ [%]	Observed deformations of the copper conductors
Model 1	3880	2435	4016	4016	2542	65%	„Elastic“ tilting 1-2 mm
Model 2	1242	3218	>7626	>7626	1242	100%	No visible deformations
Model 3	822	2124	>7626	>7626	822	100%	No visible deformations

Table VII – Experiment with the maximum allowable force applied

Model	F_{tilt2} [kN] Calculation according to [5]	F_{tilt1} [kN] Calculation according to [3]	F_{app} [kN] Applied Force	F_{tilt3} [kN] Numerical calculation	$\frac{F_{app}}{F_{tilt2}} \cdot 100$ [%]	Observed deformations of the copper conductors
Model 1	3880	2435	2542	4016	65%	„Elastic“ tilting 1-2 mm
Model 2	1242	3218	2542	>7626	204%	„Elastic“ tilting 3-4 mm
Model 3	822	2124	2542	>7626	309%	„Elastic“ tilting 3-4 mm

6. CONCLUSION

The application of numerical calculation for the description of the behaviour of continuously transposed conductor provides a deeper insight into this type of loss of structural stability and enables the calculation of stress within the conductors and the corresponding displacements. Compared to analytical calculations, the numerical model was able to predict the deformation of the conductor under constant force more accurately. Although the 2D numerical model accurately predicted the shape of the deformation, it did not accurately predict the order of magnitude of the displacements observed in the experiment due to the model simplifications. Further research should be performed into more detailed 3D models containing all the details of winding geometry for a more precise prediction of the conductor behaviour under the influence of static forces.

REFERENCES

- [1] G. Bertagnolli, "Short-Circuit Duty of Power Transformers - The ABB Approach", 1st ed., Golinelli Industrie Grafiche, January 1996
- [2] M. R. Patel, "Dynamic stability of helical and barrel coils in transformers against axial short-circuit forces," Proc. Inst. Elect. Eng., vol. 127, no. 5, Sep. 1980, pp. 281–284.
- [3] M. R. Patel, "Instability of the Continuously Transposed Cable Under Axial Short-Circuit Forces in Transformers", IEEE Transactions on Power Delivery, Vol. 17, IEEE Power & Energy Society, January, 2002.
- [4] A. Bakshi, S. Kulkarni, "Eigenvalue Analysis for Investigation of Tilting of Transformer Winding Conductors Under Axial Short-Circuit Forces", IEEE Transactions on Power Delivery, Vol. 26, No. 4, IEEE Power & Energy Society, Toronto, Canada, October 2011
- [5] IEC 60076-5 Power Transformers – Part 5: Ability to withstand short circuit, February 2006
- [6] S. V. Kulkarni, S. Khaparde, "Transformer Engineering: Design and Practice", 3rd ed., Marcel Dekker, 2004

Igor Žiger
Končar - Instrument transformers Inc.
igor.ziger@koncar-mjt.hr

Danijel Krajtner
Končar - Instrument transformers Inc.
danijel.krajtner@koncar-mjt.hr

Zvonimir Ubrekić
Končar - Instrument transformers Inc.
zvonimir.ubrekic@koncar-mjt.hr

PUSHING THE BOUNDARIES OF INDUCTIVE VOLTAGE TRANSFORMER DESIGN

SUMMARY

Designing inductive voltage transformers for the highest voltage levels (550 kV and above) is a true challenge indeed. The main reason for this is their complex internal R-L-C structure, including an insulating system which needs to be resistant to all types of overvoltages and consequent dielectric stress it can encounter during its lifetime. This is why it is necessary to verify behavior of such transformers during the design process, and under four sets of standard test overvoltage types; the Power Frequency Withstand Voltage (PFVV), the Lightning Impulse Withstand Voltage (LIWV, i.e. BIL), Chopped Impulse Withstand Voltage (CIWV) and the Switching Impulse Withstand Voltage (SIWV).

The main idea of the paper is to demonstrate that by understanding the influence of crucial parameters of the appropriate equivalent diagram on the voltage distribution across the active part of the transformer, it is possible to define the overall design of inductive voltage transformers so that they can satisfy even the most rigorous insulation requirements, thus pushing the boundaries of design even further.

1. INTRODUCTORY CONSIDERATIONS

The inductive voltage transformer is a complex unit by nature. The main reason for this is the fact that it encompasses design features of transformer bushings and a conventional transformer winding outline in a single enclosure [1]. Insulation requirements for such units are strict in general, because it is expected for these units to function with no insulation breakdown for an approximate lifetime of 40 years, essentially without maintenance or any other user intervention during that period [2]. These requirements, as well as prescribed tests which accompany them, are more rigorous than tests required for their power transformer counterparts and vary from standard to standard [3] - [6].

In contrast to IEC-oriented European countries, Canadian standard CAN/CSA C60044-2:07 defines higher test voltages for 550 kV transformers. Test voltages appointed to that standard position are shown in table I [3].

Table I - Standard requirements for 550 kV transformers according to CAN/CSA C60044-2:07

Voltage type	Voltage Magnitude [kV]
Maximum system voltage	550
Power Frequency Withstand Voltage (PFVV)	830
Lightning Impulse Withstand Voltage (BIL)	1800
Chopped Impulse Withstand Voltage (CIWV)	2070
Switching Impulse Withstand Voltage (SIWV)	1300

For voltages that high, instrument transformer manufacturers usually resort to capacitive voltage transformers or sometimes even SF₆ insulated inductive voltage transformers instead of using paper-oil insulated inductive transformers. General belief is that with either of these principles it is easier to satisfy insulation requirements specified in Table I, while keeping the transformer dimensions (and consequently the cost as well) within reasonable margins.

However, as far as paper-oil insulated transformers are concerned, the open-core concept adds several advantages insulation and weight wise (and especially cost wise), when higher voltages are considered. This is explained in references [1], [2], [7] and [8].

Figure 1 shows the cross-section of an open-core voltage transformer. As it can be seen from the figure, the active part and most notably the primary winding are distributed along the transformer height, which favorably influences the voltage distribution on the insulator surface. The main insulation cylinder is capacitively graded, meaning that a number of semi-conductive capacitive screens is inserted in-between layers of paper insulation. Screens from the insulation are galvanically connected to the coils of the primary winding, thus adding to the longitudinal capacitance of the primary winding. This makes the transformer much more resistant to lightning impulse and quick high-frequency overvoltages [7]. Finally, because the entire transformer is essentially its own bushing, in contrast to tank and bushing principle utilized by closed core inductive voltage transformers, the dimensions and the resulting weight of the transformer are significantly decreased.

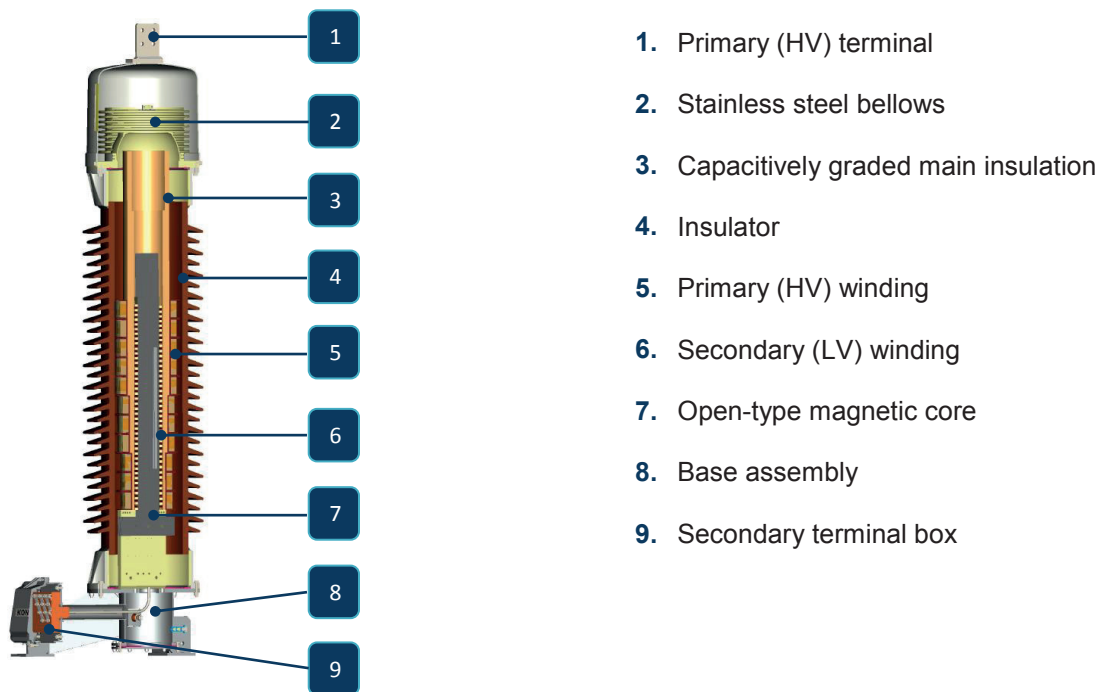


Figure 1 - Open-core inductive voltage transformer cross-section

The ensuing chapters of the paper will deal with the design challenges and principles of the insulation system for open-core voltage transformers, the influence of important parameters on the voltage distribution across the active part of the transformer and the final design, which led to successful type testing of 550 kV open-core paper-oil insulated inductive voltage transformers with insulation requirements from table I.

2. CHALLENGES AND APPROACH

Despite the advantages described in the introductory chapter, insulation design for very high voltages is not a trivial task.

The main reason is that the voltage distribution is drastically different for fast, lightning or switching impulse overvoltages, than for power frequency (over)voltages, meaning that the behavior of the main insulation system is different as well [1] [9].

Under power frequency overvoltages, the voltage distribution is mainly inductive and dependent on turn distribution of primary winding sections, meaning that the primary winding essentially determines how the main insulation is dielectrically stressed. However, it has been proven that even at low frequencies (50 - 200 Hz), the influence of capacitance from the main insulation system is not negligible [1].

On the other hand, under lightning impulse, chopped impulse or very fast overvoltages, the voltage distribution is highly capacitive by nature, meaning that the capacitances of insulation cylinder screens dictate voltage and dielectric stress distribution both across the insulation cylinder itself and across the primary winding [8] [9].

Switching impulse overvoltages are somewhere in-between the latter two. Their front time is relatively fast, meaning that the distribution is predominantly capacitive, while their tail is relatively slow, meaning that both primary winding inductances and capacitances come into play [1].

With that in mind, it is obvious that the voltage distribution under these three types of overvoltages has to be as linear and as uniform as possible. Every deviation from this can mean excessive stress on a part of the insulation and/or primary winding, which can lead to partial discharge inception, insulation ageing or insulation breakdown [1] [9].

Dielectric stress across the main insulation is not the only thing we need to worry about. Historically, it has been proven that outside insulation (i.e. air-porcelain or air-silicone boundary on the insulator surface) can become overly stressed, leading to flashovers and/or insulation breakdowns. This is especially problematic during type testing with switching impulse voltage, as this test is performed under artificial rain conditions, which worsen the electric field distribution on the insulator surface [10] [11]. This, combined with the fact that the voltage distribution varies during the waveform, is the reason why switching impulse voltage is considered critical for open-core voltage transformers [1].

Surface flashover under artificial rain conditions is an extremely complex issue on its own, notwithstanding the effect of the active part on the voltage distribution, and would require an extensive research and calculation breakthroughs which surely surpass the scope of this paper [10] - [13]. This is why this paper will disregard this issue entirely.

The proposed way of dealing with the above-mentioned issue is to ensure as uniform and as linear voltage distribution as possible, and to distribute the stress in an axial direction by ensuring a sufficient number of primary winding sections.

The approach of this paper slightly differs than previously published work on this topic. The emphasis in those papers was to verify the calculation methodology, and to observe the influence of discrete iterations (i.e. changing of primary winding turns distribution and/or capacitive screen parameters) [1] [9] [14]. Here we wished to observe the influence of total primary winding turn number and capacitance values on the voltage distribution as it has been noticed that changing of these parameters has a different effect under various types of applied voltage. This is why it was necessary to determine the optimal values of these parameters before fine-tuning the voltage distribution of the actual prototype transformer using the guidelines given in previously published work. All relevant measurements performed on the prototype are included in this paper.

3. METHODOLOGY

The proposed methodology of this paper was successfully tested thoroughly on combined instrument transformers, whose active part concept is almost identical to the one utilized by open-core voltage transformers [1] [14]. This is why the methodology is applicable in this case as well.

A simplified outline of the main insulation system (i.e. interconnected screens form the main insulation and primary winding sections) can be seen in figure 2 (a). The proposed equivalent diagram, which uses lumped parameters, can be seen in Figure 2 (b) [1].

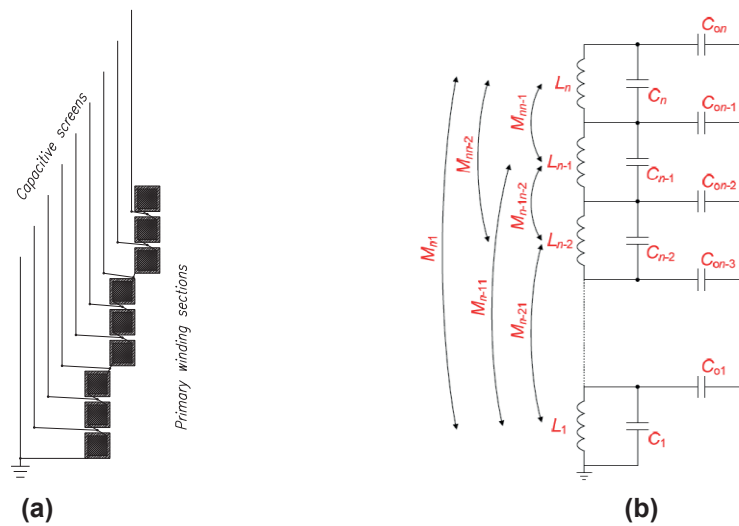


Figure 2 - (a) Simplified active part representation (b) Equivalent diagram used in the calculations

To correctly represent the active part of the transformer, we need three sets of parameters; the inductance matrix of the primary winding, the capacitance matrix of the primary winding screens and the capacitance to ground vector [1] [9]. Winding and leads resistance is neglected in this paper. As it can be seen, the secondary winding is excluded from the diagram in figure 2b. The influence of the secondary winding is however present in the magnetic flux distribution and is reflected on the values in the inductance matrix [1].

The inductance matrix itself is obtained by a numerical calculation, which takes into account the actual geometry of the transformer and properties of the magnetic core. The self-inductance of each coil is calculated according to expression (1), while the mutual inductance is calculated according to expression (2) [15] [16]. Numerical parameters necessary for the calculation were obtained using FEMM 2D solver [17].

$$L = \frac{\psi_{ii}}{I_i} \quad (1)$$

$$M_{ij} = \frac{\psi_{ij}}{I_i} \quad (2)$$

In the above equation, ψ is the flux-linkage of a designated coil, while I is the source current through the i -th coil, always set at a value of 1 A. This way the resulting flux linkage value corresponds to the appropriate inductance value.

Capacitance matrix consists only of off-diagonal elements (capacitances between main insulation screens), as each screen has a solid capacitance only towards the next screen. As the main insulation is a cylindrical system, analytical formulation given in expression (3) will suffice for an accurate capacitance calculation [9].

$$C_{ij} = 2\pi\epsilon_0\epsilon_r \cdot \frac{l}{\ln\left(\frac{R_j}{R_i}\right)} \quad (3)$$

In the above equation, l is the length of the screen, R_i and R_j are the radii of the i -th and j -th screen, respectively.

In comparison to combined transformers, the ground capacitance of voltage transformers is much smaller, because the screens in the insulation do not have a solid capacitance towards the grounded screen. The magnitude of ground capacitance was determined numerically using the formulation (4).

$$C_{i0} = 2 \frac{W}{U^2} \quad (4)$$

In the above equation U is the voltage between two electrodes, and W is the stored electric field energy.

Once all lumped parameters are determined, they are imported into EMTP solver, where an appropriate voltage shape is assigned. Power frequency withstand voltage is assigned using expression (5), while impulse and switching overvoltages are assigned using expression (6).

$$u(t) = A \cos[\omega t + \phi_0] \quad (5)$$

$$u(t) = A(e^{-\alpha t} - e^{-\beta t}) \quad (6)$$

In equation (5), A is the voltage amplitude, ω is the angular frequency and ϕ_0 is zero. In order to obtain percentage values, A is set to a value of 141. Similar principle is used for equation (6), so that the total amplitude is set at 100 V. Parameters for lightning impulse voltage are as follows: $A=103,74$ V, $\alpha=14598$ s⁻¹ and $\beta=2457002$ s⁻¹. Parameters for switching impulse voltage are as follows: $A=110,36$ V, $\alpha=318$ s⁻¹ and $\beta=16207$ s⁻¹. These values are similar to those used by other researchers [18] [19].

4. STARTING PARAMETER VARIATION

Two sets of calculations were conducted. The first set is the variation of total number of turns, while keeping the same insulation cylinder (keeping original first screen length value scr_1). The second set is the variation of the insulation cylinder capacitance (while keeping the primary winding turns at a chosen number of turns w_1).

Starting parameters (inductance and capacitances) which were considered are shown in figure 3 (a) and 3 (b). Only self-inductances of the coils are shown, instead of the entire matrix, because they illustrate the point, while keeping the representation digestible.

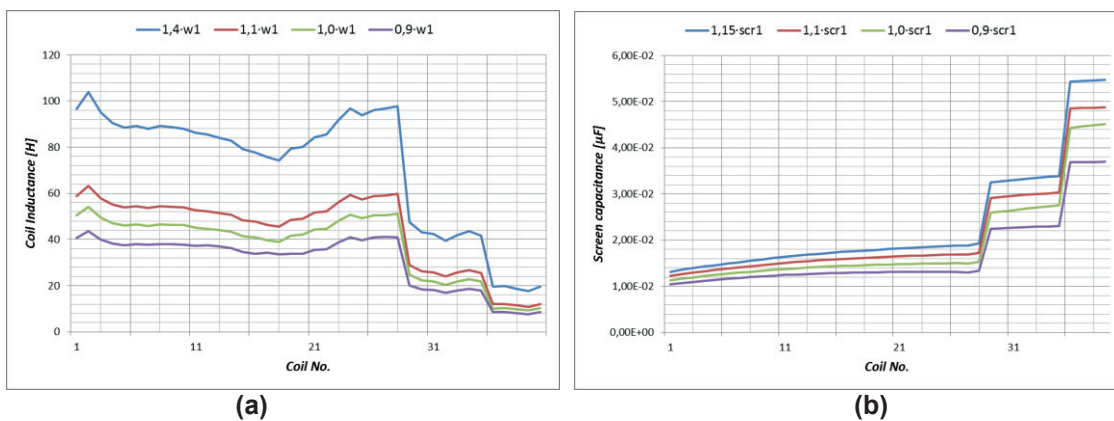


Figure 3 - (a) Inductance variation (b) Screen capacitance variation

All calculations in this part of the paper were done with the same number of primary winding coils. As it can be seen from the figure 3 (a) and (b), the upper coils have a higher corresponding capacitance and lower corresponding inductance. The reason for this is to obtain a more discrete voltage distribution on the upper portion of the primary winding in order to better control and decrease dielectric stress on the insulator surface during fast overvoltages, as explained in chapter 2.

Before getting into the calculation results, the way they are presented should be discussed. Each set of results is shown in comparison to the ideal (desired) voltage distribution, which is given as a percentage value. For each variation four sets of data are presented: voltage distribution at 60 Hz (rated frequency), voltage distribution at 120 Hz (1-minute power frequency withstand voltage test frequency), distribution of impulse voltage wave front and distribution of switching voltage wave tail. Distributions of lightning impulse front, lightning impulse tail and switching impulse front are essentially the same, so the latter two were excluded from further analysis.

4.1. Primary winding turn number and main insulation screen capacitance variation

Results for total turn number variation can be seen in figure 4 (a) - 4 (d).

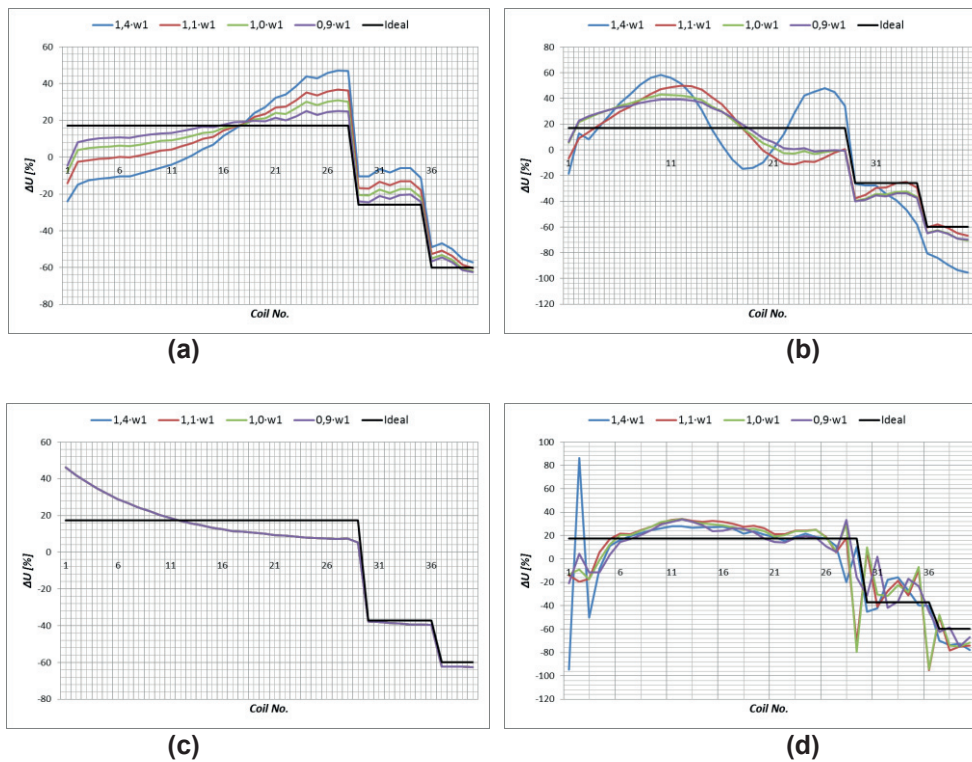


Figure 4 - (a) Voltage distribution at 60 Hz (b) Voltage distribution at 120 Hz (c) Lightning impulse front distribution (d) Switching impulse tail distribution

Results for insulation screen capacitance variation can be seen in figure 5 (a) - 5 (d).

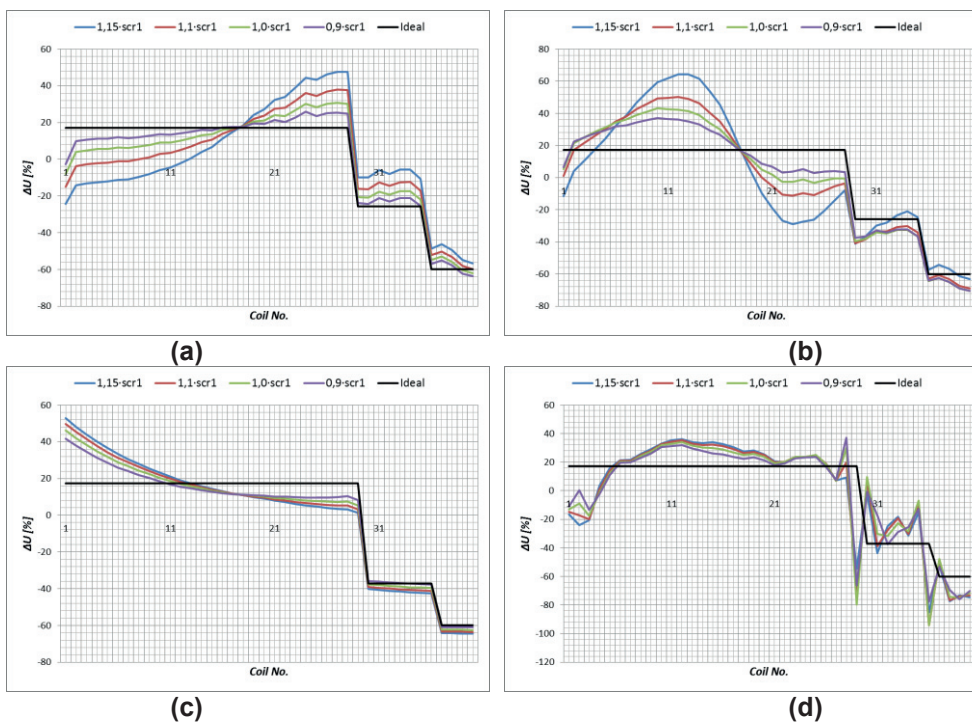


Figure 5 - (a) Voltage distribution at 60 Hz (b) Voltage distribution at 120 Hz (c) Lightning impulse front distribution (d) Switching impulse tail distribution

4.2. Result Analysis

Several trends can be observed by analyzing the charts shown in the previous chapter.

First, it is apparent that a decrease in total number of turns (and a consequent inductance drop) has a very positive effect on distribution of power frequency and switching impulse voltages. With a lower turn number, the voltage distribution becomes more “stable” and closer to the ideal distribution. As expected, lightning impulse voltage distribution is not affected by this variation.

Second, it is generally assumed that an increase in length of main insulation cylinder (and a subsequent increase in capacitance between insulation screens) has a favorable effect on lightning impulse voltage distribution, while a non-favorable effect on power frequency withstand voltage distribution. Increasing the length of capacitive screens is usually done to alleviate the stress on the upper coils. However, in this case this is already achieved by using smaller primary winding coils with less insulation between corresponding screens, thus increasing the capacitance (Figure 3 (b)). This rendered the effect of increasing the cylinder length counterproductive, because the power frequency voltage and switching impulse voltage distributions are considerably worse for a longer cylinder, and the effect on lightning impulse voltage distribution is almost negligible.

The results given in this chapter were used as a guiding beacon for final transformer design.

5. CALCULATION AND MEASUREMENTS OF THE FINAL DESIGN

The final design was set upon the foundations shown in chapter 4. Some of the parameters were updated in order to achieve a better axial dielectric stress distribution. Final parameters of the prototype design are shown in figure 6 and are contrasted with data given in figure 3.

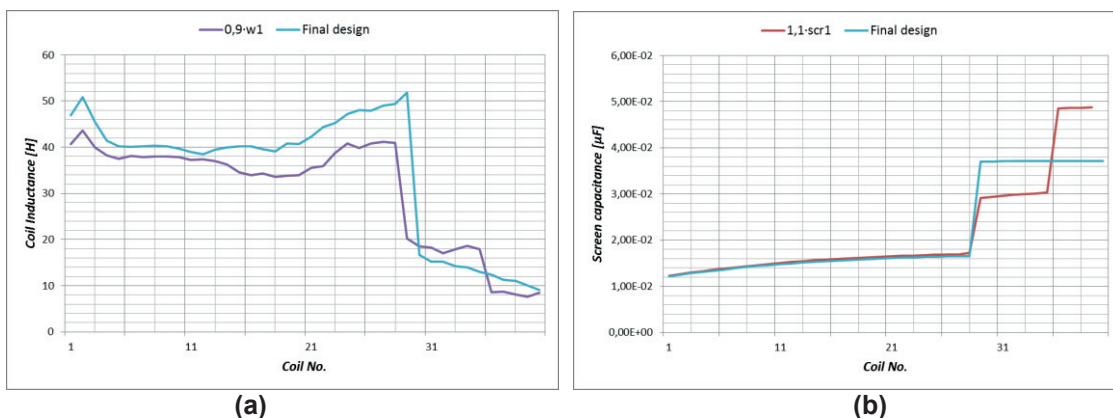


Figure 6 - (a) Final design coil inductance (b) Final design screen capacitance

The transformers entered the production process with parameters shown in figure 6. As a part of interphase testing, voltage distributions for sinusoidal, lightning impulse and switching impulse waveforms were measured. The results of these measurements were compared with calculation results. It is necessary to note that all measurements were done on an oil-impregnated active part, meaning that the transformer went through the entire drying, vacuuming and oil-impregnation process before the active part was taken out of the enclosure and measurements were performed.

Comparison of results for sinusoidal, power frequency withstand voltage distribution can be seen in figures 7 (a) and 7 (b). As it can be seen from these figures, there is some difference between measured and calculated values, although they display the same trend. The average difference is 4,1% for 60 Hz and 5% for 120 Hz. It is worth noting that, according to measurements, the voltage distribution in both cases is closer to the ideal voltage distribution than the one calculated.

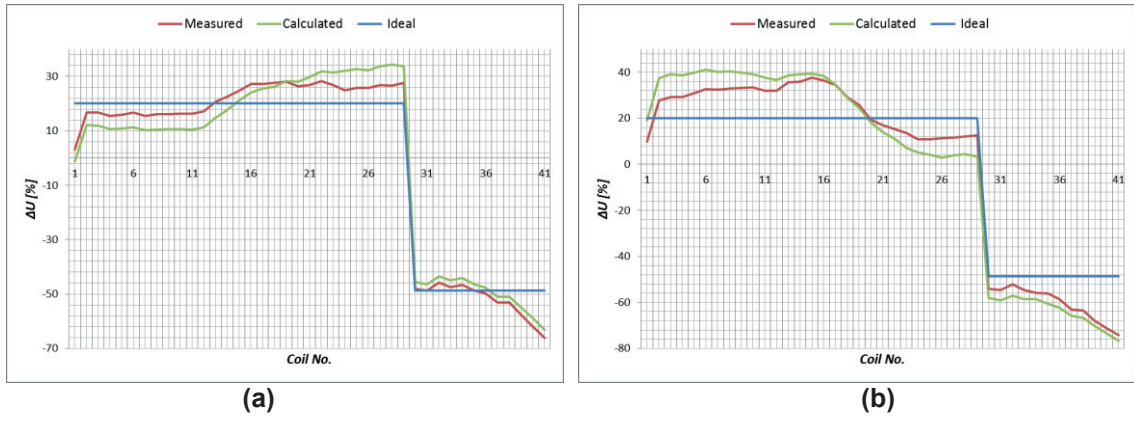


Figure 7 - (a) Voltage distribution at 60 Hz (b) Voltage distribution at 120 Hz

Calculated lightning impulse and switching impulse voltage distributions for the entire waveform are shown in figures 8 (a) - 8 (b).

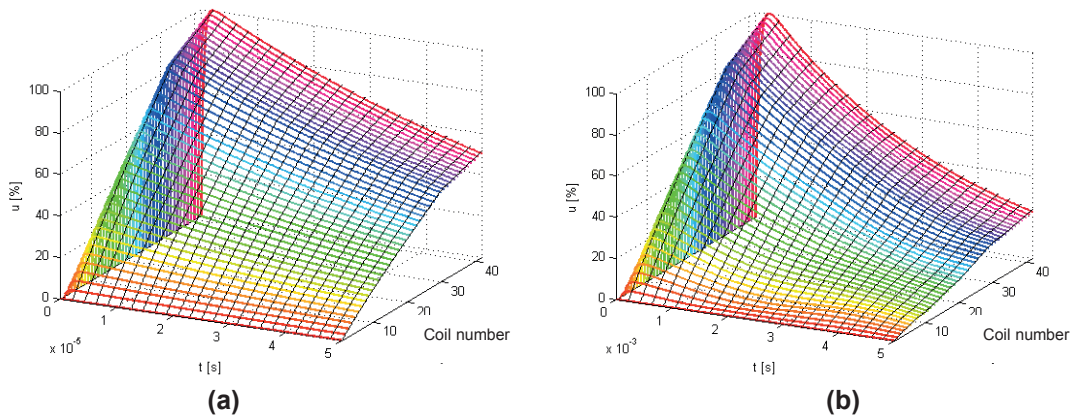
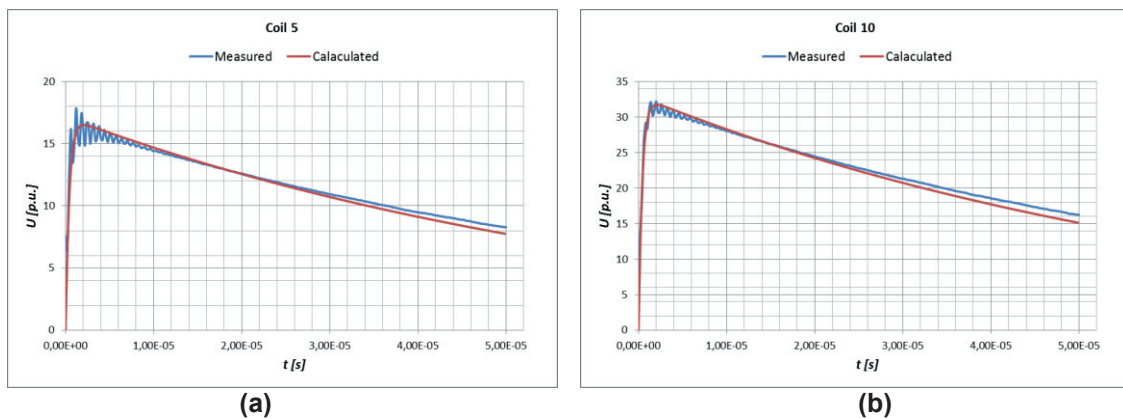


Figure 8 - (a) Calculated lightning impulse voltage distribution (b) Calculated switching impulse voltage distribution

As it would be impractical to compare the entire waveform for measured and calculated results graphically, the comparison is done on a coil-to-coil basis. Coils 5, 10, 30 and 41 are taken as example coils for voltage distribution comparison. This is done to show the behavior on lower coils and upper coils, as it sometimes differs, especially for switching impulse voltage. Comparison is shown in figures 9 (a) - 9 (d) and 10 (a) - 10 (d).



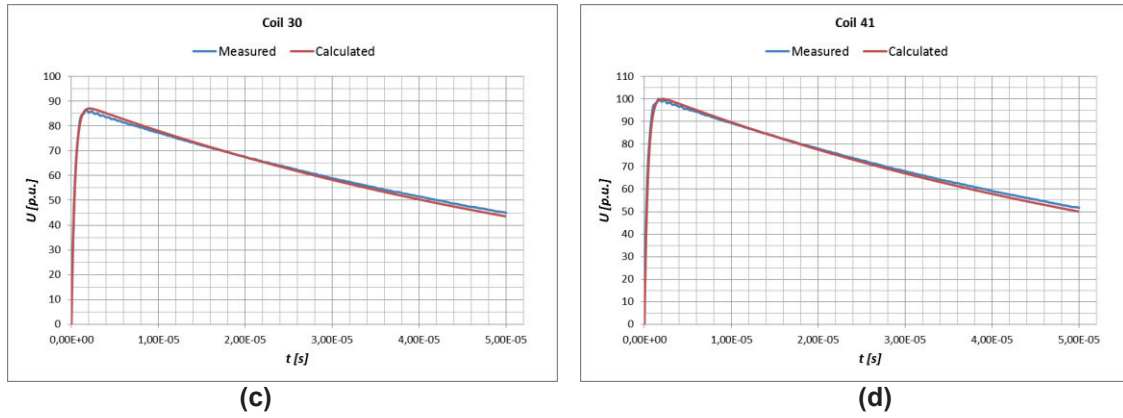


Figure 9 - Comparison of lightning impulse voltage distribution (a) Coil 5 (b) Coil 10 (c) Coil 30 (d) Coil 41

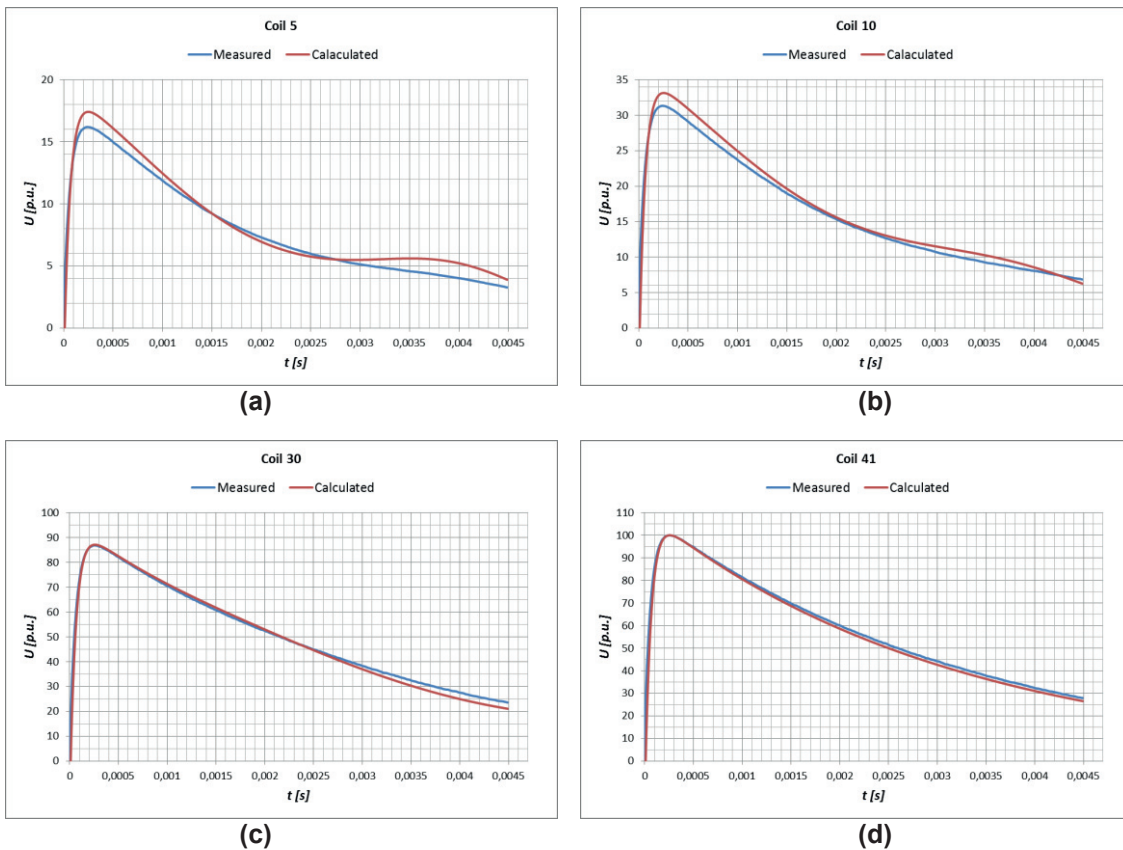


Figure 10 - Comparison of switching impulse voltage distribution (a) Coil 5 (b) Coil 10 (c) Coil 30 (d) Coil 41

As it can be seen from figures 10 and 11, the measured values correspond to the calculated ones very well, with the average difference of 2,1% for lightning impulse and 3,2% for switching impulse voltage distributions, respectively.

6. AFTERMATH

Criterion for insulation breakdown for systems of such complexity is extremely hard to determine. This is why, in some cases, it is easier to perform type testing, see how the transformer does and use this as a reference point for future design.

This was the logic for 550 kV inductive voltage transformer in question. Seeing that all interphase measurement results were satisfactory, as explained in chapter 5, the transformer was submitted to type testing according to IEC 60044-2 and CAN/CSA C60044-2:07 standards (test voltages taken from the latter).

Because of their unique insulation system, explained in chapters 1 and 2, lightning impulse voltage testing generally is not considered critical for open-core inductive voltage transformer. On the other hand, switching voltage under artificial rain conditions is the most perilous test for these transformers. This is why we wanted to emphasize the results of this particular test.

Not only did the transformer pass the type testing according to standard requirements from table I, but also withstood several impulses with higher amplitude, ending with three positive polarity impulses of 1375 kV. Neither insulation breakdown, nor any difference in wave shape was observed.

A subsequent chromatographic analysis of the transformer oil showed no evidence of any gasses appearing as a consequence of type testing. Naturally, the transformer was successfully re-tested routinely, with partial discharge intensity remaining non-existent. A photograph of the transformer during type testing can be seen in figure 11 (a), while the applied voltage magnitude can be seen in figure 11 (b).

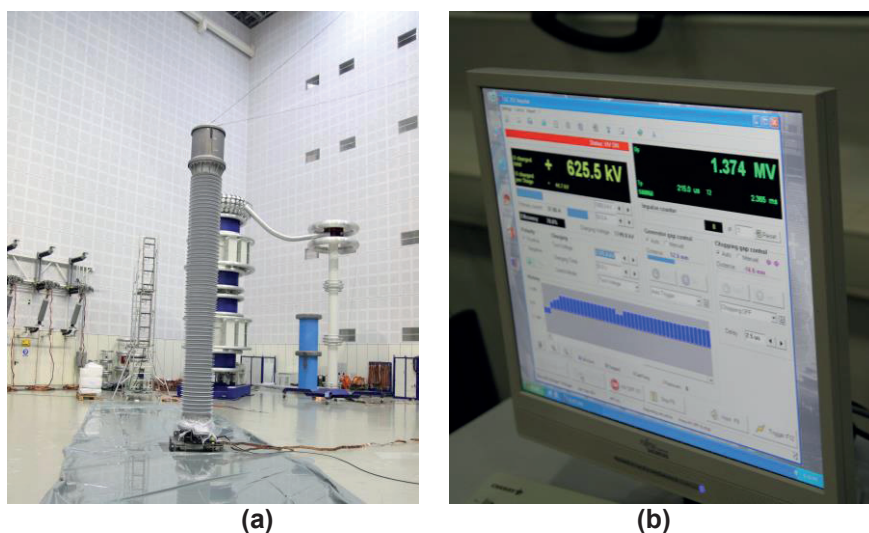


Figure 11 - (a) VPU-525 under type testing (b) Maximal applied voltage magnitude

7. CONCLUSION

The aim of this paper is two-fold. The first objective was to demonstrate the influence of starting parameters of every inductive voltage transformer design (i.e. the primary winding turn number and geometry of the screens in the main insulation) on the voltage distribution under typical overvoltages that the transformer can encounter during its lifetime. The second objective was to show that by understanding the effect of these starting parameters and by utilizing the described calculation toolset, it is possible to efficiently and swiftly calculate and assess voltage stress in the main insulation, thus essentially forcing the main insulation to behave the way the designer intended.

It is shown that decreasing the total primary turn number has a positive effect on the voltage distribution overall. Increasing the capacitances of the main insulation generally has a positive effect on voltage distribution during lightning impulse and chopped impulse overvoltages and a negative effect on power frequency voltage distribution. For this particular case, however, the effect of capacitance increase remained relatively negligible.

Transformer design based on these foundations was thoroughly checked during interphase testing, before being succumbed to final type testing. Results of interphase measurements corresponded very well with the calculated values, thus once again confirming the applicability of the proposed calculation methodology. Type testing was completely successful as well, with the transformer withstanding 830 kV PFVV, 1800 kV BIL, 2070 kV CIWV and 1300 kV SIWV without any problem whatsoever.

Such insulation design is enabled by the mentioned galvanic interconnection between primary winding sections and corresponding capacitive screens, unique to the open-core inductive voltage transformer concept. This paper has shown that the entire philosophy and background behind that design are ready to accept the next challenge in line and push the boundaries of design even further.

REFERENCES

- [1] M.Poljak, "Insulation system of combined instrument transformers", Doctoral thesis, Faculty of Electrical Engineering and Computing, Zagreb, Croatia 2006.
- [2] M. Poljak, B. Bojanić "How to prevent instrument transformer explosions" , CIGRE Croatia, Cavtat, Croatia, 2007.
- [3] "IEC 61869-1:2009, Instrument Transformers - Part 1: General Requirements", 2009.
- [4] "IEC 61869-3, Instrument Transformers - Part 3: Additional requirements for voltage transformers", 2011.
- [5] "CAN/CSA-C60044-2:07, Instrument transformers - Part 2: Inductive voltage transformers", 2007.
- [6] IEEE C57.13, "IEEE Standard requirements for instrument transformers", IEEE engineering society, 2008.
- [7] M. Poljak, B. Bojanić, "Dilemma - Inductive or Capacitor Voltage transformers", CIGRE Croatia, Cavtat, 2003.
- [8] I, Žiger, B. Bojanić, D. Krajtner, "Open-core Power Voltage Transformers: Concept, Properties, Application", Energycon 2014, Cavtat, Croatia, 2014.
- [9] D. Filipović-Grčić, "Optimization of condenser type insulation system made of oil impregnated paper", Doctoral dissertation, Faculty of Electrical Engineering and Computing, Zagreb, 2010.
- [10] M.T. Gencoglu, M. Cebeci , "The pollution flashover on high voltage insulators", Electric Power Systems Research, Elsevier, 2008.
- [11] R. Wilkins, "Mechanisms of Failure of High Voltage Insulation with Surface Contamination", Power Record Inst. El. Engrng, Vol 111, 1964.
- [12] M.W. Faranzeh, W.A. Chisholm, Insulators for Icing and Polluted Environments, IEEE, 2009.
- [13] K.Sokolija, Visokonaponski izolatori, Elektrotehnički fakultet u Sarajevu, 2000.
- [14] M.Poljak, D. Filipović-Grčić - Optimisation of Instrument Transformers Insulating Systems CIGRE Croatia, Cavtat, 2005.
- [15] Infolytica corporation, "2d case study - Self-inductance of a brooks coil", 2005.
- [16] Infolytica corporation, "2d case study - Mutual inductance of coaxial coils", 2005.
- [17] D. Meeker, "FEMM 4.2. Magnetostatics tutorial", 2006.
- [18] A.H.Soloot, A.Gholami, E.Agheb, A.Ghotbandaeipour, P.Mokhtari, "Investigation of transmission line overvoltages and their deduction approach", World Academy of Science, Engineering and Technology, 2009.
- [19] S.A. Probert, Y.H. Song, P.K. Basak, C.P. Ferguson , „Review of the basic insulation level for 400 kV oil-filled cable systems. Switching and temporary overvoltages (TOV)“, European Transactions on Electrical Power, 2003.

Branimir Ćučić
Končar - Distribution & Special Transformers Inc.
branimir.cucic@koncar-dst.hr

Nina Meško
Končar - Distribution & Special Transformers Inc.
nina.mesko@koncar-dst.hr

Martina Mikulić
Končar - Distribution & Special Transformers Inc.
martina.mikulic@koncar-dst.hr

Dominik Trstoglavac
Končar - Distribution & Special Transformers Inc.
dominik.trstoglavac@koncar-dst.hr

DESIGN IMPROVEMENTS IN MODERN DISTRIBUTION TRANSFORMERS

SUMMARY

In the paper design improvements of distribution transformers related to improved energy efficiency and environmental awareness are discussed. Eco design of transformers, amorphous transformers, voltage regulated transformers and transformers filled with ester liquids are analyzed.

As a consequence of growing energy efficiency importance, European Commission has adopted new regulation which defines maximum permissible levels of load and no-load losses of transformers with rated power ≤ 3150 kVA, and minimum peak efficiency index for transformers with rated power > 3150 kVA up to 40 MVA. The impact of new regulation on the design and economy of transformer is presented.

Amorphous transformers, with up to 70 % lower no-load losses in comparison to the conventional transformers, could be an alternative with respect to energy efficiency. Although their initial price is higher than the price of conventional transformers, some studies show that they might have economic advantages.

The increasing penetration of distributed energy sources can cause an increase in voltage variations in low voltage networks. To keep the voltage within limits defined by EN50160, voltage regulated distribution transformers could be used.

Although mineral oil has been used as a dielectric fluid in transformers for many years, there are some environmentally friendlier alternatives – natural and synthetic ester-based fluids.

Key words: energy efficiency, ecodesign, distribution transformer, ester fluids

1. INTRODUCTION

Nowadays, greenhouse gas emission in the atmosphere, considering its influence on global warming and climate change, is the biggest environmental challenge. There are many heat-trapping gases (from methane to water vapor), but carbon dioxide puts us at the greatest risk of irreversible changes if it continues to accumulate unabated in the atmosphere. In order to reduce carbon dioxide levels in the atmosphere, the energy produced from fossil fuels needs to be reduced. To do this both energy efficiency and usage of renewable energy sources (wind, solar ...) need to be increased.

At the EU level, the ecodesign of products is regulated by the Ecodesign Directive (2009/125/EC) [1]. Ecodesign requirements are aimed at improving energy efficiency by integrating environmental issues and life-cycle thinking already in the product design phase. Following those requirements, European

Commission has adopted new regulations setting new (lower) permissible maximum levels of load and no-load losses for transformers [2].

In the next paragraph the influence of new levels of losses on the design, price, weight and dimensions of modern distribution transformers is discussed, as well as the economic characteristics of amorphous transformers. Furthermore, voltage regulated distribution transformers for networks with renewables are analyzed. Finally, ecological insulations liquids are considered.

2. ENERGY EFFICIENCY

2.1. Ecodesign requirements

Having regard to Ecodesign Directive 2009/125/EC [1] and to the environmental and economic aspect of transformers, European Commission has adopted new regulations for medium power transformers. New ecodesign requirements [2] define maximum permissible levels of load and no-load losses of transformers with rated power ≤ 3150 kVA, and minimum peak efficiency index for transformers with rated power > 3150 kVA up to 40 MVA. This paper focuses on the distribution transformers. Comparing to current standard EN50464-1 [3] which defines levels Ak, Bk, Ck, Dk for load losses and Ao, Bo, Co, Do and Eo for no-load losses, new levels (Table I) are considerably lower, especially for no-load losses. No-load losses are far more reduced in comparison to reduction of load losses because of the fact that their share in total losses of distribution transformers is more than 70 % [4]. For three-phase liquid immersed distribution transformers new permissible levels from 1 July 2015 are CkAo for rated power ≤ 1000 kVA and BkAo for rated power > 1000 kVA. From 1 July 2021 levels come to an even lower level Ak(Ao-10%). New ecodesign requirements for liquid immersed distribution transformers are given in Table I.

Table I – Maximum load (P_k) and no-load losses (P_o) for three-phase liquid immersed distribution transformers with $U_m \leq 24$ kV

Rated Power (kVA)	Tier 1 (from 1 July 2015)				Tier 2 (from 1 July 2021)			
	Maximum load losses P_k (W)		Maximum no-load losses P_o (W)		Maximum load losses P_k (W)		Maximum no-load losses P_o (W)	
≤ 25	Ck	900	Ao	70	Ak	600	Ao-10%	63
50		1100		90		750		81
100		1750		145		1250		130
160		2350		210		1750		189
250		3250		300		2350		270
315		3900		360		2800		324
400		4600		430		3250		387
500		5500		510		3900		459
630		6500		600		4600		540
800		8400		650		6000		585
1000	10500	770	7600	693				
1250	Bk	11000	Ao	950		9500		855
1600		14000		1200		12000		1080
2000		18000		1450		15000		1305
2500		22000		1750		18500		1575
3150		27500		2200		23000		1980

2.2. Impact of ecodesign on a conventional transformer design and economic evaluation

In this paragraph the influence of new ecodesign requirements (lower losses) on the price of material, weight, dimensions and design of the distribution transformer is researched.

2.2.1. Influence on the price and weight of the transformer

On Figure 1 the influence of losses on the price and weight of three-phase distribution transformers (20/0.42 kV, Dyn5) for 4 different rated power; 250, 400, 630 and 1000 kVA is shown.

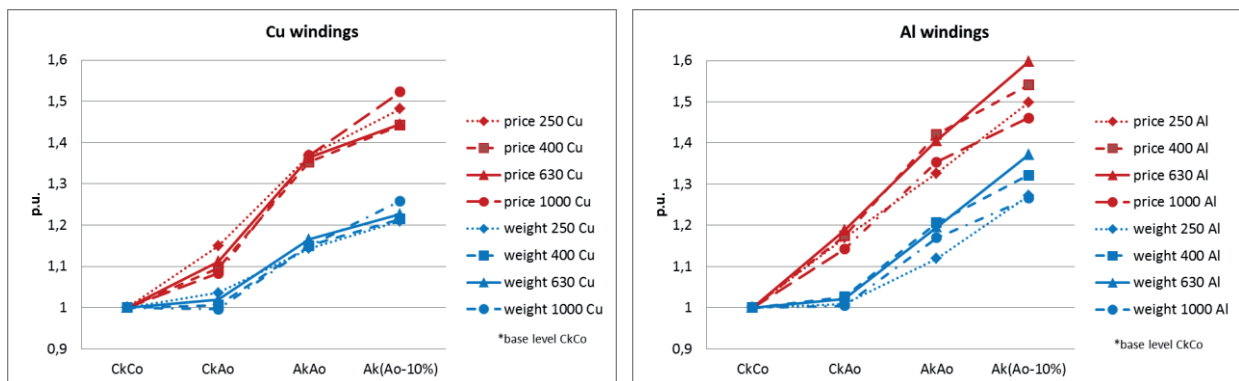


Figure 1 – Influence of the losses on the price of material and weight of the distribution transformers

As shown on Figure 1, ecodesign requirements increase the price of the transformer.

For the particular case, the average price increases for the transformers with copper (Cu) windings are 11% (CkCo->CkAo), 23% (CkAo->AkAo) and 8% (AkAo->Ak(Ao-10%)).

For the transformers with aluminium (Al) windings the price increases are somewhat higher. Average increases are 17% (CkCo->CkAo), 18% (CkAo->AkAo) and 11% (AkAo->Ak(Ao-10%)).

Regarding the weight of transformer, it approximately remains the same for both levels CkCo and CkAo. Lower levels of losses increase the weight. Transition from level CkAo to level AkAo increase the weight in average 14% (Cu) and 16% (Al). Finally, transition from AkAo to Ak(Ao-10%) increase the weight in average 7% for the transformers with Cu windings and 12% for the transformers with Al windings.

2.2.2. Influence on the dimensions of transformer

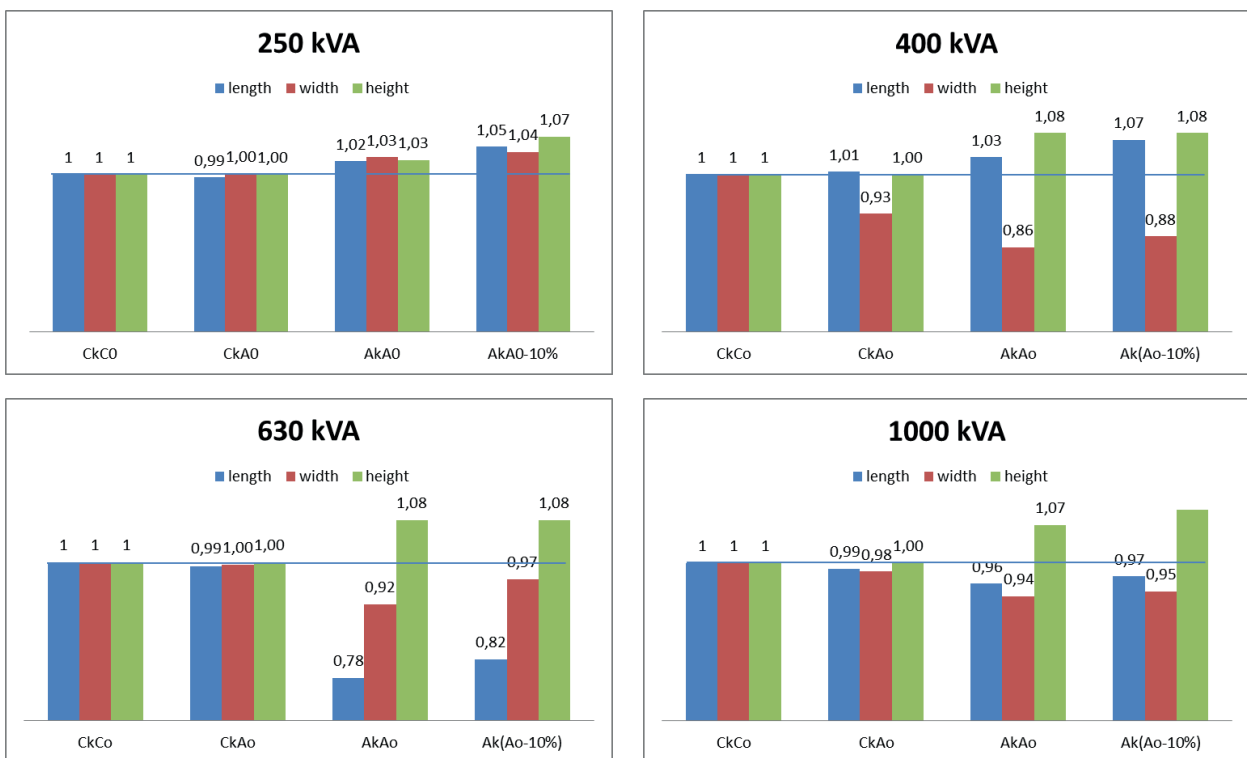


Figure 2 – Influence of the losses on the dimensions of distribution transformers (Al)

Figure 2 shows that new ecodesign requirements do not change significantly the dimensions of transformer. Similarly to weights, dimensions for levels CkCo and CkAo are almost the same. For lower level of losses, height of transformer increases but not more than 10%. Layout dimensions of transformer depend on the optimization of cooling system. Although the active parts is growing as the losses decrease, layout dimension of transformer mainly remain just a bit higher (up to 7%) or decrease. The reason for that is because lower levels of losses require less cooling system and therefore the increasing of active part doesn't reflect to the increasing of layout dimensions of the transformer. Analysis is valid for transformers with both Cu and Al windings.

2.2.3. Influence on the design of the transformer

As it can be seen from Figures 1 and 2, weight and dimensions of the transformer remain almost the same if the level CkCo is replaced with ecodesign required level CkAo. That means that the new transformer can replace the old one in the same space. In the transformer it was achieved by replacing classical grain oriented material (M5) in the core with low loss domain refined material (HGO-DR23). Further reduction of losses (to levels AkAo and Ak(Ao-10%)) requires higher cross section area of conductors and larger active part. It's interesting that, although heavier, transformers mainly keep their layout dimensions because of smaller cooling system.

2.3. Amorphous metal transformers (AMT)

The fact that AMT have up to 70 % lower no-load losses than the conventional distribution transformers makes them suitable related to ecodesign requirements. As stated before, reduction in transformer losses not only saves the current availability of electricity but also helps to reduce future generation needs. This, in turn, will help to reduce CO₂ and other gas emissions, providing a further benefit to the environment. However, amorphous transformers still have higher initial price, dimensions and noise level. Amorphous metal transformers have been used for more than 25 years, but on European market their share is negligible. Due to global movement of environmental protection, energy saving and continuous improvement of amorphous metal characteristics, their importance and share on the EU market may potentially begin to grow.

The amorphous metal used for amorphous transformers is alloy of iron, silicon and boron. To achieve an amorphous structure in a solid metal, the molten metal must be solidified very rapidly so that crystallization cannot take place. Amorphous metal is formed into ribbons, about 25 microns thick and with 3 sizes available width: 142, 170 and 213 mm, which are used to form rectangular shaped wound core. There are 2 three phase core designs types available: 3 phase 5 limbs transformer core and 3 phase 3 limbs transformer core.

2.3.1. Economic evaluation of AMT

Due to the different loss levels and initial price, the optimal way to compare cost effectiveness of amorphous and conventional distribution transformer is the Total Owning Cost (TOC) method. TOC is equal to the sum of transformer purchasing price plus the cost of transformer losses throughout the transformer lifetime. TOC can be calculated using the formula [5]:

$$TOC = PP + A \cdot P_o + B \cdot P_k, \quad (1)$$

where PP – is the purchase price of transformer
 A – represents the assigned cost of no-load losses per watt
 P_o – is the rated no-load loss
 B – is the assigned cost of load losses per watt
 P_k – is the rated load loss.

P_o and P_k are transformer rated losses. Values A and B depend on the expected loading of the transformer and energy prices. The choice of the factors A and B is difficult since they depend on the expected loading of the transformer, which is often unknown, and energy prices, which are volatile, as well as interest rate and the anticipated economic lifetime. Typically, the value of A ranges from less than 1 to 14 EUR/Watt and B is between 0.2 and 5 EUR/Watt. Below a relatively simple method for determining the A and B factor for distribution transformers is proposed.

A and B factors are calculated as follows [5]:

$$A = \frac{(1+i)^n - 1}{i \cdot (1+i)^n} \cdot C_{kWh} \cdot 8760 \quad (2)$$

$$B = \frac{(1+i)^n - 1}{i \cdot (1+i)^n} \cdot C_{kWh} \cdot 8760 \cdot \left(\frac{I_l}{I_r}\right)^2 = A \cdot \left(\frac{I_l}{I_r}\right)^2 \quad (3)$$

where: i – interest rate [%/year]
 n – lifetime [years]
 C_{kWh} – kWh price [EUR/kWh]
8760 – number of hours in a year [h/year]
 I_l – loading current [A]
 I_r – rated current [A]

Three different studies will be presented: one from USA [6], the other one from China [7] (both analyzed in [8]) and the last one from France [9].

In first two studies following values were considered: $i=5\%$, $C_{kWh}=0.04$ EUR/kWh and $n=30$ years. The load losses will have 10 % and 20 % in relation to no-load losses, which are typical values for countryside and town distributions.

USA study shows total evaluation of different types of 50 kVA liquid-filled single phase type transformers according to the Table II:

Table II – Total evaluation of different types of 50 kVA transformers in USA

Type of transformer	Amorphous core type and Cu winding	Core type M2 and Cu winding	Core type M6 and Al winding
Price	1,540 €	1,190 €	1,050 €
No-Load losses	40 W	130 W	200 W
Load losses	720 W	880 W	1,400 W
Evaluated no-load loss	216 €	702 €	1,080 €
Evaluated load losses 10% / 20%	390 € / 780 €	470 € / 940 €	760 € / 1,520 €
Total evaluation	2,146 € / 2,536 €	2,362 € / 2,832 €	2,890 € / 3,650 €

Although the amorphous transformer has the highest initial price, considering the values taken for interest rate, kWh price, lifetime and losses, it also has the lowest total owning cost which in this particular case makes it the most economic choice, considering the low values of load and no-load losses.

In the second study load losses and no-load losses are compared for distribution transformers 100 kVA and 500 kVA, classified as SBH15 and S11 type transformers. SBH15 is an amorphous core type and S11 is a typical low loss traditional liquid filled distribution transformer. The evaluation in this particular case (Table III) also shows more expensive transformer (amorphous core type) to be more economic choice considering losses and price. If a higher loss valuation would be used, the advantages for amorphous core material would be even greater.

Table III – Total evaluation of different types of 100 kVA and 500 kVA transformers in Chin

Type of transformer	100 kVA AMDT (SBH15)	100 kVA Conventional (S11)	500 kVA AMDT (SBH15)	500 kVA Conventional (S11)
Price	3,450 €	2,980 €	9,360 €	7,980 €
No-Load losses	75 W	200 W	240 W	680 W
Load losses	1,500 W	1,500 W	5,150 €	5,150 W
Evaluated no-load loss	405 €	1,080 €	1,290 €	3670 €
Evaluated load losses 10% / 20%	810/1,620 €	810/1,620 €	2,780 € / 5,560 €	2,780 € / 5,560 €
Total evaluation	4,665 € / 5,475 €	4,870 € / 5,680 €	13,430 € / 16,210 €	14,430 € / 17,210 €

From these two studies, the amorphous core material has economic advantages and shows, under these circumstances, to be the preferable option, although a relatively conservative loss valuation is used.

The third study shows different results although the values for A, B, P_o and P_k are unknown in the article. According to the study by EDF [9] made on 400 kVA 3-phase transformers with the loss level CkA_o/2 and CkB_o, the initial price of the amorphous transformer is 44 % higher and profitability is visible after approximately 27 years (Figure 3).

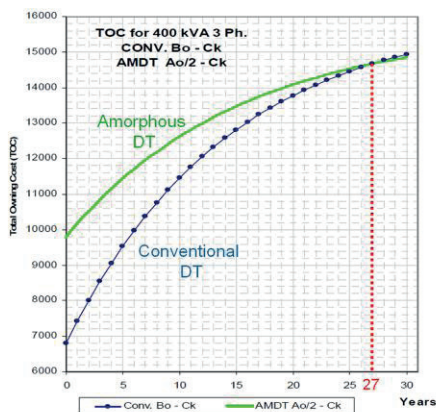


Figure 3 – Economic evaluation of AMT (EDF)

3. RENEWABLES

In the past electrical energy has predominantly been generated in large centralized power plants, but due to environment concerns and constant increase in fossil fuel price, the new trend in the modern power industry is towards renewable energy. Therefore, in 2008 the European Union has made "European plan on climate change" (also known as "European 20-20-20 targets") with three key objectives: a 20% reduction in EU greenhouse gas emissions from 1990 levels, raising the share of EU energy consumption produced from renewable resources to 20% and a 20% improvement in the EU's energy efficiency.

However, renewable energy plants have also some disadvantages: reliability of supply, large cost of initial investment, difficulty in obtaining the quantities of energy that are as large as those produced by traditional power plant and decentralized power generation. This last mentioned disadvantage has great influence on the standard design of the distribution transformer. Transformers in this distribution system have typically been designed to ensure a constant load flow from higher to lower voltage levels, but the large growth of distributed energy sources can lead to temporary reverse feeding from low voltage to medium or even high voltage.

3.1. Regulated distribution transformers (RDT)

Standard distribution transformer regulates the voltage usually in the range $\pm 2 \times 2,5\%$ or $\pm 1 \times 4\%$ of the rated voltage with off-load tap changer because it can only be switched when the transformer is de-energized.

The increasing penetration of distributed energy sources can cause an increase in voltage variations in low voltage networks. In order to keep voltage in the range $U_n \pm 10\%$, as required by standard [10], it is necessary to increase the regulation range as well as to enable automatic voltage regulation especially in relation to smart grid. Transformers capable of fulfilling those requirements are called voltage regulated distribution transformers. Basically, there are two types of those transformers. In first, on-load voltage regulator is placed directly in the low voltage (secondary) circuit. With this solution the regulation range is limited to app. $\pm 4\%$ while only one turn is switched off or on. To expand the regulation range, additional off-load tap changer in the high voltage side of transformer is used. It can only be switched when the transformer is de-energized.

In the second type voltage regulator is a part of primary circuit of transformer (Figure 4) with voltage feedback from the secondary side. With this solution completely automatic on load regulation of secondary voltage in the range $\pm 10\%$ is achieved with layout dimensions of transformers remaining the same.

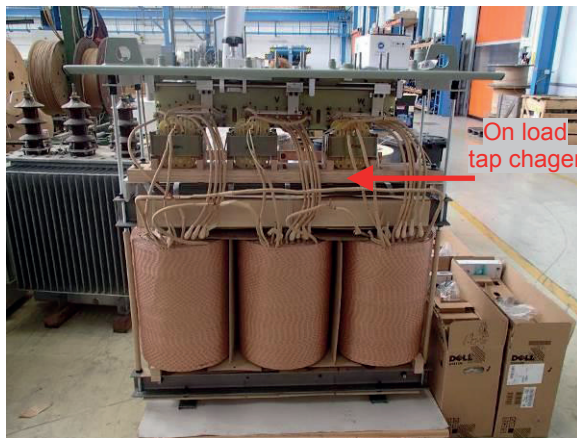


Figure 4 – Regulated distribution transformer (Končar D&ST)



Figure 5 – RDT after short circuit test

Voltage regulator is mounted at the same place as usual off load tap changer, but it requires more space in height. Such transformers must be designed with special attention in order to withstand short circuit forces. Figure 5 shows active part of RDT after successful short circuit withstand test.

Regulated distribution transformers are heavier and considerably more expensive than standard distribution transformers, mostly due to the size and price of the on-load voltage regulator.

4. ECOLOGICAL INSULATION LIQUIDS

Traditional mineral oils have been used as a dielectric fluid in generations of transformers although they have low biodegradation rate and low fire resistance. As the industry is migrating in the direction of environmental awareness, today in the market there are environmentally friendly alternatives. Natural and synthetic ester-based dielectric fluids have considerably higher both biodegradation rate and fire resistance. The flash point of such insulation liquids is 270-330 °C which is far more than 145 °C for mineral oils. Furthermore, both natural and synthetic esters are classified as being "readily biodegradable" which means that 90 % of biodegradation occurs within 28 days [11]. Figure 6 shows biodegradation rate of insulation fluids used in transformers.

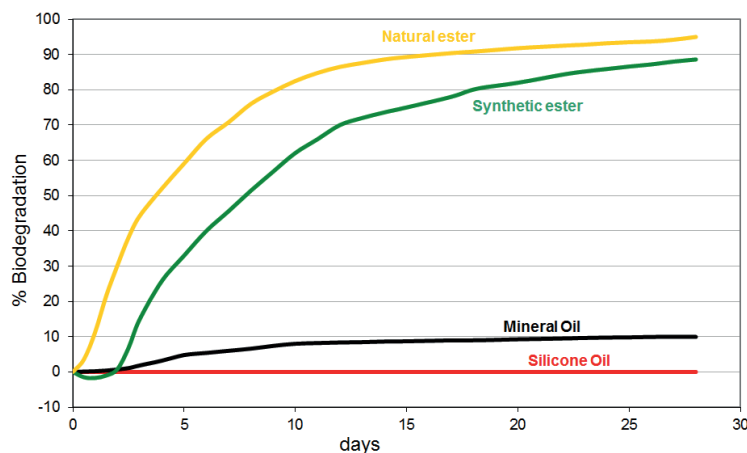


Figure 6 – Biodegradation rates of transformer insulation fluids

Ester insulation liquids have considerably higher moisture tolerance than mineral oils which means that they can absorb higher amount of water without compromising their dielectric properties. That has beneficial effect on the cellulose working life.

However, the ester immersed transformers compared to those filled with mineral oil must have larger cooling surface due to higher viscosity of esters. Furthermore, such liquids are more expensive than mineral oil (natural app. 3 times, synthetic app. 4 times). Because of that ester immersed transformers are currently approximately 25 % more expensive than conventional counterparts.

5. CONCLUSION

Industry is migrating in the direction of environmental awareness and improved energy efficiency. Distribution transformer with implemented newly adopted ecodesign requirements has basically the same design as standard transformer but with core generally made out of top quality domain refined material. Although the active parts is growing as the losses decrease, layout dimension of transformer mainly remain just a bit higher (up to 7%) or decrease.

Amorphous metal transformers with naturally up to 70% lower no-load losses than their traditional counterparts offer a noteworthy alternative. Because of higher initial price, dimensions and weight, they can be economically cost effective only if the capitalization is taken into account. Some analysis show that they are cost effective (USA, China), the other one that they are not (France).

Regulated distribution transformers with on-load tap changer in the primary side of transformer (instead of usual off-load tap changer) enable automatic voltage regulation in the secondary side in the range $\pm 10\%$. Thus the voltage can be kept within permissible range defined by EN50160 in spite of the stochastic voltage variations in the network with renewables. Such transformers keep the same layout dimensions as the standard ones.

Natural and synthetic ester-based insulation fluids are ecofriendly alternatives for minerals oils.

REFERENCES

- [1] Directive 2009/125/EC of the European Parliament and of the Council of 21 October 2009 establishing a framework for the setting of ecodesign requirements for energy-related products, Official Journal of the European Union, 2009
- [2] Commission Regulation (EU) No 548/2014 on implementing Directive 2009/125/EC of the European Parliament and of the Council with regard to small, medium and large power transformers, 21 May 2014
- [3] EN 50464-1 Three-phase oil-immersed distribution transformers 50 Hz, from 50 kVA to 2500 kVA with highest voltage for equipment not exceeding 35 kV – Part 1: General requirements, April 2007
- [4] R. Targosz, F. Topalis, "Selecting energy-efficient distribution transformers: A guide for achieving least-cost solutions", SEEDT Project, 2008
- [5] P.S. Georgilakis, "Spotlight on modern transformer design", Springer, 2009
- [6] "Energy Conservation Standards for Distribution transformers, ANPOR Public Meeting, Energy Analysis", Building Technologies Program Office of Energy Efficiency and Renewable Energy, U.S. Department of Energy, September 28, 2004
- [7] H.Wen et al., "Exploration on energy-saving effect of amorphous transformers extended in Nanning based on theoretical analysis and Total Owning Cost methods (TOC)", CICED 2008, Technical Session 4, Distributed power generation and integration technology
- [8] A. Eliasson, H. Elvfing, et al., "Amorphous Metal Core Material Shows Economic and Environmental Benefits when Pre-existing Transformers are to be Replaced within Vattenfall Group's Distribution Network", Contribution to IEEE PES, Gothenburg, Oct 2010
- [9] C. Elleau et al., "Amorphous distribution transformers trial test campaign", 21th International Conference on Electricity Distribution, Frankfurt, June 2011, Paper 0227
- [10] EN 50160 Voltage characteristics of electricity supplied by public electricity networks, March 2013
- [11] I. Radić, I. Sitar, "Synthetic esters in power and special transformers", 2. International Colloquium Transformer Research and Asset Management, Dubrovnik, Croatia, May 2012

Emanuel Almeida
EFACEC Power Transformers
emanuel.almeida@efacec.com

Pedro Pedro
EFACEC Power Transformers
pedropedro@efacec.com

Paulo Martins
Instituto Superior Técnico
pmartins@tecnico.ulisboa.pt

Carlos Silva
Instituto Superior Técnico
carlos.alves.silva@tecnico.ulisboa.pt

EVALUATION OF DIFFERENT TYPES OF STEEL UNDER HIGH LOADING RATES FOR SHORT CIRCUIT APPLICATIONS

SUMMARY

This paper draws from independent experimental results pertaining to the properties of steel loaded at high strain rates, similar to those found in power transformer short-circuits. The types of steel that were tested are common non-alloy structural steel and high strength structural steel. The experiments showed that the most common types of structural steel, when loaded at high rates, are capable of absorbing considerably more energy than in quasi-static conditions. On the other hand, the high strength structural types of steel that were tested showed no improvement in their energy absorbing characteristics at high strain rates. The paper provides some examples to show how the experimental results may be incorporated in the design of steel components for short circuit safety. The last part is focused on the plastic deformation of steel and assesses its influence on the impedance variation of the power transformer following a short circuit.

Key words: Shell form transformers, short-circuit, dynamic analysis, material high loading rate

1. INTRODUCTION

Transformers are electrical machines placed in networks that may occasionally suffer from external short-circuit. When such a fault occurs on the output line of the transformer, very high currents are pulled from the supply line of the transformer [1]. These very high currents generate heat and forces on windings that may be enormous. Standard measures to design transformers to withstand short circuit faults are provided in [2], where a standard duration of 2s is specified. During this time frame, winding temperature will increase due to the high current value. At the same time, high axial forces generated in the coil conductors are propagated across insulation elements, oil, clamping woods onto the core or tank [3]. For this reason, the tank is equipped with a specific structural short-circuit beam designed to withstand the impact of these high forces (case of a shell form transformer) [4].

The first design consideration is therefore the thermal effect brought on by the high short duration currents. As the thermal time constant of a winding is over 100 times greater than the maximum duration of the fault, it is acceptable to consider that all generated heat is retained in the conductors whose temperature will evidently rise. Analytical formulae or numerical methods may be employed to estimate the winding temperature rise, where [2] again provides maximum admissible temperatures for aluminum or copper conductors.

The second design consideration, on which this paper focuses upon, is the very high forces generated when the conductors are subject to the short circuit currents. Lying in a magnetic leakage field, conductors which carry current shall become loaded by a force of magnitude proportional to the square of that current [3]. The resultant force of a coil will be transmitted across paper and pressboard elements onto the adjacent coil. This situation repeats itself for all loaded coils. Because there are significant masses (mostly from the copper or aluminum conductors) and significant spring elements (pressboard, with non-linear characteristics), the problem of studying the movement of a winding must be performed in the dynamic domain. Clear description on the winding and core clamping schemes of shell form transformers can be found in [3][4].

In general, the structural parts of power transformers are made from non-alloy structural steel types but the selection process of the steel grade is sometimes based on the material stress response under quasi-static loading conditions derived from tensile tests performed in conventional universal testing machines (see for example [5]). Because the main goal of material selection for structural parts of power transformers is to improve mechanical performance, reduce weight and minimize costs while meeting the safety requirements during short-circuit faults, it follows that knowledge of the stress-strain mechanical behavior under medium to high rates of loading is crucial for choosing the steel grade and for designing shell form power transformers at the extreme conditions that are commonly found during short circuit faults.

The mechanical characterization of materials under different strain rate $\dot{\epsilon}$ loading conditions can be systematized into five categories; (i) mechanical characterization under extremely low rates of loading (say, $\dot{\epsilon} < 10^{-4} \text{ s}^{-1}$ and commonly designated as ‘the creep domain’), (ii) mechanical characterization under low rates of loading (say, $10^{-4} < \dot{\epsilon} < 10^{-1} \text{ s}^{-1}$ and designated as ‘the quasi-static domain’), (iii) mechanical characterization under medium rates of loading (say, $10^{-1} < \dot{\epsilon} < 10^2 \text{ s}^{-1}$ and designated as ‘the intermediate strain rate domain’), (iv) mechanical characterization under high rates of loading (say, $10^2 < \dot{\epsilon} < 10^5 \text{ s}^{-1}$ and designated as ‘the high strain rate domain’) and (v) mechanical characterization under very high rates of loading (say, $\dot{\epsilon} > 10^5 \text{ s}^{-1}$ and designated as ‘the ballistic or ultrahigh strain rate domain’) [6].

The importance of properly defining the strain rate loading conditions for designing shell form power transformers results from the generalized lack of information regarding the flow stress $\sigma(\epsilon, \dot{\epsilon})$ for strain rates acting above the quasi-static domain and may be considered one of the main reasons for designing structural elements to be more robust, heavier and more expensive than necessary for power transformers to fulfil the safety requirements.

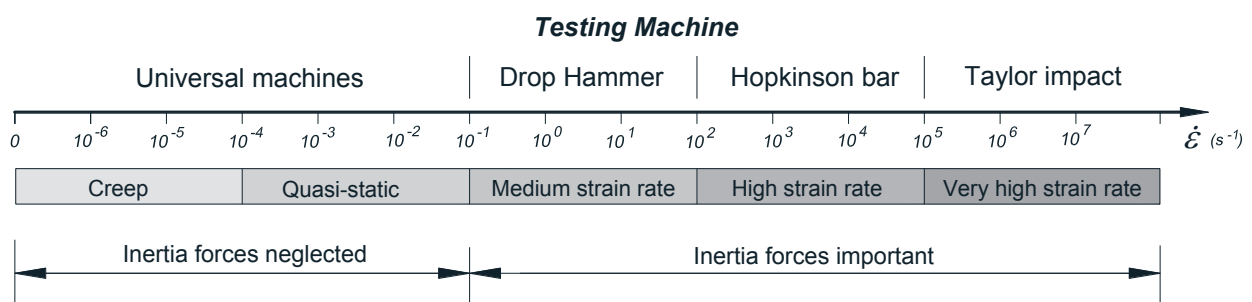


Figure 1. Strain rate operating conditions corresponding to different types of mechanical testing machines

Figure 1 presents an attempt to correlate the different types of mechanical testing machines used for material characterization with the operating conditions of strain rate that are required for a specific engineering application [3]. As seen, the mechanical characterization of materials in the creep and quasi-static strain rate domains is performed by the widely available universal testing machines operating under load, displacement or strain control. The mechanical characterization of materials in the intermediate strain rate domain is more difficult to perform and frequently involves the utilization of tailored designed drop weight (gravity), hydraulic or mechanical systems. Special purpose testing equipment based on slip Hopkinson pressure bars and Taylor impact systems are needed for the mechanical characterization of materials in the high and ultrahigh strain rate domains.

In case of material characterization for the structural parts of power transformers, the strain rate loading conditions need to be identical to those occurring in short circuit faults (around 100 s^{-1}) and , therefore, drop weight testing machines are the most adequate equipment.

This paper presents an in-house flexible drop weight testing machine to perform the mechanical characterization of the types of structural steel that are commonly used in the fabrication of shell form tanks. The flow stress $\sigma(\varepsilon, \dot{\varepsilon})$ derived from these tests is then used to obtain finite element estimates of the plastic deformation of the main structural components of a power transformer that was short circuit tested.

Results show that knowledge of the mechanical properties of the materials at medium to high strain rates is very important to estimate the plastic deformation of structural components that may arise from short circuits or other situations where the rate of loading is relatively high and the time period is short.

2. MECHANICAL CHARACTERIZATION

2.1. Equipment, methods and procedures

The investigation made use of three different types of non-alloy structural steel (S235JR, S275JR and S355JR) and a high strength structural steel (WELDOX 700). The mechanical characterization was performed by means of compression tests carried out on cylindrical test specimens with 6 mm diameter and 9 mm height that were manufactured from the supplied steel plates at strain rate levels of approximately 100 s^{-1} in order to match the loading rates originated in short circuit faults.

Figure 2 presents the in-house flexible drop weight testing machine where tests were performed with schematic charts showing its main operating features. For presentation purposes and although not corresponding to what readers directly observe in Figure 2a, the main components of the machine are split into three main groups: (1) structural, (2) mechanical and electrical, and (3) control and measurement.

The structural components of the machine comprise the frame and a plurality of individual parts that are independent of the material and mechanical tests to be performed such as, the pre-stressed columns, the anvil that holds the tool, and the support plates that are used for fixing the machine to the floor. The ram and its levering system, the tool and its active die accessories for each specific mechanical test to be performed are the most significant mechanical and electrical components. The equipment for monitoring the downward drop of the carriage and ram, the load cell, the displacement transducer, and the data acquisition system are the main control and measuring components.

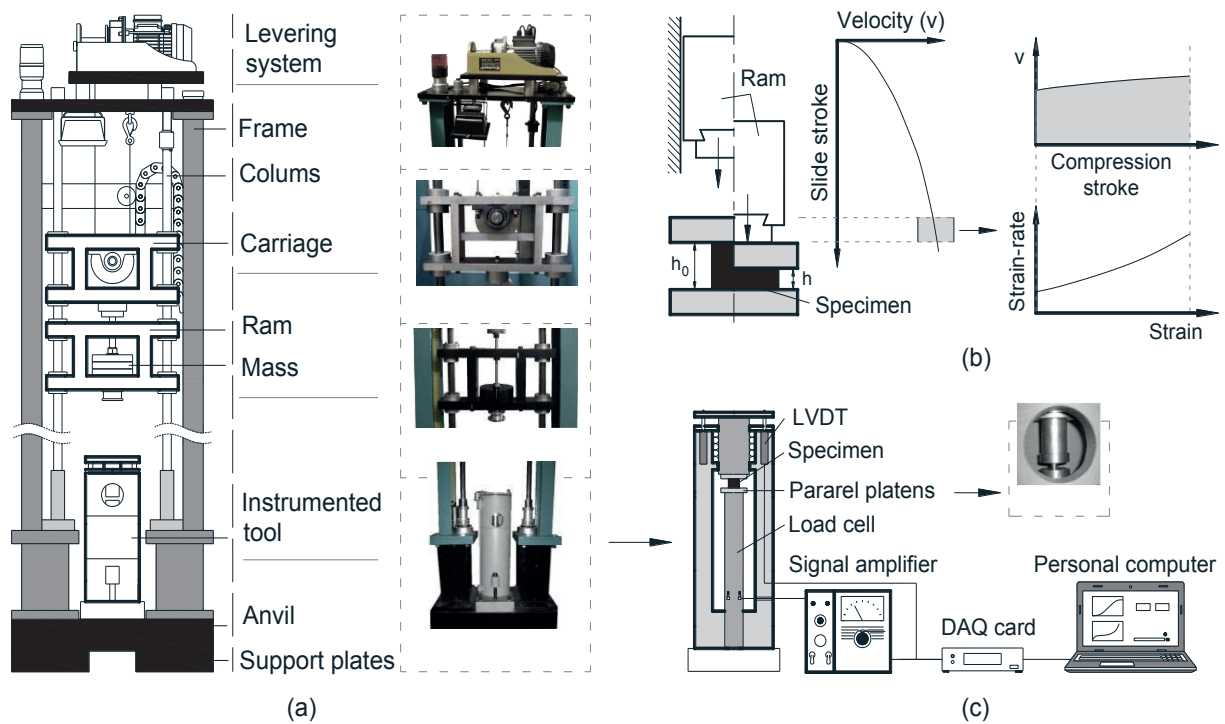


Figure 2: Flexible drop weight testing machine. (a) Schematic representation. (b) Velocity versus stroke and strain rate versus strain loading paths in the working region. (c) Detail of the tool equipped with a load cell and a displacement transducer.

The most important characteristic of this machine is the tailored-made operating conditions resulting from the flexible design of the ram and tool. In fact, the mass of the ram and the height of the fall can be easily changed so that velocity and energy of each test can be selected to match the desired strain rate loading conditions. The active die accessories of the tool can also be easily replaced in order to perform a wide variety of tests such as compression, friction, and fracture toughness, among others.

The load cell installed in the tool was fabricated by the authors and is based on traditional strain gage technology in full wheatstone bridge. The load cell has a capacity of 40 kN, a nominal sensitivity of 1 mV/V, and an accuracy class 0.7. The displacement transducer is a commercial linear variable differential transformer (LVDT Solartron AC15). Both the load cell and the displacement transducer are mounted inside the tool case where the active die components are installed (refer to the detail in Figure 2c). The load cell is connected to a signal amplifier unit (Vishay 2310B) and a personal computer data logging system based on a DAQ card (PCI-6115, National Instruments) combined with a special purpose LabView software acquires and stores the experimental data from both the load cell and the displacement transducer. The true stress and strain are determined from these experimental data as follows,

$$\sigma = \frac{F}{A} \quad \varepsilon = -\int_{h_0}^h \frac{dh}{h} = \ln \frac{h_0}{h} \quad (1)$$

where F is the experimentally measured force, A is the cross section of the compression test specimen and h and h_0 are the actual and initial height of the compression test specimens obtained from the displacement transducer.

The strain rate is determined as follows,

$$\dot{\varepsilon} = \frac{d\varepsilon}{dt} = \frac{1}{h} \frac{dh}{dt} \cong \frac{v}{h} \quad (2)$$

where v is the velocity of the testing machine.

2.2. High loading rate material test results

Figure 3 shows the stress-strain behavior of the four different types of steel obtained from compression tests before and after filtering the oscillations that are commonly found at the beginning of these curves as a result of the dynamic loading testing conditions. The fitted curves after filtering the oscillations are drawn in black and the results of compression tests performed in a universal mechanical testing machine under quasi static loading conditions are included in red for comparison purposes.

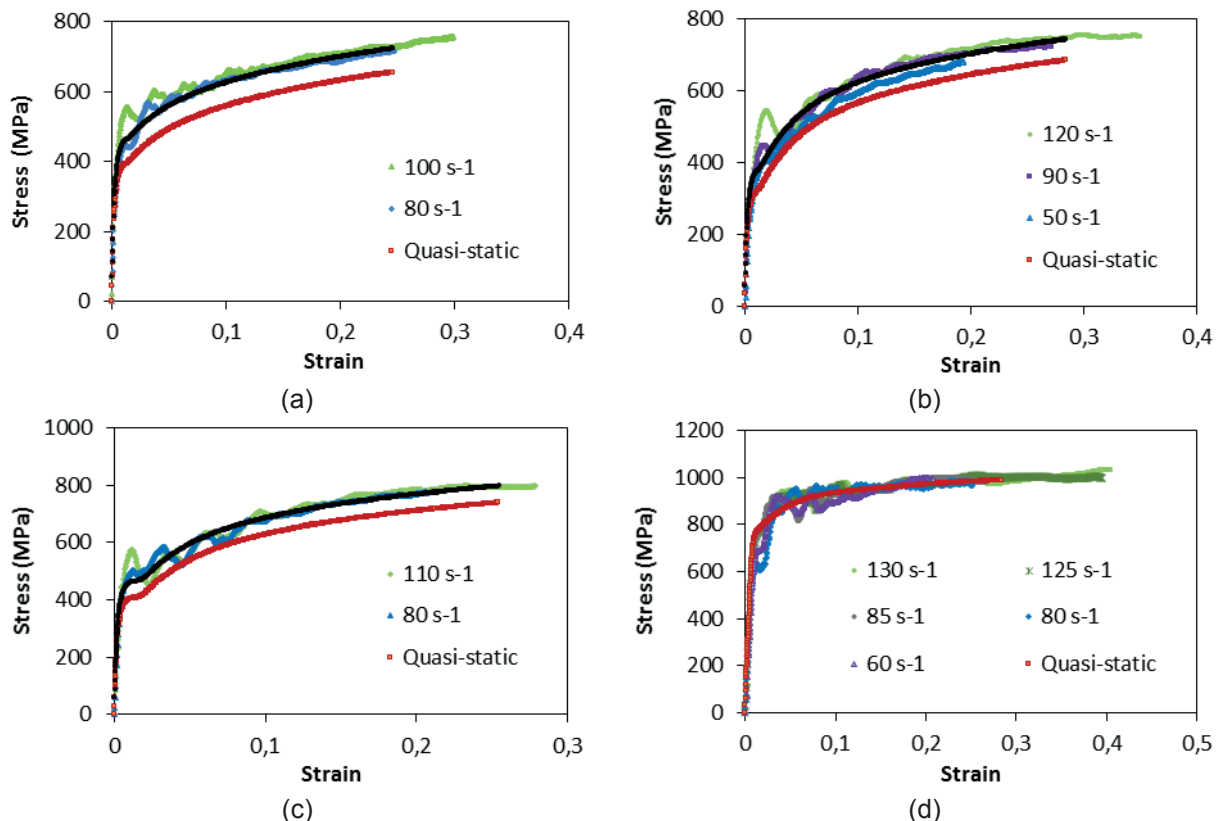


Figure 3: True stress-strain curves of the (a) S235JR, (b) S275JR, (c) S355JR and (d) WELDOX 700 types of structural steel obtained from compression tests at different strain rates

As seen in Figures 3a, 3b and 3c, the stress response of non-alloy structural steel S235JR, S275JR and S355JR increases by approximately 60 MPa~70 MPa when the strain rate loading conditions are increased from quasi-static to 100 s^{-1} . In contrast, Figure 3d, allows concluding that the stress response of the high strength structural steel WELDOX 700 remains practically unchanged when the strain rate loading conditions are increased from quasi-static to values at the vicinity of 100 s^{-1} .

3. APPLICATION OF TEST RESULTS TO SHORT-CIRCUIT DESIGN

GROPTI™ is a software tool that has been developed to estimate displacements, velocities and accelerations of winding and tank structural elements [3]. It is an EFACEC proprietary tool developed specifically to analyze shell form transformer motions during short circuit events. Through the incorporation of a carefully built genetic algorithm, the tool not only allows for the precise estimation of the movement of coils but also provides optimal design of the tank's short-circuit beams.

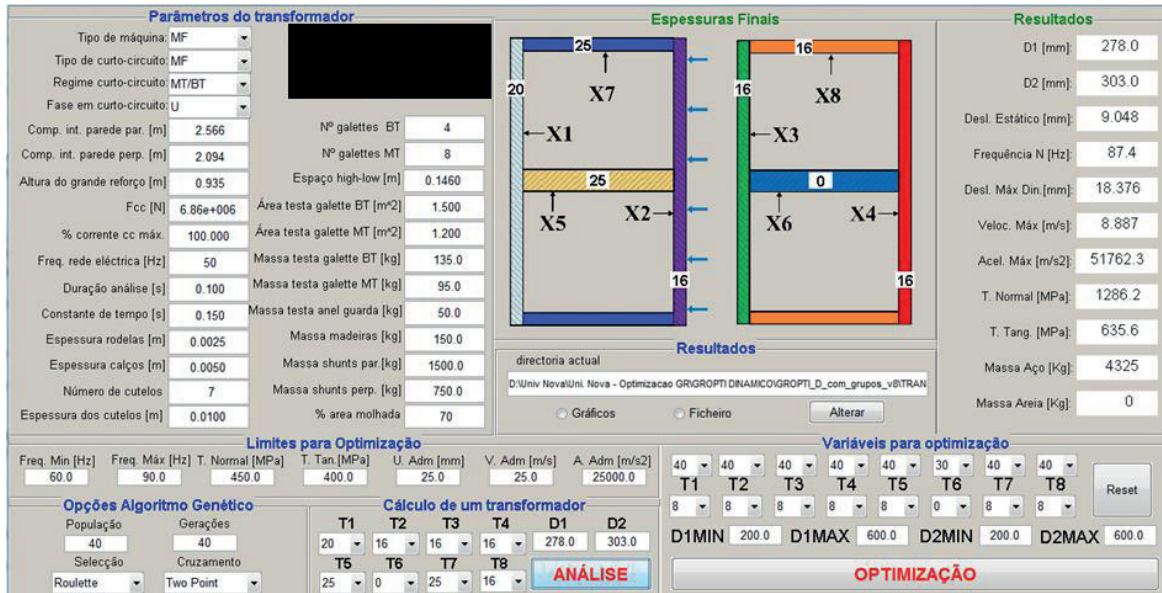


Figure 4: The GROPTI GUI. The software can evaluate the short circuit response of the coil groups, or it may determine the plate thicknesses for the box beam elements such that system response is according to specified user requirements

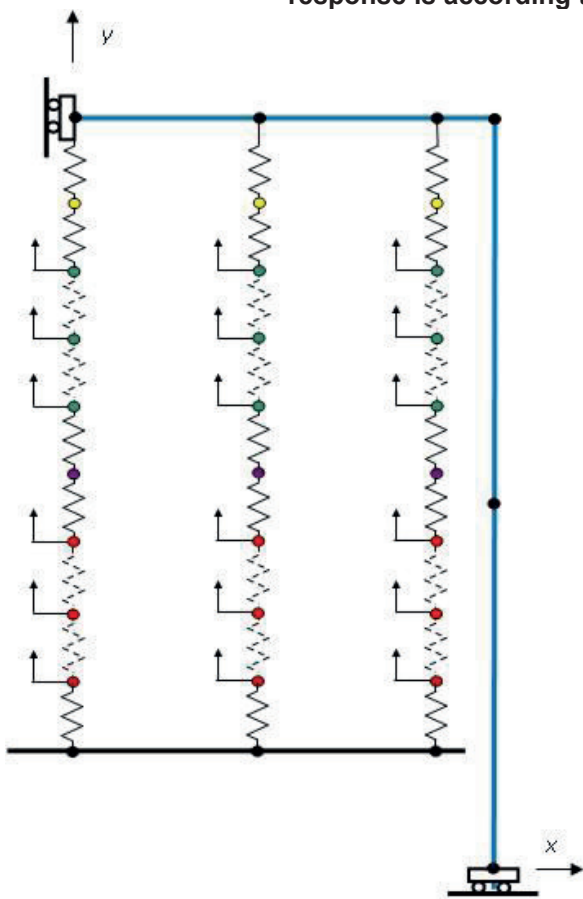


Figure 5 The FEM model that is automatically created with GROPTI for analyzing system response. The number of masses (representing coils) and springs (pressboard) vary with each short circuit, as does the application of coil forces on masses.

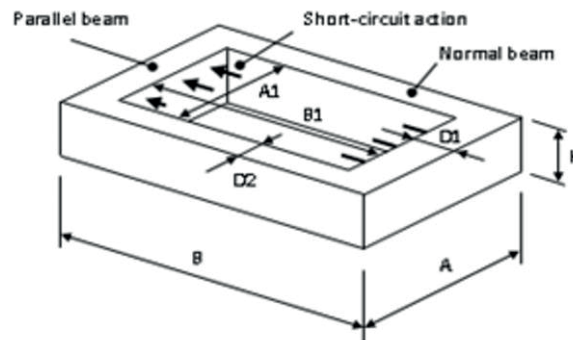


Figure 6: Some GROPTI parameters ('normal beam' also referred as 'perpendicular beam')

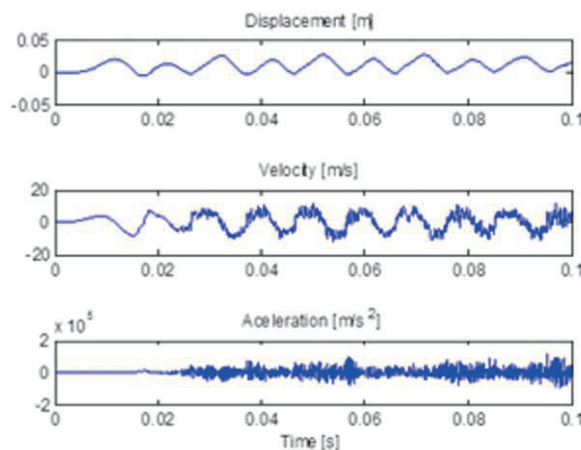


Figure 7: Displacement, velocity and acceleration of box beam mid-span during a short circuit. These outputs are graphical; other outputs are also given on the GROPTI GUI, such as material stress or box beam natural frequency

3.1. APPLICATION EXAMPLE: Transformer description and force evaluation

This example is taken from a transformer that was short circuit tested. It is a 50Hz 100MVA 400kV ONAN/ONAF/ODAF single phase autotransformer with a tertiary winding. Figure 8 shows the series winding in red, the common in green and the tertiary in blue.

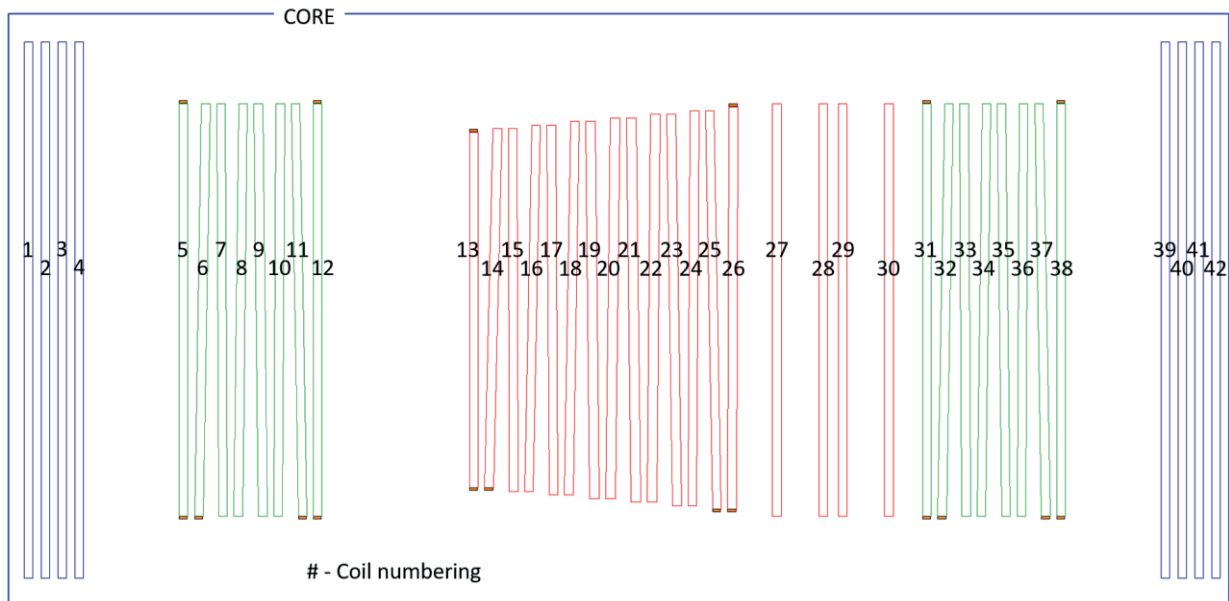


Figure 8: Window cutaway and coil numeration of transformer being short circuit tested

The first step of the process is the definition of the short circuit scenario that is going to be tested. Once the worst case short circuit was identified, a model of the transformer was built (see Figure 9) and the appropriate short circuit currents were introduced (these currents were defined based on the methodology in [2]).

Figure 10 shows the introduction of the currents into the model, where the different colors indicate currents in phase opposition. In this case, it is the common winding and the series winding that are in a short-circuit condition, whereas the tertiary winding is kept open circuited. A graph of the accumulated ampere-turns of the transformer during the fault is shown in Figure 11.

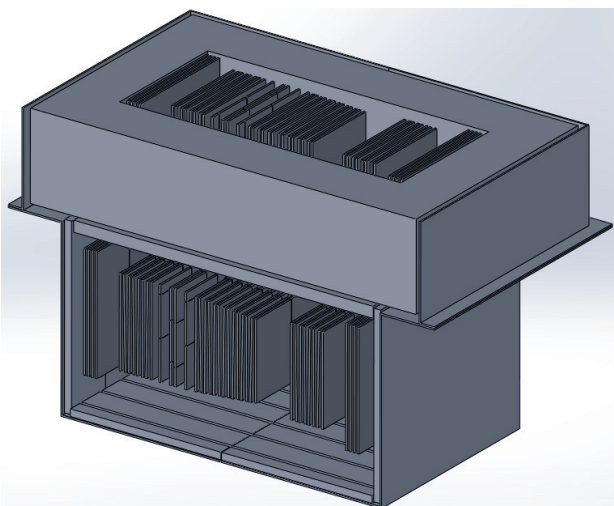


Figure 9: 1/4 transformer model for short circuit coil axial force evaluation with two symmetry planes

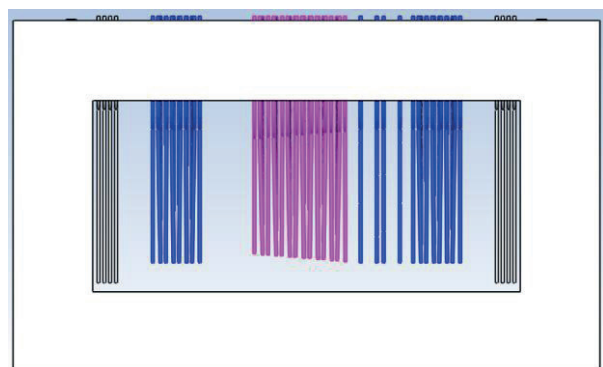


Figure 10: Short circuit condition being tested. Different colors represent opposing currents

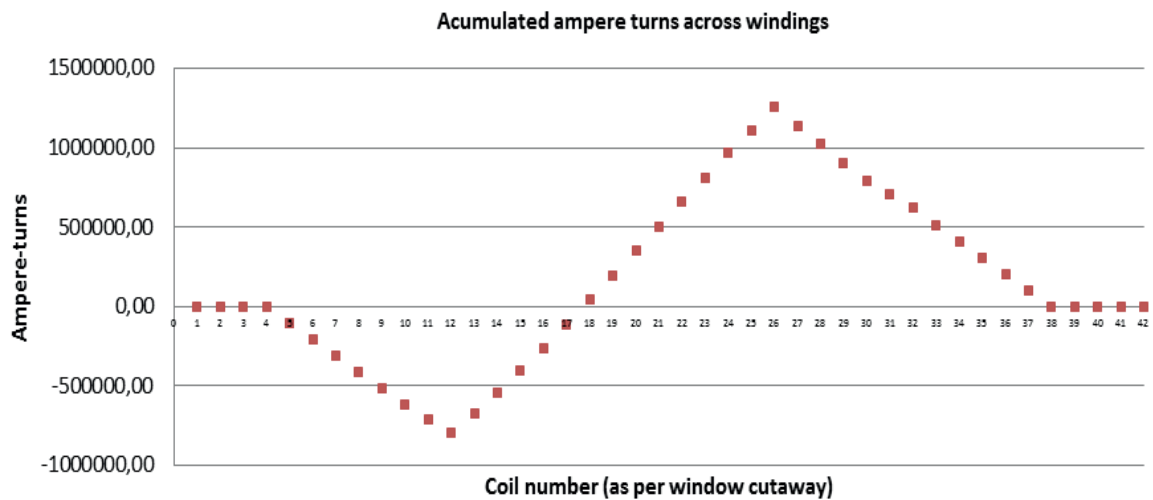


Figure 11: Graph of accumulated ampere-turns for each coil across windings

The numerical analysis of the described model yields magnetic field distributions. A boundary element method (BEM) program was used for a magnetostatic operation mode analysis. The resulting leakage induction field plot at the window cutaway symmetry plane are shown in Figure 12 and in Figure 13. Forces will be generated at coils due to this leakage and due to the current going through the conductors. Peak values for these forces are shown in Figure 14, where both the axial force acting on each coil together with the force accumulation across the window are shown. Figure 15 then shows a subdivision of the forces acting on the areas directly opposing the magnetic circuit from the forces acting on the areas directly opposing the short circuit beams. This is a very important separation to make, as the magnetic circuit shall withstand the former forces and the short circuit beams shall withstand the latter ones.

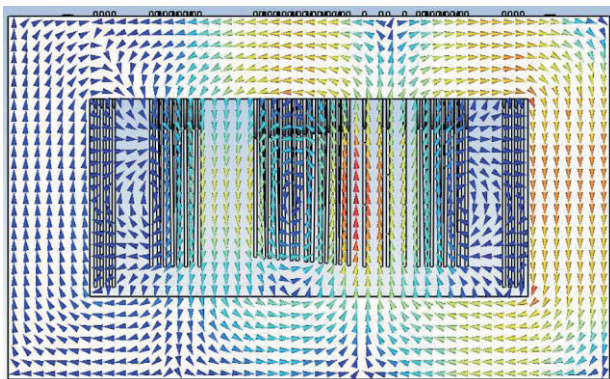


Figure 12: Leakage B-field arrow distribution at window section

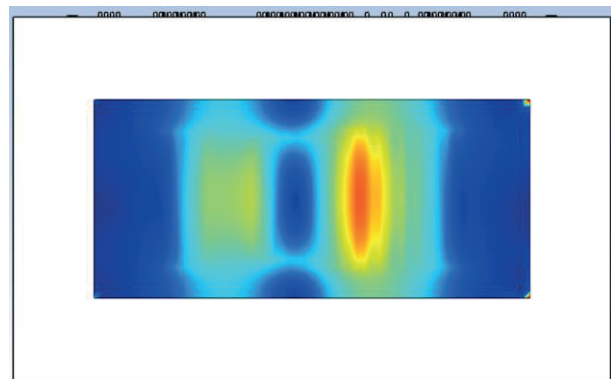


Figure 13: B-field intensity plot

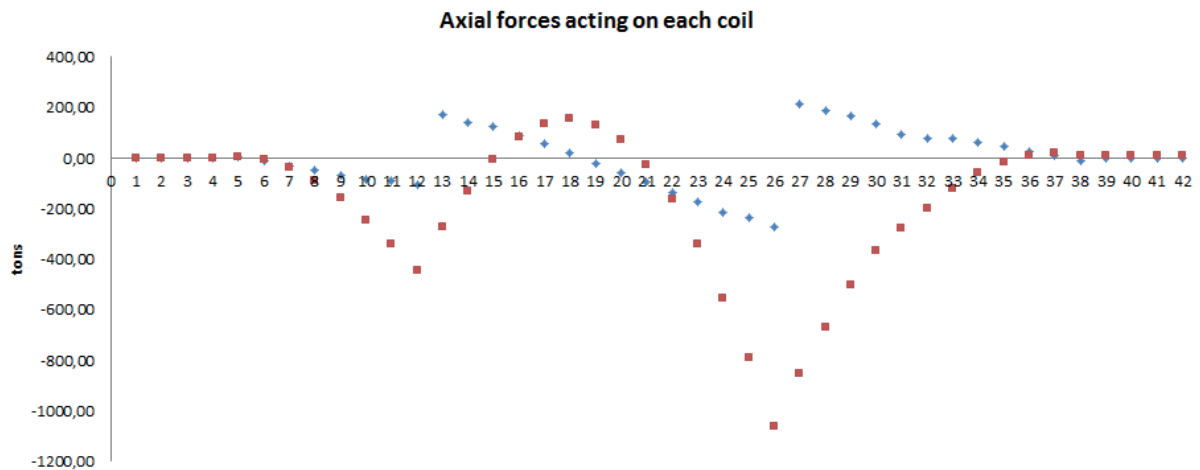


Figure 14: The blue (diamond shape graph) is the electromagnetic axial force acting on each coil, and in red is the correspondent accumulated axial force

From Figure 15 we can estimate that the peak total accumulated force acting on each short circuit beam is approximately 250 tons (this number can be found by summing all blue diamonds of Figure 15).

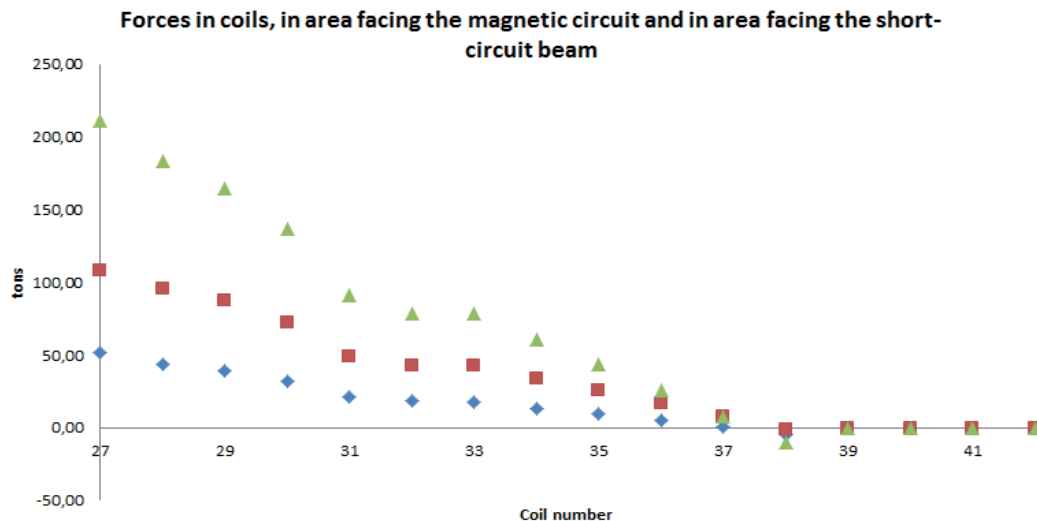


Figure 15: Axial forces in coils 27 through 42 (green triangles), with the forces acting on the areas facing the magnetic circuit (red squares) separated from the forces acting directly on the area facing the short circuit beam (blue diamonds). Note that there is always a lower and an upper short circuit beam.

3.2. GROPTI estimates for tank and coil movements

Once force estimates have been found, these may be introduced into the GROPTI software. Together with the forces, it is necessary to introduce several other input data parameters, such as the type of short circuit being analyzed, single/three phase geometry analysis, frequency, duration, line and transformer time constant, transformer geometrical dimensions, pressboard thicknesses, number of high and low voltage coils, mass of coils, impact area, mass of compression woods and static shields, magnetic shunt masses and wet area (area of oil in contact with insulated conductors). Thicknesses of steel plates used to build the short circuit beam are also necessary. These inputs are all inserted into the GUI shown in Figure 4.

Following its analysis, GROPTI outputs results, both in the GUI and in graphical format (see Figure 16). The main results are: coil and beam natural frequencies, maximum beam center point displacement, maximum beam velocity, beam peak acceleration, maximum normal stress in beam, maximum tangential stress and also the estimated beam mass.

GROPTI is also able to determine a good solution for the short circuit beam through its built in genetic algorithm. This optimization analysis requires that further inputs are given, such as for example genetic algorithm parameters, optimization constraints or acceptable range for optimization variables.

GROPTI assumes that the short circuit beam's steel is loaded in its elastic domain. In reality, there is always some plasticity that leads to permanent plastic deformation. It is important to understand the level of permanent plastic deformation which is left, as this will impact transformer properties.

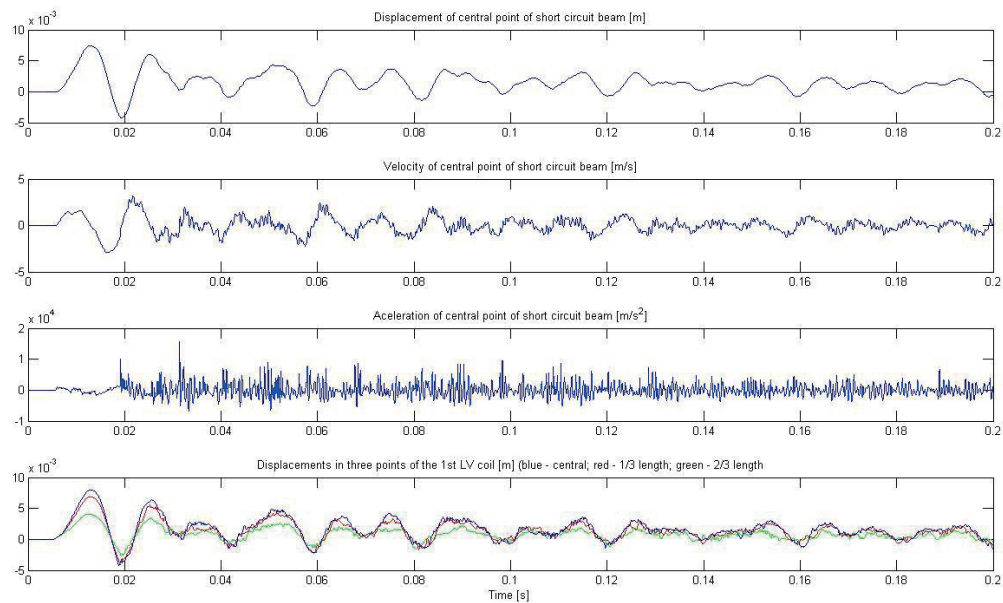


Figure 16: GROPTI displacement, velocity and acceleration results for the short circuit beam and selected coils, for the transformer that is being analyzed

4. ESTIMATION OF PERMANENT BEAM DEFORMATION

At this point we have in hand the motion estimates which assume material linearity, and we wish to assess the level of plastic deformation of the beam. In particular we are interested in determining the permanent configuration of the beam, that is, the configuration of the beam once all loads are removed. Permanent plastic deformation may be found by applying an equivalent energy method. There are 2 steps involved:

1. Assuming material linearity, determine the equivalent static force that causes the maximum dynamic displacement given by GROPTI, and compute the elastic deformation energy absorbed by the beam in that condition;
2. Apply the nonlinear material to the beam, and apply a force such that the total (elastic + plastic) deformation energy equals the elastic deformation energy of step 1.

Due to plasticity being present, even if in small proportions, it is always the case that for an equivalent energy there will always be more displacement with the nonlinear material. Residual deformation is unwanted as it will alter transformer properties permanently; therefore only very small residuals are tolerated.

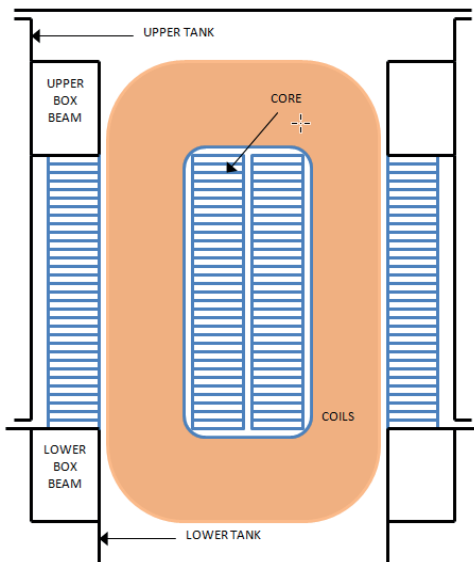


Figure 17: Location of short circuit beam in transformer tank

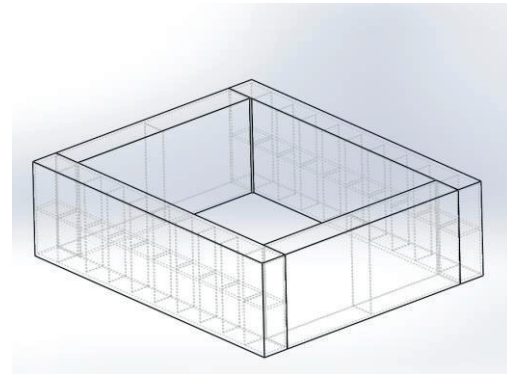


Figure 18: Short circuit box beam shown isolated from transformer. Can be seen as the upper or lower box beam of Figure 17

The procedure that has been outlined to estimate the permanent plastic deformation will be applied in two different situations. First, we shall consider that the dimensions of the beam are fixed, and we shall vary the steel material applied to the beam and then check for the residuals. Secondly, we shall design the beam for each one of the four steel materials under consideration (using GROPTI), attempting to have the same residuals for each case, so that solutions may be compared to each other.

4.1. Fixed beam solution

By applying the described procedure to the beam dimensions (that were effectively fabricated), we obtain the results of Table 1.

Table 1: FEM simulation results applying the four different types of steel (same beam for all)

FIXED BEAM SOLUTION		S235JR	S275JR	S355JR	WELDOX700
Beam mass	kg	4325	4325	4325	4325
Total deformation energy	MJ	10	10	10	10
Max Von Mises stress at corner	MPa	337	406	402	990
Max Von Mises stress at midspan	MPa	218	238	194	237
Max displacement at midspan	mm	7.46	7.46	7.49	7.45
Max residuals at midspan	mm	0.07	0.02	0.21	0

For all types of steel considered, residuals may be considered “zero”, behavior is still very linear. Even though stress levels at corners are well beyond the elastic limits, plasticity domains at the corners have little effect on the residual values. As the material curves used for the simulation were taken from the experimental results, slight deviations may occur that can well explain the slightly higher residual value for the S355JR steel. Figure 19 and Figure 20 show displacement results for the S355JR steel (the FEM package used was ANSYS 11.0, with mechanical static structural and material nonlinear simulations).

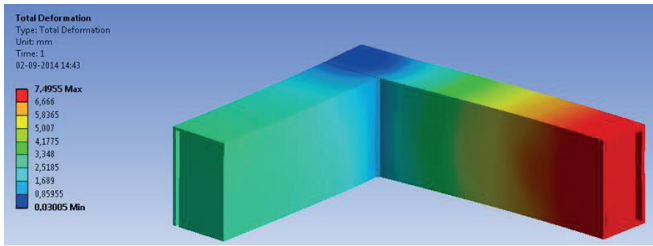


Figure 19: Beam maximum displacements (1/8 model used) for the S355JR steel

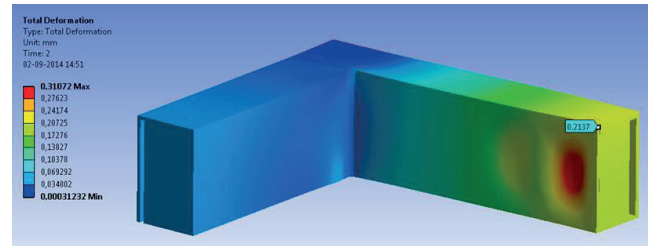


Figure 20: Maximum residual displacements (or permanent beam configuration) following load removal on the S355JR steel beam

4.2. Variable beam solution

The procedure described in the beginning of this section was then applied to 4 different beam solutions, each solution matching one of the types of steel. The beam solutions were generated by the optimization algorithm contained in GROPTI. Moreover, the solutions were sought taking in consideration the particular constraints that existed in this transformer. Should the constraints change then the solutions that are achieved as 'optimal' may change too. Table 2 shows the results for each one of the 4 solutions.

Table 2: FEM simulation results for optimal beams for all four types of steel (all beams different)

VARIABLE BEAM SOLUTION		S235JR	S275JR	S355JR	WELDOX700
Beam mass	kg	4000	3900	3580	2610
Mass variation wrt S235JR	%	-	-2.5%	-10.5%	-35%
Total deformation energy	MJ	10	10	12	14
Max Von Mises stress at corner	MPa	322	412	420	1008
Max Von Mises stress at midspan	MPa	218	278	226	403
Max displacement at midspan	mm	7.52	7.91	9.52	13.9
Max residuals at midspan	mm	0.05	0.05	0.66	0

Two points are worth mentioning. Firstly, these results confirm the 'common sense' assumption that better steel grades lead to lighter weight solutions. The answer to the question of which steel is most cost wise efficient will depend greatly on the unit acquisition price of the steel together with fabrication costs and other possible cost issues such as for example transportation costs. Nevertheless, the results from Table 2 provide a guideline to how the mass of a short circuit beam may change with application of different types of steel. Secondly, the solution shown for the WELDOX700 steel has nearly twice the admissible displacement when compared to the S235JR steel. It has become clear that higher displacements accompany higher grade steel types, up to a point where the transformer engineer does not allow for higher displacements above a certain limit. The lower grade steel would not be capable of producing the same higher displacements without increasing its stress levels and therefore compromising its permanent plastic deformation values.

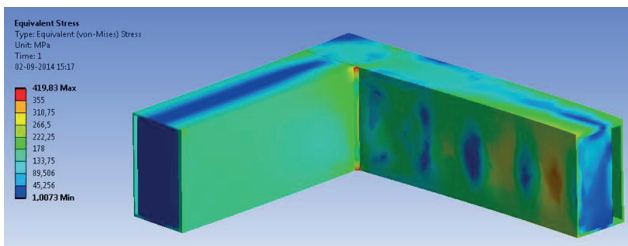


Figure 21: Stress fields in the S355JR steel

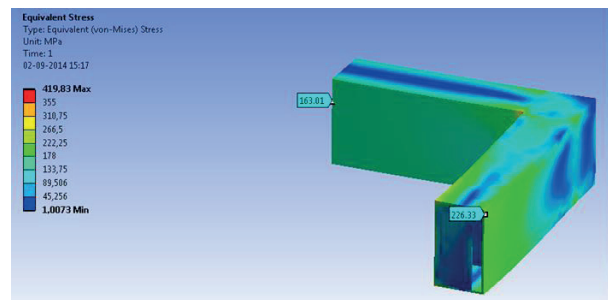


Figure 22: Stress fields from a different angle

As a last note, transformer impedance varies following a short circuit. There are movements in the coils and the phase settles to a (slightly) different configuration once forces cease. Many factors influence the impedance variation, and the good performance of the short circuit beam is only one of

them. Assurance that beam configuration settles back to its original configuration, less any residuals that may be neglected, is a necessary but not sufficient condition for impedance variation values to be within tolerances. But it is certainly one that is within the transformer manufacturer's control to assure.

5. CONCLUSIONS

Loading speed increases the energy absorbing capability of structural steel. This was found true for the lower grade (more common) steel and not true for the high grade (higher end) steel. At speeds close to 100Hz, differences in between common and high grade steel diminish, due to the enhanced performance of common steel at higher speeds. Another fact that is sometimes overlooked is that to take full advantage of a higher yield and tensile stress, higher grade steel solutions must allow for larger displacements, which are not desirable from a short circuit control standpoint. If larger displacements are not allowed, then differences in between common and higher grade types of steel are further diminished, as the higher grade structural steel is underutilized.

REFERENCES

- [1] K. Karsai, D. Kerényi, L. Kiss, "Large Power Transformers", Elsevier, 1987.
- [2] IEC 60076-5 : 2006, "Power Transformers – Part 5 : Ability to withstand short-circuit"
- [3] E. Almeida, P. Pedro, J. Cardoso, R. Ribeiro, "Design and dynamic analysis of shell form transformers under short-circuit conditions", Cigré Colloquium, Zurich, Switzerland, 2013.
- [4] J. Thierry, "Core-form and shell form transformers: Applications, design and construction", Life of a Transformer Seminar, Lake Buena Vista, Florida, USA, 2014.
- [5] E. Almeida, H. Mendes and A. Pinho, "Experimental validation of a CORE type power transformer tank", in Proceedings ASME International Mechanical Engineering Congress and Exposition, November, 2009.
- [6] C.M.A Silva, P.A.R. Rosa, P.A.F. Martins, "Innovative Testing Machines and Methodologies for the Mechanical Characterization of Materials", Experimental Techniques, 2014 (in press doi:10.1111/ext.12094).

Leonardo Štrac
Končar Power Transformers Ltd.
leonardo.strac@siemens.com

Franjo Kelemen
Končar Power Transformers Ltd.
franjo.kelemen@siemens.com

Magnetizing current of a Large Power Transformer and its Harmonic Spectrum in Normal and GIC conditions

SUMMARY

A measurement of the harmonic spectrum of magnetizing current was performed. This paper analyzes the results of the measurement of harmonic spectrum of magnetizing current in standard no-load test at various values of induction. Magnetizing current harmonic spectrum during single-phase no-load test was measured as well as the impact of combined AC and DC magnetization on core behavior and harmonic spectrum. A mathematical model of transformer core is introduced. The calculated results are presented.

Key words: power transformer, no load condition, magnetizing current, harmonic spectrum, geomagnetically-induced currents

1. INTRODUCTION

Dealing with apparent power and power factor in distribution systems is the standard part of everyday maintenance. There are many sources of higher harmonics in the system: wind farms, power convertors, SVC and nonlinear elements, such as power transformers. Also, in some countries on far north and south like Canada or South Africa the possibility of geomagnetically-induced currents (GIC) due to solar storms are high. To broaden knowledge of power transformer core behavior on distribution system and impact of GIC on transformers core magnetizing current, Končar Power Transformers (KPT) conducted a series of special measurements on a five-limb core. The harmonic spectrum of magnetizing current in standard no-load test at various values of induction in the core is analyzed. Additionally, magnetizing current harmonic spectrum during single-phase no-load test was considered and the impact of combined AC and DC magnetization on core behavior and harmonic spectrum. The measurements are compared with simulation results.

2. MEASUREMENT SETUP

The measurement of transformer core behavior and properties under special conditions was conducted at KPT. The test model was the three-phase five-limb core outside of tank equipped with custom-made temporary windings. Beside standard three-phase no load test and single phase no load test, the test setup included GIC injection. For this purpose, the special arrangement of the test windings was used to allow the possibility of simultaneous AC and DC magnetization of the core. Number of turns on both AC and DC winding is 39. AC potential is also induced in DC winding, but since DC source is located in one point of delta connection of windings there is no AC potential on DC source.



Figure 1 - Custom-made temporary windings during measurements

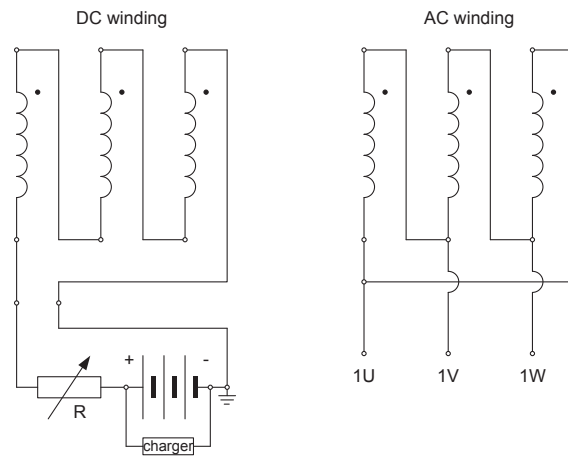


Figure 2 - Electrical schematic of DC and AC winding

3. MATHEMATICAL MODEL

The magnetic circuit model of a five-limb transformer core is derived using some usual assumptions and approximations.

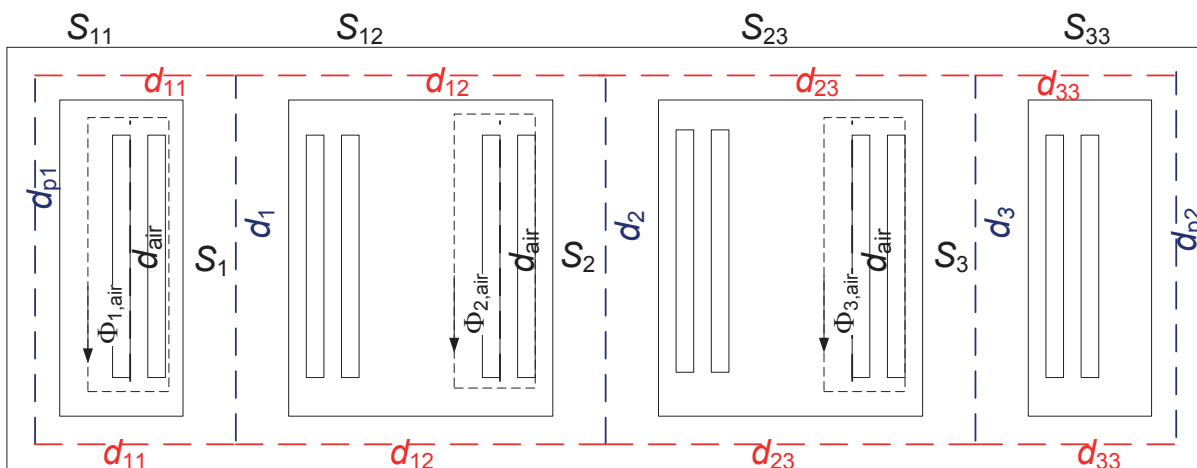


Figure 3 - Simplified schematic of a five - limb core cross section and winding arrangement.

Using the notation established in the Fig. 3, the system of equations (1)-(10) that describes the behavior of the magnetic circuit can be formed.

$$N(I_{o1}(t) + I_{DC1}) = H_1 d_1 + H_{11}(2d_{11} + d_{p1}) \quad (1)$$

$$N(I_{o1}(t) - I_{o2}(t) + I_{DC1} - I_{DC2}) = H_1 d_1 + 2H_{12} d_{12} - H_2 d_1 \quad (2)$$

$$N(I_{o2}(t) - I_{o3}(t) + I_{DC2} - I_{DC3}) = H_2 d_1 + 2H_{23} d_{23} - H_3 d_3 \quad (3)$$

$$N(I_{o3}(t) + I_{DC3}) = H_3 d_3 + H_{33}(2d_{33} + d_{p2}) \quad (4)$$

$$N(I_{o1}(t) + I_{DC1}) = H_{1,air} d_{air} \quad (5)$$

$$N(I_{o2}(t) + I_{DC2}) = H_{2,air} d_{air} \quad (6)$$

$$N(I_{o3}(t) + I_{DC3}) = H_{3,air} d_{air} \quad (7)$$

$$0 = \mu_0 \mu_{r1}(H_1)H_1 S_1 - \mu_0 \mu_{r11}(H_{11})H_{11} S_{11} - \mu_0 \mu_{r12}(H_{12})H_{12} S_{12} - \mu_0 H_{1,air} S_{air} \quad (8)$$

$$0 = \mu_0 \mu_{r2}(H_2)H_2 S_2 + \mu_0 \mu_{r12}(H_{12})H_{12} S_{12} - \mu_0 \mu_{r23}(H_{23})H_{23} S_{23} - \mu_0 H_{2,air} S_{air} \quad (9)$$

$$0 = \mu_0 \mu_{r3}(H_3)H_3 S_3 + \mu_0 \mu_{r23}(H_{23})H_{23} S_{23} - \mu_0 \mu_{r33}(H_{33})H_{33} S_{33} - \mu_0 H_{3,air} S_{air} \quad (10)$$

In equations (1)-(10) N denotes number of turns of the excited winding, I01 the alternating part of magnetizing current of the first phase, IDC1 the direct current in phase 1, H1 is the magnetic field strength and the index is given according to the geometric path in Fig. 1, d is the geometric length with index corresponding to the path leg according to Fig. 1, t is the time variable, μ_0 is the magnetic permeability of the vacuum, μ_r is relative permeability of the material followed with the index corresponding to path in Fig. 1, numbered indices 1,2,3 given to currents represent three phases of a transformer, while S represents the cross-section area of the path leg according to Fig. 1. Additional equations are obtained using the fact that the system is powered by a three-phase symmetric system of voltages without harmonic distortion. This means that the magnetic flux linkage of the windings with respect to the time variable is also a harmonic function satisfying

$$V_1 \sin(\omega t) = N \frac{d\Phi_1}{dt} \Rightarrow \Phi_1(t) = \frac{-V_1 \cos(\omega t)}{\omega N} + \Phi_{1DC}, \quad (11)$$

where V1 denotes the amplitude of the applied voltage to the first phase of a transformer, ω is the angular frequency of the voltage, and Φ_{1DC} is an integration constant representing the DC component of flux resulting from the DC current magnetization. Similar relations hold for the other two phases (denoted with indices 2 and 3, respectively), so the following three equations (12)-(14) complete the system of equations needed for the full mathematical description of a model.

$$\frac{-V_1 \cos(\omega t)}{\omega N} + \Phi_{1DC} = \mu_0 \mu_{r1}(H_1)H_1 S_1 \quad (12)$$

$$\frac{-V_1 \cos\left(\omega t - \frac{2\pi}{3}\right)}{\omega N} + \Phi_{2DC} = \mu_0 \mu_{r2}(H_2)H_2 S_2 \quad (13)$$

$$\frac{-V_1 \cos\left(\omega t - \frac{4\pi}{3}\right)}{\omega N} + \Phi_{3DC} = \mu_0 \mu_{r3}(H_3)H_3 S_3 \quad (14)$$

The magnetic behavior of the core in reality is very complex because the super oriented steel sheets are both anisotropic, and nonlinear. For the purpose of this paper, the anisotropic behavior of the material is neglected, which is equivalent to the assumption that all the magnetic flux lines coincide with the rolling direction of the steel. The nonlinear B-H curve is modeled using the simple relationship between the two field vector amplitudes and without incorporating hysteresis.

Based on the mathematical model described in this section, three series of calculations were done. The first one was to calculate (average) harmonic content of the no load current for AC magnetization of the core on different induction levels (induced voltages). The curves describing the harmonic content expressed as the percentage of the first harmonic rise with induction, and then fall off because of the influence of the active current covering the losses inside the core (Figure 4). Cases with constant DC current and variable induction, as well as the case with variable DC and “constant” induction are given in Figures 5-6. Qualitative behavior of the harmonics corresponds well to the measurements. It is important to notice that the calculated values are given as arithmetic averages of the phases. Each phase has its own signature harmonic content, which varies significantly from phase to phase. This is why the analysis should be taken as a qualitative prediction of the transformer behavior. Especially because the measurements cannot directly express the magnetizing current, but the resulting vector sum current from the active part covering the losses, magnetizing current etc. Therefore, the base harmonic differs from the one calculated using the magnetizing current only.

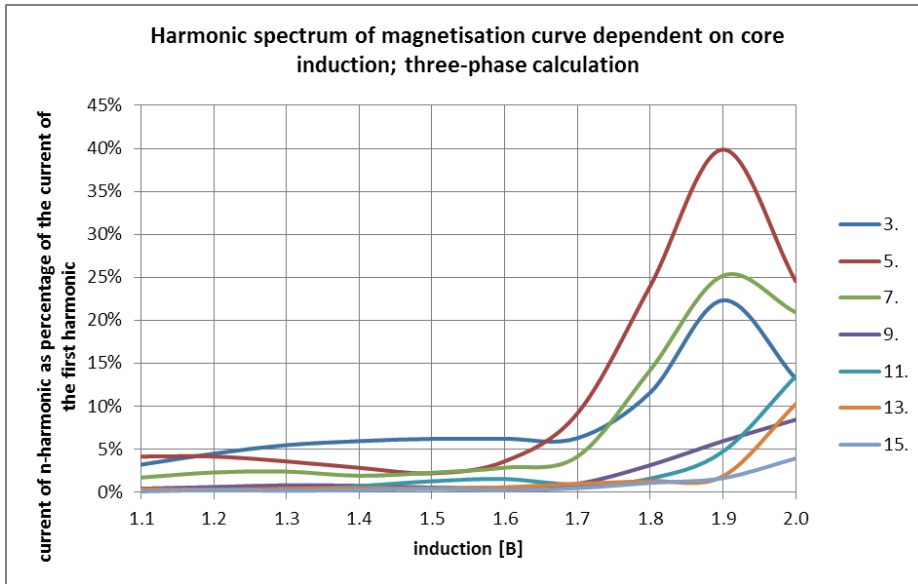


Figure 4 - Harmonic spectrum of magnetization curve dependent on core induction; three-phase calculation, phase current

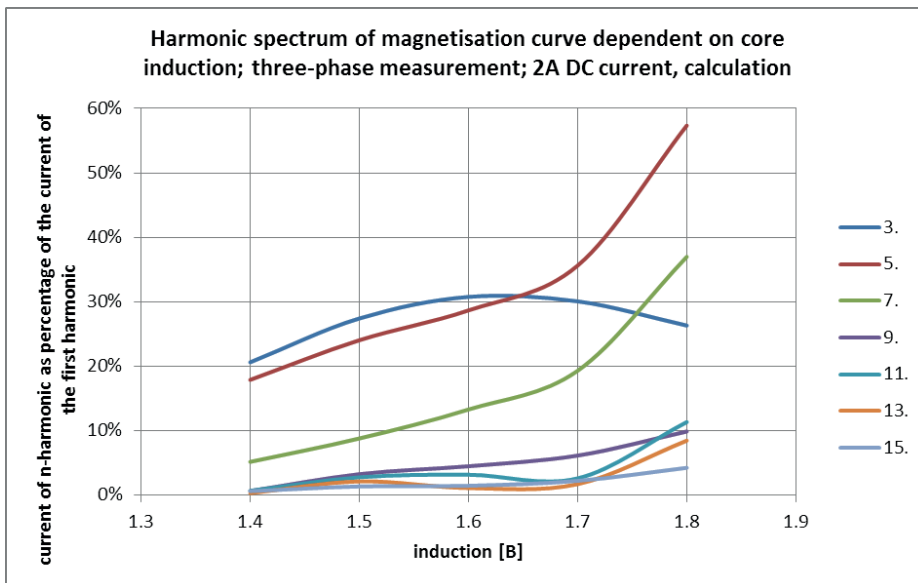


Figure 5 - Harmonic spectrum of magnetization curve dependent on core induction; 2A DC current calculation, phase current

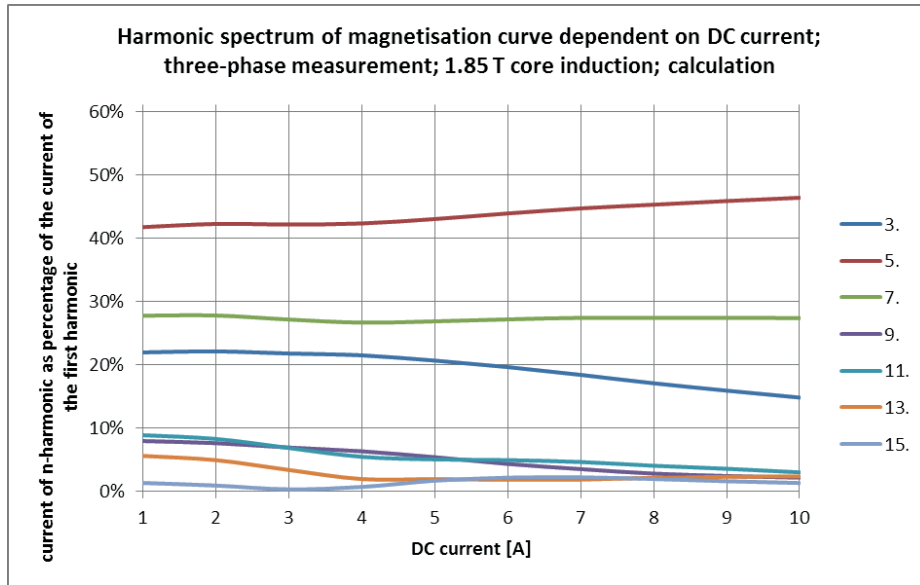


Figure 6 - Harmonic spectrum of magnetization curve dependent on DC current; 1,85 T core induction, calculation, phase current

4. MEASUREMENTS

4.1. Measurement Results for Three-Phase No Load Test

From the diagram in Figure 7 one can see that for typical working range of induction of power transformers (1.4 - 1.8 T) harmonics above the eleventh order are practically non-existent. However, thirteenth harmonic appears above the induction of 1.8 T, but only up to 5% of the first harmonic. Based on their behavior, it can be said that there are two groups of higher harmonics: the third harmonic in one group and all the others in second group. Share of the third harmonic remains rather constant (between 10% - 15%) through the range of induction, falling significantly above 1.8 T. Harmonics fifth and above increase their share constantly through the range of induction up to the saturation induction of 1.95 T when shares start to fall rapidly. Up to the induction of 1.6 T third harmonic is the dominant one, but above that higher harmonics start to dominate.

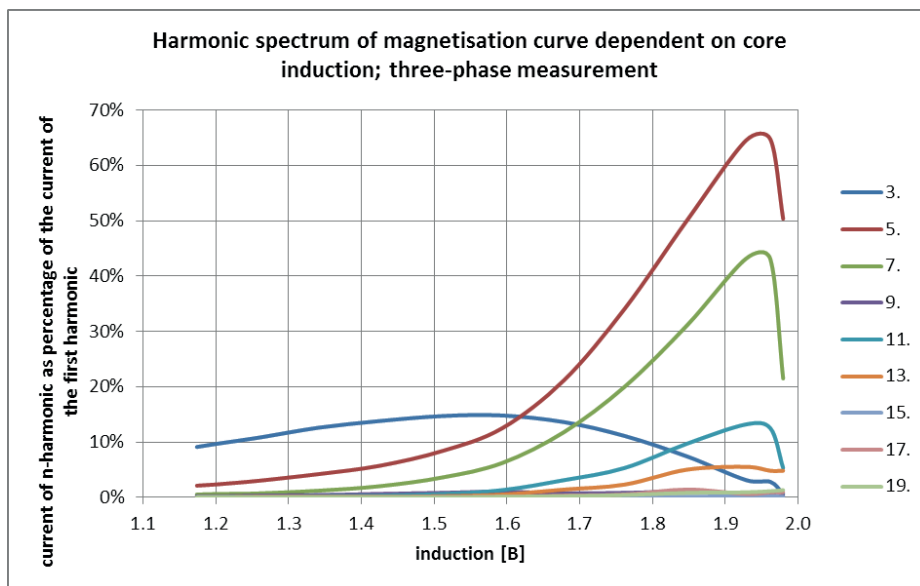


Figure 7 - Harmonic spectrum of magnetization curve dependent on core induction; three-phase measurement; phase current

4.2. Measurement Results for Single-Phase No Load Test

During the single-phase magnetization, only the limb that is magnetized can be saturated, while the other parts of the core distribute the flux through the much bigger area avoiding saturation. Since the harmonic distribution for geometrically equal limbs is practically the same, here is presented only the average values, rather than individual ones. In this situation, diagram of higher harmonics looks completely different. For all three main limbs the share of all harmonics rise linearly up to the saturation induction (Figure 8). Unlike for the three-phase magnetization, lesser the order of harmonic, higher the share of the harmonic, without line crossing.

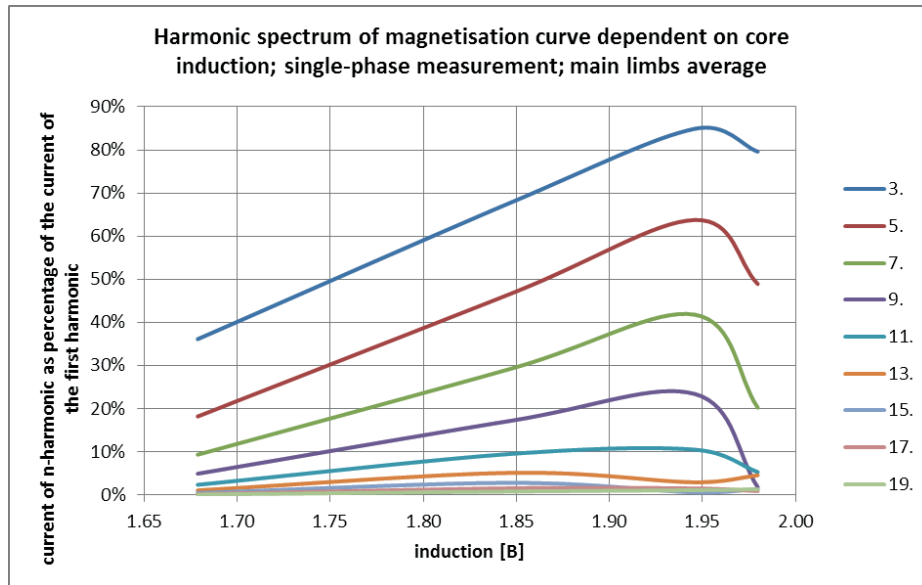


Figure 8 - Harmonic spectrum of magnetization curve dependent on core induction; single-phase measurement, phase current; main limbs average

4.3. Measurement Results for Combined AC and DC Magnetization

Although results apply to combined AC and DC magnetization, for the sake of comparison value of induction in diagrams are calculated for AC magnetization only.

Additional DC magnetization has a big impact on harmonic distribution even at only 2A DC (this correspond to $2 \times 39 = 78$ ampere turns). Third harmonic is 30% of the first harmonic which is twice as high as the share of the third harmonic without DC magnetization. Also, even at a low AC core induction of 1.34 T, core is saturated at 6A DC (this correspond to $6 \times 39 = 234$ ampere turns).

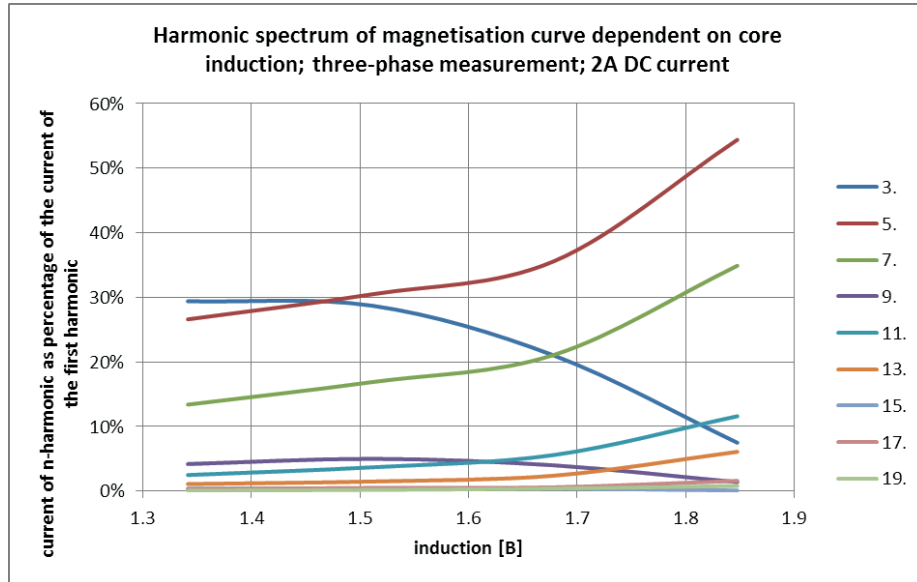


Figure 9 - Harmonic spectrum of magnetization curve dependent on core induction; three-phase measurement, phase current; 2A DC current

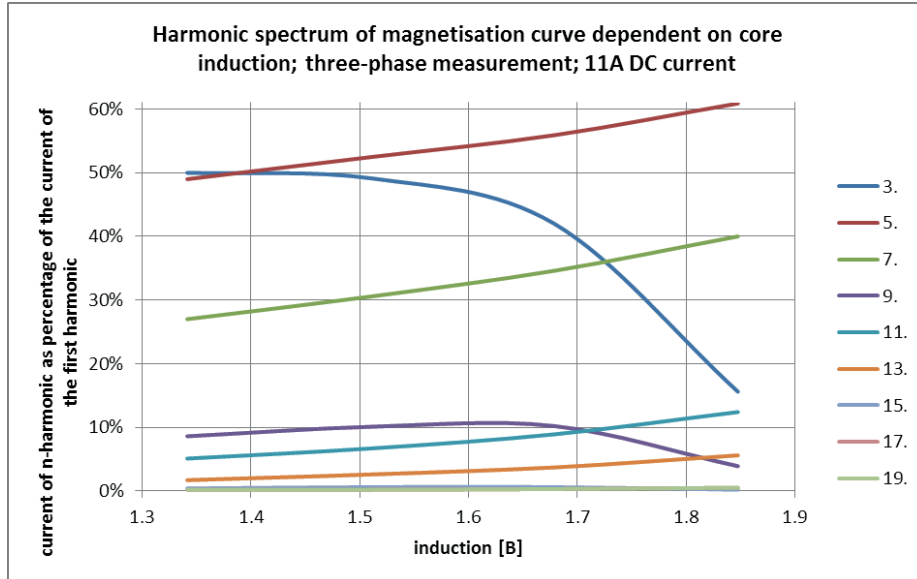


Figure 10 - Harmonic spectrum of magnetization curve dependent on core induction; three-phase measurement, phase current; 11A DC current

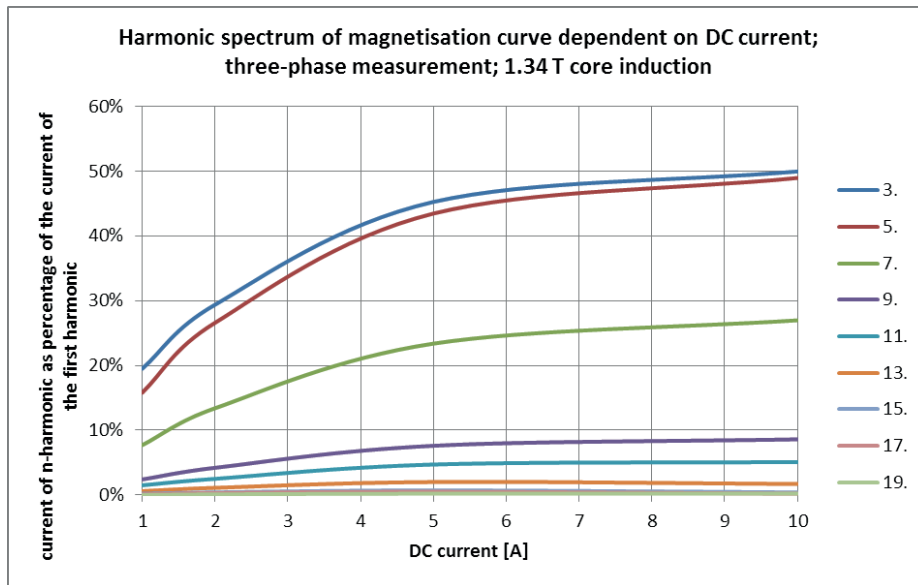


Figure 11 - Harmonic spectrum of magnetization curve dependent on DC current; three-phase measurement, phase current; 1.34 T core induction

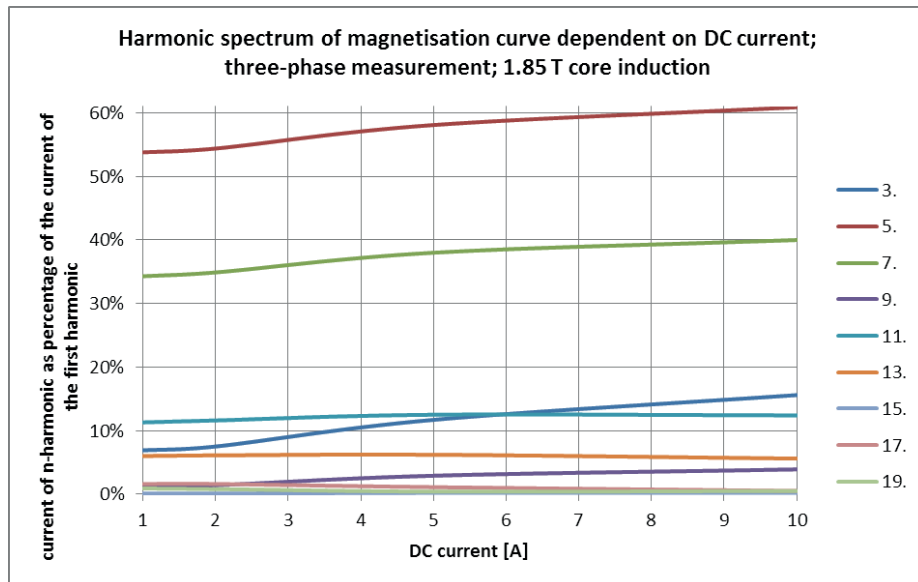


Figure 12 - Harmonic spectrum of magnetization curve dependent on DC current; three-phase measurement, phase current; 1.85 T core induction

7. CONCLUSION

Results calculated with mathematical model are qualitatively comparable with the measured ones. Precise calculation of harmonic distribution across the induction range is hard to achieve because of lack of transformers core magnetization curve. Besides that, mathematical model calculates only magnetizing current and only the total no load current which consists from magnetizing current, losses current and winding capacitance current.

Measurement results for three-phase no load test shows that for typical working range of induction of power transformers (1.4 - 1.8 T) harmonics above the eleventh order are practically non-existent. Dominant harmonics are third, fifth, seventh and ninth. Measurement also shows that harmonic share is highly dependable on core induction.

During the single-phase magnetization diagram of higher harmonics looks completely different. For main limbs the share of all harmonics rise linearly up to the saturation induction. Unlike for the three-phase magnetization, lesser the order of harmonic, higher the share of the harmonic, without line crossing.

Additional DC magnetization has a big impact on harmonic distribution even at only 2A DC (this correspond to 78 ampere turns). Third harmonic is 30% of the first harmonic which is twice as high as the share of the third harmonic without DC magnetization. Also, even at a low AC core induction of 1.34 T, core is saturated at 6A DC (this correspond to 234 ampere turns).

5. REFERENCES

- [1] F. Kelemen, L. Štrac, Impact of geomagnetically induced currents on magnetizing currents under no-load conditions, International Colloquium Transformer Research and Asset Management, Cavtat, Croatia, November 12-14, 2009
- [2] L. Štrac, F. Kelemen, Istraživanje utjecaja geomagnetski induciranih struja na energetske transformatore s trostupnom i peterostupnom jezgrom, 7. savjetovanje HO CIGRÉ, Cavtat, Croatia, November 06-10, 2005

Zoran Andjelic
Polopt Technologies GmbH, Switzerland
Zoran.Andjelic@polopt.com

Asim Fazlagic
ABB, USA
Asim.Fazlagic@us.abb.com

Claude J. Lambert
ABB Canada
Claude.J.Lambert@ca.abb.com

M. Ries
Woelfel Engineering GmbH + Co. KG, Germany
Ries@woelfel.de

Ramsis Girgis
ABB, USA
Ramsis.Girgis@us.abb.com

Alessandro Regalino
ABB Canada
Alessandro.K.Regalino@ca.abb.com

A. Seidel
Woelfel Engineering, Germany
Seidel@woelfel.de

STRUCTURAL-MECHANICS ANALYSIS OF THE 10G TRANSFORMER IMPACT

SUMMARY

Transportation of the power transformers from the site of production to the site of the exploitation is very complex and sensible task. During transportation, the transformer can be subjected to a variety of different impacts registered either during railway transportation or during on/off loading. The transformer should be designed to sustain the high accelerations appearing often during transportation.

Transformer are usually equipped with the impact recorder to registry the acceleration behavior during the transport. In the current paper, we give an overview on the structural-mechanics analysis of 10g impact on the power transformer registered during the railway transportation of the transformer from Canada to US.

1. INTRODUCTION

The main task of this study is to analyze the consequences of the mechanical impact appearing during the transportation of the single-phase transformer from ABB Varennes Factory to the customer site. The transformer was a single-phase auto transformer with rating of $746\sqrt{3}$ to $345\sqrt{3}$ kV, 450/600/750 MVA and with tertiary rating of 34.5kV,60/80/100 MVA. Two identical units were shipped at the same time. Impact events were recorded on the two impact recorders that were installed on one of those units. As the power transformer has failed in operation at its installation site afterwards, the cause of failure had to be investigated. For this purpose, numerical simulations are done. These simulations should support the clarification whether the impacts during transport are cause for the malfunction:

- A detailed finite element model is established to analyze the dynamic behavior of the transformer and to assess stress and displacement of the structural members.
- The general dynamic behavior is represented by the natural frequencies and the related mode shapes of the structure. These are the results of the free vibration analysis.

- The effects of the impact loading are calculated with RSMA (Response Spectrum Modal Analysis) method. The static load case *dead load*¹ is regarded.
- Displacements and von Misses-stresses² are calculated responses.

2 Transformer model

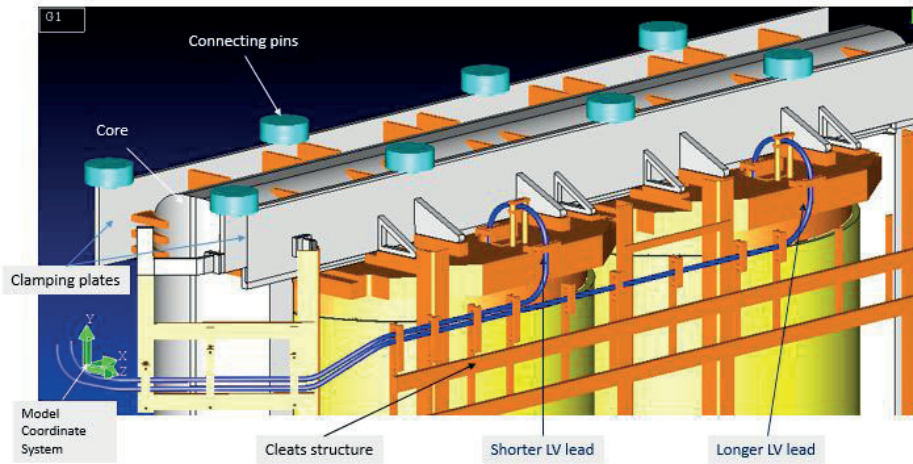


Figure 1: Transformer model

3 Mechanical Analysis Methodology

As loading conditions, the *dead load* (DL) and *impact* are specified.

3.1 Operation Loads

The response of the transformer due to *dead load* (gravity) is calculated in a 'static load' step.

3.2 Impact Loading

During the transport of the transformer an excessive impact was sensed. This impact was measured by two shock recorders mounted on the top of the tank at the manhole, Figure 2.

¹ *Dead load* is synonym for the *gravity load* defined by the weight of the structure itself.

² *Von Misses stress* is a mechanical quantity used to check if the material will withstand a given load condition

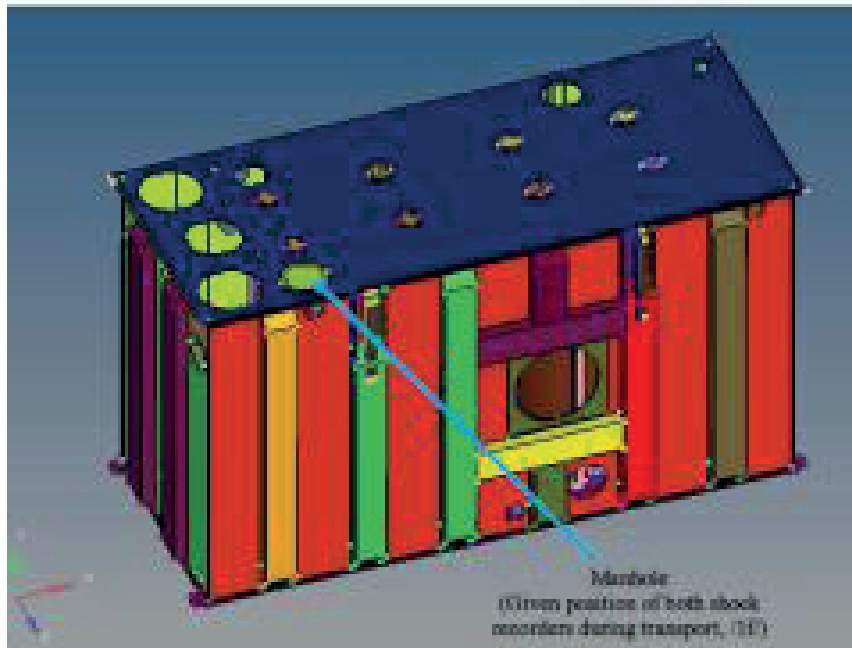


Figure 2: Position on the tank top where the recording devices were mounted

As the real impact happened at the bottom of the transformer tank, the measured information at the top of the tank was in fact the response of the real impact happening at the tank bottom. To obtain the loading at the tank bottom it was necessary to evaluate the *inverse response function* based on the measured signal³. For the impact loading the enveloped response spectra for a damping value of $D = 2\%$ are applied. As there is no information given on the structural damping of the transformer, this value is applied as a conservative approach. The enveloped response spectra are used to calculate the structural responses of the transformer due to impact in x-, y- and z-direction⁴ induced at the boundaries of the FE-Model by RSMA (Response Spectrum Modal Analysis).

The recorded time histories of both recorders are transferred into *response spectra* showing the impact signal in the *frequency domain*, Figure 3. The dominant component of the impact recorded on both recorders was the *vertical* one, but two other components were also present.

³ Nevertheless, the recorded signals were regarded as loading at the bottom.

⁴ Note: The coordinate system of the measured signal and of the simulation model differ! Vertical component in the measured signal is in "Z"-direction, whereby the vertical component in the model is in "Y"-direction.

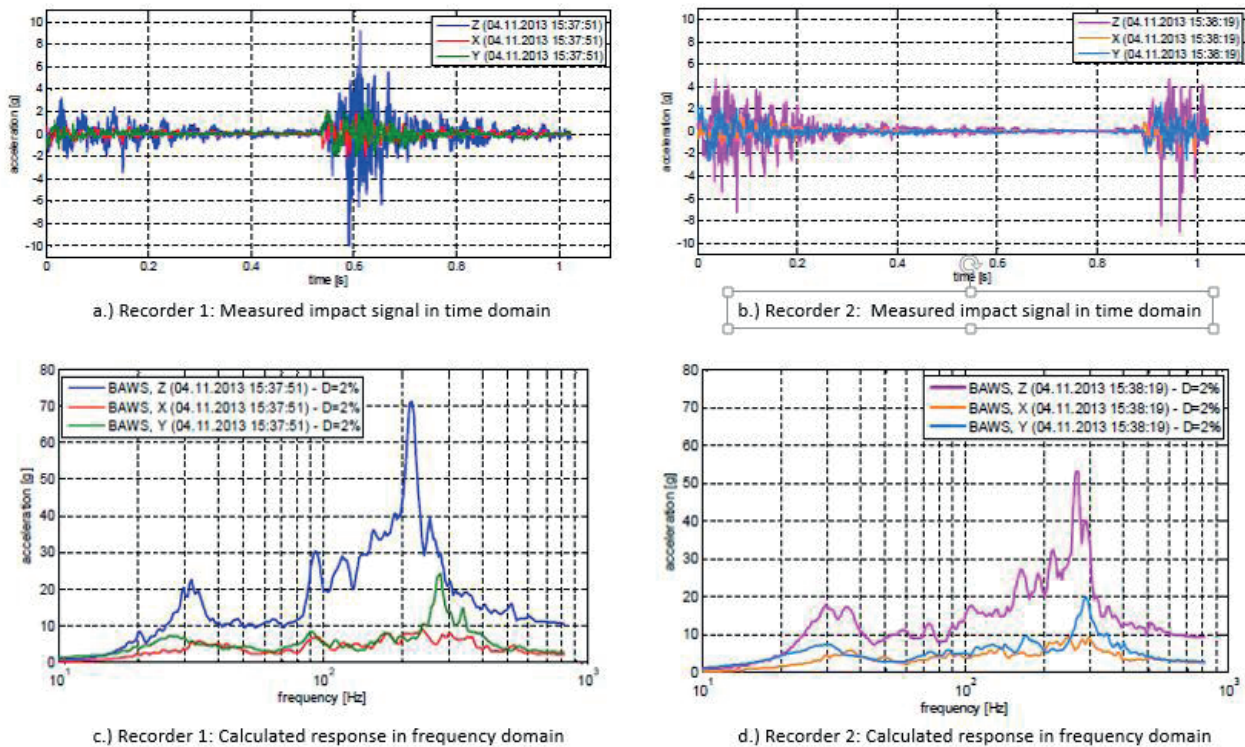


Figure 3: Impact signal in time domain (recorded) and in frequency domain (calculated as a point mass) for both recorders

The response spectrum (or shock response spectrum) shows the peak vibration response (e.g. acceleration) of a single degree of freedom system (oscillator made from a mass put on a spring and damper) due to an arbitrary transient acceleration input (e.g. shock) at its base. The abscissa gives the natural frequencies of the oscillator; the ordinate gives the corresponding peak response for a defined modal damping value.

4 RESULTS

The analysis is carried out with the software ABAQUS⁵. In [Free Vibrations](#) the results of the free vibration analysis are documented. Displacements and stresses according to *dead load* as well as displacements and stresses according to load combination *dead load* with *impact* respectively are documented in [Response to Dead Load](#) and [Response to Impact Loading and to Impact Loading with dead load](#), respectively.

4.1 Free Vibrations

With the FE- model described above the modal parameters are calculated up to a frequency of 350 Hz. The distinctive mode shapes (up to 30 Hz) with high modal masses are shown in Figure 4. It illustrates the trends how the transformer structure moves for different frequent modes (blue lines show the initial position).

⁵ Abaqus Unified FEA, Version 13.2; Dassault Systèmes

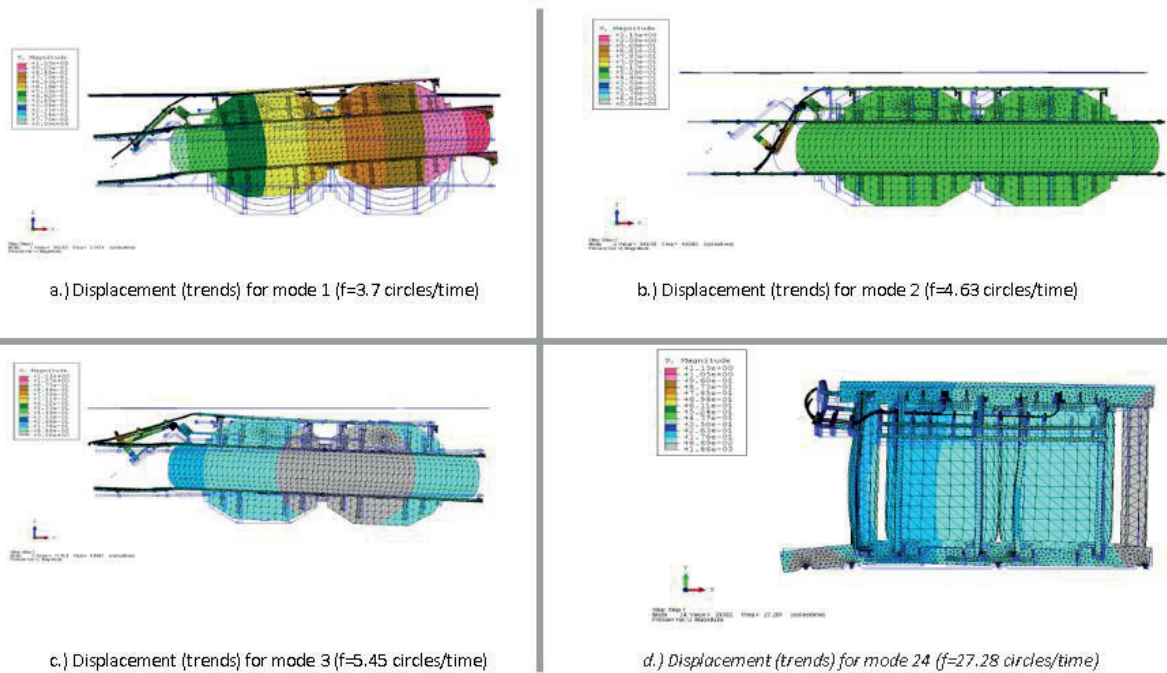


Figure 4: Distinctive Eigenmodes

The Eigen-frequencies up to 350 Hz are calculated; the contributions of higher Eigenmodes are considered insignificant as the modal effective mass of the considered modes is $> 95\%$.

4.2 Response to Impact Loading and to Impact Loading with dead load

The results due to impact loading in X-, Y- and Z-direction as well as their SRSS-combinations are regarded. The stress results are discussed for the different materials separately. The maximum displacement (algebraic-combination of impacts) in the whole transformer is approx. 38 mm and appears at the cleat structure (see Figure 5, a) which is approx. 4000 mm long.

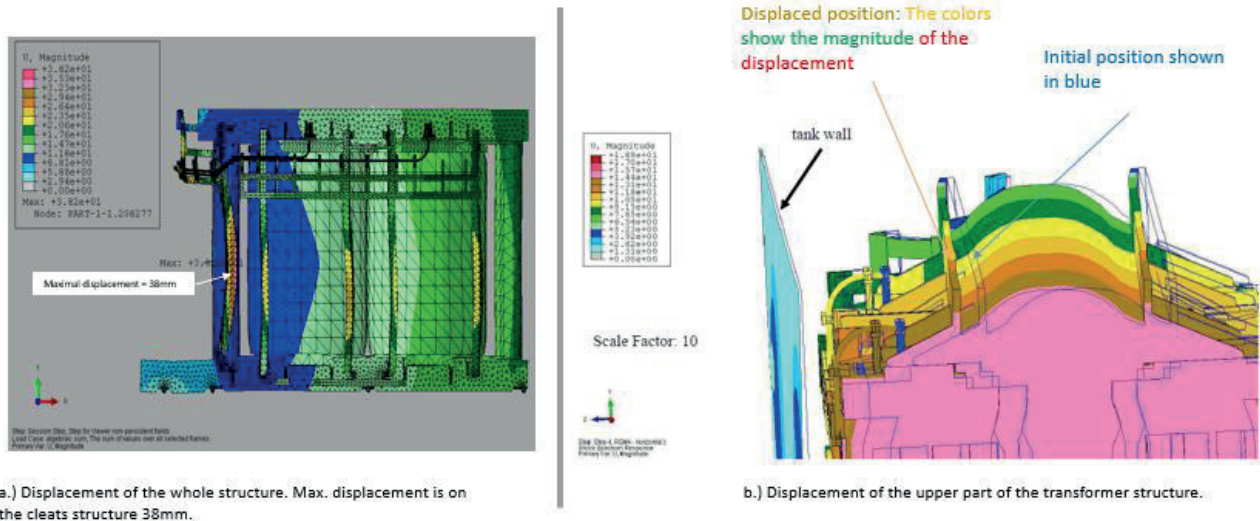


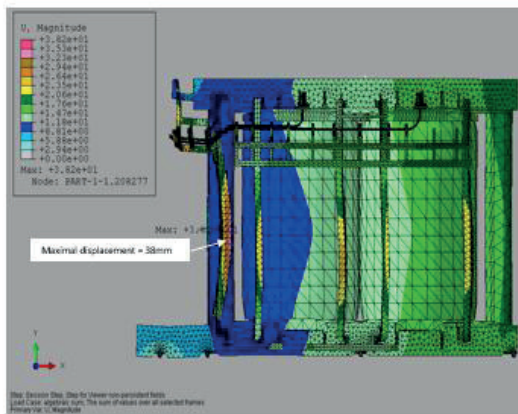
Figure 5: Displacement of the whole transformer structure

Figure 5, b) gives a closer view to the displacement of the upper part of the whole structure. Initial positions are shown in blue. Different colors represent different displacements.

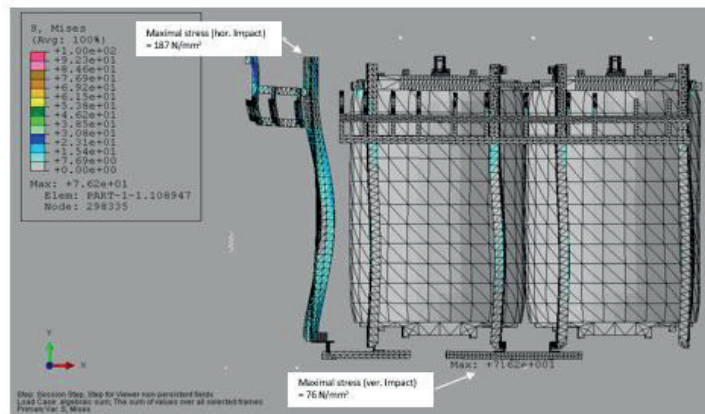
4.3 Pressboard structure

4.3.1 Pressboard Cleats Structure

Maximal displacement appearing on the cleats structure is in range of 38 mm.



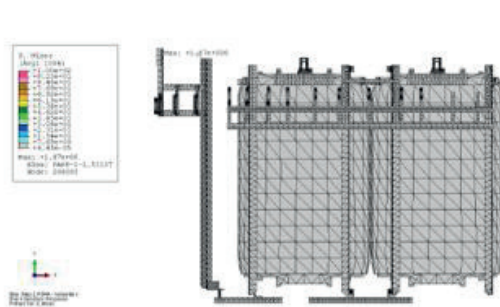
a.) Maximal displacement of the pressboard cleats structure is 38 mm



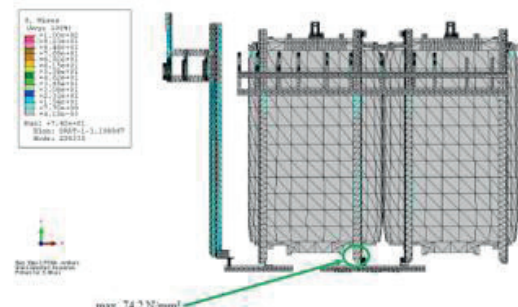
b.) Maximal stress of the pressboard cleats structure is 187 N/mm² (horizontal impact) and 76 N/mm² (vertical impact)

Figure 6: a.) Maximal displacement of the cleats = 38mm; b.) Maximal stress appearing on the cleats is around 187 N/mm² (horizontal impact) and 76 N/mm² (vertical impact).

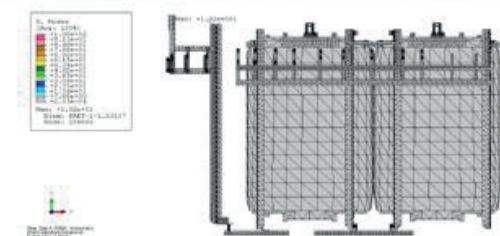
Maximal stress of the pressboard cleats structures is around 187 N/mm² for horizontal impact and 76 N/mm² for vertical impact, Figure 7. As the allowable yield stress for the pressboard is in the range 60-200 N/mm², at certain positions the calculated stress is above the minimal yield stress. It is also known, that for some types of the material (pressboard is one of those) it can cause breaking of the structure, even without achieving the “plastic” stage.



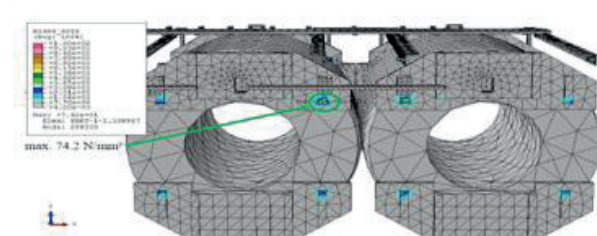
a.) Von Mises stress on the pressboard structures due to horizontal impact in X-direction (max. = 187 N/mm²)



b.) Von Mises stress on the pressboard structures due to vertical impact (max. = 74.2 N/mm²). Yield stress for pressboard varies from 60 – 200



c.) Von Mises stress on the pressboard structures due to horizontal impact in Z-direction (max. = 10.1 N/mm²)



d.) Von Mises stress (calculated as SRSS) in the pressboard bottom parts (max. 74.2 N/mm²)

Figure 7: Stresses due to impact on pressboard structures

4.4 LV Leads

The impact accelerations had a significant influence on the mechanical behavior of the LV leads. Two LV leads (“shorter” and “longer” design layout shown in Figure 1) are located at the HV side (front side) of the transformer. These leads are, with the help of the cleats structure, lead out of the tank.

4.4.1 Stresses on LV Leads

Assumptions

In the current analysis, we have assumed that the yield stress for Cu is laying between the 40 and 100 N/mm². In the real design, the LV leads are the bundled cables made of a number of the Cu wires, wrapped by the paper insulation. In the analyzed model, we assume the solid Cu structure for the LV leads. More precise information on the yield stresses of the bundled cable structure were not available during analysis.

From the detailed view on the cables bending positions shown in Figure 8, especially when considering the lower limit of 40 N/mm², the most overstressed position is near the cleats-keeping parts.

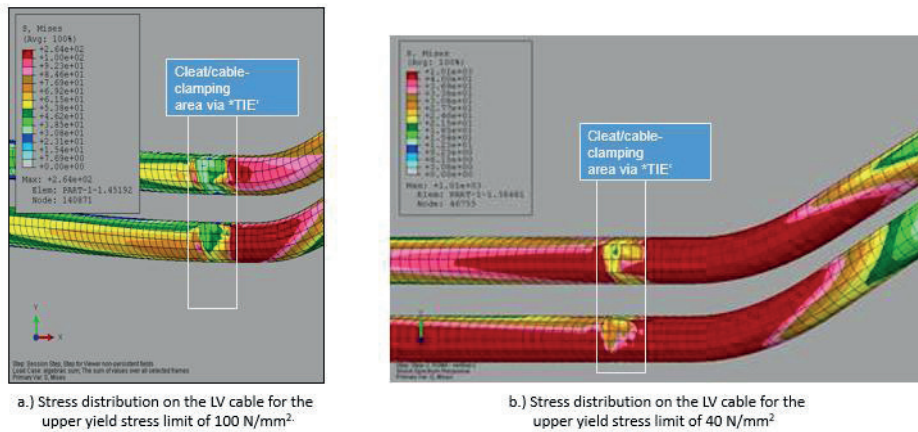


Figure 8: Stress distribution on the bending positions close to cleats

In Figure 9 it can be seen the stress distribution inside of the cable for a.) Yield limit of 100 N/mm² and b.) Yield limit of 40 N/mm² can be seen.

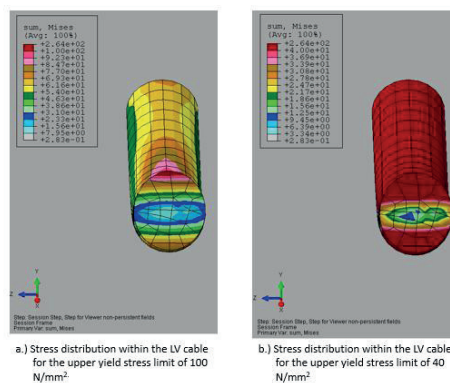


Figure 9: Stress distribution within the Cu cables

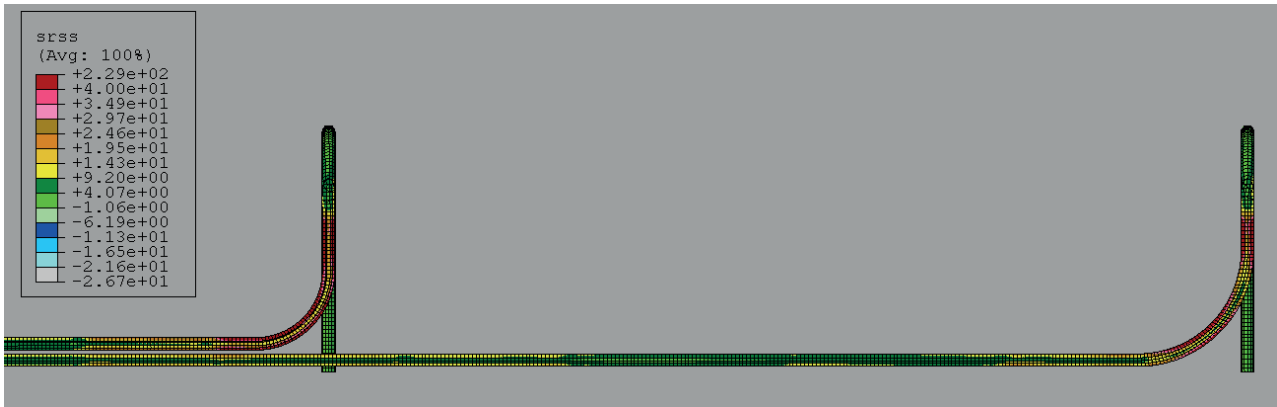


Figure 10: Comparison of the stresses on the shorter and longer LV lead (combination of impact by SRSS method)

Figure 10 shows the stress distribution on the shorter and longer lead. It is visible that the short cable has higher stresses at the bending positions than the longer cable.

Figure 11 shows the stress distribution over the cut of the conductors on the bending position in front of the limbs: a.) Shorter cable and b.) Longer cable.

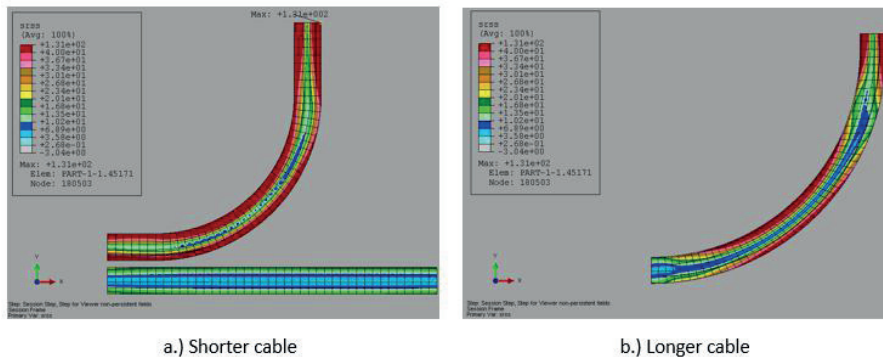


Figure 11: Stress (SRSS combination) at the bending positions of a.) Shorter cable and b.) Longer cable. Colors scaled for the lower limit of yield stress 40N/mm^2

4.4.2 Displacement of the LV Leads

All three components of the impact acceleration cause the displacement the whole structure, including the displacement of the LV leads. Figure 12 show the displacement of the LV cables in both vertical and two horizontal directions (towards and along the tank wall).

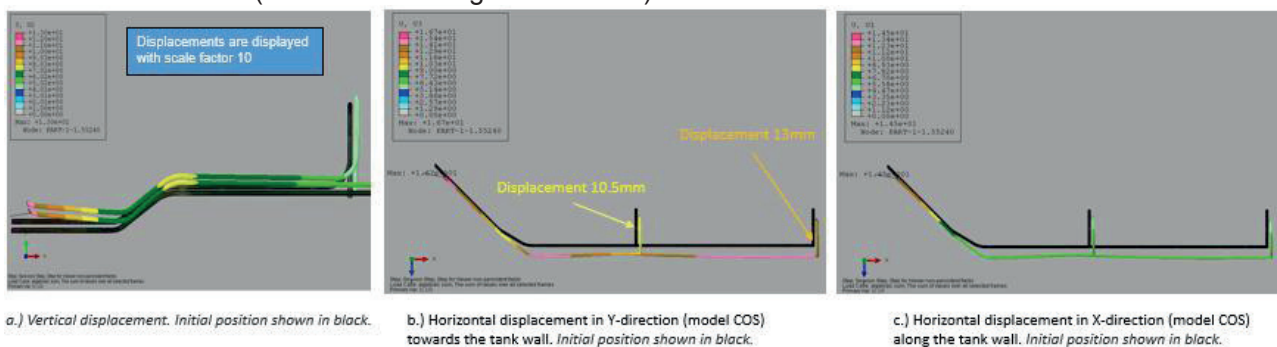


Figure 12: Displacements of the LV leads structures: a.) vertical displacement; b.) horizontal Y-displacement; c.) horizontal X-displacement

The total horizontal displacement of LV lead at the bending positions in front of the limbs is in the range of 10.5 mm (for shorter cable) to 13 mm (for longer cable), Figure 12, b.

4.5 Steel Structure

Figure 13 show the von Mises-stresses caused by the impact signals in X-, Y-, and Z-direction. The critical stresses for steel are not given, but a yield stress of 300-500 N/mm² is assumed. At the bottom connectors and bottom clamps the high values of von Mises stresses (SRSS-combination of impacts has a maximal value of 14.600 N/mm²) significantly exceed the yield stress of 300-500 N/mm² in the wide area. Material plasticity and permanent deformations in these areas are very likely.

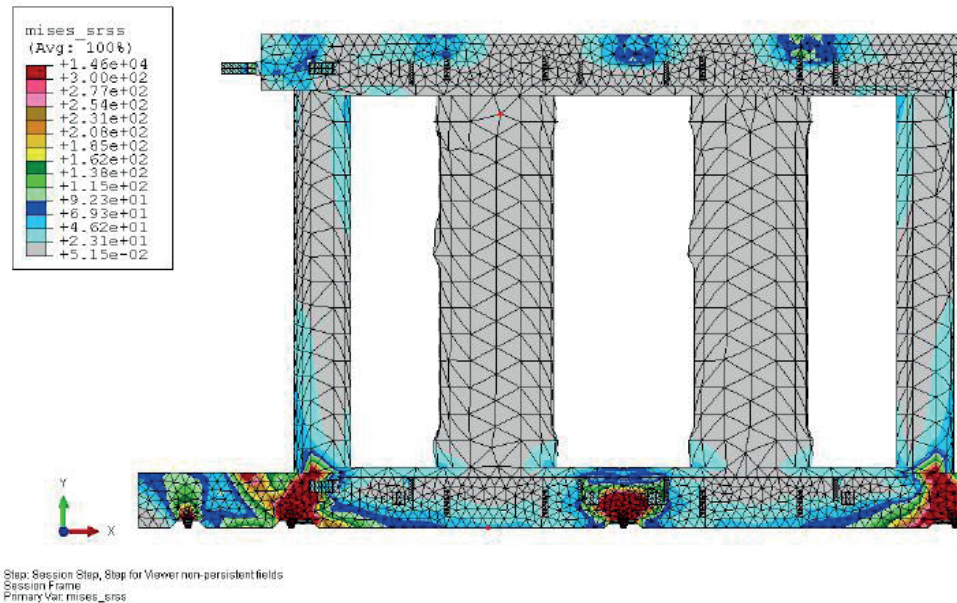


Figure 13: Very high stresses appear at the connecting pins positions. Local maximal value $1.46e^4$ N/mm² is much higher than the standard yield stress value for the steel (300-500 N/mm²).

5 CONCLUSION

The responses (stresses, displacements) of the transformer due to *dead load* and *impact* were analyzed using a linear FE-model as well as linear calculation methods. The goal was to determine whether local plastification / deformation of the structure can be expected due to the experienced impact loading during transportation thus clarifying whether the impacts during transport are potential cause for the malfunction.

The *dead load* loading was evaluated by a static analysis using -1 g vertical loading. The results show a maximum total displacement of 0.4 mm. The von Mises-stress levels in the structure are very low except areas in the clamp plates where the transformer is supported by the eight bottom connectors. In the connector regions, von Mises-stresses of approx. 213 N/mm² are reached (not shown above). This level is quite high regarding the fact, that only dead load is considered. With an assumed average yield value for steel, a usage of 71% (213/300) is already reached for Dead load.

An analysis of the Eigen-behavior of the transformer shows that the basic global horizontal modes are below 5 Hz (see [Free Vibrations](#)), in vertical direction the global motion is associated with Eigen-frequencies in the range 27.2 to 29.2 Hz. Above these frequencies the effect of the impact has (with increasing frequency) less and less effect when stressing of the copper cables or cleats is regarded. Above these frequencies the transformer is „base isolated“. This effect can be seen from the transfer functions (from the base to the transformer top in each direction, not shown).

The responses due to *impact* were analyzed by response spectrum modal analysis (RSMA). For this purpose, the recorded acceleration time histories of the two shock recorders were transferred to response spectra using a modal damping value of D = 2 %. Enveloped spectra were afterwards used to calculate the maximum responses of the transformer due to shock loading in X-, Y- and Z-direction. The responses of these three shock loadings were combined and added to the results of the *dead load* loadcase. These final results (*dead load* + *impacts*) show that:

- Von Mises-stresses in the pressboard are partially approaching the yield limit,
- Depending on the yield stress value of the copper, material plastification and local displacements are more or less likely,

- At the bottom connectors and bottom clamps of the steel structure local material plasticity, which could result in permanent displacement of the entire transformer, is likely.

6 Appendix: Index of Abbreviations

<u>Abbreviation</u>	<u>Meaning</u>
CAD	Computer-Aided Design
COS	Coordinate System
CQC	Complete Quadratic Combination
DL	Dead Load or Gravity Load
FE	Finite Elements
RSMA	Response Spectrum Modal Analysis
SRSS	Square Root of Sum of Squares
Von Misses Stress	Used to check whether the material will withstand a given load condition

Danijel Brezak
Končar - Electrical Engineering Institute Inc.
dbrezak@koncar-institut.hr

Dalibor Filipović-Grčić
Končar - Electrical Engineering Institute Inc.
d Filipovic@koncar-institut.hr

ULTRASONIC METHOD FOR TESTING OF POWER TRANSFORMERS

SUMMARY

Ultrasonic method of detecting PD is based on the fact that the electrical energy of the PD transforms in a mechanical energy, an ultrasonic acoustic wave that spreads through the transformer to the tank wall. From time difference of wave detection on different sensors, a possible location of the source can be estimated. Ultrasonic method can detect other transformer deficiencies such as loose contacts and local overheating of oil ($T > 200^{\circ}\text{C}$).

Three case studies are given in this paper. The first case was where DGA indicates the thermal problem in the oil and the result of ultrasonic testing points at OLTC contacts. In the second case an ultrasonic method was performed after electrical method detected high levels of PD at voltages much lower than the nominal. Ultrasonic method detected non-grounded parts of the returning limb electrostatic screen. In the third case, a failure of transformer, namely a breakdown from the HV bushing end shield, initiated a series of tests on similar transformers installed at the same substation. The assumption was that PD occurred in the shield epoxy insulation and eventually caused the breakdown.

Key words: diagnostics, power transformer, partial discharges, ultrasound, acoustic emission

1. INTRODUCTION

Partial discharges (PD) in power transformers occur as a result of local dielectric overstress of insulation. PD in power transformers with oil-paper insulation result in electrical, chemical and acoustic effects. Their detection can be carried out with several techniques, according to the effects that they produce. Standard method in HV testing technique is an electrical method, which is a part of the quality control in a factory (standards IEC 60270:2000 [1] i 60076-3:2000 [2]). PD in a transformer produces gases, which are the result of a chemical degradation of oil and paper. This is a basis for Dissolved Gas Analysis (DGA) method that determines the amount of characteristic gasses dissolved in oil. Disadvantage of this method is that the PD source needs to be active for a relative long period, long enough to produce measurable levels of gas. Even though these methods are useful, they only give information of the presence and/or magnitude of PD but not their location. Determination of location of the source is extremely important because the severity of the fault depends on the location of its origin. It is not necessary to accentuate that this is important for repair as well as where will it be performed, on site or in the factory. A possibility for on-site repair is always limited by the availability of the location, taking in consideration man holes on the transformer tank as well as the technical limitations, especially if there is a need for an extraction of the active part.

Short-term PD, even with high intensity often leaves no traces on the insulation, making a visual determination of the fault unlikely, even after the disassembly of the transformer. Application of electric method enables only rough approximation of the location (i.e. which phase) and determination of its

character, but only in laboratory conditions. DGA has practically no possibility of location determination, except the determination is the fault mostly in oil or in oil impregnated paper.

However, the ultrasonic method imposes as a solution for location of the PD source. Ultrasonic method of detecting PD is based on the fact that the electrical energy of the PD transforms in a mechanical energy, an ultrasonic acoustic wave that spreads through the transformer to the tank wall. These waves are detected with piezzo-electric sensors, which transform this mechanical wave in to an electrical signal. From time difference of wave detection on different sensors, a possible location of the source can be estimated. Main difference of this method is that its main feature is location of the fault and secondary its detection.

Since the method detects ultrasonic acoustic waves spreading trough the tank it can detect other transformer deficiencies such as loose contacts and local overheating of oil ($T > 200^{\circ}\text{C}$) which gives this method an unique diagnostic status[3].

2. MEASURING METHOD

Standard measuring equipment consists of 24 resonant sensors and a computer acquisition and signal analysis system. Sensors are piezzo-electric type, with resonant frequency 150 kHz, shielded for the purpose of electromagnetic disturbance elimination. Band pass is between 70 and 200 kHz which makes them sensitive to PD, and less sensitive to external noises. Position of each sensor is inputted in a coordinate system along with the transformer dimensions. Placement of the sensors mostly depends on the construction of the transformer having in mind the most critical points of possible PD origins. After the sensors are placed and the system is adjusted calibration of the sensors is performed. Calibration is performed according to Hsu-Nielsen method which gives an approximately the same character of acoustic discharge as a PD [4].

Duration of the test depends on the intensity and repeatability of the acoustic signal. Therefore there are significant differences in the test duration depending on the test location, on-site or in the factory. The duration of the test on-site is usually 24 h in order to cover the entire day cycle of transformer burden. In test stations, acoustic activity can be provoked (either by raising the voltage or current) and therefore test time could be reduced.

At least four sensors should detect the same acoustic discharge to determine its location. If less than four sensors detect discharges, some of non active sensors should be moved to the area of acoustic activity. Of course, sensor dislocation prolongs the test time.

After the test is complete, analysis is performed. During the analysis noises are eliminated, activity with mechanical character is removed and the correlation of activity with respect to working parameters of transformer (voltage, burden, operations of OLTC, cooling system operation) is evaluated.

Conclusion of the possible fault location is given after the thorough analysis of the acquired data.

Possibility of locating PD in power transformers with respect to its origin is given in table I. As the distance between PD source and the tank increases and as the number of obstacles on the wave path increases, the possibility of detection and therefore location decreases.

Table I. Possibility of acoustic source localization [5]

Origin of acoustic wave	Detection	Note
Connections and leads	Yes	High possibility of location
Inner winding	Uncertain	Depends on the position of the winding
Between first winding and core	Unlikely	Very high damping
Between the core and the tank	Yes	Moderate possibility of location
Inside the bushing	Possible	If sensors are placed near the flange of the bushing
DETC	Yes	High possibility of location
OLTC	Yes	High possibility of location

Location calculations are based on a simple relation between time, distance and the speed of an acoustic wave according to (1).

$$d = v \cdot t \quad (1)$$

The majority of the calculation modes are a variation of 2 dimensional source location in a plane, although in many cases the 2D plane will wrap around a 3 dimensional object. For 2 points in a flat plane the distance is:

$$d = \sqrt{(x_2 - x_1)^2 + (y_2 - y_1)^2} \quad (2)$$

This calculation is complicated by the lack of knowledge of the exact time the event originated. To get around that problem, all the times are considered relative to the first hit in the event. Each arrival time differences imply a difference in distance to the sensor relative to the distance to the first hit sensor. For the second hit sensor relative to the first hit sensor, a difference equation can be written as:

$$t_2 - t_1 = (d_2 - d_1) / v \quad (3)$$

or:

$$t_2 - t_1 = \left(\sqrt{(x_2 - x_s)^2 + (y_2 - y_s)^2} - \sqrt{(x_1 - x_s)^2 + (y_1 - y_s)^2} \right) / v \quad (4)$$

This equation contains two unknowns and cannot be solved without the second equation for detection on a third sensor:

$$t_3 - t_1 = \left(\sqrt{(x_3 - x_s)^2 + (y_3 - y_s)^2} - \sqrt{(x_1 - x_s)^2 + (y_1 - y_s)^2} \right) / v \quad (5)$$

When a discharge is detected by multiple sensors, using a regression analysis, the system searches possible location that best fits all the available data. [6]. An example of location determination on a plane with 3 sensors is given on figure 1.

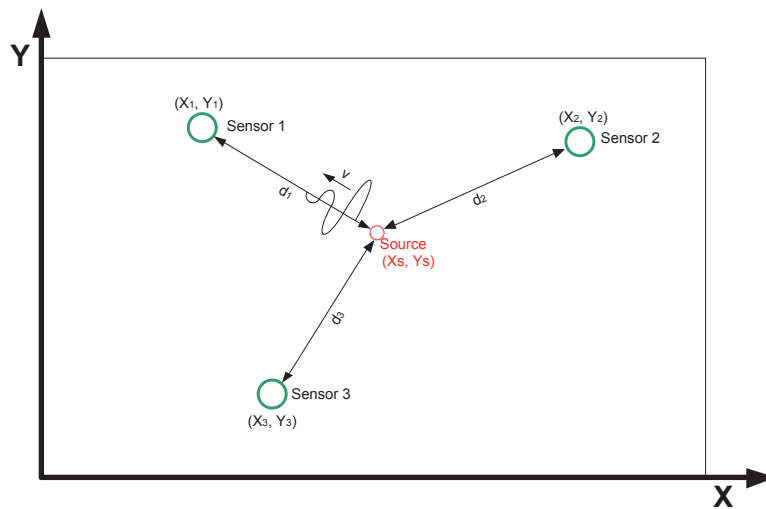


Figure 1. Determination of location on a plane

The lack of knowledge of the exact difference between time the event originated and the time when it was detected by the first sensor can be solved by the application of a Rogowski coil. A Rogowski coil is a high frequency current transformer that is placed around the transformers earthing or neutral point lead. Since the propagation of an electric signal is almost instant, the Rogowski coil detects the time when the discharge originated. Therefore, another equation is added in calculation which enhances precision of the calculations.

Since the system detects acoustic emissions spreading through the tank, the detected hits can originate not only from the actual fault but also from vibrations, external disturbance, reflections etc. In order to differentiate the origins of the signal, parameters of the recorded hits should be evaluated. For example, the system can display the amplitude, energy, duration, counts, frequency etc in respect with test time or relatively to each other. Since PD, local overheating and disturbances have different characteristics the mentioned capabilities are used during analysis.

Implementation of the method was performed in High Voltage laboratory of Končar-Electrical Engineering Institute. Source of PD (figure 2) was placed in a tank of a transformer model, 5 MVA, with dimensions 1,7x1,2x0,7 m. The measurement was performed with de-energized transformer, and the voltage was applied only to the PD source. Parallel to the acoustic method an electric method for PD measurement was used.



Figure 2. Sensor placement (left), PD source (right up) and its placement in the tank (right down).

With the level of 500 pC, system detected a possible location of PD (figure 3). The cluster with the highest density of detected locations is bounded in the green box. Green dots represent the locations of the sensor and the red dots detected locations. It is necessary to note that the dimensions of the axis are not in the same ratio (the system gives a 3D layout as a cube).

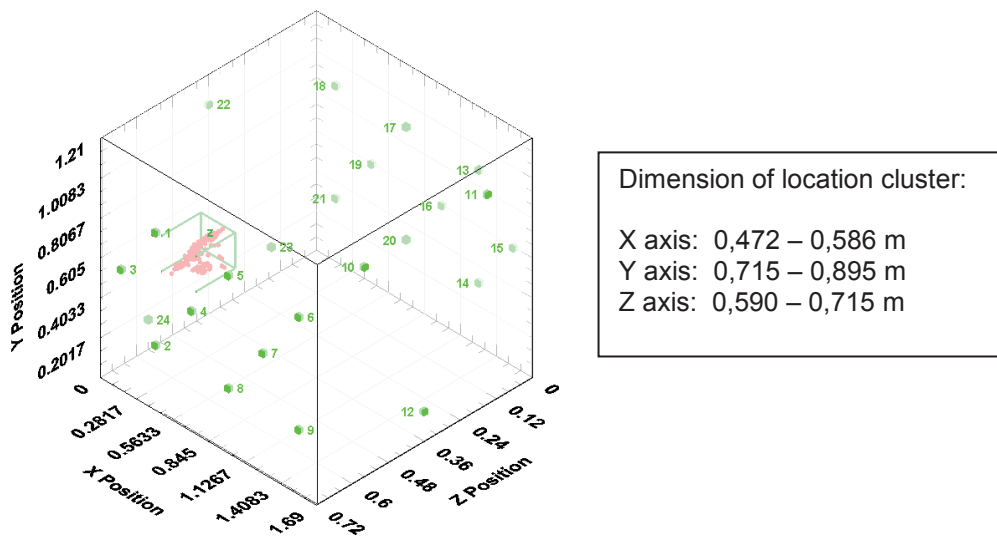


Figure 3. Cluster location at 500 pC

The actual location of the PD source was at: X= 0,530 m , Y= 0,810 m, Z= 0,690 m.

The deviation of the detected location from the actual location of the PD source is within $\pm 0,1$ m. The system was tested to determine the lowest PD level at which it gives a satisfactory precision. Sistem was tested at 100, 900, 700, 500, 70 and 50 pC. It was determined that the system still shows a correct location of the source at 70 pC while at 50 pC the locations are more dispersed, but even then the system still detects the existence of PD. (Figure 4).

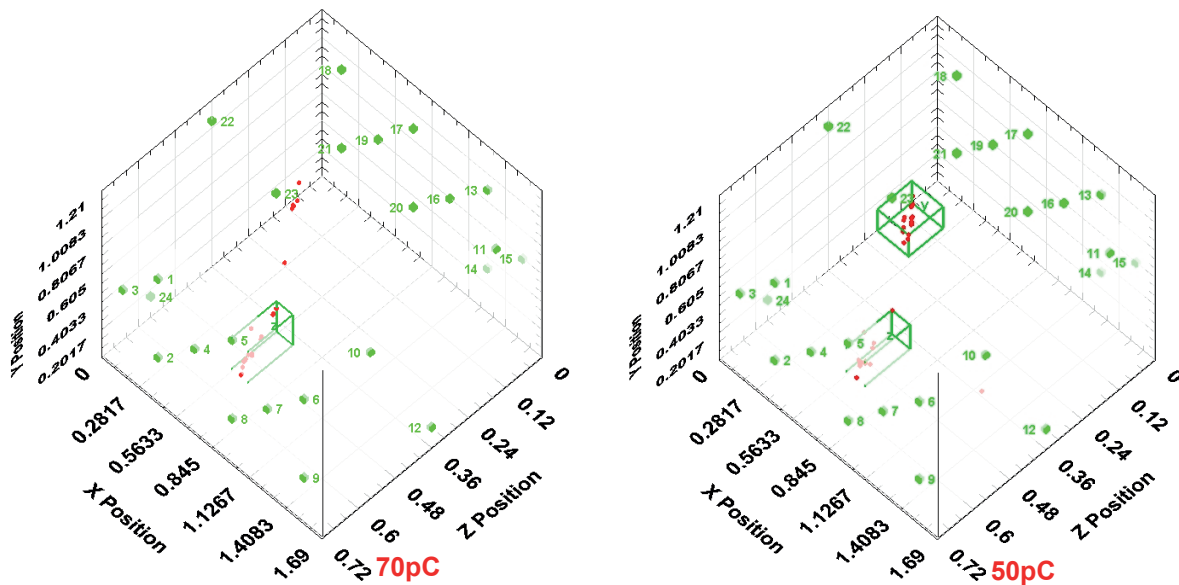


Figure 4. Location clusters at 70 and 50 pC

Even though the method detects such small levels of PD, it is an artificially generated source with a de-energized transformer. On-site it is highly unlikely to detect discharges of such small level due to surrounding interference as well as interference from the transformer itself.

3. CASE STUDIES

3.1. Case1

Ultrasonic testing of transformer 200 MVA, 220/115 kV was initiated by high levels of dissolved gasses in oil, especially ethylene (2122 ppm) and methane (1007 ppm). High levels of these gases indicate a thermal fault, local overheating without the presence of paper.

Highest acoustic activity was recorded by sensors placed in the region of OLTC. Results, before and after analysis are shown on figure 5. During the analysis noises, reflections and mechanical interference was removed, as well as the disturbance originated from the atmospheric conditions (rain, wind etc.). After the analysis locations were obtained within the blue cluster.

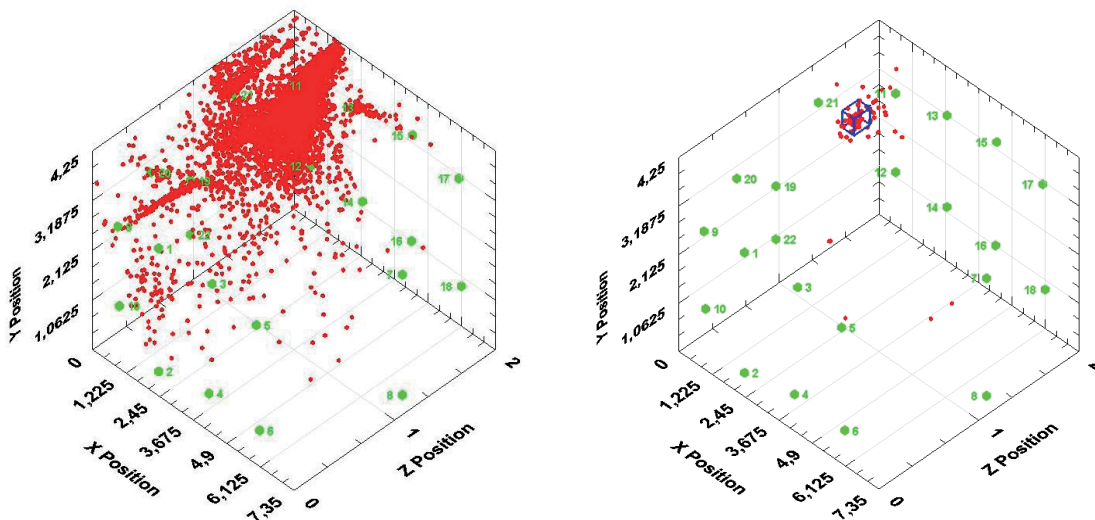


Figure 5. 3-D view of obtained locations before (left) and after the analysis (right)

Different views of the transformer are shown on figure 6 along with the sensor positions and obtained locations. OLTC position was added afterwards. Since the axes are not in the same scale OLTC has an oval shape instead of a circular.

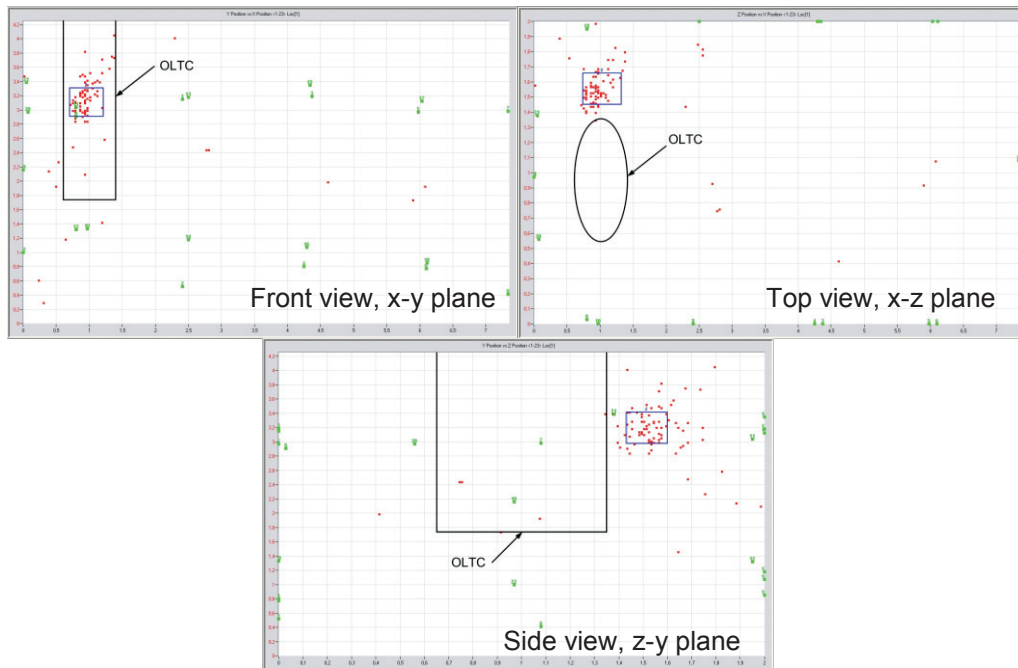


Figure 6. Obtained locations – front, top and side view

Obtained locations, a cluster of the highest density, points to a region where some of the contacts of OLTC are placed. Test result could indicate a bad connection between OLTC contacts and outputs of regulating winding. Na The most active part of the transformer is marked with a red square on figure 7.

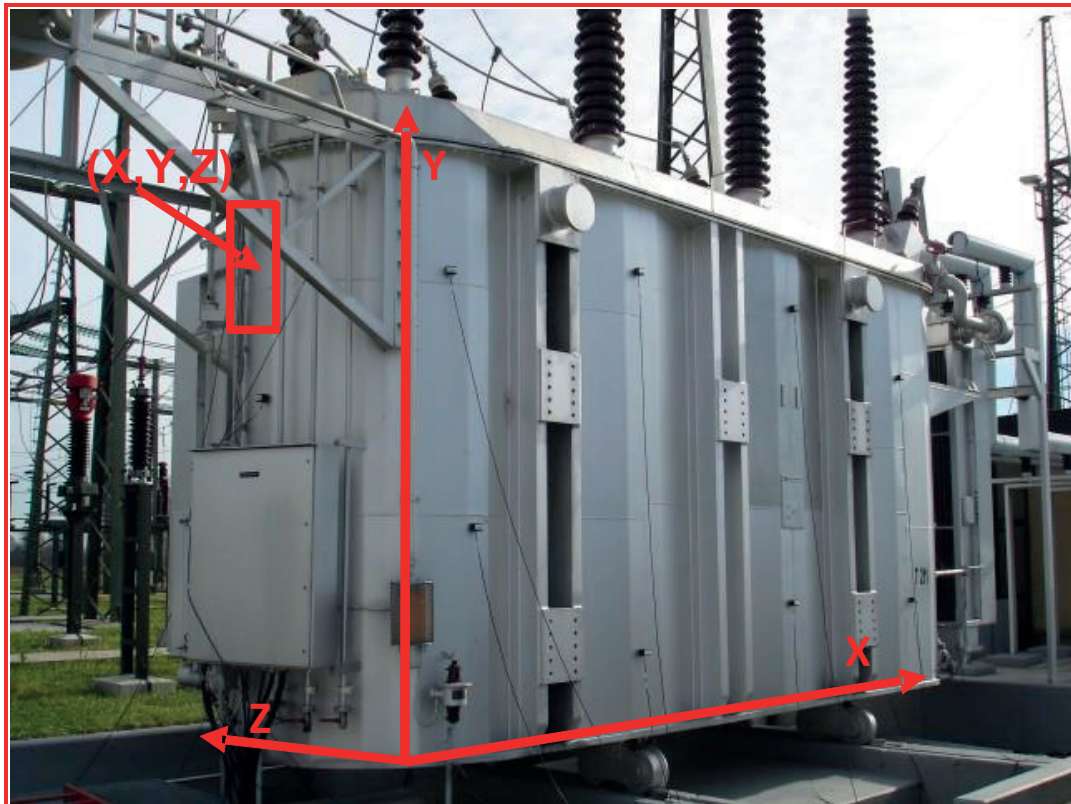


Figure 7. Area of highest activity

After the test it has been determined that there was a significant deviation of winding resistance measured in one of the OLTC positions. This position was not used and there was no further rise of dissolved gases.

3.2. Case 2

Ultrasound emission testing of a power transformer 400 MVA, 400/220 kV has been initiated because the electric method has detected partial discharges (in following text PD) during routine testing.

During the laboratory tests two independent areas of acoustic activities were obtained. Acoustic activity was recorded even at low voltages (switch on voltage). The positions of obtained locations (red dots) before the analysis are showed in figure 8. One area indicates an acoustic emission source in the region of phase 1U returning core limb (5 limb core), and another, an acoustic emission source in the region of 1W returning core limb.

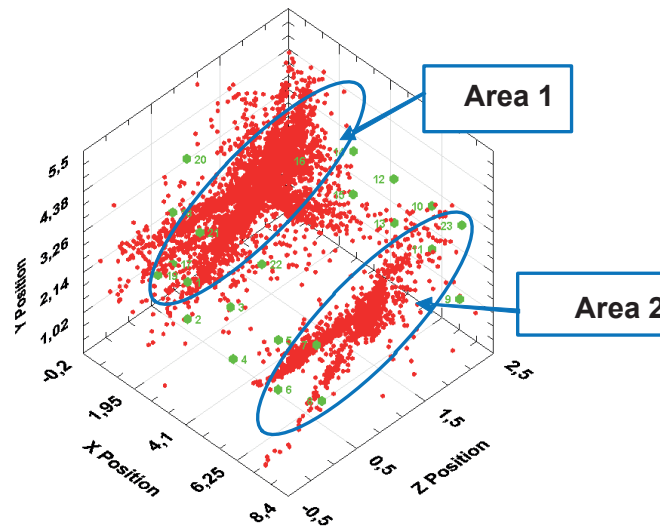


Figure 8. Obtained locations – 3D view – before analysis

After analysis, two clusters (green box on figure 9), were obtained (areas were analyzed separately).

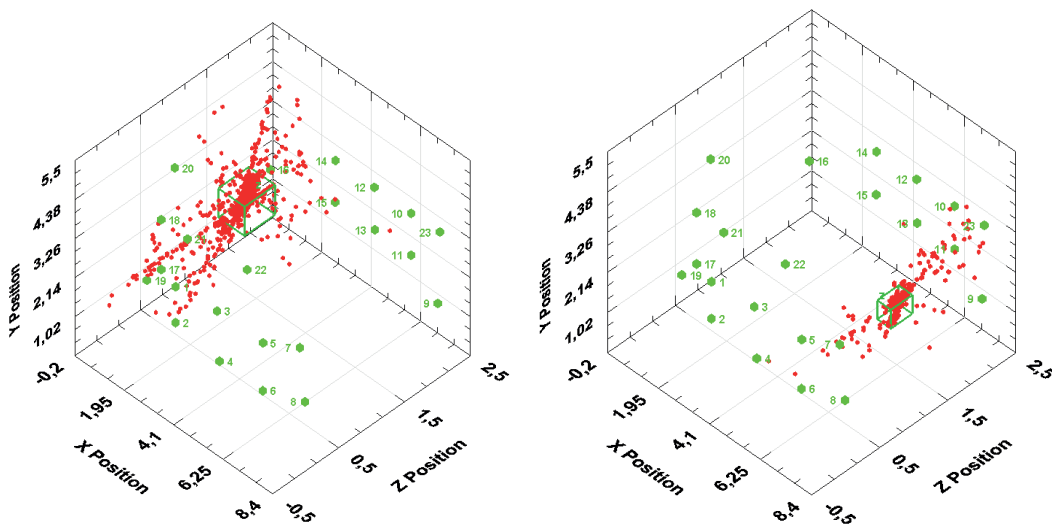


Figure 9. Obtained locations in region of returning core limb 1U (left) and 1W (right)

Areas of highest acoustic activity are shown on figure 10 (marked red). This result indicated that there are acoustic emission sources in the region of both returning core limbs.

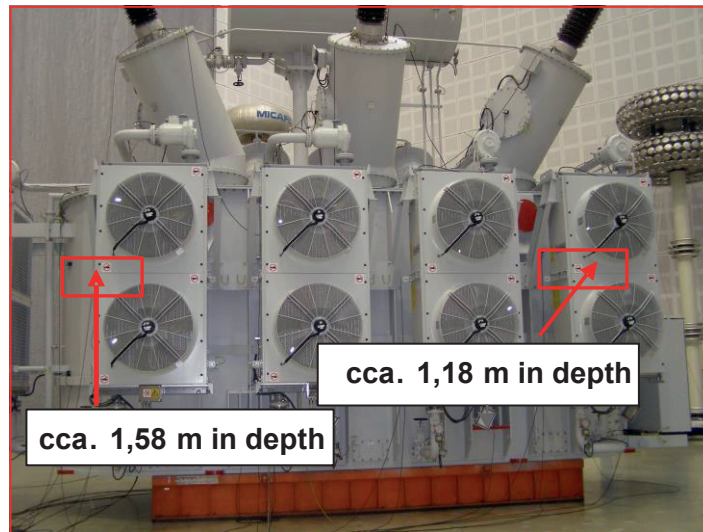


Figure 10. Areas of high acoustic activities (based on 3D clusters)

The transformer was opened and inspected. It was determined that a part of electrostatic screen of returning limb did not have defined potential, i. e. they were not properly grounded and produced sparking.

3.3. Case 3

Ultrasonic testing of bushing end shield was initiated by two breakdowns of a 400 kV in-service bushing in the region of end shield. Bushings were mounted on different transformers while the circumstances of breakdown were similar. Ultrasonic on-site testing was performed on 4 transformers with the same type of bushing and end shield, with major attention paid to the region of end shields. No significant acoustic activity was recorded. End shield consists of the screen electrode embedded in epoxy-resin so there was a possibility that acoustic activity of PD-s occurring in epoxy-resin insulation is heavily attenuated.

Therefore a laboratory test was initiated. A test setup was assembled to produce the same electric field strength as in-service (figure 11). Several end shields were tested using an electric method and ultrasonic method simultaneously.



Figure 11. Screen electrode test setup

Four sensors were placed at the bottom of the test tank. One of the end shields (screen 1, figure 12) showed high PD-s but with very low acoustic activity. This activity is within the range of surrounding noise of an on-site test.

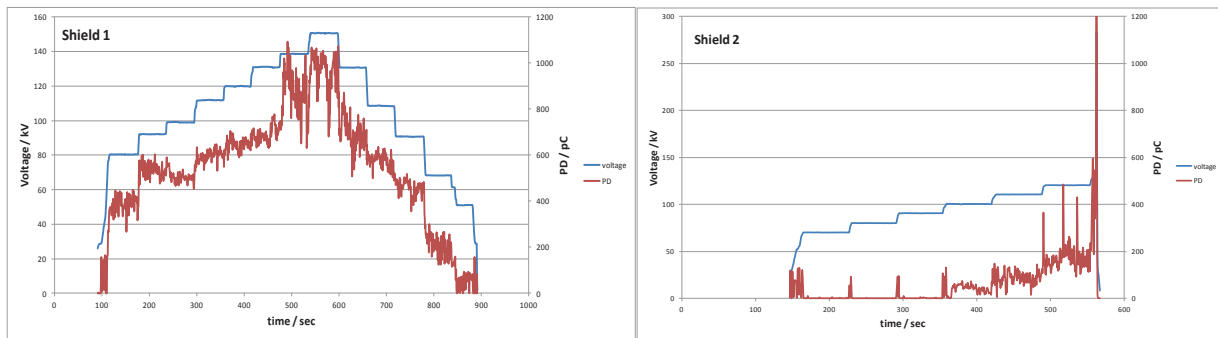


Figure 12. Plot of voltage and PD level vs. test time

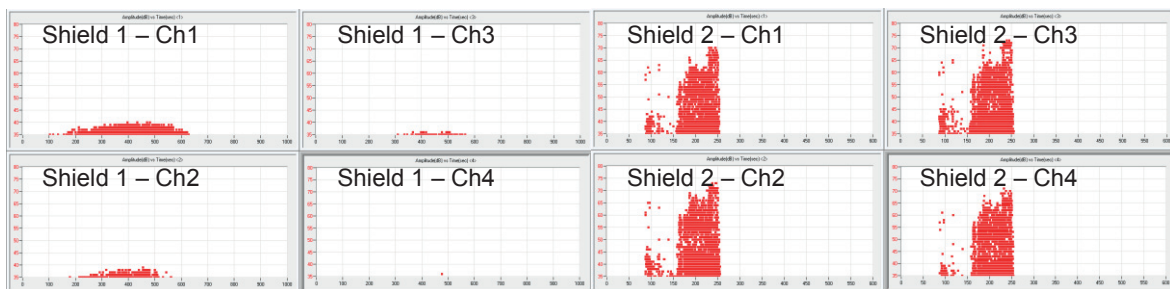


Figure 13. Plot of Acoustic activity vs. test time for both screens

As it is showed on figures 12 and 13, test of screen no. 1 showed very low acoustic activity even when PD levels were above 1000 pC.

To check the sensitivity of ultrasonic system in the existing test setup, a test of end shield no. 2 with damaged epoxy insulation (screen electrode in contact with oil) was performed. Ultrasonic system detected high acoustic activity even at PD levels lower than 10 pC. Since there was a risk of breakdown the ultrasonic system was shut off. Breakdown of shield 2 occurred at 130 kV.

Therefore it is very likely that the damping of acoustic waves generated in epoxy-resin insulation is too high and cannot be detected by the sensors placed on the tank of the transformer.

4. CONCLUSION

Partial discharges and hot spots with temperatures above 200 °C in oil impregnated insulation produce acoustic ultrasonic waves. This effect is a basis for ultrasonic testing of power transformers. Main task of this method is not detection, but to locate a possible defect inside the transformer. Entire preparation of the test and measurement can be performed during normal operation of transformer. This makes this method suitable for on-site testing, especially for important transformer, which, when switched off, can influence the stability of a power system. Besides that, a known location of the fault makes it possible to decide where the fault can be repaired, on-site or in the factory.

Possibility of locating PDs depends on the location of the fault inside the transformer. For instance, a fault on the OLTC, DECT, contacts, leads and any other part of the transformer that is located between the core and the tank is very likely to be located. Even PD-s inside the bushing can be detected in some cases. A fault inside the winding or in between the winding and the core is not likely to be detected due to high damping of an acoustic wave. As it is pointed in case study no. 3, PD inside the epoxy-resin insulation is unlikely to be detected. Laboratory test showed that acoustic activity within the epoxy-resin insulation with levels up to 1000 pC produce low acoustic activity in the range of a surrounding noise of an on-site test. Ultrasonic system detected PD levels only when they were higher than 300 pC. Therefore, a long lasting PD can damage the insulation of a screen electrode without a

possibility of detection by means of any common method (DGA shows no rise of dissolved gases). This can lead to a breakdown without warning.

Ultrasonic method is recommended when one of the standard diagnostic methods or monitoring systems indicate a possible problem, i.e. when DGA shows high electrical or thermal stress inside the transformer. It is also applicable as a fingerprint on-site test in the early stages of transformer operations which can lead to a better diagnostic conclusion of an ultrasonic testing in the later stages of transformer operations. In a combination with other diagnostic methods (DGA, electric method of PD measurement) this method represents a step forward in power transformers diagnostics and can result in a significant savings in transformer maintenance.

REFERENCES

- [1] IEC 60076-3, „Power transformers - Part 3: Insulation levels, dielectric tests and external clearances in air“, Edition 2.0, 2000.
- [2] IEC 60270, „High-voltage test techniques - Partial discharge measurements“, Edition 3.0, 2000.
- [3] Arturo Nunez, Samuel J. Ternowchek, Ronnie K. Miller, Barry Ward, „Detection, location, assessment and classification of faults in energized power transformers using acoustic emission“, CIGRÉ Transformer Colloquium, 2003
- [4] Tomasz Boczar, Marcin Lorenc, "Standard Guide for Determining the Reproducibility of Acoustic Emission Sensor Response,", Physics And Chemistry Of Solid State, V. 7, № 3 (2006) P. 585-588, 2006
- [5] IEEE PC57.127/D10.0, „IEEE Guide for the Detection and Location of Acoustic Emission from Partial Discharges in Oil-Immersed Power Transformers and Reactors“, December 29, 2006
- [6] Physical Acoustic Corporation, „Aewin™ Software Users Manual, Rev. 1.90“, 2004

Bálint Németh*
Budapest University of Technology and Economics
nemeth.balint@vet.bme.hu

István Kispál
Diagnostics Ltd.
ikispal@diagnostics.hu

Gusztáv Csépes
Diagnostics Ltd.
gcsepes@diagnostics.hu

Zsolt Laczkó
MVM OVIT Ltd.
laczko.zsolt@ovit.hu

CHECKING OF THE CONDITION OF TRANSFORMERS AND THE EFFICIENCY OF OIL REGENERATION WITH RVM (RETURN VOLTAGE MEASUREMENT)

SUMMARY

Up to now the insulation in HV power transformers has been made from oil/paper therefore the diagnosis of this kind of insulation will be also important in the next forty-fifty years. The lifetime of this equipment strongly depends on the condition of the insulation system. The ageing process of oil/paper insulating systems is a very complex and complicated phenomenon. In order to get a well-supported decision on the further operation of aged transformers, relevant information would be necessary on the condition of the oil-paper insulation. We also know that the oil-paper insulation has almost always inhomogeneous condition considering the temperature, moistening and ageing processes. The classical methods (insulation resistance, loss tangent, etc.) characterise the insulation by single measured value. This single value is not sufficient for relevant characterisation and diagnosis of such a complex system with lots of tons of insulation and with almost always inhomogeneous distribution of temperature, moisture and ageing product. If we measure the polarization spectra in three states (new insulation in equilibrium and uniform polarization spectrum, new insulation with not uniform distribution of polarization spectrum, later reaching again the uniform distributions) the shape of three polarization spectra will be different. Comparing the polarization and classical methods of this three case we can realize that sometimes the “classical single values” are almost the same but the polarization spectra are different.

The three response methods provide very practical information about the insulation system (e.g. moisture, ageing). The moistening and accumulation of ageing by-products change the distribution of interfacial polarisation in the range of long time-constants. These promising response methods measure the polarisation distribution in the range of long time-constant (with other words, in the low frequency range). The three test methods were: Return Voltage measurement (RVM), the C and $\text{tg}\delta$ measurement in range of some tens of mHz to 50 Hz (FDS=Frequency Domain Spectroscopy), and the measurement of DC charging and discharging currents (PDC=polarisation and depolarization currents) up to some thousands of sec. These equivalent methods (RVM, FDS and PDC) are able to follow the changing of condition of insulation contrary to classical methods. Therefore a little bit surprising that until now the convenient standards is missing considering the polarization methods. In an earlier Hungarian research work (Budapest University of Technology) almost all the necessary measurements have been realized, consequently we are in possession of fundamental data considering the polarization methods. This paper would like to show a short review about the RVM technique, the correct interpretation of RVM data and a case study for the checking of the efficiency of the oil reclamation with RVM technique.

Key words: transformers, Dielectric Response Methods, Return Voltage Measurement (RVM), condition assessment, ageing, moistening, life management, oil regeneration

1. INTRODUCTION

The actual lifetime of transformers strongly depends on the real operating conditions, and so the residual life of these units can spread in a broad scale. The transformer life/ageing is mainly related to the degradation of the insulation, which is caused dominantly by the thermal ageing of the insulating paper, together with the decomposition of the cellulose. The by-products of this process are water and other substances of partly polarisable and ionisable character. The humidity content and the ageing products of the paper have a decisive role in the degradation rate of the cellulose; the higher humidity accelerates very strongly the degradation. It is important to periodically check the internal conditions, diagnose the degree of its deterioration and carry out proper cost-effective preventive/corrective maintenance, refurbishment or on-site oil regeneration taking into consideration its remaining life [8] [9] [10].

The changes of the condition can be caused by certain deterioration effect, most of them can be detected using the classical methods or the polarisation (interfacial and boundary) spectrum techniques. Lots of classical methods (insulation resistance, absorption factor, loss tangent, water content measurements, etc.) have been used for many decades as testing of the solid oil impregnated paper insulation. They intend to qualify the state of inhomogeneous insulation by single measured value. This single value is not proved to be appropriate for relevant characterisation and diagnosis of the complex system of such inhomogeneous insulation considering the temperature, moistening and ageing processes. A good and suitable diagnostics system is able to distinguish the inhomogeneous distribution of the temperature, moisture and ageing product content, the good and wrong condition, the dry and wet state, the changing of condition before and after the oil regeneration, etc. [1] [2] [3] [4] [11].

When we would like to estimate the condition, we had to characterise the oil condition, the ageing phenomena of cellulose insulation (soft and hard cellulose, surface of solid insulation, the ageing product between the paper layers, etc.). Recent attention has been directed to methods of determining moisture content and ageing of the pressboard and paper more directly by measuring the effects of moisture and ageing on electrical properties. Rather than the traditional measurement of power frequency loss angle, measuring various dielectric response parameters, which characterise some known polarisation phenomena, has been in focus [5] [6]. All the three dielectric response methods (RVM, FDS, PDC) reflect the same fundamental polarisation and conduction phenomena in transformer insulation and are able to estimate this complex and complicated insulation system [1] [2] [3] [4].

Unfortunately till now a guide or a standard is still missing in this field, perhaps this is justified that the State of Arts of the polarisation spectrum methods is not well known. The main goal of this paper is to show the good efficiency of one the spectrum methods by means of the RVM (Return Voltage Measurement). For the correct interpretation of the RVM methods first of all we have to offer a brief survey of specific feature of oil-paper insulation with special attention of oil reclamation. Oil reclamation (reclaiming) is the elimination of soluble and insoluble contaminants from an insulating liquid by chemical absorption means, in addition to mechanical means, in order to restore properties as close as possible to the original values [9][11]. The oil reclamation results important and complicated changing in the condition of the oil-paper insulation. One parts of ageing contaminants is in the oil, but important parts are on the surface of the cellulose insulation. With the oil diagnostics we can check the ageing product in the oil but we have not information about the remaining ageing product in the paper insulation. The polarization spectra are able to reflect this complex mechanism, the RVM is able to follow the changing of condition of insulation, and as a consequence, the RVM is able to estimate the effectiveness of oil regeneration. It is well known that the oil regeneration "in a transformer" is far more efficient than simple oil change. In the case of oil change relatively lots of ageing products remain between the paper layers, but the RVM method is able to distinguish the difference between the oil change and the more efficient oil reclamation.

Why are we able to claim that the RVM method is very good tool to diagnose the condition of oil-paper insulation? At the Budapest University of Technology and Economics (BME) a large research work has been carried out to investigate the moistening and ageing of oil-paper insulation in 70s. In the scope of Hungarian research work - among other things - the following processes have been investigated: Return Voltage Measurements (RVM), Dielectric Frequency Domain Spectroscopy (FDS), and Charge/discharge current (measurements of polarisation and depolarization currents (PDC). In the Hungarian research work almost all the possible measurements have been realised. Based on our research work and thirty year's practical experience, we would like to clarify why the interpretation of results seems a little bit difficult. Using the results from the laboratory experiments and from field measurements, an Expert System (ES) was developed for easier interpreting the measurements. In this Expert System distinction is made between good and bad condition, it is showed the relationship between

polarisation spectrum of the new and service aged power transformers, actual condition (water content and ageing product), how to extract information from the measurement data [1] [2] [3] [4] [11].

2. BRIEFLY ABOUT THE LIFE EXPECTANCY AND OIL REGENERATION

So far, the main insulation of HV power transformers is still making from oil/paper. Transformers have designed for a 40 years lifetime therefore the management of this kind of insulation will be inevitable in the next forty years or so. The owners are concerned when to replace them and how risk increases with age. In order to minimize the cost of operation of a transformer throughout its life, it is important to periodically check the internal conditions, diagnose the degree of its deterioration and carry out proper cost-effective preventive/corrective maintenance, refurbishment or on-site oil regeneration taking into consideration its remaining life. The owner of the transformer must select - based upon technical, operational and economic considerations - one of the following alternative possibilities: repair or/and refurbishment in factory or on-site, on-site oil regeneration, replacement of damaged unit with a new or spare transformer.

It is well known that the life of the transformer is exclusively determined by the life of the insulating paper. Since the cellulose insulation in a transformer can only be replaced with a rewind and loss of production of the transformer in question, it makes sense to remove the oxidation by-products before they can do any damage to the cellulose. Since any degradation of the cellulose that occurs cannot be reversed, it would be the best to remove the oxidation by-products as quickly as possible. The simple oil purification methods do not remove the oxidation by-products associated with transformer oil aging only oil regeneration methods are capable of removing the sludge found in aged transformer oil and in cellulose insulation found in the transformer.

Regarding the behaviour of oil-paper insulation systems the oil reclamation or regeneration is very cost effective method to improve the condition of transformer insulation. During service life, the oils oxidises forming degradation products as acids and sludge. Untreated oil will attack the paper and drastically cut down on the life of transformers. As it is well known the oil reclamation is effective in removing acid compounds from oils. Knowledge of the general behaviour of an impregnated insulation system and its ageing is the key factor to understanding the possibilities for improving service conditions of insulating paper. Oil regeneration treatment restores oil quality properties, thereby extending the serviceable life of the mineral oil and the reliable life of the transformer. The regeneration will slow the aging rate of the oil, thereby extending the life of paper insulation. We had to mention some words about the simple treatment process of oil. The simple oil treatment is really filtering and drying of oil, but the ageing materials remain in the oil and on the surface of paper insulation. Since there is big difference between the simple oil treatment and the powerful oil regeneration it is essential to use such a diagnostics tool which is able to distinguish the simple and effective process [8] [9] [11].

Considering the ageing of the oil-paper insulation why is it interesting to investigate the efficiency of RVM method and the oil reclamation? The moisture and ageing products increase the dielectric loss, the dielectric loss increases the local temperature and an avalanche processes can start and in the end a dielectric failure can occur. The increased moisture, ageing products and high temperature of the oil-paper insulation accelerate the ageing processes. The evolution of free gas bubble will start with a consequent reduction of dielectric strength and sharp reduction of PD inception voltage. If we would like to specify the risk of dielectric failure of the insulation (when the bubble formation cause breakdown) we have to determine the limiting hot-spot temperature for safe operation of transformers. When free gas bubbles have been observed in transformer conductor heated to overload temperature this phenomenon influences the operation of transformer and inversely, the operation of transformer has an effect on bubble formation [7][10][11]. To avoid premature ageing of the cellulose insulation, the equipment's water and acid content must be kept to a minimum. If the transformer has a significant water and acid content, drying and oil regeneration may retard ageing of the solid insulation. As we will see below, we have to determine the whole RVM spectrum and each time constants. We had to know the limits of moisture, ageing rate, bubbling temperature, then determining the limit temperature at which the operation of transformer is safe [3] [4].

3. BRIEFLY ABOUT THE RVM TECHNIQUE

3.1. Interfacial and boundary polarisation, polarisation spectrum

Two fundamental dielectric processes, the conduction and polarisation, arise in the dielectrics under the presence of the electric field. Both processes are very strict connection to the micro-structure of the oil-paper insulation, any change in the insulation lead the changing of fundamental dielectric processes. The magnitudes of dielectric parameters are determined by the intensities of both processes. Therefore it is possible to conclude from the changing of the measured parameters to the development of deterioration of insulation, and indirectly to the decrease of its dielectric strength, as well.

The intensity of conduction can unambiguously be characterised by single quantity, the specific conductivity γ (or by its reciprocal value, specific volume resistivity (ρ)) of oil-paper insulation. The polarisation, however, is more complex process, namely a resultant of several elementary processes of different intensities and relaxation times. It can only be characterised by using the polarisation spectrum (PS) of insulation. The PS is a density function ($\alpha(T)$) what describes the distribution of the intensity of the polarisation against the time constant (Fig. 1) [3][4].

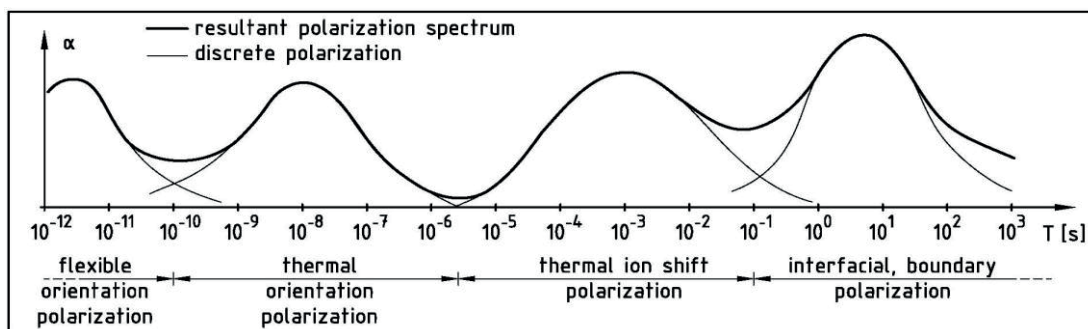


Fig. 1: Polarisation spectrum characterised by the density function of $\alpha(T)$

The interfacial polarisation spectrums contain lots of information about the insulation systems. As we can see from the technical literature, that the polarization (interfacial and boundary) spectrum techniques are able to access the condition of oil-paper insulation. The interfacial polarisation gets sorted out in the insulation when the following equality is not true: $\epsilon_1\sigma_2 = \epsilon_2\sigma_1$ (ϵ =permittivity, σ or γ =conductivity of insulation material) (Fig. 2).

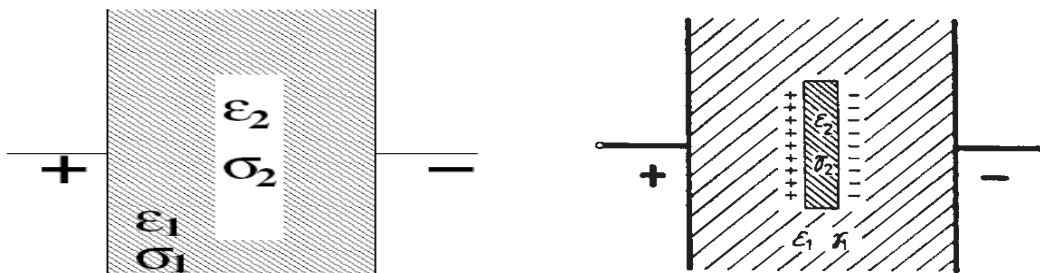


Fig. 2: interfacial and boundary polarisation

This polarisation spectrum characterises not only the material, but - because of the strict relation of the polarisation to the micro-structure - even to the condition of the insulation, as well. Consequently, by investigation this spectrum a conclusion to the deterioration (moistening, ageing, etc.) can be drawn. Regarding the diagnosis of moistening and the ageing processes in oil-paper insulation the interfacial and boundary (volumetric) polarisation is important of the whole polarisation spectra. For the simulation an equivalent circuit can be used, shown in Fig. 3 [3][4]

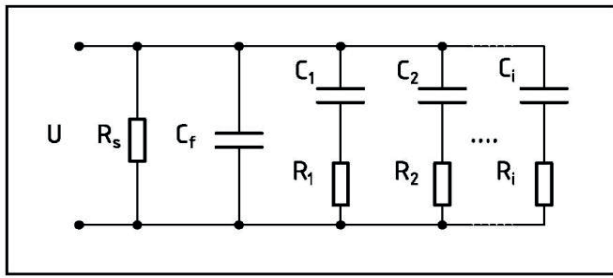


Fig. 3: Equivalent circuit of insulation

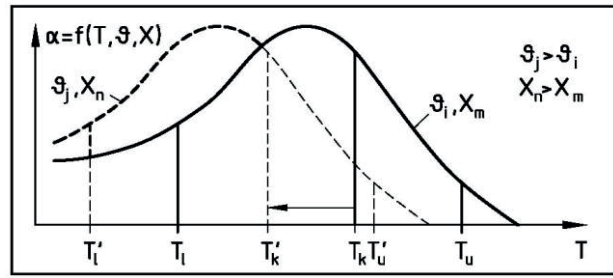


Fig. 4: The polarisation with different time constant

C_f is high frequency capacitance, R_s is the insulation resistance of the test object can. The “slow” polarization processes can be modelled by a parallel connection of series $R_i C_i$ elements, together with a “high frequency” capacitance C_f . Without going into the details the Figure 4 shows the approximation of polarisation spectrum by “elementary of number n ” processes in the related of $T_1 \dots T_u$ time constant range (α_k and T_k are the specific polarisability response the time constant ($T_i = R_i \times C_i$) of the process, parameters: X =moisture, θ =temperature) [3][4].

3.2. Technique of the Recovery Voltage Method

The Recovery Voltage Method is a DC method which investigates the slow polarisation processes in the time domain (see Fig. 7). A step voltage ($U=$) is applied over the electrodes of a completely discharged test object with geometric capacitance. During the charging period the polarisation current flows through the test object. After the charging period, the test object is short-circuited and the depolarisation current flows. After the short-circuiting period is finished, the return voltage is measured under open-circuit conditions. The source of the recovery voltage is the relaxation processes inside the dielectric material, giving rise to an induced charge on the electrodes of the test object. The charging period activates polarisation processes in the object. Depending on how long the test object is charged, different polarisation processes with different time constants become activated. Then during the short-circuiting period, the polarisation processes start to relax. Depending on how long the test object is short-circuited, different numbers of polarisation processes are almost totally relaxed. Then during the open circuit period the polarisation processes, which were not totally relaxed during short-circuit period, relax further and give rise to a recovery voltage over the electrodes of the test object [2][3][5][6].

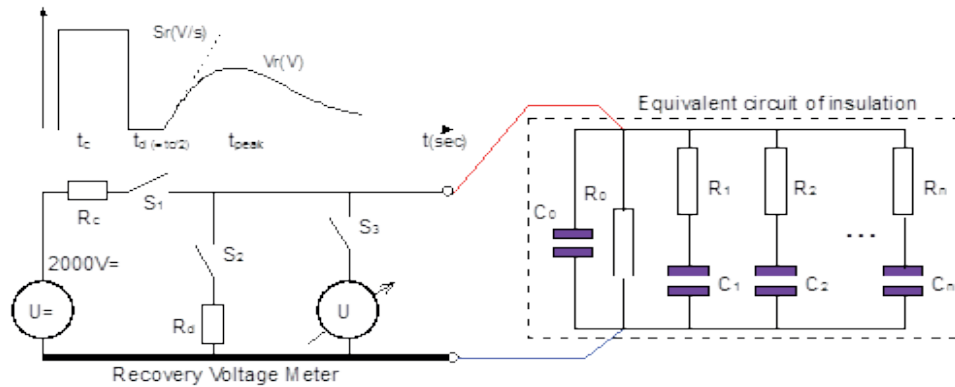


Fig. 7 – RVM measurement cycle and equivalent circuit

The RVM “quasi spectrum” is produced by applying a series of individual charging voltages $U=$ to the test object, followed by a short-circuiting period as explained in Fig. 7, at each cycle increases of the charging period, $t = t_c$ as well as the short circuiting period, $t = t_d = t_c/2$ are made (using a fixed ratio of $t_c/t_d=2$ for the measuring series). After discharging time (t_d) has elapsed, the recovery voltage $U(t)$, for a particular cycle, is recorded and from its peak value, the amplitude U is quantified with the charging period t_c for that cycle. The resulting curve, U_{max} as a function of T_c , is called the polarisation spectrum. The initial derivative, dU/dt of the recovery voltage is also found and can be plotted as a function of t_c .

The following RVM curves of the Fig. 8 and 9 show such typical cases when the investigated processes have one or two time constant.

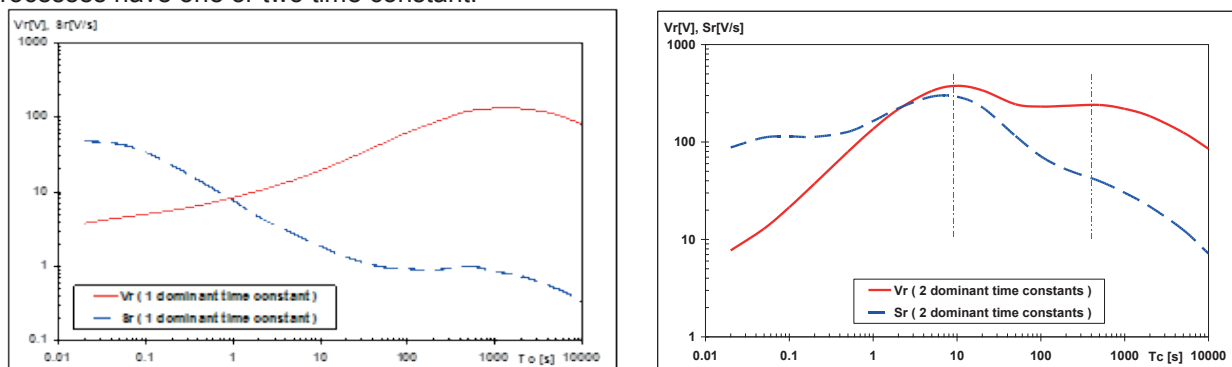


Fig. 8 and 9: typical RVM curves with one and two dominant time constant

The interpretation of an RVM measurement is based on the complete two curves (curves of V_r and S_r), namely the identification of maxima in the polarization spectra, and the estimation of the polarization intensity at the maxima. The analysis becomes much easier if the “initial slope” (S_r) spectrum and “maximum” (V_r) spectrum are used together.

The curves of Fig. 8 show the shapes of “quasi spectra” (determined by RVM) with one dominant time constants. We have to know that in this case there is only one polarization process which is characterized with single time constant. This is the case, par example, when the oil-paper insulation has a good, dry condition and the system is in equilibrium (the insulation condition is homogenous including the temperature distribution too).

The curves of Fig. 9 show such a case when there are two polarization processes which are characterized with two different time constants. This is when the oil-paper insulation has a good, dry condition and the system is not in equilibrium (the insulation condition is not homogenous), or the paper has good condition (new and dry) but the oil is aged, etc. The “quasi spectrum” is - as can be seen - a continuous curve, with two definitive maxima, at the two time constants, so, that these are well determinable of this curve. If we would like to determine the dominant time constants the “RVM quasi polarisation spectrum” is suitable in practice.

It is well known that the polarization is a more complex phenomenon, a resultant of several elementary processes. Each of the elementary polarization processes are related to a well-defined kind of charge carriers. If the density of a certain kind of charge carriers alters due to some ageing or deteriorating processes of the insulation, the intensity of the elementary polarization will change, as well. The increase in conductivity leads to an increase in dielectric loss and a decrease the time constant of elementary polarization, as well. As an example, since the chemical ageing tends to increase the dielectric loss of both paper and oil, the polarization time constant tends to shift towards lower values for ageing oil-paper insulation. Likewise, moisture in the paper resulting from over-stressing and condition tends to increase the dielectric loss and decrease the polarization time constant.

If the oil-paper insulating system is wet and aged, moisture and the ageing products influence the polarization spectra, as well. This phenomenon is very important when we analyse the condition of insulation system because, as we can see, generally it is possible to distinguish the influence of the water and the ageing. Several papers, which listed in literature, show that the methods measuring the polarization spectrum are extremely useful for assessing the condition of the oil-paper insulation comparing to those classical methods, which use single measured value (as $\text{tg}\delta$ at 50 Hz) [1][2][3][4][11].

3.3. RVM as diagnostics tool for oil-paper insulation

Fig. 10 and 11 shows curves, drawn with RVM method, measured on oil-paper insulation system models, with exactly pre-set the paper moisture content, and the temperature. Fig. 10 shows the case when the oil and the paper is new, the system is homogenous, the temperature distribution is also homogenous (the temperature was 38°C). We can see that the times constant are in unambiguous relation with the moisture content of the paper: increasing water content shift the time constant to lower value.

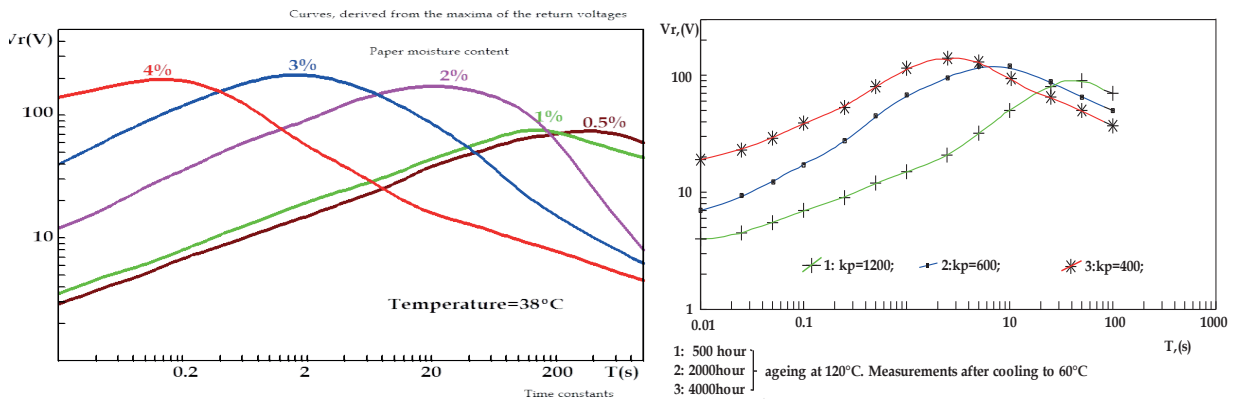


Fig. 10 and 11: Effect of moisture and ageing on the “quasi polarisation spectra” determined by the RVM

Fig. 11 shows spectra on the same oil-paper insulation model, measured on 60°C, after ageing of different time periods, at 120°C beside the determination of the polarisation spectrum with the RVM method. In each case there was also determined the depolymerisation of the paper. All other circumstances were held, or set - as far as it was possible - at, or to the same condition. It can be seen, that with the ageing the dominant time constant of the polarisation shifts - similar as with the increasing of the humidity - "forward", to the smaller values. This means, that with this method, regarding the dominant time constant, it would be theoretically better to speak of a relation to the “equivalent moisture content” of the paper, because of the fact, that the shifting of it is not only caused by H₂O, but by this, and other ageing products together.

In order to use more reliably the diagnostic techniques, it is important to summarise the most important aspects of the oil-paper insulation. The transformer life/ageing is mainly related to the degradation of the insulation, which is caused dominantly by the thermal ageing of the insulating paper, together with the decomposition of the cellulose. The moisture content, the ageing products of oil, etc. have a decisive role in the degradation rate of the cellulose, for example the higher level of humidity, temperature, acid content accelerates very strongly the degradation. Excessive water in transformers is unacceptable because it accelerates the ageing of the solid insulation, increases risk of bubble evolution, and impairs the dielectric properties of main insulation. A good insulation contains a small amount of water, which fact is important to maintain its good mechanical properties. Generally the ageing rate of insulation material is primary influenced by temperature. The water and oxygen have a significant but smaller effect. The effect of water on ageing of paper insulation is directly proportional. It is known that at 3% of moisture content in the paper the polymerization factor decreases ten times faster to its half value, with comparing if the moisture in the paper were 0,3% (dry and new paper insulation).

3.4. Interpretation of RVM results (limit values for large power transformers)

Before interpreting the RVM result we have to speak about the “safe transformer”. Considering the literature we can realise that the high temperature, the high moisture content and ageing product is dangerous for transformer. If this three parameters are high, it is risky for transformer because the inception temperature of bubbling must be far higher than the „hot spot” temperature of the transformer. It is proved that inception temperature of bubbling is water content and ageing dependent. What is the meaning of this word of „safe”? The reduced moisture and acid content allows higher reliability and overload capability (no bubbling). Until yet, the judgement of the general state of a transformer insulation could be made only by concerning the results of oil sample tests, tgδ and PD measurements. None of these can give basis for a reliable paper moisture content estimation. Thus the different operating and or production rules, standards, and recommendations could not contain regulations for the limit values for this quality determining quantity.

However now, this quantity can be in a reproducible and reliable manner easily estimated with the RVM method, with measurements made with connections at the bushings, and there has gathered meanwhile experience of thirty years of systematically made measurements on net system. So, perhaps the time is here, to recommend such limit values (Fig. 12). Fig. 12 supports the limit value for the reliable operation of MV and HV transformers. This figure shows a "spectrum" measured on a faulty 120/20 kV transformer, after an insulation breakdown. The measuring temperature was 21°C, the dominant time

constant of 0,3s refers to 5% of "equivalent moisture content" in the paper. This is the lowest dominant time constant and now not too important what is the origin (high moisture content or ageing products). Now, considering, that the dominant time constant at this moisture content, and at the operating temperature of about 60°C would be shifted forward, down to the value of 3 ms, it can be presumed, that the increased dielectric losses, and perhaps the initiated bubble and partial discharges too, had a significant role in the breakdown of the insulation.

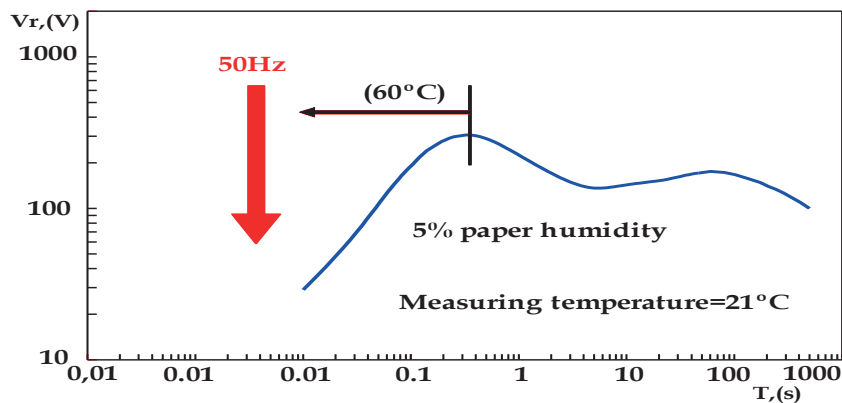


Fig. 12 Spectrum, measured on a transformer after a breakdown

Using the RVM and the "bubbling" curve [3][4][7] we will be able to determine the limit temperature at which the operation of transformer is „safe”. For the safe, reliable operation of EHV great transformers (the higher voltage is 220 kV, or higher) a limit of 2-2,5%, and for transformers of the high, and middle voltages (the higher voltage is lower than 220 kV) max. 3,5% could be a good choice, as this recommendable paper moisture content limit. At reaching, or exceeding these values should be made an on-site, or in factory drying treatment on the transformer. The "voltage dependence" of the limit values justifies the fact, which the "allowed electrical stresses" on the insulating paper are in EHV transformers generally higher, than in HV and MV transformers. For new transformers 0,5% could be a good choice for this limit value, and for the limit value after refurbishment, or drying treatment for EHV transformers 1,5%, and for HV and MV transformers 2% limit values could be recommended.

It seems that the RVM technique would be complicated but the moistening and ageing phenomena are complicated and complex and it is lucky that the RVM spectra characterise this complicated processes. If we are in possession of the fundamental database it is not too problematic to analyse these inhomogeneous systems. The RVM Expert System (RVM-ES) has been developed to determine the condition of the oil-paper insulating systems and is based on large research work.

The short recommendation for the interpretation of RVM data measured on oil-paper insulation is the following:

We have to determine the whole RVM spectrum and each time constants. We have to know the „shifting rules” of time constants determined by the temperature, the moisture content and ageing products (see the Hungarian RVM Expert System). The case of new paper/new oil we can use the „nomogram” publish in literature [1][3][4], otherwise it is recommended using the RVM Expert System based on Hungarian research work. We had to know the limits of moisture, ageing rate, bubbling temperature, then determining the limit temperature at which the operation of transformer is safe.

4. CHECKING OF EFFICIENCY OF OIL RECLAMATION WITH RVM TECHNIQUE

Some of the by-products of this degradation, mostly acids and sludge attack the chemical bonds which hold the cellulose insulation together (measured by polymerization). The main goal of the oil regeneration is to remove water and acids being formed and/or getting into the cellulose insulation from the cellulose insulation once there. Transformer oil will discolour as oxidation of the oil takes place. Colour, by itself, is not a reliable test in evaluating the condition of the oil for further use. It is a strong indication that something is happening within the transformer that requires investigation. Once transformer oil changes from the yellow colour range into the orange and red colour range, it has degraded to the point where the vital parts of the transformer are being seriously affected. As the colour of the oil changes, sludge is forming in solution with the oil due to oxidation. This causes a drop in

interfacial tension and an increase in the acid (neutralization) number. When transformer oil deteriorates to the red colour ranges, deposited sludge continues to oxidize and harden, blocking vents and insulating cooling fins, causing higher operating temperatures. Insulation shrinkage may take place, and premature failure is possible.

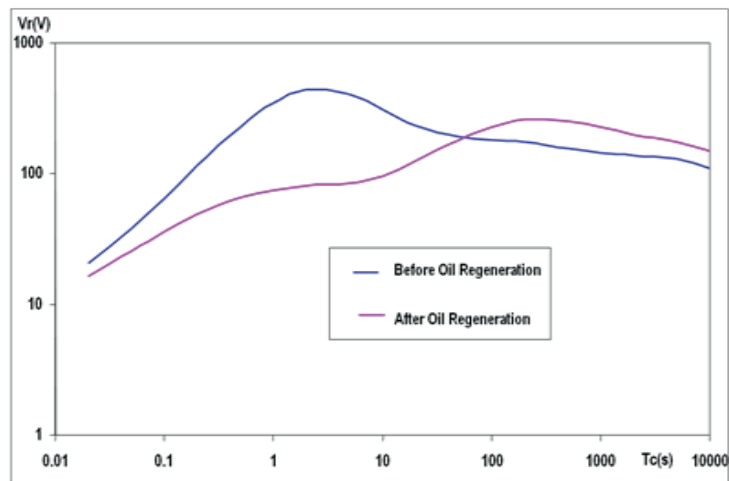


Fig. 13: RVM curves before and after the oil regeneration.

In Fig. 13 it can be seen the effectiveness of oil reclamation. The RVM curves show that the changing the polarisation spectra was important between before and after the oil regeneration, with others words, considerable quantity of ageing by-products were moved [3] [4] [11].

The case of Fig. 13 is very frequent, so it is very important the correct interpretation of RVM curves and the phenomena. In this case the transformer has the following condition: the paper insulation is medium dry and aged, the oil and the surface of the cellulose contains lots of ageing products. It is very important to recognise this condition because if the other repairing works allow us, we can repair it on-site and we will able to save lots of money. The Fig. 13 shows the influence of moisture and ageing products on RVM curves measured in real transformer (220 kV, 160 MVA, which was about 30 year old).

It can be seen that before the oil regeneration the RVM curves have at least two dominant time constants. The lower dominant time constant was mostly influenced by the ageing products, we can check this fact with using of the result of oil screen. The higher dominant time constant characterises the water content in the paper, namely the dryness of the paper insulation. At the first moment it is not too easy to observe this time constant because this part of curve is rather flat. But we can see the polarisation is very strong in the range of 100 and 1000 s. When we carried out the oil regeneration, the influence of ageing products could not totally disappear because the paper during the long service time was able adsorb lots of ageing products. The water content in the paper did not change significantly, so the time constant which characterises the moisture content of the paper remain at almost the same value. With oil regeneration, the parallel insulation resistance increased, so the peak of return voltage also increased. The polarisation which was influenced by the aging products significantly decreased, as it can be seen.

Comparing the RVM curves before and after the oil regeneration we can determine the effectiveness of oil reclamation. These RVM curves show that considerable quantities of ageing products were moved. It is very important to remark that live oil regeneration has much more benefits in comparison to replacing the oil in the transformer or just filtering the oil. Firstly, by doing it on energised transformer, from the consumer's perspective, they will not face any load shedding or supply disruption. Secondly, from the transformer's perspective, apart from reclaiming or regenerating the oil to its original condition, the transformer is also removed of sludge and other impurities from its windings. This is possible as the oil is circulated a number of times through the transformer and the process is only stopped when the oil condition at the bottom of the transformer has reached the acceptable condition and the transformer is rid of sludge, moisture and impurities. The total volume of oil is re-circulated a number of times thorough the regeneration plant and "flushing effect" of a transformer is achieved. In the case of oil change relatively lots of ageing products remain between the paper layers. Regeneration is the complete treatment of oil to like new condition.

Oil regeneration "in a transformer" is far more efficient than simple oil change. It is obvious that regeneration as a complete oil treatment method is the best technical solution to aged transformer oil. Apart from this it is also highly cost effective in comparison to an old procedure of oil change. Using the RVM technique we can check the efficiency the oil reclamation. RVM characterises the condition of the insulation with a spectrum. The traditional methods use a single parameter to characterise the condition. The RVM method is able to distinguish the changing when we remove the ageing products from the oil or from the whole solid insulation system. When we use the RVM method we measure the composite oil-paper insulation. The polarisation response influenced by the interface forming the oil and macro molecules of paper. There is big difference between the RVM spectrum if we remove the ageing product from the oil or we remove the ageing products from the layers of the paper insulation, too (oil regeneration has a flushing effect). Very important remark: the life of the transformer is determined by the life of the paper, oil regeneration is effective if we remove the acid compounds from oils and from the paper layers, too. RVM is very efficient tool to check the condition of paper after regeneration.

5. CONCLUSION

The RVM is a very good tool for getting information of insulating paper in oil - paper insulation systems. For transformers this method is applicable as an acceptance test, as a test which approves that the transport, eventually the storage, and the installation was made properly, as a periodical test, for aiding the decision whether and which transformer needs a refurbishment, a drying process on site, and last but not least, with this method the effectiveness of these renewing operations can be tested. It is also proved that the RVM provides much more information than the classical dielectric methods (insulation resistance, $\text{tg}\delta$ at power frequency, etc.) but in lack of the real guide line there are some misunderstanding using this method. This paper would like to show some selected case stories to improve the interpretation of results measured with RVM technique. The several thousand of Hungarian experimental and on-site measurements have showed that there is good correlation among the dielectric condition, the equivalent circuit and the measured results. Considering the Hungarian database these methods are useful for evaluating the uniformity of aging and/or moisture distribution and allow observation of progress of ageing moistening processes.

REFERENCES

- [1] G. Csépes, Dr. G. Woynárowich, J. Schmidt: "Dielectric Response Methods for Diagnostics of Power Transformers - Hungarian Research Work in the mid-1970s", Paper D1-242, Cigre SC D1 – Colloquium in Hungary Budapest, 2009.
- [2] Bognár, A. - Csépes, G. - Németh, E. - Schmidt, J. – "Diagnostic tests of high voltage oil-paper insulating systems (in particular transformer insulation) using DC dielectrometrics", (Proc. of the 1990 CIGRE Conference, Paris France, paper 15/33-08, 1990.
- [3] B. Németh, G Csépes, Cs. Vörös: "Applicability of RVM, FDS and PDC techniques in corrosive sulphur diagnostics", CIGRE Session 2012, D1-302, Paris
- [4] Vörös Cs., Németh B., Csépes G., Berta I.: "Investigation of complex, in-homogenous insulation system with multiple time constant by recovery voltage measurement (RVM)". IEEE EIC 2013. Ottawa, Canada, 2013. 06. 02-2013. 06. 05. Paper 173. ISBN: 978-1-4673-4739-6
- [5] CIGRE Technical Brochure 254, "Dielectric response methods for Power Transformers", TF D1.01.09 (conv. S.Gubanski), Paris, 2004
- [6] S.M. Gubanski, Chair, J. Blennow, B. Holmgren, Koch, A. Kuechler, R. Kutzner, J. Lapworth, D. Linhjell, S. Tenbohlen, P. Werelius, "Dielectric Response Diagnoses for Transformer Windings", Electra, No. 249, 2010, pp 65-71; also in CIGRE Technical Brochure, No. 414, Paris 2010.
- [7] M. Koch, S. Tenbohlen, "Systematic Investigations on the Evolution of Water Vapour Bubbles in Oil - Paper Insulations", Proceedings of the XVth International Symposium on High Voltage Engineering, ISH, Ljubljana, Slovenia, 2007
- [8] CIGRE Technical Brochure 323, "Ageing cellulose in mineral oil insulated transformer", TF D1.01.109, Paris, 2007
- [9] CIGRE Technical Brochure 413, „Insulating Oil Reclamation and Dechlorination”, WG D1.01 (TF 12), Paris, 2010

- [10] CIGRE Technical Brochure 349, "Moisture equilibrium and moisture migration within transformer insulation systems", WG A2.30, Paris, 2008
- [11] G. Csepes et al.: "On-site transformer oil reclaiming (Hungarian and Slovakian Experiences)", International Colloquium Transformer Research and Asset Management, Dubrovnik, Croatia, May 16-18, 2012

Veronika Haramija
KONČAR – Electrical Engineering Institute Inc.
veronika@koncar-institut.hr

Vedran Đurina
KONČAR – Electrical Engineering Institute Inc.
vdjurina@koncar-institut.hr

Dijana Vrsaljko
KONČAR – Electrical Engineering Institute Inc.
dvsaljko@koncar-institut.hr

Domagoj Vrsaljko
University of Zagreb, Faculty Of Chemical
Engineering And Technology
dvsal@fkit.hr

THERMAL STABILITY CHANGE OF SYNTHETIC ESTER-BASED TRANSFORMER OIL

SUMMARY

For good transformer condition assessment it is necessary to determine the condition of insulating materials, both liquid and solid. Transformer is reliable for as long as its insulation system resists deterioration. Therefore, thermal and oxidation stability are important characteristics of transformer oil. It is a measure of oil resistance for decomposition by the influence of oxygen and temperature. Oils with good thermal and oxidation stability retain their characteristics regardless the thermal stress.

Because of environmental and safety issues, the use of synthetic ester-based transformer oils is increasing. Although they have been in use in smaller transformers (distributive, traction, ...) for decades, limit values for chemical and physical characteristics are still discussed. New methods for thermal stability evaluation can be useful for insulation condition assessment.

Key words: transformer oil, synthetic ester, ageing, thermal properties, TGA, DSC

1. INTRODUCTION

Physical and chemical testings of transformer oil have proven to be worthy tools for transformer condition monitoring and evaluation. Degradation products soluble in oil are formed and analysis of liquid insulation is a convenient method for transformer condition assessment. Representative oil sample can provide information about degradation of oil itself, cellulose insulation and construction materials, as well as information about thermal and electrical processes in transformer. Decades of laboratory analysis and information gathering have resulted in recommended values for oil characteristics for normal condition of new and transformers in service, and typical concentrations of degradation products dissolved in oil (characteristic gases and furanic compounds). More important, chemical processes of mineral oil degradation are known so obtained values can be explained and understood.

Mineral oil has been used as an insulating liquid in transformers since the very beginning of oil immersed transformers. It fulfils the requirements for electrical and thermal insulation, and in normal operating conditions its characteristics can remain long-term acceptable.

Besides the fact that its availability has become questionable and thus the price can vary depending on circumstances, there are more situations where use of mineral oil is not preferable.

Environment protection and fire safety are rising up as crucial topics in expanding use of transformers. Densely populated and environmentally sensitive areas, offshore wind farms, underground

facilities, are some of the situations where use of mineral oil is not suitable. Oil leakage or transformer explosion and oil combustion are serious threats to environment and safety. Mineral oil has great impact on water systems because it blocks oxygen delivery from the atmosphere. With flash and fire point around 140 °C and 160 °C respectively, mineral transformer oil is easily ignited and when on fire produce toxic dense smoke.

For many years, alternative insulating liquids have been used, mainly in traction and distributive transformers. Synthetic esters have been used in distributive transformers (for voltages up to 66 kV) over 30 years, and in the last 10 years there has been an increasing demand for transformers up to 238 kV filled with esters [1].

Due to differences in physical and chemical characteristics between mineral and synthetic ester-based transformer oil, there must be significant change in calculation and construction of power transformers. For that reason start properties and changes during normal and irregular operation must be known. Besides that, transformer condition assessment is not complete without chemical and physical testing of insulating liquid.

Typical values needed for evaluation of ester filled transformer condition are not set. There is no standardized interpretation of DGA, known behaviour after years of operating conditions or methods for estimation of oxidation period. Various laboratory tests are conducted and useful information is gathered. But it will take some time to confirm laboratory values with in-service data.

Possibility of rapid evaluation of synthetic ester-based transformer oil was investigated [2]. Samples of synthetic ester-based transformer oil have been exposed to thermal ageing in closed vessels at 120°C and 150 °C for the period of 168, 336, 504 and 672 hours. Along with methods that show obvious changes of synthetic ester-based transformer oil properties (dielectric dissipation factor and color change), differential scanning calorimetry (DSC) and thermogravimetry (TGA) were used. DSC is widely used as an analytical, research and diagnostic tool from which relevant information, such as oxidation onset temperature (OOT) can be obtained. Decomposition kinetics can be determined by thermogravimetry (TGA), a technique in which the mass of a sample is measured as a function of temperature whilst subjected to a controlled temperature program [3]. Obtained curves are called thermograms, they show the sample mass dependence on temperature, and provide information about physical phenomena, such as vaporization, sublimation, absorption, adsorption and desorption, and about chemical phenomena, such as chemisorptions, desolvation and decomposition. Water content was determined for better understanding of decomposition reactions.

2. THERMAL STABILTY CHANGE

One of the most important characteristics of transformer oil is its thermal stability. Thermal stability of transformer oil prevents unacceptable changes of viscosity during the transformer operation at elevated temperatures. Synthetic ester-based transformer oils have superior thermal stability due to exceptional chemical stability of ester bonds [4].

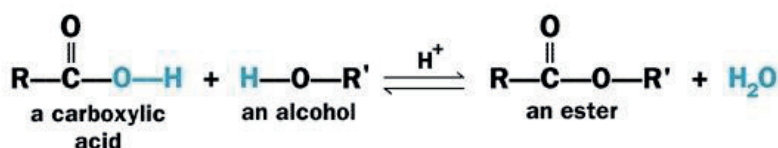


Figure 1 - Esterification reaction (R, R' are saturated hydrocarbon chains)

Synthetic esters are organic compounds formed during an esterification reaction between polyvalent alcohols and fatty acids (Figure 1). The ester linkage, bond between a hydroxyl group (-OH) and a carboxyl group (-COOH), is exceptionally stable, bond energy is more stable than the C-C bond. The absence of hydrogen atom (replaced by alkyl groups) on the β-carbon (second carbon atom to carboxyl group) of the alcohol portion of an ester leads to superior thermal stability. Decomposition occurs by a free radical mechanism which requires more energy and can occur only at higher temperatures [4].

Decomposition mechanism of ester consists of initiation, propagation and termination, but intermediates depend on oxygen presence [5]. Differences in decomposition reactions depending on oxygen presence are presented in Table I.

In presence of oxygen, initiation step gives alkyl (R•) and peroxy (HO₂•) radicals and hydrogen peroxide (H₂O₂). Unstable radicals react with each other, with oxygen and other molecules and propagation reactions give alkyl and peroxy radicals differentiated in length from initiation products. Unstable molecules react with each other forming stable molecules and terminating reaction.

In absence of oxygen, alkyl (R•) and hydrogen (H) radicals are formed in initiation step, followed by the formation of extended molecules (R₂, R₃, ...). Reactions are terminated by stable molecules formation [5].

Table I - Ester decomposition reaction steps at elevated temperature

Reaction steps	Reaction conditions	
	Oxygen present	Oxygen not present
Initiation	$RH + O_2 \rightarrow R\cdot + HOO\cdot$ $RH + RH \rightarrow 2R\cdot + H_2O_2$	$RH \rightarrow R\cdot + H\cdot$
Propagation	$R\cdot + O_2 \rightarrow ROO\cdot$ $ROO\cdot + R^2H \rightarrow ROOH + R^2\cdot$	$R\cdot + R^2H \rightarrow RH + R^2\cdot$
Termination	$ROO\cdot + ROO\cdot \rightarrow ROOR + O_2$ $R\cdot + R\cdot \rightarrow R-R$	$R\cdot + R\cdot \rightarrow R-R$

Esters of pentaerythritol and terephthalic acid (polyol esters) are widely used as insulating oils. They oxidise very slowly, at temperatures above 125°C, and darken as they do [6].

Thermal degradation of polyol ester in air is mainly due to oxidation which causes chain scission and the formation of radicals. The peroxy radical reacts with polyol ester, producing intermediate ROOH. The intermediate then decomposes to ROOR' peroxide, R"OOH peroxide and aldehyde, which decompose to form small molecules such as water or carbon dioxide. Unstable radicals also can link molecules, form large colloidal compounds (sludge) which increase viscosity [5]. The most important influence of free radicals on insulating liquids is the fact that molecules can capture their free electrons and form ions. The accumulation of ionized molecules increases the dissipation factor of oil-paper insulation [7].

3. EXPERIMENTAL SETUP

Samples of synthetic ester-based transformer oil were exposed to thermal ageing in closed vessels at 120 °C and 150°C for the period of 168, 336, 504 and 672 hours. Virgin transformer oil and aged samples were characterized.

The released heat from oxidation reactions can be measured using DSC in either isothermal or non-isothermal mode. For DSC oxidation measurements, the heat flux from the oxidized oil is compared to the heat flux from an inert reference (empty pan) both heated at the same rate. When the oxidation of the sample occurs, the recorded heat shows a peak whose area is proportional to the amount of heat released by the sample. The heat released by the oxidized oil is recorded as the heat flow signal (y-axis) as a function of temperature (x-axis) [4]. Results (oxidation onset temperature, OOT) were obtained both in an open aluminum pan and a sealed pan with a pinhole, with a heating rate of 10 °C/ min.

Thermogravimetric analyzer quantifies mass change as a function of time and temperature. It consists of a microbalance and a well regulated furnace. The test consists of precise weight loss measuring of the oil sample (initial mass 10 g) during the exposure to temperatures from 25 °C up to 625 °C with a heating rate of 10 °C/ min.

As the indicators of thermal degradation, water content, viscosity, color change and dielectric dissipation factor were determined.

Water content was determined by automatic coulometric Karl Fisher titration. The sample is mixed with a base/alcohol solution of iodide ion and sulphur dioxide. Iodine is generated electrolytically and reacts with water. Iodine is generated in proportion to quantity of electricity and the amount of water is determined directly from the quantity of electricity required for the electrolysis [8].

Dielectric dissipation factor is a measure of the dielectric losses in an electrical insulating liquid when used in an alternating electric field and of the energy dissipated as heat. A low dissipation factor indicates low AC dielectric losses. Dielectric dissipation factor of oil may be useful as a means of quality control, and as an indication of changes in quality resulting from contamination and deterioration in service or as a result of handling [9]. Higher dielectric dissipation factor indicates the presence of moisture and contaminating agents.

4. RESULTS

Oxidation onset temperatures (OOT) of virgin oil and aged samples were determined by DSC. Results are shown on Figure 2. There is no significant difference between measurements in open and sealed pan. Oxidation onset temperatures of samples exposed to 120 °C are increasing, while for samples exposed to 150 °C are decreasing with ageing duration.

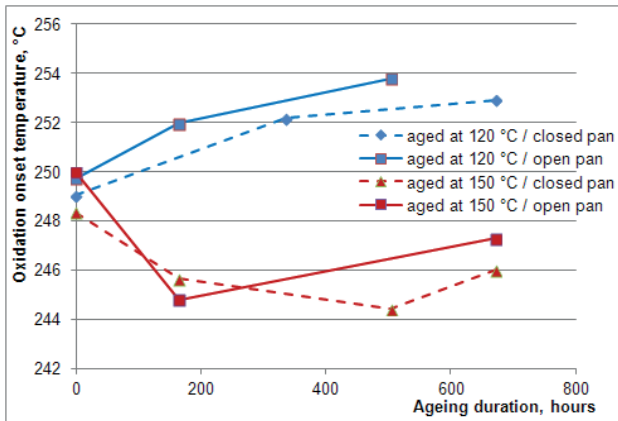


Figure 2 - Oxidation onset temperatures of aged samples;

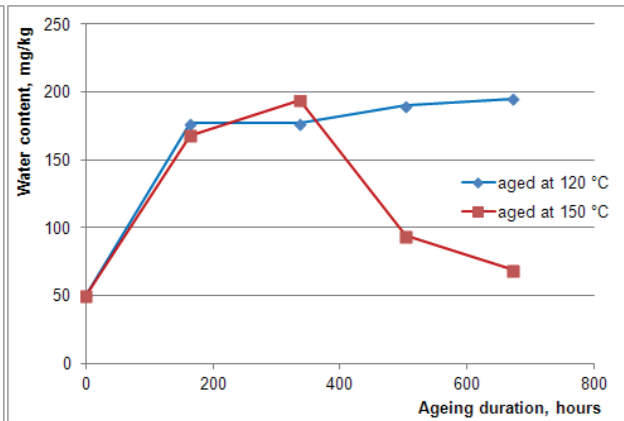


Figure 3 - Water content of aged samples

Obvious differences in oxidation onset temperature (increase and decrease after ageing at different temperatures) indicate the difference in degradation mechanism. It must be investigated if compounds that contribute to better thermal stability of synthetic ester are formed at higher temperatures. Water content of aged samples (Figure 3) confirms differences in degradation mechanism at different temperatures.

Thermograms of tested oil samples (aged at temperatures of 120 °C and 150 °C for up to 672 hours) are presented on Figure 4. All samples have lost about 5% of initial mass at the temperatures from 245 to 255 °C. For samples aged at 120 °C noticeable weight loss begins rapidly above 200 °C, while for samples aged at 150 °C weight loss is slower but begins around 160 °C.

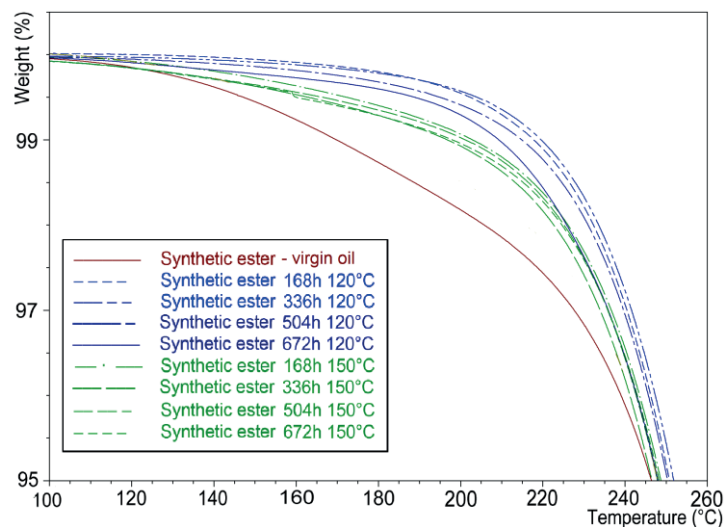


Figure 4 - Thermograms of virgin oil and aged samples

As expected, thermograms show a better thermal stability for samples aged at 120 °C than for those aged at 150 °C. Surprisingly, the fastest weight loss is measured on virgin oil. It can be assumed that water present in virgin oil evaporates during thermogravimetric analysis and causes rapid weight loss, while in aged samples it evaporates earlier, during laboratory ageing.

Comparison of aged samples weight loss at 200 °C and 220 °C is presented on Figure 5. As observed on Figure 4, samples aged at 120 °C, both at 200 °C and 220 °C, show greater difference than samples aged at 150 °C. Ageing must be extended to see whether samples aged at 150 °C show rapid weight loss.

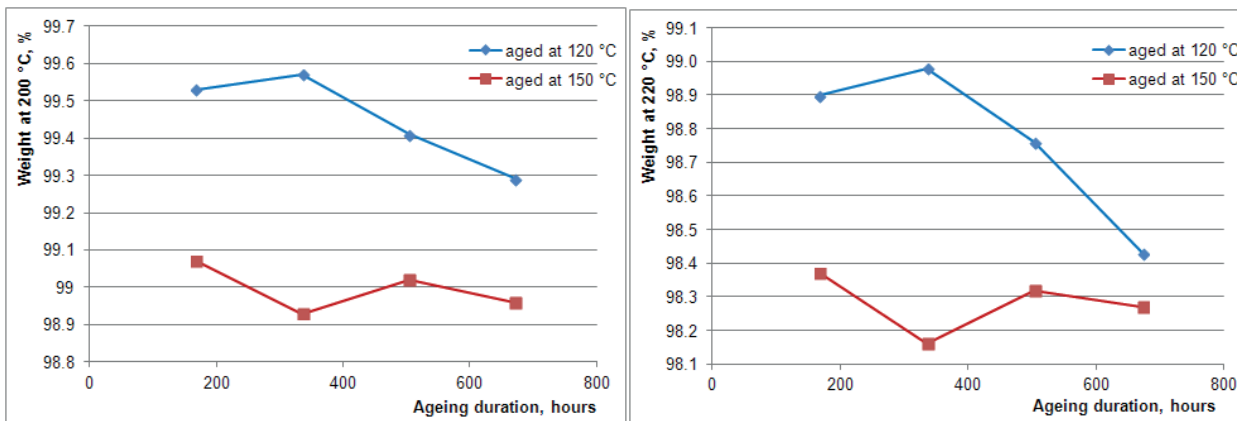


Figure 5 - Weight change at 200 °C and 220 °C of aged samples

Differences in degradation mechanism are obvious in colour change and increase of dielectric dissipation factor (Figure 6).

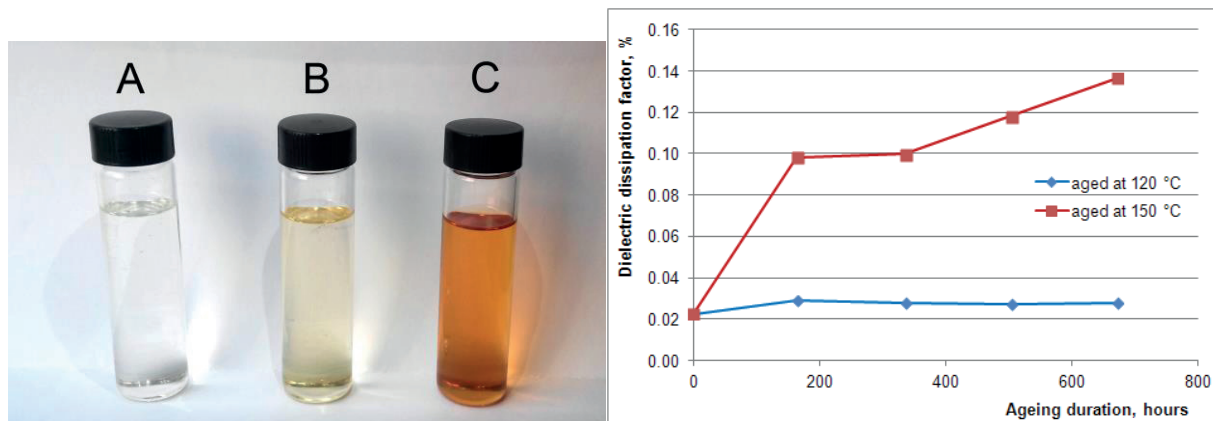


Figure 6 - colour change of virgin oil (A) after 672 hours of thermal ageing at 120 °C (B) and 150 °C (C); change of dielectric dissipation factor during laboratory ageing at 120 °C and 150 °C

There was no change in kinematic viscosity measured at 20 °C and 40 °C for virgin and aged oil (Table II). Since there is increase of the dissipation factor of oil samples aged at 150 °C, accumulation of ionized molecules occurred but unstable radicals did not form large colloidal compounds (sludge) which increase viscosity.

Table II – Kinematic viscosity measurements

Sample	Kinematic Viscosity (mm ² /s)		
	Ageing process	20 °C	40 °C
virgin oil	-	70	28
1	672 hours at 120 °C	72	28
2	672 hours at 150 °C	72	28

5. CONCLUSION

Environmentally friendly synthetic ester-based insulating liquid was aged at 120 °C and 150 °C in presence of air for 672 hours. Differential scanning calorimetry and thermogravimetric analysis were performed on virgin oil and aged samples, as well as kinematic viscosity and dielectric dissipation factor measurements, colour observations and water content determination.

Differences in oxidation onset temperature indicate different thermal ageing process kinetics at different temperatures. Oxidation onset temperatures of samples exposed to 120 °C are increasing, while for samples exposed to 150 °C are decreasing with ageing duration. Change in thermal stability of aged samples shows some regularity considering duration of ageing: samples tested after 168 hours of temperature exposure (both 120 °C and 150 °C) have better thermal stability than samples tested after 672 hours. What is not expected is that virgin oil has poorest thermal stability and the causes require further investigation. It must be determined if it is due to higher low molecular weight components content or some oxidation products or reactions contribute to better thermal stability of aged samples. Water content of aged samples confirms differences in degradation mechanism at different temperatures. Increase of dielectric dissipation factor indicates accumulation of ionized or polar molecules. However, molecules of high molecular weight, as final degradation products, are not formed in quantities sufficient to form sludge and influence kinematic viscosity.

Differential scanning calorimetry and thermogravimetric analysis have proven to be useful methods in oxidation process monitoring of synthetic esters. Additional measurements after prolonged ageing of oil samples must be performed for more knowledge of synthetic ester-based transformer oil terminal deterioration.

REFERENCES

- [1] Russel, M. Lashbrook, S. Nitin, "Synthetic esters for power transformers at >100 kV", ITMA Journal, july-august 2013
- [2] V. Haramija, D. Vrsaljko, V. Đurina, D. Vrsaljko, "Thermal Properties of Synthetic Ester-based Transformer Oil During Ageing in Laboratory Conditions", ICDL 2014: 18th IEEE International Conference on Dielectric Liquids 2014, Bled, Slovenia, June/ July 2014
- [3] R. C. Mackenzie, "Nomenclature in thermal analysis: Part IV. ", J. Thermal Anal., vol. 13, no. 2, 1978, pp. 387-392.
- [4] M. Mortier, M. F. Fox, S. T. Orszulik, (eds.), "Chemistry and technology of lubricants", Springer Science+Business Media B.V., 2010
- [5] Y. Aoyagi, "Carbon and related materials for thermal and electrical applications", ProQuest, UMI Dissertation Publishing, 2011
- [6] "Experiences in service with new insulating liquids", Cigre Working Group A2-35, 2010
- [7] I. Fofana, A. Bouaicha, M. Farzaneh, J. Sabau, "Ageing Behaviour of Mineral Oil and Ester Liquids: a Comparative Study", Annual Report Conference on Electrical Insulation Dielectric Phenomena, Quebec, QC, October 2008, pp. 87 - 90
- [8] IEC 60814 Insulating liquids – Oil-impregnated paper and pressboard – Determination of water by automatic coulometric Karl Fisher titration, August 1997
- [9] ASTM D924 Standard Test Method for Dissipation Factor (or Power Factor) and Relative Permittivity (Dielectric Constant) of Electrical Insulating Liquids, 2008

David Bidwell
Qualitrol Corporation
dbidwell@qualitrolcorp.com

Donal Skelly
Qualitrol Corporation
dskelly@qualitrolcorp.com

NEW TOOLS FOR ENHANCED DIAGNOSTICS OF DGA DATA

SUMMARY

In the last decade there has been a significant change in the way transformers are viewed. Their importance together with their obvious value to the network has been enhanced and recognized, especially in light of the ageing fleet worldwide. At the other end of the spectrum, new transformers are now being designed and built to tighter tolerances as a result of competitive market conditions, with the knock-on effect that these “modern” devices do not appear to provide the same stability and longevity as those that were entering service in the 1970s and 1980s.

Against this backdrop, the advent of transformer monitoring has emerged and continues to develop at a rapid pace. Although still considered an emerging component of asset management practice, online DGA is rapidly gaining acceptance and recognition as one of the most powerful tools in protection against asset failures. While other transformer monitoring technologies abound, many of them now online, such as partial discharge, these products collectively combine to enable the move to condition based monitoring of transformer assets.

As online DGA monitors have evolved new products and technologies are reaching the market at an ever increasing rate. However, the quiet revolution is in the analysis of the data. As more and more monitors are installed, so the burden of data analysis becomes increasingly large. New ways of extracting value from this data required. One important approach is the use of Artificial Neural Networks (ANN) for DGA data analysis. Additionally, with the recognition that data from monitors must be easily transferred into meaningful information for the end-user, diagnostic tools, such as the Duval Triangle, have evolved where the addition of Triangles 4 and 5 brings significantly more value to previously mined data.

The mute question in this paper relates to whether or not existing online monitoring hardware has sufficient accuracy and repeatability of measurement to be of use with these more advanced diagnostic tools.

Key words: DGA, Online Monitoring, TOAN, Duval Triangles, Artificial Neural Networks

1. INTRODUCTION

1.1. A Brief History on Online DGA

Prior to the emergence of online DGA monitoring, the traditional technique, still widely used today, is manual oil sampling and laboratory DGA. It is subject to a wide range of quality control measures, laid out in standards, which define procedures for obtaining and analysing an oil sample. A manual oil sample extraction would typically occur every 6 or 12 months depending on the critical nature of the transformer. Weekly sampling is a requirement under certain imminent fault conditions. The manual sample is used for other parameters associated within transformers, however, the DGA inaccuracy is well documented elsewhere and so renders the data useful for trending only.

The market conditions that have driven the evolution of online DGA relate, to a large extent in the changing structure of the electricity supply industry – liberalised and privatised markets. Many specialists with deep subject matter expertise in the area of transformers were retiring or leaving the industry as a consequence. While this has raised the number of consultants, it also left those remaining with a general lack of expertise coincident with assets which were getting older and more prone to failure.

The earliest online DGA monitors can be traced back to around 1990 – these single-gas monitors were primarily sensitive to hydrogen in oil. Some of these devices showed some cross sensitivity to other gases, meaning that the user did not always have a clear picture of the nature of the gas been reported. There were issues with measuring hydrogen. Hydrogen is the most insoluble of all the gases-in-oil, and as such has a propensity to escape from the oil. Further, hydrogen can be created in fairly large quantities due to heating within the transformer, where no fault has occurred - known as stray gassing, and can also be created in large quantities due to galvanic interaction [1]. So, by itself, the measurement of hydrogen only provides alarms related to possible fault conditions within the transformer.

The early part of this century saw the introduction of multi-gas online DGA devices as a means of determining the health of the transformer asset both in terms of discreet gas measurement, the trending of gases and most importantly the ability to diagnose a developing fault in real time. At this time IEC and IEEE call for 7 specific diagnostic gases to be measured as incipient fault gases. These gases are: Carbon Monoxide (CO), Carbon Dioxide (CO₂), Hydrogen (H₂), Methane (CH₄), Ethane (C₂H₆), Ethylene (C₂H₄) and Acetylene (C₂H₂). No specific specifications have so far emerged in support of required measurement technologies, required accuracies, repeatability or frequency of sampling although both standards do allude to performance levels best suited. While Gas Chromatography is the default technology for performing DGA in the laboratory and has been successfully employed for online monitoring, several manufacturers have chosen alternative approaches for example Infrared Spectroscopy. While Infra-red technology is employed successfully for trending in many locations one possible issue of concern is that infra-red systems may not align to laboratories with a reasonable level of confidence. Gas chromatography has the ability and requirement to field calibrate providing for a more obvious possibility of alignment to the laboratory based analysis. It can also be argued that these technologies do not provide as good a job of discriminating gases from each other as gas chromatography can.

As the market for online DGA gains market penetration, novel solid state sensors and other high-tech technologies are now emerging. It remains to be seen if any of these newer technologies will evolve to offer a higher accuracy/cost relationship than exists at present. However, with the industry moving towards conditioned based monitoring, the emphasis in real customer value resides more with interpretation of data.

2. ENHANCED DIAGNOSTICS

2.1. Artificial Neural Networks

Artificial neural networks are a computational model based on the structure of the human brain and have been used for over 50 years in weather and stock forecasting as well as process controls. ANNs are excellent classifiers for use in pattern recognition tasks where the relationship between input and output is complex and so are well suited to “big data” analytical problems. This is so with the large volumes of data in the form of alarms, frequency of analysis, and ppm changes of multiple gases reported by online DGA monitors. ANNs are taught the particular process they are analysing through a database of examples. The artificial neural network will incrementally change its internal connections between its ‘neurons’ based on previous ‘experience’. Provided the database that the artificial neural networks has been taught is sufficiently representative, then they will be able to correctly classify new unseen data from previous experience [2].

Used as part of an Expert System, an ANN is made up of a network of nodes and weighted connections. Each node sums the input from several weighted connections and applies a transfer function. The resulting value at each node is then propagated to nodes through outgoing weighted connections. These nodes are arranged in layers – the input nodes receive supplied data and each succeeding layer receiving weighted outputs from the preceding layer as it’s input. The first and last layers are called the input and output layers. Between these is the hidden layer or layers. So, the ANN learns through adjustments to the connection weights based on the error found at the output of the network. During the learning phase each set of data presented to the ANN includes known outputs and inputs and the generated output can be

compared to the expected output. The weights are adjusted backwards (back propagated) through the ANN network until the error is minimized for a specific set of data [2].

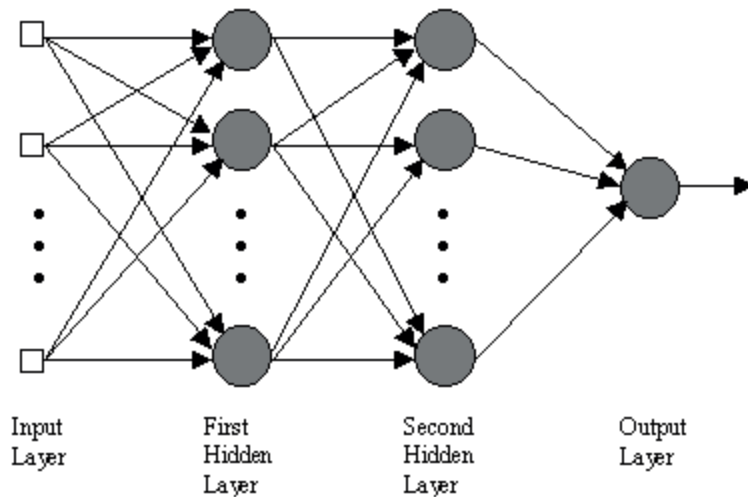


Fig. 1 –Example of an Artificial Neural Network structure

The example presented here of the use of an ANN used by Arizona Public Service (APS) company. It is a component as they of their Transformer Oil Analysis and Notification (TOAN) expert system where multiple ANNs are used.

The development of TOAN stemmed from the fact that APS has over 170 Serveron 8-gas on-line monitors on their system. Each monitor was sampling the transformer oil every 4 hours and reporting data on individual gas concentrations for Carbon Monoxide (CO), Carbon Dioxide (CO₂), Hydrogen (H₂), Methane (CH₄), Ethane (C₂H₆), Ethylene(C₂H₄), Acetylene(C₂H₂), Oxygen(O₂). Clearly the volume of data obtained from these monitors was huge, at over 350,000 samples annually with most of the data being repetitive. APS considered that what they needed was to develop or acquire an analysis engine employing highly accurate algorithms that would also allow them to incorporate an exception based reporting system. This would serve to alert on fault type and severity levels and not alarm again until these values got progressively worse. Their research into ANNs took them to some studies done in a dissertation by Zhenyuan Wang at Virginia Polytechnic (VT). Wang had developed an analysis system using ANNs, running in parallel with a rules based expert system and referred to as ANNEPS [4]. They had attempted to use traditional diagnostic tools such as seen below in Table 1. with the following success rates had being reported:

Table 1 – Conventional Fault Type Prediction.

Diagnostic Method	Success %	Error %	Not identifiable %
Doenberg Ratio	22.9	65.2	11.9
Rogers Ratio	24.8	12.4	62.8
IEC 599	42.8	24.8	32.4

Following training on a database of transformer failure autopsies testing of the ANNEPS engine showed the following success in recognizing five different fault types. These were Overheating (OH), Overheating oil (OHO), Low energy discharge or arcing (LED), High energy discharge or Arcing(HEDA) and Cellulose Decomposition(CD).

Table 2. Testing accuracy of ANNEPS

Fault Type	Success
OH	99%
OHO	98.6%
LED	98.6%
HEDA	98.6%
CD	97.6%

The initial observations were that the ANN represented the significant improvement in accuracy that APS were looking and this served as the basis for the TOAN project. There were modifications to the ANNEPS which APS implemented to improve its accuracy and flexibility. These included adaptation of the ANN to suit internal policy, a modification to the fuzzy logic models used to finalise maintenance recommendations, a change to 4 fault types: (Overheating (OH), Low energy discharge (LED), High energy discharge or arcing (HEDA) and Cellulose degradation (CD) and incorporating 6 levels of severity [6]. Added to that was a notification engine and also the incorporation of improved algorithms such as Piecewise Linear Approximation (PLA) and harmonic regression [7]. These stabilized gassing rate measurements by eliminating the harmonic effects, of time, temperate and transformer loading on gas generation. Harmonic regression is also able to provide better predictions, with a degree of certainty, on the values of dissolved gases. Later research by APS on the capabilities of TOAN revealed that these algorithms, when applied to CO and CO₂ gas concentrations show an excellent correlation to the degree of polymerisation to the point where online DGA data could be used to determine insulation ageing [4].

The key to TOANs success rate in diagnosing faults lies in both the power of the ANN and also the database used to train the system. This database is laboratory GC based and as such it was natural that the Serveron gas chromatography systems would be the optimum technology to feed in to this system. Any other non-chromatography online monitors would require some type of alignment to the TOAN database with a resulting level of uncertainty been introduced into the diagnosis. Given that all historical laboratory DGA results are gas chromatography based this is likely to be a continuing issue for the newer technologies

It is worth pointing out, and perfectly illustrates the achievement that is TOAN that its chief architect Don Lamontagne (and APS CEO Donald Branch) accepted the prestigious Edison Electric Institute Award in 2008 on behalf of APS for his team's work on TOAN.

2.2. Duval Triangle

Dr Michel Duval, a senior researcher at Hydro Quebec's Institute of Research is well known for his Duval Triangle. His research into DGA results stem from personal detailed investigations of over 200 transformer failures and autopsies. The Initial Duval Triangle was developed empirically; the fault zones in the Triangle are based on observed failures matched to laboratory gas chromatography based DGA data [5]. Duval identified that DGA data from just three gases could be mapped to a coordinate within a triangle and that this DGA data correctly matched the root cause of these failures to a very high success rate. The three gases are Methane (CH₄), Ethylene (C₂H₄) and Acetylene (C₂H₂) – as a rough estimate Methane begins to accumulate at about 150° C, Ethylene at around 350° C and Acetylene at around 700° C. The calculation is based on plotting the relative percentages of each of the three gases on a scale of 0-100%. Additionally the Triangle is divided into 6 zones which are defined in Fig. 2. These zones define certain fault conditions

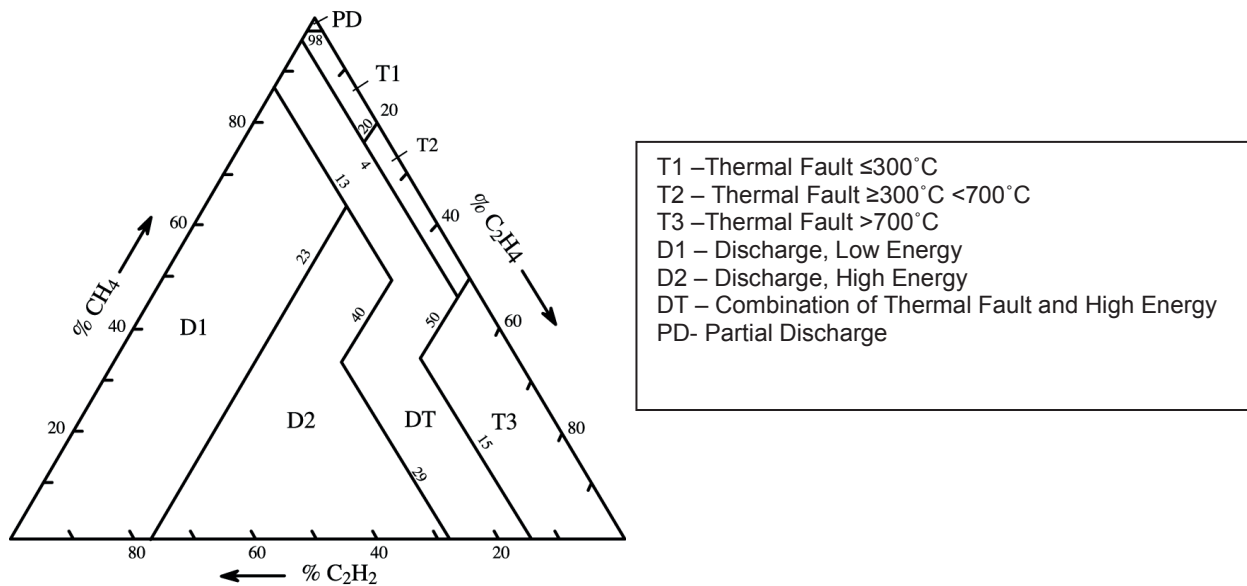


Fig. 2 Duval Triangle 1

As described by Dr. Duval T1, 2 and 3 define thermal faults in different temperature ranges [5]. T1 is for thermal faults of < 300°C normally due to overloading, blocked oil ducts or insufficient cooling evidenced by paper turning brown at around 200°C or perhaps carbonised at around 300°C. T2 is for thermal faults between 300°C and less than 700°C and generally associated with defective contacts, defective welds and circulating currents – evidenced by carbonisation of paper and formation of carbon particles in the oil. Finally T3 is for thermal faults in excess of 700°C and is exemplified by large circulating currents in oil in the tank and core and evidenced by carbon particles in the oil, metal discolouration(at 800°C) and possible fusion of metal at over 1000°C.

PD is a partial discharge of the corona type and may show discharge in gas bubbles or voids trapped in paper. It is generally evidenced by poor drying and poor oil impregnation.

D1 is for low energy discharge induced by PD of the sparking type inducing carbonized penetration in in paper and evidenced by low energy arcing inducing surface tracking of paper and particles in oil.

D2 defines discharge of the high energy variety and is evidenced by high energy arcing and flashover. This results is extensive damage to paper, large formation of carbonised particles in oil, possible metal fusion and tripping of equipment and alarms.

Faults in paper are considered more dangerous than those in oil because the paper is normally found in the HV area(windings, barriers) and is irreversible.

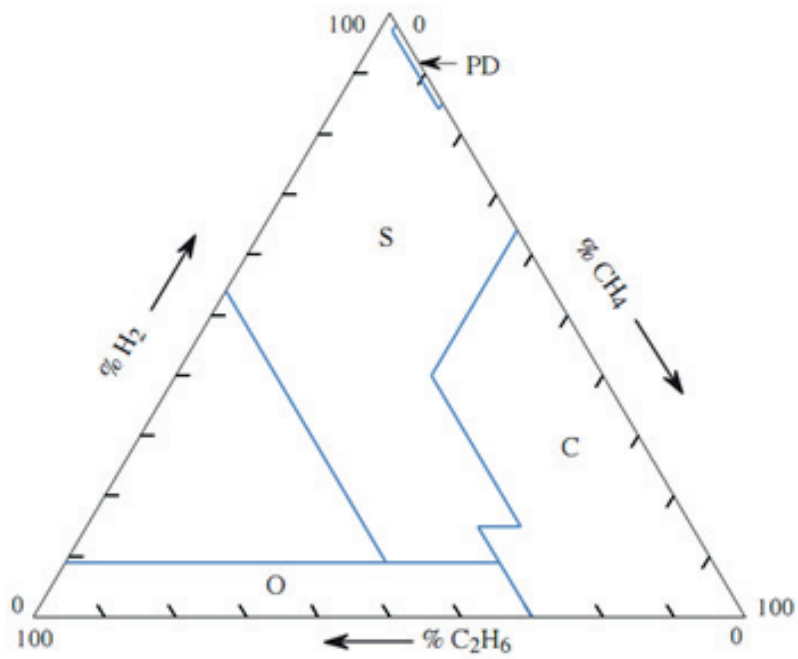
In 2008 Dr.Duval proposed an enhanced version of the traditional triangle with the introduction of 4 more triangles that further refined the ability of DGA to accurately identify a wide range of faults. Based on the same laboratory gas chromatography DGA results used to develop Triangle 1, Dr.Duval presented the following triangles:

- Triangle 2 for oil type Load Tap Changer
- Triangle 3 for Non-Mineral Oils
- Triangle 4 and 5 for low temperature faults in transformers

Considering Triangle 4 and 5, this is essentially an enhancement to the traditional Triangle 1 method. Dr Duval states that Triangle 1 is most useful for determination of a general type of fault occurring in a transformer, as described earlier. However limitations in Triangle 1 related to results being close to boundary conditions and the result of stray gassing which leads to some uncertainty. This uncertainty is removed with the inclusion of Triangle 4 and 5 which characterise low temperature faults. Employing the so called low energy gases Hydrogen (H₂), Methane (CH₄) and Ethane (C₂H₆), Triangle 4 differentiates between stray gassing and true faults.

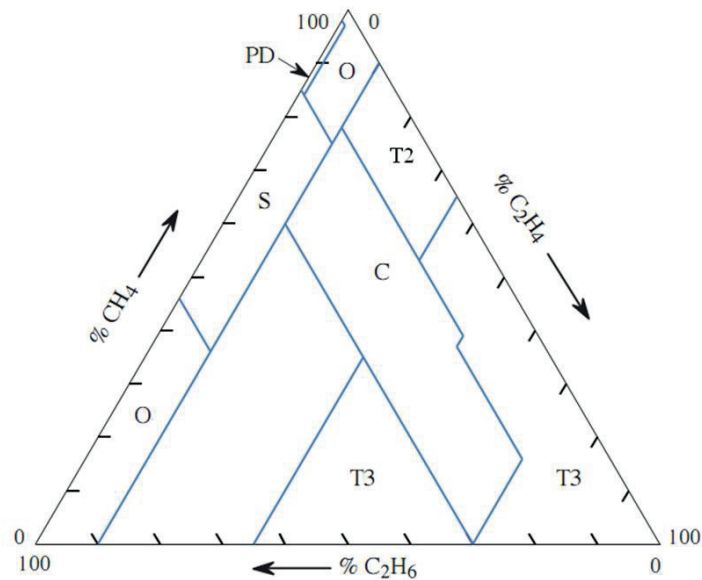
Triangle 5 further refines the interpretation of results from Triangle 4 employing the so called temperature gases; Ethylene (C₂H₄), Methane (CH₄), and Ethane (C₂H₆). It can be used to confirm fault attributes which are still uncertain from Triangle 4

Both Triangles 4 and 5 are illustrated below



PD = Corona partial discharges
 S = Stray gassing of mineral oil ($T < 200^{\circ}\text{C}$)
 C = Hot spots with carbonization of paper ($T > 300^{\circ}\text{C}$)
 O = Overheating ($T < 250^{\circ}\text{C}$)
 N/D = Not determined

Fig. 3: Duval Triangle 4



PD = Corona partial discharges
 S = Stray gassing of mineral oil ($T < 200^{\circ}\text{C}$)
 C = Hot Spot with carbonization of paper ($T > 300^{\circ}\text{C}$)

O = Overheating ($T < 250^{\circ}\text{C}$)
 T2 = Thermal faults of high temperature $300 < T < 700^{\circ}\text{C}$
 T3 = Thermal faults of very high temperature $T > 700^{\circ}\text{C}$
 N/D = Not determined

Fig. 4 – Duval Triangle 5

Given the coordinated nature of each triangle it can be easily understood that only accurate results will provide the correct location. One can consider the effect of uncertainty in results by how the target area expands and so the level of uncertainty in diagnosis expands as errors are introduced into the measurement. For this reason accuracy of DGA is critically to the successful deploying of each of the triangles both the original Duval Triangle and these refined versions.

2.3. Case Study

One of the main benefits of using online DGA is the ability to identify rapidly developing faults and their consequential gas development. In this instance we see the development of Ethylene (C_2H_4) and Methane exponentially and a significant change in Acetylene, rising from below 1ppm to over 12ppm in a matter of a few weeks. The rapid increases are correlated to the load.

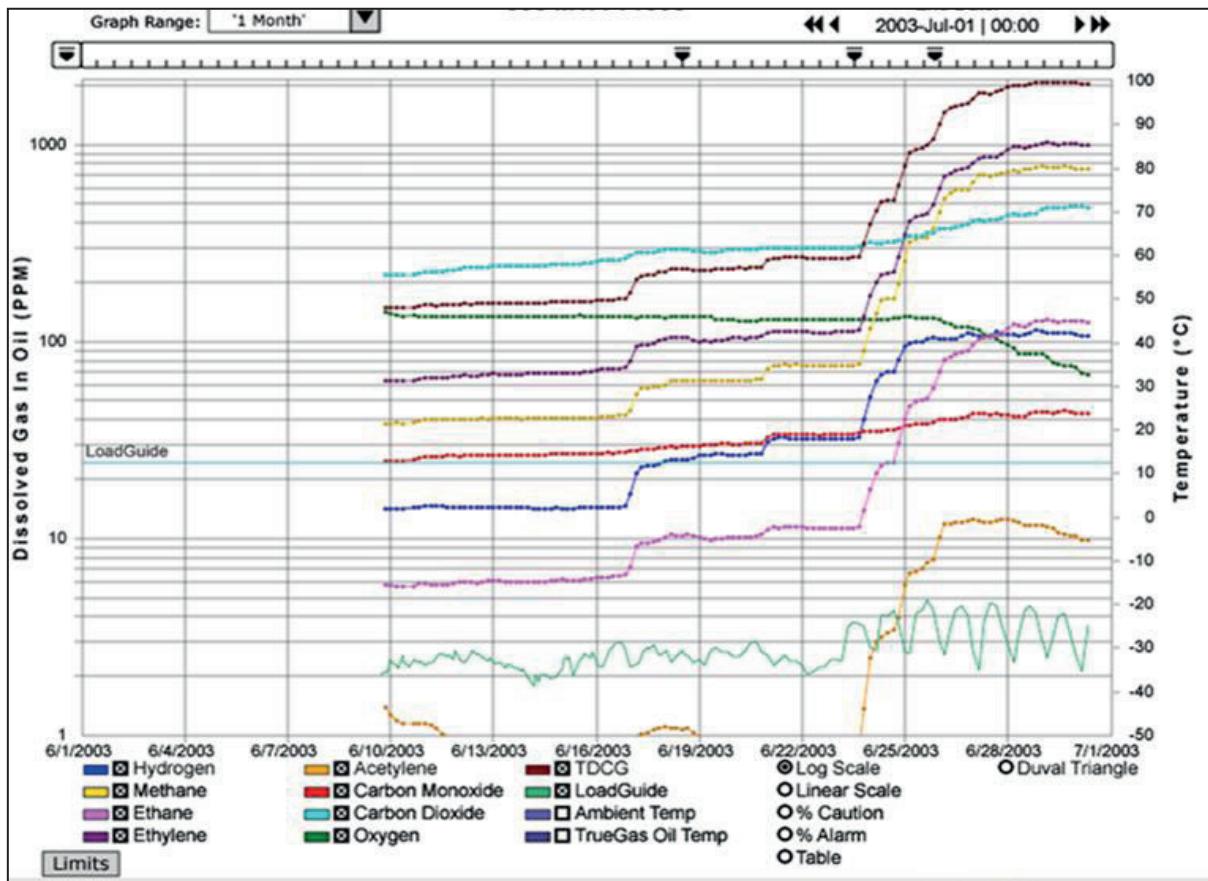


Fig.5. Gassing evolution.

As can be seen in the Duval Triangle in Fig.6 below, the gas sample accumulations are in the T3 area of the triangle thereby suggesting a thermal fault in oil.

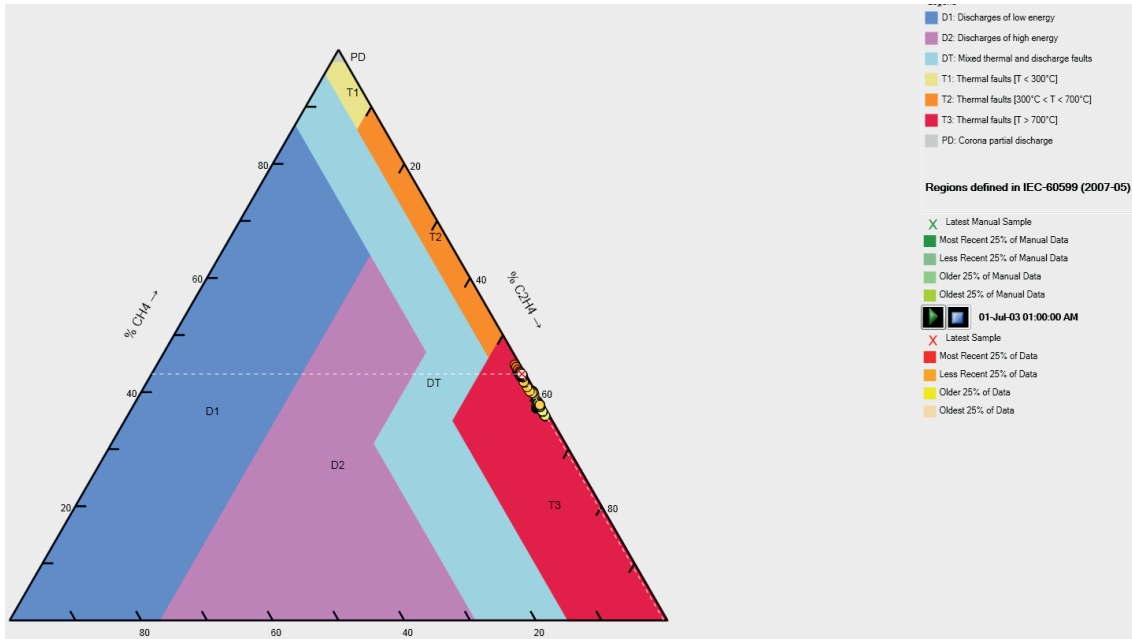


Fig 6. Triangle 1 showing T3 condition

The same data is put through TOAN and as can be seen in Fig.7 below, this fault condition is identified as being most severe (condition 1) and points to OHO (overheating oil) with a recommendation in the notification for immediate attention and a possible removal from service.

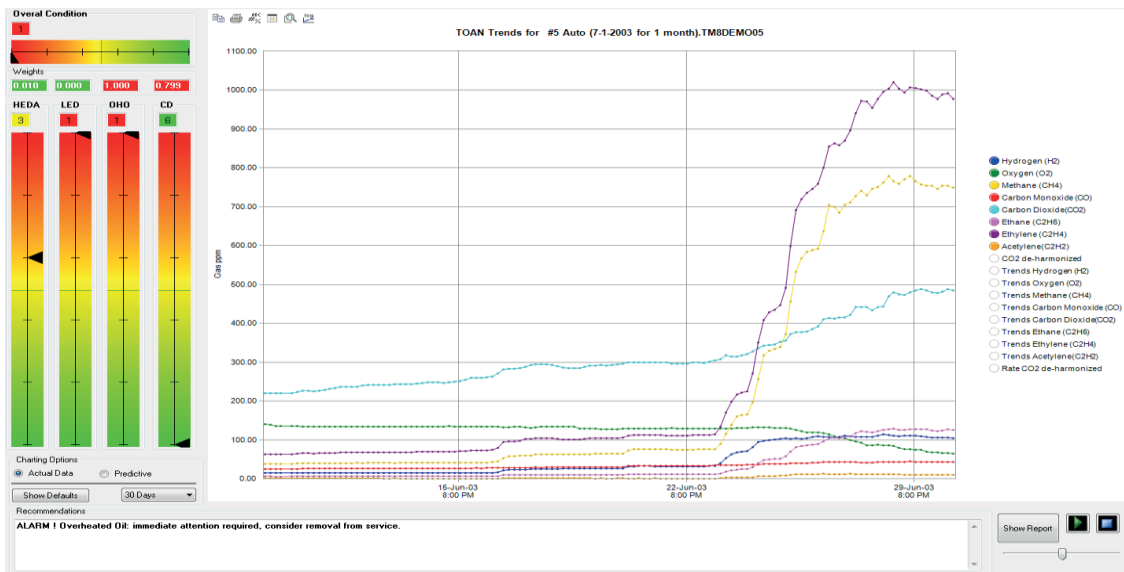


Fig.7. Representation of TOAN

The Duval Triangle is showing ppm of gases while the TOAN is actually identifying a fault condition.

3. CONCLUSION

It can be seen that diagnostic methods are emerging that are much more sophisticated than the traditional and often unreliable ratio based systems. However, accuracy and repeatability are critical both in terms of identifying the location in graphic diagnostic tools such as the Duval Triangle and for modeling such as ANNs. As such tools develop we are also seeing another leap, through TOAN, possibly representing the most significant change in DGA diagnostics in the last decade. Apart from the ability to identify a specific fault condition, the prospects of being able to identify on-line ageing of insulation adds another dimension in the monitoring of these assets.

REFERENCES

- [1] Fofana, I., et al. "The mechanism of gassing in power transformers." *Dielectric Liquids*, 2008. ICDL 2008. IEEE International Conference on. IEEE, 2008.
- [2] Ghunem, Refat Atef. *Transformer Condition Assessment Using Artificial Intelligence*. Diss. American University of Sharjah, 2010.
- [3] Cook Fraser, "Practical Long Term application UHF Partial Discharge Monitoring System on GCCIA Interconnection Network ",GCC CIGRE, 2013
- [4] Lamontagne, Donald R. "Method and system for transformer dissolved gas harmonic regression analysis." U.S. Patent No. 7,747,417. 29 Jun. 2010.
- [5] Duval, Michel. "The duval triangle for load tap changers, non-mineral oils and low temperature faults in transformers." *Electrical Insulation Magazine*, IEEE 24.6 (2008): 22-29.
- [6] D.R. Lamontagne, An Artificial Neural Network Approach to Transformer Dissolved Gas Analysis and Problem Notification at Arizona Public Service, EPRI Substation Equipment Diagnostics Conference XIV, Jul. 2006.
- [7] D.R. Lamontagne, Utilizing Piecewise Linear Approximation and Harmonic Regression to Analyze Power Transformer Insulating Oil On-Line Dissolved Gas Samples, Proceedings of TechCon®, 2010

Ivan Šulc
Končar - Electrical Engineering Institute Inc.
isulc@koncar-institut.hr

Robert Sitar
Končar - Electrical Engineering Institute Inc.
rsitar@koncar-institut.hr

Antun Mikulecky
Končar - Electrical Engineering Institute Inc.
amikul@koncar-institut.hr

AN ASPECT OF TRANSFORMER INRUSH CURRENT

SUMMARY

Paper analyzes a sparking phenomena that were observed on power transformers during their first few energizing. Sparks occurred on the flange between tank cover and tank side, in spite of the fact that a jumper (copper link) was used. The phenomenon was observed on transformers from different manufacturers, with various transformer ratings, three or five limb core.

Paper proposes a simple electromagnetic model for analyzing the phenomena. Three-phase power transformer is modeled in finite element method (FEM) magnetic software. Simplified 3D transformer model is used in order to simulate well known core saturation during the inrush current event. Voltages between tank cover and tank side are calculated for simulated conditions. The same model is used for calculation of possible currents flowing between tank cover and tank side, showing that a value of several kA can be reached.

In spite of the fact that the observed phenomenon is harmless mitigation measures are proposed. However, by doing nothing, sparking would disappear very soon.

Key words: Inrush current, core saturation, spark, copper jumper, tank coating

1. INTRODUCTION

Regardless the fact that power transformer inrush current phenomena (overcurrent, harmonics, noise, vibration, ...) has been well known for last two decades, an additional strange and visually striking phenomenon was observed. During an inrush current event, visually strong sparks appeared between the tank cover and wall in spite of the fact that a jumper (copper link) was applied between the tank cover and wall. Complete visual appearance of the phenomenon sequence is shown in set of photographs in Figure 1.

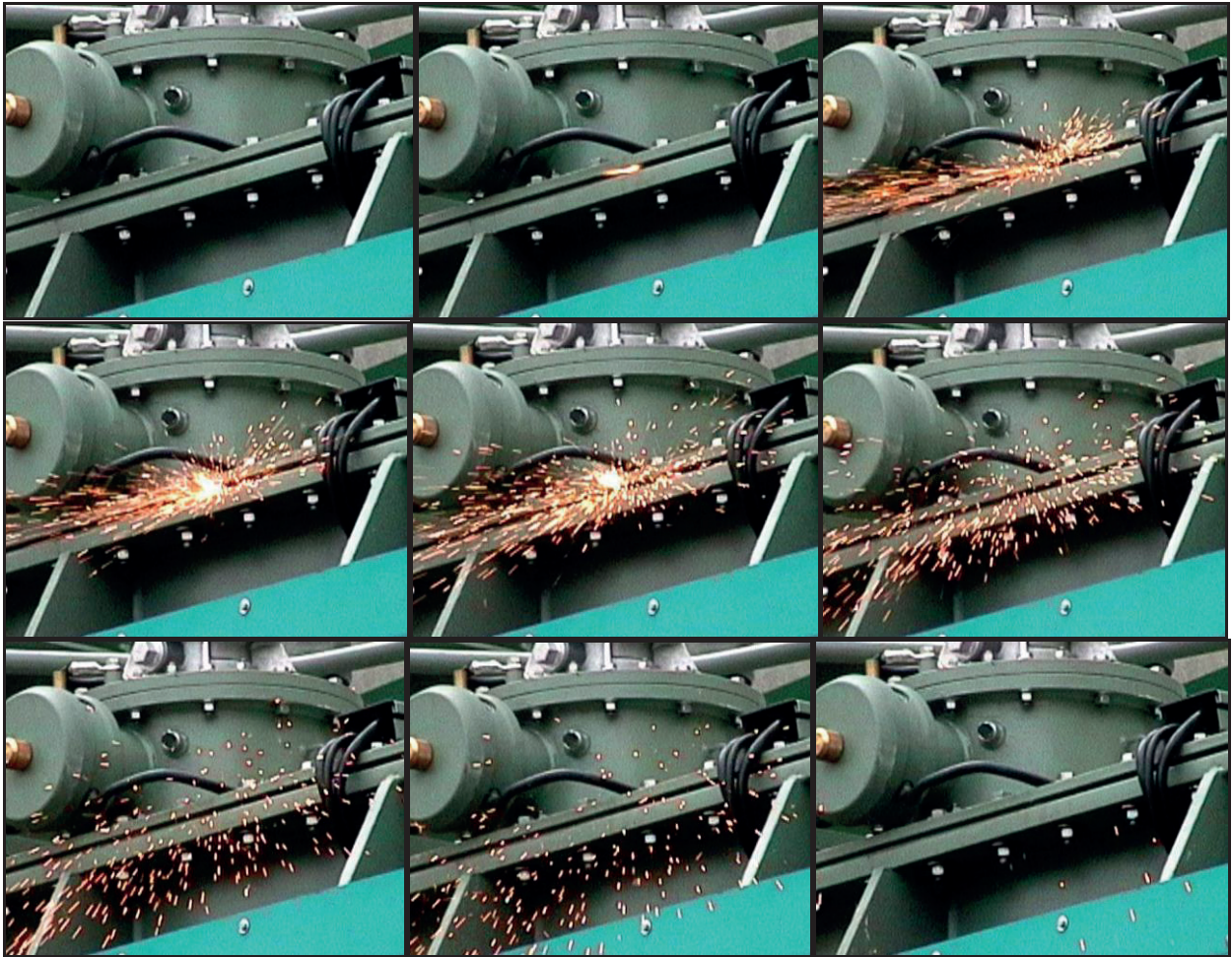


Figure 1: Sparks between tank cover and tank side (shown in detail) during inrush current event, autotransformer 220 MVA, 220 kV, sequence from left to right and from up to down

Entire phenomena in Figure 1 lasted in a range of a second. Such phenomenon was observed only on new transformers, mainly on one of the first several energizing or so, and shows a certain random behavior (in the same manner as inrush current), in a wide range of transformer power – from 40 to 500 MVA, and voltages – from 110 to 400 kV; transformers with three limb (3/0) and five limb (3/2) core type, so as from different manufactures. All observations were made on three phase transformers equipped with a bolted tank cover. It should be noted though that single phase transformers, so as three phase transformer with a bolted bell type tank, are much less abundant and this could be the reason why there has been no observations. Spark striking on 40 MVA 110 kV transformer is shown in Figure 2.



Figure 2: Sparks on tank during inrush current, transformer 40 MVA, 110 kV

Figure 1 and 2 show that the sparking may be fairly strong, astonishing the staff. Sparking does not appear on all new transformers. Moreover, it is a rare event observed only in several cases. In one case the phenomenon was observed on an about 30 years old but a completely refurbished transformer and it was also related to first energizing after refurbishment. No sparking striking events appeared on this transformer when it was new. In spite of this initial behavior, transformers operate perfectly without related complaints. Up to now there has been no evidence of any influence of the described phenomenon on dissolved gas analysis (DGA) results.

2. NUMERICAL ANALYSIS

The aim of this analysis is to find electromagnetic reasons for the reported phenomenon. First assumption is an inrush current event because the phenomenon coincides with it.

2.1. Proposed modeling approach

When switching on a transformer inrush current can drive the core into high saturation[1]. As saturation is approached, the flux is no longer confined only to the core. It is spilled to surrounding air and components. In such conditions it is quite possible that a substantial part of the flux will penetrate transformer's metal parts such as tank cover and induces eddy currents due to electrically conductive nature of tank material [2].

Closed paths of eddy currents are actually a result of different electric potentials induced by time varying magnetic flux in electrically conductive parts. However, conductive parts, such as tank cover and wall, do not have a strict electrical connection. At some places a single jumper (copper link) can be applied, but still not enabling the induced currents to have closed paths. The goal of the proposed modeling approach is to calculate differences between electric potential of the tank cover and wall at various positions on the flange. A model should include:

- 3D geometry of a transformer with modeled connections (jumpers) between tank cover and wall
- Inrush current (saturated) conditions in transformer core
- Time-varying voltage/current source

Considered three-phase 3/2 transformer model includes three basic parts; winding, core and tank (Figure 3). Tank is divided into two parts: the cover and the wall. These two parts are electrically connected only by a copper connection (jumper) and by another "test jumper" with a variable DC resistance. In order to approximate saturated conditions in the core, relative core permeability is substantially reduced to values equal or less than $\mu_r=100$. Winding currents are given with their rated values. Model is solved in time-harmonic (quasi-stationary) sinusoidal domain in order to avoid computationally expensive time "step-by-step" (transient) calculation method.

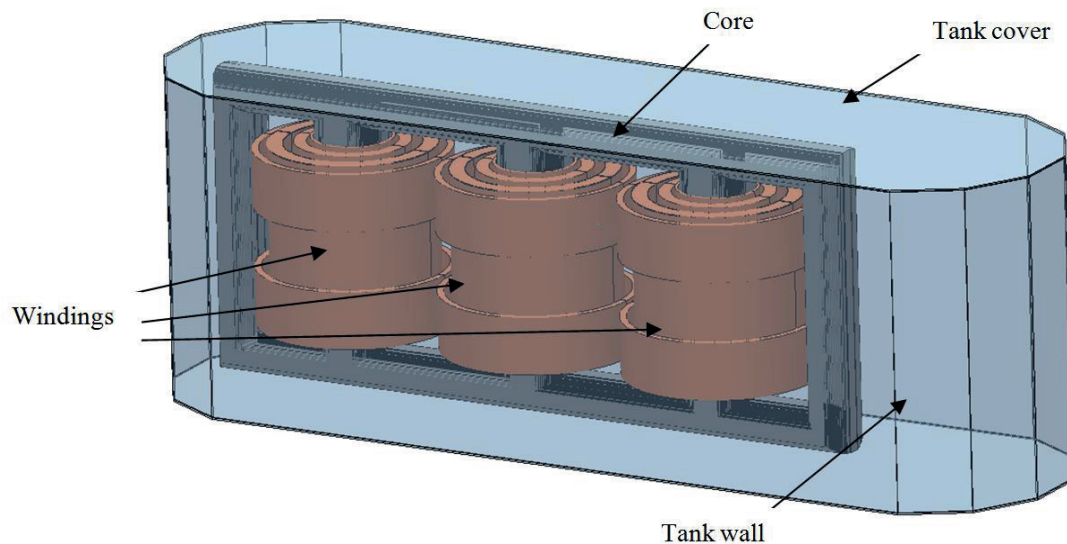


Figure 3 – 3D transformer model used in analysis

Test jumpers are placed at four different positions connecting the tank wall and cover. DC resistance of test jumpers is changed in order to observe values of currents passing through the jumper and evaluate voltage between the wall and cover at various positions. In the meantime the copper jumper has a fixed position as shown in Figure 4.

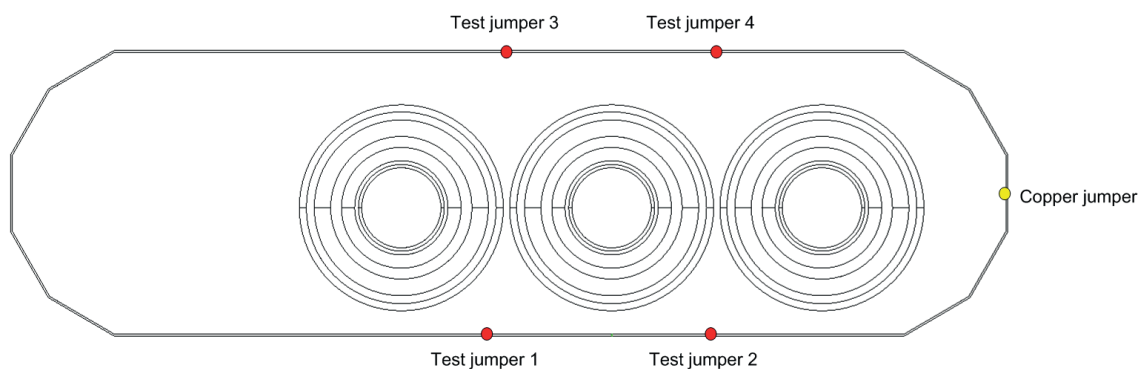


Figure 4 – Positions of test jumpers and copper jumper

2.2. Results and analysis

Several calculations have been done in MagNet [3] using FEM. Calculation model included different positions of test jumpers and different core relative permeability. Results are shown in Table I. Test jumper had a resistance of 10 kΩ. It is obvious that by reducing the permeability of the core to values close to air permeability, voltage at jumper terminals becomes higher resulting in values around 10 V. This could be considered as a voltage value that could lead to sparking at tank flanges.

Table I – Calculated voltage between test jumper terminals

Jumper	Core Rel. permeability	Voltage, V
1	100	0,652
2	100	1,397
3	100	0,361
4	100	0,990
1	1	11,811
2	1	13,484
3	1	7,997
4	1	9,515

Further on, if test jumper resistance is reduced to values of couple of mΩ, it is possible to evaluate the current flowing between the tank cover and wall. For example, test jumper 1 resistance is gradually reduced while current flowing through jumpers is observed. Results of this analysis are shown in Table II.

Table II– Calculated currents and voltages for various resistance of test jumper 1

Resistance, Ω	Current, A	Voltage, V
10000	0,001	11,89
1000	0,012	11,88
100	0,119	11,87
1	11,87	11,87
0,01	1115	11,15
0,001	8672	0,87

Results have shown that reducing the jumper's resistance, or just by short-circuiting the current path, values of currents flowing between cover and wall can go up to 10 kA.

3. SPARKING CAUSE

It is obvious that the currents calculated in previous chapter, for low jumper resistance, can have result in observed sparks but only if the majority of tank cover bolts are not able to carry the current (non-defined galvanized connection). This means that if many bolts are "insulated" from tank cover or side wall, current can become concentrated and have sparking as a consequence. This is a bit unusual because of a very high specific pressure between bolts and tank metal surface.

It is interesting to raise a question: why is this sparking happening and why has this phenomenon been recognized, by our knowledge, only for the last 15 years approximately? Actually we have no answer to this question, but some strong indication exists. According to our experience, tank coating quality (tank protection against corrosion) increased tremendously during the mentioned period. Today's tank coatings are so hard and firm providing no conductive path between the tank cover and wall in spite of the fact that all of them are properly tightened. This has been proven several times by low voltage resistance measurements performed during some other research. Because of that, the current could be concentrated (in similar manner as is simulated with a test jumper in previous chapter) and produce sparks on the "weakest place" between the tank cover and tank side wall. During transformer service, *caused by lot of similar effects*, a conductive connection between bolts and tank becomes much more likely and this side effect of inrush current event spontaneously disappears. This means that the sparking between the tank cover and wall is striking, but harmless, and will disappear quite soon in transformer service.

On the other hand, based on the facts mentioned above, the observed sparking can be understood as an unpleasant sign of a very good tank coating quality. Of course, we do not state that sparking on the tank is a desirable side effect of inrush current event.

Observed sparking can be prevented by the use of welded tank cover, but also by applying several more jumpers between the tank cover and tank side. However, by doing nothing, it will disappear soon.

4. CONCLUSION

In the paper a strange aspect of a power transformer inrush current event is explained. During this event, visually strong sparks appear between the tank cover and wall in spite of the fact that a jumper (usually copper link) between tank cover and wall is applied. Phenomenon is rare and mainly related to new transformers and transformers after detailed refurbishment which includes tank repainting. It is related especially to first several transformer energizing. There is no information about this phenomenon for (occurring on) transformers after a few months in service. Calculation revealed that during inrush current event, caused by core saturation, a huge magnetic flux may penetrate the tank. This flux may cause a very large current, up to 10 kA, between the tank cover and tank side.

This sparking seems to be caused by a large improvement in tank coating quality in last, fifteen years approximately. In that sense, observed sparking may be understood as an unpleasant sign of a very good tank coating quality, but of course, we do not state that sparking on the tank is a desirable side

effect of inrush current event. We have no evidence that this phenomenon has a noticeable influence on transformer DGA results.

Observed sparking is a striking but a harmless phenomenon and can be prevented by using a welded tank cover and also by applying several more jumpers between tank cover and wall. However, by doing nothing, it will disappear very soon causing no damages.

REFERENCES

- [1] G. Abdulsalam, et al., Estimation of Transformer Saturation Characteristics From Inrush Current Waveforms, IEE Transactions on Power Delivery, Vol. 21, No. 1, 2006.
- [2] J. C. Olivares-Galvan et al., Reduction of Stray Losses in Flange-Bolt Regions of Large Power Transformer Tanks, IEEE Transactions on Industrial Electronics, Vol. 61, No. 8, August 2014.
- [3] Infolytica MagNet software, <http://www.infolytica.com/secured/customer/elite/livedocs>

Leonid A. Darian
CJSC "Technical inspection UES", Russia
leonid.darian@gmail.com

Vladimir P. Polistchook
JIHT of RAS, Russia
polistchook@mail.ru

Alexey V. Shurupov
JIHT of RAS, Russia
shurupov@fites.ru

TESTING OF MODELS OF EXPLOSION PROTECTION SYSTEM FOR HIGH-VOLTAGE OIL-FILLED ELECTRICAL EQUIPMENT

SUMMARY

Explosions of high voltage oil-filled electrical equipment (OFEE) lead to a significant material damage. These explosions occur under action of an arc discharge (AD) which arises after internal short circuit. Modernization of OFEE design and protection systems is the possible way to achieve significant reduction of potential explosion and substantial reduction of material losses. Examination of perspective explosion-proof OFEE designs and new explosion protection systems demands the effective test methods. In present work results of development and application of an arcless source of pulse pressure (ASPP) are described. In ASPP the testing impulse is produced by the jet of powder gases (JPG) which arises at the combustion of explosive materials.

In this work results of experimental researches of AD in transformer oil (TO) at conditions typical for AD initial stage have been presented: current rise time was 3-5 ms, the maximum arc current was up to 30 kA, AD burning time was 3-20 ms. The energy released in AD amounted to 0.1 MJ. It was established, that electric field strength in AD column was about 0.2 kV/cm, gas producing factor in AD was 110 l/MJ, growth rate of pressure in TO was about 0.3 MPa/ms. These results allowed to create an ASPP with demanded parameters. Experiments proved that TO flow under action of AD and JPG are similar given that the same influence duration of the energy released in AD is equalled enthalpy of JPG at liquid inlet.

In this work the transformer fracturing behavior after explosion has been analyzed; and the requirements for protection systems have been formulated. By means of ASPP the breadboard model tests of two well-known OFEE explosion protection methods were carried out. In the first method it is assumed that the protection is reached due to fast dump of pressure inside of OFEE case when special membranes are opened. In the second protection method it is offered to establish porous coverings on internal surfaces of OFEE cases. Experiments were carried out on OFEE model with the characteristic size of 1 m at action energy up to 1.5 MJ. It was shown, that these systems cannot protect the transformer body from significant damages.

The dynamic protection system of transformer (DPS) has been described. The efficiency of this new system using ASPP has been verified in experiments with autotransformer of 25 MW. It was shown that DPS protects the transformer from considerable damages at least at dynamic impulse of about 3 MJ.

Key words: transformer explosion, arc discharge, dynamic pressure

1. INTRODUCTION

Life time of transformers or other high-voltage oil-filled electrical equipment (OFEE) is about several decades. The gradual degradation of paper-oil insulation occurs under the influence of partial discharge, heating, cavitation and other factors in service [1]. Over time the deterioration of insulation characteristics exceed a critical level, that's why untimely out of service may cause arc discharge (AD) due to internal short circuit (ISC). Electric power of discharge may range from tens to hundreds MW. Large amount of hydrogen and hydrocarbon gases is formed due to decomposition of transformer oil (TO) under action of AD. Due to oil incompressibility gas formation causes the raise of pressure that quite often ends by explosion of OFEE body. Mixture of atmospheric air and hot hydrogen and hydrocarbon gases can ignite the inflammation. In this case the explosion damage increases many times. The possibility of inflammation after OFEE explosion is about 15% [2].

In case of severe accidents only direct costs determined by cost of the replacing equipment can amount to tens of millions dollars. Therefore the improvement of explosion protection for OFEE is very important for the electrical power industry. The lack of appropriate technical and organizational solutions will make this problem worse. Firstly, there is a general trend of increasing equipment capacity, and secondly, it's not always possible to provide an adequate renewal of equipment.

The destruction degree of OFEE is mainly determined by energy Q_a released in AD. The energy Q_a depends on AD duration (or action time of protection devices), point of ISC origin, characteristics of external circuit. According to the literature data range of Q_a possible values for industrial OFEE exceed by two orders of magnitude. For example, fixed Q_a energy values in 735 kV power transformers are in a range of 1 to 147 MJ [2]. 735 kV single-phase transformer tank exploded at AD energy level of more than 8 MJ, but fire started at energy level of more than 14 MJ. Q_a energy level of 110-330 kV instrument transformers is about 0.3 - 1 MJ, Q_a energy level of 100 MVA distribution transformers can be varied in the range of 3 - 10 MJ. Q_a energy level of more powerful transformers and boxes of bushings under AD can be tens of MJ.

Loss reduction can be achieved in several ways including creation of a non-explosive OFEE design and improvement of protection systems. The solution of this problem requires an effective test method for equipment under the impact of high pressure pulse which occurs in AD. The standard test method for explosion protection of OFEE is based on electric arc ignition in the internal volume of OFEE. Together with our colleagues in works [3-6] we presented the investigations which justified an alternative test model for explosion protection of OFEE. In this method a high pressure pulse which occurs after ISC was simulated by chemical energy of explosive materials (EM). The new method allows carrying out tests directly in place of manufacture or installation site of OFEE. Estimations show that the alternative tests will cost much cheaper than the standard ones.

Joint Institute of High Temperatures of Russian Academy of Sciences (JIHT of RAS) developed an arcless source of pulse pressure (ASPP) for explosion protection tests of OFEE. The proven designs of ASPP allow producing pressure pulses with energy up to 5 MJ. Tests of protection system prototypes were carried out in OFEE models at energy effect up to 3 MJ by now.

In this work we present test results of protection system prototypes for OFEE. This work also summarizes the research results of AD in transformer oil, which was the basis for creation of ASPP. According to accepted definition explosion-proof electrical equipment is electrical equipment, where may occur structural damage after ISC, however all its components must be inside the normalized safety area close to the equipment, which is calculated as the diameter (width) of the equipment increased by two of its height but not less than 1.8 m. The energy of pulsed pressure in which the destruction of the transformer satisfies this condition can be regarded as estimation of its explosion safety.

2. ARC DISCHARGE IN TRANSFORMER OIL

Our research results of AD in OFEE test model have been described in details in works [3-6]. The AD basic parameters resulting from these studies are presented below. Experiments [3-6] were carried out under conditions similar to conditions after ISC occurrence in industrial OFEE, where discharge current increases up to 10 - 30 kA in 3-10 ms. In our experiments the maximum discharge current reached 30 kA at the rise time of 1-3 ms. The total discharge duration was 3-20 ms. The maximum heat release in the arc Q_a reached 0.1 MJ. The capacitive storage with maximum charge voltage of 5 kV was used as energy source for AD. Available electric circuit allows simulating two half-wave of heteropolar

current; however basic experiments were carried out with one half-wave voltage. The maximum of AD power was reached during the first half period, hereafter discharge voltage and power were reduced due to resistivity degradation of insulating fluid.

AD was ignited between two parallel brass electrodes about 20 mm in diameter. The distance between electrodes was varied from 17 to 30 mm. The electrodes were located in a chamber of 310 mm internal diameter and 61 liters volume. The volume of mineral TO was 35 liters. The remaining volume (26 liters) was filled with nitrogen at atmospheric pressure. The electrodes were close to the chamber axis. The distance from point of discharge origin to "liquid-nitrogen" interface was 100 mm.

AD current and voltage, the pressure in the body, the pressure of gas bubble above liquid were measured. Response time of pressure sensor was less than 0.5 ms. One pressure probe (PP) was installed close to body foot (PP1), the other was installed at 50 mm from upper level of the liquid (PP2). We used high-speed shooting of the discharge with a time resolution of 0.1 ms and motion of "liquid-nitrogen" boundary with a resolution better than 0.8 ms. The amount of hydrocarbon gases formed due to decomposition of TO was calculated from pressure increase in gas.

The arc discharge was initiated by applying voltage ($\cong 3$ kV) to a copper wire used for connecting electrodes of 0.1 mm diameter. Fig.1 and Fig. 2 present the experiment results. Fig. 1 shows "oscillograms" of current and voltage in AD. The discharge duration ($\cong 7.5$ ms) is close to half-wave voltage duration at power frequency. At start time the voltage oscillogram is on a sharp rise and then there is a rapid decline. The estimated high voltage peak duration ($\cong 20$ ms) is equal to electric explosion time of copper initiator.

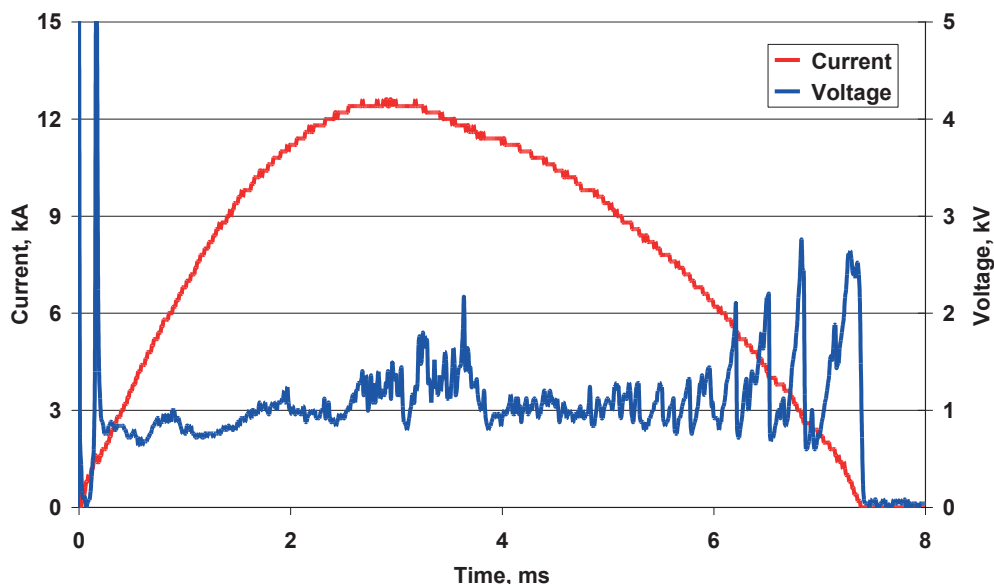


Figure 1 – Current and voltage oscillograms

There were some voltage pulsations at current fall time, which were probably associated with arc motion along the surface of electrodes. Arc velocity was about 20 m/s. Analysis revealed that AD column extends under action of its magnetic field with the result of AD voltage increase which causes shunt breakup with further voltage decrease. Estimations showed that typical electric field value in AD column was 0.1-0.3 kV/cm.

High-speed shooting of the discharge showed that plasma glow was concentrated close to electrodes at the beginning of the process. At this point the glow area started to expand at a rate of 0.3 km/s, however in 0.5 ms the rate decreased approximately threefold. Thus, the plasma expansion rate was much lower than the speed of sound in TO, which is about 1.4 km/s. Radiation flashed over the electrode spacing in about 1 ms after AD occurrence.

Fig. 2 shows "oscillograms" of pressure in TO measured by PP1. One may state that variation of pressure in TO is repetitively-pulsed. This fact is quite pictorial especially in the beginning of arcing which is about 3 ms. First pressure extremums (maxima and minima) followed at 0.8 ms interval and then one-step transition decreased to 0.6 ms. There is some correlation between the signals from pressure probe and the

discharge voltage "oscillogram". Thus the first pressure maximum is equivalent of the "smeared" voltage maximum. There was a voltage jump up to 2.2 kV in 3.64 ms after arc ignition (Fig. 1) before the absolute pressure maximum in the oil, which was fixed in 3.71 ms after AD occurrence and amounted to $\cong 1.7$ MPa (Fig. 2). Apparently, there were sound waves in the liquid under a sharp voltage decrease (breakdown).

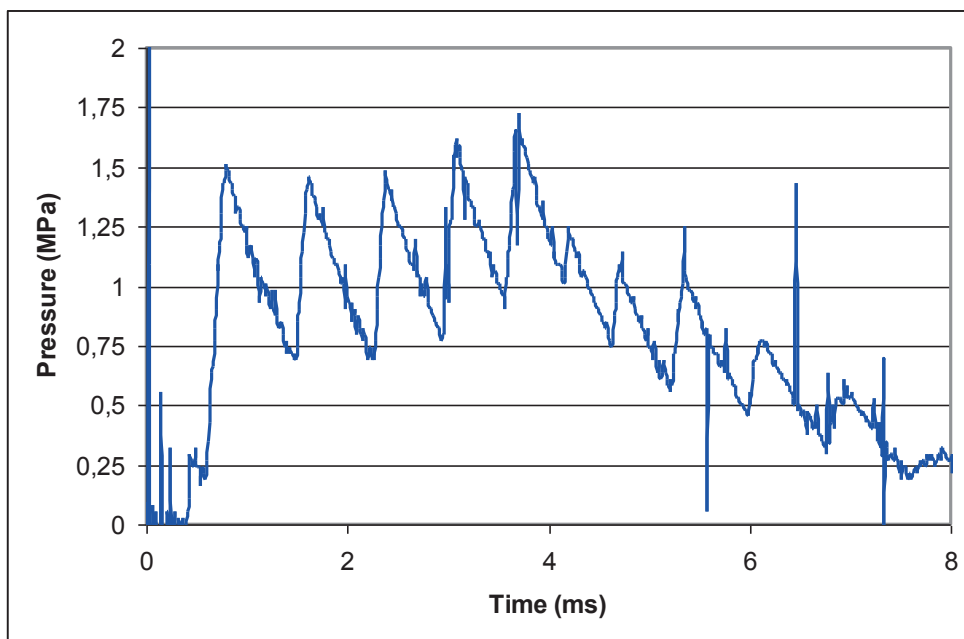


Figure 2 – Pressure in TO close to the foot of the chamber

Oil moves under the influence of expanding gas-vapor bubble, which leads to gas compression and pressure increase. According to high-speed shooting the liquid level climbs uniformly up to 0.1 m of height and then vapor-gas mixture ruptured to nitrogen volume. Typical liquid rise velocity was about 10 m/s and the kinetic energy of oil motion was 5-10 % of total energy released in AD. The main part of the energy Q_a was spent on oil heating and its decomposition.

After discharge the overpressure in nitrogen "blanket" was at 10-50 kPa level which is proportional to gas volume released due to TO decomposition. The gas formation process under AD is usually characterized by coefficient of gas formation B_g , which is the ratio of released gas volume to AD energy. According to our data $B_g = 0.11$ l/kJ.

Carried out experiments allow us to define qualitative features of AD dynamic effect to OFEE body. The main feature is the lack of shock waves in liquid. Perhaps a shock wave occurs at the moment of initiator explosion, but it quickly degenerates into a sound wave. The average pressure rise rate in liquid is 0.3 - 0.5 MPa/ms. At the background of increasing pressure of body walls there are intensive sound waves. The maximum pressure of body wall in our experiments was about 2 MPa. The pressure in the arc burning zone (vapor-gas bubble) was slightly higher. The pressure estimated from the velocity of "liquid- nitrogen" boundary (10-20 m/s) should be 5 - 10 MPa.

3. ARCLESS SOURCE OF PULSE PRESSURE (ASPP)

The research results of AD have determined the requirements for arcless source of pulse pressure (ASPP) for simulating AD effect in OFEE. In ASPP the impulse pressure is created by the enlargement of JPG which is formed due to combustion of explosive materials (EM). It is important that duration of pulse pressure effect should be about 50 ms. This requirement eliminates the use of explosive materials like TNT or hexogen in JPG generator. Therefore in our experiments we used gunpowder as EM, because it burns much slower than TNT. Gunpowder efficiency is 3.8 kJ/g; the specific gas production is 0.9 l/g.

The generator of JPG has high-pressure chamber, from which the products of EM combustion are flown through a Laval nozzle. The magnitude of impulse pressure and its duration can be controlled

by changing parameters such as nozzle area, EM mass, EM allocation in combustion body and ignition methods. Experiments with JPG were carried out in the same chamber as experiments with AD. JPG generator was attached to one of the lower windows of chamber, so that the region of JPG influence on the liquid was the same as under AD. Enthalpy Q of JPG was varied in the range of 10-50 kJ. TO and water were used as working liquids.

Pressure was measured at characteristic points of the chamber, the motion of liquid under JPG influence was studied using high-speed shooting. According to measurements jet pressure at the liquid inlet achieved about 10 MPa through about 1 ms. Duration of jet exposure to the liquid was varied from 20 to 60 ms. The typical pressure on the chamber walls was about 1 MPa. Motion of "liquid-nitrogen" boundary under JPG influence immersed in the liquid was the same as under AD under the same energy effect. This boundary while remaining flat was climbed with velocity of 10-20 m/s. It should be noted that there were no essential differences between water and TO response for JPG impact.

The experiments proved the possibility of hydraulic similarity of liquid motion under the JPG and AD effect. The equivalence of the liquid motion under effect of JPG and AD was achieved if the energy and exposure duration were equal. In this context JPG generator (ASPP) can be used in explosion protection tests for simulating AD effect in OFEE.

Fig. 3 presents ASPP for energy of 5 MJ before the control test.



Figure 3 – ASPP for energy of 5 MJ

ASPP can be used for series of tasks aimed to improve the explosion protection of OFEE:

- test of OFEE production samples;
- examination of explosion protection systems and devices efficiency;
- elaboration of OFEE new constructions with high level of explosion protection;
- basic data acquisition for development and verification of numerical methods for OFEE perspective constructions and explosion protection systems etc.

Experience of ASPP application in the tests of explosion safety of OFEE industrial samples has been described in the works [3, 4].

4. PECULIARITIES OF TRANSFORMER DESTRUCTION AFTER EXPLOSION

According to analysis of published studies, the most vulnerable elements of ISC in power transformers are bushings, oil-filled cable boxes and tap changers [2]. AD develops close to the point of a short circuit origin between transformer body ("the ground") and construction elements under high potential. The length of arc column defining AD voltage depends on OFEE construction and may range from 0.1 m to 0.3 m. AD continuously and randomly moves along internal surfaces of the transformer due to magnetic forces and convective flows. Since the typical velocity of AD is about 10 m/s and the time of its "lifetime" is about 50 ms, the surface area of the transformer under AD effect is about 0.1 m^2 . Therefore AD exists inside the volume of 10-30 liters. This fact explains the shock wave absence in OFEE despite the high power of AD.

Pressure equalization time inside transformer tank is estimated as double time of maximum sound wave transmission between opposite walls of the transformer. Pressure equalization time in typical instrument transformers of 110 and 330 kV which explosion safety has been analyzed in work [4] is about 1 ms. This time is much less than arc duration. Pressure equalization time in distribution transformers is about 15 ms. It means that there is a significant difference of pressure in large transformers during arcing. The maximum value of pressure is achieved in region of AD action. These estimations show that transformers with tank volume less than 1 m^3 should be damaged quite uniformly across the surface under the pulse pressure influence. Such faults were recorded during our safety tests of instrument transformers [4]. Faults of large transformers are local where the damaged area is less than 10% of total surface area. The example of such damage is shown in Fig. 4.



Figure 4 – Transformer in Western Siberia Substation after explosion

The maximum valid overpressure for transformer body depends on design, location and pulse duration. According to general requirements for transformer its body deformation occurs in elastic zone with static overpressure of 0.05 MPa. The tank rupture under dynamic loading can be expected if overpressure above 0.5 MPa lasts for more than 5 ms.

Apparently most probable conditions for transformer explosion are in the range of 10-30 ms after AD ignition. At early stage of AD burning for about 10 ms, internal pressure of the transformer does not reach critical values. The probability of explosion is decreased about 30 ms after arc ignition. Firstly, at that time the AD power is significantly reduced due to conductivity increase of insulating liquid. As a result there is a decrease of gas formation rate in AD and changes in pressure growth rate. Secondly, there is an increase of internal volume of the transformer tank due to its deformation under high pressure influence. This additional volume partially compensates for pressure growth due to decomposition of TO.

In the view of foregoing considerations, we can lay down basic requirements for OFEE explosion protection systems:

- the response time for internal pressure increase should not exceed 5 ms;
- the system should limit the pressure in the transformer tank at the level of 0.3-0.5 MPa;
- the protection system should be installed close to problem areas of the transformer in case it is not possible to protect the entire internal surface.

5. MODEL TESTS FOR EXPLOSION PROTECTION OF OFEE

Well-known explosion protection methods of OFEE are focused on formation of additional volume ΔV for expansion of TO in case of internal pressure growth under AD. The effectiveness of the protection system can be estimated from:

$$k = \frac{\Delta V}{B_g Q_a} \quad (1)$$

The k value that may be called a protection system reliability parameter presents itself as the ratio of TO additional volume of and gas volume $V_g=B_g Q_a$ released due to TO decomposition under AD. Approximately we can take as follows:

- $k > 0.7-0.8$, tank deformation is elastic and the equipment is explosion proof;
- $0.3 < k < 0.7$, the considerable plastic deformation of the transformer body should be taken of;
- $k < 0.1-0.3$, explosive destruction of the transformer body should be expected.

Tentatively we can take typical values of protection system reliability as $k_1 \approx 0.7-0.8$ и $k_2 \approx 0.1-0.3$.

There are two ways of additional volume formation for TO. The first method is based on using porous coverings on the internal surfaces of OFEE body [7]. It is expected that porous material is compressed under high pressure influence resulting in formation of necessary volume. In consequence pressure growth inside the body is limited. Some additional protective effect can be achieved if significant part of TO flow kinetic energy will spend on compression of the porous material. "Porous covering" method may be effective in case substantial compression of porous material takes place at a relatively low overpressure – approximately 0.3-0.5 MPa.

The second method of protection is so-called "protective membrane" method. Principle of method is installation of protective membranes on OFEE body which are destroyed under action of AD pulse pressure and used for TO flow to special container [8]. It is considered that this way internal pressure of OFEE can be kept within acceptable limits. The second protection method is widely used, for example in SERGI Transformer Protector System.

We have presented briefly the tests of the described protection systems in the work [4]; these results are discussed in details below.

In the experiments with porous covering method we used OFEE breadboard model in the form of steel cylindrical tank of 0.95 m³ volume and of 1.45 m height. Tank diameter was 1 m, thickness of wall was 7 mm. The cover has been screwed to a sidewall by 24 bolts with thread diameter of 12 mm. The plate of elastic foam plastic of 50 mm thickness has been glued on a steel cover of a breadboard model. The foam was made from extruded crumb with 0.04 kg/dm³ density. The tank was filled with water. ASPP was installed at a distance of 0.2 m from the top cover. Estimated energy of ASPP pulse was 0.35 MJ.

After test the cover of tank has lifted in 0.8 meters: only 3 bolts from 24 has survived, the cover deflection has amounted to 50 mm, the foam plastic plate has destroyed into small fractions. Hence this protection method cannot protect OFEE body from considerable deformation under action of the high pressure pulse. This result was quite expected. Indeed for the effectiveness of this protection system needed volume increase which is accessible for the liquid due to compression of porous material for its compensation in 3-5 ms - the time of pressure rise in the liquid. It is possible either at slow pressure rise rate of 0.1 MPa/ms, or at small sizes of the protected model of 0.1 m.

In general, the efficiency of the discussed protection system cannot be sufficiently high. This fact can be illustrated by following calculations. If the typical size of transformer tank is a , then the possible increase of available oil volume under covering of transformer internal surface with damper material of maximum compression h will be:

$$\Delta V \cong 6a^2 h \quad (2)$$

The porous covering uniformly compresses under action of pulse pressure only if tank size is under $\cong 0.5$ m. Taking for calculations $a \cong 0.5$ m and $h \cong 0.02$ m and using formula (2) we find that $\Delta V \cong 30$ l. It may be enough to protect the transformer from the explosion at AD energy of 0.5 MJ ($V_g \cong 55$ l).

At the increasing size of transformer tank after short circuit occurrence the covering can be effectively compressed only close to the short-circuit origin with total area of 1 m². In this case the additional volume will be $\Delta V \cong 20$ l. The effectiveness of this protection system under AD with energy $Q_a \cong 1$ MJ ($V_g \cong 110$ l) will be $k \cong 0.2$, i.e. even at a relatively low AD energy we can expect explosive destruction of tank.

In summary, porous coverings which are compressed at pulse pressure of 0.3-0.5 MPa having an effective Young's modulus of 0.5 MPa, may be used in explosion proof transformers with the tank size up to 0.5 meters if expected AD energy does not exceed 0.5 MJ. In addition this porous covering material has to maintain its properties during continuous operation.

Fig. 5 shows OFEE breadboard model which was used in the test of protective membrane method. The OFEE model had the form of steel cylindrical vessel of 1.4 m diameter filled with water. The thickness of model steel cover was 12 mm. The air volume has been separated from the water by an aluminum membrane with the thickness of 0.2 mm and diameter of 200 mm. The concrete blocks with mass of 70 kg have been installed at a distance of 300 mm from the cover to simulate transformer windings. Area of ASPP effect was between concrete blocks and cover at 0.2 m distance from the roof opening – opposite the pressure probe PP2. PP1 detected pressure in air bubble behind the membrane, PP3 and PP4 measured pressure in liquid from far field of ASPP effect. The action of pulse pressure on OFEE body was recorded by high-speed shooting. Energy of ASPP was 1 MJ, pulse duration was 50 ms.

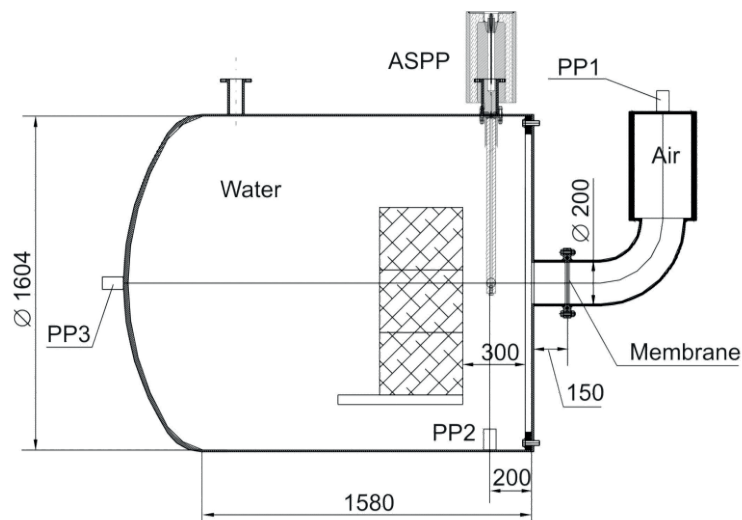


Figure 5 – OFEE breadboard model for tests using protective membrane method

Membrane contact sensor recorded its rupture in 3 ms after ASPP start. The water flow rate through membrane calculated due to air pressure changes in air bubble behind the membrane was 20 m/s. Pressure maximum in the liquid reached 1.8 MPa. High-speed shooting showed that the deformation of OFEE body had lasted for 10-15 ms. After the test we established that the residual deformation of steel cover was about 40 mm and concrete blocks were moved for 50 mm. The conditions for the discussed protection method in this test were optimal: a thin membrane of a large diameter was installed right in front of the epicenter of the pressure rise. However the present protection method was not effective enough.

The explosion prevention system in Fig. 5 is a simplified version of SERGI Transformer Protector (TP) system. This protection system is used in energy utilities of Russia in recent years, but the experience of its operation is not encouraging. On September 22, 2009 there was an explosion of AT-1 - 330 kV tank due to ISC at substation "Mashuk", where this system was installed. SERGI gave an explanation of this rupture in the report [9]. According to this report there was a peak current of 10 kA and arc duration of 60 ms at the time of rupture. In the analysis of TP system SERGI experts assumed the AD voltage was 37 kV, so that the energy released in AD was about 11 MJ. This AD voltage value seems conservative, because it was calculated without taking into account the voltage loss in inductance. According to our estimations the AD voltage was significantly lower, so that the total AD energy was about 4 MJ. The volume (gaseous products of fluid decomposition) was about 0.45 m³ under this Qa energy.

According to data [9] the protective membrane of 8 inches diameter (\cong 200 mm) was destroyed in 4.5 ms after short-circuit occurrence at pressure of 0.08 MPa. There was TO flushing through the opening which caused "depressurisation" of transformer tank in 112 ms. According to this report [9], even though the TP system did not protect the HV OFEE body from explosion, it prevented the fire occurrence. However, the data in the report [9] raise some doubts. According to this data the maximum oil flow rate through the destroyed membrane does not exceed 20 m/s. According to calculations based on values of

TO velocity [9], approximately 25l of TO leaked through the diaphragm under AD. Therefore, the reliability coefficient of the protection system (1) is $k \cong 0.07$, that's why TP couldn't protect OFEE tank from explosion. As for the lack of fire, the probability of its occurrence after rupture does not exceed 20%, so we cannot give a credit to TP system especially as Q_a energy is relatively small.

6. TESTS OF DYNAMIC PROTECTION SYSTEM

The previous analysis shows that well-known OFEE explosion protection systems are not effective enough and it's a necessary to develop new protection systems. This section briefly describes tests results of dynamic protection system (DPS) developed by JIHT of RAS. The main elements of DPS are spring-loaded moving blocks (Fig. 6). The blocks were installed on the side wall of transformer body close to the most probable place of ISC occurrence. The maximum displacement of the blocks under influence of pulse pressure was about 0.3 m. Protection of bushings was carried out using special membranes.

The tests were carried out in autotransformer (AT). The autotransformer of 25 MVA was out of service, but all elements have been preserved inside the body. Fig. 7 shows the autotransformer with established DPS elements (guard vessels are painted blue). There were 16 moving blocks under circular guard vessel and 35 blocks under rectangular guard vessel (Fig. 6). There was an ASPP inside the protective chamber from the left. DPS wasn't installed at the back side of the transformer; it was installed at one of three bushings.

ASPP with energy of 1 to 3 MJ and exposure duration of 30 to 50 ms was used in the tests. High-speed shooting (up to 2000 frames per second), four pressure probes and displacement sensors were used for diagnostics of the tank deformation. The AT tank was filled with water.

Series of experiments (10) were carried out. The pressure pulse was supplied to most likely points of short circuit origin from both sides of transformer including the bushing area. Plastic deformation of the tank with partial destruction of the structural elements but without leaks was recorded under pulsing of AT back side without DPS. High-speed shooting recorded that blocks began to move in 5 ms after ASPP start.



Figure 6 – Dynamic protection system (valve blocks without guard cover)



Figure 7 – Autotransformer with DPS before tests

According to results of these experiments it was established that:

- Pressure maximum in autotransformer increases approximately proportionally to ASPP energy: under the energy of 1 MJ pressure maximum is about 0.5 MPa, under the energy of 3 MJ the pressure exceeds 1 MPa.
- The basic body deformation without DPS begins in 20-30 ms after ASPP start.
- Displacement velocity of DPS blocks increases with ASPP energy increase: maximum velocity of blocks reaches 30 m/s at ASPP energy of 3 MJ.
- DPS has much lower response time in comparison with the factory explosion protection system in form of protective membrane.
- DPS installed in front of ASPP protects the body from plastic deformation under pulse energy up to 3 MJ.

It was estimated that DPS with tested configuration has reliability coefficient $k \cong 0.5$. The reliability of explosion protection can be increased from 30 up to 50% in case DPS is installed on the both sides of the transformer and all high-voltage bushings.

7. CONCLUSION

- 1) Dynamic effects of arc discharge (AD) and jet of powder gases on transformer oil have been investigated. It has been shown experimentally that these effects are quite similar under conditions of equal energy of action and its duration.
- 2) Arcless source of pulse pressure (ASPP) which may be used to estimate the explosion safety of OFEE under energy up to 5 MJ has been created. ASPP can be applied as an alternative to existing method which is based on AD initiation inside the equipment.
- 3) It has been experimentally shown that the protection method in the form of porous coverings on internal surfaces of OFEE which can be compressed under high pressure pulse cannot be effective for large transformers.
- 4) Test models of "protective membrane" method have shown that this method didn't protect OFEE body from considerable plastic deformation which may cause explosion. Reliability parameter of this protection method does not exceed 0.1.
- 5) Dynamic protection system (DPS) of OFEE explosion prevention has been described. Tests of DPS installed on the autotransformer of 25 MVA have shown that DPS prevents the explosive destruction of the autotransformer body at least at the energy of 3 MJ.

REFERENCES

- [1] L.A. Darian, V.G. Arakelian, "Gas-resistance of insulation liquids"// *Electrotechnika*. № 2, 1997, p. 45-49 (In Russian).
- [2] M. Foata, J.B. Dastous, "Power transformer tank rupture prevention"// Session CIGRE-2010. Paris. 2010. Report A2-102.
- [3] L.A. Darian, V.P. Efremov, A.V. Shurupov, "A new approach to design of oil-filled transformers with high oil and fire safety" // 43 CIGRE Sessions. Report A2-106. Paris. 2010 (cd).
- [4] L.A. Darian, V.E. Fortov, V.P. Polistchok, "Arcless tests of the high voltage oil-filled electrical equipment on explosion safety"// 44 CIGRE Session. Report A3-102. Paris. August 2012 (cd).
- [5] L.A. Darian L.A., A.V. Kozlov, A.V. Kotov, "Pulse arc discharge in mineral and organic oils"// Proceedings of Int. Conf. on Physics of Extreme States of Matter-2012. 1–6 March, Russia, Elbrus. Institute of Problems of Chemical Physics. Chernogolovka, 2012, p. 168.
- [6] L.A. Darian L.A., A.V. Kozlov A.V., S.N. Luzganov, "Experimental study of a flow of liquid under action of an arc discharge and jet of powder gases"// Physics of Extreme States of Matter- 2010. Chernogolovka, 2010, p. 112.
- [7] A.V. Mishuev, V.V. Kazennov, N.V. Gromov N.V., "Protection equipment of electrical transformers from fire and explosion due to short-circuiting". Patent RU 2334332 (In Russian).
- [8] F. Manie, "Explosion protection device for transformers". Patent RU 2263989 (In Russian).
- [9] SERGI company. "Substation "Mashuk". Activation of Transformer Protector on 22/09/2009. Reference Are61rr00.03e, 09/10/09.

Dario Šegović
Končar Power Transformers Ltd.
dario.segovic@siemens.com

Franjo Kelemen
Končar Power Transformers Ltd.
franjo.kelemen@siemens.com

ESTIMATION OF ZERO SEQUENCE IMPEDANCE IN POWER TRANSFORMERS USING 2D AND 3D FEM

SUMMARY

This paper describes calculation of zero sequence impedance in three phase, three leg core type power transformers using 2D and 3D finite element method (FEM) calculation on example of 100 MVA power transformer. Paper also describes how winding connection and arrangement affects the size and calculation of zero sequence impedance.

Key words: zero sequence impedance, zero sequence reactance, power transformer, finite element method, FEM

1. INTRODUCTION

In power system analysis power transformer is represented by three sets of impedances. Like other symmetrical static machines, transformers have equal positive and negative sequence impedance ($Z=Z_d=Z_i$), but zero sequence impedance (Z_0) value depends on geometry of active part and connection of windings.

The positive phase sequence impedance (Z_d short circuit impedance) allows flow of balanced symmetrical three phase positive sequence set of currents and the negative sequence impedance (Z_i) allows flow of balanced symmetrical three phase negative sequence set of currents. The zero sequence impedance (Z_0) allows flow of zero sequence set of currents that are equal to and in phase with each other in all three lines, and their sum is not zero like positive (negative) phase sequence currents, pushing the magnetic flux path outside the core in three leg core type transformers.

The positive sequence impedance of power transformer is relatively easily calculated, but its zero sequence impedance is not, and is usually estimated as $0,8\div 0,95 Z_d$ for three leg core type transformers.

Single phase transformers, shell type and five leg core type transformers have return magnetic paths, thus their zero phase impedance is nearly equal to positive and negative.

To allow the flow of set of zero phase sequence currents in three phase transformers winding arrangement is also important. Only grounded star (YN) or zig-zag connected (ZN) windings can be energized with set of zero phase sequence currents. Depending on connection of secondary winding zero sequence impedance has short circuit impedance or magnetizing impedance characteristic. For example in YNd three phase, three leg core type transformer, star connected winding energized with set of zero phase sequence currents will induce circulating current flowing in delta connected winding resulting with short circuit character impedance when viewed from primary side (YN). Since delta connected windings do not allow flow of zero phase set of currents, when viewed from secondary side transformer will have infinitely large impedance.

2. TRANSFORMER AND FEM MODELS

2.1. Transformer

In this paper all calculations and models are based on data from KPT manufactured, three phase, three leg core network transformer, 100 MVA rating, 225/13,8 kV, 50 Hz, connection symbol YNd11.

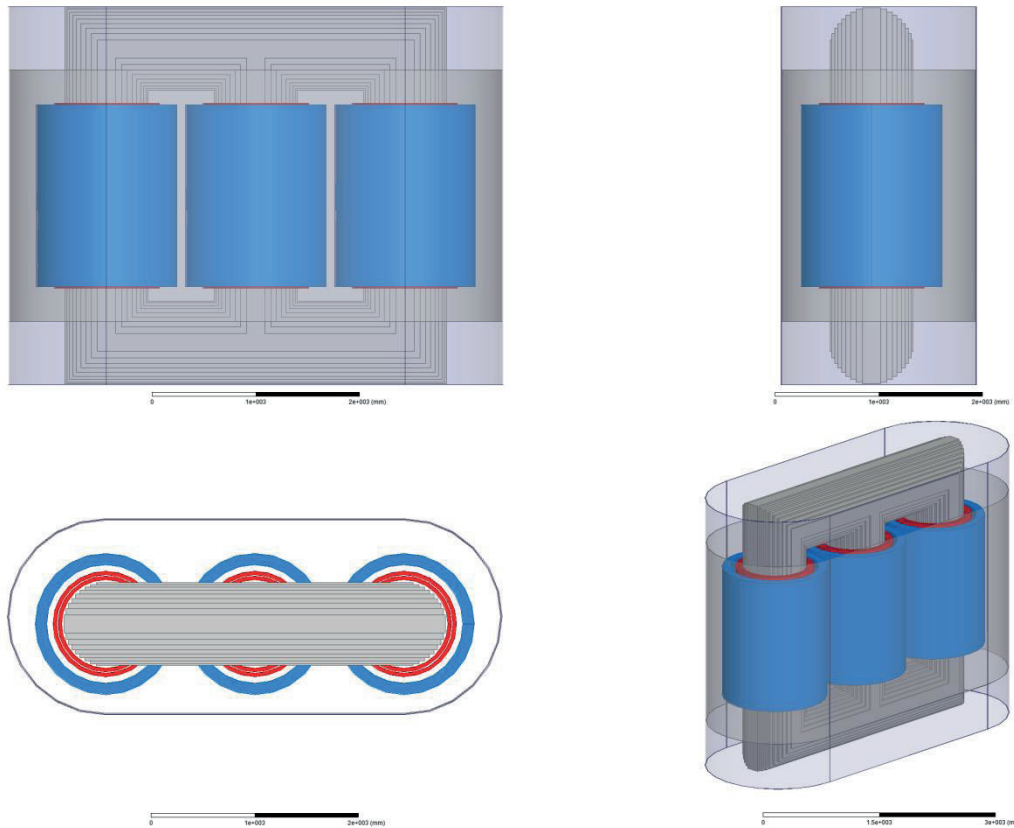


Figure 1 - Three dimensional model of example transformer

2.2. FEM models

For the purpose of zero sequence impedance finite element method calculation only the inner geometry of the transformer is important

2.2.1. 2D

Since set of zero sequence currents are equal and in phase and induced magnetic flux closes thru oil and tank, three phase transformer can be broken down in three independent single phase transformers without return limb and core yokes for purpose of calculation.

For two dimensional calculation transformer is presented with simplified axi-symmetric single phase geometry that consist of core leg, HV and LV windings and tertiary winding that represents a tank. In calculation with magnetic shield it is added in front of tank. Since the distance from windings to tank (shield) is not the same on HV and LV sides, tank is modeled on the mean distance from windings.

2.2.2. 3D

With three dimensional geometry full complexity of problem can be stressed with little simplification. For calculation of zero sequence impedance three dimensional geometry (figure 1) of transformer consists of three limb core, all windings and simplified tank and magnetic shield (if used in calculation).

2.2.3. Materials

Since resistivity is negligible compared to reactance in large power transformers only imaginary part of zero sequence impedance is calculated. Thus only important material characteristic for zero sequence reactance calculation is relative magnetic permeability. Materials used in FEM calculation are high permeability magnetic steel for core and shield, construction steel for tank and copper for windings.

3. CALCULATION

3.1. Current distribution problem

Magnetic flux that is pushed outside transformer core seeks lower reluctance path. In three phase Dyn transformers outer delta connected winding act as shield when inner star connected winding is energized with zero phase current, thus both windings have equal absolute ampere-turns. Otherwise in YNd transformers, where outer winding is star connected HV winding, when HV winding is energized with zero sequence current, tank acts like tertiary delta connected winding representing lower reluctance path for magnetic flux.

For calculating share of ampere-turns in secondary winding and tank (tertiary winding) expression for calculating reactive power of a system of windings can be used [1]. Primary winding (HV) is labeled with index 1, secondary winding (LV) with index 2, and tank with index 3.

$$Q = -\frac{1}{2} \sum_{k=1}^n \sum_{j=1}^n X_{jk} I_j I_k \quad (1)$$

$$Q = -\frac{1}{2} [2X_{12}I_1(-I_2) + 2X_{23}(-I_2)(-I_3) + 2X_{13}I_1(-I_3)] \quad (2)$$

Where: Q is reactive power,

X_{jk} is mutual reactance of pair of windings,

I_j and I_k are winding peak currents

Secondary and tank currents have negative value compared to primary current. If magnetizing current is neglected it can be stated:

$$I_1 = I_2 + I_3 \quad (3)$$

Since rated current flows in primary winding it has value of 1 per-unit ($I_1 = I_n \Rightarrow i_1 = 1 \text{ p.u.}$)

$$i_3 = 1 - i_2 \quad (4)$$

$$q = x_{12}i_2 - x_{23}i_2(1 - i_2) + x_{13}(1 - i_2) \quad (5)$$

The currents get distributed in the windings in such a way that the total energy is minimized. Hence, differentiating q with respect to current i_2 and equating it to zero results with:

$$\frac{dq}{di_2} = x_{12} - x_{23} + 2x_{23}i_2 - x_{13} = 0 \quad (6)$$

$$i_2 = \frac{x_{13} + x_{23} - x_{12}}{2x_{23}} \quad (7)$$

$$i_3 = \frac{x_{23} + x_{12} - x_{13}}{2x_{23}} \quad (8)$$

When reverted back to absolute value from per-unit value and reactance substituted with energy, since it is proportional, expressions become:

$$I_2 = \frac{W_{13} + W_{23} - W_{12}}{2W_{23}} I_1 \quad (9)$$

$$I_3 = \frac{W_{23} + W_{12} - W_{13}}{2W_{23}} I_1 \quad (10)$$

Where: W_{jk} denotes energy between winding pairs calculated with FEM

For calculation of reactance (in this case energy) for first pair of windings (HV and LV) excitation is defined as rated ampere-turns in HV and LV windings. Value is the same but directions are different. Procedure for the rest pairs is analog. In three dimensional calculations excitation in tank is three times greater due to the influence of all three phases. With calculated energy between pair of windings ampere-

turn distribution for zero sequence FEM model can be calculated using expressions 9 and 10. All calculations are done with the same geometry and in all calculations sum of ampere-turns must be zero. Magnetic shield represents lower reluctance path than oil and tank since it is made from high permeability magnetic steel and rises zero sequence impedance. In model it is represented with open circuit fourth winding that lowers induced current in tank [2]. Calculation of current distribution is same as described, only the fourth winding without any excitation is added in geometry for FEM.

3.2. Zero sequence impedance calculation

Finally zero sequence impedance can be calculated from obtained energy using expressions:

$$L_0 = \frac{2W_0}{I_1^2} \quad (11)$$

$$X_0 = 2\pi f L_0 \quad (12)$$

$$u_{0\%} = 100 \frac{S_n \cdot 2\pi f L_0}{U_n^2} \quad (13)$$

Where: W_0 denotes zero sequence energy calculated with FEM,

L_0 is zero sequence inductance,

S_n is rated power,

f is frequency,

X_0 is zero sequence reactance (impedance)

$u_{0\%}$ is percent zero sequence impedance

Defined procedures can be used to calculate zero sequence impedance of any power transformer or autotransformer.

4. RESULTS

All calculations were made using commercial Ansoft Maxwell v15 software for finite element method calculations on a two and three-dimensional computer model as magnetostatic problem. Four sets of calculations were done. Two dimensional calculations with and without magnetic shield, and three dimensional calculations with and without magnetic shield. Results obtained in calculations without magnetic shield on tank, regardless two or three dimensional method differ less than 2% from measured zero sequence impedance, while results obtained from calculation with magnetic shield are approximately 5% greater than measured ones.

Table 1 - measured and calculated values of zero sequence impedance

Zero sequence impedance	X_0 [Ω]	u_0 [%]
Measured	49,61	9,80
2D	48,95	9,66
3D	50,59	9,99
2D with magnetic shield	52,20	10,31
3D with magnetic shield	52,22	10,32

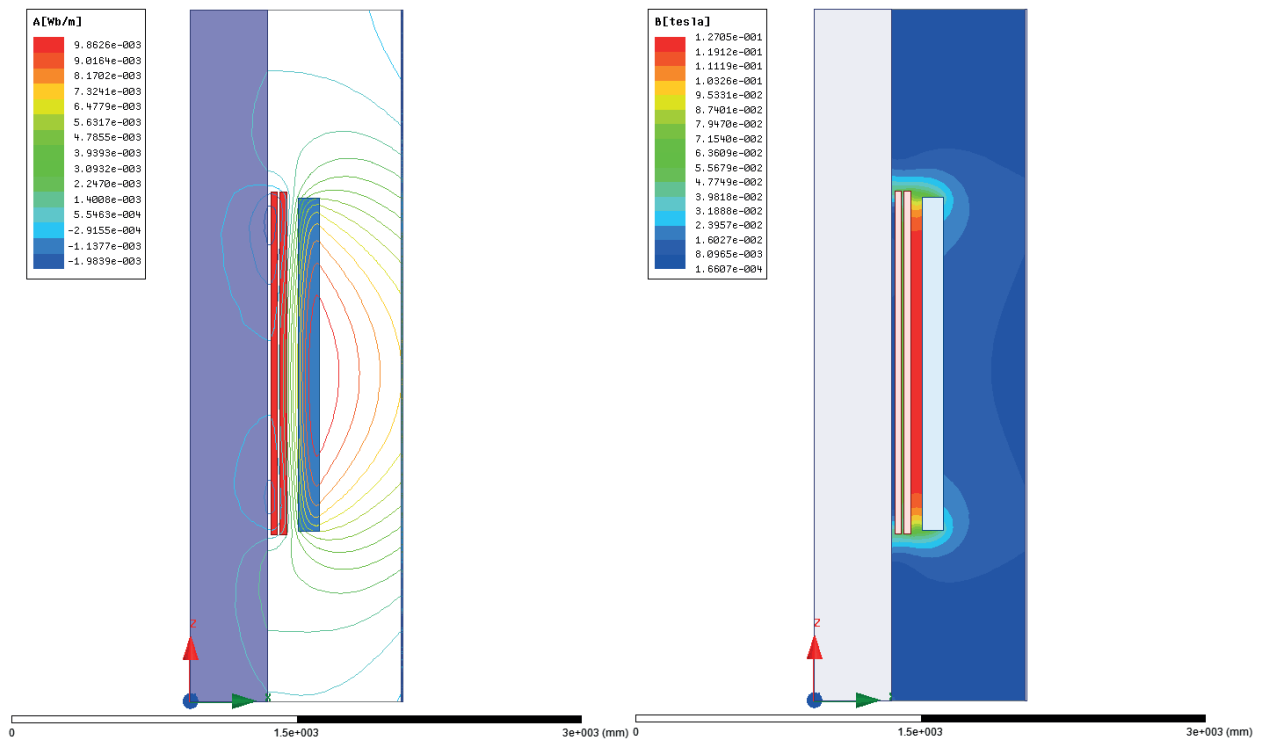


Figure 2 - magnetic flux and induction in 2D FEM model without magnetic shield

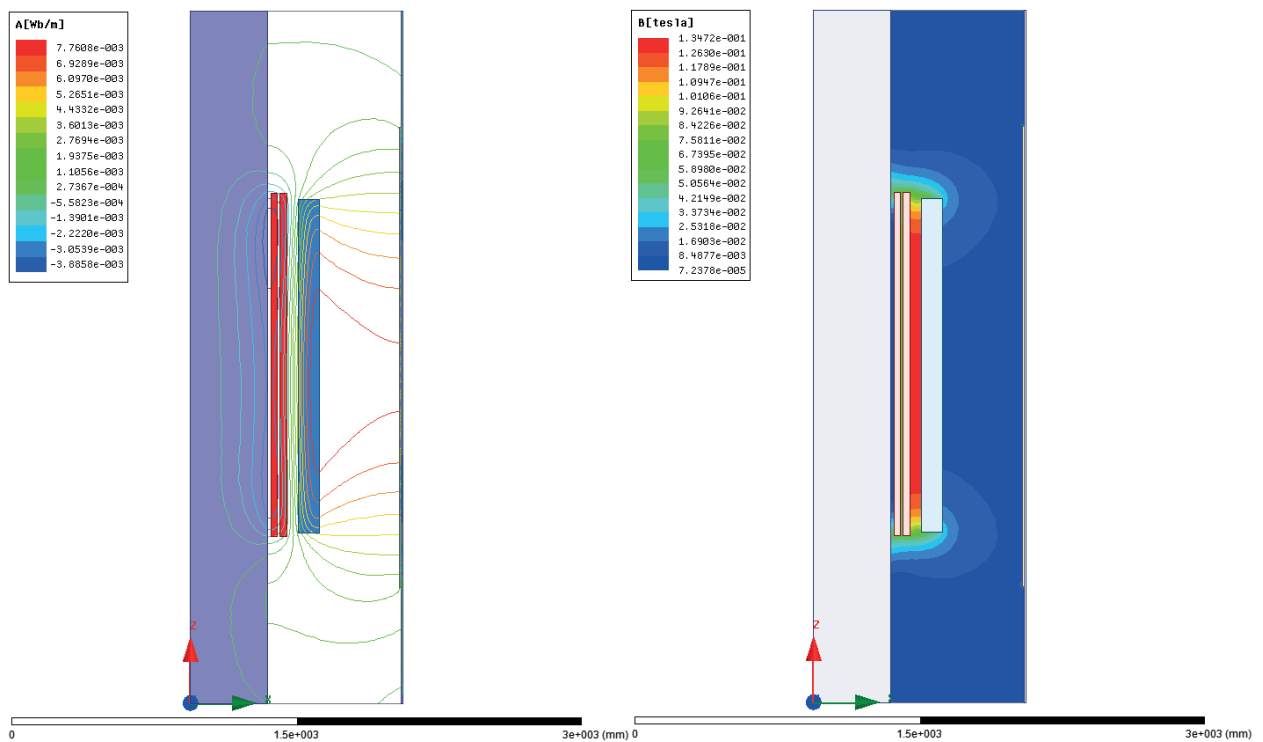


Figure 3 - magnetic flux and induction in 2D FEM model with magnetic shield

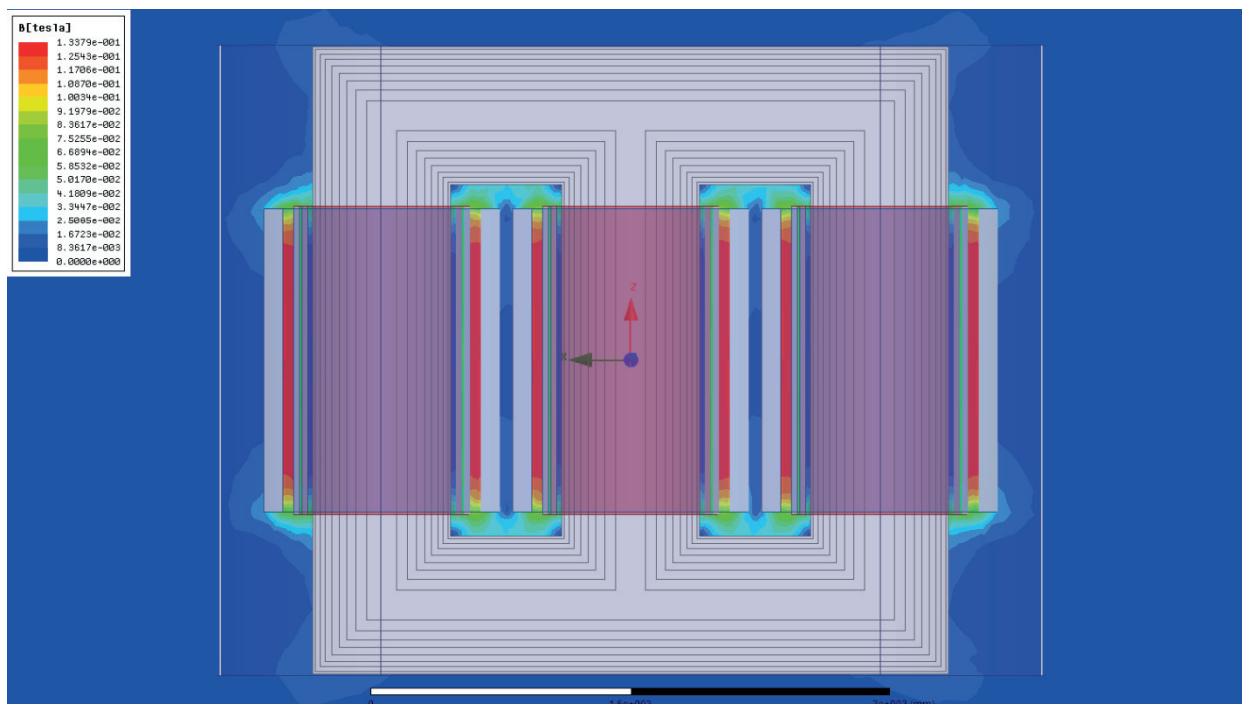


Figure 4 - magnetic induction in cross section of 3D FEM model without shield

Higher difference between measured and calculated values with magnetic shields is probably result of combination of nonlinear B-H curve and highly complex geometry of shields in real life compared to simplified geometry and material used in both 2D and 3D calculation.

5. CONCLUSION

Transformer zero sequence impedance value is important when calculating unsymmetrical short circuit currents and consequently short circuit forces especially in autotransformers. In this paper it is presented that zero sequence impedance of power transformer can be estimated using two dimensional or three dimensional finite element method calculation. Since the results in both 2D and 3D calculation are in good agreement with measured values, because of simplicity, 2D calculation without magnetic shield is recommended.

REFERENCES

- [1] Kulkarni, S.V.; Khaparde S.A.: „*Transformer engineering design and practice*“, Marcel Dekker, New York, 2004.
- [2] Ngnegueu; Mailhot; Munar; Sacotte: „*Zero Phase Sequence Impedance and Tank Heating Model for Three Phase Three Leg Core Type Power Transformers Coupling Magnetic Field and Electric Circuit Equations in a Finite Element Software*“, IEEE transactions on magnetics, vol. 31, #3, May 1995.

Saravanan Selvaraj
Crompton Greaves Ltd. India
Saravanan.Selvaraj@cgglobal.com

Geert Caluwaerts
CG Power Systems. Belgium NV.
Geert.Caluwaerts@cgglobal.com

Rafiq Mathersa
Crompton Greaves Ltd. India
Rafiq.Mathersa@cgglobal.com

Dr. Ronny Mertens
CG Power Systems. Belgium NV
Ronny.Mertens@cgglobal.com

Mahesh B. Varrier
Crompton Greaves Ltd. India
Mahesh.Varrier@cgglobal.com

INVESTIGATION OF IMPACT OF MAGNETIC SHUNT PARAMETERS ON TEMPERATURE DISTRIBUTION IN TRANSFORMER TANKS

SUMMARY

A set of reduced order models are developed to validate finite element based calculation of temperature distribution in solid and laminated magnetic structures in transformers with high current carrying conductors. Model details, measured and calculated losses and temperature of the models are presented. Effect of magnetic shunt type and its alignment with respect to stray flux direction on temperature distribution in the reduced order model are analyzed.

The magneto-thermal coupled field analysis methodology is applied to estimate the temperature distribution in Multi-Utility transformer, showed temperature higher than expected. Different cases of tank cover plate with electromagnetic shield, thicker magnetic shunts, and with non magnetic cover plate are analyzed to reduce the temperature.

With the modified shunt arrangement, the transformer passed the test as temperature were reduced by 100°C.

Key words: Transformer, HCCC, Stray losses, Magnetic shunts, FEM, Magneto-Thermal.

1. INTRODUCTION

Magnetic leakage flux emanating from the windings closes through tank and core clamps. Stray field from heavy current carrying conductor (HCCC) distributes along its length and passes through the magnetic structures [1]. As the rating of the transformer increases above 150 MVA, the magnetic leakage field strength increases proportionately [2]. This not only increases losses but also leads to local hot spots and hence shortens insulation's life. In transformers like furnace transformers, generator transformers, multi-utility transformers, excessive temperature rise can occur as a result of stray fields from HCCC. Magnetic shunts and electromagnetic shields are used to reduce the losses in core clamping structure and transformer tank. To reduce eddy current losses generated by field of constant flux i.e. winding leakage flux, magnetic shunts are widely used. The losses generated by field of constant excitation i.e. field from HCCC, can be reduced by (a) changing to non magnetic material (b) using magnetic shunts and (c) using electromagnetic shields [1]. The magnetic shunt parameters like arrangement, geometry and placement has to be selected carefully otherwise it may increase temperature of tank portions in between the shunts and also near its ends. For optimal selection of those parameters, prediction of

magnetic flux distribution in the solid and laminated magnetic structures are vital. For accurate estimation of magnetic flux distribution in solid magnetic structures, nonlinear surface impedance formulation (SIBC) is widely used [8,9] and is incorporated in most of the commercial FEA packages. Modeling of magnetic shunts and electromagnetic shields using Finite Element Software are explained in [4,7].

In this research, to improve the accuracy of Finite Element Calculations with magnetic shunts, experiments are done with a reduced order model representing magnetic structures in stray field from HCCC. The influence of shunt parameters on losses and temperature rise in the magnetic plate are tested. Based on the results, an accurate magneto-thermal coupled field analysis methodology for calculating temperature rise in magnetic structure is developed.

With that improved calculation methodology, temperature distribution in cover plate of a 440 MVA multi-utility transformer is evaluated

2. ANALYSIS METHODOLOGY

For a realistic simulation of the magnetic field distribution in magnetic structures in transformer, the computer model needs to be validated with experiments. Due to difficulties with measurement in power transformers, reduced order model representing different phenomena in transformer are widely used [3,5,6]. Such models for verifying the stray fields from HCCC are developed. To improve accuracy of calculations, properties of the Mild Steel plate and M4 grade CRGO steel sheets are measured using Electrical Steel Tester from BROCKHAUS Measurements and are used in FEA. For electromagnetic calculations and coupled field magneto thermal calculations, MagNet software and ThermNet software are used. In this section, experimental validation of calculation of temperature distribution in solid magnetic structures and laminated magnetic structures are discussed.

2.1. Bus bar- Magnetic Plate Model.

In first set of experiments, losses generated in MS plate due to magnetic field generated by copper busbar is measured. To ascertain repeatability of loss measurements, the tests are conducted at various current (1 kA- 4 kA) in the busbar and at various distances between bar and plate. Figure 1a shows the geometric details of the model. The losses in the plate is measured based on the procedure mentioned in [5]. Temperature distribution on surface of the plate is measured using Type J Thermocouples and position of the thermocouples are also shown in Figure1. Six thermocouples are fixed on MS plate and three thermocouples are used for measuring ambient temperature. Temperature is measured at regular intervals (≈ 30 minute) upto steady state condition.

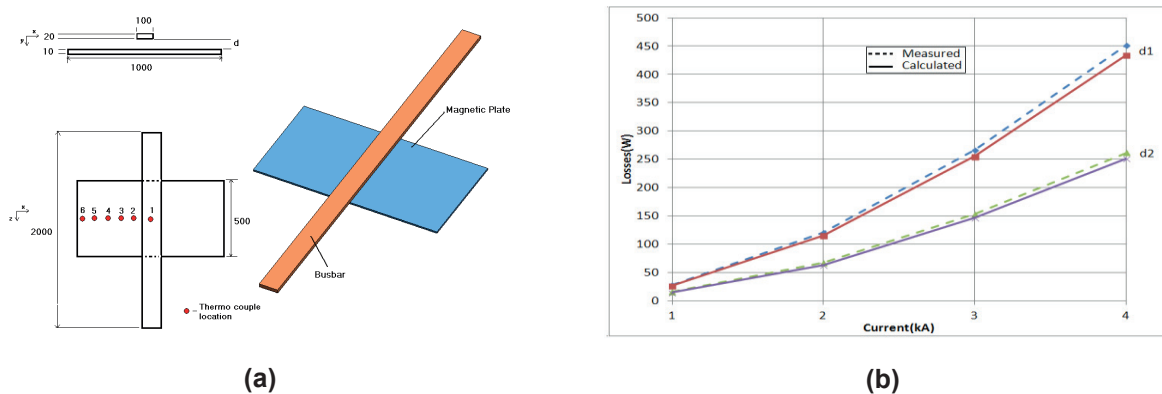


Figure 1. (a) Bar Plate model; (b) Comparison of Plate Losses

The eddy losses generated in the MS plate are calculated using non linear SIBC. Figure 1b shows the variation of the plate loss with the current and distance. Also it is clear that the calculated values are in close agreement with measured one. As shown, the losses increases squarely proportional with current flowing in the bar and to $d^{-0.5}$, where d is the distance between the bar and the plate. These data reconcile the curves published in [10].

For temperature calculation, thermal analysis of the MS plate is coupled with magnetic field analysis. In the magnetic field analysis, the eddy losses are calculated by considering the temperature dependent resistivity of MS plate. Heat transfer in the MS plate is caused mainly by natural convection

and radiation. For MS plate, natural convection heat transfer coefficient (h) is calculated using the dimensionless natural convection correlations. Figure 2a shows the temperature at the thermocouple locations with respect to time. Temperature of the MS plate reaches steady state after 3 hours. Temperature is highest in the portion of the MS plate closest to the bar and in this arrangement it decays to minimum beyond a distance of about 300 mm. Since the analysis is done with approximate h values, the calculated temperatures are slightly lesser than the measured one.

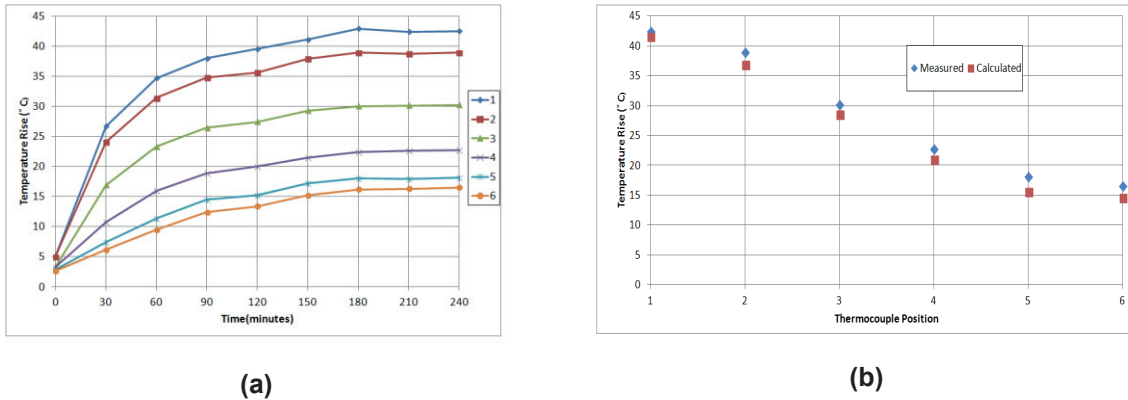


Figure 2. (a) Temperature rise at Thermocouple Positions; (b) Comparison of Temperature rise

2.2. Bus bar- Magnetic Plate and Magnetic Shunt Model.

In second set of experiments, losses generated in MS plate, shielded with width wise magnetic shunt, due to magnetic field generated by copper busbar is measured. To ascertain reduction of plate losses, losses generated in the magnetic shunts are measured separately. Figure 3a shows the geometric details of the model.

Temperature distribution on surface of the plate is measured using Type J Thermocouples and position of the thermocouples are also shown in Figure 3a. Apart from six thermocouples in MS plate, two thermocouples are placed on top surface of magnetic shunt. Temperature is measured at regular intervals (≈ 30 minute) upto steady state condition. The laminated magnetic shunts are modeled as a homogenous volume having anisotropic permeability and conductivity. Figure 3b shows variation of the plate loss with current. Also it is evident that calculated values are in close agreement with measured one. By comparing Figure 1b & 3b, it is apparent that the magnetic shunts significantly reduces ($\approx 65\%$) losses in the magnetic plate.

Thermal analysis is done similarly as explained in the previous section. For magnetic shunts, natural convection heat transfer coefficient is calculated separately and thermal conductivity is calculated based on its volume ratio. Figure 4a shows the temperature at the thermocouple locations with respect to time. Temperature of the MS plate and magnetic shunt reaches steady state after 3 hours.

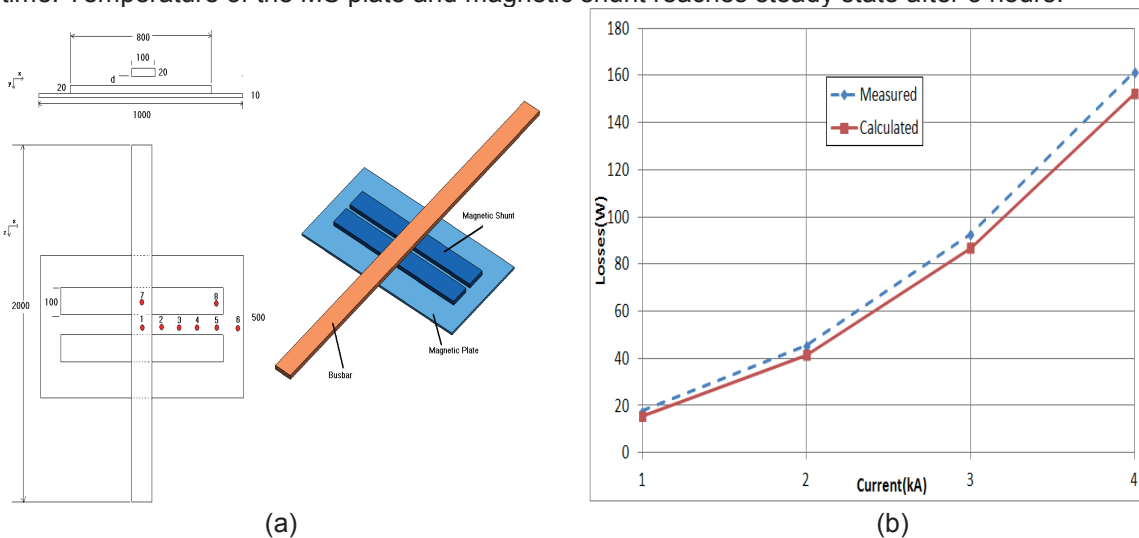


Figure 3. (a) Bar Plate Shunt model; (b) Comparison of Plate & Shunt Losses

In contrast to Figure 3a, temperature is lowest in the portion of the MS plate closest to the bar and in this arrangement it increases to maximum near the ends of the shunt. Whereas in the magnetic shunt, temperature is maximum near the busbar and minimum at its ends. This is due to the eddy currents generated in the top laminations. From Figure 2b & 4b, it is evident that with magnetic shunts, hotspot temperature in the MS plate is significantly reduced ($\approx 40\%$). Since the analysis is done with approximate h values and shunt model, the calculated temperatures are lesser than the measured one.

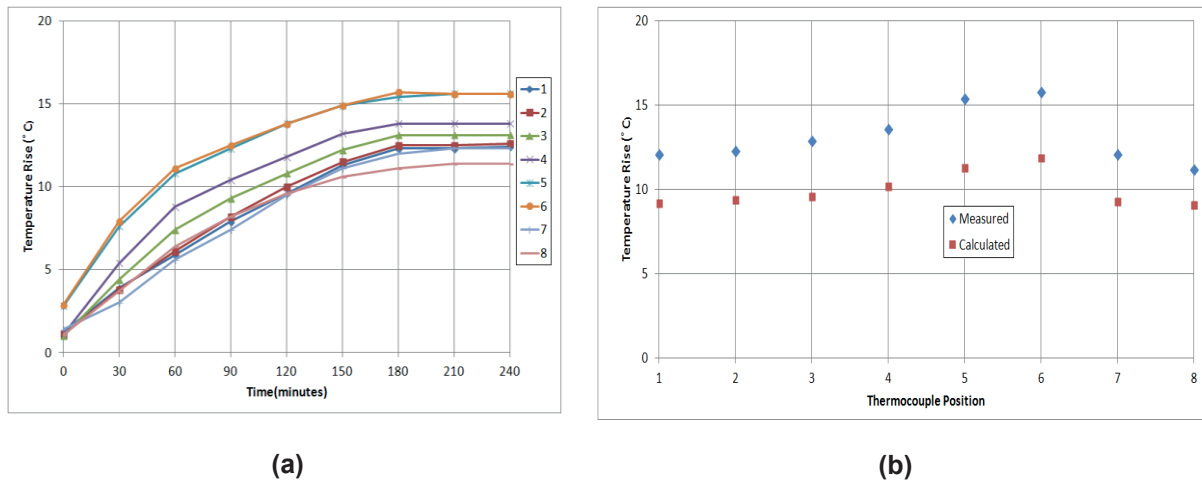


Figure 4. (a) Temperature rise at Thermocouple Positions; (b) Comparison of Temperature rise

The discussion in this section demonstrates the validity of the analysis methodology for temperature distribution in the magnetic structures.

3. RESULTS AND DISCUSSION

3.1. Effect of Magnetic Shunt Type & Alignment.

Based on the arrangement, the magnetic shunt type is referred as width-wise or edge-wise when plane of laminations is parallel or perpendicular to the tank wall respectively. As mentioned in [11], effectiveness of widthwise shunts are lesser than edge wise shunts due to its lower effective permeability. Also significant reduction of stray losses in 360 MVA/500 kV transformer with edge wise shunts is [2]. But in both the cases, stray losses due to winding leakage flux is considered and electromagnetic shield is recommended for field from HCCC [11]. Since usage of electromagnetic shield for reducing losses due to HCCC is not economical, mainly magnetic shunts are used in large power transformers.

Apart from the shunt type, alignment of shunts with respect to leakage flux direction is also important parameter. Hence for checking sensitivity of shunt type and its alignment direction on temperature distribution in magnetic plate, model shown in figure is analyzed using the methodology discussed in previous section. In figure 5a & 5b, the magnetic shunts are aligned parallel & perpendicular to magnetic flux direction respectively.

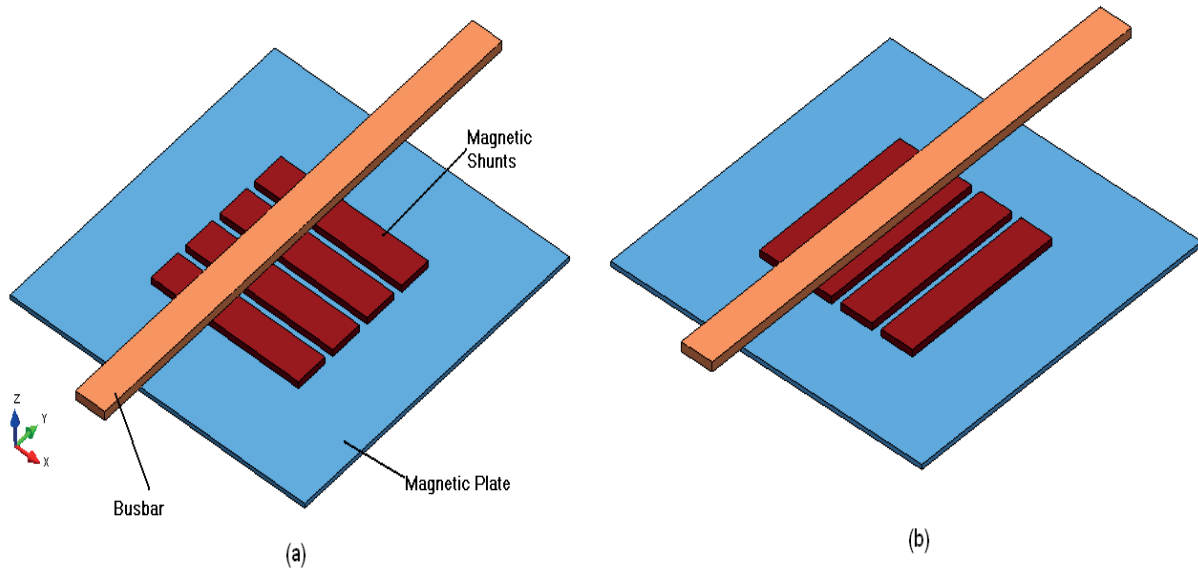


Figure 5. (a) Bar plate with parallel magnetic shunts; (b) bar plate with perpendicular magnetic shunts

Table 1. Effect of shunt arrangement of losses and temperature

Configuration	Plate losses (W)	Maximum loss density in plate (kW/m^2)	Maximum temperature in plate ($^{\circ}\text{C}$)
Without shunt/shield	464.3	1.8	67.3
Width wise Parallel	230.1	2.8	46.8
Edge wise Parallel	256	2.4	52.3
Width wise Perpendicular	341.6	3.1	57
Edgewise Perpendicular	476	1.9	76

For each configuration, losses, loss density and temperature in the magnetic plate are calculated and reported in Table 1. It manifest that the shunts, particularly edgewise shunts, kept perpendicular to leakage flux direction results in higher losses and hotspot temperatures. In width wise perpendicular case, the maximum temperature is observed between the shunts because of maximum incident flux in those regions. In remaining cases it is observed near the shunt ends.

3.2. Case Study.

Multi-Utility transformer is typically designed to accommodate various load connection configurations and various output voltage requirements. Multiple Go-Return Busbars are connected to the Low Voltage winding circuitry to achieve these requirements and excessive losses are generated in the magnetic structures in vicinity of these HCCC.

In this particular transformer, the HCCC are placed above the active parts and are closer to cover plate. Based on the incident flux density on the cover plate, magnetic shunts are designed and attached to the cover plate. During heat run test, the transformer is failed due to extreme hotspots on the cover plate. In order to troubleshoot the hotspot issues, initially stray flux distribution and temperature distribution in the cover plate are calculated without magnetic shunts and with magnetic shunts. Figure 6 shows comparison of calculated and measured temperature distribution in the cover plate. In the portion of the tank between shunts and near its ends higher temperature is observed. Basis for these excessive temperature can be appreciated from the results from previous part of this section. It is obvious that analysis methodology calculates temperatures close to measured one.

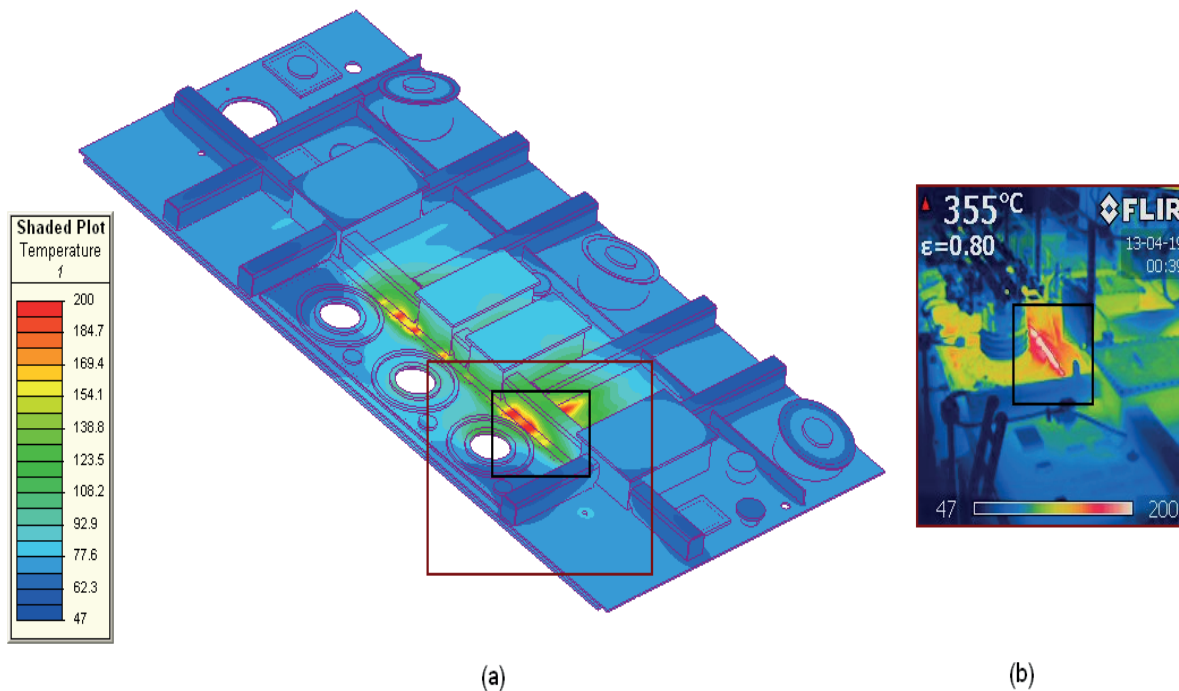


Figure 6. (a) Temperature distribution in cover plate; (b) Thermo graphic

Then various alternatives viz. nonmagnetic cover plate, copper shields, magnetic shunt with higher thickness etc.. are analyzed to reduce the hot spot temperature . From these , a cost effective & feasible solution is selected and is implemented in the transformer cover .

Temperature distribution on the cover plate calculated with modified shunt arrangement is shown in Figure 7. By comparing Figure 6a & 7 , it is clear that significant reduction (100°C) of hotspot temperature is achieved with the modified shunts. Finally the transformer is tested with modified shunt arrangement and it successfully cleared the heat run test. It is observed that the measured temperatures are well below the guaranteed values.

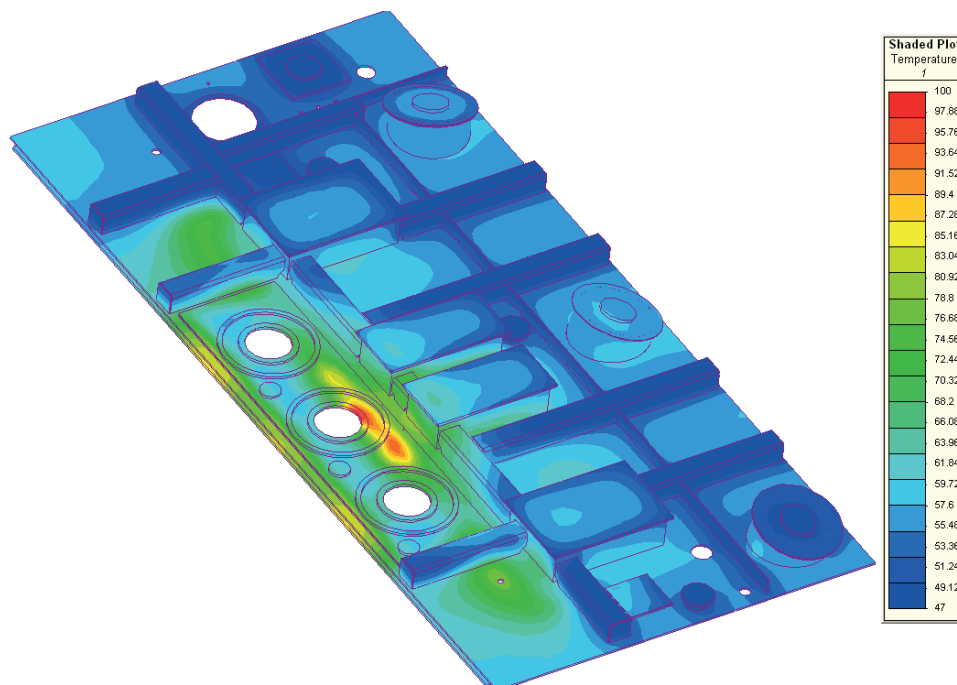


Figure 7. Temperature distribution in cover plate with modified shunt arrangement.

4. CONCLUSION

FEA calculations are validated using reduced order models. The results from reduced order models and transformer signifies the usages of magneto thermal coupled field FEA, for accurate prediction of temperature distribution in solid and laminated magnetic structures. The calculated losses and temperature are in close agreement with measured datas. Magnetic shunts , even though used for reducing losses, generates hotspots in transformer tanks due to its inappropriate arrangement.

REFERENCES

- [1] Yang Junyou et al., New Preventive Measures against Stray Field of Heavy Current Carrying Conductors, IEEE Trans. Magn. vol. 32, No. 3, pp. 1489-1492, 1996.
- [2] Chen Yongbin et al., Study on Eddy Current Losses and shielding Measures in Large Power Transformers, IEEE Trans. Magn. vol. 30, No. 5, pp. 3068-3071, 1994.
- [3] Problem 21 family and Experimental Verification, IEEE Trans. Magnetics., Vol-40, No. 2, pp. 1394-1397, 2004.
- [4] Barton, Loss calculation in Laminated steel utilizing Anisotropic Magnetic Permeability, IEEE Trans. Power Apparatus and Systems., Vol-99, No. 3, pp. 1280-1287, 1980.
- [5] Cheng et al., Large Power Transformer-Based Stray-Field Loss Modeling and Validation, IEMDC., pp. 548-555, 2009.
- [6] Cheng et al., TEAM Problem 21 Family, Compumag., 2009.
- [7] Sumei Yang et al., The Stray Loss on Magnetic Shielding in Power Transformers, 6th WSEAS International Conference on Applied Computer Science, pp. 420-425, 2007.
- [8] S.A.Holland et.al., Calculating stray losses in power transformer using surface impedance with finite elements, IEEE Trans. Magnetics., Vol-28, No. 2, pp. 1355-1358, 1992.
- [9] Janne Nerg et. al., "A Simplified FEM Based Calculation Model for 3-D Induction Heating Problems Using Surface Impedance Formulations", IEEE Trans. Magnetics., Vol-37, No. 5, pp. 3719-3722, 2001.
- [10] K. Karsai, D. Kerenyi and L. Kiss, Large Power Transformers, Elsevier, Amsterdam-Oxford-York, 1987.[11] S. V. Kulkarni & S. A.Khaparde, Transformer Engineering – Design and Practice, Marcel Dekker, New York 2004.
- [11] S. V. Kulkarni & S. A.Khaparde, Transformer Engineering – Design and Practice, Marcel Dekker, New York 2004

Ralf Wittmaack
Siemens AG, Nürnberg, Germany
Ralf.Wittmaack@Siemens.com

CFD SIMULATION OF PRESSURE LOSS IN HVDC TRANSFORMER WINDING

SUMMARY

At Siemens the in-house CFD code UniFlow is used to analyse fluid flow and heat transfer in oil-immersed and dry-type transformers, as well as transformer components like windings, cores, tank walls, and radiators. It can be employed to perform steady state as well as transient analyses. This paper describes its physical models and numerical solution methods.

Moreover, it presents an application to a valve winding of a HVDC transformer, cooled by mineral oil. This study is aimed at finding the flow induced pressure loss in the winding and the static ring assembly below and above the winding. The investigation includes isothermal runs with different inlet velocity and a conjugate heat transfer run with a conductor representation.

In the isothermal simulations a steady state is established and the pressure loss is an almost linear function of the inlet velocity. In the run involving heat transfer, the high buoyancy forces hamper the development of a steady state and the possibility to calculate a flow induced pressure loss.

Key words: Thermal design, CFD, pressure loss, physical models, numerical methods

1. INTRODUCTION

Thanks to its flexibility and accuracy, CFD (Computational Fluid Dynamics) is increasingly being used to analyse transformer thermal design. This follows the trend established in other branches of advanced technology development like aerospace, automotive, and power generation, where CFD simulations are indispensable parts of the product development cycles.

Employing commercial CFD codes, several detailed studies of disc-type transformer windings were performed, e.g., by [1] and [2]. Moreover, extended full geometry CFD analyses coupled to electrodynamic simulation of the load and no-load losses in core and windings were presented, e.g., by [3], [4]. Furthermore, combined oil and air flows in fin-type distribution transformers were investigated with commercial CFD codes, e.g., by [5], [6].

Our intention is to provide a simulation method that may be used for detailed CFD analyses on fine grids as well as for simplified coarse grid studies. The in-house code UniFlow is designed to be applicable also by users with limited experience in CFD. For this reason, e.g., material attributes are employed for a convenient coupling of fluid and solid regions in conjugate heat transfer simulations.

2. PHYSICAL MODELS AND NUMERICAL METHODS

2.1. Physical models

Our physical model is aimed at investigating flows with several kinds of heat transfer in a complex geometry. It simulates the flow of single-component, incompressible, Newtonian fluids in a three-dimensional geometry. In addition to the fluids, that may be in gaseous or liquid state, several structural materials are considered as hydrodynamic obstacles and thermodynamic heat structures. The hydrodynamics is described by the continuity and the Navier-Stokes equation. For the simulation of turbulence the algebraic Baldwin-Lomax eddy viscosity model [7] is available. To simulate the transition between laminar and turbulent flows, algebraic transition models of Drela [8] and Mayle [9] are on hand.

For temperature dependent density or material properties of the viscous stress tensor, the hydrodynamics of the fluid is coupled to the thermodynamics. For this reason, internal heat transfer (by convection and conduction) and heat generation by internal sources as well as heat transfer to the surroundings are modelled via a heat transport equation. To allow for the simulation of phase transitions it is provided in enthalpy formulation. At the rigid boundaries heat conduction is considered. For coarse grids convective heat transfer coefficients may be employed at solid-liquid interfaces. Radiant heat transfer is simulated at structural material surfaces. The material properties (density, dynamic viscosity, specific heat at constant pressure, heat conductivity, and convective heat transfer coefficient) depend on the temperature. Solids may have orthotropic heat conductivity.

2.1.1. Dynamic equations

Our dynamic equations are written in Cartesian coordinates. The continuity equation for incompressible flow is [10]

$$\frac{\partial}{\partial x^m} (\rho v^m) = 0, \quad (1)$$

where ρ is density and v velocity. x are the space coordinates and we use Einstein's summation convention for the space direction index m . Introduction of the continuity equation into the Navier-Stokes equation [10] leads to a momentum equation in strong conservation form

$$\rho \frac{\partial v_i}{\partial t} + \frac{\partial}{\partial x^m} \left[\rho v_i v^m - \mu \left(\frac{\partial v_i}{\partial x_m} + \frac{\partial v^m}{\partial x^i} \right) \right] = - \frac{\partial p}{\partial x^i} + \rho g_i, \quad (2)$$

where t is time, p pressure, and g gravitational acceleration. After inclusion of the continuity equation our heat transport equation in strong conservation form reads

$$\rho \frac{\partial h}{\partial t} + \frac{\partial}{\partial x^m} \left(\rho h v^m - \lambda \frac{\partial T}{\partial x_m} \right) = P_d. \quad (3)$$

Here h is specific enthalpy, T temperature, λ heat conductivity, and P_d density of the heat sources or sinks.

2.1.2. Radiant heat transfer model

Radiant heat transfer may be simulated between structural material surfaces adjacent to the fluid. The employed radiation model assumes that the radiating surfaces are boundaries of a hollow space with linear dimension much greater than their distance. It is applicable for, e.g., parallel plates and concentric cylinders. With this simplifying assumption the power received by surface 'a' via the heat transfer from surface 'b' is [11]

$$P_{ab} = c_{ab} A_a (T_b^4 - T_a^4); c_{ab} := \frac{\sigma}{\frac{1}{\varepsilon_a} + \frac{A_a}{A_b} \left(\frac{1}{\varepsilon_b} - 1 \right)}. \quad (4)$$

Here A is area of radiating structural material, T surface temperature, $\sigma = 5.67051 \cdot 10^{-8} \text{ W}/(\text{m}^2 \text{ K}^4)$ Stefan-Boltzmann constant, and ε emissivity of a structural material surface. Computation domain nodes undergoing radiant heat transfer may have their radiation partner nodes inside the computation domain or at the boundary.

2.2. Numerical methods

For the numerical representation of our model we developed a finite volume method and employ boundary fitted, curvilinear, non-orthogonal, block-structured grids. The blocks may be connected via 1-to-1 or patched couplings. The arrangement of the dynamic variables in the control volumes of the grid is collocated at the node centre. The dynamic equations are solved sequentially. For the solution of the momentum, pressure-correction, and heat transport equations we use implicit schemes. The system of continuity and momentum equations is solved by a SIMPLE [12], SIMPLER [13], or PISO [14] algorithm.

To speed up the code execution and to simplify the estimation of discretisation errors a FAS multi-grid algorithm is employed [15]. It is a geometric approach with standard coarsening applied to the outer iterations, visiting the grid levels in V-cycles. For steady-state problems it operates as a full multi-grid algorithm (FMG), whereas for transient problems the algorithm starts at the finest grid.

For the efficient solution of sparse linear equations several algorithms are available. The parabolic momentum and heat transport equations may be solved with SIP solvers that are modified to handle block couplings via the residual vector [12]. Additionally, for the elliptic pressure-correction equation an aggregation-based algebraic multi-grid algorithm [16] is available.

The UniFlow source code is written in C++. For multi-threaded shared memory parallelism, OpenMP is employed. In addition, for distributed memory parallelisation MPI is used.

3. APPLICATION TO PRESSURE LOSS IN WINDING OF HVDC TRANSFORMER

In this section we analyse the pressure loss in the valve winding of a HVDC transformer cooled by mineral oil. We consider natural convection of the oil, i.e., the ON cooling mode. As only a part of the natural convection loop is simulated, we employ in- and outlet boundary conditions at the entry and exit to the labyrinth.

3.1. Geometry model

Our geometry model covers the winding and its system of static rings below and above the winding. We simplify the geometry of the oil regions in the labyrinths by removing those outer parts that provide a negligible contribution to the oil flow. Furthermore, the winding geometry is simplified by considering a two-dimensional Cartesian coordinate system, where x designates the radial and z the vertical space direction. Some geometry data are listed in the table below.

Table I – Geometry data of winding

Variable	Unit	Value
Inner radius of winding	m	0.887
Outer radius of winding	m	1.059
Bottom of winding	m	0.2
Top of winding	m	2.2655
No. of coils	-	68

3.2. Grids

The following table lists some properties of the block-structured, hexahedral grids employed in our simulations. The 1st of these grids is used for the hydrodynamic runs while the 2nd grid includes a representation of the winding in addition.

Table 2 – Data of block-structured, hexahedral grids

Variable	Unit	Hydrodynamic runs	Coil representation
No. of blocks	-	259	55
No. of nodes	-	1464960	3475584
No. of fluid nodes	-	1464960	1464960
Node lengths	mm	0.16 – 0.97	0.16 – 0.97

The table shows only data of the finest geometric multi-grid level. However, 3 grid levels are used to investigate the influence of the discretisation error. Furthermore, they allow for Richardson extrapolation [12], to estimate grid independent solutions.

3.3. Boundary conditions

We consider oil velocities at the inlet of 1, 5, and 10 mm/s. The oil inlet temperature is $T_i = 343$ K. In the conjugate heat transfer simulation, adiabatic conditions are assumed at all computation domain boundaries, except the in- and outlet. Moreover, in the conjugate heat transfer run the power density of the losses in the coils is $P_d = 40.29$ kW/m³.

3.4. Properties of oil flow and estimation of boundary layer thickness

The following table lists some general properties of the oil flow. These were calculated with the half length of the longest horizontal oil flow path in the sealing ring of 0.114 m as characteristic length l , the highest considered oil inlet velocity of 10 mm/s, and the oil inlet temperature of 343 K.

Table 3 – Properties of oil flow and boundary layer thickness

Variable	Unit	Value
Reynolds number	-	300
Prandtl number	-	50.85
Hydrodynamic boundary layer thickness	mm	6.6
Thermodynamic boundary layer thickness	mm	1.8

The upper limits of the hydro- and thermodynamic laminar boundary layer thickness are estimated by

$$\delta_h \propto \frac{l}{\sqrt{R}}; \quad \delta_t \propto \delta_h Pr^{\frac{1}{3}}, \quad (5)$$

[10]. Here R is Reynolds' number and Pr Prandtl's number. According to [17], for the flow along a plate the transition from laminar to turbulent boundary layer flow occurs between $R = 3.5 \cdot 10^5$ and 10^6 . The location depends on the free stream degree of turbulence (f_{sti}). As the Reynolds number of the oil flow in the transformer winding is much below the critical range, we assume that it is laminar.

Comparison of table 2 and table 3 shows that our grids are fine enough to adequately resolve the hydrodynamic and thermal boundary layers.

3.5. Results of hydrodynamic simulations

In our hydrodynamic simulations a steady state is established. The oil temperature is the inlet temperature of 343 K in the entire computation domain. The figures in this section all refer to the run with an oil inlet velocity of 10 mm/s.

The Cartesian components of the oil velocity in the static ring labyrinth below the winding are shown in the figure below. As a result of the low oil velocity, the meandering flow is more pronounced at the inner than at the outer sides of the curves. A similar result is obtained in the upper labyrinth.

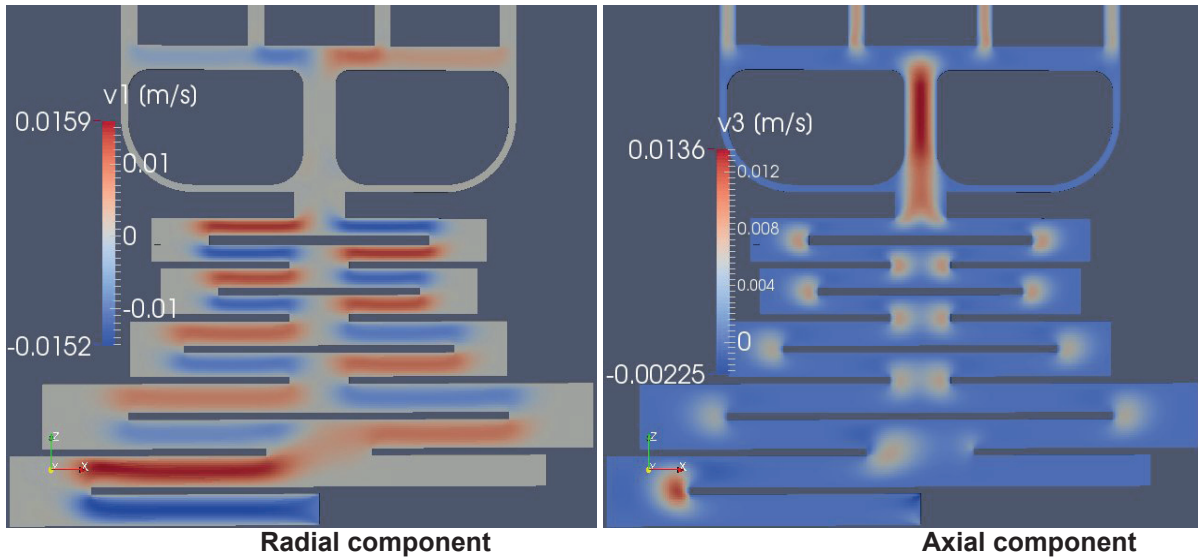


Figure 1 – Velocity in lower labyrinth of hydrodynamic simulation

The next figure shows that the calculated velocity in the winding is most pronounced in the axial oil channels and oriented almost exclusively vertically. Compared to the axial oil flow, the flow in the radial channels is negligible.

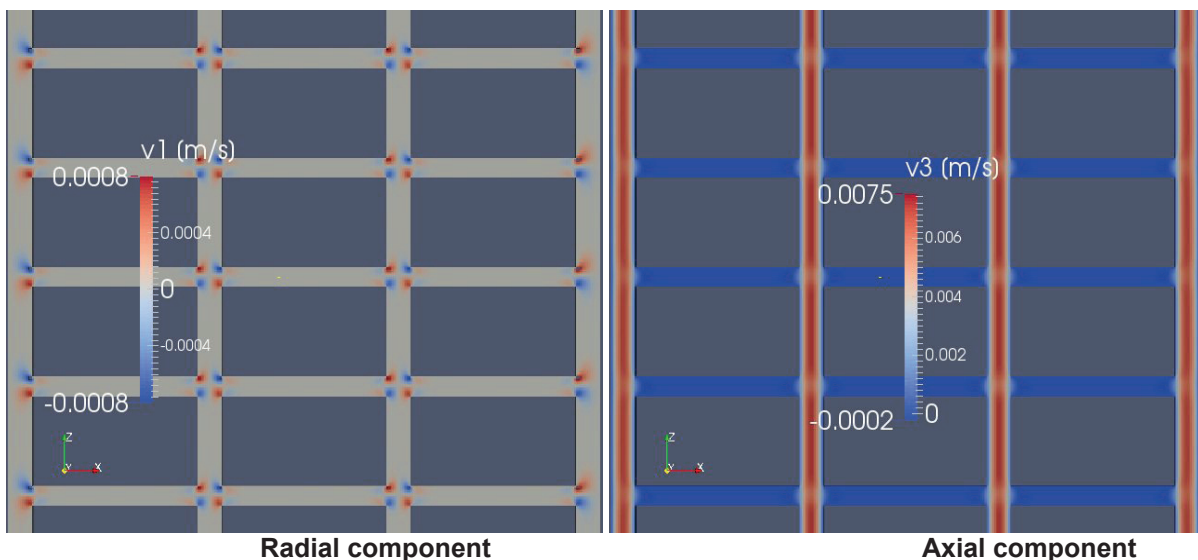


Figure 2 – Velocity in winding section of hydrodynamic simulation

The related spatial distribution of the pressure variable of the oil in the entire model and at the labyrinth below the winding is shown in the following figure. In hydrodynamic runs our pressure variable

$$p_g := p - \rho_0 g_i (z_{\max} - z); \rho_0 := \rho(T_0) = 841.2 \frac{\text{kg}}{\text{m}^3}. \quad (6)$$

omits the hydrostatic contribution to the pressure.

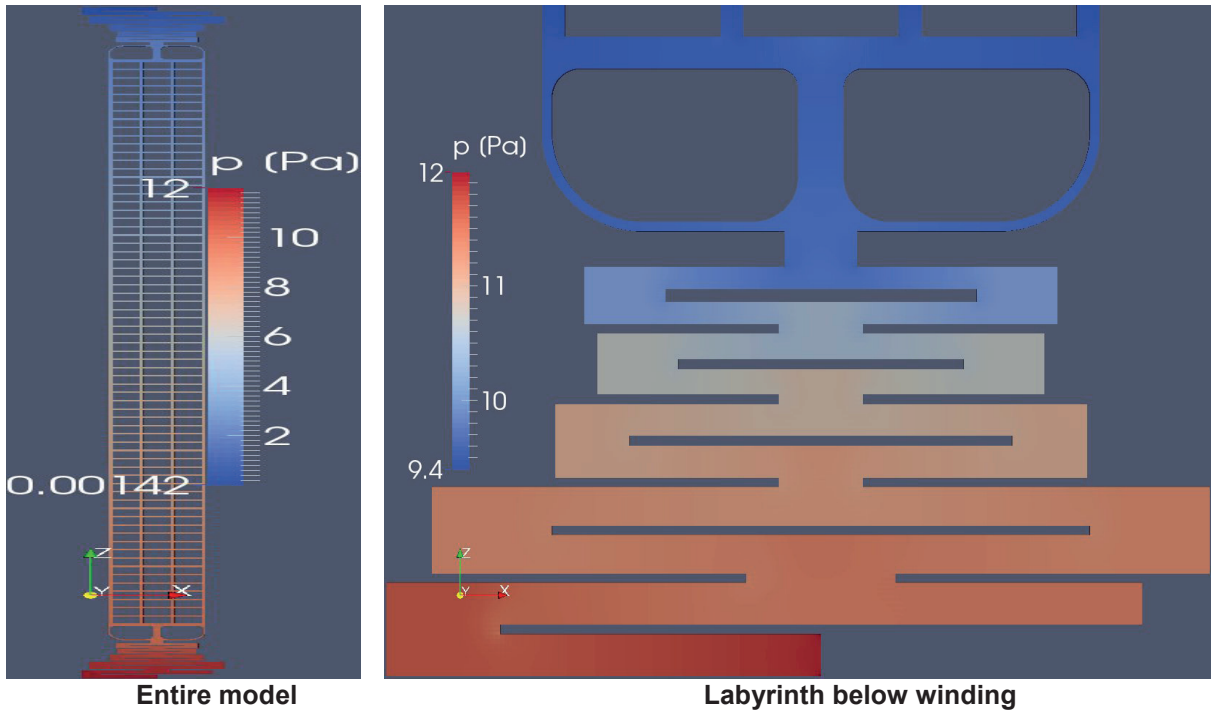


Figure 3 – Pressure variable of hydrodynamic simulation

The following table provides a list of the calculated oil flow induced pressure loss, as a function of the inlet velocity. It shows, as well as figure 4, that the dependence of the pressure loss on the inlet velocity is almost linear. Linear dependence corresponds to Hagen Poiseuille flow [10].

Table 4 – Pressure loss in hydrodynamic simulations

Inlet velocity [mm/s]	Pressure loss [Pa]
1	1.146
5	5.811
10	11.91

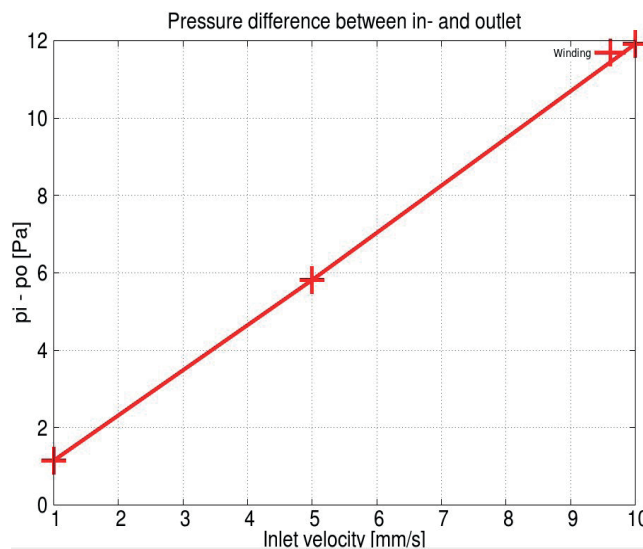


Figure 4 – Pressure loss in hydrodynamic simulations

3.6. Results of conjugate heat transfer simulation

In our conjugate heat transfer run with the coil model, a spatially constant heat source is applied inside the coils, see section 3.3. Unlike a heat flux boundary condition at the interface between coils and oil, this ensures proper matching of the temperature distribution in the oil and the heat flux at the interface.

As a result of the gravitational acceleration and the temperature dependent density of the oil, the generated heat leads to buoyancy forces and natural convection in the oil. For this reason, here we consider only the high inlet velocity of 10 mm/s. According to energy conservation, at this inlet velocity the average outlet oil temperature at the thermal steady state is

$$T_o = T_i + \frac{P}{\dot{m} c_p} = 386.16 K . \quad (7)$$

Here P is power of losses, \dot{m} mass flow, and c_p specific heat at constant pressure. In our simulation, there are varying oil flow patterns during the iterations and the residual of the specific enthalpy is not converging. This raises the presumption that there is no hydrodynamic steady state. The calculated temperature in the oil and the coils is shown in the figure below. The right part of the figure indicates that there are hot oil locations adjacent to the coils. These hot regions change their location during the iterations. This is due to the lack of axial flow barriers, that hampers the development of a steady, preferred direction of the oil flow.

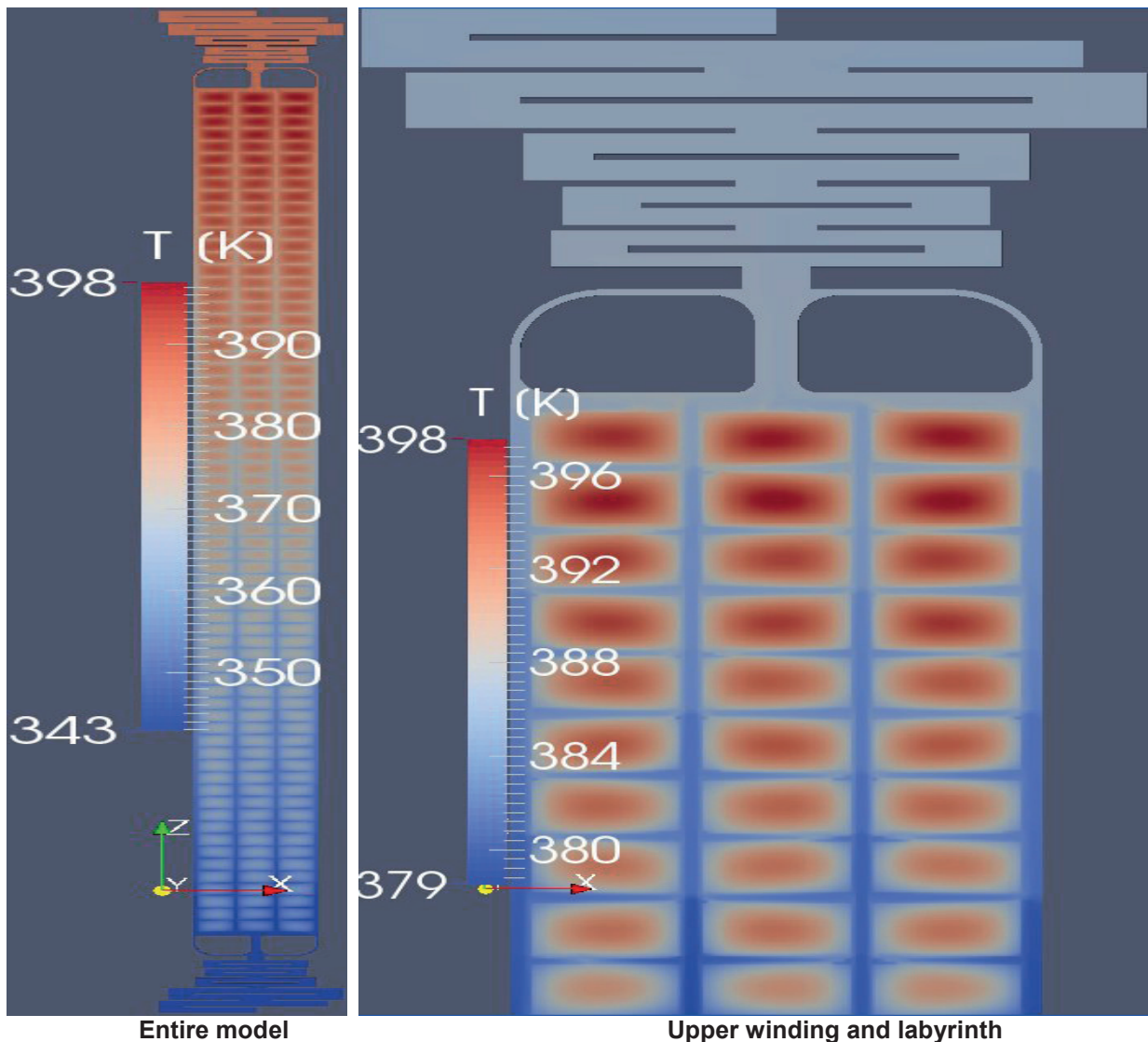


Figure 5 – Oil temperature of conjugate heat transfer simulation

As a result of our mixture material properties the heat conductivity in the coils is low. For this reason, there is a smooth temperature variation in the coil and the maximum coil temperature is high. However, as the goal of this simulation is the temperature dependent hydrodynamics, the coil temperature is of minor importance. The coil in our model is just a means to guide the heat flux from the heat source to the colder sections of the surrounding oil.

In the right part of the figure we see that the oil temperature is not constant along the radial channels. This is related to the direction of the flow. Since the flow does not reach a steady state there is also no local thermal equilibrium in the oil. The figure also shows that the oil temperature at the outlet is about 386 K. This agrees with the energy balance (7). For this reason, a global thermal equilibrium is achieved.

The next figure shows the related Cartesian velocity components at the upper section of the geometry model.

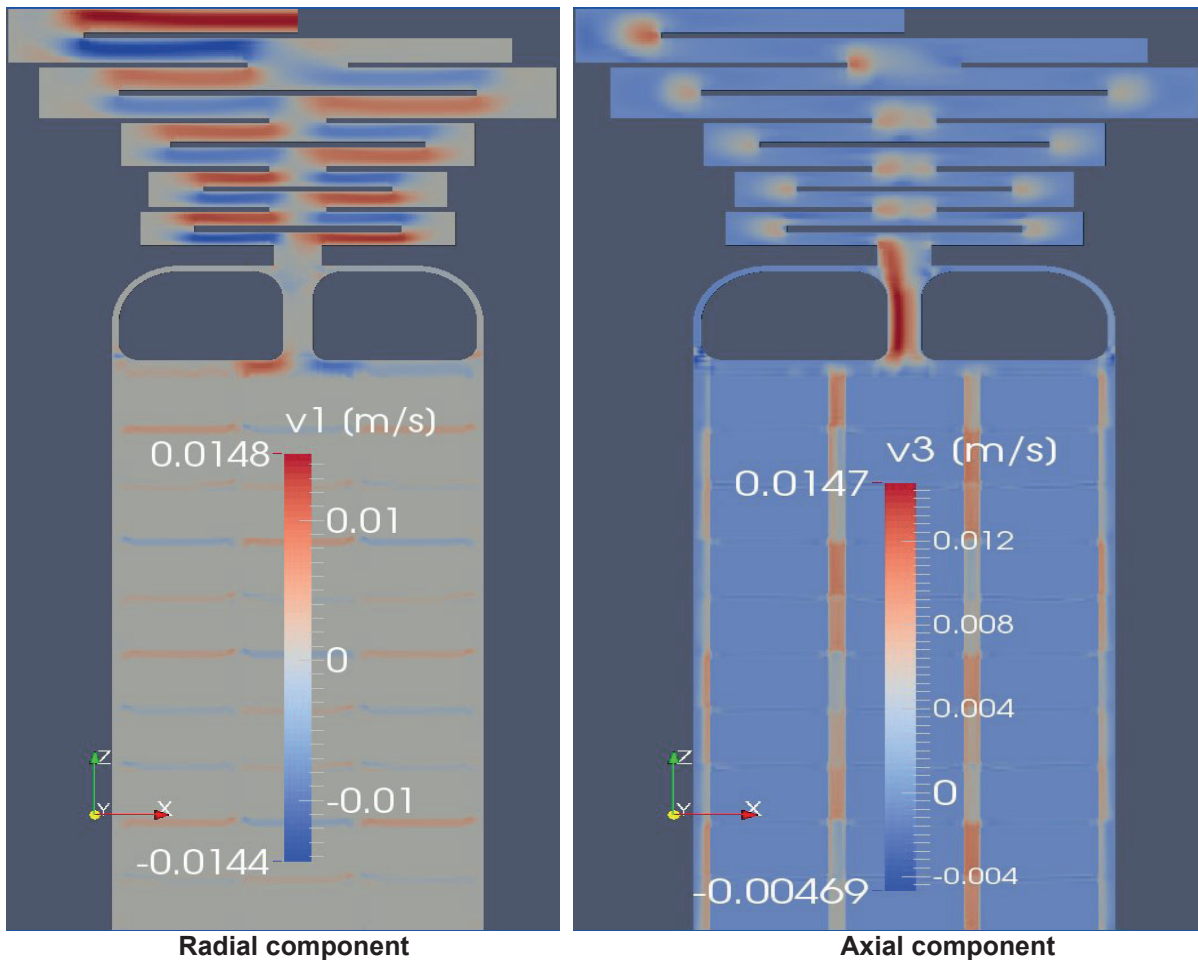


Figure 6 – Cartesian velocity components of conjugate heat transfer simulation

As mentioned before, the velocity in the winding varies during the iterations. At some iteration, e.g., the vertical velocity at certain location in an axial oil channel may be directed upward, while the flow goes down at a later iteration. Moreover, comparison of Fig. 2 and Fig. 6 shows that the velocity is higher and much more uneven than in the hydrodynamic simulation.

The higher irregularity of the flow could lead to a higher pressure loss, compared to the hydrodynamic case. However, as a result of strong heat sources and low inlet velocity, this flow is dominated by buoyancy rather than a pressure gradient caused by wall friction. The pressure merely acts as a Lagrangian multiplier that assures that the velocity is divergence-free. In order to maintain the outlet mass flow at the same low level than the inlet mass flow, the pressure variable (6) in this application increases from inlet to outlet, as shown in the following figure. Our pressure variable omits the hydrostatic contribution to the pressure in hydrodynamic simulations and causes the negative values in the figure. If heat transfer is involved, there is no such simple method to remove the hydrostatic part. The pressure itself, however, is higher at the inlet than at the outlet.

Since the buoyancy forces efficiently accelerate the flow, they may cause a higher inflow velocity than specified in our simulation, unless a high friction (e.g., caused by an inlet nozzle) prevents this.

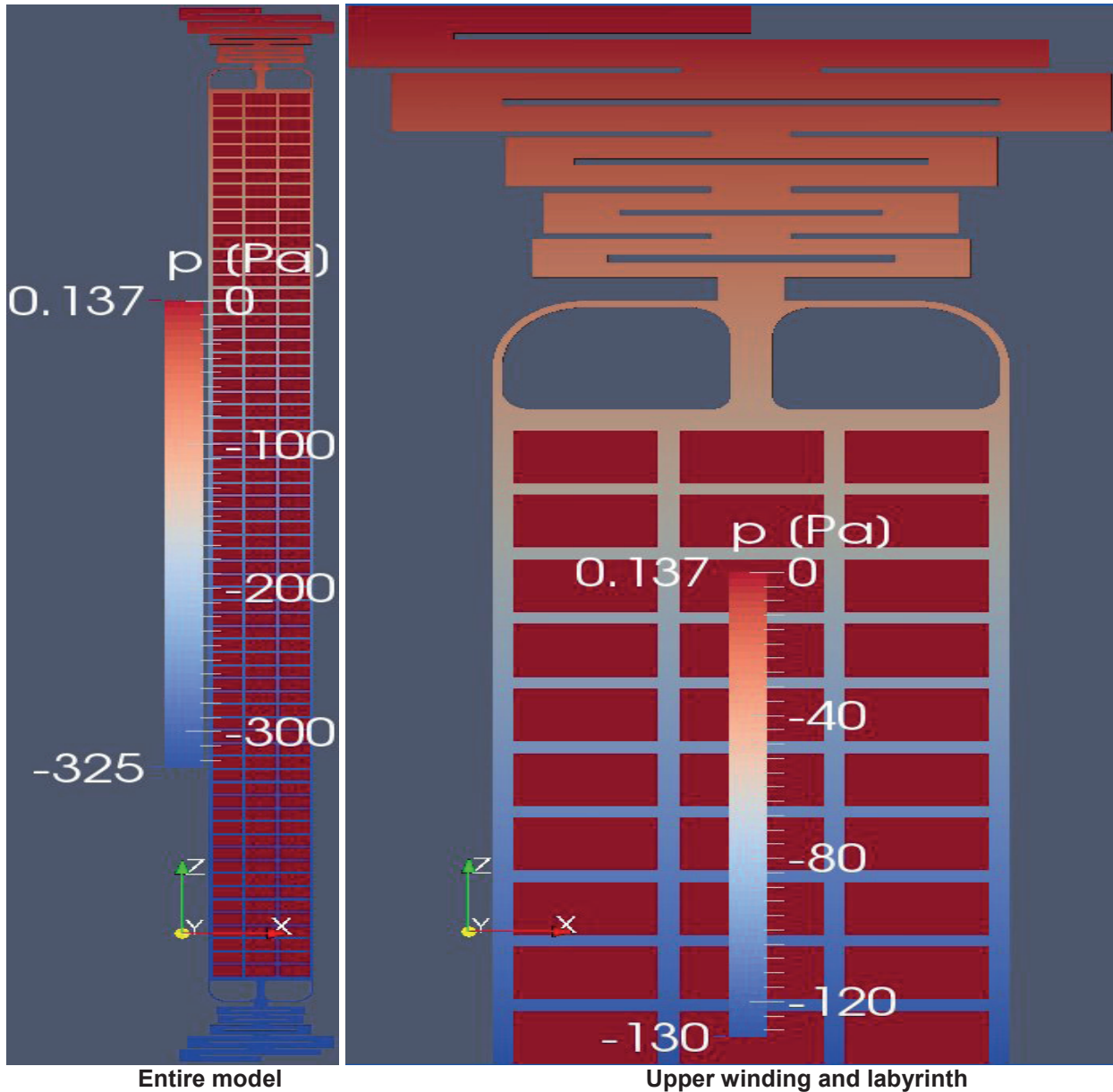


Figure 7 – Pressure variable of conjugate heat transfer simulation

4. SUMMARY AND CONCLUSIONS

We analysed the pressure loss of mineral oil flow in the valve winding of a HVDC transformer with the Siemens in-house CFD code UniFlow. In the hydrodynamic simulations a steady state is established and the pressure loss is an almost linear function of the inlet velocity. In the run involving heat transfer, the high buoyancy forces hamper the development of a steady state and the possibility to calculate a flow induced pressure loss.

The presented results indicate that UniFlow is a useful tool to analyse the thermal design of transformers. It can be used to investigate advantages and disadvantages of design features as well as to perform design optimisation.

In addition to the results shown in this paper, the temperature of insulation materials in a device subject to fluid flow may be a major result of a simulation. Furthermore, the thermal design of cast resin

transformers can be studied, including radiant heat transfer between core, windings, and radiation cylinders. This is demonstrated, e.g., in [18]. Other applications are related to detailed analyses on segments of disc windings with respect to, e.g., modelling of material compositions, width of oil channels, etc.. Another field of application are oil flows in transformer cores. Moreover, combined oil and air flows are analysed in the context of fin type distribution transformers. This is aimed at optimisation of the thermal efficiency of the fins and other tasks. Furthermore, combined oil and air flows in radiators can be investigated.

In addition to steady state analyses, transient processes are investigated. One interesting type of transient occurs at the cold start of a transformer. This matters in particular for oil transformers where the dynamic viscosity is very high at low temperatures, especially for ester fluids.

REFERENCES

- [1] Torriano, F., Pichler, P., Chaaban, M., "Numerical investigation of 3D flow and thermal effects in a disc-type transformer winding", *Applied Thermal Engineering*, 40, pp. 121-131, 2012
- [2] Jiao, Y., "CFD study on the thermal performance of transformer disc windings without oil guides", KTH School of Industrial Engineering and Management, EGI-2012-089MSC EKV915, Stockholm, Sweden, 2012
- [3] Smolka, J., Nowak, A. J., "Experimental validation of the coupled fluid flow, heat transfer and electromagnetic numerical model of the medium power dry-type electrical transformer", *Int. J. Thermal Sciences*, 47, pp. 1393-1410, 2008
- [4] Smolka, J., Biro, O., Nowak, A. J., "Numerical simulation and experimental validation of coupled flow, heat transfer and electromagnetic problems in electrical transformers", *Arch. Comput. Methods Eng.*, 16, pp. 319-355, 2009
- [5] Fonte, C. M. et. al., "CFD analysis of core-type power transformers", *CIREN*, 21st Intl. Conf. on Electricity Distribution, paper 0361, Frankfurt, Germany, 6.-7. 2011
- [6] Gastellurrutia, J. et. al., "Numerical modelling of natural convection of oil inside distribution transformers", *Applied Thermal Engineering*, 31, pp. 493-505, 2011
- [7] Baldwin, B. S., Lomax, H., "Thin layer approximation of an algebraic model for separated turbulent flows", *AIAA-paper*, 78-0257, 1978
- [8] Drela, M., "MISES implementation of modified Abu-Ghannam/Shaw criterion", MIT Aero-Astro, Boston, MA, USA, February 1995
- [9] Mayle, R. E., "The role of laminar-turbulent transitions in gas turbine engines", *ASME Journal of Turbomachinery*, 13, pp. 509-537, 1991
- [10] Landau, L. D., Lifshitz, E. M., "Course of theoretical physics, vol. 6 : Fluid mechanics", Pergamon Press, Oxford, UK, 1989
- [11] Baehr, H. D., Stephan, K., "Heat and mass transfer", Springer-Verlag, Berlin, Germany, 2006
- [12] Ferziger, J. H., Peric, M., "Computational methods for fluid dynamics", Springer-Verlag, Berlin, Germany, 1999
- [13] Van Doormal, J. P., Raithby, G. D., "Enhancements of the SIMPLE method for predicting incompressible flows", *Numer. Heat Transfer*, 7, pp. 147-163, 1984
- [14] Issa, R. I., "Solution of implicitly discretized fluid flow equations by operator splitting", *J. Comp. Phys.*, 62, pp. 40-65, 1986
- [15] Trottenberg, U., Oosterlee, C. W., Schüller, A., "Multigrid", Academic Press, New York, USA, ISBN 012701070X, 2001
- [16] Notay, Y., "An aggregation-based algebraic multigrid method", *Electronic Transactions on Numerical Analysis*, 37, pp. 123-146, Kent State University, ISSN 1068-9613, 2010
- [17] Schlichting, H., "Boundary-layer theory", McGraw-Hill, New York, USA, 1979
- [18] Wittmaack, R., "Thermal design of power transformers via CFD", 11th World Congress on Computational Mechanics (WCCM XI), Barcelona, Spain, July 21-25, 2014

Bruno Bošnjak
Siemens AG Power Transformers Nürnberg
bruno.bosnjak@siemens.com

Andreas Hauck
SIMetris GmbH
andreas.hauck@simetris.de

Hermann Landes
SIMetris GmbH
hermann.landes@simetris.de

COUPLED MAGNETO-MECHANICAL FINITE ELEMENT ANALYSIS OF A POWER TRANSFORMER IN SHORT CIRCUIT CONDITIONS

SUMMARY

External short circuit is one of the most demanding load conditions a transformer can be subjected to. Short circuit withstand capability of power transformers is therefore quintessentially important in order to ensure the proper functioning of a power transformer during its lifetime. Accurate calculation of the forces and stresses a transformer is subjected to during a short circuit is a prerequisite for better, optimized design of the active part. Main focus of this paper is the investigation into dynamic electromagnetic and mechanical behaviour of a transformer winding subject to an external short circuit. For purposes of this simulation, a single-phase 100 MVA autotransformer active part was modelled using ANSYS and NACS software. Particular areas of the winding were modelled to a greater degree of detail in order to observe the effects of Lorentz forces during a short circuit on individual conductors. A transient coupled magneto-mechanical simulation of the transformer under short circuit conditions was carried out.

When subject to dynamic short circuit forces, the winding discs exhibited a profoundly resonant behaviour indicating a strong relationship between the natural frequency of the winding and the resulting stresses and displacements incurred during a short circuit. It has been shown that the position of the yoke changes the orientation and the distribution of the magnetic field vectors at the top and the bottom of the winding, causing a non-uniform distribution of forces along the top discs of the winding. This non-uniform distribution of forces along the circular shape of the winding conductor caused high stresses at the positions within the winding which were previously considered to be under lower stress when calculated using 3D static FEM and analytical methods.

Key words: Transformer, Short Circuit, Lorentz Forces, Stress, Multiphysics, Transient, FEM

1. INTRODUCTION

During its lifetime, a power transformer is subjected to a variety of electrical, thermal and mechanical stresses that can significantly lower its life. An external short circuit can cause high currents to flow through the transformer windings. The interaction between the current-carrying conductors and the stray magnetic field results in the generation of Lorentz forces acting on the transformer windings and adjacent mechanical structures. These forces can potentially damage the conductor insulation, insulation on the winding ends or leads which can result in a flashover or plastically deform the copper conductors themselves which might change the nominal electrical parameters of the transformer or render the transformer inoperable.

Importance of adequately describing and quantifying the forces and stresses occurring during short circuit is further underlined by the fact that an average of 2 short-circuits occur on busbars per 100 busbar years with a 90% percentile of 4 busbar short circuits occurring per 100 busbar-years. From a statistical standpoint, a power transformer has to withstand several full short circuit and many small short circuit currents during its lifetime [1].

In this paper, a coupled magneto-mechanical finite element method (FEM) model is established for a transient simulation of the magnetic and mechanical effects that occur in the transformer windings during a short circuit in accordance with the IEC 60076-5 standard [2]. The transformer simulated in this calculation was a 100 MVA single-phase Siemens autotransformer that successfully underwent short-circuit testing.

2. METHODOLOGY

2.1. Magnetic Field Calculation

The Lorentz forces acting on a transformer winding during a short circuit are caused by the interaction of the current-carrying conductors in a variable stray magnetic field. The stray magnetic field in the transformer window is generated by current-carrying conductors of both transformer windings. The governing equations of the magnetic field in terms of the magnetic vector potential \vec{A} are as follows [3]:

$$\nabla \times \frac{1}{\mu} (\nabla \times \vec{A}) = \vec{J} - \sigma \frac{\partial \vec{A}}{\partial t} \quad (1)$$

$$\vec{B} = \nabla \times \vec{A} \quad (2)$$

Further on, Lorentz forces acting on the conductors of the winding can therefore be calculated using:

$$\vec{f} = \vec{J} \times \vec{B} \quad (3)$$

where μ is magnetic permeability[H/m], \vec{A} magnetic vector potential [V s/m], \vec{J} current density [A/m²], σ electric conductivity [S/m], \vec{B} magnetic flux density [T] and \vec{f} force density [N/m³].

2.2. Structural Calculation

The structural behaviour of the transformer winding is governed by the following equation of motion written in matrix form:

$$M\ddot{x}(t) + C\dot{x}(t) + Kx(t) = f(t) \quad (4)$$

where M, C and K are the mass, damping and stiffness matrices of the dynamic system, $x(t)$ is the displacement of nodes of the system and the $f(t)$ are the volume forces. Materials used are assumed to be linear elastic, and therefore the relation between stress tensor and the strain tensor is given by Hooke's law:

$$\sigma_{ij} = k_{ijkl} \cdot \varepsilon_{kl} \quad (5)$$

where σ_{ij} is the stress tensor [N/mm²] and k_{ijkl} is the stiffness tensor which can be calculated from displacement using the following relation:

$$\varepsilon = \frac{1}{2} [\nabla x + (\nabla x)^T] \quad (6)$$

The two calculations are coupled through an iterative process where the calculated Lorentz forces within the magnetic calculation are provided as input of the structural calculation which in turn alters the geometry of the initial magnetic calculation. This process is iterated until set precision is met as per a well-established method in [8].

2.3. Short Circuit Current

Short circuit in an electrical network is a system disturbance that generally causes high currents to flow through the network and the transformer. The transient waveform of current was directly set at the winding terminals according to the IEC 60076-5 standard [2]:

$$i(t) = I_m \left(\cos(\omega t) - e^{-\frac{R_k}{X_k} t} \right) \quad (7)$$

where I_m is the maximal short-circuit current [A], ω is the angular frequency [rad^{-1}], R_k and X_k the sum of resistances and inductances of the transformer and the system respectively [Ω]. The calculated current waveform is graphically represented in Figure 1.

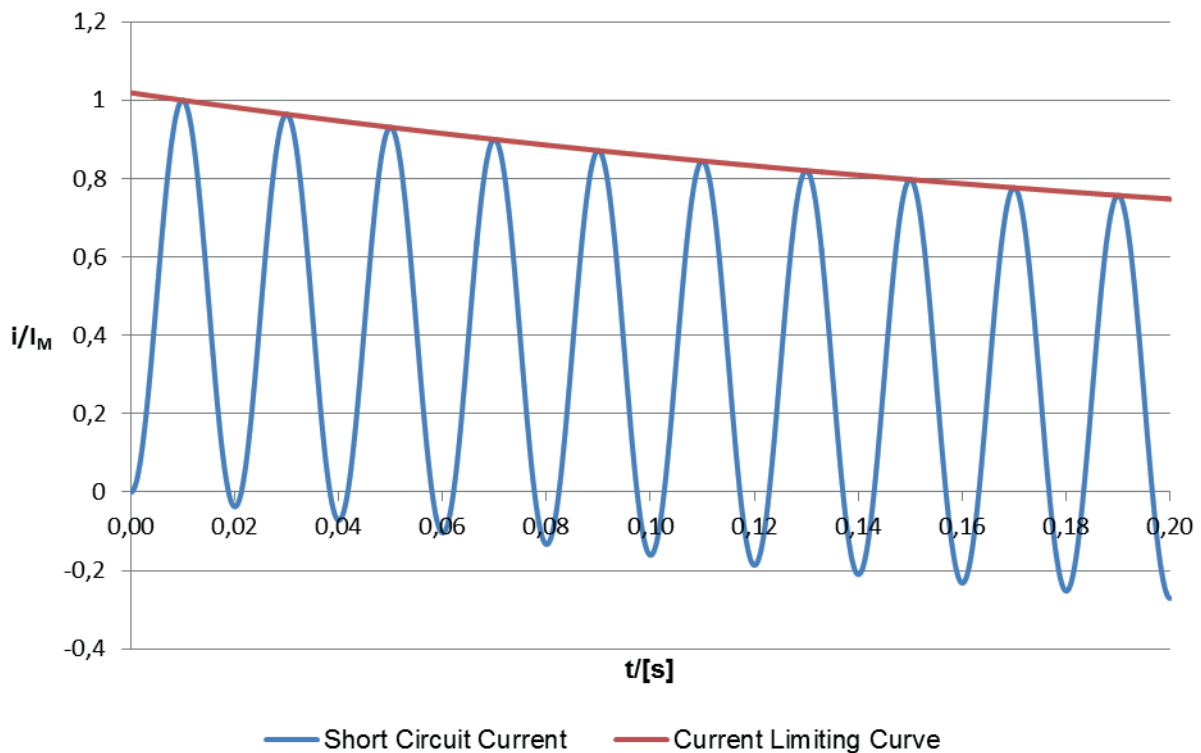


Figure 1 – Short circuit current waveform

2.4. ANSYS/NACS Model

For the purposes of this simulation, the model pre-processing and post-processing was performed using ANSYS Mechanical and Paraview, while the simulation was run using NACS magneto-mechanical solver [5]. Figure 2 shows the model prepared for solving. The primary focus of the investigation was the definition of stresses acting on the low voltage winding since forces acting on the low voltage are usually greater than those acting on the high voltage winding due to lower current density in the winding [6][7]. Hence, the top four conductors of the low voltage winding were modelled to a greater detail than the rest of the winding in order to closer observe the effects short circuit forces have on these conductors. Top four conductors of the low voltage winding are shown in Figure 3.

The top four conductors of the low voltage winding were modelled using actual material properties while the rest of the of low voltage winding, as well as the whole high voltage winding, were modelled as a homogenized isotropic hybrid material designed to emulate to the closest possible degree the structural behaviour of a complex winding structure consisting of high-yield copper, laminated transformerboard and insulation paper.

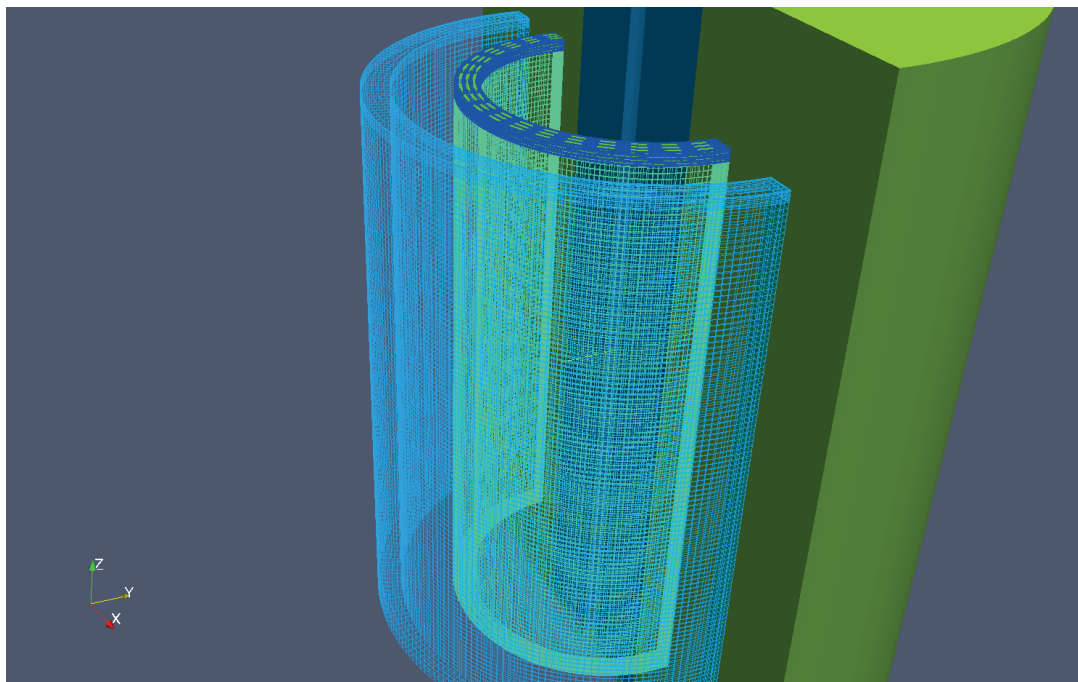


Figure 2 – Active part model prepared for solving

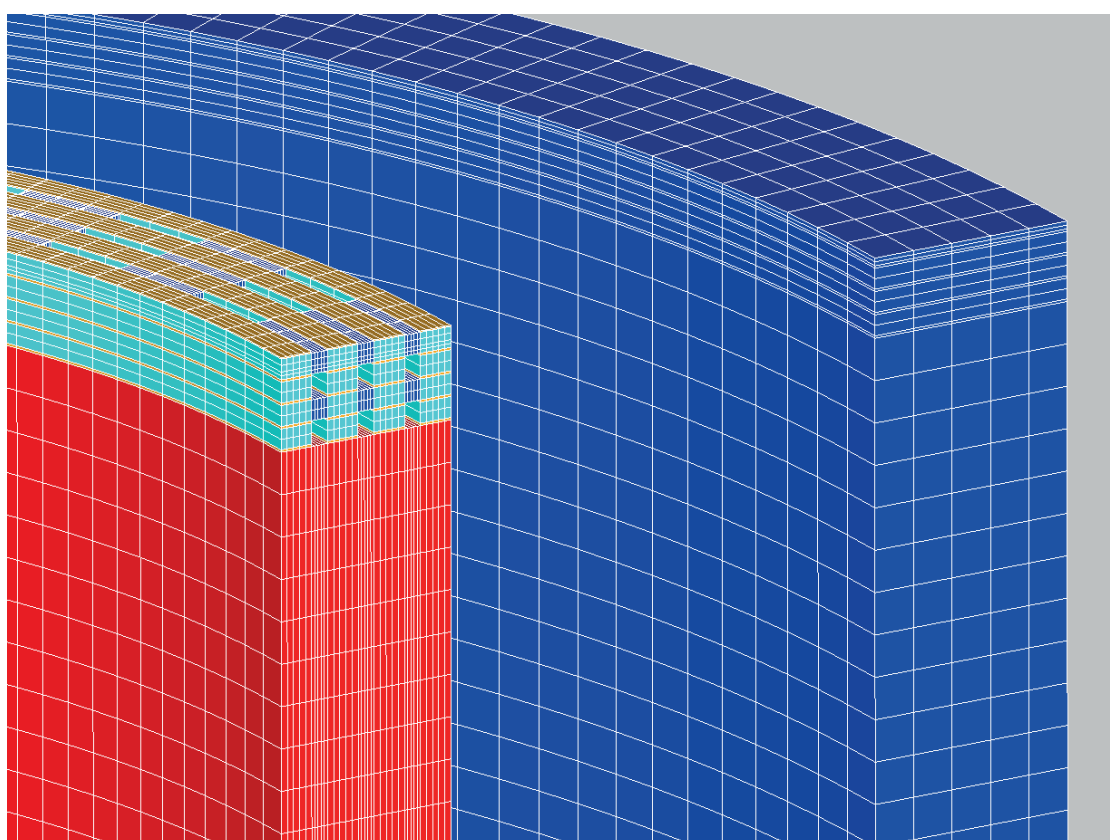


Figure 3 – Top conductors of the low voltage winding modelled to a greater detail

3. SIMULATION RESULTS

The coupled magneto-mechanical simulation was run until $t=0.04\text{s}$ after the occurrence of the short circuit. Focus was on the distribution of magnetic field and stresses within the top four conductors of the low voltage winding. First peak of the short circuit current happens at $t=0.01\text{s}$ and at $t=0.03\text{s}$ as per Figure 1. Distribution of magnetic flux density at current peaks is shown in Figures 4 and 5.

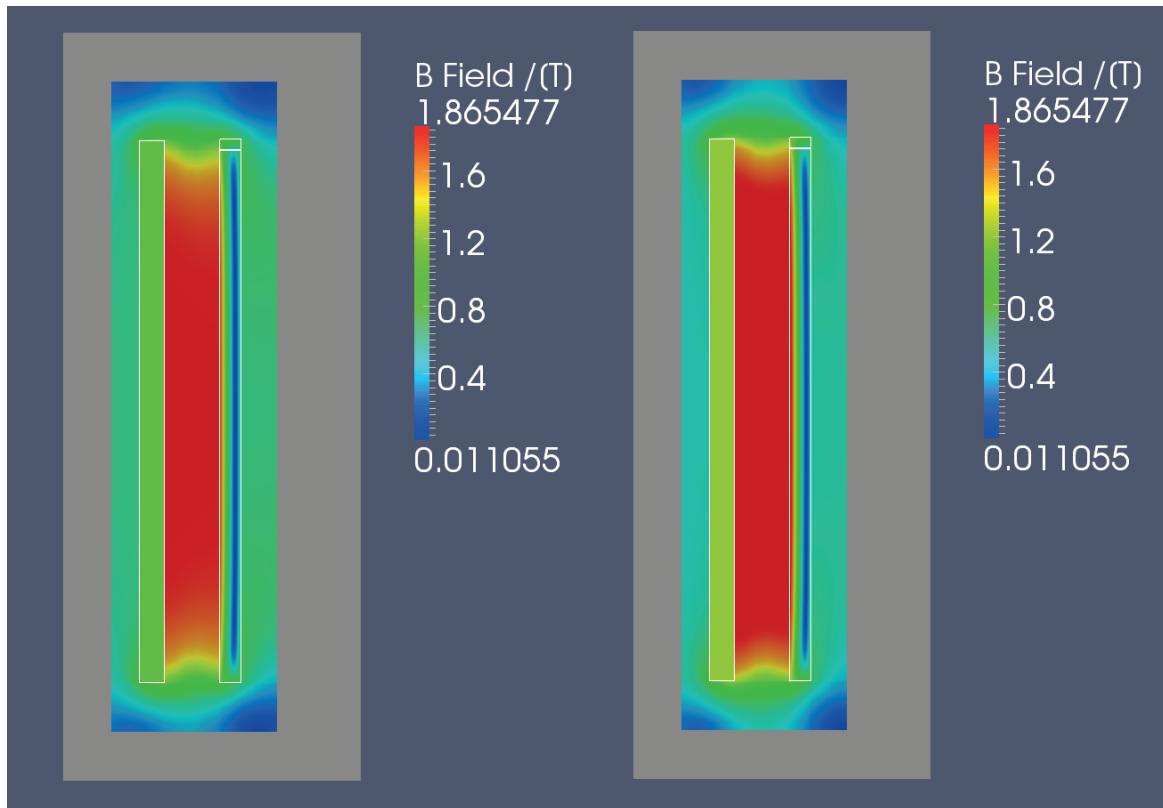


Figure 4 – Distribution of magnetic flux density at $t=0.01\text{s}$ (left) and at $t=0.03\text{s}$ (right) in the plane under the yoke

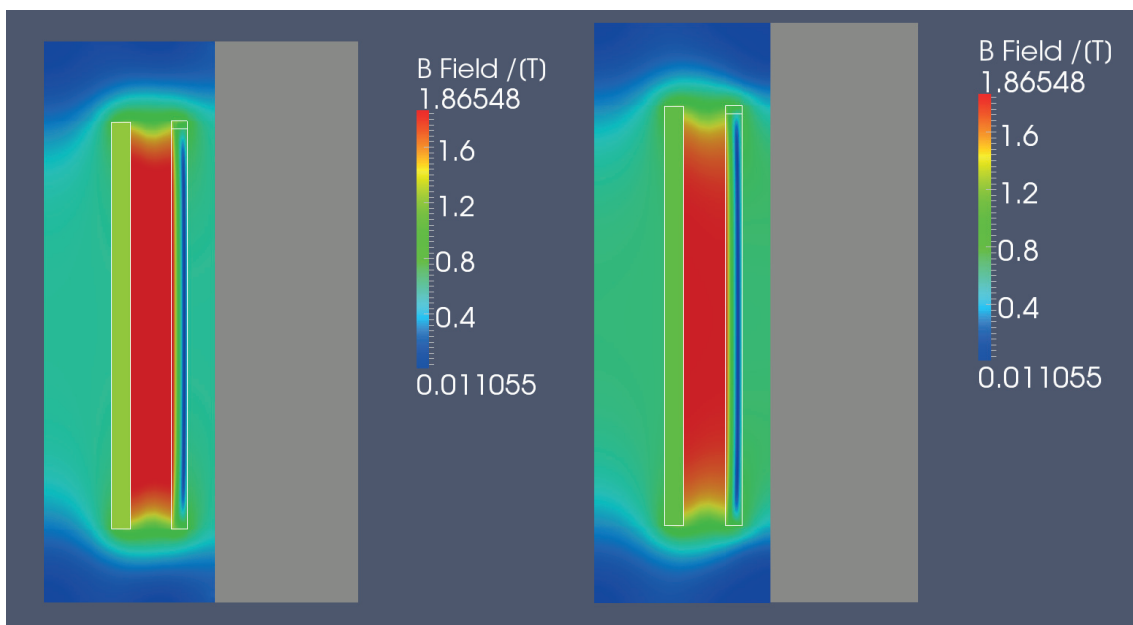


Figure 5 – Distribution of magnetic flux density at $t=0.01\text{s}$ (left) and at $t=0.03\text{s}$ (right) in the plane not under the yoke

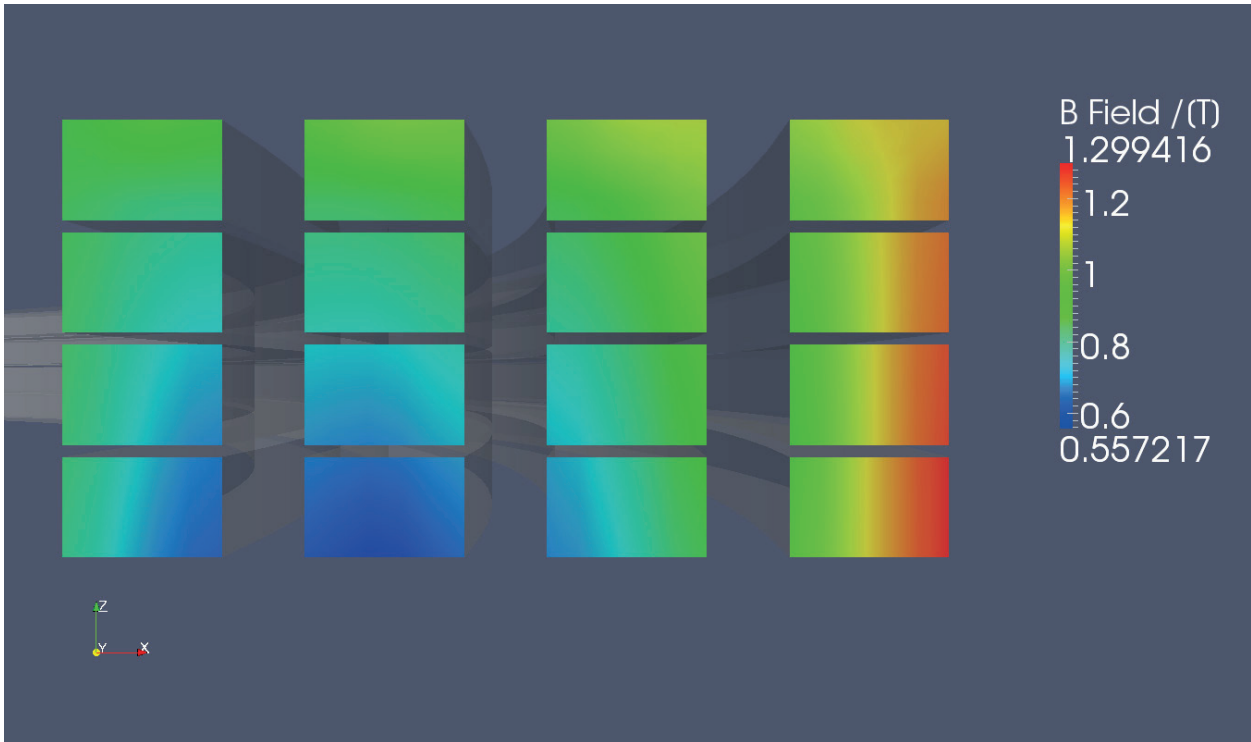


Figure 6 – Distribution of magnetic flux density in the top four conductors at $t=0.01s$ in the plane not under of the yoke

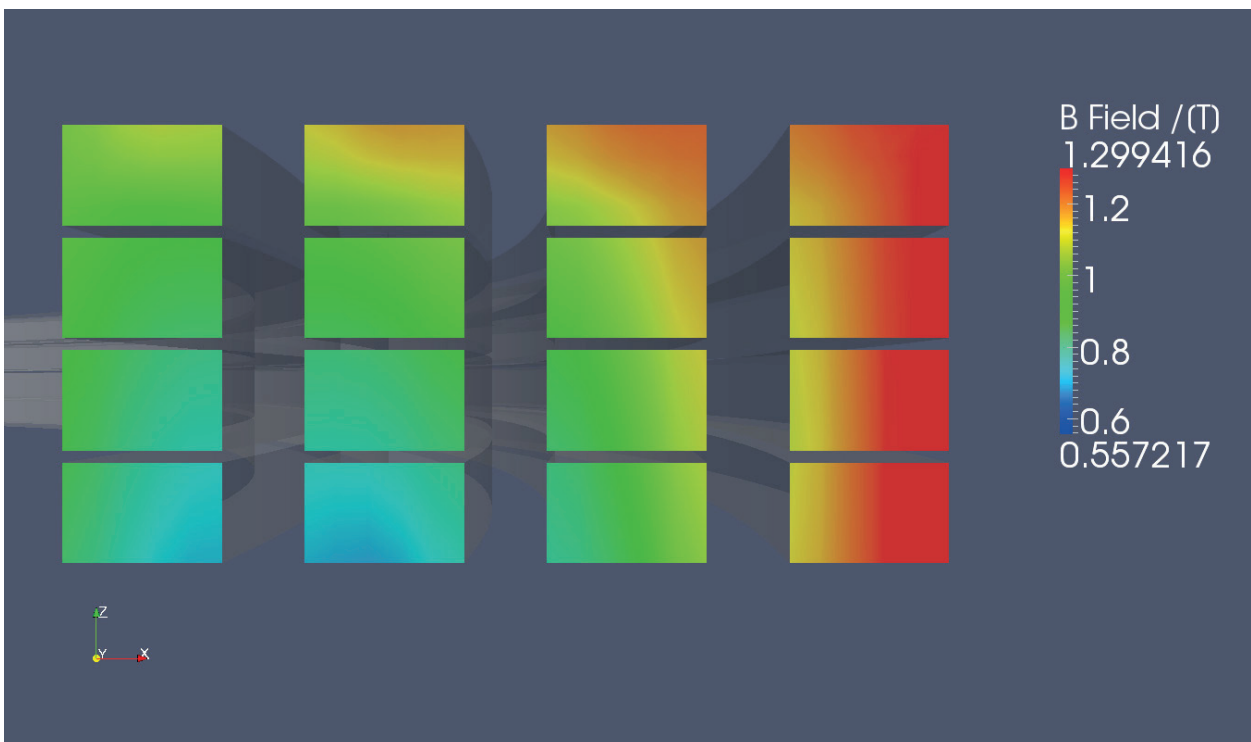


Figure 7 – Distribution of magnetic flux density in the top four conductor at $t=0.03s$ in the plane not under the yoke

From Figures 6 and 7 it is obvious that the magnetic field density is higher at 0.03s peak compared to that at the 0.01s peak. Although the peak current at $t=0.03$ is approximately 3% lower than peak current at $t=0.01s$, the magnetic field density in the conductors is higher at $t=0.03$ due to the mechanical displacement of the winding caused by Lorentz forces which pushes the conductor deeper in

the main stray channel in the plane not under the yoke. This phenomenon stems from the magneto-mechanical coupling, i.e. the low voltage winding is pushed towards the core in the plane under the core and pushed outwards into the main stray channel in the perpendicular plane. Figures 8 and 9 illustrate this phenomenon graphically.

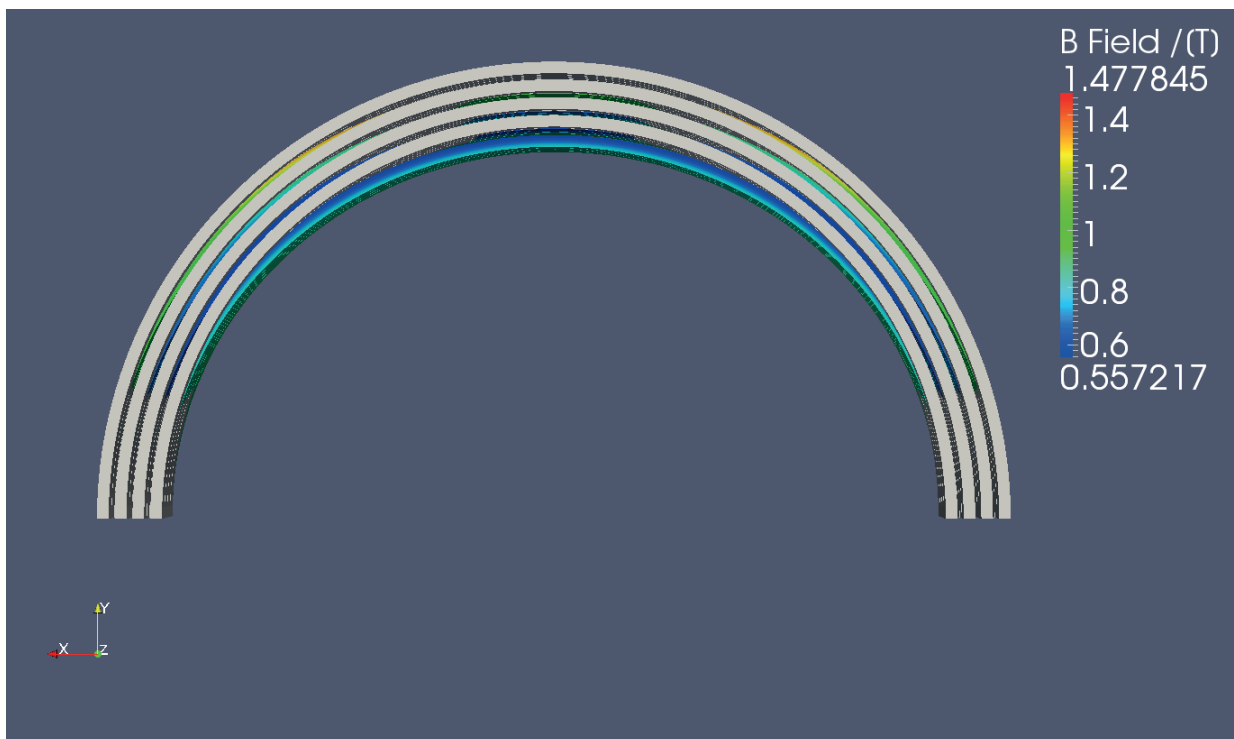


Figure 8 – Winding warped by the displacement vector at $t=0.01s$ with magnetic flux density plotted in comparison with the original winding geometry

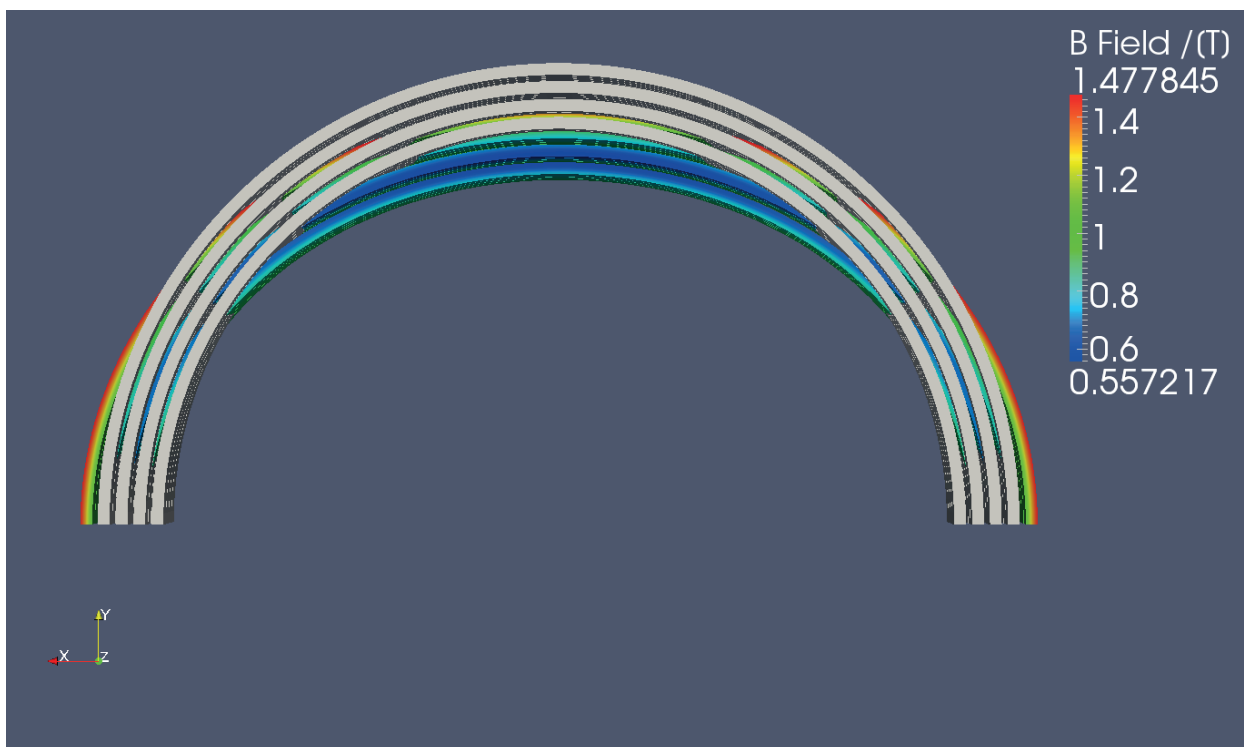


Figure 9 – Winding warped by the displacement vector at $t=0.03s$ with magnetic flux density plotted in comparison with the original winding geometry

The cause of this mechanical and magnetic behaviour of the low voltage winding is the initial non-uniform distribution of the magnetic field along the winding circumference. Due to this non-uniform distribution of magnetic field and consequentially forces, the Lorentz forces act in such a fashion that tries to achieve the uniform distribution of forces along the winding circumference in the conductors. The distribution of the radial component of the magnetic flux density on the first topmost conductor nearest to the core along the circumference at the first current peak at $t=0.01s$ is graphed in Figure 10.

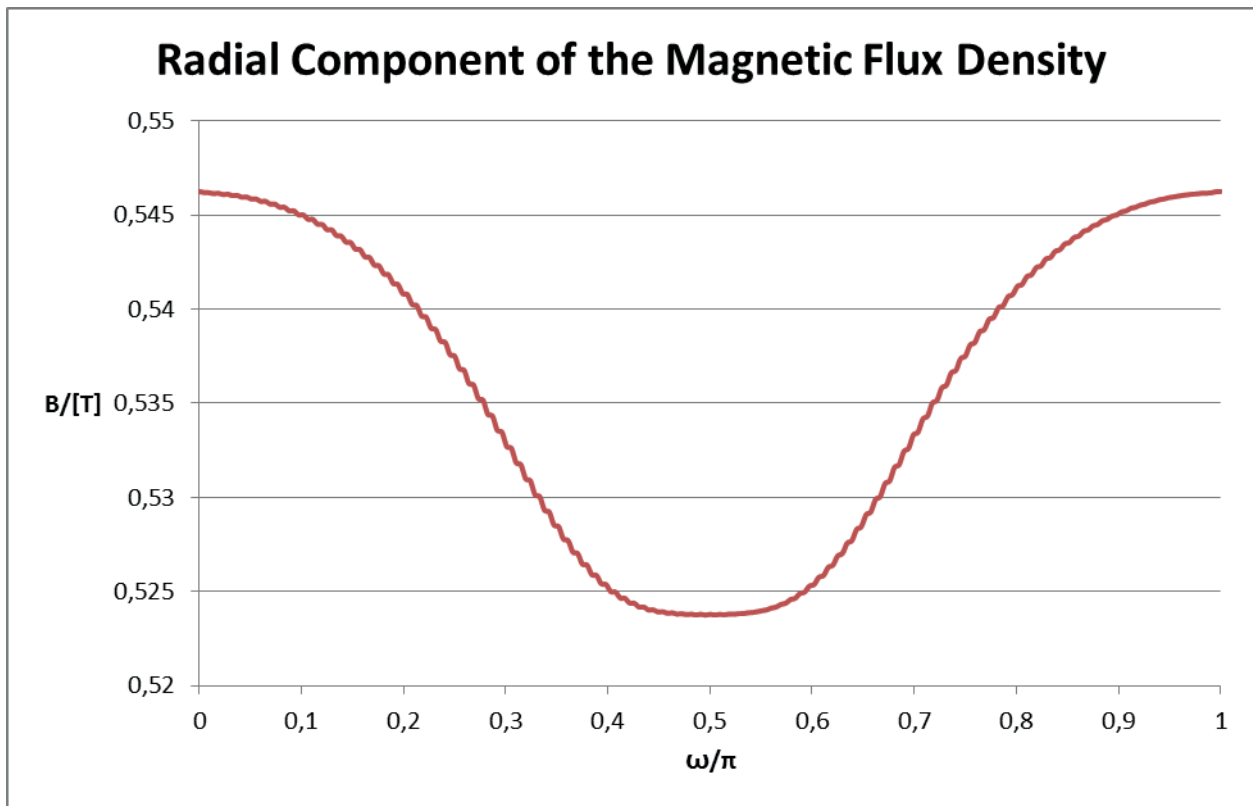


Figure 10 – Distribution of the radial component of the magnetic flux density along the first topmost conductor nearest to the core along the circumference at $t=0.01s$

This distribution results in distribution of stresses inside the top four conductors of the winding as per Figures 11 and 12. The orientation of the yoke is in the direction of the y-axis shown on Figures 11 and 12. On both Figures we can see typical hoop stress behaviour of the winding. There are three interesting phenomena that have been observed within the simulation.

- a) First, it appears that the stresses and displacements are the highest during the second peak of the short circuit current, rather than during the first peak, which is contrary to the existing knowledge [9]. Due to the model limitations, no axial supports (on the inner and outer diameter) were modelled which would support the winding in a realistic case, hence the changes in the model geometry are overestimated in this model, but the basic mechanical behaviour of the winding under short circuit conditions should not be far away from the one modelled here – the non-uniform distribution of forces along the winding circumference will increase local stress in the two principal planes of the transformer unless the transformer winding is properly supported on the inner and outer diameter in order to restrain the winding's radial movement.
- b) Second, the winding seems to exhibit a profoundly resonant behaviour under the influence of a sinusoidal short circuit current. If the relaxation of the winding after the first current peak coincides with the second current peak, an amplification of the displacement magnitude occurs. Modal analysis should enable the prediction and avoidance of such phenomena by ensuring that the natural frequencies of the investigated winding lie at a safe distance from the principal excitation frequency.
- c) Thirdly, on Figure 12 it can be seen that the stresses appearing on the innermost conductor of the winding are of the same magnitude as the stresses appearing on the outermost

conductor. It is usually considered that the outermost conductor is under highest stress in the winding when taking only magnetic calculation into consideration. This increase in stress is caused by the mechanical reaction of the winding to the Lorentz forces acting in the negative radial direction.

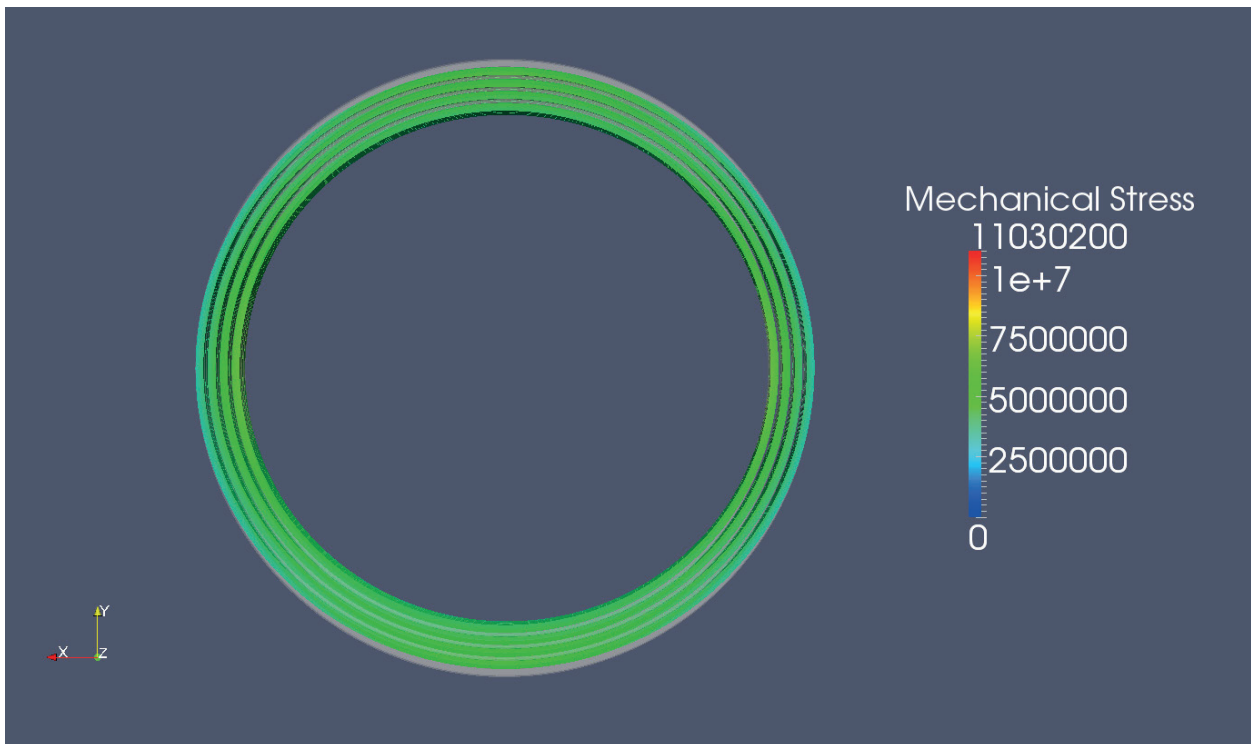


Figure 11 – Distribution of mechanical stress in the top four conductors at $t=0.01s$, geometry warped by mechanical displacement vector

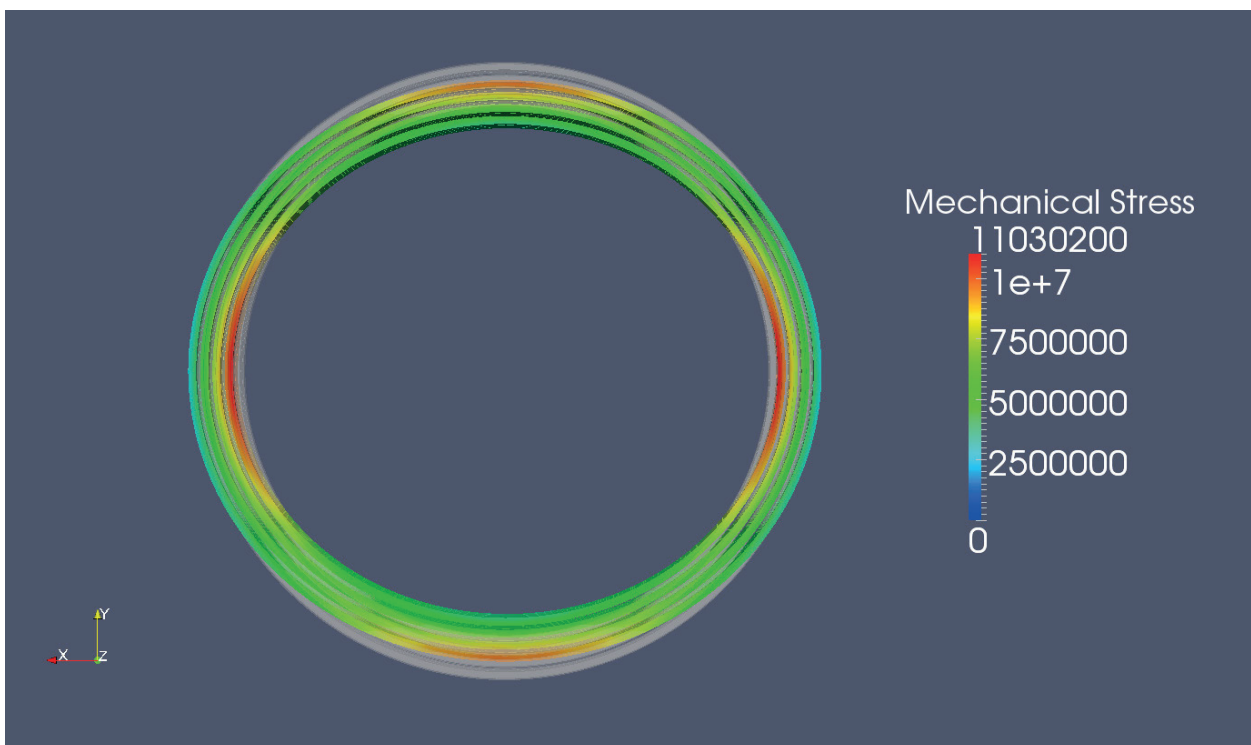


Figure 12 – Distribution of the mechanical stress in the top four conductors at $t=0.03s$, geometry warped by mechanical displacement vector

4. CONCLUSION

In this paper, a coupled magneto-mechanical transient simulation was used to predict the transient electromagnetic forces and consequent mechanical stresses and displacement of the transformer windings during a short circuit event. The mechanical displacements caused by the Lorentz force acting on the transformer windings cause the changes in the principal geometry of the simulation which has a number of repercussions on the calculation of stress. The simulation performed in this paper indicates that the mechanical displacements as well as the non-uniform distribution of magnetic flux along the winding circumference can increase the local and overall stresses in the windings, as well as alter the point in time during a short-circuit when these maximum stresses occur. Also, the windings exhibited a profoundly resonant behaviour depending on the natural frequency of the windings. All these conclusions require a more detailed investigation using models with a higher degree of details modelled as the model used here has a greater number of simplifications in comparison to the realistic winding geometry.

REFERENCES

- [1] A. Janssen, L. Passke, "Short-Circuit Testing Experience with Large Power Transformers", CIGRE Paris Session 2000, Paper No. 12-105, Paris, France, August 2000
- [2] IEC 60076-5 Power Transformers – Part 5: Ability to withstand short circuit, February 2006
- [3] Z. Haznadar, Ž. Štih, "Electromagnetic Fields, Waves and Numerical Methods", IOS Press, January 2000
- [4] R. Del Vecchio et al. "Transformer Design Principles: With Applications to Core-Form Power Transformers", 2nd ed., CRC Press, January 2010
- [5] NACS 1.7 Multiphysics Suite Documentation, SIMetris, September 2012
- [6] B. Bosnjak, F. Kelemen, "Comparison of 2D and 3D Calculation of Stray Magnetic Field and the Application of the Results in the Calculation of Short-Circuit Withstand Capability of a Power Transformer", 10th HRO CIGRE Session 2011, Report A2-04, Cavtat, Croatia, 2011
- [7] H. Ahn, et. al, "Finite-Element Analysis of Short-Circuit Electromagnetic Force in Power Transformer", IEEE Transactions on Industry Applications, Vol. 47, No. 3, May 2011
- [8] M. Kaltenbacher, "Numerical Simulation of Mechatronic Sensors and Actuators", 2nd ed., Springer, 2007
- [9] G. Bertagnolli, "Short-Circuit Duty of Power Transformers - The ABB Approach", 1st ed., Golinelli Industrie Grafiche, January 1996

Kosjenka Capuder
Končar Power Transformers Ltd
kosjenka.capuder@siemens.com

Goran Plišić
Končar Power Transformers Ltd
goran.plisic@siemens.com

Željko Štih
University of Zagreb, Faculty of Electrical Engineering and Computing
zeljko.stih@fer.hr

GENERIC APPROACH TO CALCULATION OF SHORT CIRCUIT CURRENTS IN POWER TRANSFORMERS

SUMMARY

Power transformer in service is exposed to various voltage and current stresses. The ability to withstand short circuit is an essential requirement for power transformers.

There are different types of short circuit: single - phase to earth, double - phase with or without simultaneous earth fault and three - phase short circuit. These various short circuit conditions result in different stress conditions for the windings. Mesh analysis and symmetrical components are the two methods most commonly used for determining the magnitude of short circuit currents. In this paper, both methods will be presented with results compared on a real-case transformer. Also, a generic scheme using the symmetrical components approach is designed in order to standardize the short-circuit currents calculation for all power transformer types and to reduce the time required for obtaining results.

Key words: power transformer, symmetrical components, short circuit, inductance matrix, model, mesh analysis

1. INTRODUCTION

For each winding, the short circuit currents with highest magnitudes are the input for the calculation of mechanical forces and stresses for which the transformer is then dimensioned. The worst mechanical stresses arise in different conditions for different types of transformers and network configurations (autotransformers and full transformers, parallel loading cases etc.). Additionally, the costumers requests related to transformer documentation often include calculation of currents for all types of short - circuit faults, with all cases of interest included. This can exceed to more than one hundred calculations per transformer.

Input parameters for the calculation vary for each power transformer, which complicates the standardization of the calculation process. A power transformer can be two or three - winding transformer, it can be fed by one, two or more active networks, its windings can be delta or star connected, its neutral point can be isolated or earthed (solid or through impedance) etc. All of the mentioned parameters influence the structure of the model used for the calculation. Detailed analysis has shown that theory of symmetrical components is more suitable for the development of a standardized approach. In this paper, a generic scheme for positive-sequence, negative-sequence and zero-sequence system is presented, with built-in variables covering all calculation and model possibilities. Application of these schemes provides standardized short-circuit currents calculations for all types of power transformers. This enables automatization of the calculation process and significantly reduces the time required for obtaining all required results. It also allows simple upgrading of the calculation system with additional possibilities due to oncoming requirements and requests.

2. MODELS FOR SHORT-CIRCUIT CURRENTS CALCULATIONS

The calculation of short-circuit currents is most commonly performed with one of the two methods – mesh analysis method or symmetrical components method. [1]

2.1. Mesh Analysis Method

This method is based on creating a transformer model consisting of winding self-inductances and corresponding mutual inductances between windings. In power transformers the resistance component of the impedance is negligible in comparison with the inductance component. Using mesh analysis and by applying Kirchoff's voltage law, short-circuit currents are calculated according to formula:

$$[I] = [U] \times [Z]^{-1}, \quad (1)$$

where voltage matrix [U] consists of rated voltages according to the specified model. This method is in detail described in [2], [3].

It is important to emphasize that the model varies for each transformer configuration, as well as each short circuit type.

This method will be used as a comparison method to verify the results obtained with symmetrical components method, extended by using generic approach to the calculation.

2.2. Symmetrical Components Method

Symmetrical components method is commonly used to analyze unsymmetrical faults in three-phase power systems. This method is based on the fact that each asymmetrical system can be analysed using three symmetrical systems: positive-sequence, negative-sequence and zero-sequence system. Impedances of each of the three symmetrical systems (z_1 - positive sequence impedance, z_2 - negative sequence impedance and z_0 – zero sequence impedance) are calculated separately and the short-circuit currents (i_1 , i_2 , i_0) are calculated for each case according to the specified models (Figure 1). Corresponding formulas are presented in relative units, with electromotive force of 1 p.u. (100%) [4].

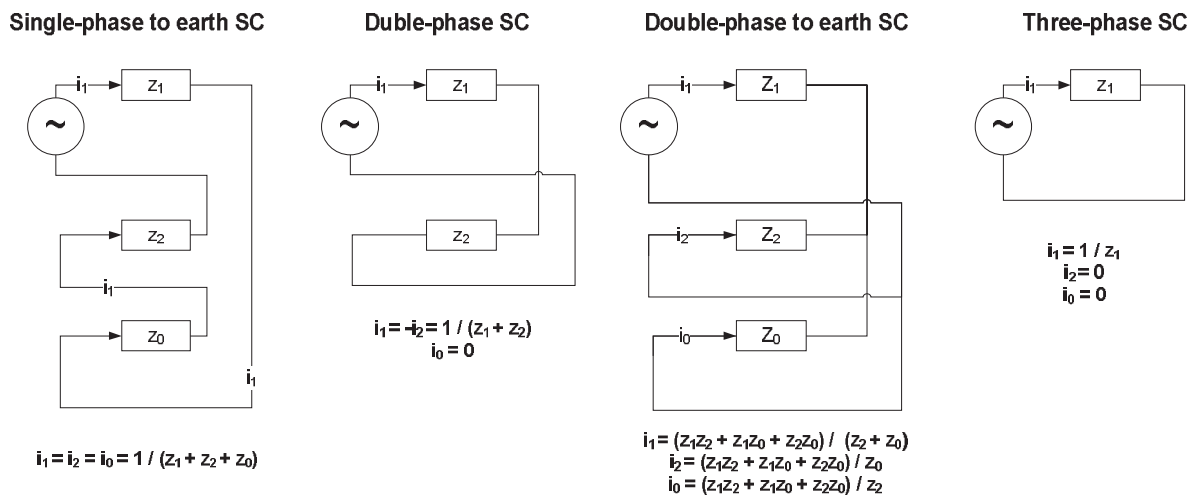


Figure 1 - Symmetrical components models for different types of short-circuit

Impedances for positive-sequence, negative-sequence and zero-sequence system are influenced by a number of parameters. In order to insure simple, and unified calculation for these impedances, a generic formula has been developed and presented in the next chapter.

3. GENERIC APPROACH FOR SYMETRICAL COMPONENTS METHOD

Negative-sequence impedance is equal to positive-sequence impedance; therefore they will be presented on a mutual model. Zero-sequence impedance is influenced by more parameters and is presented on a separated model.

3.1. Positive- and negative-sequence model

Basic positive-sequence model for three – winding transformer is presented in Figure 2.

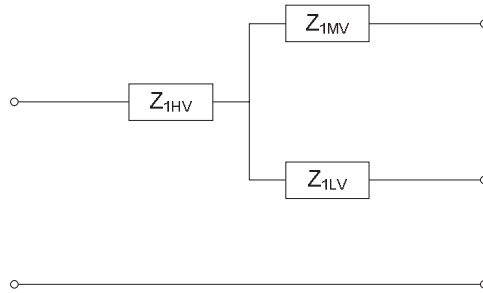


Figure 2 - Basic positive-sequence model

Impedances for each transformer winding presented in Figure 2 are calculated according to equations (2) - (4) and are usually equal for all three systems:

$$Z_{1HV} = Z_{2HV} = Z_{0HV} = \frac{1}{2}(u_{scHV/MV} + u_{scHV/LV} - u_{scMV/LV})j/100 \text{ [p.u.]} \quad (2)$$

$$Z_{1MV} = Z_{2MV} = Z_{0MV} = \frac{1}{2}(u_{scHV/MV} + u_{scMV/LV} - u_{scHV/LV})j/100 \text{ [p.u.]} \quad (3)$$

$$Z_{1LV} = Z_{2LV} = Z_{0LV} = \frac{1}{2}(u_{scHV/LV} + u_{scMV/LV} - u_{scHV/MV})j/100 \text{ [p.u.],} \quad (4)$$

where $u_{scHV/MV}$, $u_{scHV/LV}$ and $u_{scMV/LV}$ are percentage rated short-circuit voltages between windings referred to rated power S_r .

Positive-sequence model must take into account active networks to which the transformer is connected. This influence is presented in extended model in Figure 3.

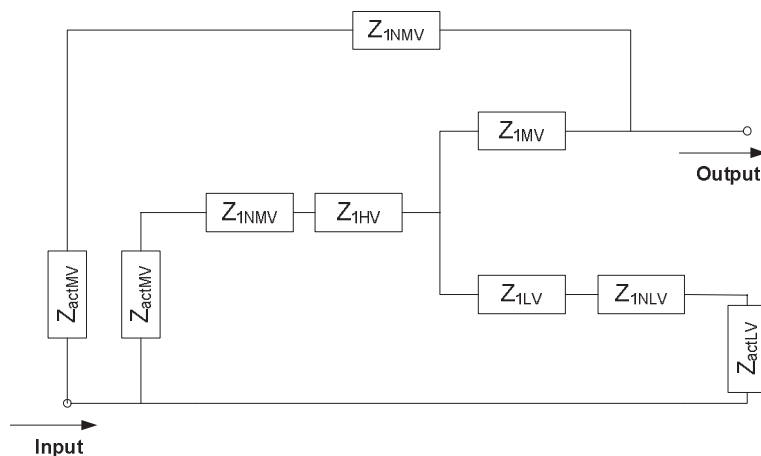


Figure 3 - Extended positive-sequence model

Z_{actHV} , Z_{actMV} , Z_{actLV} in Figure 3 determine whether the corresponding winding is connected to the active network or not. All combinations are presented in Table I.

Table I - Active network impedances

Active networks	Z_{activHV}	Z_{activMV}	Z_{activLV}
HV	0	∞	∞
MV	∞	0	∞
LV	∞	∞	0
HV and MV	0	0	∞
HV and LV	0	∞	0
MV and LV	∞	0	0
HV, MV and LV	0	0	0

If connected to the active network, impedance of the network must be taken into account. This is presented with network impedances $Z_{1\text{NHV}}$, $Z_{1\text{NMV}}$, $Z_{1\text{NLV}}$ for each voltage side of the transformer, and calculated according to:

$$Z_{1\text{NHV}} = Z_{2\text{NHV}} = z_{0\text{NHV}} = \frac{S_r}{S_{\text{scHV}}} j \text{ [p.u.]} \quad (5)$$

$$Z_{1\text{NMV}} = Z_{2\text{NMV}} = z_{0\text{NMV}} = \frac{S_r}{S_{\text{scMV}}} j \text{ [p.u.]} \quad (6)$$

$$Z_{1\text{NLV}} = Z_{2\text{NLV}} = z_{0\text{NLV}} = \frac{S_r}{S_{\text{scLV}}} j \text{ [p.u.]} \quad (7)$$

Impedance of the entire model z_1 is calculated with:

$$z_{1\text{HV}}' = z_{\text{activHV}} + z_{1\text{HVN}} + z_{1\text{HV}} \text{ [p.u.]} \quad (8)$$

$$z_{1\text{LV}}' = z_{\text{activLV}} + z_{1\text{NLV}} + z_{1\text{LV}} \text{ [p.u.]} \quad (9)$$

$$z_1 = z_2 = [(z_{1\text{HV}}' \parallel z_{1\text{LV}}') + z_{1\text{MV}}] \parallel (z_{\text{activMV}} + z_{1\text{NMV}}) \text{ [p.u.]} \quad (10)$$

Coefficients used to recalculate the positive-sequence current to currents through each winding are as follows:

$$k_{1\text{HV}} = \frac{(z_{1\text{HV}}' \parallel z_{1\text{LV}}')}{z_{1\text{HV}}'} = \frac{z_{1\text{LV}}'}{z_{1\text{HV}}' + z_{1\text{LV}}'} \text{ [p.u.]} \quad (11)$$

$$k_{1\text{LV}} = \frac{(z_{1\text{HV}}' \parallel z_{1\text{LV}}')}{z_{1\text{LV}}'} = \frac{z_{1\text{HV}}'}{z_{1\text{HV}}' + z_{1\text{LV}}'} \text{ [p.u.]} \quad (12)$$

$$k_{1\text{MV}} = \frac{z_1}{(z_{1\text{HV}}' \parallel z_{1\text{LV}}') + z_{1\text{MV}}} \text{ [p.u.]} \quad (13)$$

3.2. Zero-sequence impedance

Zero-sequence model is analog to the positive-sequence model, but influenced by an additional parameter – winding connection. This is presented with impedances Z_{YDHV1} , Z_{YDHV2} , Z_{YDMV1} , Z_{YDMV2} , Z_{YDLV1} , Z_{YDLV2} depicted in Figure 4 which are determined according to the Table II.

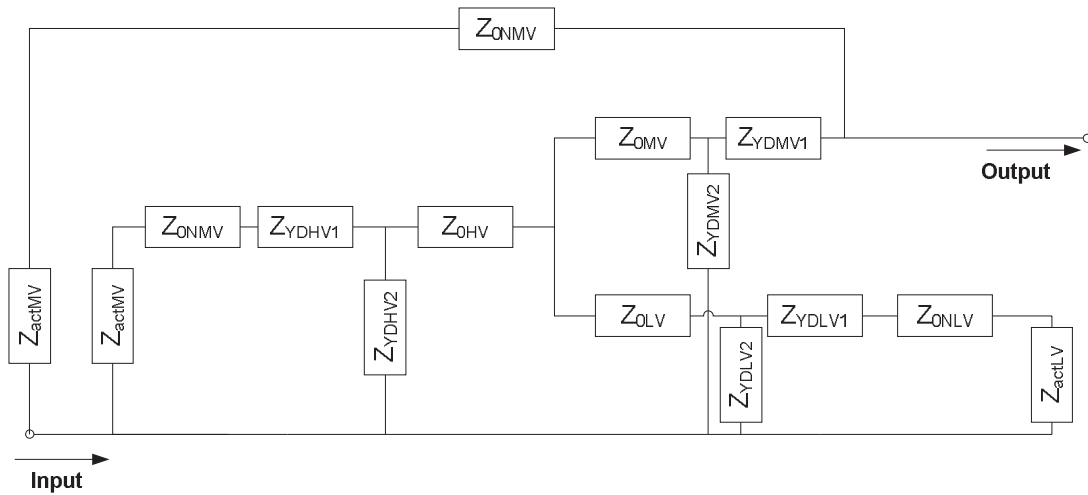


Figure 4 - Extended zero-sequence model

Table II - Winding connection impedances

	Z_{YDHV1}	Z_{YDHV2}	Z_{YDMV1}	Z_{YDMV2}	Z_{YDLV1}	Z_{YDLV2}
Y y y	∞	∞	∞	∞	∞	∞
YN y y	0	0	∞	∞	∞	∞
Y yn y	∞	∞	0	0	∞	∞
Y y yn	∞	∞	∞	∞	0	0
YN yn y	0	∞	0	∞	∞	∞
YN y yn	0	∞	∞	∞	0	∞
Y yn yn	∞	∞	0	∞	0	∞
YN yn yn	0	∞	0	∞	0	∞
Y d y	∞	∞	∞	∞	∞	∞
Y y d	∞	∞	∞	∞	∞	∞
D y y	∞	∞	∞	∞	∞	∞
YN d y	0	∞	∞	0	∞	∞
YN y d	0	∞	∞	∞	∞	0
Y yn d	∞	∞	0	∞	∞	0
Y d yn	∞	∞	∞	0	0	∞
D yn y	∞	0	0	∞	∞	∞
D y yn	∞	0	∞	∞	0	∞
YN d yn	0	∞	∞	0	0	∞
YN yn d	0	∞	0	∞	∞	0
D yn yn	∞	0	0	∞	0	∞
Y d d	∞	∞	∞	∞	∞	∞
D y d	∞	∞	∞	∞	∞	∞
D d y	∞	∞	∞	∞	∞	∞
YN d d	0	∞	∞	0	∞	0
D yn d	∞	0	0	∞	∞	0
D d yn	∞	0	∞	0	0	∞

Impedance of the entire model z_1 is calculated according to equations (14)-(16):

$$z_{0HV}' = [(z_{activHV} + z_{0NHV} + z_{YDHV1}) \parallel z_{YDHV2}] + z_{0HV} \text{ [p.u.]} \quad (14)$$

$$z_{0LV}' = [(z_{activLV} + z_{0NLV} + z_{YDLV1}) \parallel z_{YDLV2}] + z_{0LV} \text{ [p.u.]} \quad (15)$$

$$z_0 = [(z_{0HV}' \parallel z_{0LV}' + z_{0MV}) \parallel z_{YDMV2} + z_{YD;V1}] \parallel (z_{activMV} + z_{oNMV}) \text{ [p.u.]} \quad (16)$$

Coefficients used to recalculate the zero-sequence current to currents through each winding are as follows:

$$k_{0HV} = \frac{(z_{0HV}' \parallel z_{0LV}')}{z_{0HV}'} = \frac{z_{0LV}'}{z_{0HV}' + z_{0LV}'} \text{ [p.u.]} \quad (17)$$

$$k_{0LV} = \frac{(z_{0HV}' \parallel z_{0LV}')}{z_{0LV}'} = \frac{z_{0HV}'}{z_{0HV}' + z_{0LV}'} \text{ [p.u.]} \quad (18)$$

$$k_{0MV} = \frac{z_{activMV} + z_{oNMV}}{[(z_{0HV}' \parallel z_{0LV}' + z_{0MV}) \parallel z_{YDMV2} + z_{YDMV1}] + z_{activMV} + z_{oNMV}} \cdot \frac{z_{YDMV2}}{z_{0HV}' \parallel z_{0LV}' + z_{0MV} + z_{YDMV2}} \text{ [p.u.]} \quad (19)$$

4. CASE STUDY

Calculation of short-circuit currents will be performed on a real case transformer, using both methods. The aim is to illustrate how the generic approach simplifies the calculation process, and is also less time consuming. The mesh analysis method requires separated models for each short-circuit case.

Input data for transformer T1 are presented in Table III, where S_r is rated power of the transformer; U_{rHV} , U_{rMV} and U_{rLV} are rated voltages; $u_{schV/MV}$, $u_{schV/LV}$ and $u_{schMV/LV}$ are rated short-circuit voltages between windings referred to rated power S_r .

Table III - Input data for transformer T1

S_r [MVA]	Winding connection	U_{rHV} [kV]	U_{rMV} [kV]	U_{rLV} [kV]	$u_{schV/MV}$ [%]	$u_{schV/LV}$ [%]	$u_{schMV/LV}$ [%]	S_{schV} [MVA]	S_{schMV} [MVA]
400	YNynd	400	115	10.57	12.24	86.46	69.95	12000	5000

Tertiary (LV) winding has a function of stabilization so the calculations will be performed with short-circuit on MV side of the transformer. Both, HV and MV side are connected to an active network.

4.1. Mesh Analysis Method

4.1.1. Single-phase to earth short circuit on MV side

Model for single-phase to earth short circuit on MV side is presented in Figure 5, where U_{rHV_U} , U_{rHV_V} and U_{rHV_W} are rated voltages for each phase on HV side of the transformers with corresponding network inductance Z_{NHV} . U_{rMV_U} , U_{rMV_V} and U_{rMV_W} are rated voltages for each phase on MV side of the transformers with corresponding network inductance Z_{NMV} .

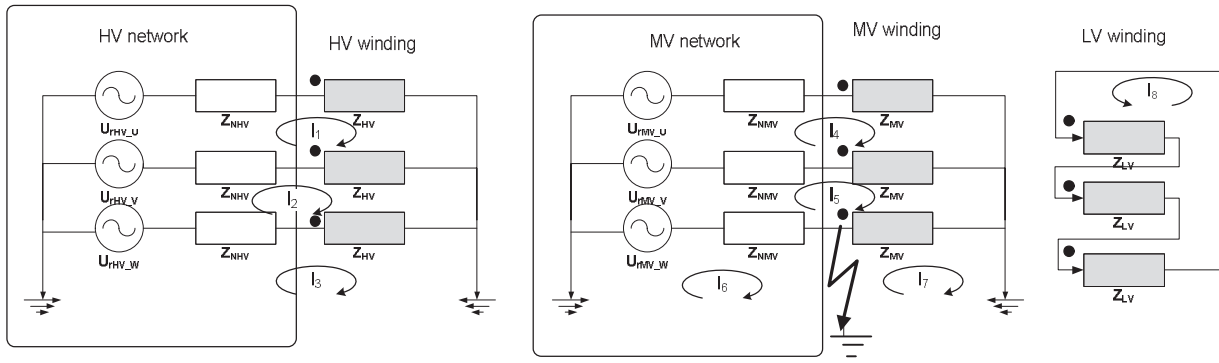


Figure 5 - Model for single-phase to earth short circuit on MV side

Network impedances on Figure 5 are calculated according to the formulas:

$$Z_{NHV} = j \frac{U_{rHV}^2}{S_{scHV}} \quad (20)$$

$$Z_{NMV} = j \frac{U_{rMV}^2}{S_{scMV}} \quad (21)$$

Z_{HV} , Z_{MV} and Z_{LV} are transformer inductances for each winding calculated from the expressions:

$$Z_{HV} = \frac{U_{rHV}^2}{i_0 \cdot S_r} \cdot 100, \quad (22)$$

$$Z_{MV} = \frac{U_{rMV}^2}{i_0 \cdot S_r} \cdot 100, \quad (23)$$

$$Z_{LV} = \frac{U_{rLV}^2}{i_0 \cdot S_r} \cdot 100, \quad (24)$$

where i_0 is the magnetizing current in percent of the rated current.

Mutual inductances between the winding $M_{HV/MV}$, $M_{HV/LV}$ and $M_{MV/LV}$ are not shown in Figure 5 and are calculated from the following expressions:

$$M_{HV/MV} = \sqrt{Z_{MV} \cdot \left(Z_{HV} - \frac{u_{scHV/MV} \cdot U_{rHV}^2}{S_r} \right)}, \quad (25)$$

$$M_{MV/LV} = \sqrt{Z_{LV} \cdot \left(Z_{MV} - \frac{u_{scMV/LV} \cdot U_{rMV}^2}{S_r} \right)}, \quad (26)$$

$$M_{HV/LV} = \sqrt{Z_{LV} \cdot \left(Z_{HV} - \frac{u_{scHV/LV} \cdot U_{rHV}^2}{S_r} \right)}, \quad (27)$$

Kirchhoff's voltage law equations are given in matrix form in (28):

$$\begin{bmatrix} I_1 \\ I_2 \\ I_3 \\ I_4 \\ I_5 \\ I_6 \\ I_7 \\ I_8 \end{bmatrix} = \begin{bmatrix} j(2 \cdot Z_{NHV} + 2 \cdot Z_{HV}) & -j(Z_{NHV} + Z_{HV}) & 0 & j(2 \cdot M_{HVMV}) & -j(M_{HVMV}) & 0 & 0 & 0 \\ -j(Z_{NHV} + Z_{HV}) & j(2 \cdot Z_{NHV} + 2 \cdot Z_{HV}) & -j(Z_{NHV} + Z_{HV}) & -j(M_{HVMV}) & j(2 \cdot M_{HVMV}) & 0 & -j(M_{HVMV}) & 0 \\ 0 & -j(Z_{NHV} + Z_{HV}) & j(Z_{NHV} + Z_{HV}) & 0 & -j(M_{HVMV}) & 0 & j(M_{HVMV}) & j(M_{HVLV}) \\ j(2 \cdot M_{HVMV}) & -j(M_{HVMV}) & 0 & j(2 \cdot Z_{NMV} + 2 \cdot Z_{MV}) & -j(Z_{NMV} + Z_{MV}) & 0 & 0 & 0 \\ -j(M_{HVMV}) & j(2 \cdot M_{HVMV}) & -j(M_{HVMV}) & -j(Z_{NMV} + Z_{MV}) & j(2 \cdot Z_{NMV} + 2 \cdot Z_{MV}) & -j(Z_{NMV}) & -j(Z_{MV}) & 0 \\ 0 & 0 & 0 & 0 & -j(Z_{NMV}) & j(Z_{NMV}) & 0 & 0 \\ 0 & -j(M_{HVMV}) & j(M_{HVMV}) & 0 & -j(Z_{MV}) & 0 & j(Z_{MV}) & j(M_{MVLV}) \\ 0 & 0 & j(M_{HVLV}) & 0 & 0 & 0 & j(M_{MVLV}) & j(3 \cdot Z_{LV}) \end{bmatrix}^{-1} \begin{bmatrix} u_{HV,U} - u_{HV,V} \\ u_{HV,V} - u_{HV,W} \\ u_{HV,W} \\ u_{MV,U} - u_{MV,V} \\ u_{MV,V} - u_{MV,W} \\ u_{MV,W} \\ 0 \\ 0 \end{bmatrix} \quad (28)$$

4.1.2. Three-phase short circuit on MV side

Model for three-phase short circuit on MV side of the transformer is presented in Figure 6.

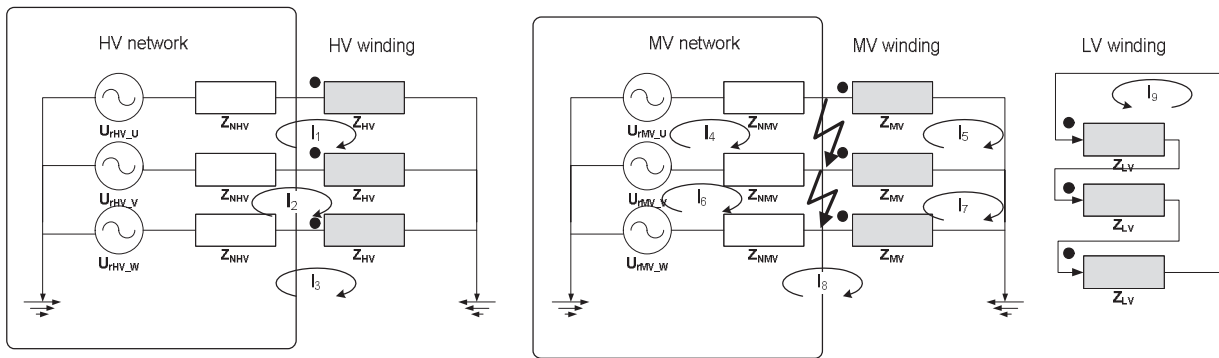


Figure 6 - Model for three-phase short circuit on MV side

Kirchhoff's voltage law equations are given in matrix form in (29).

$$\begin{bmatrix} I_1 \\ I_2 \\ I_3 \\ I_4 \\ I_5 \\ I_6 \\ I_7 \\ I_8 \\ I_9 \end{bmatrix} = \begin{bmatrix} j(2 \cdot Z_{NHV} + 2 \cdot Z_{HV}) & -j(Z_{NHV} + Z_{HV}) & 0 & 0 & j(2 \cdot M_{HVMV}) & 0 & -j(M_{HVMV}) & 0 & 0 \\ -j(Z_{NHV} + Z_{HV}) & j(2 \cdot Z_{NHV} + 2 \cdot Z_{HV}) & -j(Z_{NHV} + Z_{HV}) & 0 & -j(M_{HVMV}) & 0 & j(2 \cdot M_{HVMV}) & -j(M_{HVMV}) & 0 \\ 0 & -j(Z_{NHV} + Z_{HV}) & j(Z_{NHV} + Z_{HV}) & 0 & 0 & 0 & -j(M_{HVMV}) & j(M_{HVMV}) & j(M_{HVLV}) \\ 0 & 0 & 0 & j(2 \cdot Z_{NMV}) & 0 & -j(Z_{NMV}) & 0 & 0 & 0 \\ j(2 \cdot M_{HVMV}) & -j(M_{HVMV}) & 0 & 0 & j(2 \cdot Z_{MV}) & 0 & -j(Z_{MV}) & 0 & 0 \\ 0 & 0 & 0 & -j(Z_{NMV}) & 0 & j(2 \cdot Z_{NMV}) & 0 & -j(Z_{NMV}) & 0 \\ -j(M_{HVMV}) & j(2 \cdot M_{HVMV}) & -j(M_{HVMV}) & 0 & -j(Z_{MV}) & 0 & j(2 \cdot Z_{MV}) & -j(Z_{MV}) & 0 \\ 0 & -j(M_{HVMV}) & j(M_{HVMV}) & 0 & 0 & -j(Z_{NMV}) & -j(Z_{MV}) & j(Z_{NMV} + Z_{MV}) & j(M_{MVLV}) \\ 0 & 0 & j(M_{HVLV}) & 0 & 0 & 0 & 0 & j(M_{MVLV}) & j(3 \cdot Z_{LV}) \end{bmatrix}^{-1} \begin{bmatrix} u_{HV,U} - u_{HV,V} \\ u_{HV,V} - u_{HV,W} \\ u_{HV,W} \\ u_{MV,U} - u_{MV,V} \\ u_{MV,V} - u_{MV,W} \\ u_{MV,W} \\ 0 \\ 0 \\ 0 \end{bmatrix} \quad (29)$$

4.2. Symmetrical Components – Generic Approach

The calculation is performed for single-phase to earth and three-phase short circuit on MV side of the transformer. Both HV and MV side are connected to active network. According to Table I, active impedances for this case are $Z_{\text{activHV}} = 0$, $Z_{\text{activMV}} = 0$, $Z_{\text{activLV}} = \infty$; and according to Table II, winding connection impedances are $Z_{YDHV1} = 0$, $Z_{YDHV2} = \infty$, $Z_{YDMV1} = 0$, $Z_{YDMV2} = \infty$, $Z_{YDLV1} = \infty$, $Z_{YDLV2} = 0$. Hence, formulas (8)-(10) for positive-sequence system are transformed to:

$$z_{1HV}' = z_{1HVN} + z_{1HV} \text{ [p.u.]} \quad (30)$$

$$z_{1LV}' = \infty \text{ [p.u.]} \quad (31)$$

$$z_1 = z_2 = [z_{1HV}' + z_{1MV}] \parallel z_{1NMV} \text{ [p.u.]} \quad (32)$$

Coefficients used to recalculate the positive-sequence current to currents through each winding, according to expressions (11)-(13), are as follows:

$$k_{1HV} = 1 \text{ [p.u.]} \quad (33)$$

$$k_{1LV} = 0 \text{ [p.u.]} \quad (34)$$

$$k_{1MV} = \frac{z_1}{z_{1HV}' + z_{1MV}} \text{ [p.u.]} \quad (35)$$

For zero-sequence system, formulas (14)-(16) are transformed to:

$$z_{0HV}' = z_{0NHV} + z_{0HV} \text{ [p.u.]} \quad (36)$$

$$z_{0LV}' = z_{0LV} \text{ [p.u.]} \quad (37)$$

$$z_0 = (z_{0HV}' \parallel z_{0LV}' + z_{0MV}) \parallel z_{0NMV} \text{ [p.u.]} \quad (38)$$

Coefficients used to recalculate the zero-sequence current to currents through each winding, according to expressions (17)-(19), are as follows:

$$k_{0HV} = \frac{(z_{0HV}' \parallel z_{0LV}')}{z_{0HV}'} = \frac{z_{0LV}'}{z_{0HV}' + z_{0LV}'} \text{ [p.u.]} \quad (39)$$

$$k_{0LV} = \frac{(z_{0HV}' \parallel z_{0LV}')}{z_{0LV}'} = \frac{z_{0HV}'}{z_{0HV}' + z_{0LV}'} \text{ [p.u.]} \quad (40)$$

$$k_{0MV} = \frac{z_{0NMV}}{(z_{0HV}' \parallel z_{0LV}' + z_{0MV}) + z_{0NMV}} \text{ [p.u.]} \quad (41)$$

4.2.1. Single-phase to earth short circuit on MV side

According to Figure 1 short-circuit current for each system is calculated as:

$$i_1 = i_2 = i_0 = \frac{1}{2z_1 + z_0} \quad (42)$$

Short-circuit currents through each winding are calculated with:

$$i_{HV} = 2i_1 k_{1HV} + i_0 k_{0HV} \quad (43)$$

$$i_{MV} = 2i_1 k_{1MV} + i_0 k_{0MV} \quad (44)$$

$$i_{LV} = 2i_1 k_{1LV} + i_0 k_{0LV} \quad (45)$$

4.2.2. Three-phase short circuit on MV side

According to Figure 1, short-circuit current for each system is calculated as:

$$i_1 = \frac{1}{z_1}; \quad i_2 = i_0 = 0 \quad (46)$$

Short-circuit currents through each winding are calculated with:

$$i_{HV} = 2i_1 k_{1HV} + i_0 k_{0HV} = i_1 k_{1HV} \quad (47)$$

$$i_{MV} = 2i_1 k_{1MV} + i_0 k_{0MV} = i_1 k_{1MV} \quad (48)$$

$$i_{LV} = 2i_1 k_{1LV} + i_0 k_{0LV} = i_1 k_{1LV} \quad (49)$$

4.3. Comparison and Analysis

Results obtained using both methods for single-phase to earth short circuit are presented and compared in Table IV.

Table IV - Results for single-phase to earth short circuit in W phase

Single-phase to earth SC	HV			MV			LV
	U phase	V phase	W phase	U phase	V phase	W phase	
Inductance Matrix (1)	73.5 A	73.5 A	3748 A	771.5 A	771.5 A	14060 A	6442 A
Symmetrical Components (2)	73 A	73 A	3748 A	770 A	770 A	14061 A	6443 A
$\frac{(1)-(2)}{(1)} \cdot 100\%$	0.68%	0.68%	0%	0.19%	0.19%	-0.007%	-0.015%

Results obtained using both methods for three-phase short circuit are presented and compared in Table V.

Table V Results for three-phase short circuit results

Three-phase SC	HV			MV			LV
	U phase	V phase	W phase	U phase	V phase	W phase	
Inductance Matrix (1)	3707 A	3707 A	3707 A	12890 A	12890 A	12890 A	0 A
Symmetrical Components (2)	3707 A	3707 A	3707 A	12895 A	12895 A	12895 A	0 A
$\frac{(1)-(2)}{(1)} \cdot 100\%$	0%	0%	0%	-0.039%	-0.039%	-0.039%	0%

5. CONCLUSION

Requirements for short-circuit calculations for power transformer are an essential part of the transformer design process. Short circuit currents are input for the calculation of mechanical forces and stresses, as well as an important part of required transformer documentation.

In this paper, two methods for short circuit currents calculation are presented – mesh analysis method and symmetrical components method, with results compared on a real case transformer. Symmetrical components method is then extended using generic approach in order to obtain a standardized system applicable for all transformer types, all transformer configurations and for all short-circuit faults. Presented generic formula simplifies the calculation process and is less time consuming. Its application enables the automatization of the calculation process and also allows simple upgrading of the calculation system with additional possibilities due to oncoming requirements and requests.

6. REFERENCES

- [1] L.Song, *Transformer Short Circuit Current Calculation and Solutions*, Bachelor's Thesis, Electrical Engineering, Vaasa, Finland, 2013
- [2] G. Bertagnolli, *Short-circuit duty of power transformers*, Italy, 2007
- [3] D. Filipović-Grčić, B. Filipović-Grčić, K. Capuder, *Modeling of three-phase autotransformer for short-circuit studies*, International Journal of Electrical Power&Energy Systems, Volume(s) 56, 03-Dec-2013, Pages 228-234
- [4] H. Požar, *Visokonaponska rasklopna postrojenja*, Tehnička knjiga, Zagreb, 1990
- [5] IEC 60909-0, *Short-circuit currents in three-phase a.c. systems – Part 0: Calculation of currents*, 2001

Robert Platek
ABB Sp. z o.o. Corporate Research, Poland
robert.platek@pl.abb.com

Grzegorz Juskiewicz
ABB Sp. z o.o. Corporate Research, Poland
grzegorz.juskiewicz@pl.abb.com

SEISMIC ANALYSES FOR POWER TRANSFORMERS

SUMMARY

Reliability and security of power systems, especially in areas prone to earthquakes, depends on the seismic withstand of its components and interaction of these components with other elements. All relevant power products and components should be designed and tested to guarantee high seismic performance. Option which is strongly recommended for seismic qualification is shake table test. This way is very expensive and in some cases like power transformers impossible due to its weight and size. Because of this the numerical analyses can be very helpful to determine the dynamic characteristic of the system. This way is more and more used during evaluation of seismic performance of power products, especially in the design phase.

In the paper a different numerical approaches for seismic analyses of the power transformers have been presented. In the first part of the article focus was put on typical simulation methods defined by IEEE and IEC standards. This approach is dedicated only for transformer's components. Due to fact that standards do not provide clear information about fluid influence on power equipment during seismic events, some investigations related with oil filled transformers were done and summarized. Three different numerical methods were investigated. First one is built based on the Fluid-Structure Interaction (FSI) methodology. In this approach combination of different software (CFD, structural, and coupling code) is used to cover phonemes related with fluid dynamics and structural analyses. FSI methodology gives a wide possibility but, it's very complex however, is very complex which can be a disadvantage for very complex objects. Next one uses acoustic elements, where the fluid is modeled as acoustic medium. This is method which allows to take into account fluid during seismic simulations in simplified way. The last one uses Lagrange and Euler element formulations (CEL) in which sloshing effect of the oil in power products can be considered. All this approaches can be very helpful to determine the dynamic characteristic of the transformers and its equipment including fluid.

Key words: transformer, seismic, Finite Element Method (FEM), acoustic medium, Fluid-Structure Interaction (FSI), Coupled Euler – Lagrange (CEL)

1. INTRODUCTION

1.1. Seismic Performance Overview

Seismic forces with which we meet mostly during the earthquake is a natural phenomenon arising in the Earth's crust in the form of seismic waves, generating low frequency vibrations and weakening during propagation. Seismic loads are some of the dynamic loads which may affect not only the buildings, but also in power devices. Power transformers are one of the critical components in power systems. Their reliability and safety exposed to earthquake loading is dependent upon the seismic response of its selected components and interaction of these components with other elements. As a result, all relevant

power products and components, operating in seismically active areas, should be designed and tested to guarantee high seismic performance.

The standards indicate that the seismic qualifications should be done for critical elements (bushings, conservator system) of transformer by shake table testing. It is acknowledged that the supporting structure of the bushing or conservator (tank, top plate, etc.) amplifies the ground acceleration. The latest studies indicate that the dynamic response of bushings mounted on transformer tank is greatly different than to the rigid frame used in standards testing. Its dynamic characteristics are influenced by flexibility of the top plate of the transformer tank [1, 2]. Another issue is fluid, that exists in such product like transformer. Standards does not provide clear information about fluid influence on the supporting structure of bushings and changing dynamic characteristic under seismic loads.

Making power products earthquake-proof is no easy task. However, many years of ABB experience in this field helped to understand nature of seismic events. Efficient analyses of seismic loads based on the standards go far towards to develop innovative approaches to this type of problems.

1.2. Standards for Power Transformers

Several different methods that have been used for the investigating the seismic performance of electrical equipment, including transformers and bushings there are known. Two main standards groups are widely used: IEEE 693 in America and IEC in Europe.

IEEE Std 693-2005 "Recommended Practice for Seismic Design of Substations" [3] is a newly revised document covering the procedures for qualification of electrical substation equipment for different seismic performance level. The IEEE 693 strongly recommends that the equipment shall be qualified on the support structure that will be used at the final substation. In contrast, the IEC 61463 "Bushings-Seismic qualification" [4] is an IEC recommendation covering the seismic qualification of power bushings. It recommends executing of a dynamic analysis or vibration test. It is based mainly on static calculations introducing the coefficients to amplify the severity from the ground to the transformer. It must be noted, that bushings meeting the requirements of IEEE 693 will, in most cases, meet the requirements of IEC 61463.

Even if shake table tests are strongly recommended for seismic qualification of substation, the numerical analyses can be very helpful to determine seismic withstand of these products. Furthermore in some cases, where the tests are impossible because of weight and size (e.g. power transformers), this the only one way to determine the dynamic characteristic of the system.

1.3. Traditional Simulation Approaches

Seismic analysis of power systems is realized by estimation of the impact of a specific seismic loads on an object or part thereof (equipment). Methods of Seismic analyses methods can be divided into the following types which are based on:

- a) static approach,
- b) quasi-dynamic approach,
- c) dynamic approach.

Static analyses and quasi-static method are often used to simple equipment having the main frequency modes out of the dangerous seismic range (above 33 Hz). Such objects are qualified as 'rigid' ones. In the first method series of loads acting on the structure to represent the effect of earthquake ground motion are defined and applied to the component's centre of gravity. The second method can be used for equipment having a few important modes in the seismic range. Forces shall be obtained by multiplying the values of the components mass by the coefficients which are used to amplify the ground accelerations: K – super-elevation factor, R – the response factor, and S – static coefficients.

For complex structures of power products with many modes within the seismic range the modal dynamic analysis is recommended by the standard, and this approach was used in the analyzed case. The standard specifies also explicit time history dynamic analysis (also based on modal dynamic approach), which should be performed if the results cannot be verified by measurements (for multiple, inter-connected heavy equipment). Alternatively response spectrum can be used for rough, conservative evaluation. Those two methods usually are based on the Finite Element Method (FEM).

1.4. Finite Element Method (FEM) for seismic analyses

The modal dynamic analysis of the bushing under seismic loads is presented below. In this method, the object under examination is represented by its geometrical CAD model. Once the geometric model has been created, a set of boundary conditions has to be specified (constraints and exciting forces) and applied to the geometrical model (Figure 1). Afterwards, a meshing procedure is used to define and break the model up into small volume elements (Figure 1).

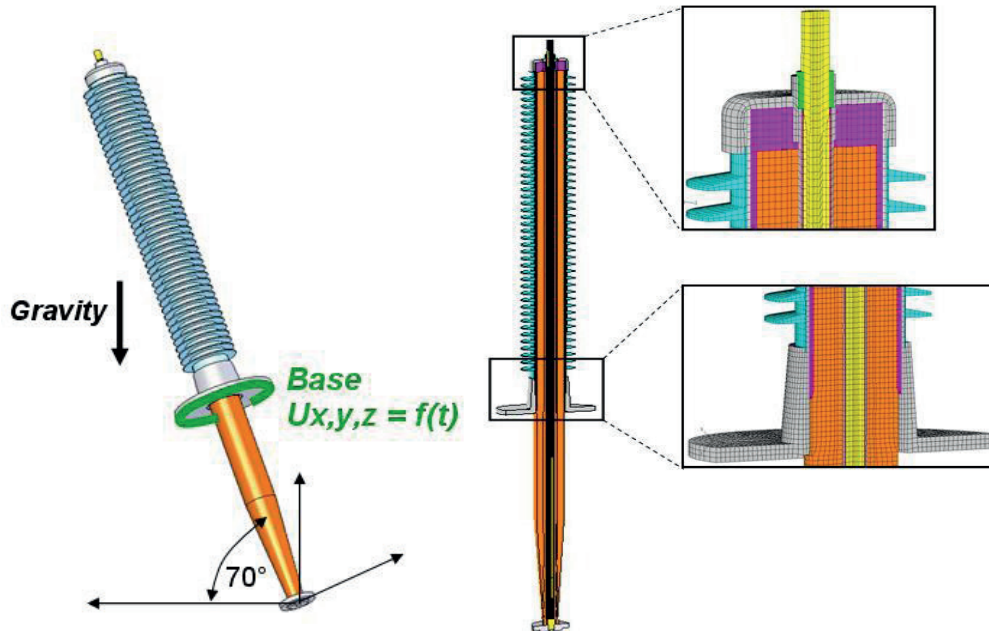


Figure 1 – Boundary conditions (left) and mesh of analyzed RIP bushing 230 kV (right)

In the final stage the results (accelerations, displacements, stresses and strains) are analyzed and compared with experiment (if possible).

In the presented approach, the structural evaluation for seismic events is based on linear analysis, using the structure's modes up to a limiting cut-off frequency, (33 Hz). Nonlinear effects such as contact or plasticity material model cannot be include in this approach.

The eigenvalue problem for natural frequencies (undamped finite model) is:

$$(-\omega^2 \mathbf{M} + \mathbf{K}) \Phi = 0 \quad (1)$$

where:

M - matrix (which is symmetric and positive definite)

K - stiffness matrix (which includes initial stiffness effects if the base state included the effects of nonlinear geometry and pre stress caused by gravity)

Φ - eigenvector (the mode of vibration)

ω - is the natural frequency

Once the modes are available, their orthogonality property allows the linear response of the structure to be constructed as the response of a number of single degree of freedom systems. In other words, the mechanical behavior of the bushing structure under base-motion is derived as linear superposition of its natural frequency modes.

Using this numerical approach for seismic analyses of HV transformer bushings, three different excitations referred to as sine sweep, earthquake time history and sine beat are usually performed. It was verified that the applied FEM methodology is able to predict the relative natural resonant frequencies, acceleration, and displacement for seismic qualification with good accuracy [5] presented in Table 1.

Table 1 - Natural resonance frequencies for simulated and tested transformer bushing

Natural resonance frequencies [Hz]			
Mode	Simulations	Measurements	Difference [%]
1	12.77	12.4	3
2	12.79	12.5	3
3	20.17	19.5	4
4	20.28	20.1	1
5	76.52	n.a.	n.a.

The application of advanced numerical simulations shows the potential to minimize further the experimental efforts on shake table qualification.

2. ADVANCED SEISMIC ANALYSES OF POWER TRANSFORMERS

2.1. Dynamic Behavior of the Bushing-Transformer System

In the literature we can find a lot of claims that the dynamic behavior of the bushing, mounted on transformer, is different than separate bushing that is seismically tested. The seismic response of the transformer-bushing system can be complex by interconnecting components. Furthermore, installed equipment can cause damage through connectors (bolts, rivets, weld). Thus, the seismic bushing tests with rigid frame will not take all critical situations into account. To quantify the effect of transformer on bushing dynamic characteristic and its seismic response, further investigation is needed [6]. The Finite Element Method (as for RIP bushing 230 kV) seems to be good for additional research in order to understand the dynamic response of transformer-bushing system. The study was prepared based on the modal analyses (similar as for RIP bushing 230 kV) in order to find natural frequencies of the analyzed model.

Three models: bushing, bushings together with turrets and top cover, transformer (without oil) were prepared and analyses were performed. The main results obtained are resonant frequencies presented in Table 2 and stress distribution shown in Figure 2.

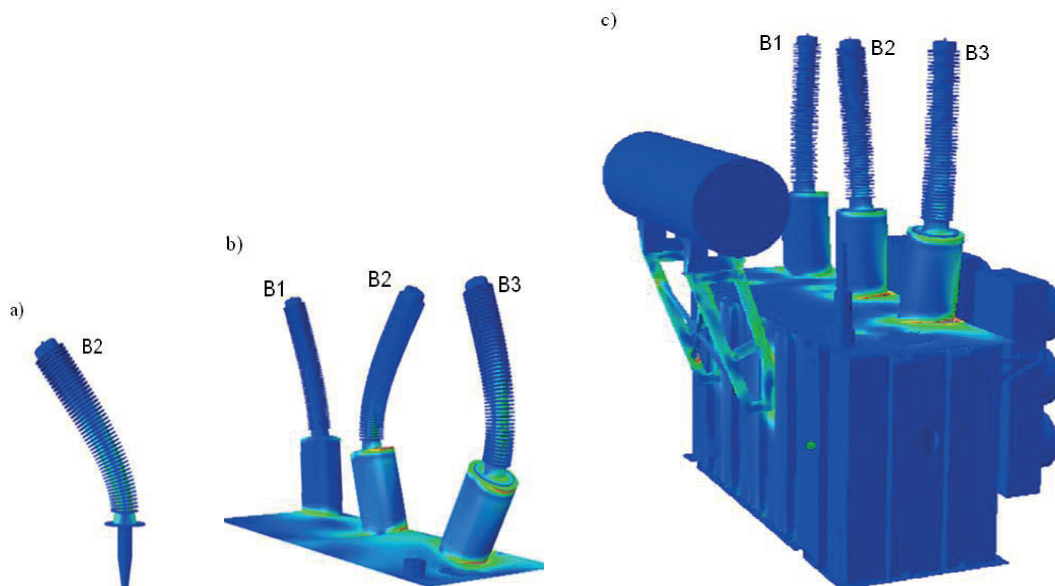


Figure 2 – Modes during modal analyses of a) bushing, b) bushings with top cover, c) transformer. B1 – bushing No. 1, B2 – bushing no. 2, B3 – bushing No. 3

Table 2 - Comparison of first natural frequencies [Hz] obtained from simulations for bushing, bushings with top cover, and the whole transformer

Bushing	Bushings with top cover			Bushing-Transformer system		
B2	B1	B2	B3	B1	B2	B3
14.13	5.54	18.38	20.34	6.4	7.08	6.1
14.13	22.99	26.46	25.83	8.36	7.38	7.08
	27.32	30.99	26.46	8.74	8.36	11.18
	33.28	33.28	32.04	10.44	8.74	17.47

Natural frequencies found were limited up to 33 Hz or 15 modes. For the last two cases frequencies are listed for both: the whole analyzed structure and separate bushings. The natural frequencies differ for three analyzed cases. For the last case (transformer) there are lower ones than for the first case (separate bushing). The performed simulations show that for comprehensive seismic analyses of transformer bushing whole system should be considered. Moreover, for power products that are liquid (oil) filled influence of the liquid on seismic loads should be verified.

2.2. Fluid-Structure Interaction (FSI) Co-Simulations

To find the right dynamic characteristic of the transformer-bushing system including tank, top plate, turrets and bushings numerous studies exist [1, 2]. Some activities are done in the area of seismic analyses of elevated tanks [7, 8, 9], ship industries and sea transport [10, 11] or storage tanks [12, 13] or its road transport of liquids [14]. But, generally, there is no clear statement about fluid influence on dynamic behavior of the transformer-bushing system.

Currently, usual approach in cases where strong interaction between fluid flow phenomena and stress effects exists is to perform structure and CFD analysis separately. Thus, the impact of flow induced forces on a structure and the impact of structure on the fluid flow are not considered. In an FSI co-simulation the analysis domains are coupled in that way, that the equations for each domain are solved separately. Loads and boundary conditions are exchanged between two domains at the common interface e.g. using MpCCI code [15]. Fluid-structure simulation capability allows fully coupled simulation approach and more precise modeling.

In the CFD the structure (tank) with fluid is modeled while in structural calculations only the structure is considered. CFD code is responsible for calculation of fluid flow. As a result, forces on the structure walls were delivered to the structural code and used as loads and boundary conditions. The new shape of the structure is given back to the CFD where the mesh update is prepared for next time increment. Finally we can get stresses, strains and deformation for the structure taking into account fluid dynamics. The scheme of the approach is presented in Figure 3.

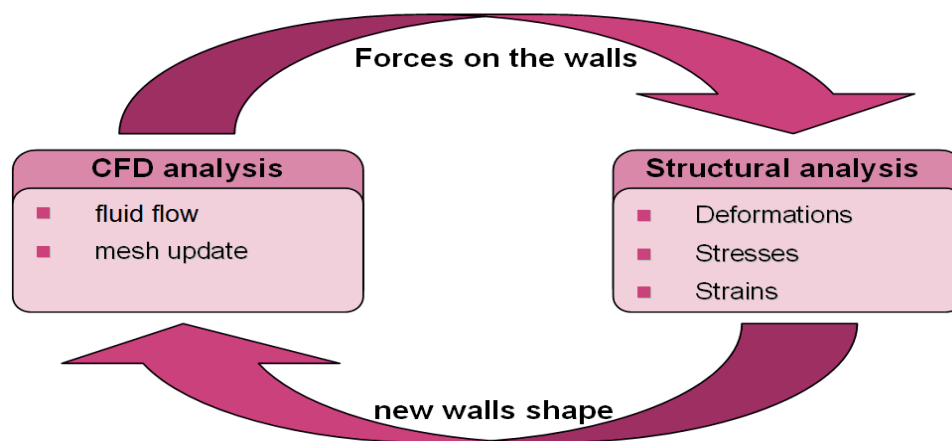


Figure 3 – FSI co-simulations seismic analysis approach

2.3. Acoustic Medium Approach for seismic analyses

Another approach to examine fluid influence during seismic loads is the way where a fluid is modeled as an acoustic medium. In case of an acoustic medium the equilibrium equation for small motions of a compressible, inviscid fluid flowing through a resisting matrix material can be represented by equation:

$$\frac{\partial p}{\partial x} = \gamma \dot{u} + \rho \ddot{u} = 0 \quad (2)$$

where:

p - is the dynamic pressure in the fluid (the pressure in excess of any initial static pressure),

x - is the spatial position of the fluid particle,

\dot{u} - is the fluid particle velocity,

\ddot{u} - is the fluid particle acceleration,

ρ - is the density of the fluid,

γ - is the "volumetric drag" (force per unit volume per velocity) caused by the fluid flowing through the matrix material.

Main assumptions of the constitutive behavior of the fluid are both inviscid and compressible. Thus, the bulk modulus of an acoustic medium relates the dynamic pressure in the medium to the volumetric strain by:

$$p = -K\varepsilon \quad (3)$$

where:

$\varepsilon = \varepsilon_x + \varepsilon_y + \varepsilon_z$ is the volumetric strain.

Both the bulk modulus K and the ρ density of an acoustic medium must be defined. The bulk modulus K can be defined as a function of temperature and field variables but does not vary in value during an implicit dynamic analysis using the subspace projection method or a direct-solution steady-state dynamic analysis [16]. For these procedures the value of the bulk modulus at the beginning of the step is used.

2.4. Coupled Euler-Lagrange Method

CEL (Coupled Euler - Lagrange) method implements possibility of interaction between Lagrange and Euler mesh formulation. In typical Lagrangian approach nodes of the finite elements are fixed within material. Consequently the finite element deforms as the material deforms. Precise values of displacement and distortion are defined by nodes coordinates. Lagrangian formulation is commonly used for solid mechanics problems. The difficulty arises in case of large deformations of analyzed objects. Excessive deformation of discrete mesh often occurs, what might lead to convergence problems and often inaccurate and useless results. In the opposite Eulerian approach introduces numerical grid and corresponding to it nodes as a discrete domain fixed in space. The material flows through the elements which not deforms as in Lagrange approach.

The CEL approach combines the advantages of Lagrange and Euler formulation and can be used in advanced seismic simulations. Sloshing of the fluid (oil domain) is solved using Eulerian formulation on a Cartesian grid that overlaps the Lagrange structure.

In considered case fluid like material was defined using linear U_s - U_p Equation Of State (EOS) model governed by the Mie-Gruneisen equation of motion. This relates to incompressible fluid model. In the EOS U_s - U_p Hugoniot form there are three input variables which must be defined before simulation. These are: c_0 - bulk speed of sound, s - is linear relationship between the linear shock velocity, U_s , and the particle velocity, U_p and Γ_0 - Gruneisen's gamma at the reference state.

Described approach was used to simulate transformer conservator tank partially filled with oil. Such setup would be difficult in representation using coupled acoustic-structural approach with expected large motions of the fluid (sloshing). Whole assembly was subjected to three axial time history ground motion which definition was based on "High level required response spectrum" defined in IEEE693 standard [3].

FE model was built using Eulerian solid and Lagrangian shell elements. All interfaces between structural parts were bonded - welded connection. At the bottom of the support structure ground motion accelerations were defined. Gravity load was applied globally.

Oil motion during time history test for first seconds of the ground motion is presented in Figure 4. One can see that CEL approach caught strong inertia of the fluid and its impact on the structure. This effect was not observed using coupled structural – acoustic approach. Concluding evaluation of fluid sloshing is one of the main benefits of presented method.

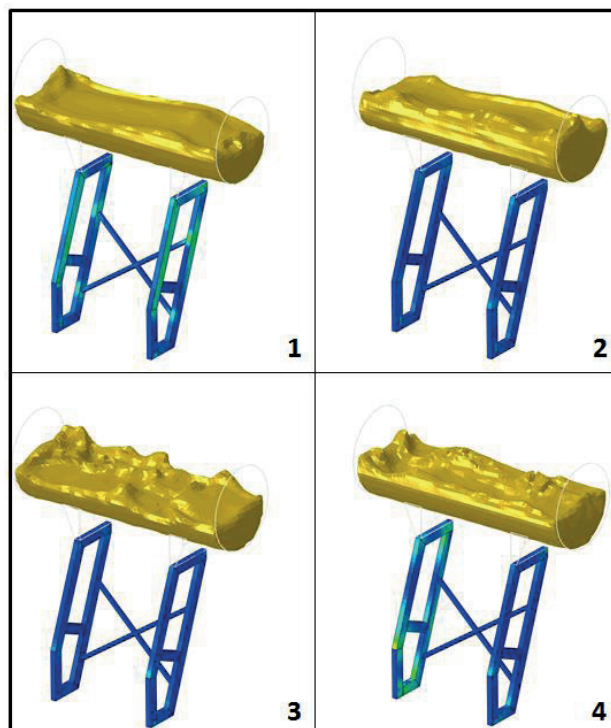


Figure 4 – Fluid motion during predefined ground motion

Important note is that CEL approach is usually solved using dynamic explicit integration scheme. This implicates several consequences. One of it is that stable time increment is strictly related to element size and density of material. More refined mesh requires very low time increment to keep on track solution stability. On the other hand Euler domain requires very fine mesh to represent fluid behavior and its interaction with Lagrange/structural component properly. Another issue is related to contact modeling and the interface between fluid and structural domain. During simulation it was observed that fluid has been separated from the structural domain. One can conclude that one of the possible reasons of such effect has been caused by imprecise definition of the viscosity of the fluid. Implemented methodology did not resolve near boundary layer effects. Presented approach was solved in time domain. Input based motion lasted ca. 30 s and covered all important dangerous frequency values.

3. CONCLUSION

Key components of substations are transformers and bushings. Past earthquakes show that their seismic performance has not been satisfactory. Understanding the seismic interactions between substations equipment like transformer-bushings-foundations and fluids is very important to proper assessments of seismic performance of substations and in qualifications of equipment.

In this paper the first results of study in ABB related to fluid influence on dynamic behavior of the system like transformer-bushing was presented. In order to simulate these complex phenomena three different approaches for seismic analyses were presented. One of them is built based on the FSI and combination of different software (CFD, structural, and coupling code) to cover Fluid dynamics and structural analyses. Other is based on acoustic modeling of fluid. The last one is based on the coupled Euler Lagrange formulations.

Consequently presented methods are introducing advantages and disadvantages. In case of full FSI approach where CFD and FEM method are coupled one can evaluate in details behavior of the fluid and its influence on the structural response. In case of complex geometries difficulty in mesh generation and remeshing process arises. In this method iteration stability requires very low time increment what implies excessively long calculation time. Acoustic-structural approach is convenient and relatively fast method. Main benefit is that external coupling code is not required. By using acoustic elements user can evaluate maximum pressure which is generated by the fluid during vibration excitation. One must be aware that this method gives reasonable results when expected response of the structure has relatively low amplitude. In case of high structural amplification possible sloshing effect will not be captured. Acoustic-structural approach is often limited to time history calculations therefore it cannot be used in eg. response spectrum method. The last method (CEL) introduces coupling between Lagrange and Euler domain. Thus, it is possible to simulate large deformation and sloshing of the fluid. In this method integration scheme is based on explicit formulation what many times results in very small time increment and consequently long calculation time.

Taking into account above, all this approaches can be very helpful to determine the dynamic characteristic of the transformers and its equipment including fluid and can reduce time of design phase if there are used appropriate for analyzed cases.

REFERENCES

- [1] A. S. Whittaker., G. L. Fenves., A. S. J. Giliani; Evaluation of seismic qualification procedures for high-voltage substation equipment. *A Structural Engineering Odyssey*. section 25. chapter 5. doi (document identification number) 10.1061/40558(2001)52. 2001
- [2] A. Filiatrault., M.EERI., H. Matt; Experimental Seismic Response of High-voltage Transformer-Bushing Systems. *Earthquake Spectra*. Vol. 21. 1009-1025. November 2005.
- [3] IEEE Std 693-2005. IEEE Recommended Practice for Seismic Design of Substations. IEEE Standard Department. 2005.
- [4] IEC 61463 Technical Report II; Bushings – seismic qualifications. Luglio. 1996
- [5] J. Rocks. N. Koch. R. Płatek. T. Nowak; Seismic Response of RIP-transformer bushing. *Insulator News & Market Report (INMR) World Congress on insulators, arresters and bushings*. Brazil. 2007
- [6] S. Ersoy. M. A. Saadeghvaziri; Seismic response of transformer-bushing systems. *IEEE Transaction on Power Delivery*. Power Engineering Society. Institute of Electrical and Electronics Engineers. 19. 131-137. 2004
- [7] R. Livaoglu. A. Dogangun; Seismic evaluation of fluid-elevated tank-foundation/soil systems in frequency domain. *TECHNO-PRESS LTD. STRUCTURAL ENGINEERING AND MECHANICS*. Vol. 21. Numb 1. 101-119. 2005
- [8] Gareane A. I. Algreane., Siti Aminah Osman, Othman A. Karim, Anuar Kasa, Behavior of Elevated Concrete Water Tank Subjected to Artificial Ground Motion, *Electronic Journal of Geotechnical Engineering*, Vol. 16 [2011], Bund. D, 387-406, 2011.
- [9] Kalani Sarokolayi L., Navayineya B., Hosainlibegi M., Vaseghi Amiri J., Dynamic analysis of water tanks with interaction between fluid and structure, *The 14th World Conference on Earthquake Engineering* October 12-17, Beijing, China, 2008.
- [10] M. Warmowska; Numerical simulation of liquid motion in a partly filled tank. *Opuscula Mathematica*. vol. 26. No. 3. 529-540. 2006
- [11] M. Warmowska; Określenie parametrów ruchu cieczy w zbiorniku okrętowym z uwzględnieniem zjawisk nieliniowych. PB No. 5 T12C 057 24. Politechnika Gdańska. Gdańsk. 2005.
- [12] Priestley M.J. and all, Seismic design of storage tanks, Recommendation of a Study Group the New Zealand Society for Earthquake Engineering, New Zealand, 1986, pp.180.
- [13] Rammerstorfer F.G., Scharf K., Fischer F.D., Storage tanks under earthquake loading, *Appl. Mech. Reviews*, 43, 1990, 261-281.
- [14] Jimin Z., Yongqiang W., Jun L., Load distribution of railway tank car in fluid sloshing, *fifth International Conference on Natural Computation*, 2009.
- [15] MpCCI. Mesh-based parallel Code Coupling Interface. www.mpcci.de. Fraunhofer-Institute SCAI. 2008
- [16] Abaqus Analysis User's Manual. Dassault Systèmes. 2008

Mladen Marković
Končar Distribution & Special Transformers
mladen.markovic@koncar-dst.hr

Ivanka Radić
Končar Distribution & Special Transformers
ivanka.radic@koncar-dst.hr

Vlatka Matun
Končar Distribution & Special Transformers
vlatka.matun@koncar-dst.hr

STATISTICAL AND NUMERICAL ANALYSIS OF TRANSFORMER OIL AC BREAKDOWN

SUMMARY

Transformer oil AC breakdown research is an important part of transformer insulation design. Research presented in this paper consists of statistical and numerical analysis of breakdown data measured in portable oil tester. Statistical analysis is done by modeling measured data as a random process with Gaussian and Weibull probability function. Numerical analysis uses statistical data for calculation of stressed oil volume, stressed electrode area and safety factors of “cumulative stress” method. Both statistical and numerical analysis showed how breakdown withstand depends on different variables and why they are important in measurement interpretation.

Key words: oil breakdown, Gaussian distribution, Weibull distribution, FEM, stressed oil volume, stressed electrode area, “cumulative stress” method

1. INTRODUCTION

Aim of this paper is to statistically and numerically compare three methods which describe AC breakdown of transformer oil: stressed oil volume (*SOV*), stressed electrode area (*SEA*) and cumulative stress method [1 – 6].

Experimental part consists of three different test variables: electrode type, electrode distance and transformer oil treatment. Tests are performed with Megger OTS100AF oil testing device, with oil breakdown range up to 100 kV. Transformer oil in all experiments was Ergon’s Hyvolt III mineral oil.

Numerical part is done with *Infolytica ElecNet* software and custom written VBA scripts.

Statistical analysis was influenced by work done by Martin and Wang in 2008 [7].

2. TRANSFORMER OIL TESTING

Table I shows different values of test variables.

Table I - Test variables names and abbreviations

Test Variable	Value	Abbreviation
Electrode type	 36 mm Mushroom Electrodes	A
	 12.7 mm Spherical Electrodes	B
Electrode distance	1 mm	1
	2 mm	2
	3 mm	3
Transformer oil treatment	Mineral oil degassed	D
	Mineral oil non-degassed	N

This makes a total sum of twelve measurement sets. Each set is coded according to variable abbreviations. For example, test with “B” type of electrodes, electrode distance of “1 mm” and “Degassed” transformer mineral oil is abbreviated “B1D”. For each measurement set, a number of 40 breakdown voltages are documented, with 1 minute pause between breakdowns (no stir).

2.1. Statistical analysis

Visualization and analysis of acquired data was done with the help of the *Wolfram Mathematica 10.0* and *Microsoft Excel 2010*. Figure 1 shows histogram plots, with estimated censored Weibull distribution (continuous line) and Gaussian distribution (dashed line).

Weibull probability [8] density function $P(x)$ is defined for $x \in [0, \infty)$ with parameters α and β as:

$$P(x) = \frac{\alpha}{\beta} \left(\frac{\alpha}{\beta} \right)^{\alpha-1} e^{-\left(\frac{x}{\beta}\right)^\alpha} \quad (1)$$

Gaussian probability [9] density function $P(x)$ is defined for $x \in (-\infty, \infty)$ by μ and σ as follows:

$$P(x) = \frac{1}{\sigma\sqrt{2\pi}} e^{-\frac{(x-\mu)^2}{2\sigma^2}} \quad (2)$$

Table II shows statistic parameters of these two distributions (α , β and μ , σ), and also goodness-of-fit (*GOF*), as well as percentiles P_1 and P_{50} for both parametric and non-parametric evaluation of the data. For Gaussian distribution 50th percentile equals mean value ($P_{50} \equiv \mu$).

Table II - Statistical evaluation of measured data

	Weibull distribution					Gaussian distribution					Non-parametric	
	<i>GOF</i>	α	β	P_1 [kV]	P_{50} [kV]	<i>GOF</i>	μ	σ	P_1 [kV]	P_{50} [kV]	P_1 [kV]	P_{50} [kV]
B1N	0.91	11.58	39.42	26.50	38.20	0.72	37.70	3.89	28.64	37.70	30.40	38.20
B2N	0.75	17.02	68.31	52.13	66.85	0.83	66.27	4.44	55.94	66.27	55.90	66.40
B3N	0.69	15.46	94.13	69.90	91.93	0.15	90.71	8.19	71.65	90.71	57.10	93.10
B1D	0.80	13.59	43.58	31.06	42.42	0.96	42.00	3.43	34.01	42.00	34.10	42.00
B2D	0.86	16.68	72.45	54.99	70.87	0.95	70.26	4.83	59.03	70.26	57.00	70.00
B3D	0.10	18.05	98.30	76.18	96.32	0.35	94.76	4.65	83.93	94.76	83.40	94.40
A1N	0.71	10.87	32.94	21.58	31.85	0.76	31.53	3.12	24.28	31.53	24.70	32.20
A2N	0.92	13.36	60.15	42.64	58.53	1.00	57.95	4.88	46.59	57.95	45.10	57.80
A3N	0.16	6.13	74.28	35.06	69.96	0.30	69.40	10.75	44.40	69.40	48.50	65.90
A1D	0.98	13.11	37.43	26.35	36.40	0.38	35.94	4.01	26.62	35.94	17.70	36.40
A2D	0.64	9.48	73.94	45.50	71.13	0.20	70.03	10.31	46.04	70.03	34.90	71.20
A3D	0	1.54	311.09	15.71	245.23	0	97.84	3.79	89.03	97.84	85.30	100.00

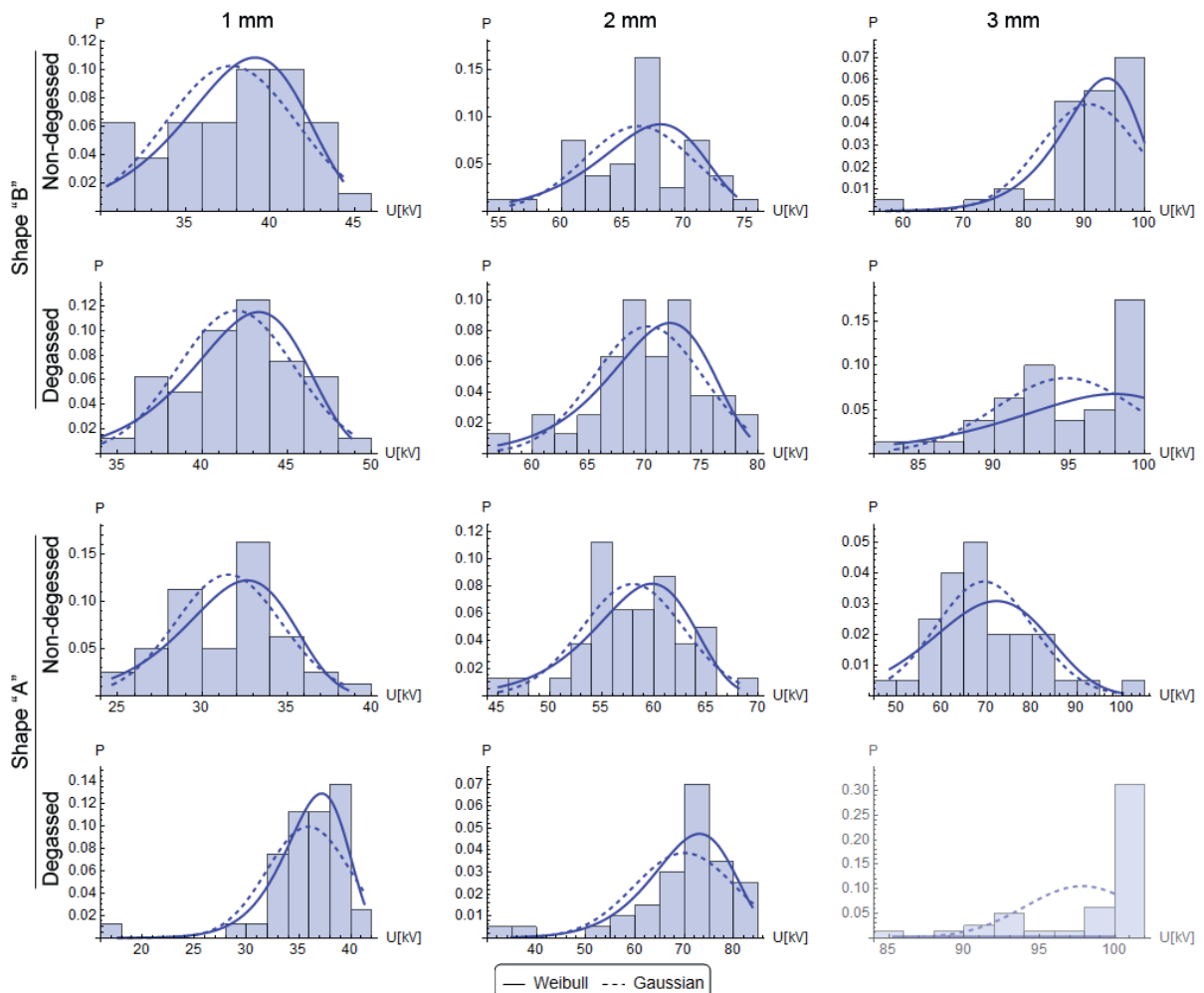


Figure 1 – Histogram plot of measured data

Figure 2 shows both first and fiftieth percentile for Weibull, Gaussian and non-parametric distribution of acquired voltage breakdown data.

GOF values for Weibull and Gaussian distribution are shown on Figure 3. They represent measure of the deviation of a sample from expectation.

Table III shows percent of breakdowns (per test set) that did not occur.

All voltage breakdown values are shown on Figure 4. It contains four graphs that show forty breakdown values for one, two and three millimeters, depending on electrode shape and oil treatment.

Figure 5 shows Gaussian parameters μ and σ from Table II normalized to 1 mm (i.e. average breakdown field between electrodes), according to Eq. (3).

$$\bar{E} = \frac{\bar{U}}{d} = \frac{\mu \pm \sigma}{d} \quad (3)$$

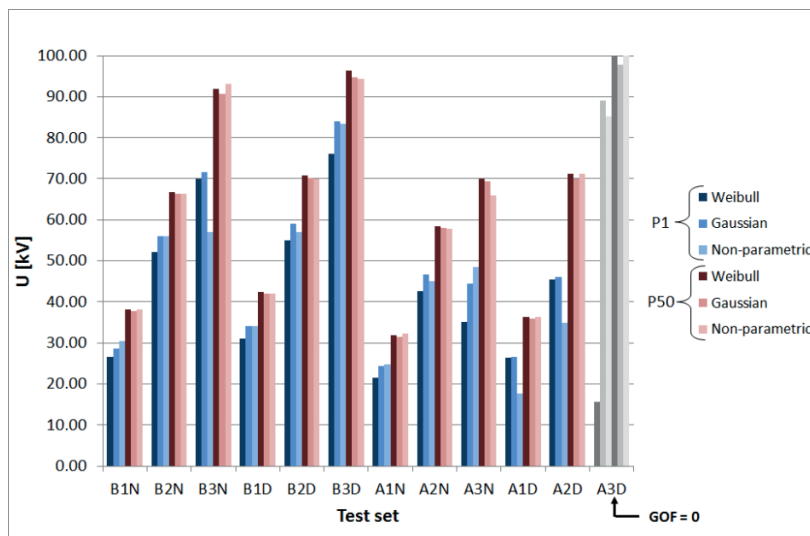


Figure 2 – First (P_1) and fiftieth (P_{50}) percentile for three distributions from Table II

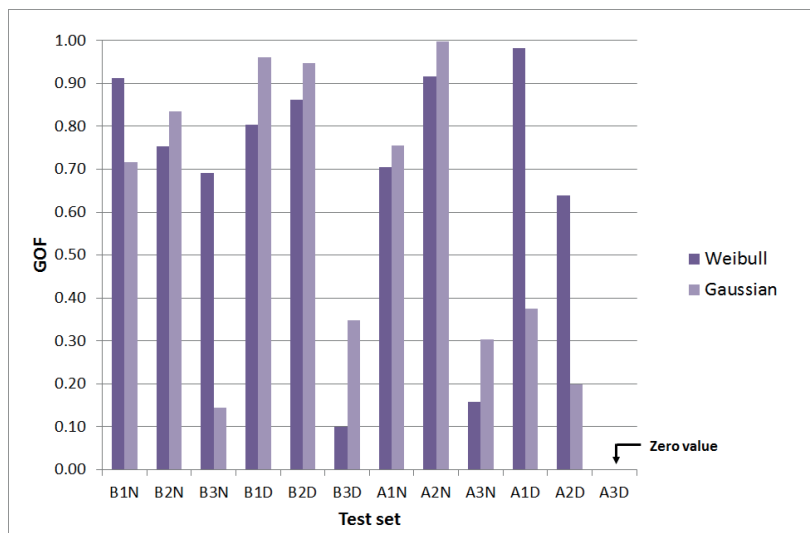


Figure 3 – Goodness-of-fit for parametric distributions in Table II

Table III - Percent of measurement in which breakdown did not occur

	"No-breakdown" rate [%]
B3N	7.5%
B3D	30.0%
A3N	2.5%
A3D	65.0%

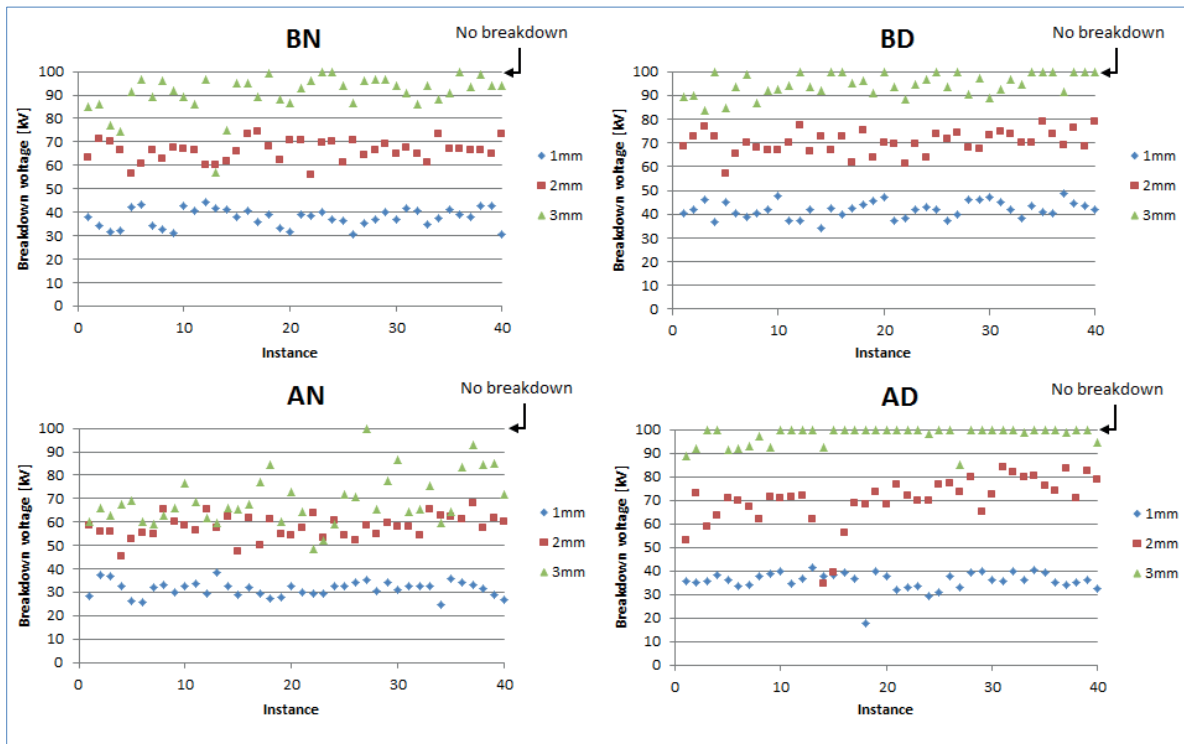


Figure 4 - Dot plot of measured breakdown data

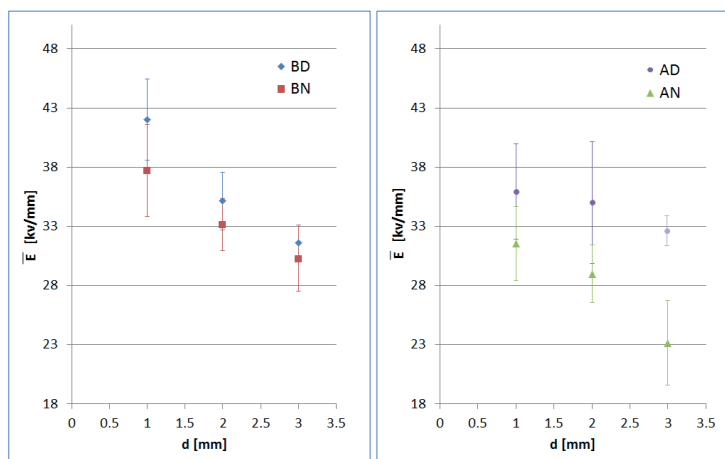


Figure 5 – Value of \bar{E} according to Eq. (3) for 1, 2 and 3 mm distance

From previous figures and tables, the following observations can be made:

- a) P_{50} varies less than P_I across distributions for all measurements (Figure 2)
- b) σ increases with electrode distance (Table II)
- c) GOF has lowest values for 3 mm distances (Figure 3)
- d) \bar{E} decreases with electrode distance (Figure 5)

Measurements taken on 3 mm electrode distance could have lowest GOF values because of greater dispersion of data (i.e. higher σ) or a fact that certain percent of breakdowns did not occur for this distance (Table III). For instance, A3D measurement has the highest rate of non-occurring breakdowns (65%) and zero GOF value (Figure 3). To highlight this, all results referring to this measurement were faded.

It was expected that the censored Weibull distribution would give overall better GOF values for 3 mm distance than Gaussian distribution, since Gaussian distribution does not support data censoring. However, this is true only for B3N measurement. Looking at Figure 3, GOF values presumably do not

follow any pattern either for Weibull or Gaussian distribution, thus a noteworthy conclusion based on significance of only one of the parametric distributions cannot be made (the higher the *GOF*, the more significant distribution is; however, in this circumstance, a statement that one distribution is “better” than other cannot be made, since *GOF* is inconsistent for both distributions).

Results have also confirmed that degassed oil has higher breakdown values than non-degassed oil. However, an investigation to which extent this relates to moisture content was not made, since authors weren’t able to control the absolute moisture content of oil samples. Therefore, rather than choosing continuous variable of “moisture content”, research was simplified by choosing discrete (or binary, to be exact) variable of oil “treatment”, which was able to have only two conditions:

- a) “Degassed” – meaning it had been filtered and dried.
- b) “Non-degassed” – meaning it had been taken out of the storage tank without any treatment.

It has been assumed that all samples of degassed oil for “A” and “B” electrodes (in measurements A1D, A2D, A3D and B1D, B2D, B3D) have “equal” moisture content, since they passed same standard process of drying and filtering, although oil samples were not drawn from the same oil “population” (they were sampled at different time with four weeks’ time span). In other words, difference between moisture content for electrodes “A” (4 ppm) and electrodes “B” (5 ppm) had been neglected, although moisture for “A” electrodes was 20 % lower. This cannot be said for non-degassed measurements, since their moisture content differed significantly. This withdraws a fact that only AD and BD measurements can be compared regarding electrode shape, which will be done in next part after numerical calculation.

3. NUMERICAL CALCULATION

Two-dimensional (2D) axisymmetric FEM model (Figure 6) is used to calculate stressed oil volume (*SOV*), stressed electrode area (*SEA*) and safety factors (*q*) of “cumulative stress” method for each of twelve testing sets.

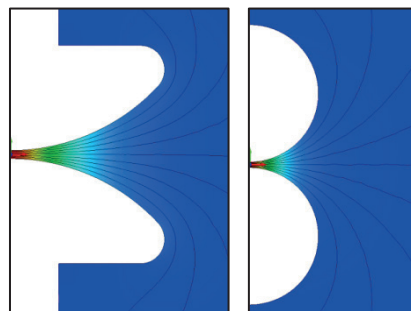


Figure 6 - 2D axisymmetric FEM model for electrodes type “A” and “B”

3.1. Stressed oil volume

Stressed oil volume is equal to “region in which calculated electric stress values are between the maximum value and 90% of the maximum value” [10]. For a case of mushroom electrodes, it has been assumed that 90% of maximum electric stress is within their spherical part. Considering this, *SOV* for both sphere and mushroom electrodes is calculated according to the formulas:

$$SOV = V_2 - V_1 - V_3 \quad (4)$$

$$V_i = \pi \int_{z_1}^{z_2} r^2 dz \quad i = [1, 2, 3] \quad (5)$$

where:

SOV – stressed oil volume

V_i – volumes of rotational bodies, created by rotation of curves *C₁*, *C₂* and *C₃* around *z* axis [12]

Figure 7 shows curves *C₁* and *C₃* defined with circle arcs formed by electrodes in a cross section plane, while curve *C₂* is the result of a contour plot of $0.9 \cdot |E|_{\max}$, where $|E|_{\max}$ is maximum electric field in solved model [10].

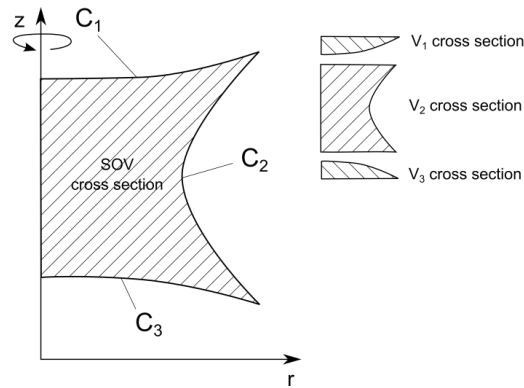


Figure 7 - Cross section of a stressed volume between electrodes

3.2. Stressed electrode area

Stressed electrode area for one electrode is calculated according to equation (6) for a sphere cap shown on Figure 8.

$$SEA = 2\pi R h \quad (6)$$

where:

SEA – stressed electrode area

R – electrode radius

h – height of a sphere cap obtained from geometry of curve C_1 or C_3 on Figure 7

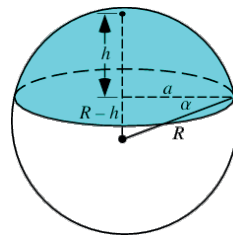


Figure 8 - Area of a sphere cap [11]

3.3. “Cumulative stress” method

Safety factor q of one streamline is calculated [6], [10] according to Eq. (7) and (8).

$$q = \frac{E_{pd}(x)}{E_{av}(x)} \quad (7)$$

where: E_{pd} is low probability PD/breakdown and E_{av} is calculated according to:

$$E_{av}(x) = \frac{1}{x} \int_0^x E(x) dx \quad (8)$$

where: q – safety factor value

E_{pd} – low probability PD/breakdown

E_{av} – average field along streamline

$E(x)$ – electric field stress (numerically calculated)

3.4. Choosing FEM model boundary value

To calculate electric stress in kV/mm between electrodes, boundary values (namely electrode voltage in kV) should be applied to 2D axisymmetric model. This poses a question which of the measured results should be applied.

In insulation design practice, it is common to use P_1 voltage breakdown value of Weibull distribution, but with additional safety margins [6], [7]. In case of measurements provided in this paper, it seems that number of breakdowns is insufficient to compensate scattering of measurements, especially for the 3 mm case. Thus, although parametric fit of first percentile of Weibull distribution should represent 1 % probability that breakdown will occur, the significance of these results provided in Table II is doubtful. However, since the primary aim of this paper is not investigation of oil breakdown criteria, the question of threshold determination is left for future research.

Regarding FEM model boundary values, authors made a decision that one of the electrodes should have fiftieth percentile of Gaussian distribution ($U_1=P_{50}$), while the other electrode consequentially has $U_2=0$ kV.

The first reason for this decision was that Gaussian P_{50} is used in standardized oil testing according to IEC 60156 [13], even though it does not have a practical meaning in insulation design.

The second reason was that the Gaussian P_{50} does not differ significantly from Weibull P_{50} and even non-parametric P_{50} , which was a sort of counterweight to GOF inconsistency seen on Figure 3.

3.5. Numerical results

Gaussian P_{50} values from Table II are inserted into FEM model, and calculated results are presented in Table IV.

Table IV- Results of numerical calculation

	B1N	B2N	B3N	B1D	B2D	B3D
$ E _{\max}$ [kV/mm]	38.2	34.0	31.5	42.6	36.1	32.9
SOV [mm ³]	6.9	26.3	54.9	6.9	25.8	54.6
SEA [mm ²]	5.4	12.7	21.7	5.3	12.5	21.7
q_{\min}	0.363	0.368	0.357	0.411	0.436	0.432
	A1N	A2N	A3N	A1D	A2D	A3D
$ E _{\max}$ [kV/mm]	32.1	29.9	24.1	29.9	30.2	30.5
SOV [mm ³]	13	47.5	104.6	13	47.5	104.6
SEA [mm ²]	9.4	20.6	35.4	9.4	20.6	35.4
q_{\min}	0.438	0.422	0.472	0.590	0.524	0.467

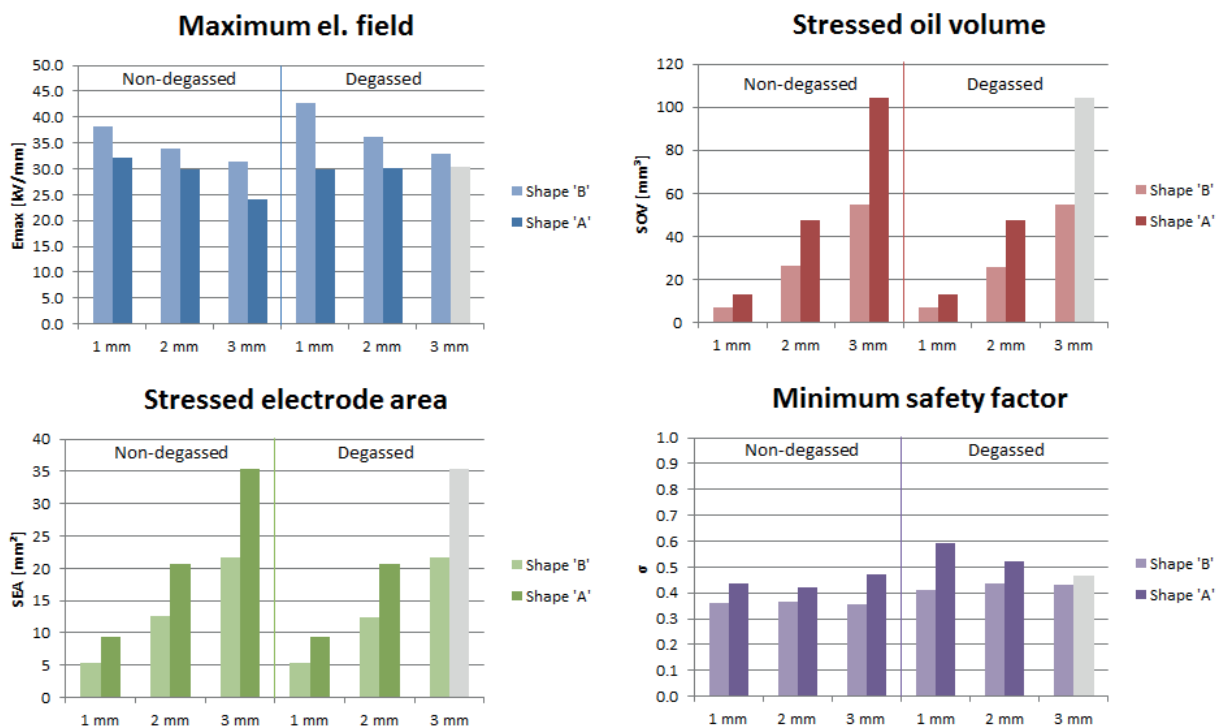


Figure 9 – Visualization of results from Table IV

From the results above, the following observations can be made:

- a) $|E|_{\max}$ is greater for "B" electrodes
- b) $|E|_{\max}$ decreases with electrode distance for "B" electrodes
- c) *SOV* and *SEA* depend solely on electrode geometry (shape and distance)
- d) *SOV* and *SEA* values are higher for "A" electrodes
- e) *SOV* and *SEA* increase with electrode distance
- f) Safety factors have values less than one ($q < 1$)
- g) Safety factors values are higher for "A" electrodes

It would be expected that by having smaller radius, "B" electrodes should have withstood smaller voltage because of the higher electric stress. However, Figure 5 showed that "B" electrodes, having higher value of \bar{E} , withstood higher voltage.

Indeed, the results have confirmed that "with the increase in stressed volume, the dielectric strength of the insulation system reduces. If the electrode radius is increased, the stress values reduce; but at the same time the stressed oil volume (between maximum value and 90% of maximum value) increases reducing withstand", as states in [10], page 342. Same thing applies with stressed electrode area, as authors showed in [2].

Regarding "cumulative stress" method, safety factors values are as expected ($q < 1$), since values taken for their configuration (Eq. (7) and (8)) are defined by low probability (first percentile or lower) PD/breakdown, while for this particular case they were calculated with fiftieth percentile. Although electrodes "A" showed higher safety factor values (meaning that the withstand voltage should also be relatively higher than for "B" electrodes), it should be noted that the method itself depends on field homogeneity, which was not discussed in this paper.

4. CONCLUSION

Paper has considered statistical and numerical analysis of transformer oil AC breakdown. By using twelve different measurement sets, authors have presented how breakdown voltage depends on electrode distance, electrode shape and transformer oil treatment. Stressed oil volume, stressed electrode area and safety factors of "cumulative stress" method were calculated using 2D FEM model, confirming that by increasing *SOV* and *SEA*, breakdown withstand of transformer oil decreases.

Any future research that considers oil breakdown measurement should presume large number of repetitive tests, especially for large electrode distances, for which dispersion of data rises. It should be taken into account that in the case of a research which includes devastative measurements (such as solid insulation breakdown research), expenditures (such as time and material) could easily reach very high cost levels.

Authors believe that any oil breakdown measurement represented in kV/mm, aside from oil properties, should also have a note regarding electrode distance and electrode shape, since the breakdown results themselves do not describe completely the oil ability to withstand electrical breakdown. In addition, this means that oil breakdown results should not be compared between different electrode geometries. Lacking of electrode geometry information (or international standard) by which transformer oil is to be tested, could be misleading in customer inquiries. For example, if a customer requests only oil breakdown withstand values without proper definition of testing equipment setup, a transformer manufacturer could give valid test results according to test setup that suits his interests (instead of 'mushroom' electrodes with 2.5 mm distance, he could use 'spherical' electrodes on 1 mm distance and get higher kV/mm breakdown values).

For a final note, both statistical and numerical analysis have proven to be useful in description of oil breakdown, and will be used for future research as well.

REFERENCES

- [1] Siodla, K.; Ziomek, W.; Kuffel, E., "The volume and area effect in transformer oil," *Electrical Insulation, 2002. Conference Record of the 2002 IEEE International Symposium on*, vol., no., pp.359,362, 7-10 Apr 2002

- [2] Weber, K. H.; Endicott, H. S., "Area Effect and Its Extremal Basis for the Electric Breakdown of Transformer Oil [includes discussion]," *Power Apparatus and Systems, Part III. Transactions of the American Institute of Electrical Engineers* , vol.75, no.3, pp.,, Jan. 1956
- [3] Del Vecchio, R.M., "Geometric effects in the electrical breakdown of transformer oil" *Power Delivery, IEEE Transactions on* , vol.19, no.2, pp.652,656, April 2004
- [4] Kawaguchi, Y.; Murata, H.; Ikeda, M., "Breakdown of Transformer Oil," *Power Apparatus and Systems, IEEE Transactions on* , vol.PAS-91, no.1, pp.9,23, Jan. 1972
- [5] Nelson, J.K.; Shaw, C., "The impulse design of transformer oil-cellulose structures," *Dielectrics and Electrical Insulation, IEEE Transactions on* , vol.13, no.3, pp.477,483, June 2006
- [6] Tschudi, D., & Heinzig, P., "State of the art solid insulation after 125 years of transformer practice" *International Colloquium Transformer Research and Asset Management, Report MC&NT-01*, Cavtat, 2009
- [7] Martin, D.; Wang, Z.D., "Statistical analysis of the AC breakdown voltages of ester based transformer oils," *Dielectrics and Electrical Insulation, IEEE Transactions on* , vol.15, no.4, pp.1044,1050, August 2008
- [8] Weisstein, Eric W. "Weibull Distribution." From MathWorld--A Wolfram Web Resource. <http://mathworld.wolfram.com/WeibullDistribution.html>, 15/08/2014
- [9] Weisstein, Eric W. "Normal Distribution." From MathWorld--A Wolfram Web Resource. <http://mathworld.wolfram.com/NormalDistribution.html>, 15/08/2014
- [10] Kulkarni, S. V.; Khaparde, S. A. "Transformer Engineering: Design and Practice", 1st edition, CRC Press, 2004
- [11] Weisstein, Eric W. "Spherical Cap." From MathWorld--A Wolfram Web Resource. <http://mathworld.wolfram.com/SphericalCap.html>, 15/08/2014
- [12] Weisstein, Eric W. "Method of Disks." From MathWorld--A Wolfram Web Resource. <http://mathworld.wolfram.com/MethodofDisks.html>, 15/08/2014
- [13] IEC 60156, *Insulating liquids - Determination of the breakdown voltage at power frequency - Test method*, 1995

Mladen Marković
Končar Distribution & Special Transformers
mladen.markovic@koncar-dst.hr

INSULATION OPTIMIZATION OF POWER TRANSFORMER LEADS

SUMMARY

Power transformers reliability, amongst other things, depends on its insulation system. High voltage leads are a part of the insulation system and should be properly insulated. This includes positioning an insulation barrier between the leads and a tank on a certain distance. This distance affects the safety factors (breakdown probability) for such system. The paper presents optimization process with which both the breakdown probability and leads vs. tank distance could be minimized. It also proposes a method with which this optimization process could be confirmed.

Key words: power transformer, insulation, numerical calculation, optimization

1. INTRODUCTION

1.1. Electrodes in transformer

Power transformer with properly designed insulation is likely to be more reliable during its lifetime. One of the main tasks of insulation design process is to determine allowable distances between parts under voltage (electrodes). Electrodes of a transformer can be roughly divided into two groups: windings and leads. The purpose of leads is to form a conductive connection between transformers bushing (i.e. phase connector) and its associated winding.

1.2. Transformer leads

Transformer leads are made of copper wire, which varies by cross-section and paper thickness, depending on current density and voltage level, respectively. Low voltage (LV) leads represent no potential threat for insulation breakdown; however, more attention in design process must be given to high voltage (HV) leads, as their insulation must be properly chosen in order for partial discharge (PD) or oil breakdown not to occur.

1.3. Insulation of transformer leads

One of the measures for proper HV leads insulation, apart from paper thickness, is the setting of an insulation barrier between HV leads and transformer tank, as can be seen on typical transformer configuration on Figure 1, page 2.

1.4. Motivation

Main motive for conveying this research is to demonstrate how the barrier location, i.e. its horizontal distance from the leads and the tank, affects the insulation reliability of this system, and also how it influences the overall transformer dimensions.

This demonstration will be done according to the FEM numerical model and insulation will be designed according to “cumulative stress” method [1].

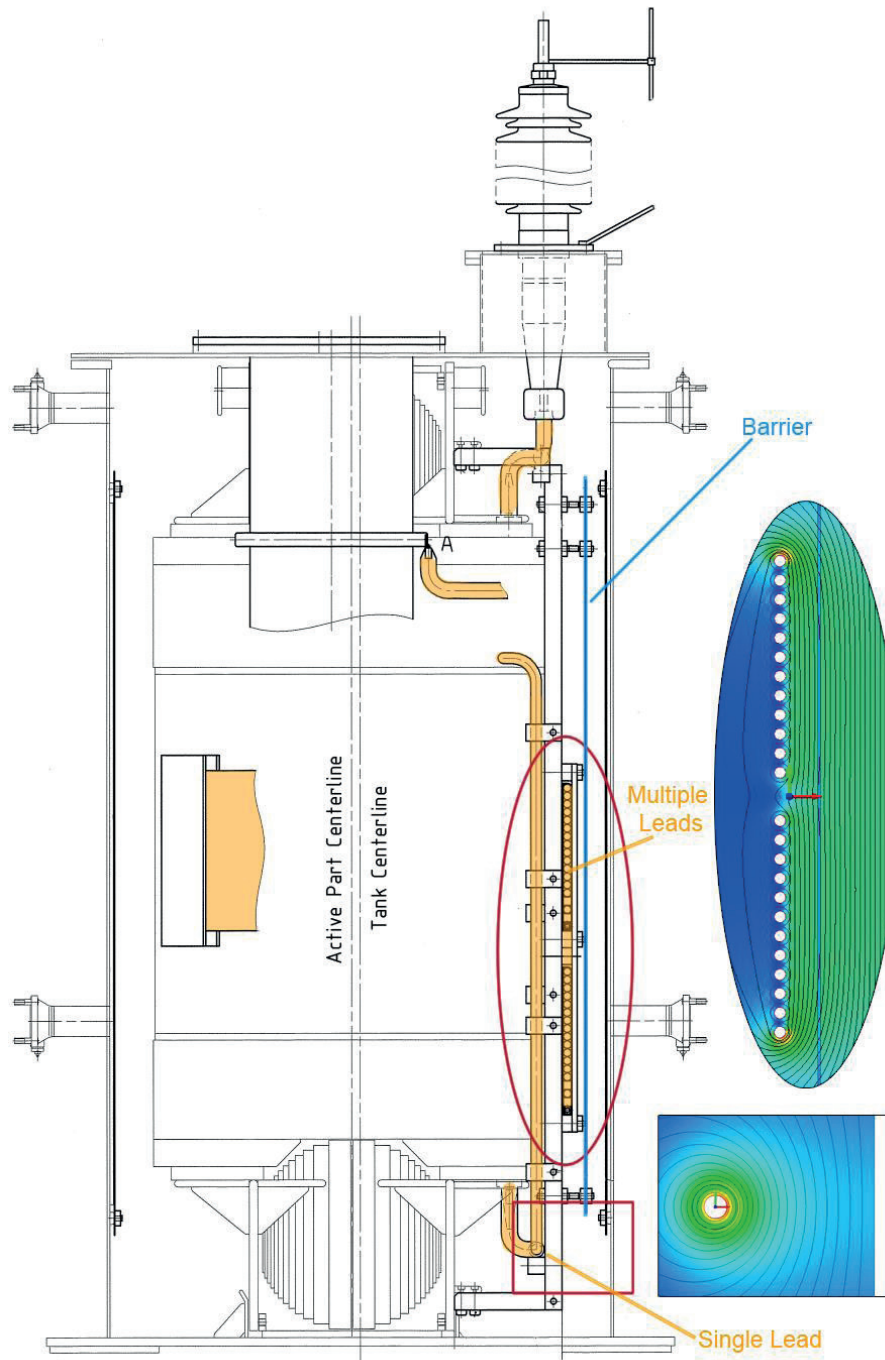


Figure 1 - Leads in transformer

2. INSULATION CALCULATION

2.1. Calculation of safety factors

According to cumulative stress method, probability of PD occurrence depends on average electric field along its streamline [2], with electrode voltage levels defined by international standard [3].

Safety factor σ of each streamline is calculated according to:

$$\sigma = \frac{E_{pd}(x)}{E_{av}(x)} \quad (1)$$

where E_{pd} is low probability PD/breakdown, and E_{av} is calculated according to Eq. (2):

$$E_{av}(x) = \frac{1}{x} \int_0^x E(x) dx \quad (2)$$

where:

$E(x)$ – electric field stress.

2.2. Optimization principles

Safety factors of each streamline are shown on Figure 2, separately for *left side of the barrier* (between leads and barrier) and *right side of the barrier* (between barrier and the tank). For this system to be optimized, two principles must be fulfilled:

- a) safety factor values for left and right side streamlines must be greater than one

$$\begin{aligned} \sigma_L &> 1 \\ \sigma_R &> 1 \end{aligned} \quad (3)$$

- b) minimum safety factor values for left and right side must be approximately equal

$$\sigma_L \approx \sigma_R \quad (4)$$

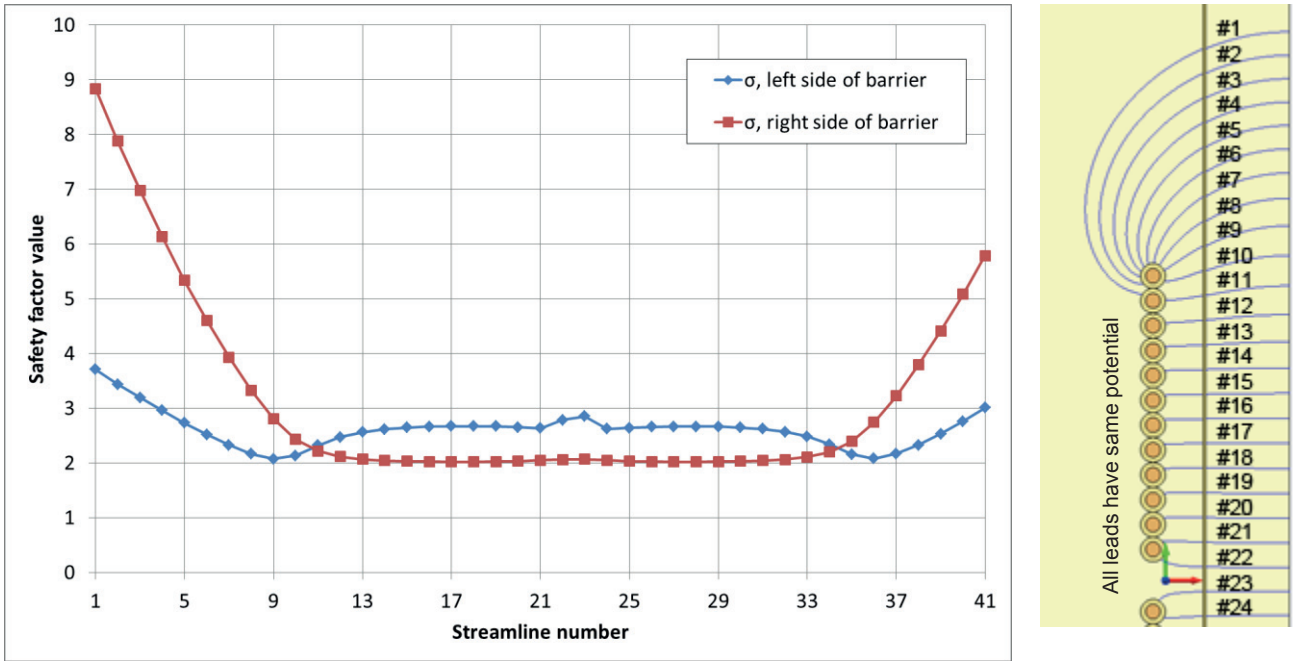


Figure 2 - Safety factors of streamlines on left and right side of the barrier

2.3. Optimization process

The optimization process consists of plotting safety factor values for different barrier distance, as shown on Figure 3.

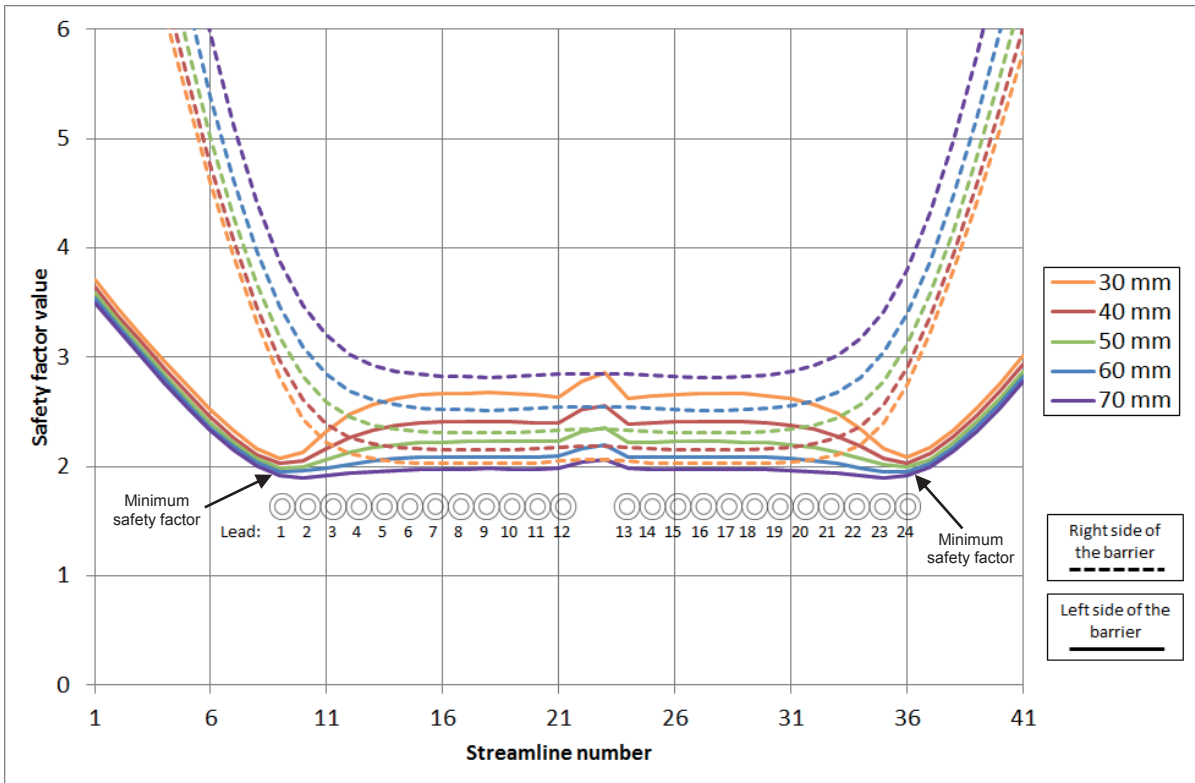


Figure 3 – Distance optimization according to principles a) and b)

From Figure 3, it can be seen that for the distance between barrier and leads of 50 mm (marked green), safety factors have approximately equal values in range of $2.2 \leq \sigma \leq 2.4$ for the leads in the center part of the bundle (for 7th to 19th lead, i.e. 16th to 31st streamline, green dashed line is equal to green continuous line), but they do not represent minimum values. In order to properly design the insulation, minimum safety factors should be observed, as they define weakest point in insulation [2].

These minimum safety factors (weakest points) are defined by 9th and 36th streamline, which occur on the first and the last lead of the bundle (where leads have the largest local electric field of 5.9 kV/mm in paper, Figure 4), but this is not always a case.

Figure 3 also shows that for the distance of around 30 mm (marked orange) these minimum safety factors of the *left* side of the barrier are equal to minimum safety factors on the *right* side of the barrier, with which principles a) and b) are both satisfied.

More detailed inspection of 30 mm barrier distance is shown on Figure 5.

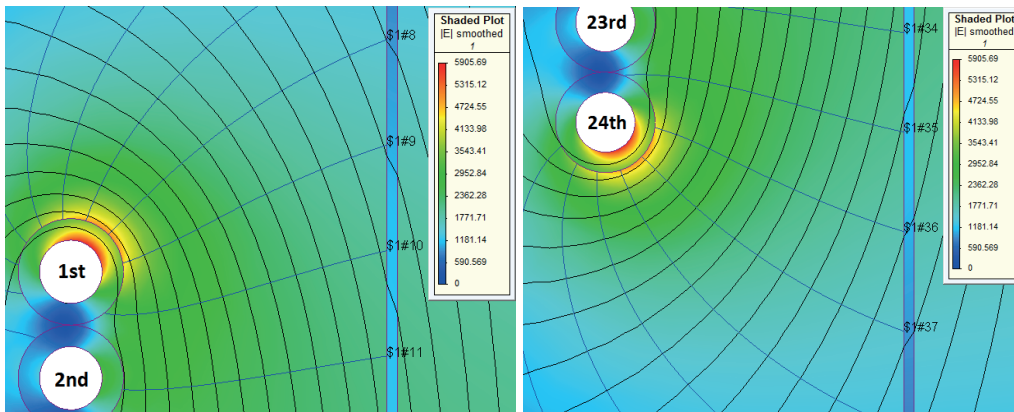


Figure 4 - Shaded electric field plot in V/mm, on first and last lead in bundle of 24 leads

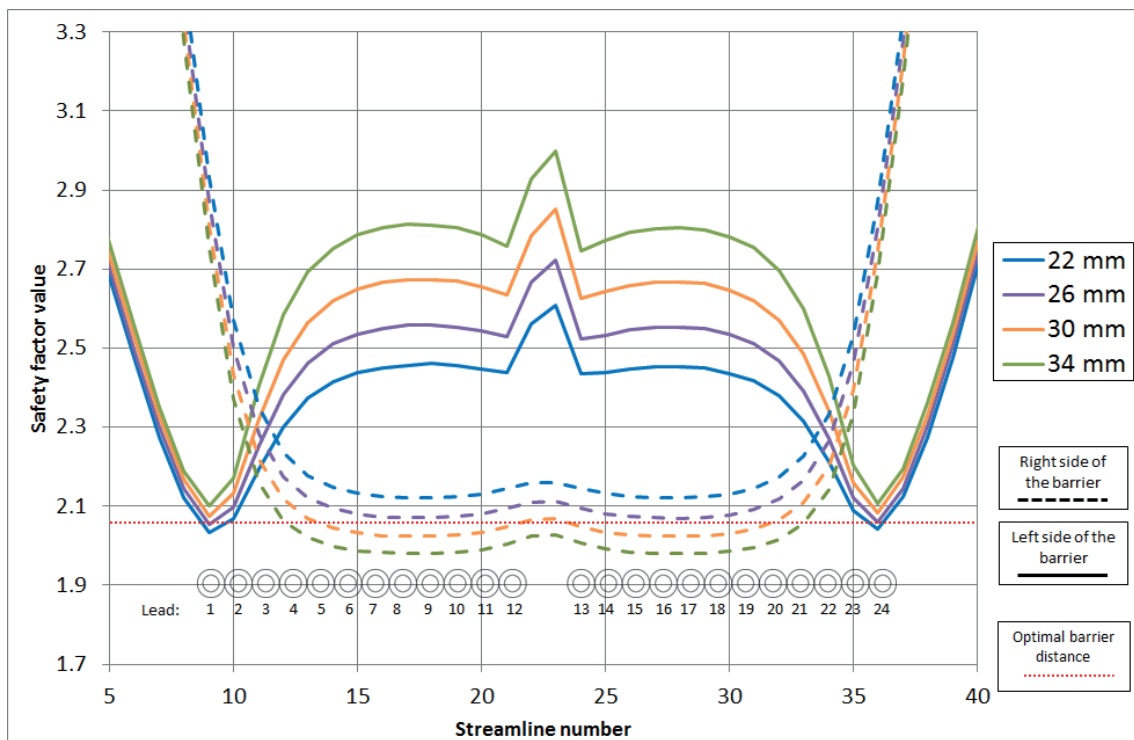


Figure 5 – Close-up of safety factor values in range of 22 mm and 34 mm barrier distance

Red dotted line on Figure 5 presents optimal safety factor which is reached for the barrier distance of 26 mm (marked purple). At this distance, both principle a) and b) is fulfilled with safety factor which is approximately $\sigma = 2.05$.

The reason that this value is optimal lies in the fact that whether the barrier moves left or right from current position, safety factor will be further decreased, i.e. there is greater probability that the oil breakdown will occur.

For example, if the barrier is moved closer to the leads (22 mm), safety factor *on the left side* of the barrier will be reduced to $\sigma = 2.03$ (part of the blue continuous line is beneath red dotted line), and if the barrier moves farther of the leads (30 mm), safety factor *on the right side* of the barrier will be reduced to $\sigma = 2.02$ (part of the orange dashed line is beneath red dotted line). Thus, the existing distance with $\sigma = 2.05$ is optimal.

3. CONFIRMATION METHOD PROPOSAL

In order to prove this concept of optimization, the following method is proposed:

- a) an experimental model is simplified and it consists of a single lead and a barrier (as shown in Figure 6)
- b) various distances between the lead and the barrier will be defined, upon which breakdown voltage will be measured
- c) for this lead/barrier system, multiple set of voltage breakdown measurements will be performed

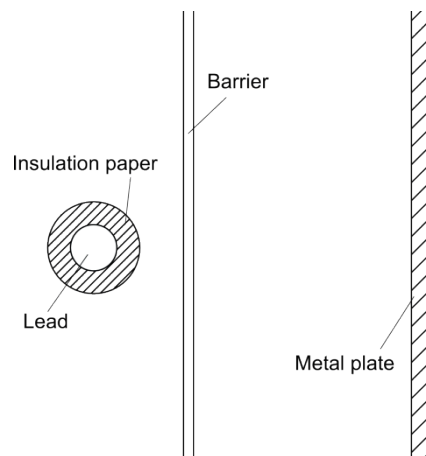


Figure 6 - Proposed method model

Three hypotheses which need to be accepted or rejected are defined as follows:

- a) in the proposed experimental system of a lead and a barrier, an optimal barrier distance exists
- b) the optimal barrier distance is based on safety factor calculation ("cumulative stress" method)
- c) expected appearance of voltage breakdown curve is according to Figure 7

Following assumptions are taken into account:

- a) the streamline with minimum safety factor is formed on the shortest path between the lead and the barrier
- b) tolerances of the model are small enough not to affect the final result of the experiment
- c) difference between optimum and minimum safety factor (marked with δ on Figure 7) is large enough to be statistically significant

For numerical part of the research, 2D FEM model will be used (Figure 8).

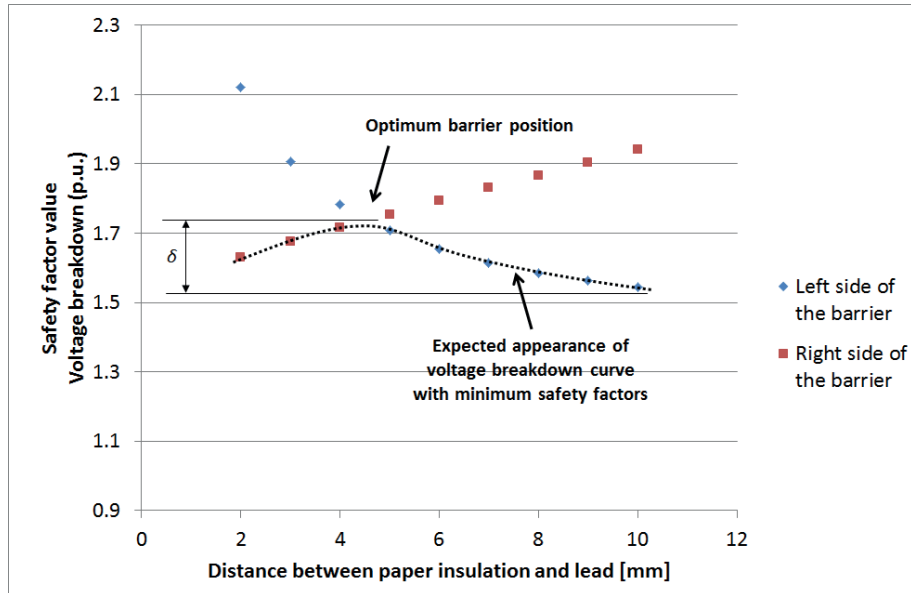


Figure 7 - Expected outcome of measured results

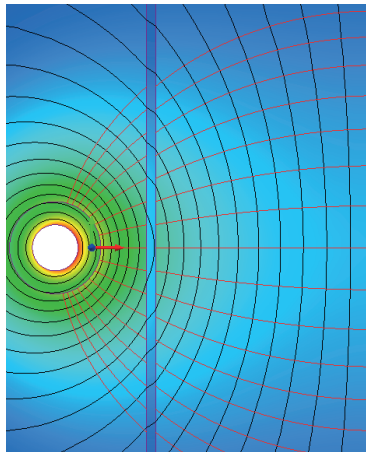


Figure 8 - FEM model for proposed research

4. LEAD OPTIMIZATION EFFECT TO TRANSFORMER WEIGHT

If the experimental part of the study confirms the proposed hypotheses, distance between HV leads and transformer tank could be reduced. This has two benefits

- a) Total mass of a transformer could be reduced. This is shown on Figure 9 for a 40 MVA / 110 kV transformer
- b) Overall transformer dimensions could be reduced. In situations with space limitations, this can be crucial factor in obtaining customers' tender

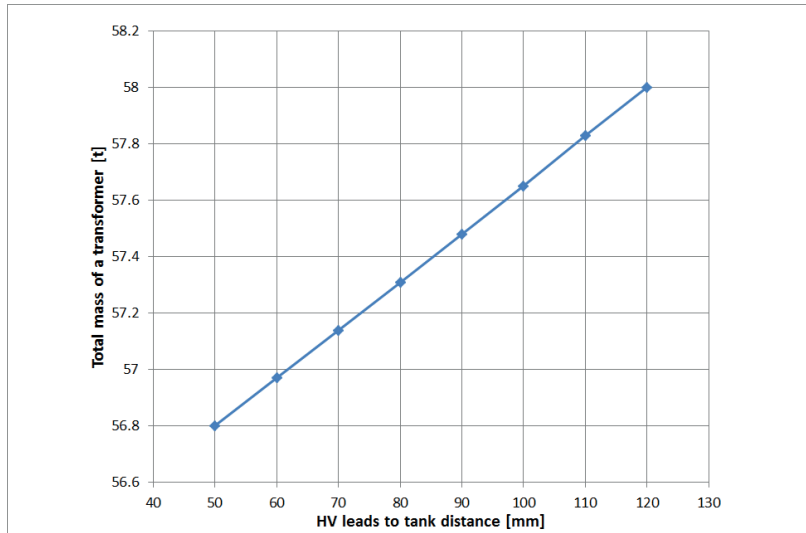


Figure 9 – “Total mass of a transformer” vs. “HV leads to tank distance” plot

5. CONCLUSION

The paper has presented how numerical calculation can be used for possible optimization of present transformer geometry. It has been shown that barrier position affects oil breakdown probability. Before taking any further steps in geometry alteration, this optimization concept has yet to be confirmed with a research which has also been presented. Depending on the results, transformer mass and dimensions could be altered, which would lead to production benefits and reduction of costs.

6. REFERENCES

- [1] Nelson, J.K.; Shaw, C., "The impulse design of transformer oil-cellulose structures," *Dielectrics and Electrical Insulation, IEEE Transactions on* , vol.13, no.3, pp.477,483, June 2006
- [2] Tschudi, D., & Heinzig, P. State of the art solid insulation after 125 years of transformer practice. *International Colloquium Transformer Research and Asset Management*, Report MC&NT-01, Cavtat, 2009
- [3] IEC 60076-3: 2013-01: Power Transformers. Part 3: Insulation levels, dielectric tests and external clearances in air.

Jasmin Smajic, Roman Obrist, Martin Rüegg
University of Applied Sciences of Eastern Switzerland (HSR)
jasmin.smajic@hsr.ch

Bogdan Cranganu-Cretu
ABB Switzerland Ltd.
bogdan.cranganu-cretu@ch.abb.com

Carlos Roy
ABB SA, Zaragoza, Spain
carlos.roy@es.abb.com

Benjamin Weber
ABB AG, Brilon, Germany
benjamin.weber@de.abb.com

Ebrahim Rahimpour
ABB AG, Bad Honnef, Germany
ebrahim.rahimpour@de.abb.com

LIGHTNING IMPULSE MODELING AND SIMULATION OF DRY-TYPE AND OIL-IMMERSED POWER- AND DISTRIBUTION TRANSFORMERS

SUMMARY

This paper presents in detail numerical methods and techniques for lightning impulse (LI) modeling and simulation of power and distribution transformers. The modeling methods are based on equivalent circuits of transformer winding entities resulting from the initial winding discretization determined by the required accuracy. The parameters of the equivalent circuit such as resistances and self- and mutual capacitances and inductances are obtained from field simulations (FEM). The circuit equations of the transformer's equivalent circuit written in the state space form yield a large system of differential equations that is solved in time-domain by using the standard Runge-Kutta numerical integration technique. The obtained solution represents the voltage distribution over the winding in each moment of the LI-time (50 μ s). The results verification by comparison against measurements is presented in detail.

Key words: Lightning impulse, transformer winding modeling, transient simulation, electric and magnetic coupling, lumped parameters, and distributed parameters.

1. INTRODUCTION

Dielectric winding design of power- and distribution transformers is a complex task involving several conflicting requirements. The distances between the windings as separate entities, the internal winding arrangement (topology), and the spatial separation of the sections within a single winding are mainly determined by the basic lightning-impulse (LI) insulation level (BIL) (more severe) and/or by the AC-test voltage levels (less severe) [1]. The geometrical arrangement of the winding system is defined in such a way that the electric field between and within the windings stays below critical values of the involved insulation materials for both the LI- and AC-test voltage levels. On the other hand, if the winding system is dielectrically oversized, the winding losses and material cost are increased and they consequently reduce the competitiveness of the design on the market. The ultimate goal of the dielectric design is a reliable winding system capable of withstanding the expected overvoltage surges in operation over the required lifetime (some tens of years) at the minimal material cost and electromagnetic losses.

To reach a sub-optimal solution for winding system from the dielectric design point of view a reliable simulation tool is required. Within the framework of this tool an accurate transformer modeling and simulation over the entire frequency range of the standardized 1.2 μ s/50 μ s LI-surge should be possible. An FFT-Analysis of the LI-surge reveals the wide frequency range (0-1MHz) that poses a difficult numerical problem for accurate transformer modeling considering the underlying complicated capacitive and inductive couplings.

Due to its relevance and importance for the design, the modeling and simulation of the LI voltage distribution over transformer windings has a long history. Already in the 1940s and 1950s a solid theoretical basis of this analysis was developed [3]. The dominant idea from the beginning of this development was to translate a geometrically complicated winding structure into a simple equivalent circuit described by the known circuit's differential equations. Early models from the 1950s were very simple and relatively easy to solve with early computers. Over the years the models of increasing complexity and predictive power emerged, as reported for example in [4], [5], and [6].

The common characteristics of the existing models can be summarized as follows: (a) they are based on various analytical approximation methods for computing the capacitive and inductive coupling between different winding sections; (b) they represent radically simplified winding structures in order to stay within an affordable CPU-time; and (c) they are not general but they are valid only for a certain winding type and voltage range.

The original contribution of this paper is manifold: (a) to present a fast and experience enhanced method for simulating the LI-voltage distribution based on analytical computation of distributed winding parameters and based on the second order (wave) differential equations, (b) to present a new recently developed method based on a detailed lumped parameters modeling of the highest possible resolution (each turn is a separate entity) and based on the first order ordinary differential equations, and (c) to show the obtained results and their experimental verification for several real-life transformers.

The paper is organized as follows. Section 2 describes in detail the developed numerical methods and techniques. Section 3 shows the obtained results and their experimental verification. Section 4 concludes the paper.

2. NUMERICAL METHODS AND TECHNIQUES

If the LI-distribution over transformer winding is considered, it is evident that full-Maxwell modeling and simulation of the transformer and its surrounding space in time-domain is required [7]. This practically means that the second order partial differential equation describing the electromagnetic field in and around the transformer should be numerically solved. As shown in [7] this approach is possible for a relatively simple 3-D structures but not for real-life transformer windings due to their complex geometrical arrangement (the corresponding CPU-time would be unacceptable and the memory requirements are simply unrealistic) [7].

What remains after the full-Maxwell approach is, for the above practical reasons, eliminated is the so-called equivalent circuit approach. The basic idea of this approach is rather simple. The winding is split into several winding sections (entities) and at the beginning of each section the transient voltage over the entire LI-time should be computed. Each section is, of course, coupled electrically (capacitance) and magnetically (inductance) with all the other sections. The matrix of the magnetic and electric couplings between the winding sections could be obtained analytically. Since the LI covers the frequency range up to 1MHz, the corresponding voltage waves propagating along a straight conductor far from the ground in free space (air) would cover the wavelength range down to 300m [7]. Considering the fact that voltage waves initiated by the LI travel along the transformer winding system, they wavelength is significantly shorter than 300m for two reasons: the electric permittivity of the insulation around winding turns is higher than that of air (epoxy resin for example $\epsilon_r \approx 4$) and the speed of the waves of a transmission line is lower compared to the speed of the EM-wave in free space. Thus the wavelength limit of the LI voltage wave inside of the winding system insulated with epoxy resin could be roughly estimated to 100m. This practically means that each winding entity used in the modeling longer than 10m (this is again a rough estimate) must not be represented by simple lumped parameters in its equivalent circuit but the distributed parameters must be used and correspondingly the second order differential equations (wave equations) must be solved. Until recently, this approach was almost exclusively used for LI simulations of transformers [2]. The drawbacks of this approach are obvious: low resolution of the obtained data (the voltage is obtained at the beginning of each modeling entity, i.e. at the beginning of each winding section), the electric and magnetic couplings within the modeling entities are neglected, the need for empirically obtained correction factors and consequently the lack of generality.

As an alternative to the above approach based on the distributed parameters and wave equations a new numerical method was recently suggested [2]. The new method abandons from the beginning any winding simplification and considers the winding system as it is in its full complexity by taking into account each single turn and its capacitive and inductive couplings against all the other turns of the system. Moreover, these couplings are determined by performing 2-D or 3-D electric and magnetic field

simulations (a highly accurate analytical approach remains as a possible alternative). To clarify this method a simple four-turn winding is modeled and its equivalent circuit is depicted in Figure 1. It is worth mentioning that the state space variables of the system are the voltages and currents of each turn.

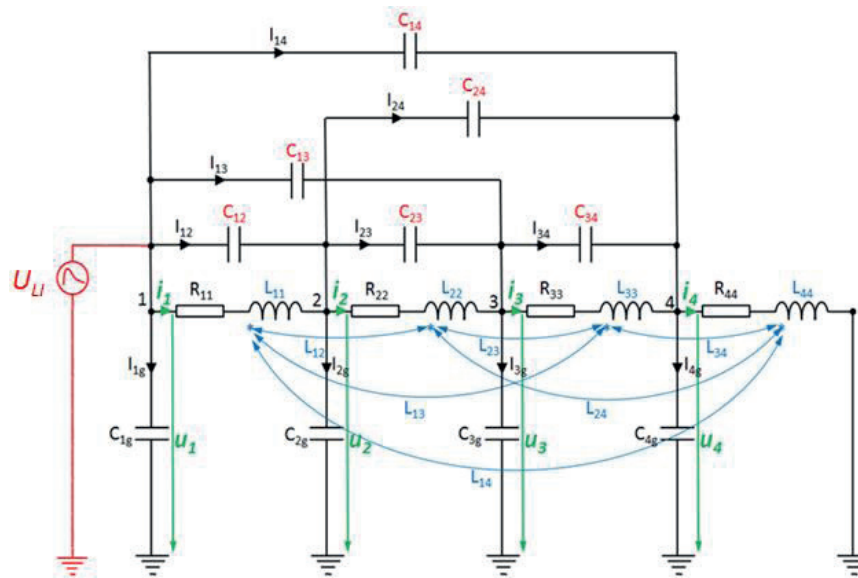


Figure 1 – An equivalent circuit of a simple four-turn winding chosen as a modeling example

According to the well known circuit theory equations, it is possible for the equivalent circuit shown in Figure 1 to write the following:

$$\begin{bmatrix} L_{11} & L_{12} & L_{13} & L_{14} & 0 & 0 & 0 & 0 \\ L_{21} & L_{22} & L_{12} & L_{24} & 0 & 0 & 0 & 0 \\ L_{31} & L_{32} & L_{33} & L_{34} & 0 & 0 & 0 & 0 \\ L_{41} & L_{42} & L_{43} & L_{44} & 0 & 0 & 0 & 0 \\ 0 & 0 & 0 & 0 & C_{21} + C_{2g} + C_{23} + C_{24} & -C_{23} & -C_{24} & \\ 0 & 0 & 0 & 0 & -C_{32} & C_{31} + C_{32} + C_{3g} + C_{34} & -C_{34} & \\ 0 & 0 & 0 & 0 & -C_{42} & -C_{43} & C_{41} + C_{42} + C_{43} + C_{4g} & \end{bmatrix} \cdot \begin{Bmatrix} \frac{di_1}{dt} \\ \frac{di_2}{dt} \\ \frac{di_3}{dt} \\ \frac{di_4}{dt} \\ \frac{du_2}{dt} \\ \frac{du_3}{dt} \\ \frac{du_4}{dt} \end{Bmatrix} =$$

$$= \begin{bmatrix} -R_{11} & 0 & 0 & 0 & -1 & 0 & 0 & 0 \\ 0 & -R_{22} & 0 & 0 & +1 & -1 & 0 & 0 \\ 0 & 0 & -R_{33} & 0 & 0 & +1 & -1 & 0 \\ 0 & 0 & 0 & -R_{44} & 0 & 0 & +1 & 0 \\ +1 & -1 & 0 & 0 & 0 & 0 & 0 & 0 \\ 0 & +1 & -1 & 0 & 0 & 0 & 0 & 0 \\ 0 & 0 & +1 & -1 & 0 & 0 & 0 & 0 \end{bmatrix} \cdot \begin{Bmatrix} i_1 \\ i_2 \\ i_3 \\ i_4 \\ u_2 \\ u_3 \\ u_4 \end{Bmatrix} + \begin{Bmatrix} u_1 \\ 0 \\ 0 \\ 0 \\ C_{21} \cdot \frac{du_1}{dt} \\ C_{31} \cdot \frac{du_1}{dt} \\ C_{41} \cdot \frac{du_1}{dt} \end{Bmatrix} \quad (1)$$

Provided that the structure of Equation (1) is clear, it is straightforward to generalize it to the level of winding system with N turns:

$$\begin{bmatrix} [L] & [0] \\ [0] & [C] \end{bmatrix} \cdot \frac{d}{dt} \begin{Bmatrix} \{i\} \\ \{u\} \end{Bmatrix} = \begin{bmatrix} [R] & [K] \\ [K^T] & 0 \end{bmatrix} \cdot \begin{Bmatrix} \{i\} \\ \{u\} \end{Bmatrix} + \begin{Bmatrix} \{a\} \\ \{b\} \end{Bmatrix} \quad (2)$$

where: $[L]$ is the inductance L-matrix,
 $[C]$ is the capacitance C-matrix,
 $[R]$ is the resistance R-matrix,
 $\{i\}$ is the vector of the unknown turn-currents,
 $\{u\}$ is the vector of the unknown turn-voltages,
 $[K]$ is a special topological matrix, and
 $\{a\}$ and $\{b\}$ are the source terms.

Due to the fact that the L-matrix and C-matrix are obtained from electromagnetic field simulations, this approach is very demanding in terms of the geometrical modeling and CPU- time. On the other hand, the method is general, mathematically well founded, accurate and applicable in every situation. This method has an additional important advantage. Due to the fact that each turn is a separate modeling entity it is possible to use a lump parameters equivalent circuit (a turn is shorter than 10m, which is not fullfilled in large power transformers). The resulting equation system is a first order ordinary differential equation system which is more stable and faster to solve from the numerical integration point of view.

At the end of this section it is important to emphasize that the following two numerical methods for simulating the LI-distribution over transformer windings are considered:

- **Method 1:** a fast and experience enhanced method based on analytical computation of distributed parameters (capacitances and inductances) of the winding sections and based on the second order ordinary differential equations describing the voltage wave propagation along the winding structure.
- **Method 2:** a recently developed new method [2] based on a detailed lumped parameters modeling of the highest possible resolution (each turn is a separate entity) and based on the first order ordinary differential equations describing the voltage transients in the winding structure. This method is represented by Equation (1) and (2).

Method 1 is widely used in daily design due to its high speed and reliable results. Method 2, however, requires much longer CPU-time, but offers a very high level of accuracy. Therefore, it is used only for highly accurate simulations in development of new winding technologies and new transformers of exceptional importance. The main reason for the long CPU-time and the high accuracy of Method 2 is its accurate computation of the capacitive and inductive couplings between the winding turns by using electric and magnetic field simulations [2]. Thus, Method 2 is somewhere between the analytical Method 1 and the previously reported full-Maxwell modeling [7].

Method 2 utilizes a general time-dependent voltage source and can be used for simulation of various transients interactions of the transformer and adjacent equipment such as cables, vacuum circuit breakers, reactors, etc. (for example the analysis of the fast EM transients).

3. RESULTS AND THEIR VERIFICATION

For testing of Method 1 the oil-immersed 40MVA , 115kV \pm 15% / 11 kV power transformer was used. The winding arrangement of this transformer for the LI-testing is shown in Figure 2.

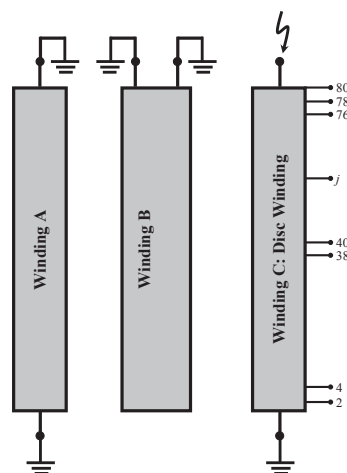


Figure 2 – Terminal condition of the oil-immersed 40MVA power transformer during the LI-test

The HV disc winding consists of 80 discs and is a partially interleaved winding. The discs from 1 to 44, numbered from bottom of the winding, are ordinary disc, while the discs from 45 to 80 are interleaved. The LI voltage source was connected to the disc 80 and the disc 1 was grounded. In the upper part of winding (the discs from 38 to 80) the voltages between two successive disc pairs and the voltages between the discs and ground were measured and calculated. In other words, the following voltages were computed and measured:

- disc-to-disc voltages: 80-78, 78-76, 76-74, ... , 44-42, and 42-40
- disc-to-ground voltages: 80-Grd, 78-Grd, 76-Grd, ... , 40-Grd, and 38-Grd

These results are presented in Figure 3. Evidently, the accuracy in terms of the voltage peaks and frequency of the winding eigenoscillations is very good. At the beginning of the LI-time the curves almost overlap. Later on, however, the difference between the curves is slightly increasing which is normal in time domain simulations (the disagreement accumulates over time). This is, however, not so significant as the voltage peaks are at later stage of the simulation not so high due to the internal damping (the resistance of the turns).

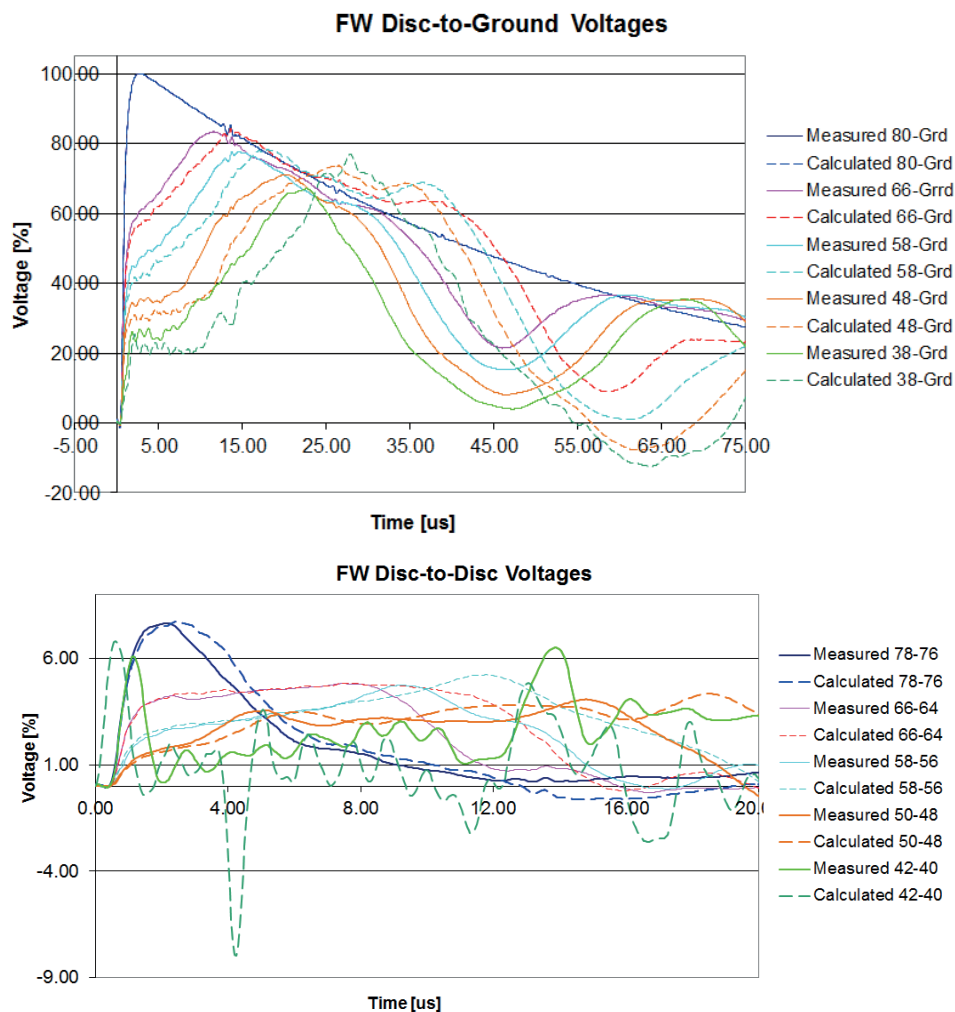


Figure 3 – The comparison of the simulation and measured results for the oil-immersed 40MVA power transformer

Method 2 has been tested on two dry-type distribution transformers. The first of them is the 24kV / 900kVA Resibloc[®]-transformer. The following Figure 4 shows a principal sketch of a layer winding design with four sections of a cast-resin Resibloc[®]-transformer. The obtained results in form of the differences of layer-to-layer voltages and section-to-section voltages are shown in Figure 5. Evidently in the first 20 μ s the agreement between simulation and measurement is very good. In this time interval occur the highest and most hazardous voltage peaks. Therefore is the accuracy in this time interval of paramount importance. For the reasons already emphasized, the disagreement accumulates of the LI-time and later on (for the time period longer than 20 μ s) and is getting more and more significant.

For testing of Method 2 also a dry-type 1600 kVA, 20 kV / 725 V distribution transformer was used. In fact only a HV and a LV phase, without magnetic core, were used. The test arrangement of this transformer is shown in Figure 6 (left). The HV winding consists of 22 ordinary discs e.g. not interleaved. The links connecting adjacent discs in series also were used as measuring points and so it is there were the voltages were simulated. The numbering of the HV measuring taps is shown in Figure 6 (right). The LI voltage source was connected to tap 1 and tap 0 was grounded, while the LV winding had both terminals grounded. The tap to ground voltages were measured and simulated in all taps.

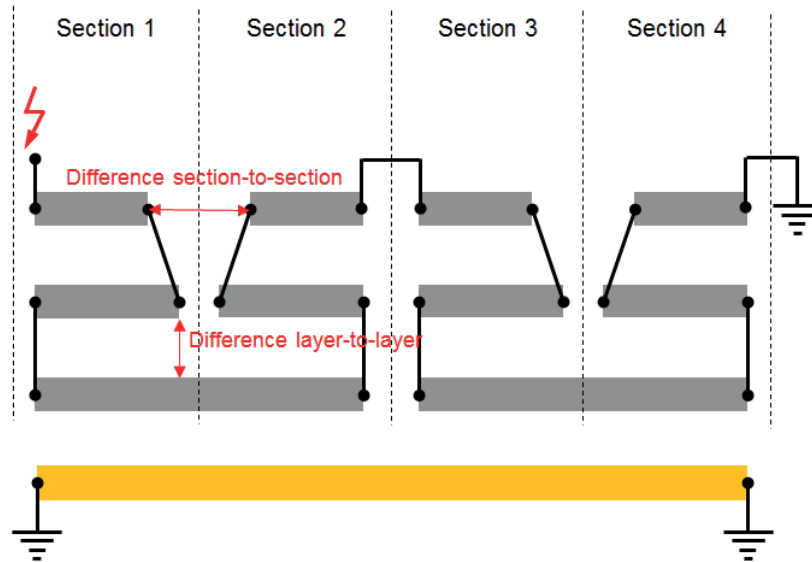
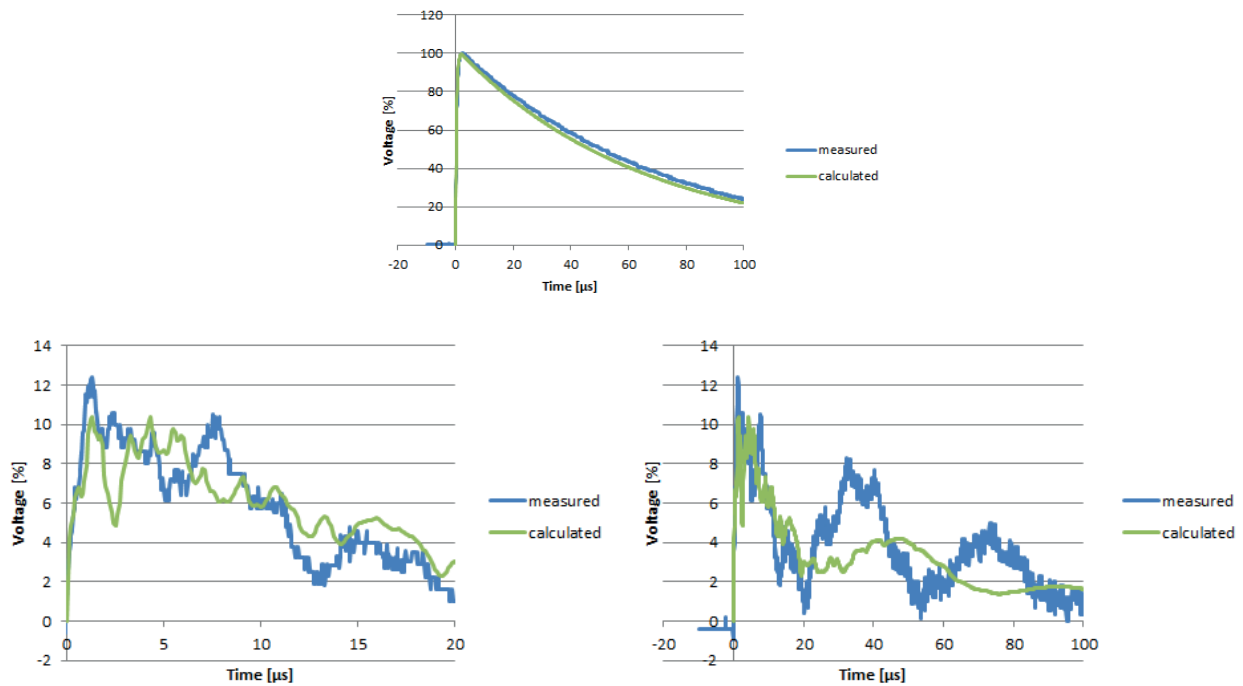


Figure 4 –Principal cross sectional sketch of a 4-section layer winding design



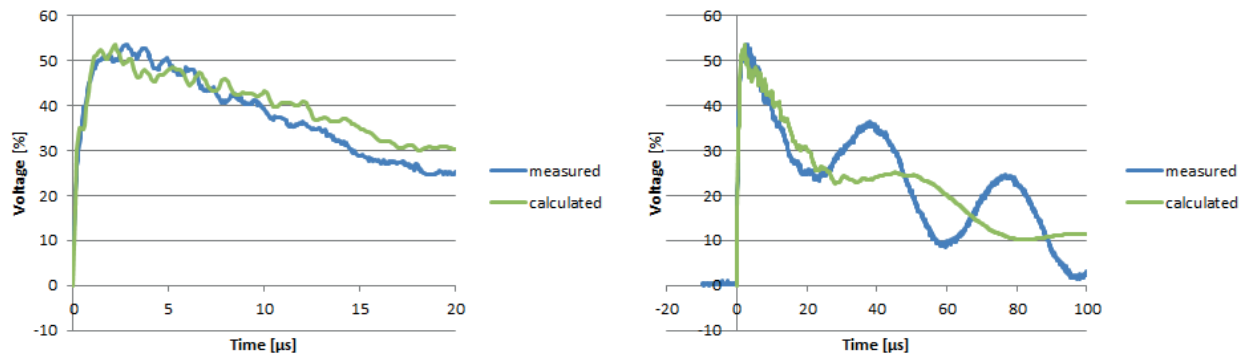


Figure 5 - Comparison of the simulation and measured results for the cast-resin Resibloc[®]-transformer, top: at winding input, center: layer-to-layer insulation, bottom: section-to-section-insulation.



Figure 6 – Test arrangement (left) and HV measuring taps for the dry-type 1600 kVA transformer (right)

The comparison of the simulation and measured results are presented in Figure 7. The degree of approximation is good, as can be seen comparing the characteristic points of the curves e.g. maximums, minimums and its corresponding delays. Anyway, as in the first case, the difference between simulation and measurement increases with the time, and from around 50 μs and later on it is quite evident. As stated before it is not so important since the voltage is quite reduced then from its first peak.

In order to illustrate the structure of the equation system (2) the capacitance and inductance matrix of the 1600kVA transformer are depicted in Figure 8. Those matrices are obtained by performing electric (C-matrix) and magnetic (L-matrix) field simulations. This is the most time consuming part of the simulation algorithm.

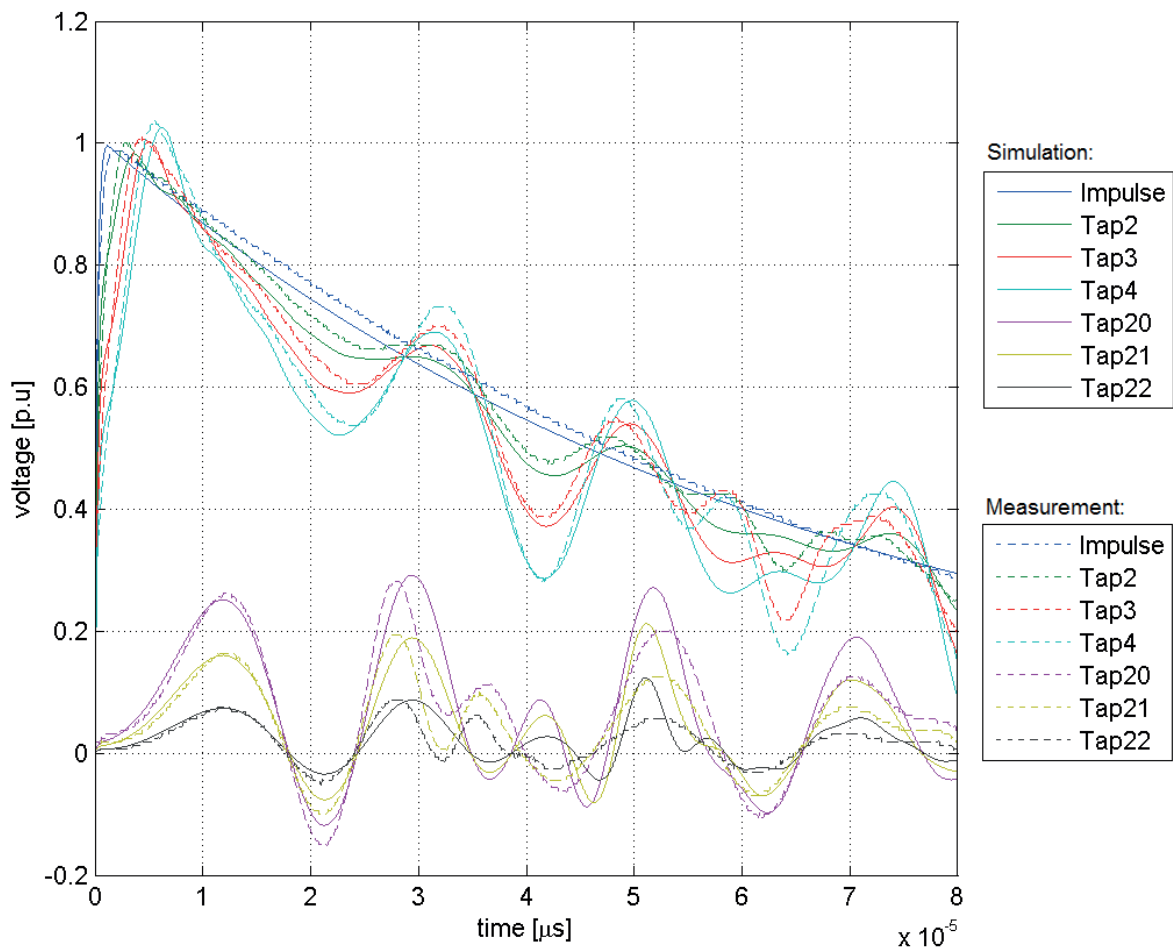


Figure 7 – Comparison of the simulated and measured results for the dry-type 1600 kVA transformer (disc to ground voltages)

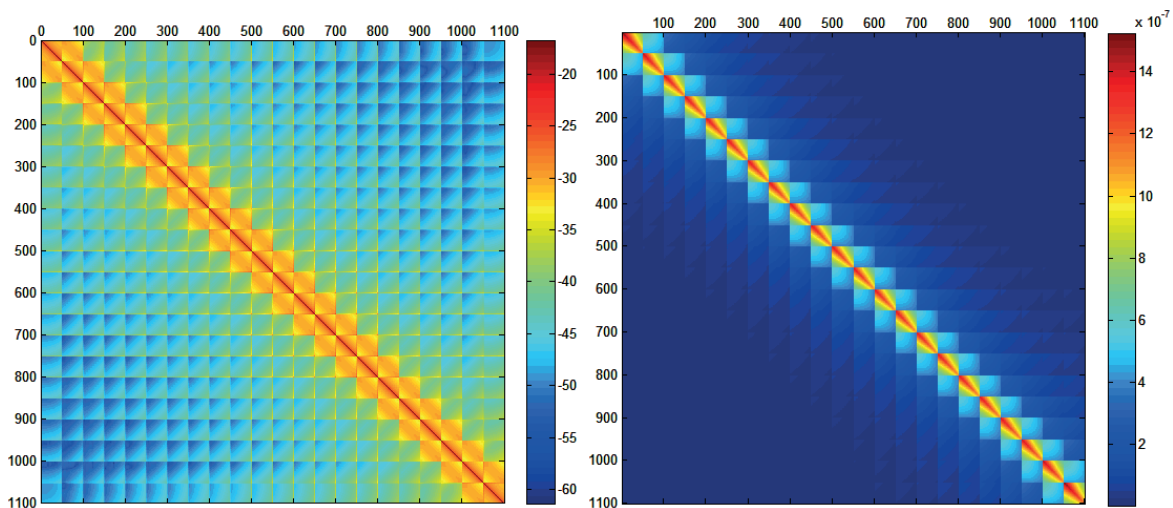


Figure 8 – The capacitance (left) and inductance (right) matrix of the dry-type 1600 kVA transformer, according to Equation (2).

4. CONCLUSIONS

Two general, mathematically well founded, stable, accurate and efficient methods for high frequency modeling of transformer windings are presented in detail. The obtained numerical results for the chosen transformers are verified by comparison against measurements.

The presented methods have a high accuracy level in the critical time interval of the LI ($t < 20\mu\text{s}$) where the highest and most hazardous voltage peaks appear. Due to the transient nature of our simulation methods the disagreement accumulates over time and, later on, it is getting more and more significant. The internal damping of the system, however, radically reduces the voltage peaks in the later time interval ($t > 20\mu\text{s}$) thus making the simulation error in this time-frame insignificant.

Considering the complexity of the winding structure and its high frequency modeling, the demonstrated level of accuracy of the suggested methods is sufficient for industrial transformer design.

REFERENCES

- [1] IEC International Standard, IEC 60076-11, *Power Transformers – Part 11: Dry-type Transformers*, International Electrotechnical Commission (IEC), Geneva, Switzerland, 2004.
- [2] J. Smajic, T. Steinmetz, M. Rüegg, Z. Tanasic, R. Obrist, J. Tepper, B. Weber, M. Carlen, “*Simulation and Measurement of Lightning-impulse Voltage Distributions Over Transformer Windings*”, IEEE Transactions on Magnetics, Vol. 50, No. 2, Article#: 7013604, February 2014.
- [3] J. H. McWhirter, C. D. Fahrnkopf, J. H. Steele, “*Determination of Impulse Stresses within Transformer Windings by Computers*”, Power Apparatus and Systems, Part III. Transactions of the AIEE, 1956, pp. 1267-1274.
- [4] A. Miki, T. Hosoya, K. Okuyama, “*A Calculation Method for Impulse Voltage Distribution and Transferred Voltage in Transformer Windings*”, IEEE Transactions on Power Apparatus and Systems, Vol. PAS-97, No. 3, 1978, pp. 930-939.
- [5] F. de Leon, A. Semlyen, “*Complete Transformer Model for Electromagnetic Transients*”, IEEE Trans. on Power Delivery, Vol. 9, No. 1, 1994, pp. 231-239.
- [6] S. Okabe, M. Koto, G. Ueta, T. Saida, S. Yamada, “*Development of High Frequency Circuit Model Oil-immersed Power Transformers and its Application for Lightning Surge Analysis*”, IEEE Trans. on Dielectrics and Electrical Insulation, Vol. 18, No. 2, 2011, pp. 541-552.
- [7] J. Ostrowski, R. Hiptmair, F. Krämer, J. Smajic, T. Steinmetz, “*Transient Full Maxwell Computation of Slow Processes*”, in Mathematics in Industry, B. Michielsen, J. R. Poirier, Eds., Springer, Berlin, 2012, pp. 87-95.

Goran Plišić
Končar Power Transformers Ltd
goran.plisic@siemens.com

Kosjenka Capuder
Končar Power Transformers Ltd
kosjenka.capuder@siemens.com

INFLUENCE OF WINDING CAPACITANCES TO GROUND MODELLING ON THE CALCULATION OF TRANSFERRED VOLTAGES IN POWER TRANSFORMER

SUMMARY

During voltage transients, the windings of a transformer are coupled by electric and magnetic fields. To calculate the transients inside the transformer, a network model is typically used. The accuracy of obtained calculation results depends mainly on this model in which the windings are lumped into R, L and C circuit components. The windings are usually represented by discs, or groups of discs, with the corresponding resistances, inductances (self and mutual) and capacitances (series and to the ground) [1]. In case of impulse voltage, wave's steep front and consequently high frequency oscillations are the main reason why capacitances modelling is of major importance for the calculation of voltage distribution in winding and between windings.

Key words: power transformer, overvoltages, lightning, capacitances, model, 3D FEM

1. INTRODUCTION

In order to calculate the transient and oscillatory responses of windings to impulse waves, the appropriate model of the transformer is used in practice. It includes inductances and capacitances of the windings and resistive elements as representation of damping. Finally, a network of finite number of lumped elements is formed. The inductive network consists of branches and nodes, with each branch between two neighbouring nodes. The lumped capacitances are then assigned to the nodes. There are capacitances between nodes, as well as between nodes and ground (Figure 1). To ensure validity of the circuit for the requested calculations, the model complexity is chosen to accurately represent behaviour in the frequency range of interest. It means that one element of lumped parameters is small enough to correctly represent oscillations with this frequency. In this case the biggest elements are discs in a disc winding and with this specific geometry the calculation is valid for a range of frequencies up to several hundreds of kHz.

During some special impulse voltage tests in the factory measurements of transferred voltages between windings of a transformer were conducted. HV side was impulsed on two phases simultaneously and LV side voltages were measured. Tests included different combinations of grounding of HV and LV terminals to correspond to realistic situations occurring during transformer operation in a power system.

Comparison with the calculation showed some deviation. After analysis of all the results and influences, especially focused at different grounding combinations, the idea was to check modelling of capacitances. The emphasis is on shunt capacitances since, as stated in [2], even the bushing and terminal bus capacitances have the effect of reducing the transferred electrostatic component of voltage. This is also valid for the other capacitances to metal parts in the vicinity of windings / winding connections. To check the adequacy of existing analytical calculation of capacitances a 3D transformer model was built and capacitances of interest were calculated using FEM (finite element method) software, Ansys Maxwell (v.15).

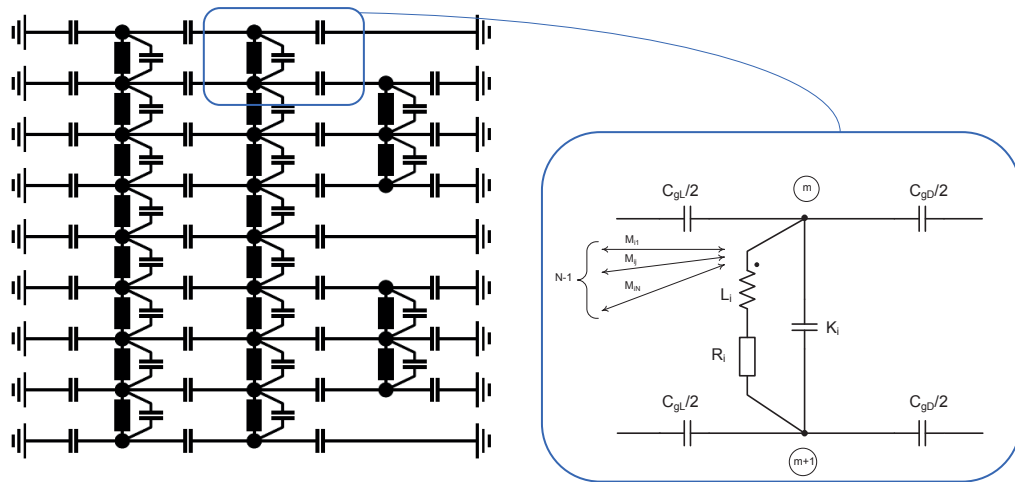


Figure 1 – simplified, one phase network model with lumped elements

- K_i – series capacitance of the element "i"
- R_i – resistive component of the element "i"
- L_i – self inductance of element "i"
- M_{ij} – mutual inductances between elements "i" and "j"
- C_{gL} – shunt capacitance between element "i" and left neighbouring element or earth
- C_{gD} – shunt capacitance between element "i" and right neighbouring element or earth

As mentioned, two phases are impulsed at the same time, so for this specific case, a three phase model is needed. This means that three one-phase models are connected to form a three-phase model while basic principle of the network per phase stays the same. Also, there are some capacitances modelled between windings of neighbouring phases.

2. CAPACITANCES

2.1 Standard, analytical model

2.1.1 Series Capacitances

Values of series capacitances are calculated as equivalent capacitances based on the electrostatic energy stored in the network of elementary capacitances. In the described model the details include elementary turn-to-turn and disc-to-disc capacitances and their connection depending on a type of winding [3]. These capacitances will not be tested in this paper.

2.1.2 Shunt Capacitances inside one phase

Capacitances between winding and core, neighbouring windings and winding and tank are calculated with simple analytical formulas for capacitance between concentric cylinders:

$$C = 2\pi\epsilon_0\epsilon_r \frac{H}{\ln \frac{D_2}{D_1}} \quad (1)$$

- Where:
- ϵ_0 - permittivity of vacuum ($\epsilon_0 = 8.854 \text{ pF/m}$)
 - ϵ_r - relative permittivity of the relevant material between electrodes
 - H - length of cylinder (m) (electrical winding height)
 - D_2 - diameter of outer cylinder (inner diameter of outer winding)
 - D_1 - diameter of inner cylinder (outer diameter of inner winding)

Similar formula, with some corrective factors, is in the used transient calculation. Corrective factors are taking into account the real geometry with conductor insulation and radial ducts.

2.1.3 Shunt capacitances between phases

Similarly to the ones described in previous paragraph, capacitances between windings of neighbouring phases are calculated with analytical formula for capacitance between parallel cylinders:

$$C = \frac{\pi \varepsilon_0 \varepsilon_r H}{\ln \left(\frac{a}{D} + \sqrt{\left(\frac{a}{D} \right)^2 - 1} \right)} \quad (2)$$

Where: a - distance between cylinders' (windings') axes
 D - outer diameter of cylinders

However, formulas for shunt capacitances are used for all the lumped elements regardless of their position in the transformer core window. So, in this case even the 2D FEM (or BEM) would be an improvement, keeping in mind to avoid errors when using 2D rotational symmetric model, since it doesn't describe the transformer core/yoke in the right way. In addition to the aforementioned capacitances of windings, there are also capacitances of winding connections that are not taken into account. They can also influence the result. Winding connections are typically a geometry that is difficult, if not impossible, to represent and calculate in 2D.

2.2 3D FEM model

To check the adequacy of existing analytical approach, 3D FEM calculation is chosen since it allows simultaneous solution to the mentioned capacitances with one model.

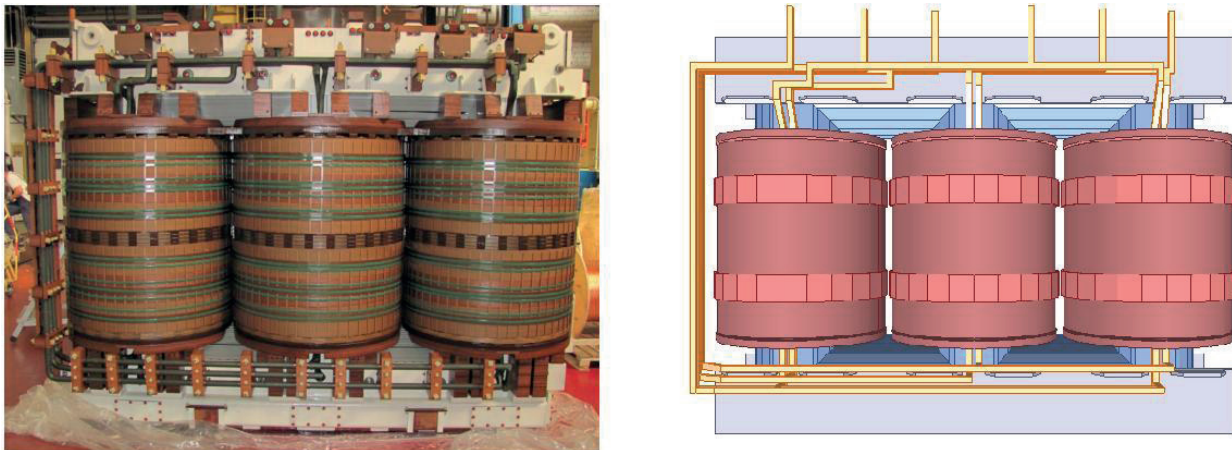


Figure 2 – Transformer active part in the production / 3D transformer model in Ansys Maxwell v.15

FEM Model (shown in Figure 2) consisted of the transformer active part in the tank, including LV side winding connections. Insulation cylinders between windings, as well as some wooden parts near the windings were modelled. Permittivity used in the model:

Table I – permittivity values used

ε_r, oil	$\varepsilon_r, paper$	$\varepsilon_r, transformerboard$	$\varepsilon_r, wood$
2.2	3.4	4.4	4.4

Because of the size of the model and large differences in dimensions, one compromise that had to be done is that only end parts of windings were modelled to the size of disc/turn, and not the whole winding height. Otherwise the model would become too large and the calculation too slow on available computer resources. Nevertheless, from the results shown, it can be seen that the assumption of homogeneity of field is proved valid, when going deeper in the winding. In Figure 3 an illustration of voltage distribution is given looking at intermediary results obtained when calculating capacitances. Maxwell 3D software allows

user to generate capacitance matrix from chosen electrodes, so this part of work was straightforward and easy to accomplish.

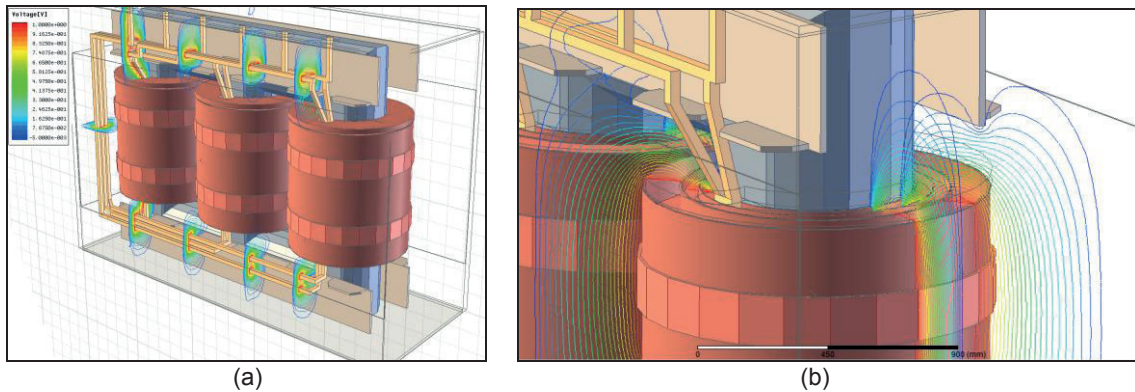


Figure 3 – Illustration of voltage distribution around electrodes of interest – (a) LV winding connections, (b) windings

3. RESULTS

3.1 Capacitances

The main differences between two calculations are in the parts where electric field is not homogeneous and areas which are not covered with analytical expressions at all. That said, it's obvious that winding ends, top and bottom, are the places to look at. Main differences are shown in Tables II and III. Shunt capacitances between windings and grounded parts are shown with results given for top part since bottom is nearly the same.

Table II – Capacitances between turns of LV winding and ground

Turns, top to bottom	Analytical formula	FEM 3D	
	C_r in pF	C_r in pF, phases 1,3	C_r in pF, phase 2
Turn 1	60,1	133,2	130,3
Turn 2	60,1	58,6	58,9
Turn 3	60,1	58,9	59,0
Turn 4	60,1	59,6	59,2
Turn 5	60,1	59,5	59,2
Turn 6	60,1	59,5	59,1
Rest, average per turn	60,1	59,8	59,4

Table III – Capacitances between discs of HV winding and ground

Discs, top to bottom	Analytical formula	FEM 3D	
	C_r in pF	C_r in pF, phases 1,3	C_r in pF, phase 2
Disc 1	5,76	103,5	116,2
Disc 2	5,76	10,6	12,0
Disc 3	5,76	7,3	8,5
Disc 4	5,76	6,4	7,5
Disc 5	5,76	6,0	7,1
Disc 6	5,76	5,7	6,7
Rest, average per disc	5,76	5,3	5,5

LV winding connections in this specific transformer are of such configuration, which can be seen in Figure 2, that their capacitances are not negligible, especially if we compare values with those inside windings. Capacitances between LV winding connections and connections to the ground are shown in Table IV.

Table IV – Capacitances between LV winding connections and to the ground (FEM 3D)

LV1 :	a1-b1	a1- c1	b1-c1	a1-ground	b1-ground	c1-ground
C in pF	142,44	25,51	81,08	159,52	110,55	123,36
LV2 :	a2-b2	a2-c2	b2-c2	a2-ground	b2-ground	c2-ground
C in pF	291,31	47,04	317,99	325,40	156,35	328,42

3.2 Measurement

Equipment used for the measurement was:

- Haefely Recurrent Surge Generator (RSG), type 481
- Tektronix Digital Oscilloscope, type TDS 544A, 1Gs/sec

The transformer is 64MVA, 24/6,8/6,8 kV, connection YNd11d11. Test connection is shown in Figure 4, with possible values of capacitances C of 250 and 500 pF, and resistance R of 600 and 1000 Ω .

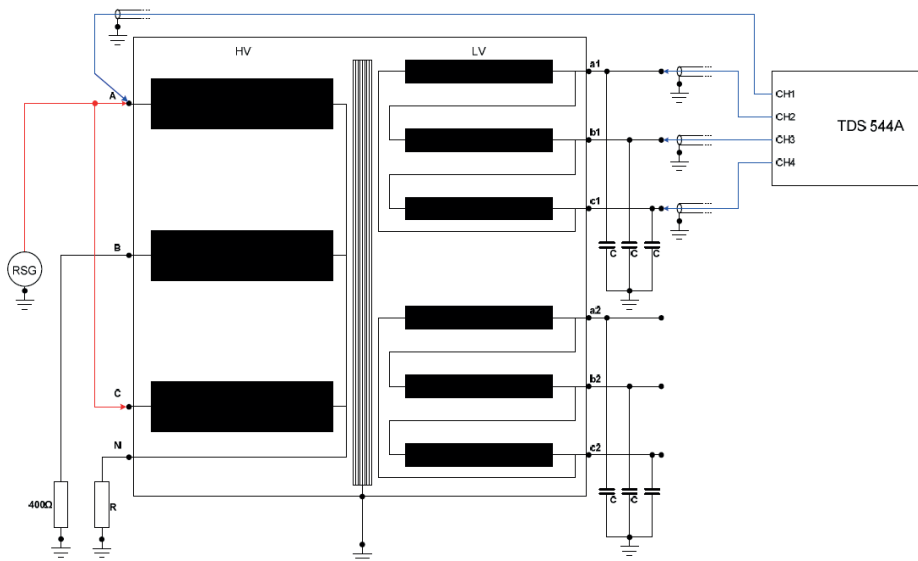


Figure 4 – Test connection for RSO measurement

3.3 Transient calculation

To check the influence of corrected or newly added capacitances one case from the measurements is chosen, the case with all of the LV winding terminals being isolated and HV neutral grounded with 600 Ω .

Table V gives a comparison between voltages calculated on LV side with, in the first case, capacitances calculated according analytical expressions and, in the second, those obtained from 3D FEM calculation.

Table V – Maximum voltages on LV windings terminals (in percent of impulse voltage on HV side)

<i>terminal</i>	<i>Measurement</i>	<i>Standard transient calculation</i>	<i>Calculation with FEM 3D capacitances</i>
	<i>U in %</i>	<i>U in %</i>	<i>U in %</i>
a1	68,0	73,0	69,1
b1	15,7	20,0	18,9
c1	41,9	45,4	43,2
a2	68,9	73,9	68,2
b2	16,6	21,4	19,3
c2	42,5	46,4	40,8

In Figures 5 to 10, calculated voltage waveshapes of LV windings terminals are shown in comparison to measurement. Influence of capacitances values on amplitudes and waveshapes is clearly seen. In this case it's more visible on the LV2 side (terminals a2, b2, c2) which can be explained with higher values of capacitances of windings connections.

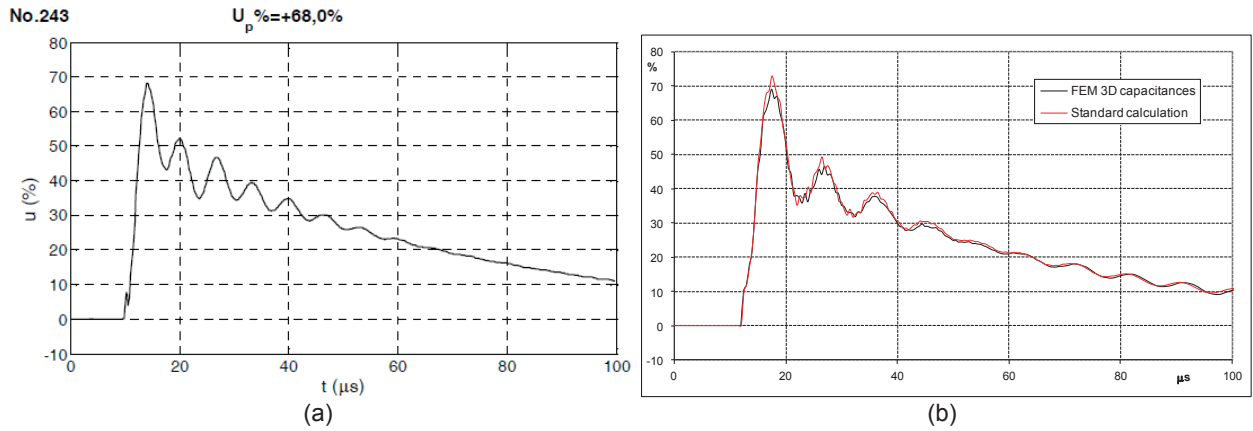


Figure 5 – Measured (a) and calculated (b) voltage waveshape on terminal a1

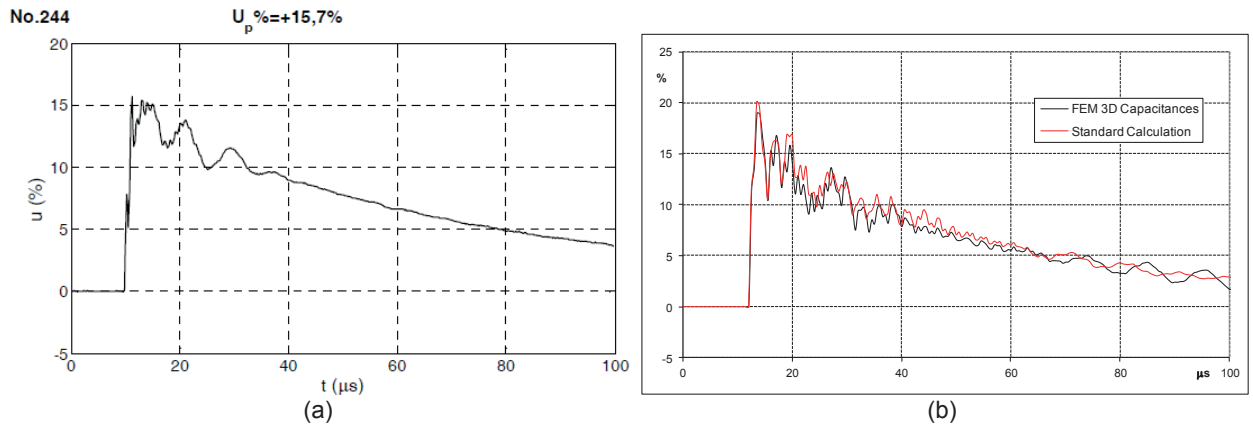


Figure 6 – Measured (a) and calculated (b) voltage waveshape on terminal b1

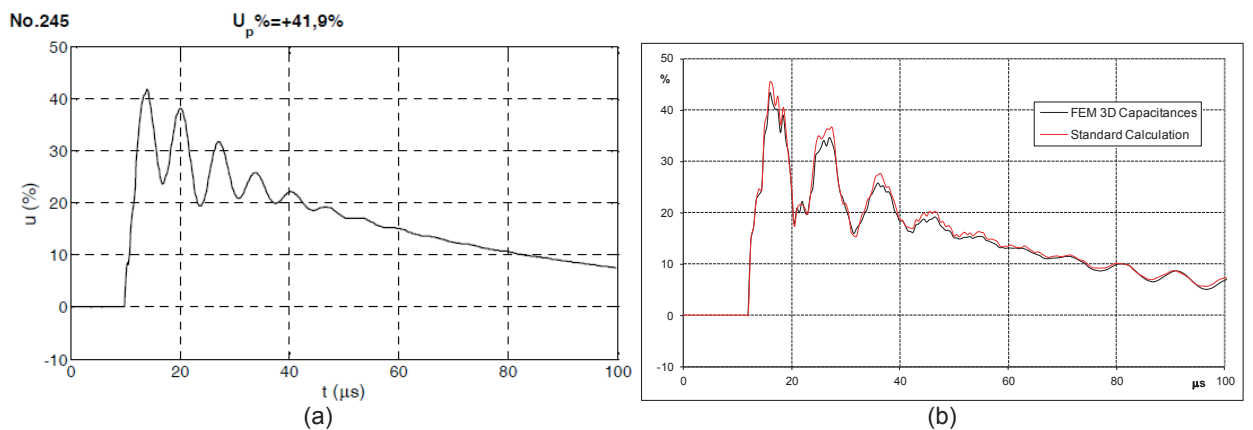


Figure 7 – Measured (a) and calculated (b) voltage waveshape on terminal c1

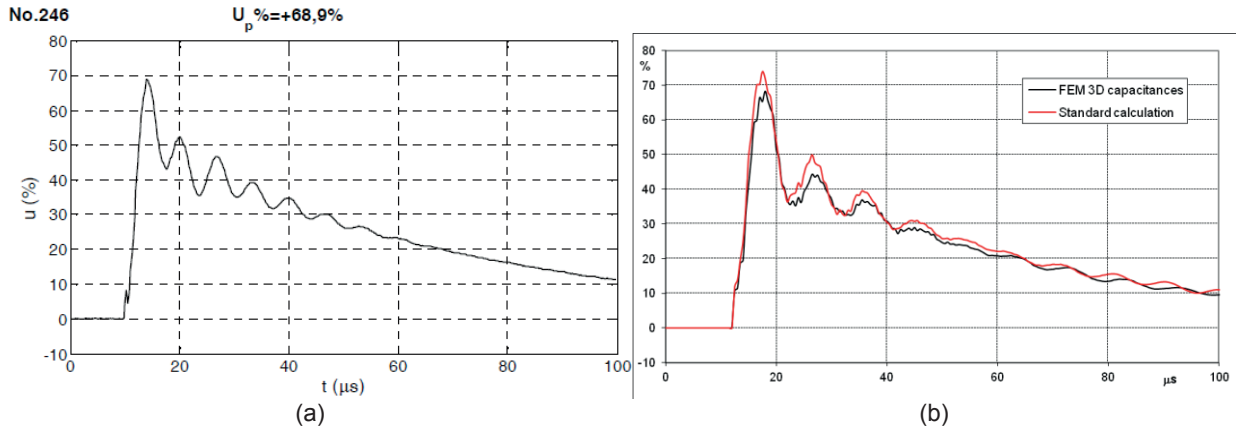


Figure 8 – Measured (a) and calculated (b) voltage waveshape on terminal a2

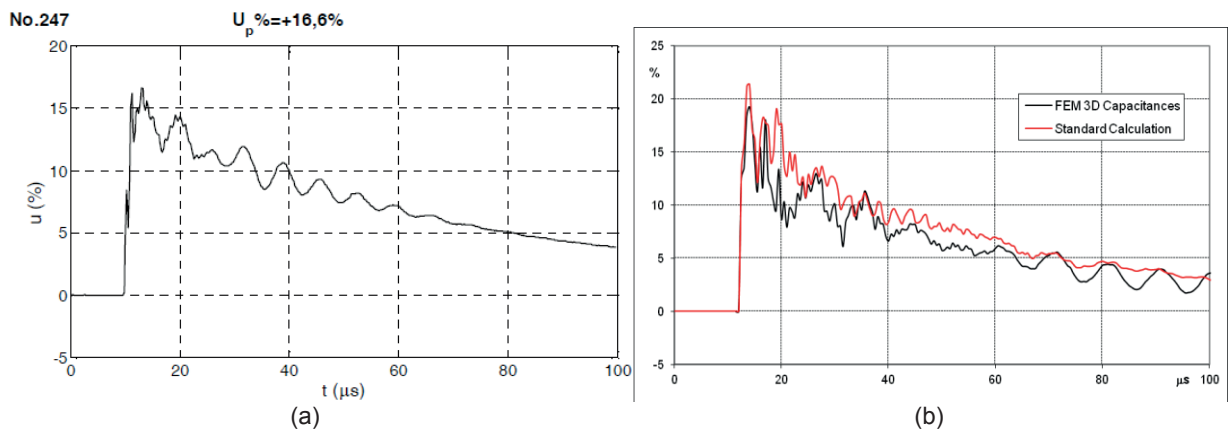


Figure 9 – Measured (a) and calculated (b) voltage waveshape on terminal b2

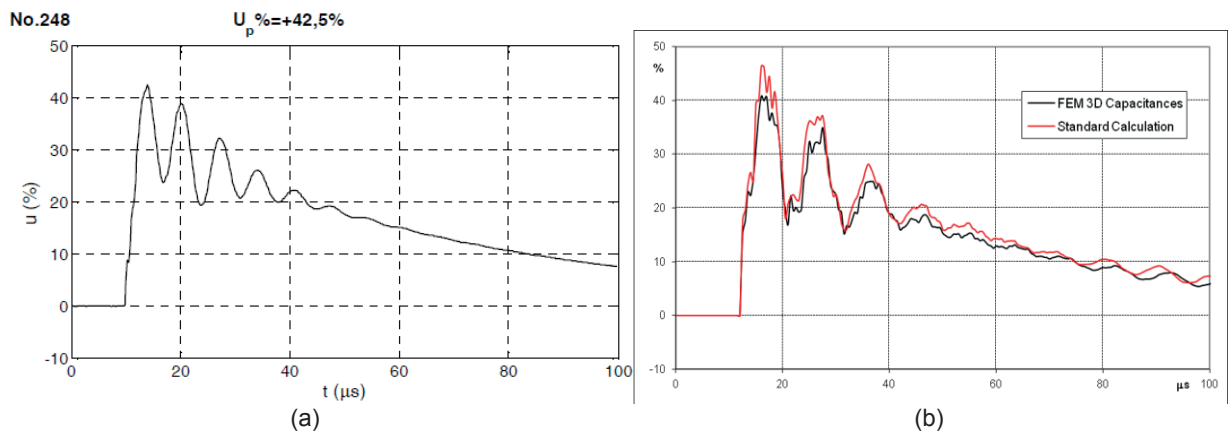


Figure 10 – Measured (a) and calculated (b) voltage waveshape on terminal c2

4. CONCLUSION

The main idea behind the influence of capacitance modelling on transferred overvoltages has been described through one example. The results showed the importance of adequate modelling of capacitances that are not usually taken into account or their influence is underestimated. This includes shunt capacitances of windings to grounded parts (i.e. core, clamping plates, tank etc.) and capacitances of winding connections to each other and to ground too. Influence on the final result, i.e. transferred voltages, was shown with transient calculation and two different sets of capacitance values (standard and FEM based) while other parameters remained the same. Transient calculation results were compared to

measurement and both the amplitudes as well as voltage waveshapes showed good agreement, especially after corrected capacitance values have been introduced. If we look at the difference (in percent) of all calculated values to measurement, their root mean square value went down from 17.5% to 10.9% with FEM 3D calculated capacitances. This puts the calculation results practically in the area of measurement uncertainty.

It was once again confirmed that FEM 3D analysis, although powerful, for certain problems is too time consuming, while the results obtained can be reached through simpler methods, but with appropriate complexity. For the future analyses the solution may be in using some of the capacitive weighting techniques as mentioned in [4].

5. REFERENCES

- [1] V. Kulkarni, S. A. Khaparde, *Transformer Engineering: Design and Practice*, Marcel Dekker, Inc., 2004
- [2] Abetti, P.A., *Electrostatic voltage distribution and transfer in three-winding transformers*, AIEE Transactions, December 1954, p. 1407–1416.
- [3] Ambrozic, C., *Berechnung der Ersatzkapazität einer Scheibenspule von einer Normalscheibenspule-transformatorwicklung*, *Etz-A*, Vol. 93, No. 8, 1972, pp.446-450
- [4] Adam J. Thomas, Satish M. Mahajan, *Capacitive weighting technique for estimating the 3D turn-level capacitance in a transformer winding*, *Electric Power Systems Research* (2011), vol. 81 issue 1 p. 117-122
- [5] Robert M. Del Vecchio, Bertrand Poulin, Pierre T. Feghali, Dilipkumar M. Shah, Rajendra Ahuja, *Transformer design principles, with applications to core-form power transformers*, second edition, Taylor and Francis Group, LLC, 2010
- [6] M. Popov, L. van der Sluis, R.P.P. Smeets, *Evaluation of surge-transferred overvoltages in distribution transformers*, *Electric Power Systems Research* (2008) vol. 78 issue 3 p. 441-449

Vasily Larin
All-Russian Electrotechnical Institute (VEI)
Moscow, Russia
vlarin@vei.ru

Daniil Matveev
Moscow Power Engineering Institute (MPEI)
Moscow, Russia
dmatveev@tpn-moscow.ru

Alexey Volkov
All-Russian Electrotechnical Institute (VEI)
Moscow, Russia

Study of Transient Interaction in a System with Transformer Supplied from Network through a Cable: Assessment of Interaction Frequencies and Resonance Evolvement

SUMMARY

Transformer together with its windings is a complex oscillatory system. The interaction between the transformer and an electric network during transients can cause the development of resonance phenomenon in the windings leading to overvoltages and the risk of transformer fault.

This report presents the results of studies of resonance phenomena in transformer windings, caused by interaction with an electric network containing the feeder cable. The approach to a simple assessment of dominant oscillation frequency of a voltage in the system “feeder cable – transformer” and estimation of the resonant frequencies of transformer winding is considered. The report also describes the technique for measurement of winding resonance voltages. The resonance phenomenon evolvement in transformer windings is considered and the impact of decaying oscillating applied voltage on maximum ratio of resonance overvoltages is estimated.

Key words: Transformer windings, resonance overvoltages, winding natural oscillation frequencies, frequency response analysis, FRA, voltage measurement in transformer windings.

1. INTRODUCTION

Power transformers are the key and crucial elements in the chain of transmission and distribution of electrical energy. In transient conditions caused by switching or short-circuit faults in power networks the transformers actively interact with other elements of electrical network [1, 2]. This electrical interaction is complex and it may result in transformer insulation faults under adverse circumstances.

One of the instances of electrical interaction with the supplying network is an internal resonance in transformer windings in the case when the oscillation frequency of the voltage at its input terminals is close to one of the windings natural oscillation frequencies. If the secondary winding of the transformer is not loaded, such resonant phenomena can be accompanied by significant overvoltages in internal insulation of transformer in which the voltage on the certain parts of the winding insulation is comparable or exceeds the voltage at transformer input terminals. The harmfulness of the resonance phenomenon in transformer windings is aggravated by the fact that the external arresters installed at the input terminals of the transformer are not able to limit such overvoltages that occur on the certain elements inside the transformer.

For the above reasons resonant overvoltages potentially pose a threat to the internal insulation of transformer. In general, resonant overvoltages impact on both the longitudinal insulation of windings (primarily in the entrance area) and the main insulation (at some distance from the entrance area of the winding). These resonant overvoltages can manifest themselves by damaging corresponding winding insulation elements.

It should be noted that the internal insulation of oil-immersed transformers is a composition consisting of many layers. For example, the insulation of wires may consist of three or more layers (per one side) of craft paper; the main insulation of windings, in general, may comprise more than one insulation barrier. Repetitive exposure of resonant overvoltages can lead to subsequent degradation of the solid insulation and to significant decrease of the transformer internal insulation electric strength. The cumulative effect may cause the damage of the transformer internal insulation under normal operating voltage after some time since this transformer had been put into operation.

To assess the possibility of the resonant overvoltages development in the transformer windings and the degree of their severity for the internal insulation it is necessary, first of all, to determine the dominant frequencies of possible voltage oscillations in the network, the resonant frequencies of the transformer windings and to make an assessment of the voltages on the elements of the windings insulation.

2. VOLTAGE OSCILLATION IN THE SYSTEM “FEEDER CABLE – TRANSFORMER”

The necessary conditions of the internal resonance evolvement in the transformer are the absence of load on the transformer secondary side and the presence of voltage oscillations on the supply side with a frequency close to one of the natural frequencies of the transformer windings.

Natural frequencies of high voltage and intermediate voltage windings of medium and high power transformers are typically tens of kHz. One of the main sources of voltage oscillations at these frequencies are oscillations in feeder cables or overhead lines having length of the order of hundreds of meters, caused by multiple reflections of waves in these lines due to any switching. In this regard, the networks, in which a transformer is energized together with a feeder line from its remote end, are a subject to potential danger.

The following typical situations in power facilities [3] causing high-frequency voltage oscillations in the system “feeder cable – transformer” may be identified:

- 1) short-circuit earth fault on one of the phases at the beginning of the cable (including faults at the substation busbars);
- 2) energization of the system “feeder cable – transformer” from the busbar to which several cable lines with a low total surge impedance are connected;
- 3) energization of the system “feeder cable – transformer” from the busbar to which one or more cables with similar parameters and lengths are connected.

In the considered systems “feeder cable – transformer” an approximate evaluation of the dominant oscillation frequency may be performed by solving the following transcendental equation [4]:

$$f = \frac{v}{4L} \left[1 - \frac{2}{\pi} \arctan 2\pi f C_T Z_c \right], \quad (1)$$

where v – wave propagation speed in the feeder cable; L – length of the feeder cable; C_T – transformer surge capacitance; Z_c – characteristic impedance of the feeder cable.

It follows from the expression (1) that the dominant frequency in the system is determined primarily by the parameters of the feeder cable and by the transformer surge capacitance. Meanwhile, the greater the oscillation frequency and the characteristic impedance of the cable, the greater the effect of transformer surge capacitance. In the case of long cables with low characteristic impedance the last term in the expression (1) can be neglected for the approximate estimation of the oscillation frequency.

3. ESTIMATION OF TRANSFORMER WINDINGS NATURAL OSCILLATION FREQUENCIES

3.1. Theoretical evaluation of the windings natural frequencies

The evaluation of the transformer windings natural frequencies is often one of the main stages of impulse transients calculation and longitudinal insulation design. To date, there are a large number of publications which address the issues of theoretical determination of natural frequencies, for example [5]. However, due to a complex mutual magnetic and electrical interaction between the individual elements of a single winding and/or adjacent windings the expressions for natural frequencies cited in the literature typically are based on a number of significant simplifying assumptions, therefore they are suitable only for qualitative evaluation.

For a uniform winding with earthed neutral by neglecting the mutual magnetic influence of individual elements of this winding and the influence of adjacent windings the following expression for the k -th natural frequency (k -th harmonic) can be obtained [5]:

$$f_k = \frac{k}{2\sqrt{LC\left(1 + \frac{K}{C}(k\pi)^2\right)}}, \quad (2)$$

where L – inductance of winding; C and K – capacitance to earth and series capacitance of winding.

Considering the fact that the natural frequency f_k is related to the winding wave propagation speed V_k by the formula

$$f_k = \frac{kV_k}{2l}, \quad (3)$$

where l – the “electrical length” of the winding. From the expression (2) the formula for V_k may be obtained:

$$V_k = \frac{l}{\sqrt{LC\left(1 + \frac{K}{C}(k\pi)^2\right)}}. \quad (4)$$

It follows from the expression (2) that for windings with low series capacitance the first few natural frequencies are determined mainly by the capacitance to earth and are close to the oscillation frequencies of the line with the same electrical length grounded at the far end.

It follows from the expression (4) that in the case of a winding with low series capacitance the wave propagation speed is equal to $V_1 \cong \frac{l}{\sqrt{LC}} = \frac{c}{\sqrt{\epsilon_s}}$, where c – speed of light, ϵ_s – equivalent dielectric

permittivity of the winding surrounding medium which determines the capacitance of the winding to the ground. Meanwhile, the harmonic’s wave propagation speed decreases with the increase of the harmonic’s number.

It should also be noted that estimation of the first natural frequencies can be made by the expression (3) provided that the estimations of the wave propagation speeds and the electrical length of the winding are known, which often happens in practice. For example, in oil-immersed transformers, in general, the first natural frequency corresponds to the propagation speed of about 140–180 m/ μ s, and in dry-type transformers with open windings – 240–300 m/ μ s.

3.2. Evaluation of the winding natural frequencies by means of numerical modeling

For a more accurate evaluation (as compared with theoretical formulae) of the winding natural frequencies a high-frequency model of the transformer can be used. It is based on an equivalent circuit with distributed or lumped parameters which is implemented in software programs for calculation of impulse transients in transformer windings.

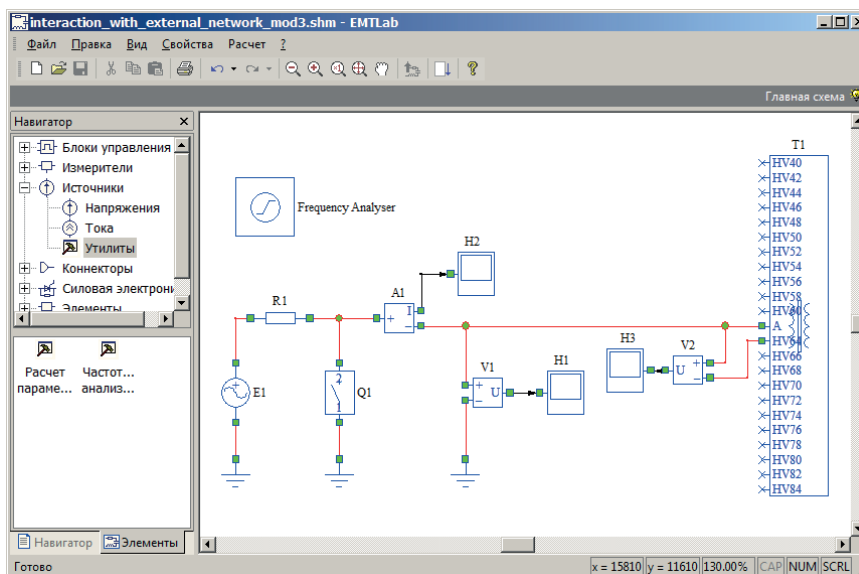


Figure 1 - A high frequency transformer model in the EMTLab software program: calculation of frequency response

In order to determine natural frequencies by means of numerical modeling authors use an approach described in [4]. It is based on a combined application of two software programs. The first one (TT) is used for generation of a high-frequency lumped parameters model of a transformer which is afterwards exported to the second program (EMTlab). EMTlab is designed for simulation of transients in electrical networks (EMTlab, figure 1) and features the frequency analyzer module which calculates transfer functions in frequency domain (figure 2).

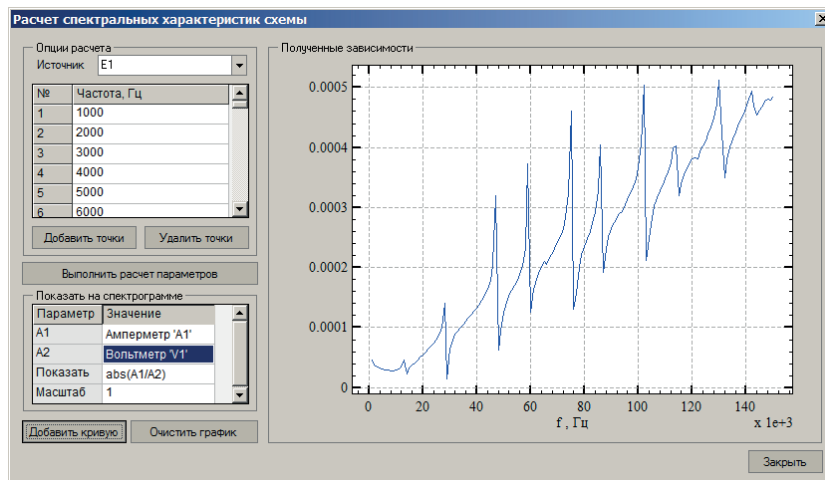


Figure 2 - The EMTlab's frequency analyzer module and calculated winding admittance

3.3. Experimental determination of windings natural frequencies

When a power transformer is fed by AC voltage with frequency equal to one of its resonant frequencies relatively high resonant oscillating voltages develop in its windings. Corresponding currents which flow mainly within these windings are high too. These oscillating currents are accompanied by loss of energy and, therefore, the highest active power is consumed from power source in the resonance mode. While changing the frequency of the applied voltage in a wide range it becomes close to one of the resonant frequencies and the energy losses in the transformer grow up. Thus, the local maximum of consumed active power may be used as an indication of achievement of one of the transformer resonant frequencies.

The problem of consumed power maximum determination in a certain frequency range can be reduced to the problem of determination of maximum real part of input admittance of a fed transformer winding [1]. To solve this problem in practice it is quite convenient to use Frequency Response Analysis (FRA) measuring systems.

The principle of FRA systems is based on determination of frequency response of transformer windings by means of signal injection through one of transformer terminals and measurement of an input voltage \bar{U}_1 and an output voltage \bar{U}_2 induced at a certain transformer terminal [6]. The result is a transfer function represented by corresponding absolute value $A = |\bar{U}_2 / \bar{U}_1|$ (usually expressed in dB) and phase angle $\varphi = \angle(\bar{U}_2, \bar{U}_1)$. The transfer function is defined in a broad frequency range (from tens of Hz to thousands of kHz).

In FRA systems measuring cables are about 5–15 m long; to eliminate their possible influence on measurement results at high frequencies these cables are terminated by matching resistors with resistance equal to cable surge impedance (usually 50 Ohms). The measured output voltage is proportional to an output current \bar{I}_2 flowing to earth through a shunt (matching resistor of 50 Ohms), which resistance is small enough compared to the impedance of the winding at high frequencies. Thus, the winding admittance is defined as

$$\bar{Y}_{12} = \frac{\bar{U}_2}{Z_c(\bar{U}_1 - \bar{U}_2)} = \frac{1}{Z_c \left(\frac{1}{A \angle \varphi} - 1 \right)}. \quad (5)$$

It is necessary to note that when measuring the frequency response of individual windings the matching impedance of 50 Ohms is shunted by capacitance to earth C_s of high voltage bushing and leads that connect the winding with bushing and other windings as well as by capacitance of measuring cables and wires. The value of this shunt capacitance may have order of hundreds or thousands of pF. At frequencies of several MHz the impedance of this capacitance C_s becomes comparable with the

resistance of a matching resistor and, therefore, output current of measured winding partially flows through capacitance C_s instead of 50 Ohm resistor. Taking into account the shunt capacitance C_s formula (5) takes the form:

$$\bar{Y}_{12} \approx \frac{\frac{1}{Z_c} + j\omega C_s}{\frac{1}{A \angle \varphi} - 1} \quad (6)$$

Thus, neglecting the earth capacitance leads to an error in active and reactive component of input admittance of the winding achieved by FRA measurements and expression (5). However, the first natural frequencies of high-voltage transformer windings typically are few tens or few hundreds of kHz while the effect of shunt capacitance on the active component of input admittance is generally not so significant in this frequency range. So the first natural frequencies can be evaluated from FRA measurement but it needs to be mentioned that this is just an estimation rather than accurate measurement.

As an illustration of abovementioned statements the results of continuous disc-type winding transfer functions and frequency response measurements are presented. The winding model (figure 3) has an average diameter of about 1000 mm, height of 1100 mm and consists of 52 discs of 10 turns in each. For the purpose of measurements the winding has intermediate terminals at outer transitions between every pair of discs. The measurement results are shown in figure 4, which shows the transfer function voltages at the terminals of junctions between discs 14 and 15, 26 and 27 and 38 and 39 (hereinafter, terminal “14-15”, “26-27”, “38-39”), roughly corresponding to 1/4, 2/4 and 3/4 of the electrical length of the winding.

It should be noted that this model is continuous disc-type and has relatively low longitudinal capacitance. For these reasons, the obtained frequency response contains a pronounced resonance peaks corresponding to the winding natural frequencies. As can be seen from figure 4, the resonance peaks of the frequency responses of the winding are located at the same frequencies as the resonant peaks of the transfer functions of the terminal voltages.



Figure 3 – Model of continuous disc-type winding

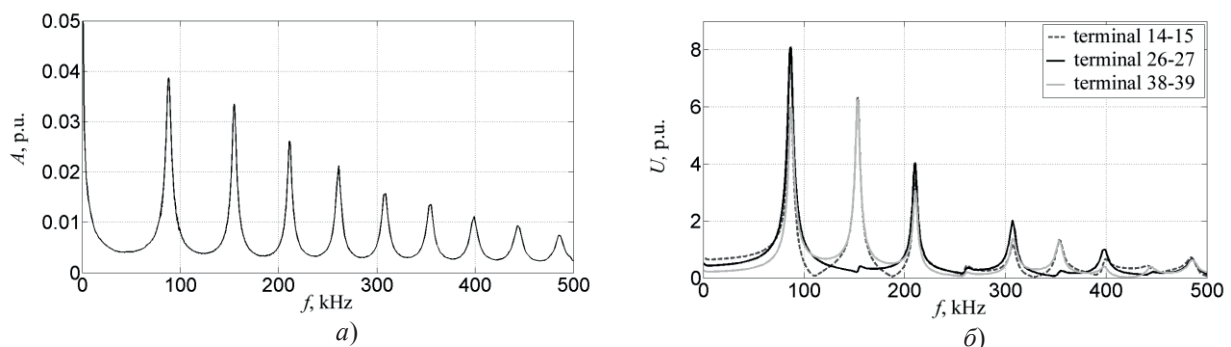


Figure 4 – Frequency response of the winding (a) and the transfer function of the terminal voltages (b)

In general, the resonant frequencies represented in the frequency response of the individual winding correspond not only to winding natural frequencies. The resonance frequency of individual windings can be distinguished from the frequencies corresponding to the interaction between windings as follows.

The transient voltages in any winding can be expanded as a combination of standing waves at self-frequencies. For the winding to which the voltage is applied the standing wave at the first winding

natural frequency has the nodes at the ends of this winding. Current distribution of this standing wave at the first natural frequency is shifted from voltage distribution by 1/4 of spatial period [7], thus, the current has a node in the middle of the winding and different polarities in the upper and lower halves of the fed winding. This leads to the fact that the EMF induced in the discs of the secondary winding are mutually compensated and the magnetic flux generated by the primary winding flows through the magnetic core without reaction from the secondary winding. Thus, at the frequency corresponding to the first natural frequency of the primary winding, the short circuiting of secondary winding has almost no influence on the input impedance of this primary winding. As a result, the frequency responses of the primary winding of the transformer obtained for open and short-circuited secondary winding are very close to each other starting from frequencies close to the first natural frequency of the primary winding.

However at frequencies much lower than the first natural frequency the open or short-circuit state of the secondary winding affects the magnetic flux and the flux return path and, therefore, significantly affects the value of input admittance of the primary winding and resonant frequency of interaction between windings.

Thus, the first natural frequency of the primary winding can be determined using FRA-measurements of this winding with respect to the input terminals with open and short-circuited secondary winding and subsequent identification of the first resonant frequency which achieves a local maximum of the real part of input admittance of the primary winding and the coincidence of frequency responses for open and short-circuited states of secondary winding.

Example below presents the frequency response and the real part of the admittance G_{12} of high-voltage winding (HV) of two-winding transformer (figures 5,a and 5 b, respectively), obtained when voltage is applied to the line terminal and measured at the neutral N of HV winding with open and short-circuited secondary low voltage winding (LV).

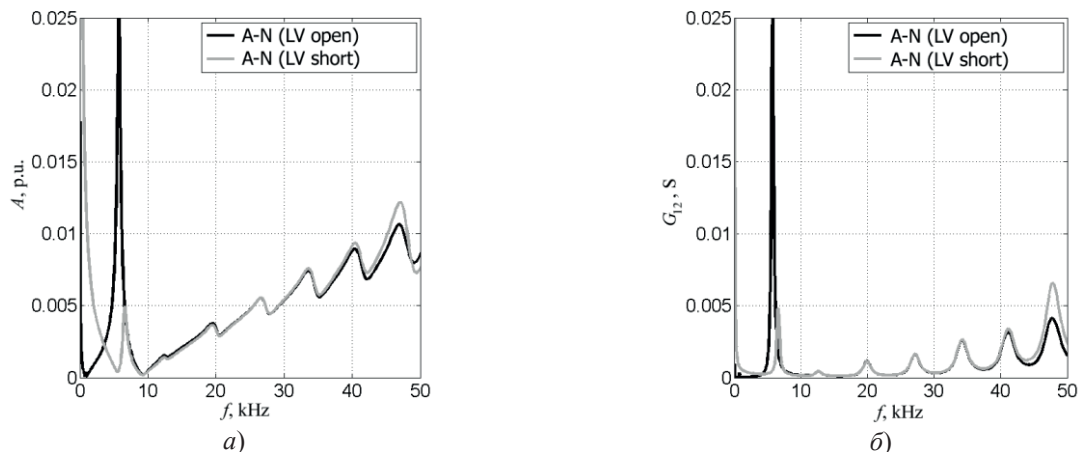


Figure 5 - Frequency responses (a) and real part of admittance (b) for the primary winding

As it can be seen from figure 5, the frequency responses of HV winding with open and short-circuited LV winding are significantly different up to the frequency of 8-10 kHz, both in magnitude and frequencies of resonance peaks; for the frequencies of about 13 kHz and higher frequency responses match each other. Thus, in this example, the resonant peaks at frequencies of about 5-7 kHz are related to frequencies of the interaction between windings and the resonant peak at a frequency of about 13 kHz corresponds to the first natural frequency of HV winding.

4. MEASUREMENTS OF WINDING VOLTAGES AT RESONANT FREQUENCIES

4.1. The technique

One of the crucial points in the resonant overvoltages problem is that the transformer in operation is exposed to the impact of *decaying* voltages. Therefore maximum possible values of overvoltage ratio may not have enough time to be achieved. However, these possible maximum ratios are definitely of interest as they represent the worst case.

In practice, the estimation of the maximum possible ratio of the resonant overvoltages in transformer windings can be performed by feeding the primary winding of the transformer by continuous AC voltage with a peak value of few tens of volts and by measuring the voltage at the intermediate points of the winding. Obviously, it is possible only in factory conditions. These measurements actually have a lot in common with repetitive surge oscillography (RSO) by low impulse voltages, and therefore they could be combined with it.

However, compared with RSO measurements the voltage measurement under resonant conditions has its own features, most important of them are listed below.

1) RSO measurements of oil-immersed transformers are usually performed without oil, resulting in roughly twice smaller values of equivalent dielectric permittivity of the environment (which determines the earth capacitance of the windings). Measured voltage peaks and resonant frequencies will be slightly higher than the values obtained in oil-filled conditions. Thus, the measurement results should be considered as an upper estimation.

2) As a rule, connection of measuring equipment to intermediate points of the winding is carried out by means of connection cables or wires, which leads to addition of their earth capacitances to these points. If the capacitance of connected objects is comparable with the capacitance to earth of individual sections of winding in these intermediate points, the distortion of values of resonant frequencies and voltage peaks is to be expected. As a consequence to ensure accurate measurements it is necessary to avoid the use of measurement cables with high capacitances and long connecting wires and, in general, to use the connection between measuring system and winding with the lowest possible capacitance to the earth.

3) With respect to the abovementioned statements we may state that the measurement of voltages at fixed frequencies corresponding to expected winding natural frequencies gives inaccurate estimations. In the presence of measuring wires the maximum voltage values at specific points of winding are achieved at slightly different frequencies. Due to the strong frequency dependence of the resonant voltages even a small shift in frequency leads to a significant change of measured voltages. In order to make more accurate determination of highest voltage values at certain intermediate points of the winding it is advisable to make measurements in fairly wide frequency range.

Considering the above, the measurement of resonant overvoltages in windings may be performed most correctly using FRA measurement systems, which output signal frequency varies in frequency range from a few Hz up to few MHz. Regular measuring cables and termination resistor of 50 Ohms are to be excluded from the winding response measurement circuit and replaced by digital oscilloscope probe with built-in divider (10:1 for example) with a bandwidth of tens or hundreds of MHz, input impedance of 10 M Ω and low input capacitance not bigger than 10–20 pF.

As an example, the results of measurements of transfer functions and voltages in the resonant conditions for the described above winding model are presented below. The completeness of measurement results is largely determined by the amount of winding intermediate terminals available for measurement. In the considered model the winding has intermediate terminals after each two discs. Point-by-point measurement of transfer functions for each terminal allows to build a spatial-frequency spectrum for maximum voltage values (figure 6) and the voltage distribution along the winding at natural frequencies of the winding (figure 7).

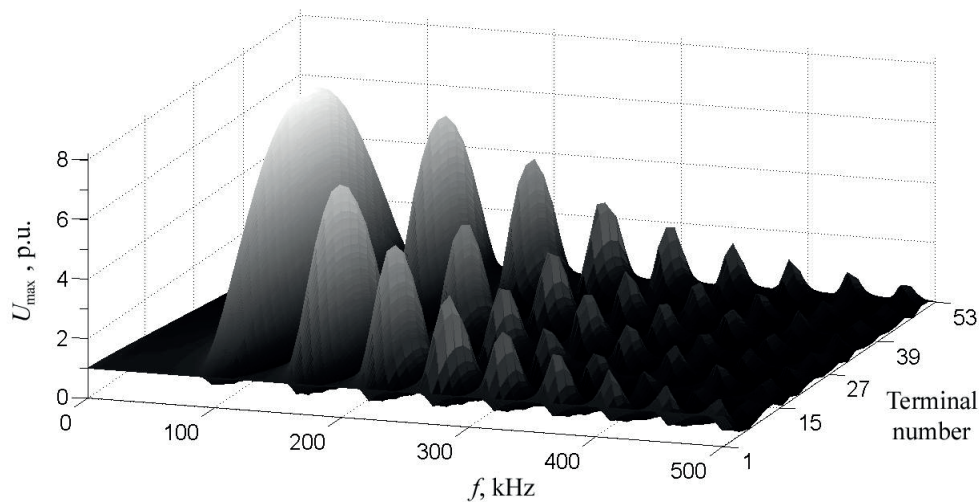


Figure 6 - Spatial-frequency spectrum of maximum voltages in the winding

Studies conducted on the winding model show that in case of connection to intermediate point of the winding made by the measurement circuit with the input capacitance not greater than 10-20 pF the expected voltage measurement error is not greater than 10%. The deviation of measured resonant frequencies from winding natural frequencies can be used as an indicator of measurement circuit influence.

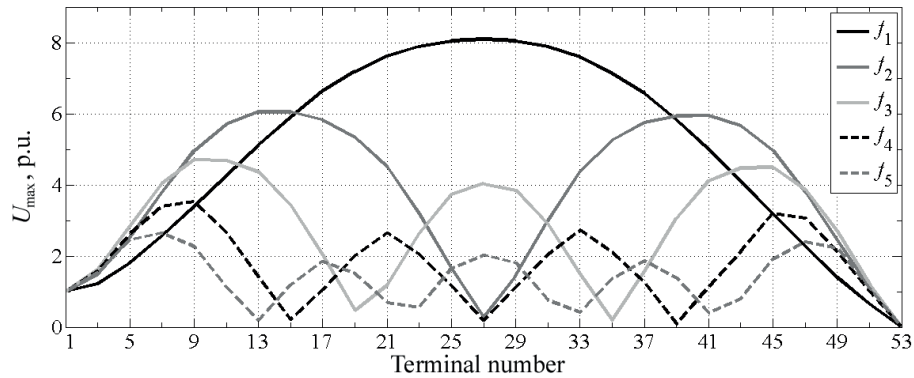


Figure 7 - Voltage distribution along the winding at first five natural frequencies

4.2. Analysis of the resonant voltage increase in the windings under the influence of an alternating voltage

Resonant voltages in transformer windings may be thought of as a combination of standing waves. The sum of these waves leads to voltage rise in certain parts of the windings. To achieve the maximum overvoltage ratio in the windings it is necessary to apply periodic input voltage for a sufficient amount of time, greater than the winding wave travel time.

With this in view, the attenuation of voltage oscillations in the network plays an important role in the development of dangerous resonance phenomena in transformer windings. The time required to reach the steady state with maximum overvoltage ratio may be of the order of tens of periods of applied oscillating voltage. Thus, if the input voltage decays with time the maximum overvoltage ratio may just not have time to develop. Moreover, the greater is the attenuation of the applied voltage, the less is the ratio of resonant overvoltages.

Using the measurement technique described above and the generator of sinusoidal voltage with a frequency equal to one of the winding natural frequencies, it is possible to perform oscillography of resonant rise of voltages in certain parts of the winding.

For example, the oscillograms of voltages at model terminals are presented in figure 8. For the frequencies of applied voltages equal to the first (86,4 kHz) and to the third (210,5 kHz) winding natural frequencies voltages were measured in the middle of the winding. For the second natural frequency (153,4 kHz) the voltage was measured at 1/4 of the winding length.

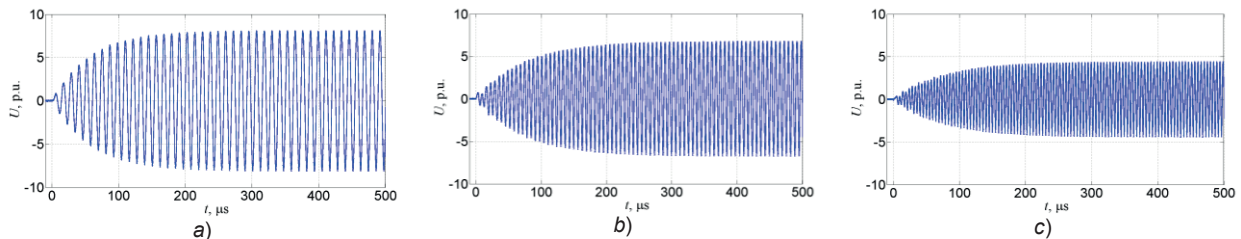


Figure 8 – Waveforms of voltages at model terminals

a - terminal "26-27", applied voltage frequency is 86.4 kHz; b - terminal "14-15", applied voltage frequency is 153,4 kHz; c - terminal "26-27", applied voltage frequency is 210,5 kHz

As may be seen from figure 8, the terminal voltages have the form of exponentially growing periodic voltage. Due to wave propagation the terminal voltage has time delay with reference to applied voltage. The voltage at antinode of standing wave (which is actually the maximum voltage) has time delay equal to $T_k/4 + (m - 1)T_k/2$, where m – voltage antinode number.

Assuming that the applied voltage is $u_s(t) = U_s \sin(2\pi f_k t)$, the maximum terminal voltage at corresponding natural frequency may be approximately represented by the following expression

$$u_k(t) = U_s A_k \sin(2\pi f_k t + \varphi_k) \cdot \left(1 - e^{-\frac{t}{\tau_k}} \right), \quad (7)$$

where k – number of winding natural frequency; t – time; U_s – peak value of applied voltage; A_k – maximum ratio of terminal voltage at k -th winding natural frequency; f_k – k -th winding natural frequency; φ_k

– represents time-delay in reference to applied voltage; $\varphi_k \approx \pi/2 + (m - 1)\pi$ for terminal corresponding to voltage antinode; τ_k – time constant of terminal voltage rise at the k -th winding natural frequency.

For the received waveforms the values of time constant τ_k and its ratio to the period of winding natural frequencies T_k are given in table 1.

Table 1 – Time constant of terminal voltage rise

Number of harmonics k	Frequency f_k , kHz	Period T_k , μ s	Time constant τ_k , μ s	τ_k / T_k
1	86,4	11,6	56,7	~5
2	153,4	6,5	72,8	~11
3	210,5	4,7	71,9	~15

In order to estimate maximum value of terminal voltage for the case of decaying sinusoidal applied voltage $u_d(t) = U_s \sin(2\pi f_k t) \cdot \exp(-t/\tau_d)$ using the Laplace transform and neglecting time-delay for simplicity, the following expression can be obtained for the terminal voltage

$$u_{kd}(t) = U_s A_k \left[\sin(2\pi f_k t) e^{-\beta t} + \frac{A \cos(\omega_k t) (e^{-\alpha t} - e^{-\beta t}) + \sin(\omega_k t) (B e^{-\alpha t} - C e^{-\beta t})}{(\beta - \alpha)(4\omega_k^2 + (\beta - \alpha)^2)} \right] \quad (8)$$

where τ_d – time constant of applied voltage damping; $\omega_k = 2\pi f_k$; $\alpha = 1/\tau_k$; $\beta = 1/\tau_d$;

$$A = 2\omega_0 \alpha \beta; \quad B = \alpha \alpha^2 - \alpha \beta + 4\omega_0^2; \quad C = \beta \beta^2 - \alpha \beta + 4\omega_0^2.$$

Typically, the transient voltage at high frequencies is characterized by a fast decay, the value of τ_d may be equal to several periods of transient voltage dominant frequency. At a known value of τ_d expression (8) may be used to estimate the maximum terminal voltage that may develop with regard to the attenuation of applied voltage. For example, with $A_k = 8$ p.u., $\alpha = 1/(5T_k)$, $\beta = 1/(4T_k)$ the terminal voltage under decaying supply voltage will reach the maximum value of 2.6 p.u.

5. CONCLUSION

To assess the possibility of resonant overvoltages in transformer windings and the degree of their severity for the internal insulation it is necessary, first of all, to determine the dominant frequency of possible voltage oscillations in the network, the resonant frequencies of the transformer and the voltages on the elements of winding insulation in resonance conditions.

Potential subjects to danger are networks in which transformers are commutated together with supplying lines to remote busbars with identical cables of similar length or with a large number of cables with low total surge impedance. An estimation of the dominant oscillation frequency of the system “feeder cable – transformer” can be made analytically on the basis of the wave propagation speed, characteristic impedance and length of the cable line, and the transformer surge capacitance.

Evaluation of the winding resonant frequencies with different degrees of accuracy may be performed analytically or with the help of numerical modeling. More precise determination of the natural frequencies can be accomplished experimentally by measuring the frequency response of the winding using FRA measurement systems and subsequent determination of frequencies corresponding to maxima of the real part of the transformer primary winding input admittance.

The recognizing of the resonant frequencies associated with winding natural frequencies can be performed by measuring the frequency response of this winding at the input terminals with open and short-circuited secondary winding with subsequent identification of frequencies, at which local maxima of the real part of input admittance coincide in both cases of open and short-circuited secondary winding.

For measurement of maximum ratio of resonant overvoltages it is advisable to use FRA systems that give the picture in a wide range of frequencies. For purposes of overvoltages ratio measurement the regular measuring cables and the termination impedance of 50 Ohms should be excluded.

Any connection to intermediate points of windings leads to inclusion of additional capacitances and to an error in the obtained maximum overvoltages ratio both in frequency and in peak value. To ensure high precision, it is necessary to use connections, with the lowest possible input capacitance of the measuring circuit, for example, high-frequency measuring probes of the digital oscilloscope with an input capacitance of less than 10 pF.

The time required to reach the steady state with maximum overvoltages ratio is of the order of tens of periods of the applied voltage. If primary winding is supplied by decaying oscillating voltage the overvoltages with maximum ratio may just not have enough time to develop. To evaluate overvoltages at

individual points of windings in this case the Laplace transform may be applied to the combination of the decaying input voltage and the continuous AC solution. It constitutes a simple analytical approach.

6. REFERENCES

- [1] CIGRE Brochure 577A, "Electrical Transient Interaction between Transformers and the Power System – Part 1: Expertise", 2014.
- [2] CIGRE Brochure 577B, "Electrical Transient Interaction between Transformers and the Power System – Part 2: Case Studies", 2014.
- [3] Bjørn Gustavsen. Study of Transformer Resonant Overvoltages Caused by Cable-Transformer High-Frequency Interaction // IEEE Transactions on Power Delivery, Vol. 25, No. 2, April 2010, pp. 770–779.
- [4] V.S. Larin, D.A. Matveev, A.V. Zhuikov. Approach to analysis of resonance phenomena and overvoltages due to interaction between power transformer and external network // CIGRE SC A2 & C4 JOINT COLLOQUIUM, 8 – 14 September 2013, Zurich, Switzerland.
- [5] Power transformers. Reference book / Ed. by D.S. Lizunov, A.K. Lokhanin // Moscow: Energoatomizdat, 2004 (in Russian).
- [6] IEC 60076-18 ed. 1. Power transformers – Part 18: Measurement of frequency response.
- [7] Dolginov A.I. High-voltage engineering in electric-power industry // Moscow: Energy, 1968 (in Russian).

Bruno Jurišić
EDF R&D, France
bruno.jurismic@edf.fr

Alain Xemard
EDF R&D, France
alain.xemard@edf.fr

Philippe Guuinic
EDF R&D, France
philippe.guuinic@edf.fr

Ivo Uglešić
University of Zagreb, Croatia
ivo.uglesic@fer.hr

Françoise Paladian
Université Blaise Pascal, France
francoise.paladian@lasmea.univ-bpclermont.fr

CASE STUDY ON TRANSFORMER MODELS FOR CALCULATION OF HIGH FREQUENCY TRANSMITTED OVERVOLTAGES

SUMMARY

Events such as lightning, switching of vacuum circuit breaker or switching operations in gas insulated substation (GIS) generate high frequency overvoltages. An equipment in a transmission or a distribution system has to be protected against such phenomena.

Unfortunately, the traditional transformer models available in Electromagnetic transient simulations program (EMTP-like) software packages are not capable of representing transformer behavior in a transient state, which includes high frequencies. Moreover, high frequency transformer models are often too complex or require confidential information on transformer geometry. However, in the design stage of insulation coordination it is particularly important to accurately calculate transmitted overvoltages through transformers.

In the scope of this paper two different transformer models for high frequency, are developed in an EMTP-type software program. The first model named “Black box” derives solely from the values measured on the transformer terminals and does not require any knowledge of the transformer inner geometry. The second model named “Grey box”, is based on a lumped RLC parameters network, whose values are derived from the simple geometry of the transformer window and from the nameplate data. Furthermore, the models’ capabilities to characterize a transformer at high frequencies are analyzed. The case study is done on a distribution transformer which is to be located inside a power plant. The transmitted overvoltages calculated with the models in the EMTP-type software program are compared with measurements.

Key words: “Black box”, EMTP-type software, “Grey box”, high frequency transients, lightning, rational approximation, transformer modelling

1. INTRODUCTION

Surges, which occur in a power system, are often caused by events such as lightning. Besides the risk of failure on the high voltage side of the transformer, surges can be transmitted through the transformer and can cause failure either of the transformer itself or the components, which are located after the transformer (i.e. for instance distribution network in a power plant). Therefore, the protection of the equipment in the power system against such phenomena should be carefully investigated.

In the design stage of insulation coordination, which is usually based on electromagnetic transient simulations, transmitted overvoltages through transformers should be accurately calculated in order to have an adequate protection of the system components. Since those overvoltages include high frequency components, the traditional, low frequency transformer models cannot be used for accurate calculation of overvoltages. Therefore, it is particularly important to have a proper transformer model, accurate also for representing the high frequency transformer behavior [1].

Two different transformer models, which are able to represent transformer high frequency behavior, are developed in the EMTP-RV software program [2]. The models are derived from the information, which are usually provided to the transformer buyer's company, since the detailed inner geometry of the transformer is the property of the transformer manufacturer.

The first model named "Black box", is derived solely from the values measured on the transformer terminals and does not require any knowledge on the transformer inner geometry. The voltage ratio between the transformer's terminals voltages is measured using a frequency response analyzer; this equipment is usually used for FRA measurement [3], [4]. This approach includes the transformer's admittance matrix calculation from the measurement results, the approximation of its elements by using rational approximation, and a state space block representation in EMTP-RV software program [5], [6]. The transformer admittance matrix's elements can also be derived from scattering parameters measurement [7].

The second model is a "Grey box", based on a lumped RLC parameters network, whose values are derived from the simple geometry of the transformer window. Model parameters are calculated using analytical expressions and finite element calculation method (FEMM software program) [8]-[11].

In this paper, we propose to analyze the capabilities of a "Black box" model and a "Grey box" model to characterize a transformer at high frequencies. The case study is done on a distribution transformer which is to be located inside the power plant. Both models presented in this paper are used to represent the same transformer. The overvoltages calculated with the models in the EMTP-RV software program are compared with measurements. The comparison is done for several connections of transformer terminals in order to validate the models.

2. "BLACK BOX" MODEL PRINCIPLE

In this section, a basic approach for deriving the "Black box" model based on state space equations from measurement results is described. More precisely, a procedure for measuring the admittance (Y) matrix elements of a transformer with FRA equipment and building from these measurements a model compatible with EMTP-RV is presented.

2.1. Measurements of admittance matrix elements

The frequency response analyzer, which is used for the measurement, is only capable of measuring the ratio (H) between the input (V_{in}) and the output (V_{out}) voltages.

$$H(f) = \frac{V_{out}(f)}{V_{in}(f)} \quad (1)$$

Since the FRA measurement equipment is not normally used for measuring Y matrix, a procedure for measuring this matrix is established. This measurement procedure stems from the following expression:

$$\begin{pmatrix} I_1 \\ I_2 \\ \vdots \\ I_{N-1} \\ I_N \end{pmatrix} = \begin{pmatrix} Y_{1,1} & \cdots & Y_{1,N} \\ \vdots & \ddots & \vdots \\ Y_{N,1} & \cdots & Y_{N,N} \end{pmatrix} \begin{pmatrix} V_1 \\ V_2 \\ \vdots \\ V_{N-1} \\ V_N \end{pmatrix} \quad (2)$$

Expression (2) is valid for the transformer with N terminals. However, the transformer considered in this paper has 11 terminals: 3 terminals of HV winding (A, B, C), neutral of HV winding (N), 6 terminals of two secondary LV windings (a1, b1, c1, a2, b2, c2) and a tank (optional).

2.1.1. Off-diagonal elements

The electric circuit, which represents the frequency network analyzer connection for measuring off-diagonal Y matrix elements, is given in the figure 1. The coaxial cables are shown in blue and the flat braids are shown in red.

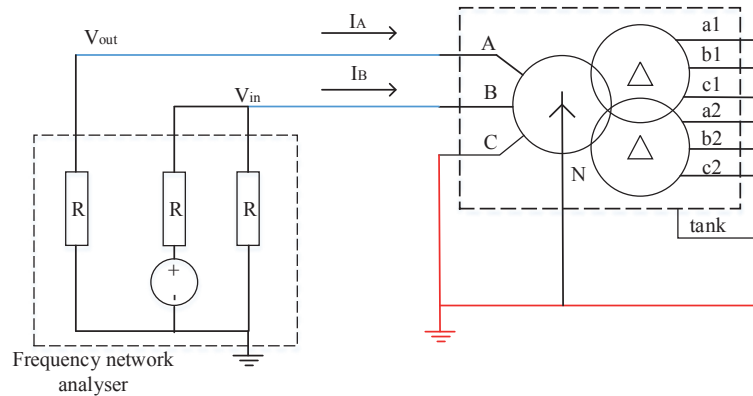


Figure 1 - Electric scheme for measuring off-diagonal Y matrix

In the equipment, which was used, the source and the reference leads use the same coaxial cable, as it is shown in the figure 1. The matching resistances (R) of frequency network analyzer terminals (source, reference and response) should be the same value as the characteristic resistance of the coaxial cables in order to avoid wave reflections (which can have some effect on the measurement results) at the connection between the network analyzer and the coaxial cables. Therefore, in our calculations we are neglecting the resistance of the coaxial cables. Furthermore, the influences of the connections which are made by straight braids are also neglected.

Note that the measurements of the reference and the response signals are made across the matching resistance of the equipment.

In the figure 1, the measurement configuration for measuring the $Y_{1,2}$ element of the admittance matrix is shown. Since all the terminals which are not under measurement are grounded, their voltages are equal to 0 V (if the effect of the flat braids is neglected). Therefore, from the equation (2), for the connection from the figure 1, the following general expression for calculating the matrix off-diagonal elements can be deduced:

$$Y_{i,j}(f) = -\frac{V_i(f)}{V_j(f)} * \left(Y_{i,i}(f) + \frac{1}{R} \right) \quad (3)$$

2.1.1. Diagonal elements

For measuring the diagonal elements of the admittance matrix, the matching resistance of the response lead is used as a shunt in order to connect the value of the current flowing through the response lead with its voltage (V_{out}). Therefore, there was no need to use an additional shunt for the measurements.

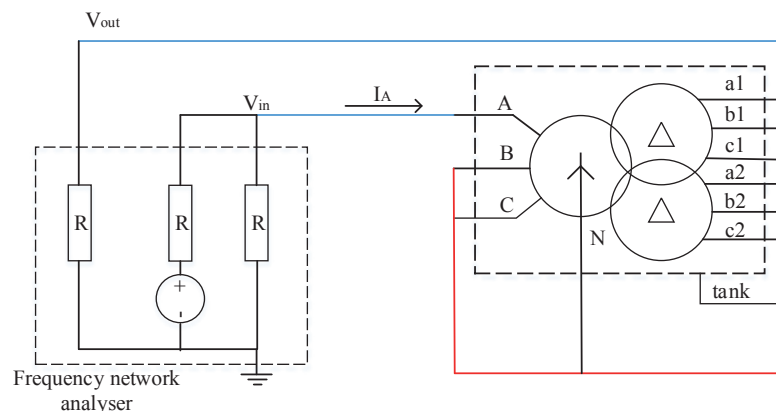


Figure 2 - Electric scheme for measuring diagonal Y matrix

Based on the connection of the figure 2, a general expression for calculating the matrix diagonal elements can be deduced:

$$Y_{i,i}(f) = \frac{I_i(f)}{(V_{in}(f) - V_{out}(f))} = \frac{V_{out}(f)}{R * (V_i(f) - V_{out}(f))} \quad (4)$$

Note that the procedure described in this section of the document is valid for a N terminal admittance matrices.

2.2. Measurements results

The measurements are done on a 64 MVA, 24/6,8/6,8 kV, YNd11d11 transformer. The matching resistance of the frequency network analyzer is 50 Ω and the accuracy better than ± 1 dB in the measurement range 0-75 dB. The frequency range of the apparatus is 20 Hz-2 MHz. The measurements are done with the tank grounded (as it is on site). Therefore, we can model the transformer as a 10 terminal system. This simplification reduces the number of measurements needed to make a model (in this case from 121 to 100), which is equivalent of almost 2 hours if we consider that the time spent per measurement for one element is approximately 5 minutes.

Measured admittance matrix elements versus frequency are shown in the figure 3. Expressions used to calculate the admittance matrix from the measurements were already given in the text (expression (3) and (4)).

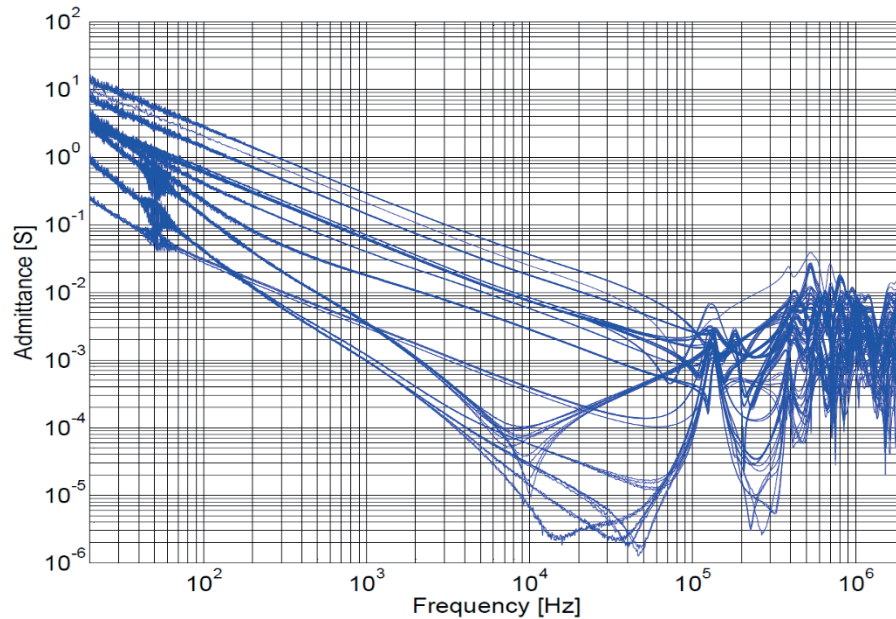


Figure 3 - $Y(f)$ amplitude for transformer with the tank grounded

Each curve shown in the figure 3 consists of the 1040 frequency points over the full frequency range of the equipment (from 20 Hz to 2 MHz). The calculated values are in accordance with the values of the measured voltage ratios, H and similar to the ones obtained in recent similar studies [7].

Noise which occurs around 50 Hz, from the figure 3, is probably caused by interferences with the power frequency of a power supply of the measurement equipment. Noise which occurs when the measurements amplitude is low is probably caused by the lack of accuracy of the measurement equipment outside its rated measurement area (0-75 dB).

2.3. Inclusion of the measurements data in EMTP-type software

Since the transformer model has to be built in an EMTP-type software program, the results of the measurement have to be prepared for the input in the computer software. This can be done by using the fitting method to approximate each admittance matrix element $Y_{ij}(f)$ with a rational expression [12]-[16] of the type given below:

$$Y_{ij}(s) \approx \sum_{n=1}^N \frac{c_{n,ij}}{s - a_{n,ij}} + d_{ij} + s * e_{ij} \quad (5)$$

In the equation (5) $a_{n,ij}$ represents the poles which can be either real or complex conjugated pair, $c_{n,ij}$ represents the residues which can also be either real or complex conjugated pair, d_{ij} and e_{ij} are the real values constant. s stands for $j2\pi f$ where f is frequency. N is number of poles used for approximating each matrix element.

These rational functions have to be both stable and passive since the transformer is a passive component of the electric grid. Stability is obtained by keeping only the poles which are stable. Passivity is enforced by perturbation of the residues and constants values in order to match the passivity criterion [17]-[20]:

$$P = \text{Re}\{v^* Y_{i,\text{fit}} v\} > 0 \quad (6)$$

Rational expression (5) allows using state space equations as shown below:

$$sX(s) = A * X(s) + B * U(s) \quad (7)$$

$$I(s) = C * X(s) + D * U(s) + sE * U(s) \quad (8)$$

Matrices A, B, C, D and E for state space representation can be input directly into the state space block in EMTP-RV. These matrices are obtained by using the values of poles and residues from rational functions (5) and forming the function given below:

$$I(s) = Y(s) * U(s) = \left[\frac{C * B}{(s[I] - A)} + D + sE \right] * U(s) \quad (9)$$

Expression (9), in which [I] is the identity matrix, can be obtained from equations (7) and (8). It represents the relation between the terminal currents and voltages of the transformer, suitable to represent the rational function given by expression (5).

If some of the matrices elements are complex (as they usually are, since some poles and residues can be complex), a transformation to real values should be done [21]. This transformation does not have any effect on the accuracy of the model. State space representation is used to describe a linear network. Therefore, it can be used to represent a transformer, since transformer behavior is linear at high frequencies. The advantage of using these equations is the straightforward conversion from the frequency (measurements) to the time domain (EMTP-type software), without changing the values of the A, B, C, D and E matrices.

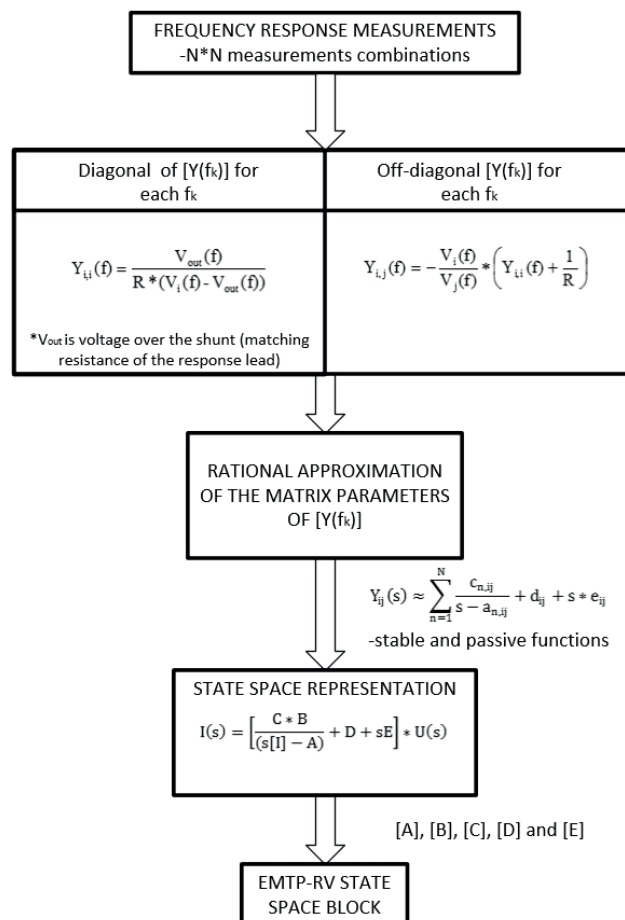


Figure 4 - Procedure for deriving the "Black box" transformer model in EMTP-RV.

The complete procedure for building the "Black box" transformer model in EMTP-RV, from the frequency response measurement is shown in the figure 4. Note that the given procedure is directly applicable for transformers with N terminals.

2.4. EMTP-RV model

As it was already indicated, the model of the transformer in EMTP-RV uses inbuilt state space block, from the standard library. The 10 terminal model of 64 MVA, distribution transformer unit, developed in EMTP-RV, is shown in the figure 5.

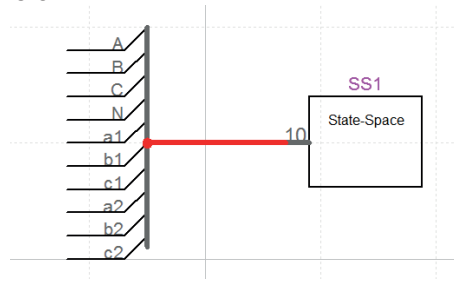


Figure 5 -10 terminal transformer model in EMTP-RV

3. THE “GREY BOX” MODEL: PRINCIPLE

A simple “Grey box” transformer model, derived from the basic geometry of the transformer window, and suitable for the calculation of transmitted overvoltages through transformer was developed.

In this section the idea of the “Grey box” RLC models is first presented. Then, the method for deriving the RLC parameters from the geometry of the transformer window is described. Model parameters are derived from the data provided by the transformer manufacturer, using analytical expressions and a finite element calculation method (FEMM software program). Furthermore, the model implementation in EMTP-RV is presented.

The model which is explained further in this paper can be called “Grey box” model, since the information required to build such a model is basic and freely accessible to the power utility. It is based on lumped RLC equivalent network [8]-[10]. Its elements values can be derived from the geometry of the transformer window and from capacitances inside the transformer, whose measurements can be requested during the transformer production process. Each RLC element represents a physical part of the transformer. The example of a RLC network which represents one phase of a two winding transformer is given below:

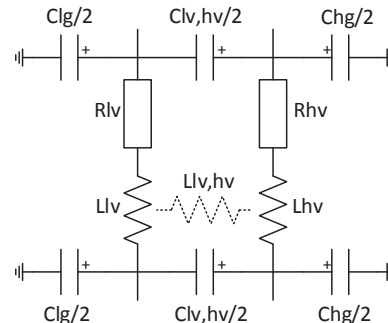


Figure 6 - RLC network for one phase of a two winding transformer

From the figure 6, it can be seen that the transformer is represented with the inductances and resistances of the windings itself, the mutual inductance, capacitance between the windings and capacitances to the ground of each winding.

3.1. Parameters calculation

3.1.1. Resistances

The values of the resistance parameters for the RLC model are usually derived from nameplate data which includes the transformer configuration and the windings resistances. Note that the variation of resistance with frequency due to the skin effect is not included.

3.1.2. Inductances

The inductances values are calculated using the magnetostatic solver in FEMM. For magnetostatic model, FEMM solver calculates magnetic potential (A) distribution from which magnetic field intensity (H) and flux density (B) can be deduced. To define a magnetostatic problem, the following input parameters should be given: complex material relative permeability in each axes direction (it can be linear or nonlinear); source current density for each material; type of lamination of the material; boundary conditions; current flowing through the windings and number of turns.

After all the parameters are set, the calculation of inductance in FEMM can be done in two different ways: by calculating the integrals of magnetic potential (A) over the windings area or from the stored magnetic energy. Since the calculation of inductance from the magnetic energy stored in the system is very time consuming due to the calculation of the integrals over the whole geometry of the model for each inductance, in this paper only the calculation of inductances from the magnetic potential is presented.

In order to represent self inductances as a function of magnetic potential, the following expression is introduced [22]:

$$L_{ii} = \frac{\int_{V_i} J_i A_i dV}{I_i^2} \quad (10)$$

, where A_i is a magnetic potential caused by the i -th winding, I_i is a current flowing through the i -th windings. J_i is the density of the current in i -th winding while V_i is the volume of the same winding.

The integral in the numerator of the expression (10) can be calculated in FEMM as an integral $A \cdot J$ over the area of winding in which current I_i is flowing while currents in all the other windings is set to 0 A.

In order to represent mutual inductances as a function of magnetic potential, the following expression is introduced:

$$L_{ij} = \frac{\int_{V_j} J_j A_i dV}{I_i I_j} = \frac{\int_{V_i} J_i A_j dV}{I_i I_j} \quad (11)$$

The integral of the numerator of the expression (11) can be rewritten into a simpler form, since $n_j = J_j \cdot a_j$, where a_j is a cross section surface of j -th winding [22]:

$$L_{ij} = \frac{\int_{V_j} J_j A_i dV}{I_i I_j} = \frac{\int_{V_j} \frac{n_j I_j}{a_j} A_i dV}{I_i I_j} = \frac{n_j \int_{V_j} A_i dV}{a_j I_i} \quad (12)$$

The integral from the equation (12) can be calculated in FEMM as an integral A (FEMM can calculate directly A/a_j) over the area of j -th winding while the current I_i is flowing through the i -th winding and generates the magnetic potential (A_i) in the system. Note that all the other currents should be set to 0 A [22].

3.1.3. Capacitances

The capacitances values can be calculated from the analytical expression or using the electrostatic solver in FEMM.

For the electrostatic model, FEMM solver calculates potential (V) distribution from which electric field intensity (E) and electrical charge density (D) can be determined. To define a problem, the following input parameters should be given: material relative electrical permittivity in each axes direction; charge density for each material; boundary conditions for each material region (fixed voltage is used); prescribed voltage or total charge in the conductor.

The capacitances are calculated in two different ways: by using the analytical expression or by using the FEMM software (from the electrostatic energy or from the charge) [22]. In this document only the capacitance calculation by using the analytical expression is presented.

Since the windings are concentrically wound around the leg of the core, the analytical expression for capacitance of cylindrical capacitors can be used for calculating the capacitance [8]:

$$C = 2\pi\epsilon_0\epsilon_r \frac{l + d}{\ln\left(\frac{R_1}{R_2}\right)} \quad (13)$$

In the expression (13), l is the height of the winding, R_1 is the outer diameter of the inner winding, R_2 is the inner diameter of outer winding and d is distance between the windings. ϵ_r from the expression (13) represents the relative permittivity of the transformer oil. Since the real value of this parameter is not known, it is assumed that it is equal to 2,2 [10]. The same value for ϵ_r is used in the calculations in FEMM.

In the numerator of the expression (13), d is added to l in order to compensate for the fringing of the fields at the ends of the cylinders [8].

3.2. EMTP-RV model

In this section the model implementation in EMTP-RV is explained and a short procedure for deriving the “Grey box” model is given. In the figure 7, below, a comparison between the electric scheme of 1-phase of the transformer model and its implementation in EMTP-RV is made.

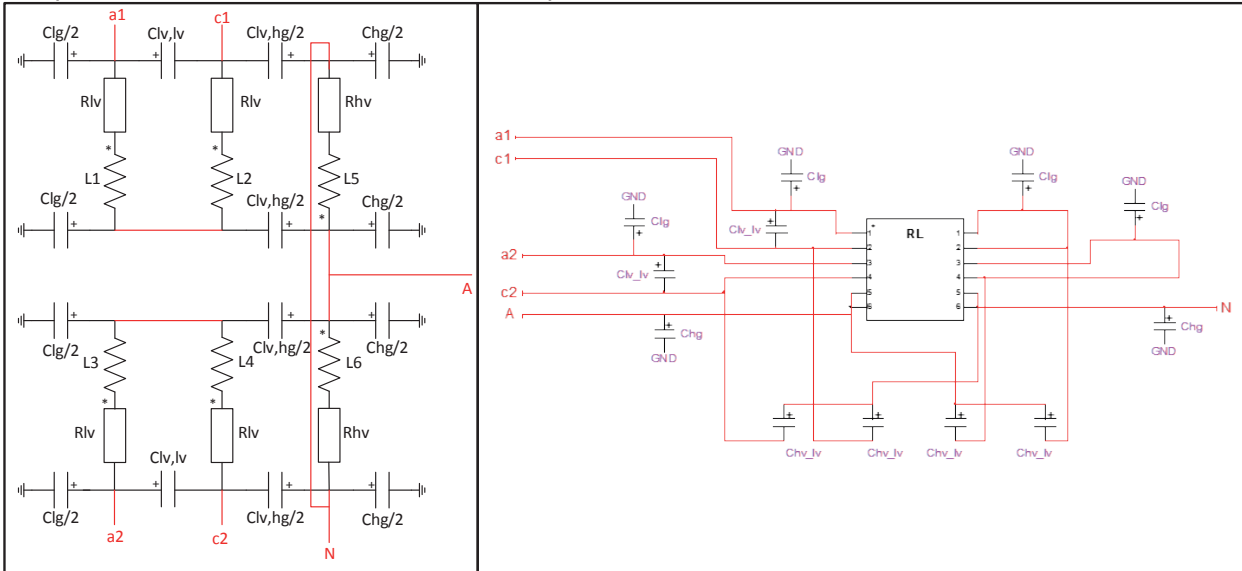


Figure 7 - The electric scheme of a 1-phase of the transformer model (left) and its implementation in EMTP-RV (right)

Note that in the electric scheme of the figure 7, the mutual inductances are not shown. Nevertheless, they exist between each part of the windings. It can also be seen that the inductance matrix together with the self-resistances of the parts of the windings are implemented in EMTP-RV with RL block. The capacitances are given in addition, outside the block.

3-phase transformer model is constructed from three 1-phase transformer models. 1-phase transformer models are connected together in YNd11d11 connection.

Besides the connections between phases, the transformation from 1-phase model to 3-phase model is straightforward if the interphases mutual inductances and capacitances are neglected, as they are in the model that has been developed. The differences between the phase inductances and capacitances, which depend on the location of each phase winding inside the transformer tank, are also neglected in the model.

The complete procedure for building the “Grey box” transformer model in EMTP-RV, from the nameplate and the simplified transformer window geometry data is shown in the figure 8.

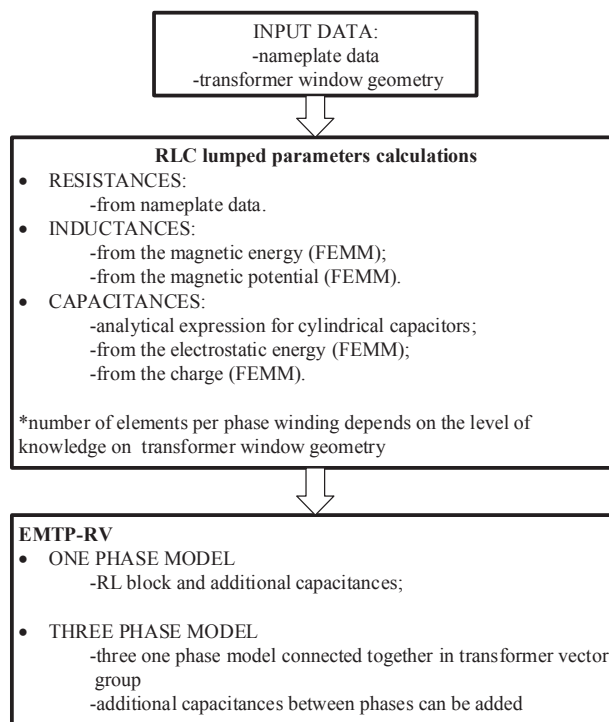


Figure 8 - Procedure for deriving the "Grey box" transformer model in EMTP-RV.

4. CASE STUDY

The transformer models we developed are tested on several configurations. In the scope of this paper, the responses of the EMTP-RV models are investigated on two different cases: lightning impulse applied on phase A and C, phase B grounded with 400 Ω resistance, neutral grounded with 1000 Ω, secondary terminals isolated (case 1); lightning impulse applied on phase A and C, phase B grounded with 400 Ω resistance, neutral grounded with 1000 Ω, secondary terminals grounded with 250 nF capacitances (case 2);

The responses of the real transformer are also measured in the laboratory, for the same cases. To investigate the models accuracy, comparisons between the maximum values of transferred overvoltages calculated with the models in EMTP-RV and those obtained by the measurements, are presented. The values are given for each phase and case.

Table 1 - Comparison between simulation and measurements results (the values are given in percentage of the amplitude of the impulse applied at the primary terminals)

		Signal shape	a1 / %	b1 / %	c1 / %	a2 / %	b2 / %	c2 / %
case 1	Measurements	1,43/55 μs	69,3	18,5	43,6	70,1	18,6	44
	„Black box“	1,2/50 μs	70,0	17,8	40,0	68,4	19,5	44,6
	„Grey box“	1,2/50 μs	71,6	26,0	38,6	71,7	26,0	38,6
case 2	Measurements	1,4/42,2 μs	13,7	-13,2	1,0	13,7	-13,0	1,1
	„Black box“	1,2/50 μs	18,8	-16,9	1,7	18,4	-17,0	1,5
	„Grey box“	1,2/50 μs	16,3	-15,5	1,1	16,4	-15,5	1,1

Note that in the case study, measurement equipment is not modelled and the signal shape of the lightning impulse is ideal 1,2/50 μs wave. During the measurements the shape of the applied wave slightly differs from the ideal, as it can be seen from the table 1. Nevertheless, the models gave accurate amplitudes of the overvoltages transferred to the secondary side. Only noticeable difference between the measurements and the simulation results can be observed for the phases b1 and b2 in the case 1. This

can be explained through the fact that no interphase mutual (capacitances and inductances) are modelled in the Grey Box model. The shapes of the transferred waves are not in the scope of this paper. They will be studied in the future.

5. CONCLUSION

In this paper the “Black box” and the “Grey box” model of the 64 MVA distribution transformer is developed in EMTP-RV. “Black box” is based on FRA measurement (done with the equipment proposed in the Standard IEC 60071-18 [3]), rational approximation and state space equations. This model is used since it requires only the data measured from the transformer terminals, which is available to the power utility. “Grey box” is based on simple RLC network whose parameters are derived from the transformer window geometry and the nameplate data.

The models we developed gave an accurate response for the calculation of the maximum values of the transmitted overvoltages for the cases observed in this document.

In the future we will strive to analyze more measurements techniques for developing the “Black box” model and to include more details in the “Grey box” model such as additional elements like regulation windings, interphase inductances and capacitances and frequency dependence of the RLC components. These advanced models should help to detect a minimum knowledge on the transformer data required to build a transformer model accurate enough for a wideband frequency range, which is the aim of the research.

6. ACKNOWLEDGMENT

The authors express their thanks to Siemens Končar Power Transformers for providing the measurement results which were used for the development and validation of the models presented in this paper.

7. REFERENCES

- [1] CIGRE Working Group A2/C4.39, “Electrical transient interaction between transformers and the power systems” (2013.)
- [2] EMTP-RV documentation – www.emtp.com. (20th February 2014.)
- [3] International Standard IEC 60076-18: “Power Transformers – Part 18: Measurement of frequency response” (First edition, 2012.)
- [4] Filipovic-Grcic, D., Filipovic-Grcic, B., Uglesic, I., “High-Frequency Model of Power Transformer Based on Frequency Response Measurements” (IEEE PES Transaction on Power Delivery, Submitted for publishing, 2013.)
- [5] Gustavsen, B., “Wide band modeling of power transformers” (IEEE Transactions on Power Delivery, vol. 19, pp. 414-422, 2004.)
- [6] Legrand, X., Xemard, A., Nucci, C.A. and Auriol, P., “A Method to Interface Electromagnetic Models of Grounding Systems with Transients Programs” (CIGRE C4 Colloquium on Power Quality and Lightning, Sarajevo, May 2012.)
- [7] Jurisic, B., Xemard, A., Uglesic, I. and Paladian, F., “High frequency transformer model for calculations of transferred overvoltages” (CIGRE International Colloquium on Lightning and Power Systems, Lyon, May 2014.)
- [8] Bjerkan, E., “High frequency modeling of power transformers,” (PhD Thesis, 2005.)
- [9] Bjerkan, E. and Hoidalén, H.K., “High frequency FEM-based power transformer modeling: Investigation of internal stresses due to network-initiated overvoltages” (IPST 2005, Montreal, Canada, June 19-23, 2005.)
- [10] Uglesic, I., “Calculating Lightning Overvoltages Transferred through a Transformer” (Proceeding of 24th International Conference on Lightning Protection, UK, September 1998.)
- [11] Meeker, D., “Finite Element Method Magnetics” – www.femm.info/wiki/HomePage (17th February 2014.)
- [12] Gustavsen, B., Semlyen, A., “Rational approximation of frequency domain responses by vector fitting” (IEEE Transactions on Power Delivery, vol.14, no.3, pp.1052-1061, 1999.)
- [13] Gustavsen, B., “Improving the Pole Relocating Properties of Vector Fitting” (IEEE Transactions on Power Delivery, vol. 21, no. 3, pp. 1587-1592, July 2006.)

- [14] Ye, Z., Li, Y., Gao, M. and Yu, Z., "A novel framework for passive macromodeling" (48th IEEE Design Automation Conference, USA, 2011.)
- [15] Ye, Z., "pmm: A Matlab Toolbox for Passive Macromodeling in RF/mm-wave Circuit Design" (IEEE 10th International Conference on ASIC, 2013.)
- [16] Deschrijver, D., Mrozowski, M., Dhaene, T. and Zutter, D. D., "Macromodeling of Multiport Systems Using a Fast Implementation of the Vector Fitting Method" (IEEE Microwave and Wireless Components Letters, vol. 18, no. 6, pp. 383-385, June 2008.)
- [17] Grivet-Talocia, S. "Passivity enforcement via perturbation of Hamiltonian matrices" (IEEE Transactions on Circuits and Systems I: Regular Papers, vol.51, no.9, pp.1755-1769, 2004.)
- [18] Gustavsen, B., Semlyen, A., "Enforcing passivity for admittance matrices approximated by rational functions" (IEEE Transactions on Power Delivery, vol. 16, no. 1, pp. 97–104, 2001.)
- [19] Semlyen, A., Gustavsen, B., "A Half-Size Singularity Test Matrix for Fast and Reliable Passivity Assessment of Rational Models" (IEEE Transactions on Power Delivery, vol. 24, no. 1, pp. 345-351, January 2009.)
- [20] Gustavsen, B., "Fast Passivity Enforcement for Pole-Residue Models by Perturbation of Residue Matrix Eigenvalues" (IEEE Transactions on Power Delivery, vol. 23, no. 4, pp. 2278-2285, October 2008.)
- [21] Gustavsen, B., Semlyen, A., "Fast Passivity Assessment for S -Parameter Rational Models Via a Half-Size Test Matrix" (IEEE Transactions on Microwave Theory and Techniques, vol.56, no.12, pp.2701-2708, 2008.)
- [22] Meeker, D., "Finite Element Method Magnetics" (User's Manual Version 4.2, 2013.)

Journal
of Energy

AN
ENERGY